Universidade de Aveiro
2024

José Pedro de Sousa Cardoso

Estudos por Espetroscopia Ótica em Heteroestruturas de III-Nitretos Modificadas por Feixe de Iões para Emissão no Verde e Vermelho

Optical Spectroscopy Studies of III-Nitrides Heterostructures Modified Using Ion Beams for Green and Red Solid-State Emitters

Universidade de Aveiro
2024

José Pedro de Sousa Cardoso

Estudos por Espetroscopia Ótica em Heteroestruturas de III-Nitretos Modificadas por Feixe de Iões para Emissão no Verde e Vermelho

Optical Spectroscopy Studies of III-Nitrides Heterostructures Modified Using Ion Beams for Green and Red Solid-State Emitters

Tese apresentada à Universidade de Aveiro para cumprimento dos requisitos necessários à obtenção do grau de Doutor em Engenharia Física, realizada sob a orientação científica da Doutora Maria do Rosário Pimenta Correia, Professora Associada do Departamento de Física da Universidade de Aveiro, e coorientação da Doutora Nabiha Ben Sedrine (Castros S. A., 4410-160 São Félix da Marinha, Portugal).

Apoio financeiro da FCT – Fundação para a Ciência e a Tecnologia através da bolsa de doutoramento DAEPHYS-FCT (PD/BD/142780/2018) comparticipada pelo Fundo Social Europeu e por fundos nacionais do MCTES. Apoio financeiro do laboratório associado i3N (UIDP/50025/2020, UIDB/50025/2020 e LA/0037/2020) comparticipado por fundos nacionais através da FCT/MCTES. Apoio financeiro através das bolsas de investigação EdtlB.18-DFis/2022_8242 e EdtlB.38-DFis/2022_30302 (projeto DEOFET – PTDC/CTM-CTM/3553/2020), comparticipadas por fundos nacionais através da FCT/MCTES.

Dedico esta tese aos meus avós e aos meus pais

o júri

Presidente

Doutor João Paulo Davim Tavares da Silva
Professor Catedrático, Universidade de Aveiro

Doutora Ana Cros Stotter
Professora Catedrática, Universidad de Valencia

Doutor Mikhail Igorevich Vasilevskiy
Professor Catedrático, Universidade do Minho

Doutor Eduardo Jorge da Costa Alves
Investigador Coordenador, Universidade de Lisboa

Doutor Luis Miguel Rino Cerveira da Silva
Professor Auxiliar, Universidade de Aveiro

Doutora Maria do Rosário Pimenta Correia
Professor Associada, Universidade de Aveiro (Orientadora)

Acknowledgment

Aproveito este espaço para agradecer a todos aqueles que me acompanharam ao longo desta aventura.

Em primeiro lugar, agradeço à minha orientadora, a Professora Doutoral Maria do Rosário Correia, por todo o conhecimento científico transmitido ao longo destes anos. Também pela amizade e companheirismo demonstrados, estando sempre lá nos bons e nos maus momentos. Estou-lhe muito grato por tudo o que fez por mim e por toda a dedicação que se sempre demonstrou. Estou certo de que não podia ter tido melhor orientadora.

Agradeço à Doutora Nabiha Ben Sedrine pela ajuda na fase inicial deste percurso.

Agradeço a todos aqueles que contribuíram e colaboraram diretamente nos trabalhos de investigação realizados ao longo desta tese. De entre todos eles, quero agradecer em especial ao Doutor Bruno Daudin, por me ter recebido tão gentilmente no seu laboratório no CEA-Grenoble por dois meses e meio, permitindo-me experienciar um ambiente totalmente diferente daquele que havia vivido, e ao Doutor Rémy Vermeersch, por me ter ensinado tanto nesse período e por estar sempre disponível para me ajudar, sem esperar nada em troca. Agradeço também à Professora Doutora Katharina Lorenz e à Professora Doutoral Teresa Monteiro pela disponibilidade e contributo essencial para esta tese.

Agradeço ao grupo de espetroscopia do i3N-UA, a todos os técnicos do Departamento de Física da UA e a todos os colegas do Departamento de Física com que me cruzei ao longo destes anos, nem que fosse para tomar um café.

Agradeço à minha família. Tentei e tentarei sempre fazer o melhor por vocês, tal como sei que o fazem por mim. Os esforços que sempre fizeram por mim não têm preço.

Agradeço à Beatriz. Sem ti não tinha chegado até ao fim desta aventura. Foste a pessoa que mais sofreu com o facto de eu estar presente e ao mesmo tempo ausente, mas estiveste sempre lá para mim e a apoiar-me nos momentos mais difíceis.

Agradeço a todos os meus amigos sem exceção.

Palavras-chave

Nitretos do Grupo III, Dispositivos Emissores de Luz, AlGaN, Nanofios, Európio, Implantação Iónica, InGaN, Poços Quânticos, Iões Pesados de Alta Energia, Irradiação iónica, Fotoluminescência, Espetroscopia Raman

Resumo

Os nitretos do grupo III (III-N) encontram-se atualmente entre os semiconductores mais importantes nas áreas da optoeletrónica e electrónica. De entre as várias aplicações que estes apresentam sobressai a utilização em díodos emissores de luz (LEDs) azul. Através do controlo da composição das ligas de AlGaN e InGaN na região ativa dos LEDs, é possível sintonizar a cor da emissão desde o ultravioleta até ao infravermelho próximo.

A realização de LEDs vermelhos, verdes e azuis (RGB) eficientes baseados em III-N é essencial para a integração monolítica (ou *quasi*-monolítica) de emissores RGB, o que deverá permitir a realização de LEDs brancos mais eficientes e uma integração mais facilitada de *displays* multi-cor à micro e à nanoescala. No entanto, a eficiência quântica externa (EQE) dos LEDs vermelhos (~10 %) e verdes (~60 %) é muito inferior à EQE dos LEDs azuis (~80-90 %), resultado da utilização de ligas de InGaN com frações molares de InN altas (>20 %). Nesta tese, foram utilizadas duas estratégias de modificação de estruturas III-N por irradiação iónica e estudadas as suas propriedades óticas e estruturais. O objetivo era avaliar a viabilidade destas estratégias para a obtenção futura de LEDs vermelhos e verdes mais eficientes.

A primeira abordagem consistiu na implantação de nanofios (NWs) de AlGaN com Eu^{3+}, procurando tirar partido da luminescência intensa e de reduzida largura de banda das transições intra-$4f^6$ para obter LEDs vermelhos mais eficientes. Este estudo pretendeu avaliar que fração molar de AlN, em nanofios de (NWs) AlGaN, dá origem a uma luminescência do Eu^{3+} mais intensa e eficiente. A partir de estudos de espetroscopia ótica, identificou-se que é na matriz de AlN NWs que essa luminescência é mais intensa e eficaz após o recozimento térmico rápido (RTA). Comparativamente ao RTA realizado a 1000 ºC, o RTA a 1200 ºC permite melhorar o desempenho da emissão vermelha destes sistemas. Partindo destes resultados, foram implantados com Eu^{3+} NWs de AlN, com junções p-n axiais, ficando demonstrada a prova de conceito de LEDs vermelhos. Embora longe da otimização, estes resultados evidenciam o potencial desta abordagem para a obtenção de emissores vermelhos à micro e à nanoescala.

A segunda abordagem estudada consistiu na irradiação de múltiplos poços de potencial (MQWs) InGaN/GaN com iões pesados de alta energia (SHIs) de ^{129}Xe com diferentes energias de feixe, com o objetivo de obter uma mistura composicional nos poços (QWI) e melhorar a eficiência dos LEDs verdes. Os resultados sugerem a ocorrência de QWI para energias de irradiação superiores a 74 MeV. No entanto, esta leva à formação de defeitos superficiais prejudiciais à emissão dos MQWs.

Em resumo, a primeira abordagem mostra potencial para a realização de LEDs vermelhos mais eficientes, enquanto a segunda não é viável tecnologicamente.

Keywords

Group III-Nitrides, Light-Emitting Devices, AlGaN, Nanowires, Europium, Ion Implantation, InGaN, Quantum Wells, Swift-Heavy Ions, Ion Irradiation, Photoluminescence, Raman Spectroscopy

Abstract

Group III-nitrides (III-N) are among the most technologically valuable semiconductors in optoelectronics and electronics, with blue light-emitting diodes (LEDs) being their most outstanding application. Indeed, by controlling the composition of ternary AlGaN and InGaN alloys in the active region of the LEDs, it is possible to tune their emission color from ultraviolet to near-infrared.

The realization of efficient III-N-based LEDs operating in the red, green, and blue (RGB) is essential for the monolithic (or *quasi*-monolithic) integration of RGB emitters, which is expected to enable the development of more efficient white LEDs and full-color displays at micro- and nano-scale. However, in contrast to the highly efficient blue LEDs based on InGaN/GaN multi-quantum well (MQW) with external quantum efficiency (EQE) of ~80–90 %, the need for high InN molar fractions causes the green and red LEDs to have much lower EQE (~60 % and ~10 %, respectively). In this thesis, two approaches involving the modification of the optical properties of III-N by ion irradiation techniques were investigated using optical spectroscopy techniques. The goal was to evaluate their viability for potential application as red and green LEDs.

The first approach involved the implantation of AlGaN nanowires (NWs) with Eu^{3+}, aiming to take advantage of their intense and atomic-like emission (intra-4f^6 transitions) to obtain red LEDs with improved efficiency and good color purity. The presented study evaluated which AlN molar fraction in AlGaN NWs' host leads to a more intense and efficient Eu^{3+}-related luminescence. From optical spectroscopy studies, it was identified that AlN NWs result in the strongest and most efficient red luminescence after post-implantation rapid thermal annealing (RTA) treatments. Compared to RTA at 1000 ºC, RTA at 1200 ºC improves the luminescence performance of these NW systems. Considering these results, AlN p-n junction NWs were implanted with Eu^{3+}, with proof-of-concept red LEDs being demonstrated. Although far from optimization, this result highlights the potential of this approach for obtaining red micro- and nano-emitters.

The second approach studied in this thesis consisted of irradiating InGaN/GaN MQWs with ^{129}Xe swift-heavy ions (SHIs) with different beam energies, aiming to achieve quantum-well intermixing (QWI) for the realization of more efficient green LEDs. The results suggested that QWI occurs for irradiation energies higher than 74 MeV. However, at the same time, the irradiation generates superficial defects detrimental to the emission of the InGaN MQWs. This compromises the technological implementation of such a strategy.

In summary, the first approach shows potential for future application as red LEDs. In contrast, the second one is not viable for realizing more efficient green LEDs.

Table of contents

List of acronyms

2D	Two-dimensional
2DEG	Two-dimensional electron gas
$\mathbf{A}^{-}$	Ionized acceptor
$\boldsymbol{A_{rad}}$	Total spontaneous emission probability
BL	Blue luminescence band
BX	Bound exciton
BZ	Brillouin zone
$\mathbf{C_N}$	Carbon in nitrogen site
CB	Conduction band
CC	Configuration coordinate
CCD	Charge-coupled device
CF	Crystal field
CH	Split-off band
CL	Cathodoluminescence
CLT	Critical layer thickness
CTS	Charge-transfer state
$\mathbf{D}^{+}$	Ionized donor
DAP	Donor-acceptor pair
DFT	Density functional theory
$\boldsymbol{E}$	Energy
$\boldsymbol{E_d}$	Threshold energy for atomic displacement
$\boldsymbol{E_F}$	Fermi energy level
$\boldsymbol{E_{gap}}$	Bandgap energy
e*-*h	Electron-hole pair
EBL	Electron blocking layer
ED	Electric dipole
EDX	Energy-dispersive X-ray spectroscopy
EL	Electroluminescence
EQE	External quantum efficiency
ET	Energy transfer

Eu_{III}	Europium in metal-III site
FWHM	Full width at half maximum
FX	Free exciton
GL	Green luminescence band
HEMT	High-electron mobility transistor
HR	High-resolution
IE	Injection efficiency
III_N	Metal-III in nitrogen site
III-N	Group III-nitrides
III-P	Group III-phosphides
IQE	Internal quantum efficiency
IR	Infrared
ITO	Indium tin oxide
I-V	Current-voltage
JO	Judd-Ofelt
LED	Light-emitting diode
LEE	Light extraction efficiency
LO	Longitudinal optical
LPP	Longitudinal phonon-plasmon
LPP^-	Lower-frequency longitudinal phonon-plasmon
LPP^+	Higher-frequency longitudinal phonon-plasmon
LVM	Local vibrational mode
MBE	Molecular beam epitaxy
MC	Monte Carlo
MD	Magnetic dipole
Mg_{Al}	Magnesium in aluminum site
Mg_{Ga}	Magnesium in gallium site
MOVPE	Metalorganic vapor phase epitaxy
MQW	Multi-quantum well
NBE	Near-band edge
N_i	Interstitial nitrogen
N_{III}	Nitrogen in metal-III site
NW	Nanowire

$\mathbf{O_N}$	Oxygen in nitrogen site
PAMBE	Plasma-assisted molecular beam epitaxy
p-DOS	Phonon density of states
PL	Photoluminescence
PLE	Photoluminescence excitation
PMT	Photomultiplier tube
QCSE	Quantum confined Stark effect
QW	Quantum-well
QWI	Quantum-well intermixing
RBS	Rutherford backscattering spectrometry
RBS/C	Channeled Rutherford backscattering spectrometry
RDA	Randomly displaced atom
RGB	Red-green-blue
$\boldsymbol{R_p}$	Penetration depth of ions in a material
RS	Rock salt
RSM	Reciprocal space maps
RT	Room-temperature
RTA	Rapid thermal annealing
$\boldsymbol{S}$	Total stopping power
$\boldsymbol{S}_\mathrm{e}$	Electronic energy losses
$\boldsymbol{S}_\mathrm{n}$	Nuclear energy losses
SEM	Scanning electron microscopy
SF	Stacking fault
SHI	Swift-heavy ion
$\mathbf{Si_{Al}}$	Silicon in aluminum site
$\mathbf{Si_{Ga}}$	Silicon in gallium site
SNR	Signal-to-noise ratio
SO	Spin-orbit
SRH	Shockley-Read-Hall
SSL	Solid-state lighting
STEM	Scanning transmission electron microscopy
$\boldsymbol{S}_\mathrm{e}^{\boldsymbol{th}}$	Electronic energy loss threshold for track formation
$\boldsymbol{T}$	Temperature

TAT	Trap-assisted tunneling
TD	Threading dislocation
TEM	Transmission electron microscopy
TO	Transverse optical
TTM-MD	Two Temperature Model – Molecular Dynamics
UHPA	Ultra-high pressure annealing
UL	Middle-ultraviolet luminescence band
UV	Ultraviolet
UVL	Near-ultraviolet luminescence
V_{bi}	Built-in potential
V_{Ga}	Gallium vacancy
V_{host}	Crystal field potential
V_{III}	Metal-III vacancy
V_{N}	Nitrogen vacancy
WZ	Wurtzite
x	Nominal InN molar fraction of an InGaN alloy
XRD	X-ray diffraction
y	Nominal AlN molar fraction of an AlGaN alloy
YL	Yellow luminescence band
ZB	Zinc blende
ZPL	Zero-phonon line
τ_{rad}	Radiative lifetime of a transition
Φ	Luminescence quantum efficiency

Preface

The journey of GaN-based light emitters has been tremendous since the breakthroughs managed by Isamu Akasaki, Hiroshi Amano, and Shunji Nakamura. High-efficiency blue light-emitting diodes (LEDs) are everywhere, with white LEDs conceivably being their standout application. However, the potential of group III-nitrides (III-N) does not extinguish in producing the blue color because, through bandgap engineering of AlGaN and InGaN alloys, their emission can be tuned from deep ultraviolet (UV) to infrared (IR). This property of III-N semiconductors enables the realization of several lighting applications capable of enhancing human well-being and productivity, such as monolithic red-green-blue (RGB) macro- and micro-scale displays, photodetectors, or UV light emitters for disinfection and water purification.

Nevertheless, the efficiency of III-N LEDs significantly decreases when approaching the green and even more the red colors, that is, with increasing the InN molar fraction of InGaN alloys. It also decreases for high current levels. The existing challenges should be overcome to realize more efficient and reliable devices. This thesis intends to study how the optical and structural properties of different III-N structures are modified through ion beams and evaluate if they are a feasible route for obtaining more efficient green and red light emitters based on III-N in the future. Two distinct approaches are considered: one involving the implantation of AlGaN nanowires (NWs) with europium ions, and the other consisting of the irradiation of InGaN/GaN multi-quantum wells (MQWs) with high-energy – above tens of MeV – heavy ions, the so-called swift-heavy ions (SHIs).

Thesis outline

The present thesis is organized into six chapters, whose content is revealed next.

Chapter 1 corresponds to the introduction and motivation of the thesis, intending to introduce the reader to III-N and their role in lighting. The potentialities of light emitters based on such semiconductors and their performance issues are reviewed, the latter being the leading force for the research conducted in this thesis. The objectives and methodology of the approaches taken in this thesis are succinctly described at the end of the chapter.

Chapter 2 presents a miscellany of physics concepts essential for understanding and discussing the results of the upcoming chapters. The first three sections present aspects related to the crystalline structure, the lattice vibrations, and the optoelectronic properties of III-N. The fourth section discusses the electrical doping of III-N and the basics of p-n

junction LEDs. The following section is dedicated to the optical doping of III-N with trivalent lanthanoid (Ln) ions, presenting the unique fundamentals behind such ions, from the free ion case to their inclusion in a crystalline host. Here, the incorporation of trivalent europium ions (Eu^{3+}) into III-N is discussed in more detail and complemented with literature results. The last section of the chapter deals with the interaction of ion beams with matter, illustrating some consequences and opportunities provided by the ion irradiation of III-N.

Chapter 3 is the first one that includes experimental results. In this, one studies the optical activation of Eu^{3+} incorporated into AlGaN NWs grown by plasma-assisted molecular beam epitaxy (PAMBE), covering the entire range of AlN molar fractions from GaN to AlN. The crystalline damage inflicted by europium implantation to the AlGaN NWs and the posterior lattice recovery accomplished by rapid thermal annealing (RTA) are investigated using micro-Raman. The optical properties of the Eu-implanted AlGaN NWs are evaluated using a combination of luminescence techniques, like photoluminescence (PL), photoluminescence excitation (PLE), and cathodoluminescence (CL).

Based on the results of **Chapter 3**, AlN NWs are a promising system to enhance the red luminescence output of Eu^{3+}. Therefore, in **Chapter 4**, AlN p-n junction NWs are implanted with europium, aiming to demonstrate proof-of-concept red LEDs. The ion implantation effects on the crystalline lattice are again assessed by micro-Raman spectroscopy; PL, PLE, and CL techniques are employed to study the optical activation of Eu^{3+}. Finally, a brief electro-optical characterization of the light-emitting devices is carried out through electroluminescence (EL) and current-voltage (I–V) characteristic measurements.

The second approach of this thesis is utterly different from the previous one, except that it uses ion beams to modify the optical properties of III-N. This approach is presented and discussed in **Chapter 5**. InGaN/GaN MQWs emitting in the green spectral region are irradiated with highly energetic ^{129}Xe ions, whose energy varied between 82 and 36 MeV. This investigation explores the possibility of achieving quantum-well intermixing (QWI) at the InGaN/GaN interfaces without a high contribution of detrimental point defects and the absence of implanted species in the active region, common in low-energy ion irradiation. The realization of QWI has been theoretically predicted to improve the efficiency of conventional InGaN-based LEDs, particularly at high current levels.

Chapter 6 presents the main conclusions of the thesis and some proposals for future work in the field.

Finally, a list of the scientific contributions and outputs generated during the thesis period is provided.

Chapter 1

Introduction

1.1. Group III-nitrides and lighting

1.1.1. Preamble on III-N semiconductors

Group III-nitrides, including AlN, GaN, InN, and respective ternary and quaternary alloys, are among today's most technologically valuable semiconductors.[a] The progress in the growth and doping control of such materials during the last 35 years, alongside their unique physical and chemical properties, contributed greatly to their industrial implementation.

Optoelectronics is perhaps the field that benefitted the most from developing III-N technology to the current state [1–6]. This is due to some notable features of wurtzite III-N semiconductors, such as the tuning of their direct bandgap from about 6.0 eV (for AlN) to 0.7 eV (for InN), at room temperature (RT), by controlling the metallic composition [7], as well as the ability to dope them both n- and p-type. The combination of such properties makes them suitable for applications such as high-brightness light-emitting devices and photodetectors from far UV to near-IR [8–12]. Indeed, the state-of-the-art LEDs operating from near UV to green are based on III-N.

Besides optoelectronics, III-N are a suitable choice for next-generation microelectronics. This is because of their high electric breakdown fields and electron mobility, which makes III-N-based high-electron mobility transistors (HEMTs) particularly suitable for high-power and high-frequency devices, like radar systems and wireless 5G communications [13,14]. Also, the physical and chemical robustness of III-N allows their operation in harsh and hostile environments, subject to considerable temperature and humidity variations or under various radiation levels, such as in space or nuclear facilities [15–17].

The initial investigations involving III-N date back to the beginning of the 20th century with the synthesis of powder samples [18–20]. However, GaN films were first grown only in

[a] The designation group III is used to refer to the atomic species of group 13 (current designation) of the Periodic Table, as terms like III-nitrides are widely adopted by the scientific community.

1969 by H. Maruska et al. on sapphire substrates using hydride vapor phase epitaxy [21]. Then, it was employed to grow AlGaN thin films [22,23]. At that point, III-N faced critical issues that hindered their technological implementation and development, such as the poor crystalline quality caused by the inexistence of adequate lattice-matched substrates, the failure to achieve p-type doping, and the unintentional n-type conductivity.

Strategies to solve the III-N problems appeared only in the late 1980s and early 1990s due to the outstanding contributions of Isamu Akasaki, Hiroshi Amano, and Shuji Nakamura. The most significant ones consisted of *i)* the growth of high-quality GaN films on sapphire substrates by metalorganic vapor phase epitaxy (MOVPE, also referred as OMVPE) through the previous deposition of a low-temperature GaN (or AlN) buffer layer to accommodate strain [24–27] and *ii)* the achievement of p-type doping of GaN activated by low-energy electron beam irradiation or thermal annealing treatments [28,29]. Such breakthroughs allowed them to achieve the first commercial high-brightness blue LEDs and laser diodes [30–33]. This revolutionary invention brought a new breath to the III-N technology and was the tipping point for LED solid-state lighting.

From then on, the allure for III-N grew exponentially, owing to the possibility of realizing more efficient lighting solutions [6]. Notably, in 2014, the relevance of I. Akasaki, H. Amano, and S. Nakamura and their contributions to science and society would come to be recognized with the attribution of the Nobel Prize in Physics *"for the invention of efficient blue LEDs, which has enabled bright and energy-saving white light sources,"* **Figure 1.1(A)** [34–36].

Figure 1.1(B) schematizes the standard structure of a blue III-N LED, which evolved from a "simple" p-n homojunction [30] to a complex heterostructure involving an active region with InGaN/GaN multi-quantum wells (MQWs) and a p-AlGaN electron blocking layer (EBL) [33,37]. **Figure 1.1(C)** shows a commercial blue III-N LED emitting.

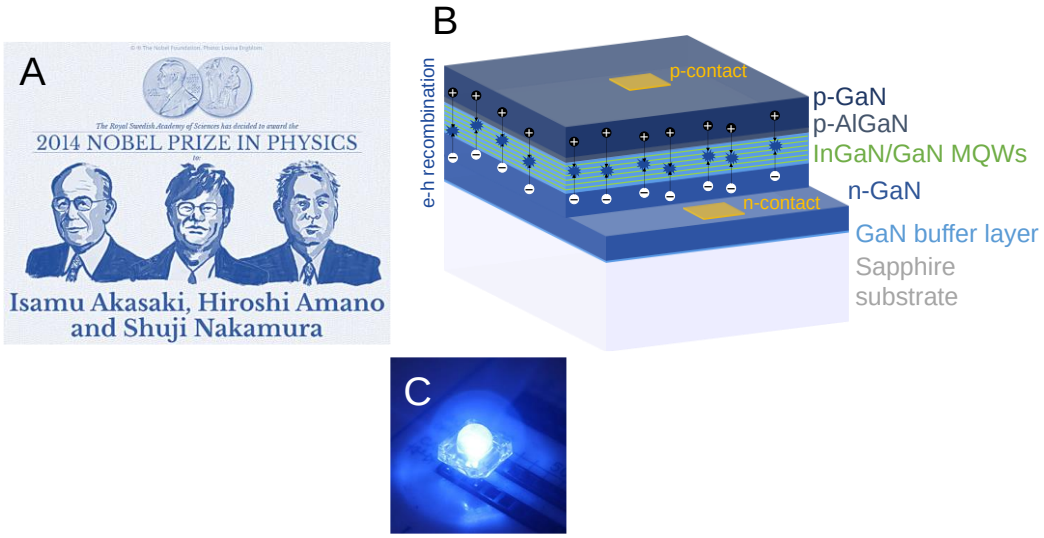

Figure 1.1 (A) 2014 Nobel Prize in Physics awarded to Isamu Akasaki, Hiroshi Amano, and Shuji Nakamura for the invention of efficient blue LEDs [34]. **(B)** Schematic structure of a typical blue III-N LED heterostructure [33,37]. The electron-hole recombination occurs in the active region (InGaN/GaN MQWs), generating blue light. **(C)** Commercial high-brightness blue III-N LED [38].

1.1.2. LED solid-state lighting

LEDs are semiconductor devices that convert electrical energy directly into light. The emitted photons result from the radiative recombination of electrons (holes) injected in the active region through the n-side (p-side) of the p-n junction when an electric voltage is applied between the two sides of the junction. The basics of p-n junctions are further discussed in **subsection 2.4.2**. The active region of an LED consists generally of MQWs, taking advantage of carrier confinement for better light-emitting properties.

Although green and red LEDs based on group III-phosphides (III-P) and group III-arsenides already existed, the realization of blue III-N LEDs was perhaps the most important milestone in solid-state lighting (SSL). The main reason was the possibility of obtaining white LEDs, which was impossible until then. It is fair to say that the breakthroughs of Akasaki, Amano, and Nakamura led to a paradigm shift in lighting, with SSL solutions emerging.

Compared with conventional white light sources (e.g., incandescent, fluorescent, or high-intensity discharge lamps), LEDs have lower power consumption and driving voltage, i.e., superior energetic performance. Therefore, and considering that lighting represents about a fifth of global electricity consumption, the implementation of SSL solutions plays a significant role in attaining the energy-efficiency goals established by the United Nations in

the 2030 Agenda and ensuring better living conditions for present and future generations [39,40].

Besides efficiency, LEDs offer advantages like long operation lifetimes (above 20000 hours), physical robustness, better-quality light output, and easier light management. They are also considered ideal for smaller and more flexible light fixtures. These properties make LEDs ideal for exploring innovative and connected lighting functionalities that promote human well-being and productivity. The cost of LED technology, which was a problem in the past, has decreased to a point where it is no longer a problem for consumers, with the current prices approaching those of fluorescent lamps.

Although LEDs are a mature technology, there is room to improve their energy efficiency [41–45]. **Figure 1.2(A)** illustrates the conventional white SSL solution, which combines a blue-emitting III-N LED with a phosphor (e.g., YAG:Ce) that absorbs part of the LED's blue light and emits in the yellow/green spectral range. The combination of the blue color of the LED with the yellow/green broad emission of the phosphor produces the white color [46]. These are called phosphor-converted white LEDs. Alternatively, white SSL emitters can be produced by mixing the light generated by LEDs emitting at different wavelengths; such LEDs are known as color-mixed white LEDs and are schematically represented in **Figure 1.2(B)**. The most common approach combines monochromatic LEDs emitting red, green, and blue (RGB) colors. In this multi-color approach, blue and green LEDs are typically based on III-N, while for the red ones, III-P are typically employed [47]. In the color-mixed approach, the various LEDs can be arranged vertically or horizontally, as displayed in the photos in **Figure 1.2(B)**.

Phosphor-converted white LEDs have a simpler structure as they avoid some complexities of the multi-color approach, such as the assembly and the different properties of the individual LED elements. Also, they are cheaper. However, in terms of efficiency, the color-mixed approach has a greater potential. Furthermore, it allows for better color control, which is beneficial and valuable for smart lighting applications [47]. The efficiency of white LEDs is usually evaluated in terms of luminous efficacy[b], which depends on each of their elements. The performance of phosphor-converted LEDs is simultaneously affected by the efficiency of the blue LED and the phosphor's energy down-conversion, while that of color-mixed white LEDs depends on the efficiency of each of the colored LEDs used.

Figure 1.2(C) shows the evolution of the luminous efficacy of phosphor-converted and color-mixed white LEDs over the years since 2005. Both approaches now outperform conventional lighting sources, and, at common operation conditions (25 ℃ and 35 $A \cdot cm^{-2}$),

[b] Luminous efficacy: ratio between luminous flux, measured in lumen (lm), and electrical power consumption, measured in watt (W). The luminous flux corresponds to the perceived optical power, that is, the optical power spectrum weighted by the human eye response.

state-of-the-art phosphor-converted LEDs have efficacies of ~190 lm · W^{-1}, which is higher than the 110 lm · W^{-1} of color-mixed LEDs. Despite this, the maximum theoretical value of the first is limited to ~255 lm · W^{-1} due to the losses inherent to the energy down-conversion process that cannot be avoided unless phosphor use is eliminated [49]. In turn, a multi-color approach enables a considerably higher maximum theoretical efficacy of ~330 lm · W^{-1}, beings usually considered ultra-efficient SSL.

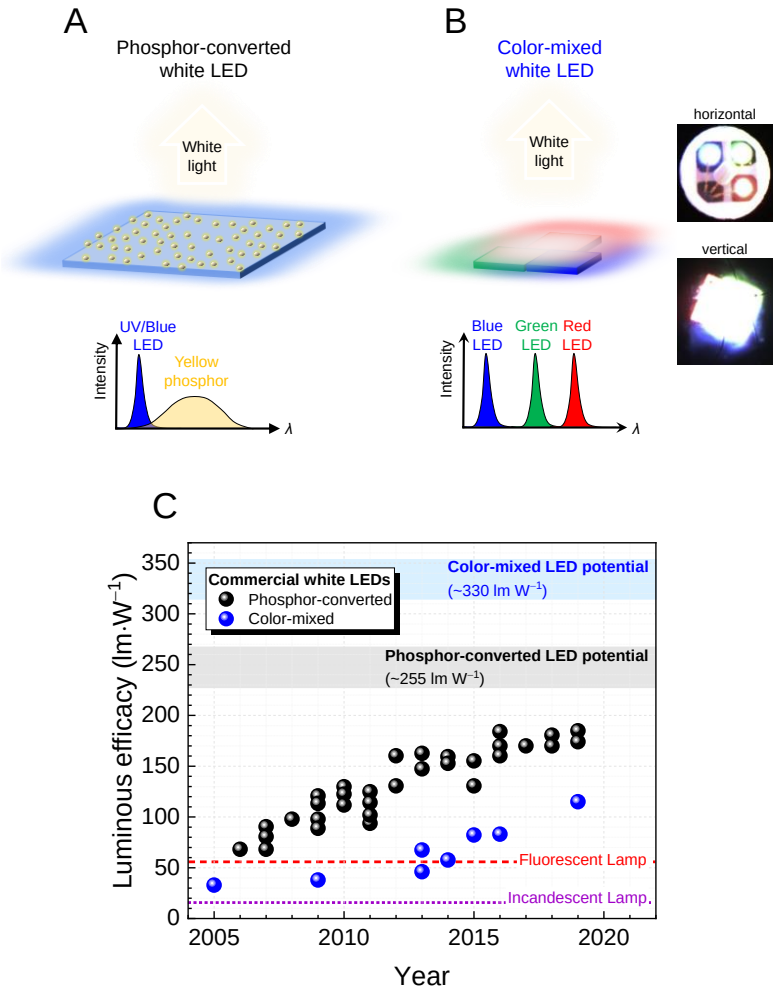

Figure 1.2 Schematic illustration of the white LEDs' structure and respective spectral shape: **(A)** phosphor-converted and **(B)** color-mixed (in the circumstance, RGB) color mixing. Photos of planar distributed and vertically-stacked RGB LEDs are also shown [48]. **(C)** Evolution of the luminous efficacy measured at 25 ℃ and 35 A · cm^{-2} over the years for different commercial white LEDs. The potential efficacy of both SSL approaches and the actual efficacy of incandescent (15 lm · W^{-1}) and fluorescent lamps (60 lm · W^{-1}) are indicated. Adapted from reference [44].

Nowadays, LEDs are widely implemented in the market. Applications such as streetlights, automotive lights, advertising and traffic signs, liquid crystal displays' backlights, and camera flashes are just a few examples [41–45]. **Figure 1.3(A)** shows an image summarizing the LED technology applications from macro to micro-scale.

Figure 1.3 (A) SSL technology applications from macro (e.g., automotive industry, large area TV panels, traffic signals, indoor/outdoor illumination) to micro-scale (e.g., micro-displays for smartwatches, smartphones, virtual/augmented reality) [56]. **(B)** 'The Wall', a micro-LED TV from Samsung [55]. **(C)** Micro-scale display from Ostendo [57].

Besides the high potential for white emitters, multi-colored LEDs allow the development of other lighting applications, such as full-color displays, sensing, and visible light communications, due to color tunability and faster response times [50,51]. Micro-LEDs[c] have attracted attention over the last few years regarding next-generation full-color displays. This relies on the fact that micro-LED displays show remarkable features that make them able to compete and predictably surpass the technologies in the market. For example, compared with liquid-crystal displays and organic LEDs, micro-LED technology can offer higher brightness, higher contrast in light environments, as well as superior resolution [51–53]. High-tech companies like Sony and Samsung have already introduced micro-LED televisions

[c] Micro-LEDs are LEDs in which the active area dimensions are below 100×100 μm^2 [51].

in the market, as represented in **Figure 1.3(B)** [54,55]. Each of the millions of micron-sized pixels that make a micro-display consists of three distinct RGB micro-LEDs individually controlled (sub-pixels). Any pixel color can be produced by adjusting the current flowing (or indirectly their color intensity) through the sub-pixels. The smaller the pixel size, the higher the resolution of the display. As a result, micro-LED technology can be used for high-tech applications, such as augmented/virtual reality displays, where high brightness and pixels with dimensions around 10 µm or below are required, **Figure 1.3(C)**. However, micro-LED applications are still expensive due to complex and costly manufacturing processes.

1.1.3. Efficiency issues of III-N LEDs

To further improve the performance of SSL solutions and fully exploit their potential, efficient monochromatic LEDs covering the visible part of the electromagnetic spectrum are required. However, this is not simple to achieve. First, the efficiency of monochromatic LEDs is not the same for different emission wavelengths, and they are usually made of different semiconductors. Second, integrating colored LEDs at the micro- and nano-scale is not easy. A monolithic approach can contribute positively due to the comparable properties of the semiconductors used, facilitating device operating conditions, as well as the possibility of growing the different LEDs in the same wafer without further complications in transferring and integrating them. III-N are the most promising and reliable group of materials to achieve it due to the possibility of tuning their direct band gap across the visible region.

When evaluating the performance of individual monochromatic LEDs, it becomes essential to consider their external quantum efficiency (EQE), the most important figure of merits. The EQE expresses the ratio of generated photons to the number of injected carriers, that is, how efficiently the device converts the injected current into light and allows it to escape from the LED. EQE can be interpreted as the product of injection efficiency (IE), internal quantum efficiency (IQE), and light extraction efficiency (LEE) [58]: $EQE = IE \times IQE \times LEE$.

IE corresponds to the fraction of injected carriers that reach the active area of the LED. IQE accounts for the radiative recombination efficiency, i.e., it quantifies the ratio of carrier recombining radiatively concerning all the recombination processes occurring in the active area. LEE defines how efficiently the generated light is extracted from the device [58]. Therefore, one can work independently to improve each of the three parameters to boost the EQE of an LED. IQE can be enhanced by growing materials with superior crystalline quality and optimizing devices' structure. At the same time, LEE can be improved by

exploring different LED geometries that favor light extraction [59,60]. The maximum theoretical EQE achievable is ~80–90 % [44].

Other relevant parameters to evaluate the performance of an LED include reliability, cost, operation lifetime, and emitting color considerations, namely color purity and color stability to the applied current and temperature [51,58,61,62].

1.1.3.1. Green and red LEDs

State-of-the-art violet and blue LEDs, the most advanced technology based on III-N, have peak EQE values of ~85 % [46], i.e., close to the theoretical maximum. Such high EQE values are even more impressive considering the high density of extended defects resulting from the growth of lattice-mismatched sapphire substrates. For example, threading dislocations (TDs) densities of ~1–5×10^8 cm^{-2}, typically obtained in III-N grown on sapphire, would substantially diminish the efficiency of devices based on other semiconductors like III-P [45,58]. The "insensitivity" of carriers to extended and point defects in III-N arises from their reduced diffusion length [45,58]. Contributing to this are the intrinsic properties of III-N and the adoption of an active area consisting of MQWs. In these InGaN/GaN MQWs, compositional fluctuations promote carrier localization and reduce their probability of being captured by defects.

The conventional way to obtain longer wavelength nitride LEDs is by increasing the indium content in the active region of InGaN MQWs, i.e., through bandgap engineering. However, the EQE gradually decreases for emission wavelengths above 450 nm, such that for green LEDs, peak EQE is below 60 % [63–65], and for red ones, it is only about 3 % [66]. Z. Bi et al. mentioned, in the book *Micro LEDs*, that the company Glō achieved red InGaN-based LEDs with peak EQE between 10–20 % by substrate engineering [51]. **Figure 1.4** shows the trend of the peak EQE of III-N LEDs, emitting in the visible part of the electromagnetic spectrum, with the emission wavelength.

The reduction of the peak EQE with the emission wavelength is mainly attributed to the difficulties concerning the growth of high-quality InGaN/GaN MQWs with high indium contents (above 20–25 %). Such complications arise from the low dissociation temperature of InN (~600 °C) and the large in-plane lattice mismatch between InN and GaN (~11 %) [47,67]. The first imposes a low growth temperature for InGaN MQWs with high InN molar fraction, leading to insufficient surface adatom migration (immiscibility of In in GaN). The second is responsible for lattice strain in the active region due to the coherent growth of InGaN MQWs on GaN barriers. These effects also promote the formation of point defects and extended defects in the material, deteriorating its crystalline quality.

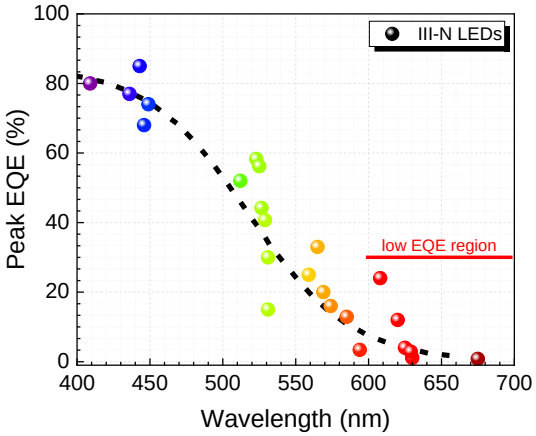

Figure 1.4 Peak EQE of III-N LEDs versus emission wavelength [51,63–66,68–72]. The dashed line is a sigmoidal function that reasonably describes the trend [68].

Defects formed in the LED structure may introduce electronic levels within the semiconductor bandgap and act as traps for carriers, promoting defect-assisted nonradiative recombination [67,73,74]. As the carriers' lifetime is inversely proportional to trap densities, a higher concentration of defects results in a higher probability of non-radiative recombination. This means that non-radiative recombination should be more pronounced for higher indium content in InGaN MQWs, for which the defects' density is expected to be higher [67,70].

Figure 1.5(A) shows the evolution of the TDs density as a function of the emission wavelength. It is possible to notice a significant increase in the concentration of TDs for emission wavelengths higher than 510 nm, i.e., where the peak EQE reduces drastically [67]. **Figure 1.5(B)** presents a transmission electron microscopy (TEM) image of an InGaN/GaN MQW structure, revealing a TD associated with the formation of an inverted pyramidal defect known as V-pit.

In addition to strain and defects, *c*-oriented InGaN/GaN MQWs experience a spontaneous polarization due to the lack of an inversion center in the wurtzite (WZ) hexagonal structure and electronegativity differences between nitrogen (3.04) and metal (Al: 1.61, Ga: 1.81, and In: 1.78) species [75]. Together with the piezoelectric polarization induced by strain, the polarization field within the active region of InGaN-based LEDs leads to a strong electric field, which can be higher than 1 $MV \cdot cm^{-1}$ [76,77]. This causes the spatial separation of electrons and holes, decreasing the carriers' wave functions overlap within the quantum well (QW); this is the well-known quantum-confined Stark effect (QCSE). With increasing the InN molar fraction in InGaN, the QCSE tends to become more severe, and consequently, the spatial separation of carriers is more significant. This reduces the spontaneous recombination rate and may also contribute to the peak EQE

reduction observed for LEDs operating in green and red [10,78]. Further discussion about this topic is provided in **subsection 2.1.3** and **sub-subsection 2.3.1.4**.

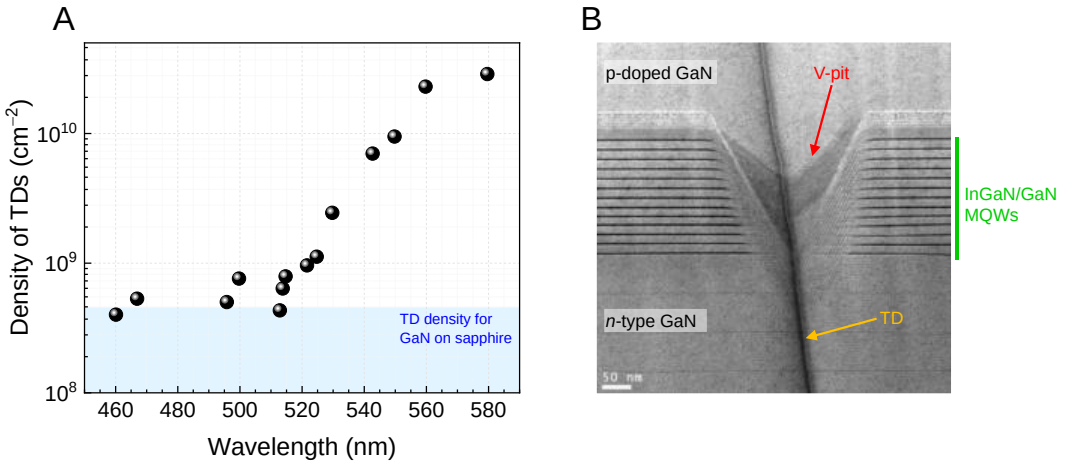

Figure 1.5 (A) Density of TDs as a function of the emission wavelength of InGaN/GaN MQWs. The density of TDs in GaN templates grown on sapphire substrates is typically 1×10^{8} to 5×10^{8} cm^{-2} [67]. **(B)** TEM image of an InGaN/GaN MQW structure, showing a TD associated with a V-pit defect (adapted from [79]).

Carrier transport along the conventional planar MQWs' structure can also impact the efficiency of green and red emitters. As the potential barrier at the InGaN/GaN interface increases with the InN molar fraction of the InGaN well, the homogeneous distribution of carriers becomes challenging. For large InN molar fractions, electrons (holes) tend to accumulate in the MQWs closer to the n-side (p-side) of the junction, reducing the spatial overlap between carriers and opposite charges [44].

III-P LEDs – the red alternative

Despite all the efforts to push up the efficiency of red III-N LEDs, they have not yet reached efficiencies comparable to those of LEDs based on III-P. State-of-the-art red LEDs (i.e., emitting wavelength above ~600 nm) have peak EQE values of ~50–70 % and are based on these materials, specifically on AlGaInP MQWs grown on GaAs substrates [68]. Such LEDs can operate in the 560–650 nm wavelength range by controlling the metal content in quaternary AlGaInP alloys.

Figure 1.6 depicts the evolution of peak EQE with the emission wavelength for III-P LEDs. As can be noticed, their efficiency decreases abruptly as the emission peak blueshifts. This droop is due to the indirect-direct band gap transition at ~540 nm [80], conditioning an efficient radiative recombination probability [81,82]. This leads to a spectral region

between 510 nm and 600 nm where neither III-P nor III-P LEDs can operate efficiently, known as the "green gap" region. Moreover, the efficiency of III-P LEDs is conditioned by the high refractive index (~3 between 560–650 nm), which makes light extraction more challenging compared to III-N LEDs [82–84].

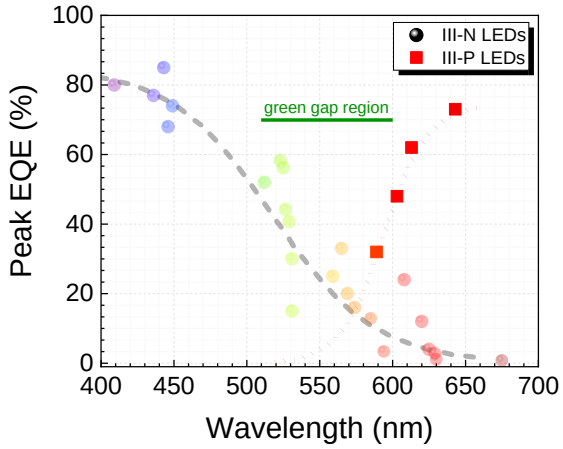

Figure 1.6 Peak EQE of III-P LEDs versus emission wavelength [68]. The dotted line corresponds to a sigmoidal function that reasonably describes the evolution. The data for III-N LEDs, already presented in Figure 1.4, is faintly plotted in the background for comparison.

1.1.3.2. Efficiency droop

Another problem of III-N LEDs is that efficiency does not remain constant with current density. This becomes particularly critical for high current densities (above 50 $A \cdot cm^{-2}$), where EQE is compromised, the so-called efficiency droop. This strongly impacts the device's performance since high current levels are required for high-brightness applications.

Figure 1.7(A) exemplifies the EQE dependence on current density for blue, green, and red III-N LEDs. As discussed previously, the peak EQE decreases with increasing the emission wavelength and occurs at low current density levels (~1–10 $A \cdot cm^{-2}$). Increasing the current density leads to a gradual decrease in EQE for all cases shown. Such a decrease becomes particularly relevant if one considers the typical operating conditions of III-N LEDs that lie at about 20–50 $A \cdot cm^{-2}$.[d] Indeed, mitigating the efficiency droop maximizes LEDs' output power while lowering the cost per lumen. Higher brightness also diminishes the number of LEDs needed to achieve a given luminous flux, minimizing the cost, weight, and size of the light sources.

[d] Note that a compromise between efficiency and output optical power is needed when defining device's operating conditions.

Figure 1.7(B) depicts the light output power density evolution with current density for blue, green, and red III-N LEDs. Although it does not provide additional information compared to the discussion above, it allows one to look at the problem from another angle. As expected, the output power increases with increasing the current flowing through the device. However, the growth trend tends to slow down at high current levels due to reduced efficiency. Furthermore, and in analogy with the efficiency results, the output power density is reduced when the emission wavelength redshifts from blue to red. For instance, at 50 $A \cdot cm^{-2}$, the output power density of blue LEDs is about four and forty times that of green and red LEDs, respectively.

Despite having a preponderant role at low current densities, nonradiative recombination at defects is not the limiting mechanism for reducing the efficiency at high current levels. The scientific community has debated this issue for years, and Auger effects have been identified as the primarily responsible mechanism for such an efficiency droop. Auger nonradiative recombination corresponds to the case in which the energy of the electron-hole pair (e–h) recombination is transferred to a third carrier (electron or hole), promoting it to a high-energy state in the electronic bands. Hence, this mechanism does not result in photon emission but in releasing energy by phonons or in the escape of high-energy carriers from the active region. As Auger recombination is a three-particle process, it tends to be more and more relevant as the carrier density increases, i.e., for high current levels, cloaking the contribution of nonradiative recombination at defects [8,10].

In addition to Auger nonradiative recombination, other effects like carrier leakage from the active region can contribute to the efficiency droop. In this process, electrons injected from the n-side cross the entire active region without recombining and escape into the p-side of the junction, where they can recombine either in radiative or nonradiative ways with the available holes. The reverse effect, i.e., holes reaching the n-side, is also possible; however, electrons escape is more likely because their mobility is higher than that of holes. Like Auger effects, this one tends to further aggravate for higher current levels. To mitigate electron leakage, a p-type AlGaN EBL is typically grown at the end of the MQWs active region (in the p-type side), as schematized previously in **Figure 1.1(B)** [10,45,60].

Potential fluctuations in the MQWs are also indirectly considered to reduce the efficiency at high carrier densities. This happens because slight changes in the growth parameters introduce fluctuations in the composition or the quantum-well width, modifying the electronic potential of the MQWs. Consequently, carriers tend to become localized at potential minima. Carrier localization implies a reduced light-emitting volume and an increased carrier density that favors high-order loss processes such as Auger recombination [10,45,58]. The combination of Auger recombination, carrier leakage, and

potential fluctuations alters the probabilities of radiative and nonradiative recombination processes, impairing LEDs' performance at high current levels.

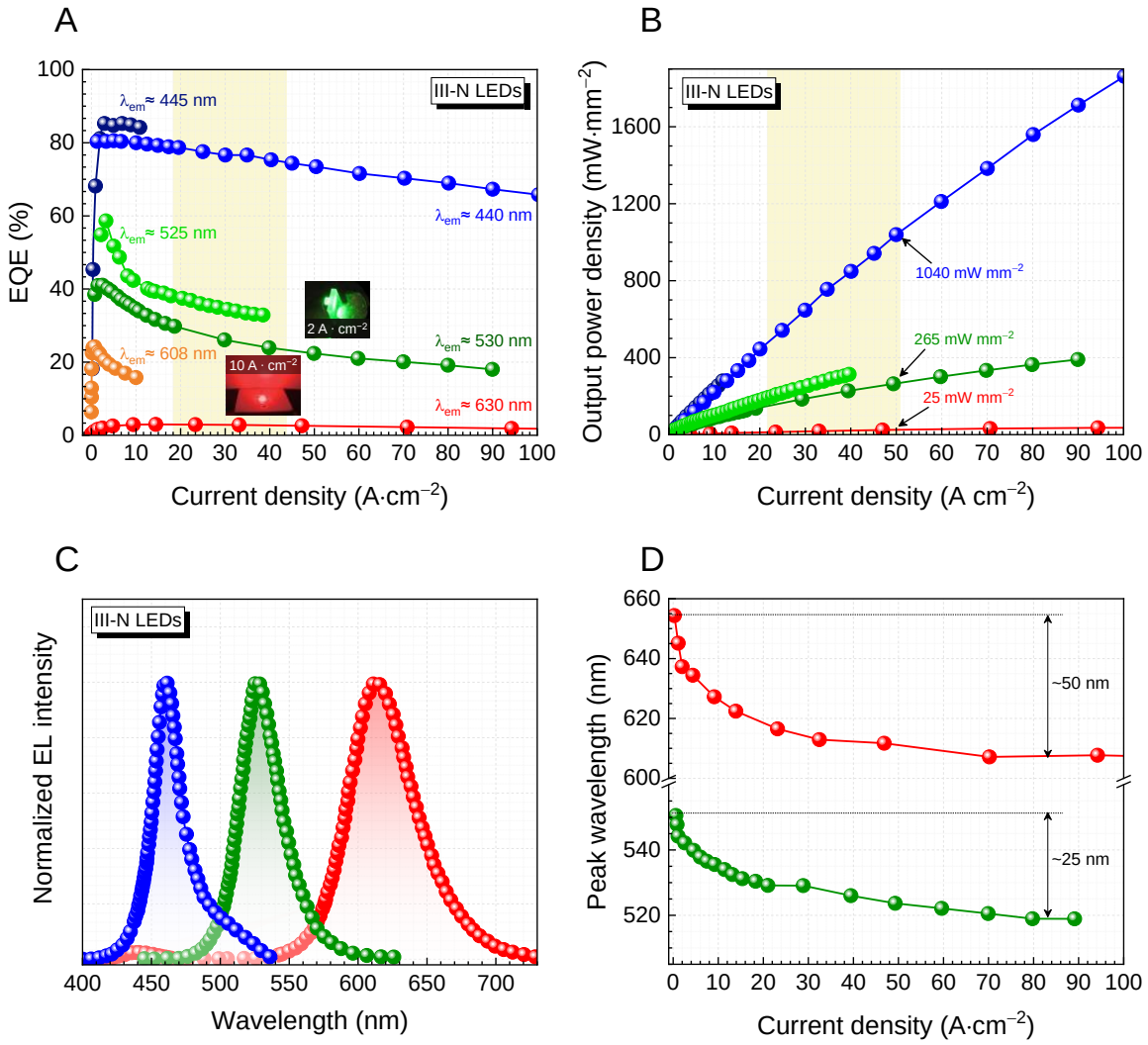

Figure 1.7 (A, B) EQE and light output power versus current density for blue, green, and red III-N LEDs [46,64–66]. The yellow region denotes the typical operation conditions of III-N LEDs. **(C)** Normalized EL spectra of blue, green, and red III-N LEDs (operating at 20 A · cm^{-2}) [46,64,66]. **(D)** Peak wavelength as a function of current density for green and red III-N LEDs [64,66].

From **Figure 1.7(A)**, it is also possible to notice that the magnitude of the EQE reduction depends on the emission wavelength. For instance, by comparing the EQE curves of blue and green III-N LEDs, the efficiency droop is more significant for the latter. Since peak EQE is significantly lower for longer wavelength emitters, the larger reduction with increasing the current density further contributes to the poorer performance of green and red III-N LEDs compared to blue ones at common operating conditions. At 50 A · cm^{-2},

efficiency is only 90 % and 50–60 % of the peak EQE values for blue and green LEDs, respectively. Considering the discussion above, this is likely due to the increased compositional fluctuations as the InN molar fraction of the QW increases, leading to a higher concentration of carriers in a reduced volume and, consequently, an enhanced Auger recombination probability.

Figure 1.7(C) shows the electroluminescence (EL) spectra of blue, green, and red III-N LEDs operating at 20 $A \cdot cm^{-2}$. For longer emission wavelengths, the full width at half maximum (FWHM) of the peak widens from ~25 nm to ~55 nm due to random alloy fluctuations, among others [85]. This poses an additional issue, particularly for red emitters, as the emission must be as narrow as possible to achieve ultra-efficient SSL solutions.

The stability of the LED emission color with the current density is another issue that must be considered in III-N technology; this particularly affects applications for which color control is required. The trend of the emission peak wavelength with the current density is shown in **Figure 1.7(D)** for green and red III-N LEDs. When the current rises, the emission peak blueshifts due to carrier de-trapping from localized states and screening of the internal electric field [86]. Like the other problems mentioned, this is also exacerbated for longer wavelength emitters. The blueshift is typically around 15 nm and 35 nm for green and red III-N LEDs as the current density increases from 1 $A \cdot cm^{-2}$ to 40 $A \cdot cm^{-2}$ [67]. For extremely high current densities above 100 $A \cdot cm^{-2}$, the EL peak might experience a slight redshift because thermal effects become dominant [8,67,86]. A thermal droop may also impact the performance of III-N LEDs at elevated temperatures, which can be obtained if the device is operated in certain hostile environments or if heat dissipation is inefficient. Device heating tends to gain importance as the current density increases. For reference, one should consider that EQE can decrease by more than 20 % for commercially available LEDs as the device temperature increases from 25 to 125 ℃ at typical operating conditions [60].

1.1.3.3. Miniaturization to micro- and nano-scale

Shrinking the LED size to the micro- and nano-scale, **Figure 1.8(A)**, poses an additional issue for the efficiency of III-N devices. Given the current technological trend of miniaturization and the key role that micro-LEDs are already beginning to play, this problem constitutes a challenge for the scientific community. In fact, mitigating the reduction in efficiency with LED downsizing has been one of the biggest challenges for III-N technology in recent years.

The traditional approach to manufacturing micro-LEDs is plasma (dry) etching of conventional large-area LED structures using proper masks defined by photolithography; consequently, the maximum achievable efficiency of micro-LEDs is limited by that of the starting devices. As a result of the etching, sidewall damage, i.e., introduction of surface

defects, is not avoided, contributing to an increase in the rate of nonradiative recombination at defects and a negative impact in EQE. The increase in perimeter-to-area ratio makes surface recombination and sidewall damage more relevant, affecting EQE as the size decreases. J. Kou et al. demonstrated numerically that the efficiency of blue III-N micro-LEDs would decrease drastically as the device size shrinks below 100 μm if surface defects are present [87]. Other authors have also demonstrated a similar behavior experimentally [88–92].

Figure 1.8(B) shows the dependence of peak EQE evolution of blue, green, and red III-N LEDs and red III-P LEDs on the lateral size. In all cases, it is possible to notice a decrease in EQE with LED downsizing due to the sidewall damage introduced during fabrication and the increased surface contribution. Looking at the EQE of blue III-N LEDs, one might note that despite their high peak of about 80 % for large-scale devices, it hardly surpasses 10 % for dimensions below 10 μm; this becomes even more critical for micro-LEDs with smaller sizes. At this point, the peak EQE of green micro-LEDs becomes comparable to or even higher than the blue ones. J. Smith et al. attributed this behavior to the smaller surface recombination velocities with increasing the InN molar fraction of InGaN due to the enhanced carrier localization caused by alloy disorder [92]. This is also the likely explanation for the peak EQE independence on lateral size for red III-N LEDs.

Red LEDs based on III-P are also not free from reduced efficiency when lateral dimensions are reduced to the micro-scale. Indeed, they suffer even more than III-N LEDs from size reduction. This happens because the nonradiative recombination processes at the surface are intensified due to the faster surface recombination velocities (for AlGaInP alloys: ~10^4–10^6 cm · s^{-1}, and for InGaN alloys: ~10^2–10^5 cm · s^{-1}) and the larger minority carrier diffusion lengths (at least one order of magnitude) compared to III-N [93,94].

Moreover, it must be added that most of the data in **Figure 1.8(B)** concern micro-LEDs subjected to surface treatments, such as sidewall passivation. These treatments partially camouflage the effects of downsizing due to the reduction of the surface damage introduced during the dry etching [51]. Sidewall passivation is accomplished by depositing SiO_2 or Al_2O_3 thin layers (thicknesses of about tens of nanometers) by atomic layer deposition. Before that, a chemical etching with KOH or KF is usually employed to remove oxygen impurities and provide a better nucleation surface [98]. Different works have demonstrated the positive impact of passivation on EQE and light emission homogeneity [51,87,88,98–100]. R. Ley et al. reported an increase in the peak EQE with LED downsizing and attributed it to enhanced backside light extraction due to a larger critical angle allowed by the lower refractive index of the surface passivation dielectric layer compared to III-N [101]. It is worth mentioning that recently, M. Sheen et al. published in *Nature* the state-of-the-art blue III-N nano-LEDs, with peak EQE as high as 20.2 %, through

a sol-gel deposited SiO_2 passivation layers in substitution to the conventional atomic layer deposition [102].

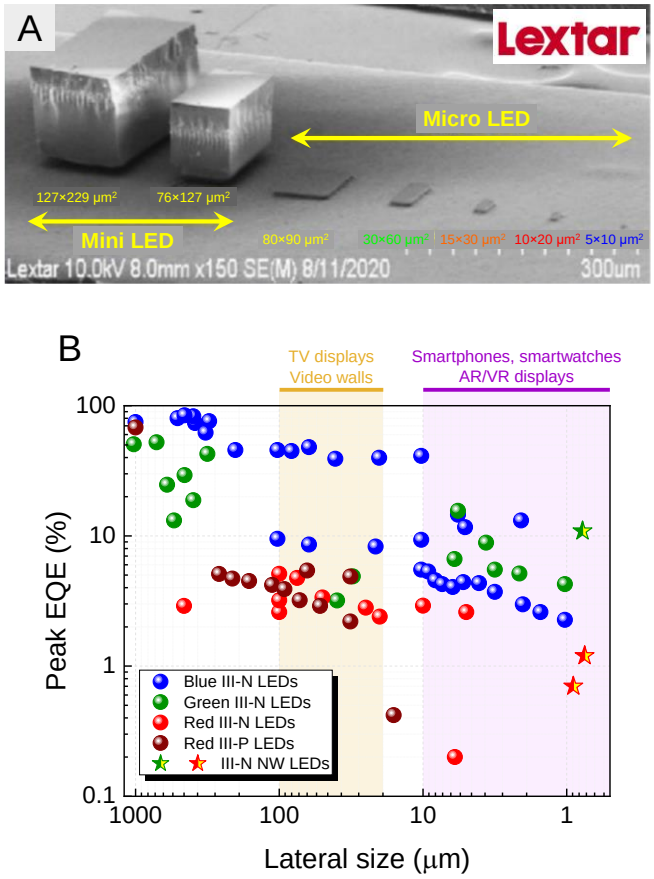

Figure 1.8 (A) Electron microscopy image of LEDs with sizes from macro- to micro-scale (reprinted from [95]). **(B)** Peak EQE evolution of blue, green, and red III-N LEDs, as well as red III-P LEDs, as a function of the lateral size (data from [92,96,97] and references within).

In contrast to III-N micro-LEDs, limited improvements were achieved by passivation for III-P micro-LEDs [103]. Consequently, for sizes below ~100 µm, red III-N micro-LEDs can compete with or surpass III-P LEDs in terms of efficiency and light output power, as observed in **Figure 1.8(B)** [104–106]. Recently, P. Li et al. reported 5×5 µm^2-sized red InGaN micro-LEDs emitting at 607 nm with a maximum EQE of 2.6 %, corresponding to the state-of-the-art red micro-LEDs [107]. From a different perspective, N-polar InGaN nanowire (NW) LEDs are also gaining much interest since there is no need to do plasma etching treatments, making their EQE virtually "independent" of LED size dimensions [96,97]. The presented results suggest that, despite there being challenges to solve, III-N are the most promising solution for obtaining quasi-monolithic RGB micro-LED displays, particularly at the micro-scale.

1.2. Thesis scope

Tackling the efficiency challenges of III-N LEDs has been a *"hot topic"* for years, particularly since the attribution of the 2014 Nobel Prize. The trend of miniaturization and the emergence of micro-LED technology has also been driving interest in obtaining green and red LEDs with better performance. Several efforts and strategies have been considered to solve the efficiency challenges of III-N LEDs, including *i)* the optimization of growth processes [64,108,109], *ii)* the re-design of the LED structure (by adding, removing, or replacing layers) [65,110–112], *iii)* the adoption of non- or semi-polar crystallographic orientations [113–118], or *iv)* the use of NW structures [96,97,119].

This thesis aims to contribute to the field by exploring two approaches that modify the luminescence characteristics of III-N through ion irradiation techniques. Ion beams have been widely used to tune these semiconductors' properties (optical, electrical, structural) according to the desired application [120–124]. The main goals of this thesis consist of studying the fundamental optical properties of the modified III-N without forgetting the additional impact that ion irradiation can introduce (e.g., crystalline damage) and evaluating the viability of such strategies for realizing future light emitters.

The two approaches studied in this thesis consist of *i)* implanting AlGaN NWs with Eu and *ii)* irradiating InGaN/GaN MQWs with swift-heavy ions (SHI). While both rely on ion irradiation, the interaction between ions and matter proceeds differently because of the distinct ions' species and energy; this topic is further discussed in **section 2.6**. Consequently, despite sharing a common goal, the motivation, the individual objectives, and the methodology used differ for the two approaches. A more detailed presentation of these two strategies is done in the following subsections.

1.2.1. Eu-implantation of AlGaN NWs

The first strategy explores the implantation of AlGaN NWs, grown by plasma-assisted molecular beam epitaxy (PAMBE), with Eu. It aims to benefit from the characteristic and atomic-like intra-4*f* luminescence of trivalent europium ions (Eu^{3+}), which in III-N hosts usually results in an intense $^5D_0 \rightarrow {}^7F_2$ transition that peaks at ~620 nm [125–128]. The research of Eu^{3+}-doped III-N for their use as light emitters is not properly groundbreaking, with several reports in this field, particularly involving GaN hosts [129–131]. Nevertheless, the recent results of the group of Professor Y. Fujiwara and collaborators, in which they demonstrated red LEDs based on Eu-doped GaN with performances as high as the conventional InGaN/GaN MQW LEDs (peak EQE of 9.2 % at 2 mA), led to a renewed interest in this approach [132–138].

In this thesis, one intends to study the role of the AlN molar fraction of AlGaN NWs on the optical activation of Eu^{3+} and evaluate if an increase in AlN molar fraction can enhance the luminescence characteristics towards the development of more efficient light emitters. Indeed, investigations on this topic are scarce and limited to two-dimensional (2D) planar AlGaN structures [139–144]; the results showed that the red luminescence intensifies with increasing the Al-composition from 0 to 0.2–0.5, decreasing after that until reaching AlN. Still, the intensity of Eu^{3+} emission in AlN hosts was higher than in GaN hosts. Furthermore, it was reported that AlGaN hosts with successively higher Al-contents lead to a lower thermal quenching of the Eu^{3+} luminescence, suggesting a potential improvement by suppressing the non-radiative de-excitation paths [139,142]

The interest also relies on the adoption of the NWs, as it allows for direct growth of AlGaN NWs (nearly free of extended defects compared to thin film technology) in lattice-mismatched substrates, such as Si substrates, providing a potentially cost-effective and scalable platform for device integration with current microtechnology [12]. As discussed above, NWs are promising for micro-LEDs since their EQE is virtually "independent" of LED size [96,97]. Moreover, the NW geometry favors the incorporation of dopants [145,146] and may lead to an increased light extraction than thin films [147,148]. Studies on doping GaN hosts with Eu^{3+} suggest that the red luminescence could be intensified in NWs compared to thin films [149–151].

Currently, most successful red LEDs based on Eu-doped III-N involve in situ doping during growth [131–138]. Notwithstanding, numerous studies demonstrated the possibility of optically activating Eu^{3+} in III-N using ion implantation [125,149–155]. As ion implantation is a non-equilibrium process, it can reach concentration levels beyond equilibrium and without precipitation [156]. Furthermore, it is a routine technique in the microelectronics industry that allows in-depth doping profile control and lateral patterning at the nano-scale using lithographically defined masks [157–159]. Nevertheless, because of the ballistic nature of the process, ion implantation results in the introduction of crystalline damage, which is an undesirable complication. Subsequent thermal annealing treatments are needed to remove implantation-induced damage and optically activate Eu^{3+} [153,156].

Despite the optical activation of the ions in Eu-implanted III-N structures, the remaining damage after annealing has been proven a limiting factor under electrical injection. Consequently, obtaining an EL response from Eu-implanted planar III-N LED structures has not been possible to date [120,126]. D. Faye et al. observed an ohmic behavior in implanted LED structures after annealing. They attributed this behavior to parasitic conducting paths forming across the diode structure, likely due to the interaction between implantation-induced defects and dislocations (inherently formed during the growth of III-N on sapphire substrates) during annealing [160]. In this sense, AlGaN NWs with high AlN

molar fractions (y) are a potential choice for obtaining red LEDs based on Eu-implanted III-N since implantation with fluences typically below 10^{15} cm^{-2} generates lower damage levels in hosts containing high Al-compositions [143,144,161,162]. Besides, GaN NWs were found to be less prone to residual implantation damage, and the formation of extended defects was suppressed compared to layered structures [151].

In the investigation provided in this thesis, $Al_yGa_{1-y}N$ NWs, with y ranging from 0 (GaN) to 1 (AlN), grown by PAMBE on GaN NW templates on Si substrates were implanted with Eu for the first time.[e] In order to assess the crystalline damage inflicted by implantation and its recovery after annealing, micro-Raman spectroscopy is used. To further look at the optical properties, photoluminescence (PL), photoluminescence excitation (PLE), and cathodoluminescence (CL) experiments are conducted.

The main goal of this study is to answer the following questions:

- What is the role of y on the optical activation of Eu^{3+}?
- Which y results in a stronger red Eu^{3+} luminescence?
- Does the adoption of the NW geometry influence the luminescence of Eu^{3+}?
- Is the annealing temperature a critical parameter to recover the implantation-induced damage and to optically activate the implanted ions?

Once the previous questions have been answered, p-n junction NWs will be grown to test the possibility of obtaining red LEDs based on Eu-implanted III-N for the first time. The chosen host will be the one that gives rise to a more intense Eu^{3+} luminescence. Initially, a structural and optical characterization like that made for Eu-implanted AlGaN NW is carried out. Next, the electro-optical performance of the devices is evaluated through EL and current-voltage (I–V) measurements; nevertheless, only initial studies are provided.

1.2.2. Irradiation of InGaN/GaN MQWs with SHIs

The second approach involves irradiating InGaN/GaN MQWs with high-energy (above tens of MeV) heavy ions, the so-called SHIs. The idea is to understand if it is possible to achieve In/Ga compositional intermixing at the InGaN/GaN interfaces and, if so, without forming detrimental defects to the luminescence. Introducing InN molar fraction gradients in the active region of InGaN/GaN MQW is expected to boost the EQE of LEDs, particularly at high current levels [85,163–165]. The explanation for this relies on reducing the QCSE and nonradiative Auger recombination probability, as well as improving the spatial overlap of electron and hole wavefunctions [163,164].

[e] From then on, for the sake of simplicity, one will refer to $Al_yGa_{1-y}N$ as AlGaN, omitting y in the nomenclature.

Since nano-scale control of the In-composition gradients is challenging during growth, post-growth treatments are usually employed, namely thermal annealing and low-energy (tens to hundreds of keV) irradiation followed by thermal annealing [166–169]. The first does not generate sufficient atomic diffusion, while in the second, the nuclear interactions generate point defects that act as nonradiative recombination centers and degrade emission efficiency; furthermore, as the penetration depth of the ion species used is reduced, a high concentration of unwanted ions reside in the active region, affecting the electrical and optical properties of the device.

SHI irradiation emerges as a possible solution to overcome the previous problems because their interaction with the matter occurs mainly through electronic interactions, and the ions penetrate the entire sample without becoming implanted in the active region [170]. Due to the intense local ionization provoked by the passage of the ions, solid-liquid-solid transitions can be induced in the material for some picoseconds, forming straight cylindrical tracks along the ion path, where atomic diffusion can occur during the molten state [171–173]. The electronic energy losses should be higher than a threshold that depends on material properties like density and specific heat capacity [174].

The study carried out in this thesis involves the structural and optical characterization of green-emitting InGaN/GaN MQWs irradiated with ^{129}Xe SHI with energies between 82 and 38 MeV. These energies correspond to electronic losses at the surface above and below the threshold values found for GaN in the literature [175–177]. The samples are characterized based on optical transmittance, micro-Raman, PL, and PLE techniques. The analysis is compared with independent channeled Rutherford backscattering spectrometry (RBS/C) experiments in order to validate the methodology adopted.

The main goal of this research is to answer the following questions:

- Is it possible to obtain quantum-well intermixing (QWI) in InGaN/GaN MQWs? If yes, what are the optimal ion beam conditions?
- How are the structural and optical properties of InGaN/GaN MQWs affected by SHI irradiation?
- Is it a viable approach for realizing more efficient III-N LEDs?

In the end, it is intended to evaluate the pertinence of this approach as a tool for obtaining QWI in InGaN/GaN MQWs for realizing more efficient green LEDs. Understanding how irradiation affects their optical and structural properties can help identify and analyze the SHI irradiation phenomena in InGaN/GaN MQWs. It can also give insight into the possibility of using III-N semiconductors for applications in harsh high-energy radiation conditions, such as nuclear facilities and space.

1.3. References

[1] S.J. Pearton et al., GaN: Processing, defects, and devices, *J. Appl. Phys.* **86** (1999) 1–78. https://doi.org/10.1063/1.371145.

[2] D. Zhu et al., Prospects of III-nitride optoelectronics grown on Si, *Reports Prog. Phys.* **76** (2013). https://doi.org/10.1088/0034-4885/76/10/106501.

[3] O. Ambacher, Growth and applications of group III-nitrides, *J. Phys. D. Appl. Phys.* **31** (1998) 2653–2710. https://doi.org/10.1088/0022-3727/31/20/001.

[4] H. Amano et al., The 2020 UV emitter roadmap, *J. Phys. D. Appl. Phys.* **53** (2020). https://doi.org/10.1088/1361-6463/aba64c.

[5] M.S. Wong et al., Review—Progress in High Performance III-Nitride Micro-Light-Emitting Diodes, *ECS J. Solid State Sci. Technol.* **9** (2020) 015012. https://doi.org/10.1149/2.0302001JSS.

[6] S. Nakamura et al., The Blue Laser Diode, 1st ed., Springer-Verlag Berlin Heidelberg, Germany, 1997.

[7] P.P. Paskov et al., Optical Properties of III-Nitride Semiconductors, in: Handb. GaN Semicond. Mater. Devices, 1st ed., CRC Press, United States, 2017: pp. 87–116.

[8] T.-Y. Seong et al., eds., III-Nitride Based Light Emitting Diodes and Applications, 2nd ed., Springer Nature Singapore Pte Ltd, Singapore, 2013.

[9] F.A. Ponce et al., Nitride-based semiconductors for blue and green light-emitting devices, *Nature.* **386** (1997) 351–359.

[10] J. Li et al., III-Nitrides Light Emitting Diodes: Technology and Applications, 1st ed., Springer Nature Singapore Pte Ltd, Singapore, 2020.

[11] S. Cuesta et al., Effect of Bias on the Response of GaN Axial p-n Junction Single-Nanowire Photodetectors, *Nano Lett.* **19** (2019) 5506–5514. https://doi.org/10.1021/acs.nanolett.9b02040.

[12] S. Zhao et al., III-Nitride nanowire optoelectronics, *Prog. Quantum Electron.* **44** (2015) 14–68. https://doi.org/10.1016/j.pquantelec.2015.11.001.

[13] F. Ren et al., eds., Wide Bandgap Semiconductor-Based Electronics, IOP Publishing, United Kingdom, 2020.

[14] M. Meneghini et al., GaN-based power devices : physics , reliability and perspectives, *J. Appl. Phys.* **130** (2021) 227. https://doi.org/10.1063/5.0061354.

[15] S.J. Pearton et al., Review of radiation damage in GaN-based materials and devices, *J. Vac. Sci. Technol. A Vacuum, Surfaces, Film.* **31** (2013) 050801. https://doi.org/10.1116/1.4799504.

[16] S.J. Pearton et al., Review—Ionizing Radiation Damage Effects on GaN Devices, *ECS J. Solid State Sci. Technol.* **5** (2016) Q35–Q60. https://doi.org/10.1149/2.0251602jss.

[17] D. Verheij et al., Radiation sensors based on GaN microwires, *J. Phys. D. Appl. Phys.* **51** (2018). https://doi.org/10.1088/1361-6463/aab636.

[18] E. Tiede et al., Über phosphorescenzfähiges, durch Silicium aktiviertes Aluminiumnitrid, *Berichte Der Dtsch. Chem. Gesellschaft (A B Ser.* **61** (1928) 1568–1573. https://doi.org/10.1002/cber.19280610721.

[19] W.C. Johnson et al., Nitrogen Compounds of Gallium. III, *J. Phys. Chem.* **36** (1932) 2651–2654. https://doi.org/10.1021/j150340a015.

[20] R. Juza et al., Über die Kristallstrukturen von Cu_3N, GaN und InN Metallamide und Metallnitride, *Zeitschrift Für Anorg. Und Allg. Chemie.* **239** (1938) 282–287.

https://doi.org/10.1002/zaac.19382390307.

[21] H.P. Maruska et al., The preparation and properties of vapor-deposited single-crystal-line GaN, *Appl. Phys. Lett.* **15** (1969) 327–329. https://doi.org/10.1063/1.1652845.

[22] W.M. Yim et al., Epitaxially grown AlN and its optical band gap, *J. Appl. Phys.* **44** (1973) 292–296. https://doi.org/10.1063/1.1661876.

[23] J. Hagen et al., Growth and properties of Ga x Al 1-x N compounds, *J. Phys. C Solid State Phys.* **11** (1978) L143–L146. https://doi.org/10.1088/0022-3719/11/4/005.

[24] H. Amano et al., Metalorganic vapor phase epitaxial growth of a high quality GaN film using an AlN buffer layer, *Appl. Phys. Lett.* **48** (1986) 353–355. https://doi.org/10.1063/1.96549.

[25] H. Amano et al., Effects of the buffer layer in metalorganic vapour phase epitaxy of GaN on sapphire substrate, *Thin Solid Films.* **163** (1988) 415–420. https://doi.org/10.1016/0040-6090(88)90458-0.

[26] S. Nakamura et al., Novel metalorganic chemical vapor deposition system for GaN growth, *Appl. Phys. Lett.* **58** (1991) 2021–2023. https://doi.org/10.1063/1.105239.

[27] S. Nakamura, GaN Growth Using GaN Buffer Layer, *Jpn. J. Appl. Phys.* **30** (1991) L1705–L1707. https://doi.org/10.1143/JJAP.30.L1705.

[28] H. Amano et al., P-type conduction in Mg-doped GaN treated with low-energy electron beam irradiation (LEEBI), *Jpn. J. Appl. Phys.* **28** (1989) L2112–L2114. https://doi.org/10.1143/JJAP.28.L2112.

[29] S. Nakamura et al., Thermal Annealing Effects on P-Type Mg-Doped GaN Films, *Jpn. J. Appl. Phys.* **31** (1992) L139–L142. https://doi.org/10.1143/JJAP.31.L139.

[30] S. Nakamura et al., High-Power GaN P-N Junction Blue-Light-Emitting Diodes, *Jpn. J. Appl. Phys.* **30** (1991) L1998–L2001. https://doi.org/10.1143/JJAP.30.L1998.

[31] S. Nakamura et al., Candela-class high-brightness InGaN/AlGaN double-heterostructure blue-light-emitting diodes, *Appl. Phys. Lett.* **64** (1994) 1687–1689. https://doi.org/10.1063/1.111832.

[32] S. Nakamura et al., High-brightness InGaN blue, green and yellow light-emitting diodes with quantum well structures, *Jpn. J. Appl. Phys.* **34** (1995) L797–L799. https://doi.org/10.1143/JJAP.34.L797.

[33] S. Nakamura et al., Continuous-wave operation of InGaN/GaN/AlGaN-based laser diodes grown on GaN substrates, *Appl. Phys. Lett.* **72** (1998) 2014–2016. https://doi.org/10.1063/1.121250.

[34] The Nobel Prize in Physics 2014, (2014). https://www.nobelprize.org/prizes/physics/2014/summary/ (accessed March 3, 2021).

[35] S. Nakamura, Nobel Lecture: Background story of the invention of efficient blue InGaN light emitting diodes, *Rev. Mod. Phys.* **87** (2015) 1139–1151. https://doi.org/10.1103/RevModPhys.87.1139.

[36] I. Akasaki, Fascinating journeys into blue light (Nobel Lecture), *Ann. Phys.* **527** (2015) 311–326. https://doi.org/10.1002/andp.201500803.

[37] M. Yamada et al., InGaN-based near-ultraviolet and blue-light-emitting diodes with high external quantum efficiency using a patterned sapphire substrate and a mesh electrode, *Jpn. J. Appl. Phys.* **41** (2002) L1431–L1433. https://doi.org/10.1143/JJAP.41.L1431.

[38] Cambridge Center for Gallium Nitride - Nitrides for the 21st Century, (n.d.). https://www.gan.msm.cam.ac.uk/projects/platform (accessed April 9, 2022).

[39] UN Environment - Global Environment Facility, Accelerating the global adoption of energy-efficient lighting, 2017. https://www.unep.org/resources/publication/accelerating-global-adoption-energy-efficient-lighting.

[40] United Nations - Take Action for the Sustainable Development Goals, (2020). https://www.un.org/sustainabledevelopment/sustainable-development-goals/ (accessed April 4, 2022).

[41] J. Li et al., eds., Light-Emitting Diodes, 1st ed., Springer International Publishing, Switzerland, 2019. https://doi.org/10.1007/978-3-319-99211-2.

[42] A. De Almeida et al., Solid state lighting review - Potential and challenges in Europe, *Renew. Sustain. Energy Rev.* **34** (2014) 30–48. https://doi.org/10.1016/j.rser.2014.02.029.

[43] P. Morgan Pattison et al., LED lighting efficacy: Status and directions, *Comptes Rendus Phys.* **19** (2018) 134–145. https://doi.org/10.1016/j.crhy.2017.10.013.

[44] M. Pattison et al., DOE BTO Lighting R&D Program, "2019 Lighting R&D Opportunities," 2020. https://www.energy.gov/sites/default/files/2020/01/f70/ssl-rd-opportunities2-jan2020.pdf.

[45] C. Weisbuch et al., The efficiency challenge of nitride light-emitting diodes for lighting, *Phys. Status Solidi Appl. Mater. Sci.* **212** (2015) 899–913. https://doi.org/10.1002/pssa.201431868.

[46] Y. Narukawa et al., White light emitting diodes with super-high luminous efficacy, *J. Phys. D. Appl. Phys.* **43** (2010). https://doi.org/10.1088/0022-3727/43/35/354002.

[47] M.H. Crawford, LEDs for solid-state lighting: Performance challenges and recent advances, *IEEE J. Sel. Top. Quantum Electron.* **15** (2009) 1028–1040. https://doi.org/10.1109/JSTQE.2009.2013476.

[48] Y.F. Cheung et al., Colour tuneable LEDs and pixelated micro-LED arrays, in: Nitride Semicond. Light. Diodes, 2nd ed., Woodhead Publishing, 2018: pp. 415–439.

[49] C.J. Humphreys, Solid-state lighting, *MRS Bull.* **33** (2008) 459–470. https://doi.org/10.1557/mrs2008.91.

[50] C.-C. Sun et al., Introduction of LED solid-state lighting, in: Opt. Des. LED Solid-State Light., 1st ed., IOP Publishing, 2022.

[51] H. Jiang et al., eds., Micro LEDs, 1st ed., Academic Press, United States, 2021.

[52] Z. Chen et al., MicroLED technologies and applications: Characteristics, fabrication, progress, and challenges, *J. Phys. D. Appl. Phys.* **54** (2021). https://doi.org/10.1088/1361-6463/abcfe4.

[53] H.X. Jiang et al., III-nitride blue microdisplays, *Appl. Phys. Lett.* **78** (2001) 1303–1305. https://doi.org/10.1063/1.1351521.

[54] Sony Develops Next-generation Display, "Crystal LED Display", Ideal for High Picture Quality on Large screens, (2012). https://www.sony.com/en/SonyInfo/News/Press/201201/12-005E/ (accessed February 22, 2022).

[55] Samsung Unveils "The Wall," the World's First Modular MicroLED 146-inch Display, (2018). https://news.samsung.com/global/samsung-unveils-the-wall-the-worlds-first-modular-microled-146-inch-tv (accessed February 22, 2022).

[56] ams-OSRAM, Light Emitting Diodes (LED), (2022). https://www.osram.asia/os/applications/application-notes/index.jsp (accessed August 15, 2022).

[57] Ostendo, (2022). https://www.ostendo.com/story (accessed September 18, 2022).

[58] C. Weisbuch, Review—On The Search for Efficient Solid State Light Emitters: Past, Present, Future, *ECS J. Solid State Sci. Technol.* **9** (2020) 016022. https://doi.org/10.1149/2.0392001JSS.

[59] J. Cho et al., Efficiency droop in light-emitting diodes: Challenges and countermeasures, *Laser Photon. Rev.* **7** (2013) 408–421. https://doi.org/10.1002/lpor.201200025.

[60] M. Meneghini et al., Thermal droop in III-nitride based light-emitting diodes: Physical origin

and perspectives, *J. Appl. Phys.* **127** (2020). https://doi.org/10.1063/5.0005874.

[61] A. David et al., LED-based white light, *Comptes Rendus Phys.* **19** (2018) 169–181. https://doi.org/10.1016/j.crhy.2018.02.004.

[62] M. Buffolo et al., Defects and Reliability of GaN-Based LEDs: Review and Perspectives, *Phys. Status Solidi Appl. Mater. Sci.* **219** (2022). https://doi.org/10.1002/pssa.202100727.

[63] Q. Lv et al., Realization of Highly Efficient InGaN Green LEDs with Sandwich-like Multiple Quantum Well Structure: Role of Enhanced Interwell Carrier Transport, *ACS Photonics.* **6** (2019) 130–138. https://doi.org/10.1021/acsphotonics.8b01040.

[64] A.I. Alhassan et al., Development of high performance green c-plane III-nitride light-emitting diodes, *Opt. Express.* **26** (2018) 5591. https://doi.org/10.1364/oe.26.005591.

[65] P. Li et al., Highly efficient InGaN green mini-size flip-chip light-emitting diodes with AlGaN insertion layer, *Nanotechnology.* **30** (2019). https://doi.org/10.1088/1361-6528/aaf656.

[66] J.-I. Hwang et al., Development of InGaN-based red LED grown on (0001) polar surface, *Appl. Phys. Express.* **7** (2014) 071003. https://doi.org/10.7567/APEX.7.071003.

[67] B. Damilano et al., Yellow-red emission from (Ga,In)N heterostructures, *J. Phys. D. Appl. Phys.* **48** (2015). https://doi.org/10.1088/0022-3727/48/40/403001.

[68] K.A. Bulashevich et al., Optimal ways of colour mixing for high-quality white-light LED sources, *Phys. Status Solidi Appl. Mater. Sci.* **212** (2015) 914–919. https://doi.org/10.1002/pssa.201431576.

[69] D. Iida et al., Recent progress in red light-emitting diodes by III-nitride materials, *Semicond. Sci. Technol.* (2021) 0–23. https://doi.org/10.1088/1361-6641/ac3962.

[70] D. Schiavon et al., Wavelength-dependent determination of the recombination rate coefficients in single-quantum-well GaInN/GaN light emitting diodes, *Phys. Status Solidi Basic Res.* **250** (2013) 283–290. https://doi.org/10.1002/pssb.201248286.

[71] S. Zhang et al., Efficient emission of InGaN-based light-emitting diodes: toward orange and red, *Photonics Res.* **8** (2020) 1671. https://doi.org/10.1364/prj.402555.

[72] A.I. Alhassan et al., High luminous efficacy green light-emitting diodes with AlGaN cap layer, *Opt. Express.* **24** (2016) 17868. https://doi.org/10.1364/oe.24.017868.

[73] D.S.P. Tanner et al., Polar (In, Ga) N / Ga N Quantum Wells: Revisiting the Impact of Carrier Localization on the "green Gap" Problem, *Phys. Rev. Appl.* **13** (2020) 1. https://doi.org/10.1103/PhysRevApplied.13.044068.

[74] M.D. McCluskey et al., Defects in Semiconductors, *J. Appl. Phys.* **127** (2020) 190401. https://doi.org/10.1063/5.0012677.

[75] The periodic table of the elements, (n.d.). webelements.com (accessed August 28, 2023).

[76] O. Ambacher et al., Pyroelectric properties of Al(In)GaN/GaN hetero- and quantum well structures, *J. Phys. Condens. Matter.* **14** (2002) 3399–3434. https://doi.org/10.1088/0953-8984/14/13/302.

[77] A. Hangleiter et al., Composition dependence of polarization fields in GaInN/GaN quantum wells, *Appl. Phys. Lett.* **83** (2003) 1169–1171. https://doi.org/10.1063/1.1601310.

[78] B. Ding, Improving radiative recombination efficiency of green light-emitting diodes, *Mater. Sci. Technol.* **34** (2018) 1615–1630. https://doi.org/10.1080/02670836.2018.1461587.

[79] C.K. Li et al., 3D numerical modeling of the carrier transport and radiative efficiency for InGaN/GaN light emitting diodes with V-shaped pits, *AIP Adv.* **6** (2016). https://doi.org/10.1063/1.4950771.

[80] S. Jungthawan et al., Direct enumeration studies of band-gap properties of AlxGa yIn1-x-yP alloys, *J. Appl. Phys.* **105** (2009). https://doi.org/10.1063/1.3153948.

[81] P. Altieri et al., Internal quantum efficiency of high-brightness AlGaInP light-emitting

devices, *J. Appl. Phys.* **98** (2005) 18–21. https://doi.org/10.1063/1.2085308.

[82] A. Yadav et al., Temperature effects on optical properties and efficiency of red AlGaInP-based light emitting diodes under high current pulse pumping, *J. Appl. Phys.* **124** (2018). https://doi.org/10.1063/1.5020266.

[83] M. Broell et al., New developments on high-efficiency infrared and InGaAlP light-emitting diodes at OSRAM Opto Semiconductors, in: K.P. Streubel et al. (Eds.), Light. Diodes Mater. Devices, Appl. Solid State Light. XVIII, 2014: p. 90030L. https://doi.org/10.1117/12.2039078.

[84] E. Ochoa-Martínez et al., Refractive indexes and extinction coefficients of n- and p-type doped GaInP, AlInP and AlGaInP for multijunction solar cells, *Sol. Energy Mater. Sol. Cells.* **174** (2018) 388–396. https://doi.org/10.1016/j.solmat.2017.09.028.

[85] M. Auf der Maur et al., Efficiency Drop in Green InGaN/GaN Light Emitting Diodes: The Role of Random Alloy Fluctuations, *Phys. Rev. Lett.* **116** (2016) 027401. https://doi.org/10.1103/PhysRevLett.116.027401.

[86] C.H. Oh et al., Current- and temperature-dependent efficiency droops in InGaN-based blue and AlGaInP-based red light-emitting diodes, *Jpn. J. Appl. Phys.* **58** (2019). https://doi.org/10.7567/1347-4065/ab09db.

[87] J. Kou et al., Impact of the surface recombination on InGaN/GaN-based blue micro-light emitting diodes, *Opt. Express.* **27** (2019) A643. https://doi.org/10.1364/oe.27.00a643.

[88] M.S. Wong et al., High efficiency of III-nitride micro-light-emitting diodes by sidewall passivation using atomic layer deposition, *Opt. Express.* **26** (2018) 21324. https://doi.org/10.1364/oe.26.021324.

[89] F. Olivier et al., Influence of size-reduction on the performances of GaN-based micro-LEDs for display application, *J. Lumin.* **191** (2017) 112–116. https://doi.org/10.1016/j.jlumin.2016.09.052.

[90] F. Olivier et al., Shockley-Read-Hall and Auger non-radiative recombination in GaN based LEDs: A size effect study, *Appl. Phys. Lett.* **111** (2017). https://doi.org/10.1063/1.4993741.

[91] S.S. Konoplev et al., From Large-Size to Micro-LEDs: Scaling Trends Revealed by Modeling, *Phys. Status Solidi Appl. Mater. Sci.* **215** (2018) 1–6. https://doi.org/10.1002/pssa.201700508.

[92] J.M. Smith et al., Comparison of size-dependent characteristics of blue and green InGaN microLEDs down to 1 μ m in diameter, *Appl. Phys. Lett.* **116** (2020). https://doi.org/10.1063/1.5144819.

[93] K.A. Bulashevich et al., Impact of surface recombination on efficiency of III-nitride light-emitting diodes, *Phys. Status Solidi - Rapid Res. Lett.* **10** (2016) 480–484. https://doi.org/10.1002/pssr.201600059.

[94] J.-T. Oh et al., Light output performance of red AlGaInP-based light emitting diodes with different chip geometries and structures, *Opt. Express.* **26** (2018) 11194. https://doi.org/10.1364/oe.26.011194.

[95] Lextar, Lextar Offerings for Automotives, 2021.

[96] X. Liu et al., N-polar InGaN nanowires: breaking the efficiency bottleneck of nano and micro LEDs, *Photonics Res.* **10** (2022) 587. https://doi.org/10.1364/prj.443165.

[97] A. Pandey et al., N-polar InGaN/GaN nanowires: overcoming the efficiency cliff of red-emitting micro-LEDs, *Photonics Res.* **10** (2022) 1107. https://doi.org/10.1364/PRJ.450465.

[98] M.S. Wong et al., Size-independent peak efficiency of III-nitride micro-light-emitting-diodes using chemical treatment and sidewall passivation, *Appl. Phys. Express.* **12** (2019) 097004. https://doi.org/10.7567/1882-0786/ab3949.

[99] P. Tian et al., Size-dependent efficiency and efficiency droop of blue InGaN micro-light

emitting diodes, *Appl. Phys. Lett.* **101** (2012). https://doi.org/10.1063/1.4769835.

[100] F. Olivier et al., Investigation and improvement of 10 μm pixel-pitch GaN-based micro-LED arrays with very high brightness, *Dig. Tech. Pap. - SID Int. Symp.* **48** (2017) 353–356. https://doi.org/10.1002/sdtp.11615.

[101] R.T. Ley et al., Revealing the importance of light extraction efficiency in InGaN/GaN microLEDs via chemical treatment and dielectric passivation, *Appl. Phys. Lett.* **116** (2020). https://doi.org/10.1063/5.0011651.

[102] M. Sheen et al., Highly efficient blue InGaN nanoscale light-emitting diodes, *Nature.* **608** (2022) 56–61. https://doi.org/10.1038/s41586-022-04933-5.

[103] R. Horng et al., Study on the effect of size on InGaN red micro-LEDs, *Sci. Rep.* **12** (2022) 1324. https://doi.org/10.1038/s41598-022-05370-0.

[104] D. Iida et al., 633-nm InGaN-based red LEDs grown on thick underlying GaN layers with reduced in-plane residual stress, *Appl. Phys. Lett.* **116** (2020). https://doi.org/10.1063/1.5142538.

[105] Z. Zhuang et al., 630-nm red InGaN micro-light-emitting diodes (<20 μm×20 μm) exceeding 1 mW/mm^2 for full-color micro-displays, *Photonics Res.* **9** (2021) 1796. https://doi.org/10.1364/PRJ.428168.

[106] M.S. Wong et al., Improved performance of AlGaInP red micro-light-emitting diodes with sidewall treatments, *Opt. Express.* **28** (2020) 5787. https://doi.org/10.1364/oe.384127.

[107] P. Li et al., Demonstration of ultra-small 5×5 μm^2 607 nm InGaN amber micro-light-emitting diodes with an external quantum efficiency over 2%, *Appl. Phys. Lett.* **120** (2022) 041102. https://doi.org/10.1063/5.0078771.

[108] D. Iida et al., Growth of GaInN by raised-pressure metalorganic vapor phase epitaxy, *Appl. Phys. Express.* **3** (2010) 2–3. https://doi.org/10.1143/APEX.3.075601.

[109] R. Hashimoto et al., High-efficiency green-yellow light-emitting diodes grown on sapphire (0001) substrates, *Phys. Status Solidi Curr. Top. Solid State Phys.* **10** (2013) 1529–1532. https://doi.org/10.1002/pssc.201300238.

[110] A. Even et al., Enhanced In incorporation in full InGaN heterostructure grown on relaxed InGaN pseudo-substrate, *Appl. Phys. Lett.* **110** (2017) 1–5. https://doi.org/10.1063/1.4989998.

[111] D.D. Koleske et al., On the increased efficiency in InGaN-based multiple quantum wells emitting at 530-590 nm with AlGaN interlayers, *J. Cryst. Growth.* **415** (2015) 57–64. https://doi.org/10.1016/j.jcrysgro.2014.12.034.

[112] W. Sun et al., Integrating AlInN interlayers into InGaN/GaN multiple quantum wells for enhanced green emission, *Appl. Phys. Lett.* **112** (2018). https://doi.org/10.1063/1.5028257.

[113] T. Wernicke et al., Indium incorporation and emission wavelength of polar, nonpolar and semipolar InGaN quantum wells, *Semicond. Sci. Technol.* **27** (2012). https://doi.org/10.1088/0268-1242/27/2/024014.

[114] Y. Zhao et al., 30-mW-class high-power and high-efficiency blue semipolar (10$\bar{1}$1) InGaN/GaN light-emitting diodes obtained by backside roughening technique, *Appl. Phys. Express.* **3** (2010) 10–12. https://doi.org/10.1143/APEX.3.102101.

[115] A.E. Romanov et al., Strain-induced polarization in wurtzite III-nitride semipolar layers, *J. Appl. Phys.* **100** (2006). https://doi.org/10.1063/1.2218385.

[116] H. Li et al., Efficient Semipolar (11-22) 550 nm Yellow/Green InGaN Light-Emitting Diodes on Low Defect Density (11-22) GaN/Sapphire Templates, *ACS Appl. Mater. Interfaces.* **9** (2017) 36417–36422. https://doi.org/10.1021/acsami.7b11718.

[117] H. Li et al., Study of efficient semipolar (11-22) InGaN green micro-light-emitting diodes on

high-quality (11-22) GaN/sapphire template, *Opt. Express.* **27** (2019) 24154. https://doi.org/10.1364/oe.27.024154.

[118] Y. Zhao et al., Toward ultimate efficiency: progress and prospects on planar and 3D nanostructured nonpolar and semipolar InGaN light-emitting diodes, *Adv. Opt. Photonics.* **10** (2018) 246. https://doi.org/10.1364/aop.10.000246.

[119] Aledia, Strategic agenda by G.Anania, (2021). https://www.aledia.com/en/news/strategic-agenda-by-g-anania (accessed April 8, 2022).

[120] K. Lorenz, Ion Implantation into Nonconventional GaN Structures, *Physics (College. Park. Md).* **4** (2022) 548–564. https://doi.org/10.3390/physics4020036.

[121] M. Sall et al., Synergy between electronic and nuclear energy losses for color center creation in AlN, *EPL (Europhysics Lett.* **102** (2013) 26002. https://doi.org/10.1209/0295-5075/102/26002.

[122] K. Lorenz et al., Enhanced red emission from praseodymium-doped GaN nanowires by defect engineering, *Acta Mater.* **61** (2013) 3278–3284. https://doi.org/10.1016/j.actamat.2013.02.016.

[123] Z. Islam et al., Heavy ion irradiation effects on GaN/AlGaN high electron mobility transistor failure at off-state, *Microelectron. Reliab.* **102** (2019). https://doi.org/10.1016/j.microrel.2019.113493.

[124] A. Kumar et al., In-situ transport and microstructural evolution in GaN Schottky diodes and epilayers exposed to swift heavy ion irradiation, *J. Appl. Phys.* **123** (2018) 1–7. https://doi.org/10.1063/1.4995491.

[125] T. Monteiro et al., Photoluminescence and lattice location of Eu and Pr implanted GaN samples, *Phys. B Condens. Matter.* **308–310** (2001) 22–25. https://doi.org/10.1016/S0921-4526(01)00656-1.

[126] N. Ben Sedrine et al., Eu-Doped AlGaN/GaN Superlattice-Based Diode Structure for Red Lighting: Excitation Mechanisms and Active Sites, *ACS Appl. Nano Mater.* **1** (2018) 3845–3858. https://doi.org/10.1021/acsanm.8b00612.

[127] A.J. Steckl et al., Multiple color capability from rare earth-doped gallium nitride, *Mater. Sci. Eng. B.* **81** (2001) 97–101. https://doi.org/10.1016/S0921-5107(00)00745-5.

[128] Y. Fujiwara et al., Present understanding of Eu luminescent centers in Eu-doped GaN grown by organometallic vapor phase epitaxy, *Jpn. J. Appl. Phys.* **53** (2014) 05FA13. https://doi.org/10.7567/JJAP.53.05FA13.

[129] J. Heikenfeld et al., Red light emission by photoluminescence and electroluminescence from Eu-doped GaN, *Appl. Phys. Lett.* **75** (1999) 1189–1191. https://doi.org/10.1063/1.124686.

[130] J. Heikenfeld et al., Low-voltage GaN:Er green electroluminescent devices, *Appl. Phys. Lett.* **76** (2000) 1365–1367. https://doi.org/10.1063/1.126033.

[131] A. Nishikawa et al., Room-Temperature Red Emission from a p-Type/Europium-Doped/n-Type Gallium Nitride Light-Emitting Diode under Current Injection, *Appl. Phys. Express.* **2** (2009) 071004. https://doi.org/10.1143/APEX.2.071004.

[132] B. Mitchell et al., Utilization of native oxygen in Eu(RE)-doped GaN for enabling device compatibility in optoelectronic applications, *Sci. Rep.* **6** (2016) 18808. https://doi.org/10.1038/srep18808.

[133] W. Zhu et al., High-Power Eu-Doped GaN Red LED Based on a Multilayer Structure Grown at Lower Temperatures by Organometallic Vapor Phase Epitaxy, *MRS Adv.* **2** (2017) 159–164. https://doi.org/10.1557/adv.2017.67.

[134] B. Mitchell et al., Perspective: Toward efficient GaN-based red light emitting diodes using europium doping, *J. Appl. Phys.* **123** (2018) 160901. https://doi.org/10.1063/1.5010762.

[135] B. Mitchell et al., Color-Tunablility in GaN LEDs Based on Atomic Emission Manipulation under Current Injection, *ACS Photonics.* **6** (2019) 1153–1161. https://doi.org/10.1021/acsphotonics.8b01461.

[136] Y. Fujiwara et al., High Brightness and RGB Integration of Eu-doped GaN-based Red LEDs for Ultrahigh-resolution Micro-LED Display, *IEICE Tech. Rep.* (2020).

[137] S. Ichikawa et al., Eu-doped GaN and InGaN monolithically stacked full-color LEDs with a wide color gamut, *Appl. Phys. Express.* **14** (2021) 031008. https://doi.org/10.35848/1882-0786/abe603.

[138] Y. Fujiwara et al., Eu-Doped GaN Red LEDs for Next-Generation Micro-LED Displays, *J. Imaging Soc. Japan.* **60** (2021) 593–605. https://doi.org/10.11370/isj.60.593.

[139] A. Wakahara, Impact of AlGaN on luminescence capability of rare-earth ions in AlGaN, *Opt. Mater. (Amst).* **28** (2006) 731–737. https://doi.org/10.1016/j.optmat.2005.09.011.

[140] T. Fujiwara et al., Photoluminescence properties of Eu-implanted $Al_xGa_{1-x}N$ ($0 \leq x \leq 1$), *Phys. Status Solidi.* **2** (2005) 2805–2808. https://doi.org/10.1002/pssc.200461431.

[141] K. Wang et al., Luminescence of Eu ions in $Al_xGa_{1-x}N$ across the entire alloy composition range, *Phys. Rev. B.* **80** (2009) 125206. https://doi.org/10.1103/PhysRevB.80.125206.

[142] A. Koizumi et al., In situ Eu doping into $Al_xGa_{1-x}N$ grown by organometallic vapor phase epitaxy to improve luminescence properties, *Opt. Mater. (Amst).* **41** (2015) 75–79. https://doi.org/10.1016/j.optmat.2014.11.005.

[143] Y. Nakanishi et al., Effects of Al composition on luminescence properties of europium implanted $Al_xGa_{1-x}N$ ($0 \leq x \leq 1$), *Phys. Status Solidi.* **96** (2003) 2623–2626. https://doi.org/10.1002/pssc.200303440.

[144] K. Lorenz et al., Structural and optical characterisation of Eu implanted $Al_xGa_{1-x}N$, *Nucl. Instruments Methods Phys. Res. Sect. B Beam Interact. with Mater. Atoms.* **257** (2007) 307–310. https://doi.org/10.1016/j.nimb.2007.01.020.

[145] A.M. Siladie et al., Dopant radial inhomogeneity in Mg-doped GaN nanowires, *Nanotechnology.* **29** (2018). https://doi.org/10.1088/1361-6528/aabbd6.

[146] Z. Fang et al., Si Donor Incorporation in GaN Nanowires, *Nano Lett.* **15** (2015) 6794–6801. https://doi.org/10.1021/acs.nanolett.5b02634.

[147] J. Chesin et al., Light extraction in individual GaN nanowires on Si for LEDs, *Nanoepitaxy Mater. Devices IV.* **8467** (2012) 846703. https://doi.org/10.1117/12.970456.

[148] J. Chesin et al., Comparing directed efficiency of III-nitride nanowire light-emitting diodes, *J. Nanophotonics.* **8** (2014) 083095. https://doi.org/10.1117/1.jnp.8.083095.

[149] J. Rodrigues et al., Spectroscopic Analysis of Eu^{3+} Implanted and Annealed GaN Layers and Nanowires, *J. Phys. Chem. C.* **119** (2015) 17954–17964. https://doi.org/10.1021/acs.jpcc.5b05101.

[150] A. Sukegawa et al., Self-Organized Eu-Doped GaN Nanocolumn Light-Emitting Diode Grown by RF-Molecular-Beam Epitaxy, *Phys. Status Solidi.* **216** (2018) 1800501. https://doi.org/10.1002/pssa.201800501.

[151] D.N. Faye et al., Incorporation of Europium into GaN Nanowires by Ion Implantation, *J. Phys. Chem. C.* **123** (2019) 11874–11887. https://doi.org/10.1021/acs.jpcc.8b12014.

[152] W.M. Jadwisienczak et al., Visible emission from AlN doped with Eu and Tb ions, *J. Appl. Phys.* **89** (2001) 4384–4390. https://doi.org/10.1063/1.1357467.

[153] K. Lorenz et al., Rare earth doping of III-nitride alloys by ion implantation, *Phys. Status Solidi.* **205** (2008) 34–37. https://doi.org/10.1002/pssa.200776714.

[154] I.S. Roqan et al., Optical and structural properties of Eu-implanted $In_xAl_{1-x}N$, *J. Appl. Phys.* **106** (2009) 1–5. https://doi.org/10.1063/1.3245386.

[155] M.A. Ebdah et al., Studies of III-nitride superlattice structures implanted with lanthanide ions, *Mater. Res. Soc. Symp. Proc.* **1111** (2009) 103–108. https://doi.org/10.1557/proc-1111-d04-12.

[156] K. O'Donnell et al., eds., Rare Earth Doped III-Nitrides for Optoelectronic and Spintronic Applications, 1st ed., Springer Netherlands, Netherlands, 2010.

[157] C. Ronning et al., Ion implantation into gallium nitride, *Phys. Rep.* **351** (2001) 349–385. https://doi.org/10.1016/S0370-1573(00)00142-3.

[158] S. Sato et al., Photoluminescence properties of implanted Praseodymium into Gallium Nitride at elevated temperatures, *Nucl. Instruments Methods Phys. Res. Sect. B Beam Interact. with Mater. Atoms.* **479** (2020) 7–12. https://doi.org/10.1016/j.nimb.2020.06.007.

[159] S. Sato et al., Optical properties of neodymium ions in nanoscale regions of gallium nitride, *Opt. Mater. Express.* **10** (2020) 2614. https://doi.org/10.1364/OME.401765.

[160] D.N. Faye et al., Study of damage formation and annealing of implanted III-nitride semiconductors for optoelectronic devices, *Nucl. Instruments Methods Phys. Res. Sect. B Beam Interact. with Mater. Atoms.* **379** (2016) 251–254. https://doi.org/10.1016/j.nimb.2016.03.028.

[161] S.O. Kucheyev et al., Structural disorder in ion-implanted $Al_xGa_{1-x}N$, *Appl. Phys. Lett.* **80** (2002) 787–789. https://doi.org/10.1063/1.1445478.

[162] D.N. Faye et al., Crystal damage analysis of implanted $Al_xGa_{1-x}N$ ($0 \le x \le 1$) by ion beam techniques, *Surf. Coatings Technol.* **355** (2018) 55–60. https://doi.org/10.1016/j.surfcoat.2018.01.020.

[163] M. Auf Der Maur et al., Band gap engineering approaches to increase InGaN/GaN LED efficiency, *Opt. Quantum Electron.* **44** (2012) 83–88. https://doi.org/10.1007/s11082-011-9536-x.

[164] K.P. O'Donnell et al., It's not easy being green: Strategies for all-nitrides, all-colour solid state lighting, *Phys. Status Solidi - Rapid Res. Lett.* **6** (2012) 49–52. https://doi.org/10.1002/pssr.201100206.

[165] S.-H. Han et al., Improvement of efficiency droop in InGaN/GaN multiple quantum well light-emitting diodes with trapezoidal wells, *J. Phys. D. Appl. Phys.* **43** (2010) 354004. https://doi.org/10.1088/0022-3727/43/35/354004.

[166] K. Lorenz et al., Quantum well intermixing and radiation effects in InGaN/GaN multi quantum wells, in: J.-I. Chyi et al. (Eds.), Proceeding SPIE - Gall. Nitride Mater. Devices XI, 2016: p. 97480L. https://doi.org/10.1117/12.2211429.

[167] M.A. Sousa et al., Luminescence studies on green emitting InGaN/GaN MQWs implanted with nitrogen, *Sci. Rep.* **5** (2015) 6–11. https://doi.org/10.1038/srep09703.

[168] C.C. Chuo et al., Interdiffusion of in and Ga in InGaN/GaN multiple quantum wells, *Appl. Phys. Lett.* **78** (2001) 314–316. https://doi.org/10.1063/1.1339991.

[169] M.D. McCluskey et al., Interdiffusion of In and Ga in InGaN quantum wells, *Appl. Phys. Lett.* **73** (1998) 1281–1283. https://doi.org/10.1063/1.122149.

[170] W.J. Weber et al., The role of electronic energy loss in ion beam modification of materials, *Curr. Opin. Solid State Mater. Sci.* **19** (2015) 1–11. https://doi.org/10.1016/j.cossms.2014.09.003.

[171] M. Lang et al., Fundamental Phenomena and Applications of Swift Heavy Ion Irradiations, in: Compr. Nucl. Mater., Elsevier, 2020: pp. 485–516. https://doi.org/10.1016/B978-0-12-803581-8.11644-3.

[172] W. Bolse, Interface modification by swift heavy ions, *Radiat. Meas.* **36** (2003) 597–603. https://doi.org/10.1016/S1350-4487(03)00208-7.

[173] M. Toulemonde et al., Thermal spike model in the electronic stopping power regime, *Radiat. Eff. Defects Solids.* **126** (1993) 201–206. https://doi.org/10.1080/10420159308219709.

[174] D.K. Avasthi et al., Swift Heavy Ions for Materials Engineering and Nanostructuring, Springer Netherlands, Dordrecht, 2011. https://doi.org/10.1007/978-94-007-1229-4.

[175] M. Sall et al., Track formation in III-N semiconductors irradiated by swift heavy ions and fullerene and re-evaluation of the inelastic thermal spike model, *J. Mater. Sci.* **50** (2015) 5214–5227. https://doi.org/10.1007/s10853-015-9069-y.

[176] F. Moisy et al., Optical bandgap and stress variations induced by the formation of latent tracks in GaN under swift heavy ion irradiation, *Nucl. Instruments Methods Phys. Res. Sect. B Beam Interact. with Mater. Atoms.* **431** (2018) 12–18. https://doi.org/10.1016/j.nimb.2018.06.014.

[177] M. Karlušić et al., Response of GaN to energetic ion irradiation: conditions for ion track formation, *J. Phys. D. Appl. Phys.* **48** (2015) 325304. https://doi.org/10.1088/0022-3727/48/32/325304.

Chapter 2

Group III-nitrides: intrinsic properties and their tailoring

2.1. Crystalline structure

III-N commonly crystallize in the hexagonal WZ structure since it is the thermodynamically stable phase at RT and atmospheric pressure. Besides, these materials can be found in cubic crystalline structures like the zinc blende (ZB) or the rocksalt (RS). The ZB phase can be stabilized by epitaxial growth on cubic substrates [1–3]. The RS structure is only possible under high-pressure growth conditions; for instance, a phase transition is observed at 16.6 GPa for AlN and at ~65 GPa for GaN [4,5]. Besides the atomic arrangement, crystallization in different phases also leads to distinct physical properties. Given that the samples studied in this thesis have hexagonal symmetry, the structure of the WZ III-N and their fundamental physical properties are further discussed below.

Figure 2.1(A) shows the hexagonal WZ structure of III-N, which is defined by two lattice parameters, a and c. It is also characterized by the ratio between the two lattice constants, c/a, which ideally is equal to $1/\sqrt{u} \approx 1.633$, with $u = 3/8$, the internal parameter that defines the metal–N bond length (in units of c).

The WZ structure belongs to the space group C_{6v}^4 ($P6_3mc$) in the Schoenflies notation (Hermann-Mauguin notation) [1]. It consists of two interpenetrating hexagonal close-packed (hcp) sublattices, one of each kind of species, where the metal atom is surrounded by four N atoms in a tetrahedral configuration and vice-versa. The sublattices are shifted by uc along the c-axis (i.e., the [0001] direction, defined according to the Miller-Bravais index system [6]).

The unit cell that can describe the entire WZ structure, also represented in **Figure 2.1(A)**, consists of four atoms (two of each kind) occupying sites with C_{3v} symmetry. In Cartesian coordinates, the basis coordinates of the unit cell atoms are $(0, 0, 0)$ and $(0.5a, a\sqrt{3}/6\,, 0.5c)$, for one atomic specie, and $(0, 0, uc)$ and $(0.5a, a\sqrt{3}/6\,, [u + 0.5]c)$, for the other. This means that the stacking sequence of the atomic planes along the c-axis is of the type AaBbAaBbAaB [1].

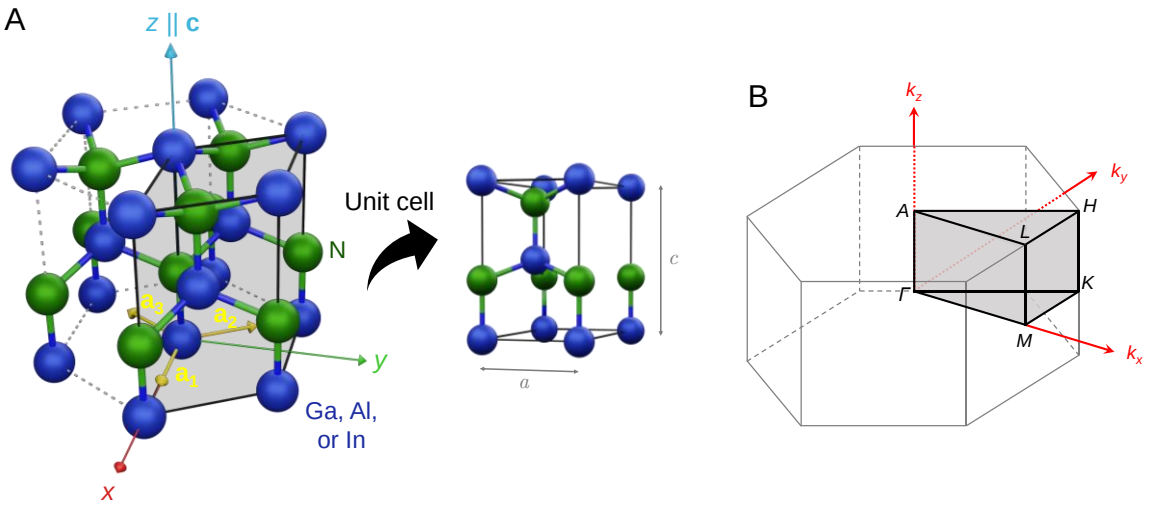

Figure 2.1 (A) WZ structure and respective unit cell. The lattice parameters a and c correspond to the edge length of the basal hexagon and the height of the hexagonal prism, respectively. **(B)** First BZ of the WZ structure. Adapted from reference [7].

Like any other crystalline structure, the WZ structure has two associated lattices: the previously described crystal lattice in the real space and the reciprocal lattice in the Fourier space (also known as reciprocal space or **k**-space). The reciprocal lattice is a mathematical construction that can be obtained by applying a Fourier transform of the direct lattice, ensuring that both have the same definite periodicity. In the reciprocal space, each point defines a specific wave vector, **k**, that describes a wave's propagation direction. The concept of reciprocal lattice is particularly relevant in solid-state physics since the periodicity of the crystal creates an ideal solution for Fourier analysis [8].

Figure 2.1(B) depicts the first Brillouin zone (BZ) of the WZ structure, which can be interpreted as the Wigner-Seitz primitive cell in the **k**-space. The corresponding BZ has the shape of a hexagonal prism with height $2\pi/c$. The Γ point, located at the center of the BZ ($\mathbf{k} = 0$), defines the highest symmetry point in the crystalline lattice. Other high symmetry points can be defined at the BZ boundaries: A with coordinates $(0, 0, \pi/c)$, L with coordinates $(2\pi/a)(1/\sqrt{3}, 0, a/2c)$, M with coordinates $(2\pi/a)(1/\sqrt{3}, 0, 0)$, H with coordinates $(2\pi/a)(1/\sqrt{3}, 1/3, a/2c)$, and K with coordinates $(2\pi/a)(1/\sqrt{3}, 1/3, 0)$. These points provide convenient reference points for analyzing the electronic band structure and other properties of crystals [7].

Table 2.1 presents the experimental observed structural parameters, including the lattice constants a and c, as well as the c/a ratio and the internal parameter u, for AlN, GaN, and InN semiconductors in the WZ phase. It includes other relevant parameters like

thermal expansion coefficients (α_c and α_a), thermal conductivity (κ), density (ρ), and atomic density (N_{at}).

Table 2.1 Relevant physical properties of AlN, GaN, and InN grown in the WZ phase and for the most common substrates. Data was taken from reference [1].

		AlN	**GaN**	**InN**	**α-Al_2O_3**	**6H-SiC**	**Si**
a	(Å)	3.110	3.199	3.585	4.758	3.0817	5.4301
c	(Å)	4.994	5.226	5.801	12.991	15.1123	
c/a		1.606	1.634	1.618			
u		0.382	0.377	0.379			
α_a ($\times 10^{-6}$)	K^{-1}	4.2	5.59	3.8	7.5	4.46	3.59
α_c ($\times 10^{-6}$)	K^{-1}	5.3	3.17	2.9	8.5	4.16	
κ	($W \cdot cm^{-1} \cdot K^{-1}$)	2.85–3.2	2.3	0.45–1.76	0.3–0.5	4.9	1.5
ρ	($g \cdot cm^{-3}$)	3.23–3.28	6.11–6.15	6.81–6.98			
N_{at}	(cm^{-3})	9.6×10^{22}	8.9×10^{22}	6.4×10^{22}			

The internal parameter u slightly deviates from $3/8 = 0.375$, meaning that the lattice is distorted from the ideal one. This distortion happens because of the electronegativity difference between nitrogen (3.04) and metallic species (Al: 1.61, Ga: 1.81, and In: 1.78) [9], with the bonding electrons tending to be distributed more closely to the N atoms. This causes a non-uniform charge distribution over the bonds and confers a mixed covalent and ionic character to them, such that N species are considered as being triply negative charged anions (N^{3-}) and metallic species as triply positive charged cations (III^{3+}).

The lattice parameters of the most common substrates (Al_2O_3, Si, and 6H-SiC) for III-N are also included in **Table 2.1**, demonstrating the disagreement in the lattice constant a and c, as well as in the thermal expansion coefficients of substrates and III-N [10]. In the growth of III-N on (0001)-oriented α-Al_2O_3 substrates, a 30° in-plane rotation (around the c-axis) between both unit cells is done, for a better lattice accommodation. Consequently, the effective a-lattice parameter of the substrate is 2.747 Å. On the other hand, Si crystallizes in a cubic diamond structure; to "match" the symmetry, the growth of III-N is done along the Si (111) face, resulting in an effective lattice parameter of 3.8397 Å.

For ternary III-N alloys, the thermodynamically stable crystalline phase is still the WZ [1]. Under the assumption of a random distribution of the atomic species A and B in a ternary alloy $B_xA_{1-x}N$, with x corresponding to the BN molar fraction, the lattice parameter can be estimated considering a linear variation between the values of the two binaries, AN and BN.[f] This corresponds to using the empirical Vegard's law [11]:

$$a(x) = xa^{\mathrm{BN}} + (1-x)a^{\mathrm{AN}} \quad \text{and} \quad c(x) = xc^{\mathrm{BN}} + (1-x)c^{\mathrm{AN}}. \tag{2.1}$$

2.1.1. Strain effects

Commonly, III-N experience stress (or strain) that elastically distorts the crystalline lattice. The introduced stress can have different natures and factors contributing to it, namely *i)* the disagreement in lattice parameters and thermal expansion coefficients between substrate and material in the plane perpendicular to the growth direction and *ii)* the presence of defects. The first may lead to uniaxial stress parallel to the *c*-axis or biaxial stress in the basal plane if the growth direction is parallel to the *c*-axis [12]. In the second case, defects uniformly distributed in the lattice induce a tri-dimensional stress known as hydrostatic pressure [12,13]. It should be noted that different stress contributions may co-exist in the same crystal lattice [13], even if subsequent analysis treats them independently.

Within the elastic regime, the stress sources mentioned above deform the crystalline lattice without breaking the C_{6v}^4 space group symmetry. Therefore, the strain tensor $\boldsymbol{\epsilon}$ has only the following diagonal components [12]:

$$\epsilon_{xx} = \epsilon_{yy} = \frac{a_{\mathrm{s}} - a_0}{a_0}, \text{and} \tag{2.2}$$

$$\epsilon_{zz} = \frac{c_{\mathrm{s}} - c_0}{c_0}. \tag{2.3}$$

ϵ_{xx} (and ϵ_{yy}) correspond to the strain induced in the basal plane (in-plane), while ϵ_{zz} is the strain along the *c*-axis (out-of-plane) strain; a_0 (a_{s}) and c_0 (c_{s}) are the relaxed (strained) lattice parameters.

[f] A and B represent the two metallic species of the ternary alloy, i.e., Al, Ga, or In.

For slight deviations from equilibrium ($\epsilon \lesssim 1$ %), Hooke's law (general strain-stress relation) gives the corresponding diagonal stress tensor $\boldsymbol{\sigma}$ with components [12]:

$$\sigma_{xx} = \sigma_{yy} = (C_{11} + C_{12})\epsilon_{xx} + C_{13}\epsilon_{zz}, \text{ and} \tag{2.4}$$

$$\sigma_{zz} = 2C_{13}\epsilon_{xx} + C_{33}\epsilon_{zz}. \tag{2.5}$$

C_{11}, C_{12}, C_{13}, and C_{33} are four of the five independent stiffness constants C_{ij} of the WZ crystal.

By convention, a positive strain is considered as follows: $\epsilon_{zz} > 0$ and $\epsilon_{xx}, \epsilon_{yy} < 0$ for uniaxial strain, $\epsilon_{xx} = \epsilon_{yy} > 0$ and $\epsilon_{zz} < 0$ for biaxial strain, and $\epsilon_{xx}, \epsilon_{yy}, \epsilon_{zz} > 0$ for hydrostatic strain [12].

In the case of uniaxial stress along the c-direction, i.e., $\sigma_{xx} = \sigma_{yy} = 0$ and $\sigma_{zz} \neq 0$, the lattice relaxes elastically in the c-plane. The relation between the induced strain in-plane and the deformation along the stress direction is expressed by the Poisson ratio (ν). By substituting in equation (2.4), the relationship between ϵ_{xx} and ϵ_{zz} is:

$$\epsilon_{xx} = -\frac{C_{13}}{C_{11} + C_{12}}\epsilon_{zz} = -\nu\epsilon_{zz}. \tag{2.6}$$

Isotropic biaxial stress in the plane perpendicular to the c-axis of the WZ lattice is described by $\sigma_{xx} = \sigma_{yy} \neq 0$ and a vanishing component along the c-direction $\sigma_{zz} = 0$. The relationship between the strain components ϵ_{xx} ($=\epsilon_{yy}$) and ϵ_{zz} is given by the biaxial relaxation ratio, R^{B}. Then, from equation (2.5), it comes:

$$\epsilon_{zz} = \frac{2C_{13}}{C_{33}}\epsilon_{xx} = -R^{\mathrm{B}}\epsilon_{xx}. \tag{2.7}$$

In the case of hydrostatic pressure, all the diagonal components of the stress tensor are non-zero and have equal magnitude, i.e., $\sigma_{xx} = \sigma_{yy} = \sigma_{zz} = 0$. From Hooke's law, the relationship between ϵ_{xx} and ϵ_{zz} is given by:

$$\epsilon_{zz} = \frac{C_{11} + C_{12} - 2C_{13}}{C_{33} - C_{13}}\epsilon_{xx} = R^{\mathrm{H}}\epsilon_{xx}, \tag{2.8}$$

where R^{H} is the hydrostatic relaxation ratio. When $R^{\mathrm{H}} \approx 1$, the lattice deforms in an isotropic manner, i.e., the induced strain is equal in all the crystal's directions [12].

2.1.2. Crystallographic defects

In a perfect crystal, the unit cell associated with the crystalline structure repeats itself periodically without any imperfections. However, in a "real" crystal, it is impossible to avoid the formation of crystallographic defects during growth or post-growth treatments (e.g., thermal annealing, doping, etching) that disrupt the three-dimensional periodicity of the crystal. Depending on their extension, they can be classified as point defects or extended defects. The former involves periodicity breaks at a scale of the order of the lattice constants, while the second extends spatially throughout the crystal, involving many lattice sites and forming along specific planes or directions of the crystal.

Point defects can be *i)* vacancies, which are absences of N atoms (V_N) or metal atoms (V_{III})[g] from their regular site; *ii)* interstitials that correspond to N or metal atoms occupying positions between the regular sites (N_i and III_i, respectively); and *iii)* substitutional defects, where N atoms occupy metal atoms' sites (N_{III}), and vice-versa (III_N). The defects mentioned above involve only the crystal's atoms; therefore, they are called native defects. Nevertheless, interstitial and substitutional positions can also be occupied by foreign species, introduced intentionally (dopants) or not (impurities). In both cases, the nomenclature of the defect is done using the chemical symbol of the respective atomic species involved. Nearby point defects can interact and form complex defects (if thermodynamically stable) [14–17].

Extended defects involve imperfections spatially extended through the crystal that can occur at the one, two, or three dimensions. Dislocations are line (one-dimensional) defects involving a series of atoms not in their regular lattice sites. The discontinuity on a specific area of the plane forms many dangling bonds. These often result from the plastic relaxation of the lattice. Because of the lattice mismatch between III-N and common substrates, for a layer thickness above a critical value, the critical layer thickness (CLT), heteroepitaxial growth occurs with III-N relaxing plastically (irreversible), with a high density of dislocations being formed [18]. Dislocations are designated as misfit dislocations if the direction of the lattice distortion (Burgers' vector) is parallel to the interface or threading dislocations if the Burgers vector points from the interface towards the surface. Stacking faults (SFs) correspond to the plane of atoms in the wrong sequence (two-dimensional defects). In III-N, SFs can transform the WZ into the zinc blende phase and vice-versa [14,17].

[g] The subscript 'III' refers to the metal atom and is replaced by Al, Ga, and In, when it is intended to specify the atomic specie involved. The same is valid for the nomenclature of other defects.

Surface defects are another type of two-dimensional extended defects that arise from the irregularities and incomplete bonding at the surface; consequently, they become increasingly important when the surface area-to-volume ratio increases, i.e., at the micro and nano-scale (e.g., in nanowires and chemically etched LEDs) [19–21]. Voids and clusters of atoms (precipitates) are examples of three-dimensional extended defects [17].

In general, crystallographic defects manifest themselves by modifying the physical properties of the materials, in most cases negatively, impairing the performance of devices. In III-N, the formation of defects during growth is inevitable, even in samples with high crystalline quality. Whether point or extended defects, they tend to trap charge carriers and introduce non-intended recombination paths (radiative and non-radiative), usually detrimental to the efficiency and reliability of optoelectronic devices [16–18]. Still, taking advantage of some defects to improve devices' performance is possible in certain situations, as is the case of point defects related to dopants, which are purposely introduced in the lattice to improve the material's properties (e.g., electrical, optical, or magnetic) with a view of a given application. Therefore, their influence on the device's performance is expected to be beneficial.

Doping III-N is necessary to achieve n- and p-type conductivity and can be accomplished in situ during growth or post-growth by thermal diffusion or ion implantation [18,22,23]. Besides the electrical properties, doping can also modify the optical properties of III-N; in particular, incorporating Ln^{3+} allows for tailoring the emission range throughout the visible and infrared regions [24,25].

2.1.3. Polarization-related phenomena

The absence of an inversion center in WZ III-N implies that the [0001] and the $[000\bar{1}]$ directions are not equivalent. This, alongside the different electronegativities between bonding atoms, makes III-N exhibit crystallographic polarity. By convention, the [0001] direction corresponds to the case where the vector points from the metal to the N atom for bonds along the *c*-direction. When III-N grow in this direction, they are said to have metal-polarity. In contrast, the $[000\bar{1}]$ direction defines the N-polarity [10].

The non-uniform distribution of charge over the bonds induces a spontaneous polarization in III-N along the *c*-axis, which is given by $\mathbf{P}_{\mathrm{sp}} = P_{\mathrm{sp}}\,\mathbf{z}$. The magnitude of the polarization field, P_{sp}, is equal to $-0.081\ \mathrm{C\cdot m^{-2}}$ (for AlN), $-0.029\ \mathrm{C\cdot m^{-2}}$ (for GaN), and $-0.032\ \mathrm{C\cdot m^{-2}}$ (for InN) [10]. The spontaneous polarization field is opposite to the [0001] direction, pointing from the N atom (higher electronegativity) to the metal atom, and the greater the difference in electronegativity, the stronger the induced field. Therefore, because of the induced spontaneous polarization, polarity has several consequences in the electronic band structure of III-N heterostructures, affecting their optical and electrical properties

[10,26,27]. Furthermore, polarity also has a strong impact on growth because of the different incorporation rates of dopants and impurities, as well as the different adatom mobility in (0001) and $(000\bar{1})$ surfaces [28–30].

Besides the spontaneous contribution, an additional polarization field arises in III-N because of the biaxial stress that results from the heteroepitaxial growth on lattice-mismatched substrates. The lattice deformation changes the metal–N bond lengths, leading to a redistribution of the charges and, consequently, to the appearance of a piezoelectric polarization field [1]. Considering once again that the induced stress is within the elastic regime, the piezoelectric polarization field is given by $\mathbf{P}_{\mathrm{pz}} = P_{\mathrm{pz}}\ \mathbf{z} = 2\left(e_{31} - e_{33}\frac{C_{13}}{C_{33}}\right)\epsilon_{xx}\ \mathbf{z}$, with e_{31} and e_{33} the piezoelectric coefficients (e_{ij}) [1,31]. The direction of the piezoelectric field depends on whether the III-N layer is tensile or compressive biaxially strained. As the quantity $\left(e_{31} - e_{33}\frac{C_{13}}{C_{33}}\right)$ is a negative quantity for III-N, P_{pz} is negative for crystals under biaxial tensile strain ($\epsilon_{xx} > 0$) and positive for those biaxially compressed ($\epsilon_{xx} < 0$) [1,31]. Such a contribution does not only arise when III-N are grown on (0001) α-Al_2O_3, Si, and 6H-SiC substrates; it also appears in heterostructures involving III-N solely (e.g., InGaN/GaN or AlGaN/GaN) since these also present incompatibility in the lattice constants.

Thus, in the absence of external electric fields, the total macroscopic polarization of the crystal, $\mathbf{P}$, is given by $\mathbf{P} = \mathbf{P}_{sp} + \mathbf{P}_{pz}$, having a unique component along the crystal's *c*-axis. Such polarization results in the accumulation of charges at surfaces and interfaces, which culminates in strong electric fields inside the III-N layers, profoundly affecting optoelectronic applications.

The polarization fields, particularly the spontaneous contribution, can be mitigated by growing the III-N along directions other than the typical [0001] polar direction. For example, the growth along non-polar planes (e.g., the *a*-plane $\{11\bar{2}0\}$ and the *m*-plane $\{1\bar{1}00\}$) or semi-polar planes (e.g., the family of planes $\{11\bar{2}2\}$) have been explored for developing InGaN-based LEDs with superior performance. However, up to now, the results have not been as good as those of *c*-plane LEDs because of the low crystalline quality, the need for specifically oriented substrates, and poor light extraction [32–35].

Table 2.2 summarizes the values of the used independent stiffness and piezoelectric constants of WZ AlN, GaN, and InN, as well as the relationship between ϵ_{xx} and ϵ_{zz} for uniaxial, biaxial, and hydrostatic strain in the elastic regime for the same crystals.

Table 2.2 Stiffness and piezoelectric constants of WZ AlN, GaN, and InN, as well as their Poisson, biaxial relaxation, and hydrostatic relaxation ratios [1,36]. Data from reference [12] is given in parentheses.

		AlN	**GaN**	**InN**
C_{11}	(GPa)	410 ± 10	390 ± 15	223
C_{12}	(GPa)	149 ± 10	145 ± 20	115
C_{13}	(GPa)	99 ± 4 (113)	106 ± 20 (104)	92
C_{33}	(GPa)	389 ± 20 (370)	398 ± 20 (414)	224
ν		0.177 (0.210)	0.198 (0.202)	0.272
R^{B}		0.509 (0.611)	0.533 (0.502)	0.821
R^{H}		1.25 (1.21)	1.11 (0.99)	1.17
e_{33}	($\mathrm{C \cdot m^{-2}}$)	1.54	0.83	0.95
e_{31}	($\mathrm{C \cdot m^{-2}}$)	-0.45	-0.45	-0.52

2.2. Lattice vibrations

The unit cell of the WZ structure is composed of four atoms, two of each species, meaning that 12 normal vibrational modes (or phonons – quanta of energy associated with lattice vibrations in a crystal) exist in the WZ structure ($N_{\mathrm{vib}} = 3 \times N^{\mathrm{atoms}}_{\mathrm{unit\ cell}}$). Three of these phonons are acoustic – in-phase vibrations of all the lattice atoms that fall in the low-frequency range –, while the other nine are optical – higher frequency vibrations, in which metal and N atoms oscillate differently [37].

At the BZ center ($\mathbf{q} = 0$, with $\mathbf{q}$ the wave vector associated with the phonons), group-theory predicts the following irreducible representation for a crystal belonging to the C_{6v} point group: $\Gamma = \Gamma_{\mathrm{ac}} + \Gamma_{\mathrm{op}} = (A_1 + E_1) + (A_1 + 2B_1 + E_1 + 2E_2)$ – in Mulliken's notation. A_1 and B_1 are non-degenerate representations, while E_1 and E_2 are doubly degenerated, leading to the 12 normal vibrational modes. A set of phonons with A_1 and E_1 symmetry correspond to the acoustic branch; all the others are optical modes.

B_1 and E_2 modes consist of out-of-phase vibrations of atoms of the same sub-lattice. Along the c-direction, depending on whether atoms of one sub-lattice vibrate in-phase or out-of-phase with the atoms of the other sub-lattice, the frequency is higher or lower, respectively. Their nomenclature includes a subscript h (l) to make the distinction. The E_2

modes are Raman active, while the B_1 modes are neither Raman nor IR active (silent modes) [37,38].[h]

A_1 and E_1 vibrations are polar modes, simultaneously allowed by Raman and IR, which is only possible because the WZ structure does not have an inversion center. Such vibrations induce a polarization field in the unit cell that interacts with the incident electromagnetic wave, resulting in a split of these optical phonons into longitudinal (LO) and transversal (TO) components, depending on whether the lattice oscillates parallel or perpendicularly to the propagation direction of the interacting electric field, respectively. For LO modes, as the oscillation dipole moment is aligned with the incident electromagnetic wave, the resulting frequencies are typically higher than in TO modes [37]. In III-N, the long-range electrostatic forces predominate over the anisotropic short-range forces, causing the TO–LO splitting (in the order of ~100 cm^{-1}) to be larger than the A_1–E_1 splitting (in the order of ~10 cm^{-1}) [39]. As a result, A_1 and E_1 modes can mix if the incident or scattered radiation is not strictly parallel or perpendicular to the *c*-axis, yielding *quasi*-TO and *quasi*-LO modes, whose frequency varies between the frequency of A_1, $\omega_{A_1(\mathrm{LO})}$, and E_1, $\omega_{E_1(\mathrm{LO})}$, depending on the angle θ between the *c*-axis and the phonon wave vector (varies between 0° and 90°). The frequency of the *quasi*-LO is given by $\omega^2_{quasi\text{-LO}} = \omega^2_{A_1(\mathrm{LO})}\cos^2\theta + \omega^2_{E_1(\mathrm{LO})}\sin^2\theta$ [40].

Figure 2.2 shows the atomic displacements corresponding to Raman active optical phonons in the WZ structure.

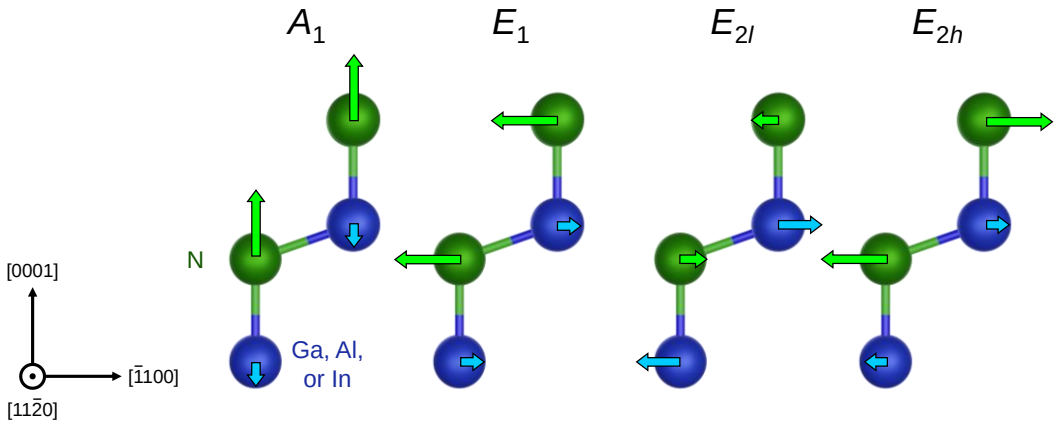

Figure 2.2 Representation of the optical vibrational modes of the WZ lattice at the BZ center ($\mathbf{q} = 0$). Adapted from reference [41].

[h] From the interaction of a light wave with lattice vibrations, IR active modes are vibrations that cause a change in the dipole-moment, and Raman active modes are those that cause a change in the susceptibility [37].

The frequencies of the phonons of WZ III-N at the BZ center are listed in **Table 2.3**. The presented values were measured on WZ III-N layers grown on (0001) α-Al_2O_3 substrates. The AlN and GaN layers have a thickness of ~50–70 µm; therefore, they can be considered fully relaxed [39,42]. Then, the tabulated values are considered the relaxed frequencies associated with each phonon in GaN and AlN. For InN, as the thickness is ~0.1–0.7 µm, considering these frequencies as the relaxed ones may not be correct, as they can be affected by remaining stress existing in the lattice (i.e., partial relaxation) [43].

Table 2.3 Phonon frequencies of WZ AlN, GaN, and InN layers measured by Raman spectroscopy at $T = 300$ K (those of B_{1l} and B_{1h} modes were calculated numerically). Data are from reference [42] for GaN and AlN, and from reference [43] for InN.

Symmetry	**Phonon frequency** (cm^{-1})		
	AlN	**GaN**	**InN**
E_{2l}	248.6	144.0	87
B_{1l}	571	319	
A_1(TO)	611.0	533.8	447
E_1(TO)	670.8	560.2	476
E_{2h}	657.4	567.6	488
B_{1h}	778	728	
A_1(LO)	890.0	734.0	586
E_1(LO)	912.0	741.0	593

2.2.1. Coupling between LO phonons and plasmons

In polar semiconductors, like WZ III-N, the free carrier plasma (plasmon) interacts with the LO phonons via their macroscopic electric fields, forming LO-phonon plasmon (LPP) coupled modes [44]. Raman scattering from LPP modes occurs through the following mechanisms: *i)* modulation of the optical polarizability by the atomic displacements (deformation potential scattering) and by the macroscopic longitudinal electric field (electro-optical scattering) or *ii)* scattering due to density fluctuations of the free carriers. These interactions can result in scattering events that reduce or increase the oscillation frequency. As a result, instead of a pure plasmon and a pure LO phonon, two LPP modes appear at frequencies below and above that of the respective LO phonon, designated as LPP^- and LPP^+, respectively [44].

In the presence of a plasma of free carriers, the dielectric constant, $\varepsilon(\omega)$, is given by [44]:

$$\varepsilon(\omega) = \varepsilon_\infty \left\{ 1 + \frac{\omega_{\mathrm{LO}}^2 - \omega_{\mathrm{TO}}^2}{\omega_{\mathrm{TO}}^2 - \omega^2 - i\omega\gamma} - \frac{\omega_{\mathrm{p}}}{\omega(\omega + i\Gamma_{\mathrm{d}})} \right\}, \tag{2.9}$$

with ω_{LO} and ω_{TO} are the LO and TO frequencies associated with the respective phonon, ε_∞ is the high-frequency dielectric constant, Γ_{d} is the phonon damping coefficient, γ is the electron damping constant, ω corresponds to the frequency of the measured phonon (in the case, that of the LPP modes), and ω_{p} is the plasma frequency.

The plasmon frequency (in cm^{-1}) is connected to the free carriers, n, through the following expression [44]:

$$\omega_{\mathrm{p}} = \frac{1}{2\pi c} \sqrt{\frac{e^2 n}{\varepsilon_\infty \varepsilon_0 m^*}}, \tag{2.10}$$

where e is the elementary charge ($= 1.60217663 \times 10^{-19}$ C [45]), m^* is the effective mass of the free carriers (in units of m_0, with $m_0 = 9.1093837015(28) \times 10^{-31}$ kg [46]), c is the speed of light in vacuum ($= 299792458\ \mathrm{m \cdot s^{-1}}$ [45]), and ε_0 is the vacuum permittivity ($= 8.8541878128(13) \times 10^{-12}\ \mathrm{F \cdot m^{-1}}$ [46]).

Assuming that the damping terms can be neglected[i], the frequencies associated with the LPP modes (ω^-, for LPP^-, and ω^+, for LPP^+) are roots of equation (2.9) and correspond to [47]:

$$\omega_\pm^2 = \frac{1}{2}\left[\omega_{\mathrm{LO}}^2 + \omega_{\mathrm{p}}^2 \pm \sqrt{(\omega_{\mathrm{p}}^2 + \omega_{\mathrm{LO}}^2)^2 - 4\omega_{\mathrm{p}}^2 \omega_{\mathrm{TO}}^2} \right]. \tag{2.11}$$

With the experimentally measured frequency of LPP^+, one can derive the plasma frequency and, consequently, estimate the free carrier concentration (and respective mobility). Indeed, this is a widely adopted methodology to estimate the free carrier concentration in III-N [47–50].

[i] For a more accurate estimation, one must consider the damping terms [49].

2.2.2. Strain effects

Within the elastic regime, the contraction or expansion of the crystalline lattice due to strain leads to a variation in bonding length while maintaining the hexagonal unit cell. This culminates in different force constants and, consequently, in a frequency shift of the phonons. For a given phonon i, the frequency shift depends on the two deformation potentials associated with that phonon (a_i and b_i), and it is given by [12]:

$$\Delta\omega_i = 2a_i\epsilon_{xx} + b_i\epsilon_{zz}. \tag{2.12}$$

Therefore, knowing the nature of the elastic stress present in the crystal (i.e., uniaxial, biaxial, or hydrostatic), it is possible to estimate the magnitude of the strain by considering the proper relations between ϵ_{xx} and ϵ_{zz} (defined already in **subsection 2.1.1**).

Figure 2.3 shows how strain affects the frequency of **(A)** E_{2h} and **(B)** A_1(LO) phonons in WZ GaN for the cases of uniaxial, biaxial, and hydrostatic strain. One can notice that both E_{2h} and A_1(LO) phonons are affected by strain; regardless of the phonon, a positive strain (consider the convention defined in **subsection 2.1.1**) decreases its frequency. However, due to the polar nature of A_1(LO) and the respective influence of the concentration of free carriers, the E_{2h} phonon is the choice for determining strain in III-N.

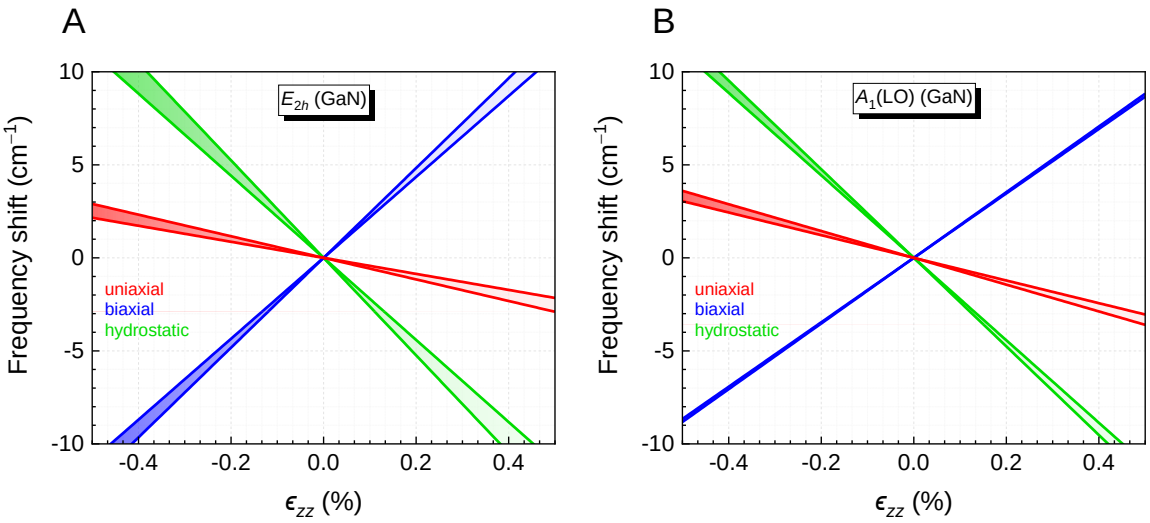

Figure 2.3 Frequency shift of the **(A)** E_{2h} and **(B)** A_1(LO) phonons in GaN as a function of ϵ_{zz} (in %) considering the three types of elastic strain, i.e., uniaxial, biaxial, and hydrostatic strain. The calculations considered the dispersion in the values found for the phonon deformation potentials for GaN (indicated in Table 2.4) [12,51,52]. The values used for ν, R^B, and R^H were those calculated by J. Wagner et al. (indicated in **Table 2.2**) [12].

The deformation potentials associated with the E_{2h} and A_1(LO) phonons, which will be needed later in this thesis, are specified in **Table 2.4**. A significant disparity in the values of these deformation potentials can be found in the literature, particularly in the case of InN (up to ~20 %).

Table 2.4 Deformation potentials associated with E_{2h} and A_1(LO) phonons calculated by J. Wagner et al. for AlN and GaN [12]. Experimental values from references [51,52] and [53,54] are given in parentheses for GaN and InN, respectively.

Phonon	**Deformation potential** (cm^{-1})	**AlN**	**GaN**	**InN**
E_{2h}	$a_{E_{2h}}$	−877	−740 (−818, −850)	(−610, −960±48)
	$b_{E_{2h}}$	−911	−727 (−797, −920)	(−857, −498±82)
A_1(LO)	$a_{A_1(LO)}$	−743	−663 (−685)	(−915±48)
	$b_{A_1(LO)}$	−735	−877 (−997)	(−642±82)

2.2.3. Ternary alloys – compositional effects

Assuming that in a ternary alloy $B_xA_{1-x}N$, the two metallic species B and A are randomly distributed in cation sites, the frequency of a given optical phonon lies between that in AN and BN. The frequency evolution with the molar fraction can follow a one-mode or a two-mode behavior [39].

The one-mode behavior corresponds to the case in which the phonon frequency of a varies linearly with the composition x between the frequencies of the two binaries, AN and BN, and the force constants associated with the vibrational modes remain practically constant [39].

Two sets of vibrational modes are available in the two-mode behavior, with frequencies close to that of AN and BN binaries. These modes are analogous to AN and BN impurity modes perturbed respectively by B and A atoms in the lattice; they are commonly referred to as AN-like and BN-like modes. As they are analogous to impurity modes, they slightly shift with the composition towards the frequency of the other binary, although they remain close to the binary frequencies. Furthermore, the strength of each mode tends to be proportional to the molar fraction, i.e., the intensity of the AN-like (BN-like) mode increases with increasing (decreasing) the composition [39].

Besides the two behaviors mentioned above, some crystals present a mixed behavior; the phonons exhibit a one-mode behavior in a given range of compositions and a two-mode behavior in the remaining range [39].

Figure 2.4 shows the frequency evolution of E_{2h} and A_1(LO) phonons in **(A)** $In_xGa_{1-x}N$ alloys with the InN molar fraction, x,[j] and **(B)** AlGaN alloys with y. The presented dependencies correspond to experimental results from the literature.

For InGaN alloys, both phonons typically exhibit a trend congruent with the one-mode behavior [55,56]. Therefore, considering the relaxed frequencies of the binaries tabulated in **Table 2.3**, the frequency shifts of E_{2h} and A_1(LO) phonons relative to the frequency of the same modes in GaN can be estimated by:

$$\Delta\omega^{x}_{E_{2h}} = \omega^{\mathrm{InGaN}}_{E_{2h}} - \omega^{\mathrm{GaN}}_{E_{2h}} = -79.6x \text{ and} \tag{2.13}$$

$$\Delta\omega^{x}_{A_1(LO)} = -153x, \tag{2.14}$$

respectively.

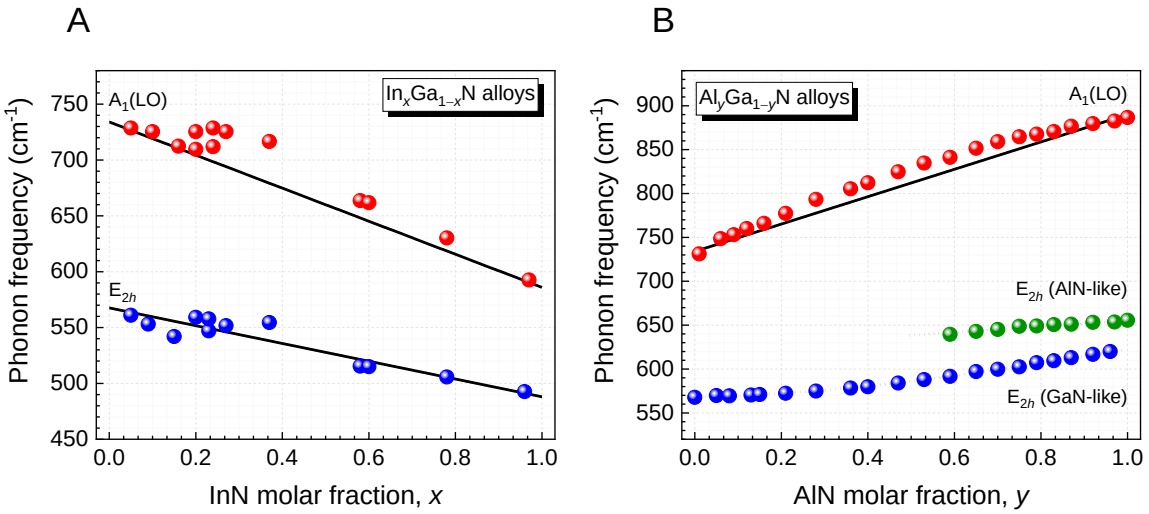

Figure 2.4 Frequency evolution of E_{2h} and A_1(LO) phonons in **(A)** InGaN and **(B)** AlGaN alloys with x and y, respectively. Experimental values from references [55] for InGaN and [57] for AlGaN. Solid lines correspond to the linear one-mode evolution considering the relaxed frequencies of the binaries indicated in Table 2.3. Dotted lines are the trend of E_{2h} (GaN-like) and E_{2h} (AlN-like) modes obtained by V. Yu. Davydov et al. for AlGaN layers [57].

[j] From then on, for the sake of simplicity, one will refer to $In_xGa_{1-x}N$ as InGaN, omitting x.

For AlGaN alloys, the A_1(LO) phonon's trend follows the one-mode behavior; therefore, its frequency shift with composition can be reasonably determined by $\Delta\omega^{x}_{A_1(LO)} = 156x$. In contrast, a two-mode behavior is found for the E_{2h} phonon with two phonon modes, E_{2h} (GaN-like) and E_{2h} (AlN-like), close to the frequencies of the respective binaries. In this case, an increase of y leads to a blueshift of the E_{2h} (GaN-like) from that of the E_{2h} (GaN), while the E_{2h} (AlN-like) blueshifts towards the E_{2h} (AlN) phonon frequency. In addition, the scattered intensity of the E_{2h} (GaN-like) and E_{2h} (AlN-like) impurity modes depends on alloy composition, with the first (second) one being enhanced for a low (high) AlN molar fraction, making that usually only one of the peaks is detectable in Raman experiments [57–60].

At first glance, it would be easy to determine the composition of ternary alloys just by measuring the frequency of the phonon modes; however, strain also affects the frequency of the phonons, as discussed before. Indeed, strain and composition cannot be disentangled unless one is determined independently. This means one needs to know the strain state to estimate the alloy composition based on the phonon frequency correctly, and vice-versa.

In addition to the frequency shift, the phonon peaks broaden for the ternary alloys, with maximum broadening generally observed for intermediate compositions. This reflects lattice disorder to the alloy randomness and the elastic scattering of phonons by compositional fluctuations [55,57,59].

2.2.4. Crystalline disorder

In light scattering experiments, as the wave vectors associated with photons in the visible spectral range ($\mathbf{k} \approx 10^4 – 10^5$ cm^{-1}) are orders of magnitude lower than the wave vectors associated with phonons at the extremities of the BZ ($\mathbf{q} \approx 10^8$ cm^{-1}), momentum conservation implies that only phonons with $\mathbf{q} \approx 0$ can participate in first-order processes.

Crystalline defects (and compositional disorder) are perturbations to the crystalline periodicity; therefore, their presence in a crystal will affect the scattering events. When the disorder level remains low enough to preserve the long-range order (i.e., the translation symmetry), the scattering spectrum continues to be dominated by first-order processes. In this case, the phonons can experience frequency shifts due to defects-induced strain and broadening due to disorder. Furthermore, local vibrational modes (LVMs), which correspond to short-range oscillations induced around the defects, can arise at characteristic frequencies[k] [61]. The disorder can also partially relax the **q**-selection rule and activate

[k] Under the assumption that the force constants are not significantly changed by the defects involved, the frequency of the LVMs can be estimated using the diatomic model, where the reduced mass of the vibration changes according to the chemical nature of the defect [61].

forbidden or silent modes; for example, in AlGaN alloys, the silent mode B_1 can be activated by compositional randomness [57,62].

For higher disorder levels, the broadening of the first-order phonons increases, and the frequency shift (from the unstrained value) is also expected to be more significant. At some point, disorder leads to a significant loss of the translational symmetry, fully relaxing the selection rule of $\mathbf{q} \approx 0$ required for momentum conservation in a perfect crystal. In this case, phonons from the entire BZ become allowed, and the scattering spectrum resembles the phonon density of states (p-DOS) weighted by the transition matrix elements involved in the photon-phonon coupling during the scattering process [37,42].

Figure 2.5 shows the calculated phonon dispersion curves and the associated phonon density of states (p-DOS) for hexagonal bulk AlN and GaN [42]. The singularities in the p-DOS are closely associated with the flat regions of the phonon dispersion curves that describe the relationship between phonon frequency and the phonon's wave vector in the BZ of the crystal lattice [37,42].

No theoretical and experimental results are found in the literature regarding the p-DOS function for ternary III-N alloys. Nevertheless, one would expect the singularities to evolve with composition analogous to first-order phonons, with frequency varying between the singularities in the two extreme binaries.

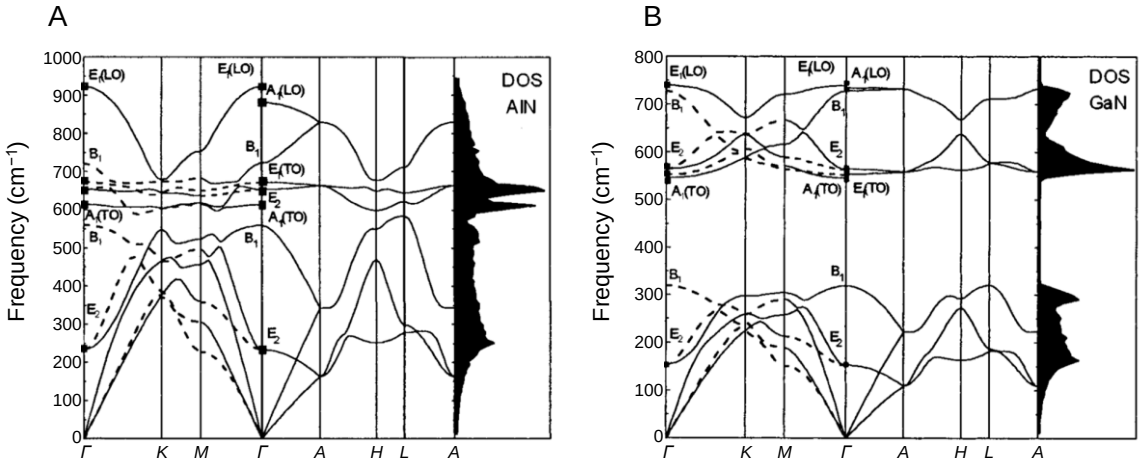

Figure 2.5 Calculated phonon dispersion curves and p-DOS for hexagonal bulk **(A)** AlN and **(B)** GaN. Reprinted from reference [42].

2.2.5. Raman spectroscopy

Raman spectroscopy is an optical spectroscopy technique that allows for obtaining valuable information concerning the crystalline structure of materials by analyzing the

inelastic scattering of photons by phonons. As the phonons' characteristics (e.g., frequency, full width at half maximum) depend on the composition, strain, free carrier concentration, or crystalline disorder, one can infer such information from the Raman spectrum [37,63,64].

When striking into matter, monochromatic light can scatter elastic or inelastically. In the first case, called Rayleigh scattering, the scattered photon has the same energy as the incident one. The inelastic processes are mediated by lattice phonons, such that scattered and incident photons have different energies. If acoustic or optical phonons mediate the process, it is called Brillouin or Raman scattering, respectively. The energy difference between the incident and scattered signal corresponds to the creation (Stokes) or annihilation (anti-Stokes) of phonons. Stokes and anti-Stokes spectra are symmetrical relative to the Rayleigh line.

The Raman scattering process can be described from a semi-classical perspective, the macroscopic theory of inelastic scattering by phonons [37,64]. Consider an infinite medium with electric susceptibility χ. An external sinusoidal electromagnetic field, $\mathbf{E}(\mathbf{r},t)$, described by a plane wave with frequency ω_{inc} and wave vector $\mathbf{k}_{\text{inc}}$, induces a time-dependent polarization, $\mathbf{P}(\mathbf{r},t)$, in the medium with equal frequency and wave vector. The amplitude of the polarization relates to the electric susceptibility of the medium by $\mathbf{P}(\mathbf{k}_{\text{inc}},\omega_{\text{inc}}) = \chi(\mathbf{k}_{\text{inc}},\omega_{\text{inc}})\mathbf{E}(\mathbf{k}_{\text{inc}},\omega_{\text{inc}})$ [37,64].

The periodic atomic vibrations in a crystal cause atomic displacements, $\mathbf{Q}(\mathbf{r},t)$, around their equilibrium position, $\mathbf{Q}_0$, associated with a phonon with frequency ω_{i} and wave vector $\mathbf{q}$. Given that $\omega_{\text{inc}} \gg \omega_i$, one can treat the phonon as an almost static deformation of the unit cell (potential deformation interaction) and define a susceptibility modulated by $\mathbf{Q}$. As the vibrational amplitudes are small compared to the lattice constant, the susceptibility can be expanded as a Taylor series in $\mathbf{Q}(\mathbf{r},t)$ [37,64]:

$$\chi(\mathbf{k}_{\text{inc}},\omega_{\text{inc}},\mathbf{Q}) = \chi_0(\mathbf{k}_{\text{inc}},\omega_{\text{inc}}) + \left(\frac{\partial\chi}{\partial\mathbf{Q}}\right)_0 \mathbf{Q}(\mathbf{r},t) + \cdots, \tag{2.15}$$

where χ_0 denotes the electric susceptibility without lattice vibrations. The second term in equation (2.15) represents the oscillating susceptibility caused by lattice vibrations. This causes the polarization of the medium to be expressed as a sum of two contributions [37,64]:

$$\mathbf{P}_0(\mathbf{r},t) = \chi_0(\mathbf{k}_{\text{inc}},\omega_{\text{inc}})\ \mathbf{E}(\mathbf{r},t), \quad \text{and} \tag{2.16}$$

$$\mathbf{P}_{\text{ind}}(\mathbf{r},t,\mathbf{Q}) = \left(\frac{\partial\chi}{\partial\mathbf{Q}}\right)_0 \mathbf{Q}(\mathbf{r},t)\ \mathbf{E}(\mathbf{r},t). \tag{2.17}$$

The first relates to a polarization vibrating in phase with the incident radiation, while the second describes the polarization wave induced by the phonon.

The induced polarization $\mathbf{P}_{\text{ind}}$ results in two scattered light contributions: *i)* Stokes, with frequency $\omega_{\text{s}} = \omega_{\text{inc}} - \omega_i$ and wave vector $\mathbf{k}_{\text{s}} = \mathbf{k}_{\text{inc}} - \mathbf{q}$, and *ii)* anti-Stokes, with frequency $\omega_{\text{as}} = \omega_{\text{inc}} + \omega_i$ and wave vector $\mathbf{k}_{\text{as}} = \mathbf{k}_{\text{inc}} + \mathbf{q}$. The frequency shift between the incident and scattered photons is called the Raman shift and is usually given in cm^{-1}. The participation of phonons guarantees energy and momentum conservation.

In Raman experiments, as the wave vectors associated with photons in the visible spectral range ($\mathbf{k} \approx 10^4$–10^5 cm^{-1}) are orders of magnitude lower than the wave vectors associated with phonons at the extremities of the BZ ($\mathbf{q} \approx 10^8$ cm^{-1}), momentum conservation implies that only phonons with $\mathbf{q} \approx 0$ can participate in first-order Raman scattering. Generally, the Raman experimental setups work with the Stokes range.

The intensity of the Raman signal depends on the polarization of the incident and scattered radiation, $\mathbf{e}_{\text{i}}$ and $\mathbf{e}_{\text{s}}$, relatively to the crystal axis. It also depends on the Raman tensor, $\mathbf{R} = (\partial\chi/\partial\mathbf{Q})_0\widehat{\mathbf{Q}}$ (with $\widehat{\mathbf{Q}} = \mathbf{Q}/|\mathbf{Q}|$), which translates the changes in the susceptibility of the medium caused by lattice vibrations. The intensity of the Raman signal is then proportional to [37,64]:

$$I_{\text{Raman}} \propto |\mathbf{e}_{\text{i}} \cdot \mathbf{R} \cdot \mathbf{e}_{\text{s}}|^2. \tag{2.18}$$

This means that for a given phonon to be Raman active, the associated atomic displacement must change the susceptibility of the medium with respect to $\mathbf{Q}_0$, i.e., $\mathbf{R}$ needs to differ from zero.

The Raman tensors associated with the phonons of the WZ structure (C_{6v} point group), describing the scattering induced by a potential deformation can be determined by recurring to the group theory. Those for the Raman-allowed modes are given by [65]:

$$A_1(z) = \begin{bmatrix} a & 0 & 0 \\ 0 & a & 0 \\ 0 & 0 & b \end{bmatrix}, \quad E_1(x) = \begin{bmatrix} 0 & 0 & c \\ 0 & 0 & 0 \\ c & 0 & 0 \end{bmatrix}, \quad E_1(y) = \begin{bmatrix} 0 & 0 & 0 \\ 0 & 0 & c \\ 0 & c & 0 \end{bmatrix}, \quad E_2 = \begin{bmatrix} d & d & 0 \\ d & -d & 0 \\ 0 & 0 & 0 \end{bmatrix}.$$

These are expressed in the cartesian coordinates (x, y, z): the z-axis coincides with the c-axis of the crystal, the x-axis corresponds to the crystallographic axis $[2\bar{1}\bar{1}0]$, and the y-axis is also in the basal plane but perpendicular to x. In the case of the polar modes, A_1 and E_1, the polarization direction is indicated in parenthesis. Moreover, the designation of the tensor components is arbitrary, but equal letters indicate components of equal magnitude.

The knowledge of the Raman tensors allows for determining the selection rules that depend also on the scattering geometry. The Porto's notation is commonly employed to identify whose phonons can be observed in each experimental configuration. This notation

is represented as $\mathbf{k}_{inc}(\mathbf{e}_i\mathbf{e}_s)\mathbf{k}_s$, where $\mathbf{k}_{inc}$ and $\mathbf{e}_i$ ($\mathbf{k}_s$ and $\mathbf{e}_s$) define respectively the direction and the polarization of the incident (scattered) radiation. Thus, the experimental observation of the phonons in Raman experiments is possible only when the components defined by $(\mathbf{e}_i\mathbf{e}_s)$ of the Raman tensor are non-null [37,64]. **Table 2.5** presents the allowed modes for the WZ structure for the various scattering geometries.

Table 2.5 Selection rules for Raman allowed phonon modes in WZ crystals.

Scattering geometry	Allowed modes
$x(y\ y)\bar{x}$	A_1(TO), E_2
$x(z\ z)\bar{x}$	A_1(LO)
$x(z\ y)\bar{x}$	E_1(TO)
$x(y\ z)y$	E_1(TO), E_1(LO)
$x(y\ y)z$	E_2
$z(y\ x)\bar{z}$	E_2
$z(y\ y)\bar{z}$	A_1(LO), E_2

The formalism presented describes only first-order Raman processes but can be expanded to higher scattering orders. The involvement of more than one phonon in the scattering process makes observation of phonons from the entire BZ possible. In this case, the spectrum reflects the p-DOS of the material [37,64].

The analysis has been restricted to the influence of potential deformation interaction on the polarization field. However, the LO phonon can induce a macroscopic polarization and consequently an electric field, which contributes with an additional restoring force to the oscillation, explaining why the frequency of the LO phonons is often higher than the corresponding TO frequency. This macroscopic field can interact with the electrons, Fröhlich interaction, producing an additional contribution to the scattering process. This interaction becomes relevant when the electronic states of a polar crystal are directly involved in the Raman scattering; when this happens, it is said that the Raman scattering occurs under resonance conditions. The electronic resonance can occur with the incident (incoming) or scattered photons (outgoing).

As a result of the Fröhlich interaction, in resonant Raman scattering experiments, the scattering efficiencies of the polar LO modes are substantially enhanced compared to other modes like E_2. This signifies that the relative scattering intensity between polar and non-polar Raman-allowed in resonant Raman experiments is higher than in non-resonant Raman conditions, where the interaction is dominated by a deformation potential [37,64–

66]. Furthermore, the Raman tensors of the polar modes obey different selection rules that depend on **q**; the respective tensors for a crystal belonging to the C_{6v} point group are indicated in **Table 2.6**.

Table 2.6 Raman tensors associated with the Fröhlich interaction for the WZ III-N and their dependence on **q** [65].

Direction of **q**	$A_1(z)$	$E_1(x)$	$E_1(y)$
x	$\begin{bmatrix} 0 & 0 & e \\ 0 & 0 & 0 \\ e & 0 & 0 \end{bmatrix}$	$\begin{bmatrix} a & 0 & 0 \\ 0 & b & 0 \\ 0 & 0 & c \end{bmatrix}$	$\begin{bmatrix} 0 & d & 0 \\ d & 0 & 0 \\ 0 & 0 & 0 \end{bmatrix}$
y	$\begin{bmatrix} 0 & 0 & 0 \\ 0 & 0 & e \\ 0 & e & 0 \end{bmatrix}$	$\begin{bmatrix} 0 & d & 0 \\ d & 0 & 0 \\ 0 & 0 & 0 \end{bmatrix}$	$\begin{bmatrix} b & 0 & 0 \\ 0 & a & 0 \\ 0 & 0 & c \end{bmatrix}$
z	$\begin{bmatrix} h & 0 & 0 \\ 0 & h & 0 \\ 0 & 0 & i \end{bmatrix}$	$\begin{bmatrix} 0 & 0 & f \\ 0 & 0 & 0 \\ f & 0 & 0 \end{bmatrix}$	$\begin{bmatrix} 0 & 0 & 0 \\ 0 & 0 & g \\ 0 & g & 0 \end{bmatrix}$

2.3. Optoelectronic properties

2.3.1. Electronic band structure

The fundamental optoelectronic properties of III-N are intrinsically linked to their electronic band structure, which describes the accessible (occupied and unoccupied) and inaccessible energies for electrons in a semiconductor. Determining the band structure involves solving the time-independent Schrödinger's equation for a many-electron system in a periodic crystalline potential. According to Bloch's theorem, the wave functions for a periodic potential are the product of a plane wave $\exp(i\mathbf{k}\cdot\mathbf{r})$, where $\mathbf{k}$ is the electron wave vector, and a function $u_{\mathbf{k}}(\mathbf{r})$ with the periodicity of the crystal lattice [8]. Generally, the electronic band structure, $E(\mathbf{k})$, is represented as a function of the electrons' wave vectors in the crystal, $\mathbf{k}$, in the first BZ [8].[1]

[1] Several approaches, like the $\mathbf{k}\cdot\mathbf{p}$ theory or the empirical pseudopotential method, have been developed to calculate the electronic band structure of WZ III-N [1]. A proper description of these methods is beyond the scope of this thesis.

Figure 2.6 shows the band structure of WZ AlN, GaN, and InN along high symmetry lines in the first BZ. These were calculated within the empirical pseudopotential method, using the model potential parameters obtained for III-N in the ZB phase and neglecting spin-orbit (SO) interactions. The energy diagrams show that the valence band (VB) maximum and the conduction band (CB) minimum occur for the same $\mathbf{k}$ ($\mathbf{k} = 0$), indicating that binary WZ III-N have a direct bandgap. The corresponding energy difference is the bandgap energy (E_{gap}).

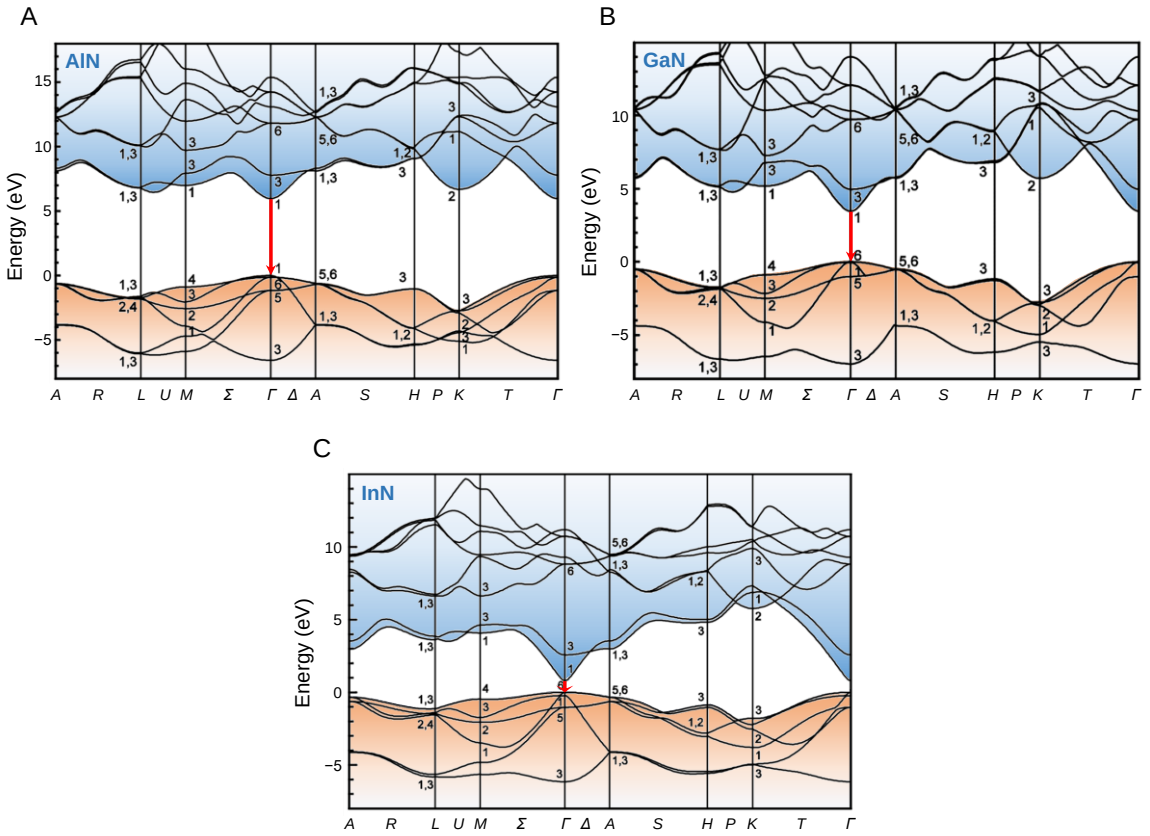

Figure 2.6 Electronic band structure of **(A)** WZ AlN, **(B)** WZ GaN, and **(C)** WZ InN along the high symmetry points and directions in the BZ, calculated within the empirical pseudopotential method. The calculations did not consider spin-orbit interactions, and the zero energy was assumed at the VB maximum. Red arrows represent the E_{gap} of each semiconductor. The numbers in the diagram denote the symmetry of the bands in Bethe's notation. Adapted from references [1,67].

The direct bandgap is one of the main reasons that makes III-N particularly suited for optoelectronic applications once direct optical transitions have a higher transition probability than indirect ones that involve the participation of phonons for the conservation of energy and momentum. As the CB minimum has an *s*-like character and the top of VB shows *p*-like, the angular momentum changes by unity at $\mathbf{k} = 0$, making the

transitions allowed by electric dipole, according to Laporte's selection rule [68]. Furthermore, the energy bandgap of InN, GaN, and AlN is respectively ~0.7 eV, ~3.4 eV, and ~6.0 eV at RT [69]; consequently, by controlling the composition in ternary III-N alloys, it becomes possible to tune the operational range of optoelectronic devices in an extended spectral range, from UV to NIR.

At the Γ point, the bottom of the CB consists of non-degenerate states whose contributions are predominantly from the *s*-orbitals of the metal atoms (Al, Ga, or In) and transform with the Γ_{1c} representation of the point group C_{6v}. In contrast, the upper VB states are formed from *p*-like orbitals associated with nitrogen and, consequently, are degenerated. The crystal field (CF) interaction energetically differentiates the p_z-like orbital from the remaining ones (p_x- and p_y-like) because of the anisotropy of the WZ structure. The VB states split into a doublet (Γ_{6v} symmetry) and a singlet (Γ_{1v} symmetry). The energy difference between these states, $\Delta_{\mathrm{cr}} = E_{\Gamma_{6v}} - E_{\Gamma_{1v}}$, lies about −220 meV, 10–40 meV, and 17 meV for AlN, GaN, and InN, respectively[m]. Changes in the crystalline structure, namely in the internal parameter u, are associated with such a behavior [1,69]. The negative sign of Δ_{cr} for AlN culminates in a distinct stacking order of the VB states, as it is possible to notice in the energy diagrams of **Figure 2.6**.

The SO interaction reflects the coupling between spin and angular momenta (**S** and **L**, respectively), and it further perturbs the electronic states and splits the VB states according to the total angular momentum ($\mathbf{J} = \mathbf{L} + \mathbf{S}$). When dealing with the electron spin (J is a half-integer), the double group notation must be adopted for a proper description according to group theory. In this case, the CB states transform according to Γ_{7c}, doubly degenerated due to spin considerations [1]. Furthermore, Γ_{1v} transforms as Γ_{7v} (split-off band, CH), while Γ_{6v} splits into two representations, Γ_{9v} and Γ_{7v}, separated energetically by Δ_{so}. Because of spin, these three configurations are doubly degenerated. The energy difference Δ_{so} is about 15–36 meV, 11–17 meV, and 3 meV for AlN, GaN, and InN, respectively [1,69].

The behavior of the valence sub-bands at $\mathbf{k} = 0$ under the action of CF and SO interactions is schematically represented in **Figure 2.7** for WZ GaN and AlN. For GaN, the order of these sub-bands is Γ_{9v}, Γ_{7v}, and Γ_{7v} (CH), in descending energy (the same for InN). For AlN, as Δ_{CF} is negative, the order changes and is Γ_{7v} (CH), Γ_{9v}, and Γ_{7v}. Even if the order of the valence sub-bands changes in GaN (and InN) and AlN, transitions between the conduction band and the three valence sub-bands are usually labeled as A, B, and C in order of ascending energy.

[m] In AlGaN alloys, the change of Δ_{cr} from positive to negative occurs for AlN molar fractions higher than about 0.10–0.25 [69,70].

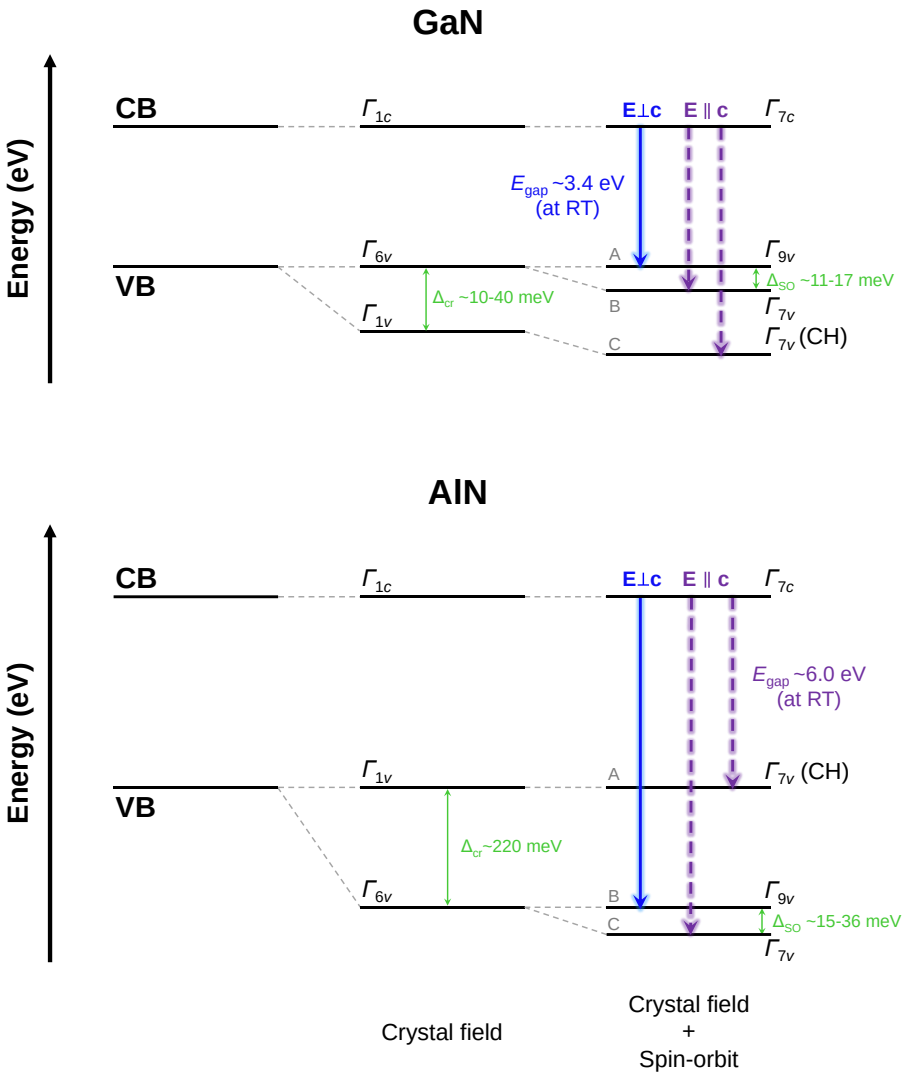

Figure 2.7 Splitting of the valence band states due to CF and SO interactions and respective band structure of GaN and AlN at the Γ point (not drawn to scale). The optical transitions between the minimum of the CB and the maximum of the various valence sub-bands are indicated, as well as the polarization of the emitted light associated with each. Adapted from references [69,70].

A natural consequence of the difference in the VB structure is the change in the optical properties. Since the upper VB has a different symmetry in GaN (or InN) and AlN, electronic transitions (absorption or emission) between the maximum of the VB and the minimum of the CB, i.e., the fundamental gap, will have a different polarization. For GaN (or InN), band-to-band transitions between the CB and the Γ_{9v} sub-band are allowed by electric dipole only for $\mathbf{E} \perp c$ polarization (transverse electric polarized), with $\mathbf{E}$ the electric field vector of the emitted (or absorbed) light. In contrast, for AlN, band-to-band transitions

between the CB and Γ_{7v} (CH) sub-band occur predominantly for $\mathbf{E} \parallel c$ polarization (transverse magnetic polarized).[n] This implies that the resulting emitted photons in GaN and AlN have a distinct propagation direction: parallel and perpendicular to the *c*-axis, respectively. Consequently, it is not possible to extract light efficiently from the top of AlN layers grown along the *c*-axis [69,70]; this has been critical for developing efficient UV LEDs based on III-N.

2.3.1.1. Strain effects

The band structure is modified in a strained crystal. An obvious consequence is the change in the bandgap energy as the metal–N bond length varies. However, because of the anisotropy of the WZ structure, the energy shifts of the various valence sub-bands in the presence of strain are different, which may lead to a change in their energetic order.

Within the elastic regime, J. Wagner et al. demonstrated how the CB and VB are modified by strain (without considering the SO interaction). In this case, the two gap energies can be calculated by [12]:

$$E_{\Gamma_{1c}-\Gamma_{6v}}(\epsilon) = E_{\Gamma_{1c}-\Gamma_{6v}}(0) + (a_1 + b_1)\epsilon_{zz} + 2(a_2 + b_2)\epsilon_{xx} \quad \text{and} \tag{2.19}$$

$$E_{\Gamma_{1c}-\Gamma_{1v}}(\epsilon) = E_{\Gamma_{1c}-\Gamma_{6v}}(0) + \Delta_{\text{cr}} + a_1\epsilon_{zz} + 2a_2\epsilon_{xx}. \tag{2.20}$$

$E_{\Gamma_{1c}-\Gamma_{6v}}(0)$ is the gap between the bands Γ_{1c} and Γ_{6v} in the absence of strain; while a_1, a_2, b_1, and b_2 are the electronic deformation potentials.

Figure 2.8 presents the evolution of the two gap energies defined above as a function of ϵ_{xx} for **(A)** WZ AlN and **(B)** WZ GaN in the three elastic regimes (uniaxial, biaxial, and hydrostatic). A positive strain (consider the definition in **subsection 2.1.1**) decreases E_{gap} and vice-versa. Consider, for example, the case of a uniaxial strain in GaN. With no strain ($\epsilon_{xx} = 0$), the fundamental E_{gap} corresponds to the energy difference between Γ_{1c} and Γ_{6v}. When a positive uniaxial strain is applied ($\epsilon_{xx} < 0$), the fundamental gap remains the same. Otherwise, for ϵ_{xx} above ~0.03 % (negative uniaxial strain), the valence sub-bands alter their order, with the fundamental E_{gap} corresponding to the difference between Γ_{1c} and Γ_{1v}. From the graphs, it is possible to notice that the order of valence sub-bands alters in certain circumstances. This implies that the bands involved in the fundamental bandgap change from $\Gamma_{1c} - \Gamma_{6v}$ ($\Gamma_{1c} - \Gamma_{1v}$) to $\Gamma_{1c} - \Gamma_{1v}$ ($\Gamma_{1c} - \Gamma_{6v}$) in GaN (AlN). Such a modification impacts the optical properties of III-N.

[n] Although allowed in both $\mathbf{E} \perp \mathbf{c}$ and $\mathbf{E} \parallel \mathbf{c}$ polarizations, the oscillator strength for the first is about three orders of magnitude lower.

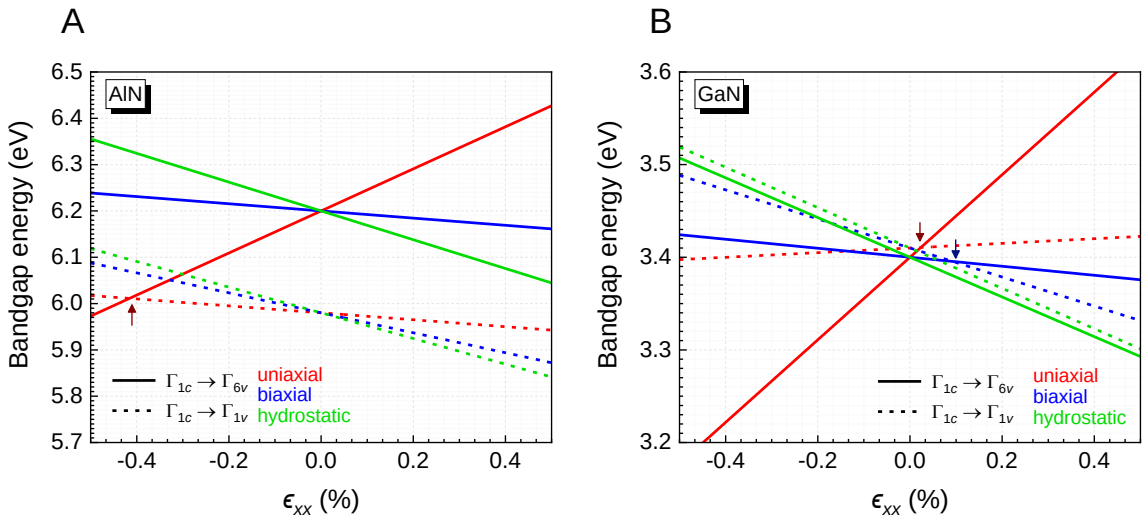

Figure 2.8 Variation of the gaps $E_{\Gamma_{1c}-\Gamma_{6v}}$ and $E_{\Gamma_{1c}-\Gamma_{1v}}$ for **(A)** WZ AlN and **(B)** WZ GaN as a function of ϵ_{xx}. Uniaxial, biaxial, and hydrostatic strain cases are considered. The electronic deformation potentials used in the calculations were: $a_1 = -4.09$ (-3.39), $a_2 = -8.87$ (-11.81), $b_1 = -7.02$ (-9.42), and $b_2 = 3.65$ (4.02) for GaN (AlN) [12]. The colored arrows mark the change in the fundamental gap associated with the respective strain regime.

2.3.1.2. Bandgap behavior with temperature

The bandgap energy of III-N depends on the temperature. In a generalized manner, such a dependence can be reasonably fitted using the empirical Varhsnii's equation [71]:

$$E_{\text{gap}}(T) = E_{\text{gap}}(0\ \text{K}) - \frac{\alpha T^2}{\beta + T}, \tag{2.21}$$

where α (in $\text{meV} \cdot \text{K}^{-1}$) and β (in K) are fitting parameters; the latter is usually compared to the Debye temperature. T is the temperature and $E_{\text{gap}}(0\ \text{K})$ is the bandgap energy at $T = 0$ K.

2.3.1.3. Ternary alloys – compositional effects

Ternary III-N in the WZ phase, like AlGaN and InGaN, are also characterized by a direct bandgap at the Γ point. In this case, the bandgap energy varies between the values of the two end binaries constituting the ternary compound. For the ternary $B_xA_{1-x}N$ with a random distribution of the atomic species A and B, the bandgap can be estimated by the empirical Vegard's rule [11]:

$$E_{\text{gap}}(x) = xE_{\text{gap}}^{\text{BN}} + (1 - x)E_{\text{gap}}^{\text{AN}}. \tag{2.22}$$

A quadratic term of the type $-b \cdot x(1-x)$ is commonly added to the empirical rule to fit the experimental data better. In this case, b is the bowing parameter; for III-N, the values found in the literature are often between 1 and 3 eV [1,69]. The quadratic term reflects, for example, strain effects, compositional fluctuations, or density of defects; therefore, the disparity of b found in the literature relates to the distinct quality of the samples.

Figure 2.9 depicts the evolution of the bandgap energy for WZ III-N at RT versus the *a*-lattice parameter. In the estimation of the bandgap energy for ternary alloys, two cases were considered: *i)* no bowing parameter, and *ii)* applying a bowing parameter reported for AlGaN, InGaN, and AlInN ternary alloys [69].

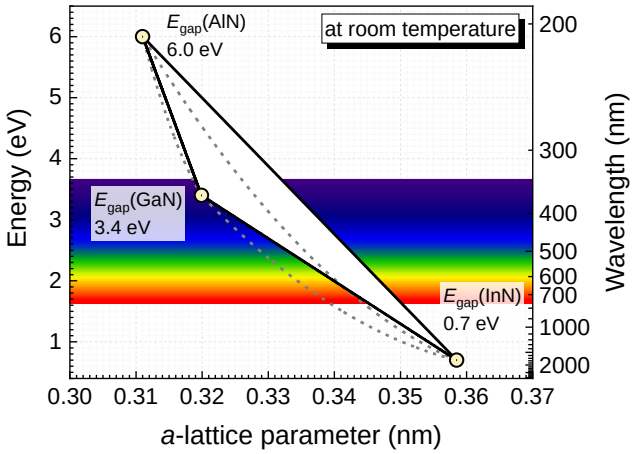

Figure 2.9 Bandgap energy versus *a*-lattice constant for WZ III-N at RT. Solid lines consider the empirical Vegard's law ($b = 0$ eV), while dashed lines consider the additional quadratic term with a bowing parameter of 1 eV for AlGaN, 1.65 eV for InGaN, and 3.1 eV for AlInN ternary alloys [69]. The *a*-lattice parameter was determined using equation (2.1).

Similar behaviors with strain are expected for ternaries, each with corresponding deformation potentials. Furthermore, as both composition and strain affect the bandgap

energy, determining the composition of a ternary alloy by evaluating the bandgap energy requires knowledge of the strain state. This is identical to the procedure needed to determine composition from lattice vibrations.

2.3.1.4. Heterostructures

A heterostructure is a structure where at least two different materials are placed in contact. As a result of their different electronic band structure, there exists a discontinuity in the valence and conduction bands at the junction's interface, resulting from the different electron affinities of the materials. Under equilibrium conditions, the Fermi energy level (E_F)[o] must be equal on both sides of the junction; therefore, charges diffuse from one side to the other, culminating in a depletion region close to the interface and consequent bending of the electronic bands. Depending on the alignment of the electronic bands, the confinement, transport, or recombination of charge carriers can be affected [72].

In III-N heterostructures, the bands align so that the minimum of the CB and the maximum of the VB occur on the same side of the junction, i.e., on the side of the material with the lower bandgap energy. A heterojunction of this type is called straddling or type-I [72,73]. In this case, it is possible to form potential wells (or barriers) by inserting a material with a smaller (larger) bandgap between two with a larger (smaller) one.

The polarization fields in III-N cause a net polarization at the interface, leading to an accumulation of charges on both sides of the heterojunction. This culminates in strong electric fields within the different layers, contributing even more to bending the bands, which is determinant to the optical and electrical properties of the heterostructure [10,31,73].

The band diagrams associated with two III-N heterostructures widely adopted in optoelectronics are schematized in **Figure 2.10**: **(A)** InGaN/GaN QWs and **(B)** n-doped AlGaN/n-doped GaN single interfaces. The first plays a pivotal role in light-emitting applications, while the second is employed in high-power and high-frequency electronics.

[o] The Fermi level defines the highest energy state possibly occupied by an electron at $T = 0$ K, according to the Fermi-Dirac distribution. In an intrinsic semiconductor, the Fermi level lies close to the mid-gap of the semiconductor [72].

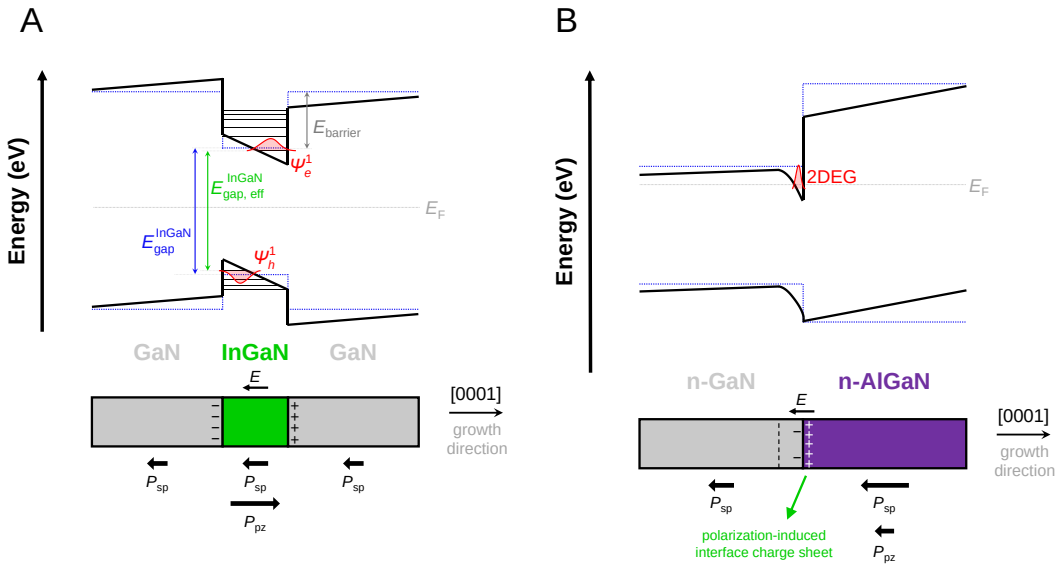

Figure 2.10 Schematic representation of the band structure of **(A)** an InGaN/GaN QW and **(B)** an n-AlGaN/n-GaN single interface. In both cases, the [0001] direction was assumed to be the growth direction (metal-polarity). Solid (black) and dashed (blue) lines correspond to the bands with and without considering polarization effects.

In the first case, a nanometric InGaN layer is inserted between two GaN barriers with a larger bandgap. The term 'QW' arises from the fact that the typical dimensions of the InGaN layer (approximately between 2–5 nm) are comparable to or smaller than the exciton Bohr radius and the de Broglie wavelength of free electrons and free holes in the semiconductor [1,74]. This confinement restricts the movement of electrons and holes to two dimensions, leading to quantized energy states. Within a simple approximation of an infinite square potential well with width L, the confinement energy, E_n, can be expressed as [64]:

$$E_\mathrm{n} = \frac{\hbar^2}{2m^*}\left(\frac{\pi n_x}{L}\right)^2, \tag{2.23}$$

where $\hbar$ is the reduced Planck constant ($= 6.582119569\ldots \times 10^{-16}$ eV $\cdot$ s [46]) and n_x is an integer quantum number (> 0) associated with the quantized energy level. Since E_n is inversely proportional to the effective mass and typically $m_e^* \neq m_h^*$ (electron and hole effective mass, respectively), the quantized energies associated with electrons in the CB and holes in the VB differ. Similarly, the quantized states involving holes in the various valence sub-bands differ in energy.

A direct consequence of quantum confinement is that the effective bandgap increases compared to the bulk value. Moreover, confined carriers should exhibit higher recombination rates due to the spatial overlap of their wave functions. However, spontaneous and

piezoelectric polarization in III-N results in strong built-in electric fields within the InGaN QWs, reaching values on the order of $MV \cdot cm^{-1}$. This effect, known as QCSE, spatially separates electrons and holes, reducing the spontaneous recombination rate and causing a redshift of the electron-hole recombination energy. Depending on the magnitude of the electric field, this redshift can compensate for the blueshift caused by confinement and result in a lower effective bandgap than the bulk value [31,75–77].

In the second example, the net polarization at the n-doped AlGaN/n-doped GaN gives rise to an accumulation of opposite charges at both sides of the interface, with different interfacial charge densities. Assuming that the structure grows with metal-polarity, electrons accumulate on the GaN side of the heterojunction, while a higher density of holes accumulates at the AlGaN side of the interface. This charge distribution creates an electric field that bends downward the bands on the GaN side close to the interface. As a result of this bending, the Fermi level lies above the CB in a nanometric region close to the interface (channel), where electrons in the CB become confined to move in the plane parallel to the interface. This is called two-dimensional electron gas (2DEG) [10,31,73]. Technologically, HEMTs take advantage of this effect since the mobility of electrons in the transistors' channel (interface) is increased [78,79]. Analogously, a two-dimensional hole gas can be formed when the AlGaN/GaN interface is grown with N-polarity.

2.3.2. Recombination mechanisms

Under an external stimulus (e.g., optical, electrical) with energy equal to or above the bandgap of a given semiconductor, electrons can be promoted from the VB to the CB, leaving holes in their "places". Once excited, the semiconductor returns to the fundamental state after a certain relaxation time. The recombination between electrons and holes is *i)* radiative if it results in the emission of photons or *ii)* non-radiative if, instead, the recombination energy is dissipated as heat through the excitation of phonons [64,74].

2.3.2.1. Band-to-band transitions and free excitons

Initially, excited electrons (holes) tend to relax intra-band towards the CB minimum (VB maximum) through multi-phonon relaxation, called thermalization. After thermalizing, such electrons and holes electrostatically attract to each other, forming *e-h* pairs, also called excitons. As these excitons involve the interaction of electrons and holes in the bands, they are said to be free excitons (FXs). Due to Coulomb attraction, excitons exhibit hydrogen-like behavior modulated by the semiconductors' dielectric constant ε ($\varepsilon = \varepsilon_r \varepsilon_0$, with ε_r the relative permittivity of the material), and considering the reduced effective mass of the system μ^* ($1/\mu^* = 1/m_h^* + 1/m_e^*$, with m_h^* and m_e^* the effective masses of holes and electrons

in the VB and CB, respectively). Consequently, excitons' bound states with energies [8,15,80]:

$$E_{\mathrm{X}}^{n_{\mathrm{x}}} = \frac{\mu^*}{m_0 \varepsilon_r^2} R_H \left(\frac{1}{n_{\mathrm{x}}}\right)^2 \tag{2.24}$$

are formed. R_{H} the Rydberg constant of the hydrogen atom ($= 13.605693122994(26)$ eV [46]), and n_{x} (integer value equal to or above 1) is the principal quantum number that indicates the exciton's energy state. The FX ground state corresponds to $n_{\mathrm{x}} = 1$ and its respective energy E_{X}^1 is the ionization energy of the exciton. The recombination energy of FXs occurs at energies slightly lower than the bandgap given by:

$$E_{\mathrm{FX}} = E_{\mathrm{gap}} - E_{\mathrm{X}}^{n_{\mathrm{x}}}. \tag{2.25}$$

The exciton Bohr radius in the energy state n_{x}, $a_{\mathrm{X}}^{n_{\mathrm{x}}}$, that describes the average distance between the electron and the hole forming the exciton is given by [8,15,80]:

$$a_{\mathrm{X}}^{n_{\mathrm{x}}} = \frac{m_0}{\mu^*} \varepsilon_r n_{\mathrm{x}}^2 a_H, \tag{2.26}$$

with a_H ($= 5.29177210903(80) \times 10^{-11}$ [46]) the Bohr radius of the hydrogen atom. When a_{X} is larger than the lattice constant, i.e., electrons and holes forming the exciton are bound together due to a long-range Coulomb interaction, excitons are called Wannier-Mott excitons. Otherwise, if the exciton Bohr radius is of the order or lower than the lattice constant, they are called Frenkel excitons. In this case, electrons and holes are tightly bound on the same or nearby crystal atoms [8,15,64].

In III-N, the VB splits into three sub-bands, each with an associated hole effective mass; therefore, three distinct excitons can be observed: $\mathrm{FX_A}$, $\mathrm{FX_B}$, and $\mathrm{FX_C}$ in order of ascending energy (as defined above). Naturally, they have different binding energies and Bohr radius. Still, the values reported for $\mathrm{FX_A}$ in the literature are often considered: E_{X}^1 is ~60 meV, ~25–34 meV, and ~9 meV, while a_{X} is ~1.4 nm, ~2.4 nm, and ~8 nm for AlN, GaN, and InN, respectively [81,82]. Thus, considering the lattice constants, the FXs correspond to Wannier-Mott excitons.

When the thermal energy, E_T, is enough to dissociate excitons, band-to-band transitions, corresponding to direct recombination of electrons in the CB and holes in the VB, can occur. In this case, the recombination energy equals the respective bandgap energy. As direct transitions depend on exciton's dissociation, they become more relevant with increasing temperature. At RT, E_T ($= k_B T$, with $k_B = 8.617333262... \times 10^{-5}$ eV $\cdot$ K^{-1} [46], the Boltzmann constant) is ~26 meV, which only allows for fully ionizing the FXs in InN. Therefore, excitons can still be observed at RT in most III-N. Regardless of being FX or

direct band-to-band recombination, A-, B-, and C-related transitions are polarized according to that defined in **subsection 2.3.1** [69,70].

In ternary III-N alloys, the random distribution of the metallic species affects the crystalline short-range order, creating potential fluctuations that result in broader emission line widths compared to binaries. Furthermore, excited carriers can be localized at potential minima induced by compositional and strain fluctuations, with the recombination of these carriers being the dominant contribution to the alloy luminescence. In contrast, light absorption maps the joint density of electronic states with the localized energy levels weakly contributing to it. This leads to an energy difference between absorption and emission called Stokes shift [83–86].

For InGaN systems, K. O'Donnell et al. observed a linear dependence of the emission peak, E_{em}, with the absorption band edge (equal to E_{gap}) over a wide range of InN molar fractions ($0 < x < 0.41$) for different kinds of structures (e.g., layers and MQWs). They obtained the following relationship between emission and absorption energies [87]:

$$E_{\mathrm{em}} = 1.453E_{\mathrm{gap}} - 1.54. \tag{2.27}$$

For instance, for $x = 0.41$, a Stokes shift of ~500 meV is presumed using the previous expression.

Several authors also found significant Stokes shifts in AlGaN alloys. T. Onuma et al. reported Stokes shifts as large as 100–250 meV that increased with increasing the AlN molar fraction up to 0.7 in nearly strain-free AlGaN layers [88]. A. Pierret et al. reported larger Stokes shifts in PA-MBE grown AlGaN NWs, reaching ~450 meV for intermediate AlN molar fractions of 0.5 [89].

2.3.2.2. Defect-related transitions

Crystalline defects introduce energy levels in the forbidden gap, which are *i)* shallow states when located within a few tens of meV from the band edges or *ii)* deep when closer to the middle of the gap. While the electronic energies of the former can be determined using the "effective-mass" theory, the same does not happen for the deep centers [64]. Depending on their nature, they can act as donors, acceptors, or isoelectronic defects. Donors have excess valence electrons and can provide those electrons to the CB at energies lower than the semiconductor's bandgap, thus becoming positively charged. Acceptors have a deficit of valence electrons and tend to capture electrons from the VB, creating holes in the VB. In turn, isoelectronic defects are those that do not have excess or missing valence electrons and, therefore, maintain the charge state in the crystal [64].

As a result of Coulomb interactions between electrons or holes of the pair and defects, excitons can become bound to defects; they are then designated bound excitons (BXs). The energy of BXs is lowered compared to FXs by the localization energy of the exciton at the defect, E_{loc}. Therefore, their recombination energy is given by:

$$E_{\mathrm{BX}} = E_{\mathrm{gap}} - (E_{\mathrm{loc}} + E_{\mathrm{X}}^{n_{\mathrm{x}}}), \tag{2.28}$$

with $E_{\mathrm{loc}} + E_{\mathrm{X}}^{1}$ representing the ionization energy of the BX [14,64]. Bound excitons can be bound to donor or acceptor states. They can also be localized at isoelectronic impurities, given that, due to differences in electronegativity, these impurities tend to act as traps for electrons or holes [14,64].

Shallow defects cause a weak disruption to the periodic potential of the lattice; therefore, they introduce energy states with smaller localization energies (a few tens of meV). Because of the weak binding between free electrons (holes) and positively charged donors (negatively charged acceptors), the wave functions of the trapped carriers are delocalized in space, and the interaction with the lattice is minimal. As a result, the recombination of excitons bound to shallow defects consists of sharp lines like those associated with FXs. Furthermore, as the energy states of donors and acceptors are close to the CB and the VB, respectively, the recombination of excitons bound to shallow defects occurs at energies similar to those of FXs [14]. The luminescence from band-to-band transitions, FXs, or excitons bound to shallow defects is called near-band edge (NBE) luminescence.

Despite the weak interaction with the lattice, the aforementioned optical transitions can be accompanied by phonon replicas at lower energies than the fundamental transition, the zero-phonon line (ZPL), by an amount of $m_v \hbar\omega_{\mathrm{LO}}$, in which ω_{LO} is the phonon frequency, and m_v is the vibrational level [14,64].

In contrast to shallow defects, deep centers induce a strong perturbation of the periodic potential around them, leading to trapped carriers with tightly localized wave functions. Because of their localized nature, they feel more disturbances of the local potential like those induced by lattice oscillations, implying a strong electron-phonon coupling [14]. The luminescence from deep centers can be described by the annihilation of bound excitons accompanied by a significant lattice relaxation or by the recombination of carriers from an excited state to the ground state of the same defect [90]. The strong electron-phonon coupling makes the recombination at deep-level defects result in broad luminescence bands.

Deep centers are often interpreted in terms of a configuration coordinate (CC) model. In this model, the energy of the vibronic states (coupling between electronic and vibrational states) of the system is represented as a function of a generalized coordinate Q that represents the spatial displacement of atoms from their positions in a fully relaxed lattice.

The change in the charge state of deep-level defects changes the equilibrium positions of the atoms, i.e., the potential minima of the vibronic states associated with those occurring at different Q. Following the Franck-Condon approximation (electronic transitions occur much faster than nuclear motion), electronic transitions in a CC diagram are represented as vertical arrows. The coupling between vibrational and electronic states explains the broader emission [14,17].

Indeed, broad luminescence bands related to deep-level defects are typical in III-N. For example, broad green/yellow emission bands are well-known to occur in GaN, being commonly attributed to V_{Ga}, carbon or oxygen impurities in nitrogen sites (C_N or O_N), or complexes involving those point defects [16,17,91–94].[p] Analogously, AlN samples show broad luminescence bands tentatively ascribed to defects similar to those in GaN; however, their emission lies in the UV–blue spectral range [16,94–100].

Figure 2.11 illustrates how the CC model can help interpret deep-level defects in III-N. To exemplify it, one recurs to the case of GaN with carbon impurities in nitrogen sites (C_N). In unintentionally doped GaN, which has n-type conductivity (Fermi level above the mid-gap) due to native defects or impurities that act as donors, C_N impurities are acceptor states, and their ground state is the C_N^-. **Figure 2.11(A)** shows the case where the excitation energy is enough to provide electrons from the VB to the CB. In this case, the acceptor state captures a free hole after band-to-band excitation. After relaxation towards the minimum of the excited vibronic state, the defect relaxes through the emission of photons. Furthermore, it is possible to excite these defects resonantly with energy below the bandgap; this is demonstrated in **Figure 2.11(B)**. In this case, the excitation directly promotes an electron from the defect to the CB, changing the defect's charge state. After relaxation, the free electron can recombine with the hole left in the defect. As a result of the strong electron-phonon coupling, phonons are emitted during the lattice relaxation, and the defect-related emission occurs at an energy lower than the resonant absorption. The energy difference between the absorption and emission maxima is called the Franck-Condon shift and defines the amount of energy lost during relaxation [14,90]. **Figure 2.11(C)** represents the electronic band diagram associated with this defect, i.e., without considering the vibrational states. Such a diagram cannot describe the lattice relaxation. **Figure 2.11(D)** depicts a schematic representation of the absorption and emission spectrum related to the deep-level defect, considering both above bandgap excitation and resonant excitation.

[p] Although unwanted, carbon and oxygen impurities are common in III-N. Typical precursors used in MOVPE contain carbon. On the other hand, oxygen has a high reactivity with gallium and aluminum, which means that, even for low concentrations of oxygen in the growth chamber, it can readily incorporate the material [2].

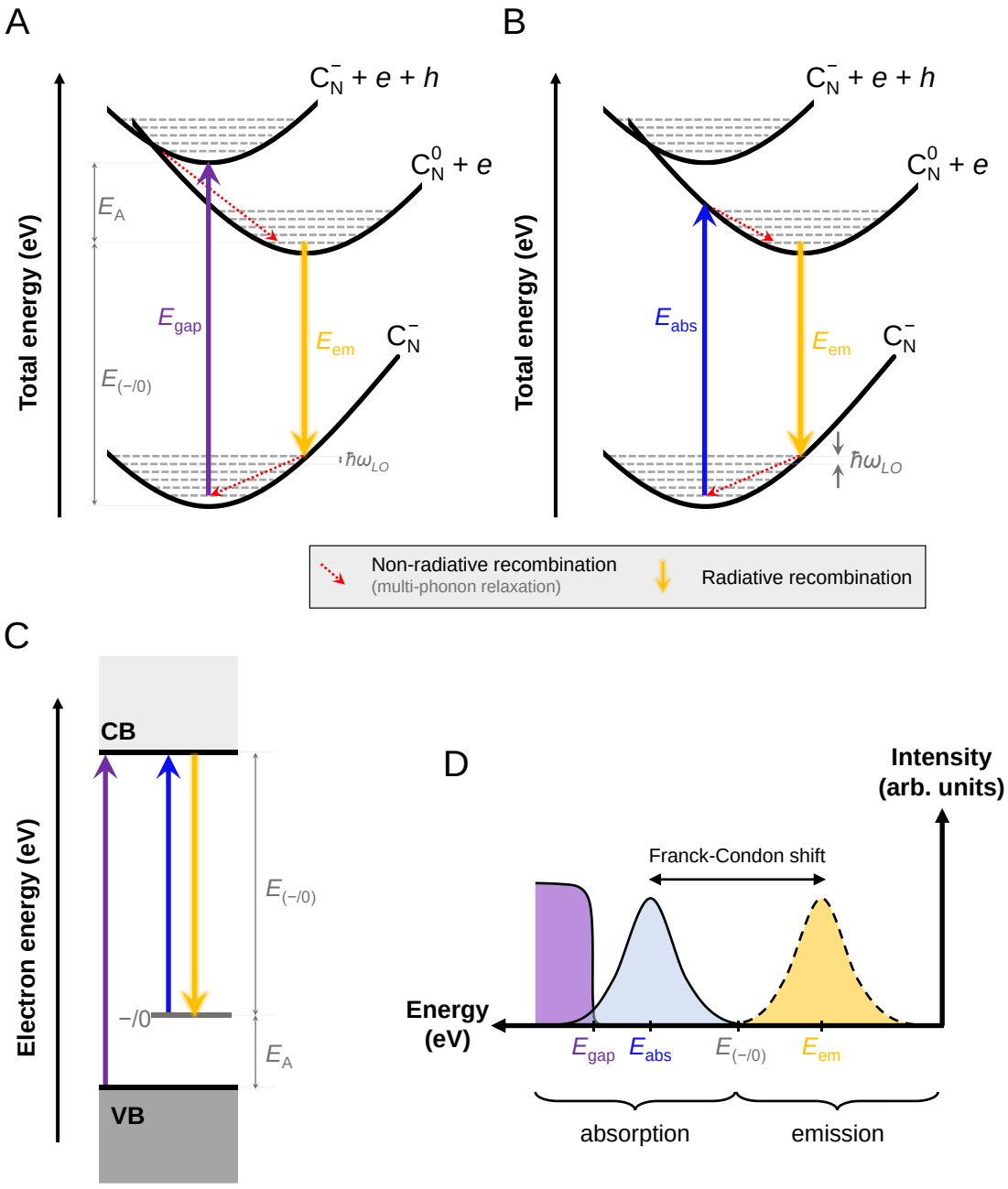

Figure 2.11 CC diagram for the C_N acceptor in GaN when the excitation energy is **(A)** equal to or above the bandgap and **(B)** resonant with the defect. **(C)** Band diagram for the same defect. **(D)** Schematic representation of the absorption (for the above bandgap and resonant excitation) and the emission spectra of the defect. Adapted from reference [90].

Commonly, a semiconductor may contain both donors and acceptors. Such semiconductors are said to be compensated because, under equilibrium, acceptors will capture some of the electrons of the donors, leaving the semiconductor with ionized donors (D^+) and ionized acceptors (A^-). The ionized defects can trap free electrons and holes excited

optically, producing neutral donor and acceptor centers. When returning to equilibrium, electrons on the neutral donors may recombine radiatively with holes on the neutral acceptors, giving rise to what is known as donor-acceptor pair (DAP) transitions. The energy of the emitted photon is given by [64]:

$$E_{\mathrm{DAP}} = E_{\mathrm{gap}} - (E_{\mathrm{D}} + E_{\mathrm{A}}) + \frac{e^2}{4\pi\varepsilon r}. \tag{2.29}$$

Here, E_{D} and E_{A} represent donor and acceptor ionization energies, respectively, and the last term accounts for the Coulomb interaction between the ionized donors and acceptors, with r denoting the distance between them [64]. It is worth noting that DAP transitions can involve both shallow and deep defects; for that reason, they can be affected by strong electron-phonon coupling.

When DAP transitions involve shallow defects, ionizing one of the defects involved in the pair can lead to free-to-bound transitions. These transitions encompass processes like the recombination of free electrons with holes localized at acceptors (e-A transitions) or the recombination of electrons localized at donors and free holes in the VB (D-h transitions) [14]. These become more likely at higher temperatures, i.e., when shallow defects are ionized, replacing DAP transitions. Additionally, if DAP transitions involve deep-level defects, they can be analyzed using the CC model, as discussed before.

Figure 2.12 presents a schematic summarizing the possible radiative recombination mechanisms involving carriers free in the semiconductor's bands or trapped at defect levels. As previously mentioned, trapping of carriers at defects usually occurs at the expense of energy loss by the emission of phonons, i.e., conversion into heat instead of light. After becoming trapped at defects, in addition to recombining radiatively, the carriers can recombine non-radiatively with the emission of phonons. This occurs predominantly at defects that introduce deep levels in the gap (e.g., vacancies, dislocations, surface states) and is known as Shockley-Read-Hall (SRH) recombination [101,102]. Non-radiative processes are, in most cases, detrimental for optoelectronic devices since they lead to heat and reduce the radiative recombination rate of the intended luminescence, which usually involves NBE luminescence.

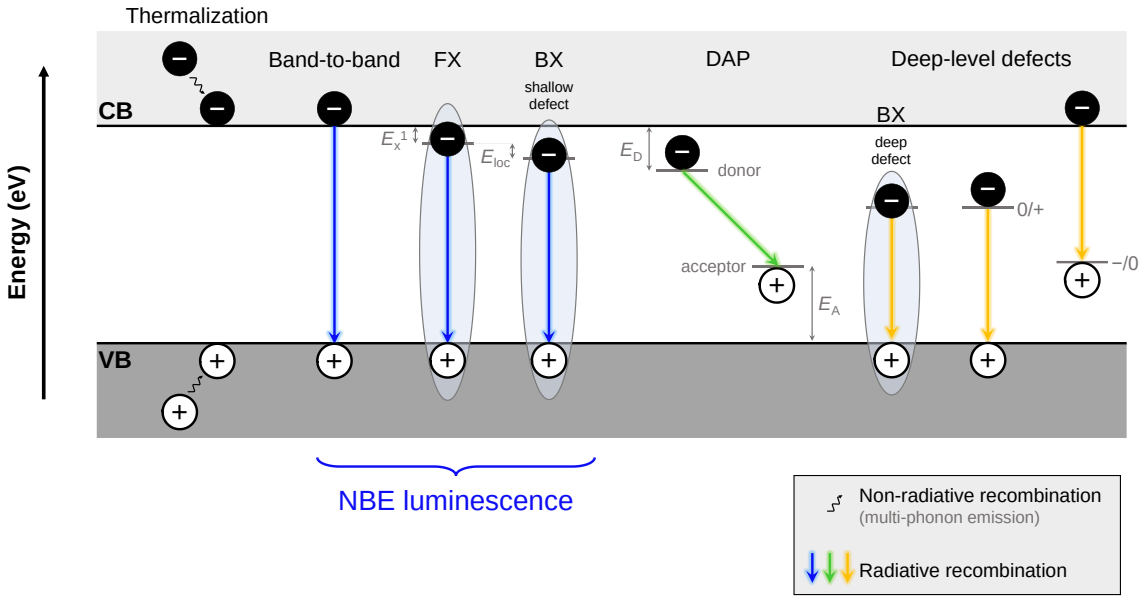

Figure 2.12 Schematic representation of the recombination mechanisms in semiconductors (at $\mathbf{k} = 0$). Thermalization of the excited carriers in the respective bands towards their energy minima is accompanied by the emission of phonons (momentum conservation). Adapted from reference [103].

2.3.3. Photoluminescence spectroscopy

PL spectroscopy is a valuable tool for probing the optical properties of semiconductors, including III-N. The basic principle of operation of the PL technique consists of optically exciting the material with a laser or lamp (fixed excitation wavelength) and then measuring the emitted signal. A PL spectrum corresponds to the variation of a signal proportional to the number of emitted photons as a function of their wavelength (or energy).

From PL spectra, it is possible to identify the radiative recombination channels present in a sample, allowing for inferring their electronic band structure and the presence of defects (and their energetic location in the forbidden gap). Variations in excitation wavelength (above and below bandgap excitation), excitation density, and measurement temperature allow one to obtain further knowledge about the nature of the radiative centers and their dynamics. For instance, by changing the excitation wavelength, one can selectively promote the excitation of different electronic states and probe varying depths within the material due to the dependence on the absorption coefficient with the radiation wavelength. Moreover, from the dependence of the PL response on the excitation density and temperature, it is possible to determine the PL IQE of the material, which is defined as the ratio of the number of emitted photons to the number of absorbed photons [17,90].

Regarding investigations of the optical properties of III-N, the PL technique is perhaps the most used, as it provides information on the crystalline quality and the existence of defects. Several studies involving the identification of defect- or impurity-related bands and their characteristics in III-N, with particular emphasis on GaN, are found in the literature [17,90]. Identifying defects and understanding their properties are needed to eliminate them or reduce their detrimental effect on optoelectronic devices.

PLE is a complementary technique to PL. It involves scanning the excitation wavelength while monitoring a specific radiative recombination path (usually a PL band maximum), i.e., the emission wavelength is fixed. The excitation source can be a lamp connected to a monochromator or a tunable laser, allowing proper control of the excitation wavelength. In its essence, PLE aids in identifying the excitation paths that promote specific electronic transitions.

It is essential to note that PL studies on ultra-wide bandgap semiconductors, such as AlN and AlGaN with high AlN molar fractions, are constrained by the non-availability of light sources operating in the far UV region in the laboratories where the experiments are carried out. As a result, band-to-band photo-excitation is not possible, with PL studies being restricted to sub-gap excitation mediated by defects with energy levels in the forbidden gap. CL spectroscopy is usually carried out to overcome the light source limitation. In these experiments, electron beams accelerated to a few tens of kV are directed towards the samples, resulting in their impact excitation and ionization by inelastic scattering of the hot electrons with the lattice atoms, which is a necessarily different mechanism from excitation in PL. Due to the high energy of the beam, CL allows to observe luminescence through all the radiative paths available in the sample. Furthermore, as CL experiments involve the introduction of electrons, they may lead to changes in the charge balance within the material, potentially affecting and modifying the recombination pathways.

EL is a different luminescence technique in which the excitation proceeds by injecting carriers in the material. This one is essential for developing light-emitting devices, as it mimics their operationalization. In such experiments, the excitation can involve *i)* the introduction of oppositely charge carriers in an active region, as in a p-n junction, and the recombination proceeds similarly to PL experiments, or *ii)* the acceleration of hot carriers in a strong electric field, in this case, the excitation is similar to CL.

2.4. Electrical doping

III-N are an established reference semiconductor family for optoelectronics. This is due to their remarkable intrinsic properties and the possibility of doping them with shallow donors and acceptors, i.e., n- and p-type doping. The latter is essential for enhancing their

electrical conductivity and, therefore, for realizing p-n junctions, which are fundamental building blocks for numerous optoelectronic devices, including light-emitting diodes [104–106].

2.4.1. n- and p-type doping of AlGaN

Before discussing the doping of AlGaN systems with n- and p-type dopants, it is essential to mention that they exhibit an n-type conductivity even when undoped. At first, native defects that introduce donor-like states, like V_N, were invoked as responsible for such background conductivity. However, J. Neugebauer and C. Van de Walle demonstrated that such conductivity would only be possible for large concentrations of these defects, which would be energetically unfavorable due to their high formation energy. Instead, they attributed the background n-type conductivity to Si and O impurities unintentionally introduced during growth [107,108].

One key concept to grasp is that the Fermi level depends on the doping level as the distribution of electrons and holes in the material changes; E_F shifts towards the CB for n-type doping and the VB for p-type doping [72]. Hence, the formation energy of defects can be changed, as well as their charge state. Indeed, to reach thermodynamic equilibrium, the system tends to form native defects that behave as compensating centers, contributing to the reduction of doping efficiency [108]. For instance, the formation of compensating V_{III} acceptors is likely to occur in n-type doped III-N; in the same way, V_N donors are more likely to be formed in p-type doped III-N [107,108]. A direct consequence of the compensation effect is that the effective doping ends up being lower than the concentration of dopants introduced, $N_{eff} = |N_D - N_A|$, with N_D and N_A the respective concentration of donors and acceptors.

The concentration of free carriers contributing to the electrical conductivity depends on *i)* the effective doping and *ii)* the combination of the dopant's ionization energy and the thermal energy. The last point implies that the ionization energy of the dopant should be as close as possible to the thermal energy, ensuring that most of the dopants are ionized and provide free carriers that contribute to the conductivity. Hence, donors (acceptors) must introduce shallow states close to the CB minimum (VB maximum) to guarantee they are ionized at RT (E_T is ~26 meV). Consequently, a high concentration of dopants does not necessarily mean a high concentration of free carriers.

Doping with Si is the typical procedure to achieve n-type conductivity in GaN (excluding background conductivity). In this case, Si dopants tend to incorporate Ga sites (Si_{Ga}), which act as shallow donors with ionization energy lying between 22–30 meV (both experimentally obtained and calculated values) [109–111]. With increasing Si concentration in the lattice, donors' electrons start interacting with each other, with the discrete donor

energy splitting into a band of energies, which can overlap with the bottom of the CB [72]. For Si in GaN, this is observed for free electron densities starting at ~10^{18} cm^{-3} [112]. In this regime, the semiconductor is said to be degenerate and presents properties similar to metals, i.e., metallic-like behavior.

Like for GaN, Si is the most used n-type dopant for AlGaN; however, with the increase in the AlN molar fraction, the ionization energy increases significantly, reaching values of about 282 meV for AlN [113]. One explanation is that Si atoms no longer occupy the cation sites responsible for the shallower donor states for high AlN molar fractions. Instead, they occupy interstitial sites, which results in a donor state *DX* with a much larger ionization energy. Furthermore, the formation energy of acceptor centers that can compensate for donor effectiveness, like V_{Al} defects or their complexes with O impurities, decreases [22]. These problems make the n-type doping of AlN more challenging than in GaN. Recently, M. Breckenridge demonstrated that ion-implanted Si can remain in the substitutional site, which introduces a shallow donor state with an ionization energy of ~70 meV after annealing at 1200 ℃, rather than relaxing into the deeper *DX* state [114].

Regarding p-type doping of III-N, Mg is the most common dopant. In GaN, Mg tends to replace the Ga atom (Mg_{Ga}), acting as an acceptor with an ionization energy of about 210–224 meV [109,115]. This value is much higher than the ionization energy of Si in GaN. Furthermore, Mg acceptors are compensated by native defects (e.g., V_N) and can be passivated by hydrogen impurities incorporated during growth, making p-type doping less effective than n-type doping. The dissociation of Mg-H complexes was achieved by post-growth thermal annealing or low-energy electron beam irradiation and was one of the reasons for the attribution of the Nobel Prize in Physics in 2014. For Mg-doped GaN growth by molecular beam epitaxy (MBE), A. Hoffman et al. reported that p-conductivity could be obtained without realizing post-growth treatments [116].

As for Si, the ionization energy of Mg acceptors in AlGaN alloys increases for higher AlN molar fractions. For Mg-doped AlN, the ionization energy is reported to be between 510–630 meV [113,117]. This implies that only a residual fraction of acceptors are ionized at RT, hindering the achievement of p-type conductivity. The poor p-type conductivity is indeed one of the bottlenecks of the AlN-based technology, and achieving a solution to this problem would significantly improve the performance of deep ultraviolet LEDs.

The doping of AlGaN NWs presents distinct particularities due to the larger surface area-to-volume ratio, allowing a more efficient strain relaxation. However, it also increases the preponderance of dangling bonds and adsorbed species at the surface [118,119]. These surface states can trap charge carriers, leading to Fermi-level pinning, which can result in a conductive or insulating layer at the surface of the NWs. The pinning of the Fermi level at the surface depends on the density and energy of the surface states, as well

as on the doping level. This complicates the comprehension of electrical transport in NWs [19].

Concerning Si doping of GaN NWs, Z. Fang et al. demonstrated that incorporating Si dopants can be enhanced in NWs compared to 2D counterparts [120]. For the most heavily doped samples, the authors measured by high-resolution (HR) energy-dispersive X-ray spectroscopy (EDX) Si concentrations of ~3×10^{20} cm^{-3} accompanied by a Si-enriched shell with a concentration of ~6×10^{20} cm^{-3} and thickness ranging from 10 to 40 nm; these values are above the predicted solubility limit of Si in GaN (~5×10^{19} cm^{-3} at N-rich conditions [121]). Free electron concentrations up to 10^{20} cm^{-3} were obtained. The mechanism responsible for this was tentatively assigned to the eased strain relaxation in NWs or a decrease in Si incorporation energy in NWs [120]. Recently, E. Aybeke et al. reported the formation of a high resistive shell in similar Si-doped GaN NWs, which was attributed to the accumulation of crystallographic defects in the periphery of the NWs due to the Si doping level above the solubility limit [122]. In the same work, E. Aybeke et al. showed that Mg concentration in GaN NWs is 4–40 times higher at the periphery (concentrations in the 10^{20} cm^{-3} range) than in the core, resulting in a highly conductive shell [122].

In the case of Si-doped AlN NWs, R. Vermeersch et al. observed that Si can incorporate the shallow Si_{Al} donor state with ionization energy of ~75 meV [123,124], similar to that obtained by M. Breckenridge in Si-implanted AlN layers [114]. Two *DX* states, with ionization energies of ~150 meV and ~270 meV, were also identified [123,124], the latter matching the *DX* state commonly observed in Si-doped AlN layers [113]. The increase in Si concentration resulted in increased incorporation in *DX* states, with the shallow donor's configuration absent for Si concentrations above ~10^{19} cm^{-3}. Between donor ionization energy of 270 and 75 meV, the increase in free electron concentration is significant at RT and would allow the realization of conductive n-AlN [123,124].

As mentioned above, Mg acceptors in AlN have ionization energies of more than 500 meV and are highly compensated by native defects with an n-type character. Despite challenges encountered in AlN layers, highly Mg-doped AlN NWs have demonstrated improved conduction properties. This has been attributed to the lower formation energy of the Mg_{Al} acceptor state when growing AlN NWs in N-rich conditions (conditions typically employed in the MBE growth of AlN NWs); at the same time, the formation of V_N-related defects that act as compensating centers is suppressed [125,126]. Furthermore, due to the band tailing effect and broadened Mg energy levels associated with the higher concentration of Mg, the ionization energy can be reduced, contributing to an enhanced p-type conductivity [126]. Free hole concentrations of ~6×10^{17} cm^{-3} have been derived for AlN NWs [127], which are orders of magnitude higher than p-type AlN layers grown by

MOVPE [113]. N. Tran et al. proposed that hole-hopping conduction in the Mg impurity band was responsible for unusually high hole concentrations [127].

Recently, A.-M. Siladie et al. proposed that the p-type efficiency in AlN NWs could be improved by co-doping with Mg and indium. Indium atoms would passivate at some extent the V_N donors that compensate for Mg acceptors, allowing for an enhanced incorporation of Mg into AlN. Despite the possible incorporation of Mg beyond a level of ~1.5×10^{20} cm^{-3} for indium concentrations of ~3×10^{18} cm^{-3}, the impact on transport properties has not been fully understood [128].

2.4.2. Basics of p-n junction LEDs

A p-n junction is the physical junction between a p-type and an n-type doped semiconductor. At the junction's interface, a concentration gradient exists due to the surplus of holes on the p-side and electrons on the n-side, leading to the diffusion of electrons from the n-side into the p-side and vice-versa for holes. As electrons diffuse, positively charged donors are left immobilized in the n-region; likewise, the diffusion of holes leaves negatively charged acceptors in the p-region. These positive and negative space charges induce an electric field in a region close to the junction's interface, known as the depletion region. This electric field, which points from the n- to the p-side of the junction, opposes the continuous diffusion of charges; that is, the field induces a drift of holes back to the p-side and electrons to the n-side [72,74].

At thermal equilibrium conditions, drift and diffusion currents cancel out each other; then, the net current is zero. In this situation, the charge distribution and the electric field acquire a stationary configuration. Furthermore, as the Fermi level must be the same on both sides of the junction, the induced electric field results in a potential difference, designated as built-in potential (V_{bi}), between the n- and the p-sides of the junction. This potential barrier prevents the flow from majority carriers: electrons from the n-side to the neutral p-doped region and holes from the p-side to the neutral n-side [72,74]. **Figure 2.13(A)** depicts the band diagram of a p-n junction at thermal equilibrium before and after physical contact (no applied bias).

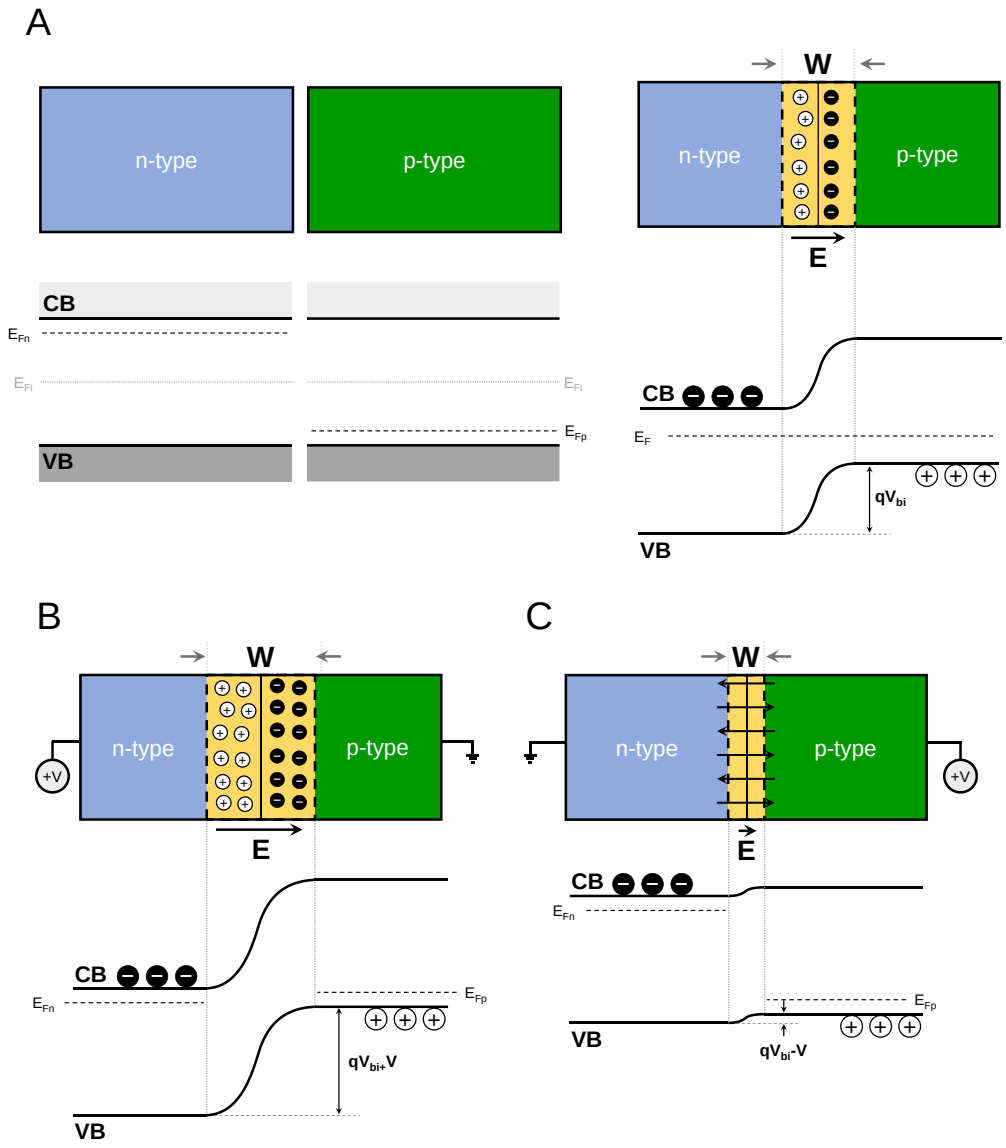

Figure 2.13 (A) Schematic representation of the energy band diagram of a p-n junction before and after physical contact in thermal equilibrium. **(B, C)** Band diagram of a p-n junction under reverse and forward bias, respectively. E_{Fi} is the intrinsic Fermi level, while E_{Fn} and E_{Fp} are the Fermi level on the n- and p-side of the junction, respectively. Adapted from reference [72].

When a p-n junction is subjected to an external bias, the physical parameters established under equilibrium conditions are changed. Such a bias can either heighten or diminish the potential across the depletion region, giving rise to two distinct operational regimes: *i)* reverse bias, in which a positive bias is applied to the n-side of the junction, and *ii)* forward bias, when the positive bias is applied to the p-side [72,74].

Figure 2.13(B) shows the energy band diagram of a p-n junction under reverse bias. In this situation, the potential barrier for the majority carriers (electrons in the n-side and

holes in the p-side) increases, further conditioning their diffusion. On the other hand, minority carriers do not feel the barriers, and their drift causes a small current, designated as saturation current, I_s. Under these conditions, the Fermi level on the n-side is located below the Fermi level on the p-side, with the difference between the Fermi level on both sides of the junction corresponding to the applied bias (in energy units) and being responsible for the increase in the potential barrier. Because of this, the number of positive and negative charges in the depletion region increases (larger depletion region), resulting in a stronger electric field [72,74].

Figure 2.13(C) illustrates the diagram of a p-n junction under forward bias. In this regime, the applied potential opposes the built-in potential, reducing the potential barrier between n- and p-regions. In contrast to the reverse bias scenario, the Fermi level on the p-side is lower than the corresponding on the n-side, and the width of the depletion region decreases. As the forward bias increases, the diffusion of majority carriers through the space charge region becomes progressively more likely. If the bias exceeds V_{bi}, electrons from the n-side can flow easily to the p-side, and vice-versa for holes. This signifies that minority carriers are injected into the n- and p-sides of the junction, generating a current across the p-n junction. Depending on the lifetime of the minority carriers in these regions, they will eventually recombine radiatively or non-radiatively with majority carriers [72,74,129]. The possible recombination mechanisms are those identified in **subsection 2.3.2**. Typically, in a semiconductor p-n junction LED, the radiative recombination associated with NBE luminescence is intended to be the favored process.

The I–V characteristics of an ideal p-n junction can be derived from the Shockley model, which is based on four assumptions. These assumptions encompass *i)* the existence of abrupt boundaries and the neutrality of the semiconductor outside of the depletion region; *ii)* the consideration of the Maxwell-Boltzmann distribution to describe carrier statistics; *iii)* the complete ionization of dopants, and a considerably lower concentration of injected minority carriers than the concentration of majority carriers (low injection conditions); and *iv)* the constancy of the total current in the junction, which is the sum of the individual electron and hole currents that remain constant throughout the depletion region and are continuous functions throughout the p-n junction. In the Shockley model, the equation that governs the relationship between I and applied voltage (V) for an ideal p-n junction is expressed as follows [72,129]:

$$I = I_s \left[\exp\left(\frac{eV}{k_B T}\right) - 1 \right]. \tag{2.30}$$

This equation can be re-written as [72,129]:

$$I = I_s \left[\exp\left(\frac{eV}{\eta k_B T}\right) - 1 \right], \tag{2.31}$$

where η is the ideality factor that accounts for additional contributions to the current in a p-n junction that cannot be solely described by the ideal case, where $\eta = 1$. For instance, when the current resulting from the loss of injected carriers into the depletion region due to recombination with oppositely charged carriers (recombination current) is the dominant contribution to the total current flowing across the p-n junction, $\eta \approx 2$ [72]. Essentially, values of η other than 1 means a deviation from the ideal p-n junction behavior.

In practice, the experimental fitting of the *I*–*V* characteristics of a p-n junction LED often considers parasitic resistances. These can be modeled by introducing a shunt resistance (R_{par}) in parallel with the ideal diode and a resistance (R_s) in series with the ideal diode and the shunt resistance. The parallel resistance accounts for current pathways bypassing the p-n junction; for example, dislocations can lead to alternative paths dodging the junction. Conversely, the series resistance describes the resistance encountered at the contacts and within the neutral regions of the p-n junction.

Considering the parasitic resistances, the potential drop across the p-n junction LED differs from the ideal case. That said, the Shockley equation can be reformulated as [129]:

$$I - \frac{V - IR_s}{R_{par}} = I_s \exp\left(\frac{e(V - IR_s)}{\eta k_B T}\right). \tag{2.32}$$

This is known as the modified Shockley equation and tends toward equation (2.31) when $R_{par} \to \infty$ and $R_s \to 0$. R_p primarily influences the reverse current, providing an alternative path that bypasses the junction, whereas, R_s tends to limit the current flowing through the device at high forward bias.

In III-N-based LEDs, an undoped (or intrinsic) region is generally introduced between the n- and p-type regions, forming a p-i-n structure. This intrinsic region often consists of multi-quantum wells (active region), which confines the carriers and promotes their recombination in the active region of the LED. Additional modifications to the device's structural design are typically employed, namely introducing an electron-blocking layer to mitigate leakage of electrons from the active region [76,130].

While III-N LEDs are the solid-state solutions with the highest EQE values for blue and green emitters,[q] experimentally extracted ideality factors can be significantly higher than 2 (between 2.5 and 50) [131–139]. Several factors have been proposed to account for

[q] The efficiency-related figures of merit of p-n junction LEDs (EQE, IE, IQE, and LEE) were already discussed in **subsection 0**.

these abnormally high ideality factors observed in III-N LEDs. These include trap-assisted tunneling effects, non-linearly doped junctions, poor doping efficiency, or non-optimized contacts (e.g., Schottky contacts instead of ohmic contacts) [140,141]. J. Shah et al. proposed that the experimentally determined ideality factors represent the summation of ideality factors associated with various individual junctions within the device (e.g., the p-n junction, metal-semiconductor junctions, and other interfaces in the device) [135].

2.5. Optical doping with lanthanoids

Lanthanoids, or lanthanides, correspond to a particular group of elements in the Periodic Table of elements that include those ranging from lanthanum (atomic number, $Z = 57$) (lanthanum) to lutetium ($Z = 71$) [142]. They have an identical electronic structure of the type [Xe] $4f^m\,6s^2$,[r] with m representing the number of electrons in the $4f$ shell ($0 \leq m \leq 14$). Lanthanum, cerium, gadolinium, and lutetium, are exceptions to this rule since they possess an extra $5d$ electron [143]. Together with scandium and yttrium, whose elementary substances have similar chemical properties, they constitute the rare-earth elements.

When incorporated into compounds, these lanthanoids tend to be stabilized in their positive trivalent charge state due to the removal of the two $6s$ electrons and one of the $4f$ electrons (or the extra $5d$ electrons, when it is the case)[s] [143]. Hence, the electronic structure of lanthanoids becomes [Xe] $4f^M$, with M assuming integer values from 1 (cerium) to 13 (ytterbium)[t]. Since the radial extension of the filled $5s$ and $5p$ orbitals is larger than that of the partially filled $4f$ orbitals (exemplified in **Figure 2.14**), $4f$ electrons are shielded from interacting with the host's ligands, i.e., with the surrounding environment. Because of this, electronic transitions within the $4f$ manifold result in sharp emission lines whose energy is almost independent of the host [143].

Doping with lanthanoids is a common approach to tailor the optical properties of III-N since different emission wavelengths can be obtained by choosing the adequate Ln^{3+} species to be incorporated. For example, when the red emission color is pretended, Eu^{3+} is a dopant of choice; samarium (Sm^{3+}) and praseodymium (Pr^{3+}) can also be used. For obtaining a blue emission, one considers the use of thulium (Tm^{3+}), while a green emission is achieved by doping with erbium (Er^{3+}) or terbium (Tb^{3+}) [144]. It should also be noted that: *i)* Ln^{3+} may

[r] [Xe]: is $1s^2\,2s^2\,2p^6\,3s^2\,3p^6\,3d^{10}\,4s^2\,4p^6\,4d^{10}\,5s^2\,5p^6$.

[s] Despite commonly found in their trivalent charge state, certain lanthanoids can also be stabilized in divalent (e.g., europium) or tetravalent (e.g., cerium) charge states [143].

[t] For the trivalent La and Lu ions, M is respectively 0 (empty $4f$ orbital) and 14 (filled $4f$ orbital); consequently, they are not of interest for optical applications and will be no longer discussed.

lead to characteristic emission lines at various wavelengths (e.g., Er^{3+} has characteristic emissions in the green and infra-red), and *ii)* the host must be transparent in the spectral region of the intended emission.

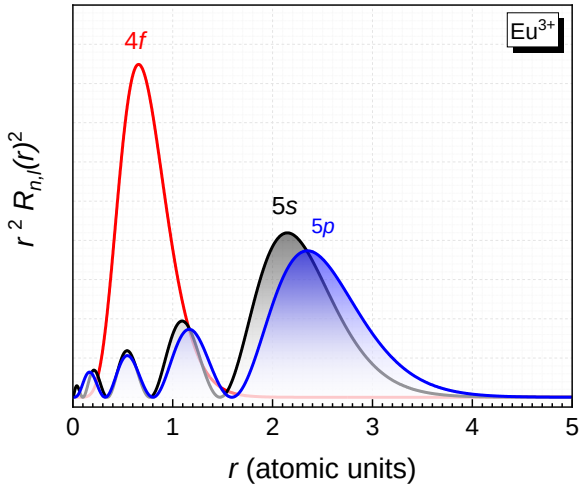

Figure 2.14 Radial function distribution of the $4f$, $5s$, and $5p$ orbitals for Eu^{3+} (in atomic units, 1 Bohr radius = 52.9 pm), constructed by assuming the central-field potential function $U(r)$ as being analogous to that of the hydrogen atom, modulated by an effective nuclear charge $Z_{\text{eff}}e$, with Z_{eff} the effective nuclear charge for the respective orbital in the ion [145].

2.5.1. Fundamentals of trivalent lanthanoid ions

A fundamental understanding of the electronic energy levels of Ln^{3+} is essential when characterizing their optical properties in different hosts. The procedure to determine the energy, E_{Ln}, of the electronic states of Ln^{3+} relies on quantum mechanics and consists of solving the time-independent Schrödinger equation, $\mathcal{H}_{\text{Ln}}\mathbf{\Psi} = E_{\text{Ln}}\mathbf{\Psi}$, where $\mathcal{H}_{\text{Ln}}$ is the Hamiltonian operator whose observable corresponds to the total energy of the ion, and $\mathbf{\Psi}$ is the wave function that describes the ion [143]. However, solving this problem for multi-electron systems is not simple, and unless certain approximations are assumed, it is impossible to find an exact solution. The standard methodology starts from the free-ion case and then treats the crystal-field interaction as a perturbation to the free-ion solutions. This is a reasonably valid approach once the $4f$ electrons are slightly affected by the crystal due to the shielding imparted by the filled $5s$ and $5p$ orbitals.

2.5.1.1. Free-ion interactions

The discussion begins by considering the free-ion problem and assuming that the nuclear mass is infinite compared to the mass of the electrons (Born-Oppenheimer approximation) [143,146]. The Hamiltonian that describes a multi-electron free-ion, $\mathcal{H}_{\mathrm{FI}}$, can be defined as $\mathcal{H}_{\mathrm{FI}} = \mathcal{H} + \mathcal{H}_{\mathrm{SO}}$, where $\mathcal{H}$ is the non-relativistic Hamiltonian for an N-electron ion with a nuclear charge Ze, and $\mathcal{H}_{\mathrm{SO}}$ is the Hamiltonian contribution that refers to the SO coupling, i.e., the interaction of the electron's spin with its orbitally induced magnetic field. These two contributions can be written as [146]:

$$\mathcal{H} = \frac{-\hbar^2}{2m_0}\sum_{i=1}^{N}\nabla_i^2 - \sum_{i=1}^{N}\frac{Ze^2}{\mathbf{r}_i} + \sum_{i<j}^{N}\frac{e^2}{\mathbf{r}_{ij}}, \text{and} \tag{2.33}$$

$$\mathcal{H}_{\mathrm{SO}} = \sum_{i=1}^{N}\xi(r_i)\ \mathbf{l}_i \cdot \mathbf{s}_i. \tag{2.34}$$

The summation involving i is over all the N-electrons of the ion. The various contributions to $\mathcal{H}$ correspond to the kinetic and potential energies of all the N electrons, as well as to the repulsive Coulomb potential energy resulting from the interaction between pairs of electrons distanced by $\mathbf{r}_{ij}$. In what concerns to the $\mathcal{H}_{\mathrm{SO}}$ contribution, $\xi(r_i)$ corresponds to the spin-orbit coupling constant and is a function of r_i, while $\mathbf{l}_i$ and $\mathbf{s}_i$ are the angular orbital and spin momentum of individual electrons, respectively.

Let one first focus on the non-relativist Hamiltonian. Exact solutions of the Schrödinger equation are impossible to obtain for multi-electron ions because $\mathcal{H}$ is not spherically symmetric. A possible methodology to solve this problem is to consider the central field approximation, which assumes each electron moves independently and feels the potential field of the nucleus and a spherically averaged potential field resulting from the interaction with all the other electrons, $U(\mathbf{r}_i)$. Each electron is said to move in a spherically symmetric central field Hamiltonian, $\mathcal{H}_{\mathrm{cf}}$, described by [146]:

$$\mathcal{H}_{\mathrm{cf}} = \sum_{i=1}^{N}\left[\frac{-\hbar^2}{2m}\nabla_i^2 + U(\mathbf{r}_i)\right]. \tag{2.35}$$

The non-spherically symmetric contributions of $\mathcal{H}$ are restrained to the difference $\mathcal{H} - \mathcal{H}_{\mathrm{cf}}$ and will be treated later as a perturbation to the solution of the central field Hamiltonian. By combining equations (2.33) and (2.35), the electrostatic potential term of the Hamiltonian is rewritten as:

$$\mathcal{H} - \mathcal{H}_{\mathrm{cf}} = -\sum_{i=1}^{N}\left[\frac{Ze^2}{\mathbf{r}_i} + U(\mathbf{r}_i)\right] + \sum_{i<j}^{N}\frac{e^2}{\mathbf{r}_{ij}}. \tag{2.36}$$

Considering the central field Hamiltonian, the solution of the time-independent Schrödinger equation can be constructed as a linear combination of the one-electron solutions (Hartree-Fock method) [146]:

$$\Psi = \sum_{i=1}^{N} \varphi_i(a^i) \quad \text{and} \quad E_{\text{cf}} = \sum_{i=1}^{N} E_i, \tag{2.37}$$

where (a^i) represents a set of quantum numbers $(n\ l\ m_l)$ that specify the electronic state of a single electron. This corresponds to saying that the i^{th}-electron is characterized by three quantum numbers: the principal quantum number n (positive integer values, $n = 1, 2, 3, ...$), the orbital angular momentum quantum number l (integer values, $l = 0, 1, ..., n-1$), and the magnetic quantum number m_l (integer values, $m_l = -l, -l+1, ..., l$), which results from the space quantization of the orbital angular momentum, i.e., is the projection of l along the z-axis.

For each electron, the quantum mechanical solution is like that of the hydrogen atom, differing only in the replacement of the potential energy $(-e^2/r)$ by the central field potential energy function, $U(r)$. A significant consequence of the spherical symmetry of the central field potential is that the wave functions can be separated in their radial (r) and angular parts (θ, ϕ). The resulting normalized wave function of the i^{th}-electron can then be expressed as [143,146]:

$$\varphi_i(a^i) = \frac{1}{r} R_{n,l}(r) Y_{l,m_l}(\theta, \phi). \tag{2.38}$$

The radial function, $R_{n,l}(r)$, will depend on the central field potential energy function $U(r)$ considered. On the other side, the angular part of the wave function, $Y_{l,m_l}(\theta, \phi)$, can be determined and corresponds to the spherical harmonics of degree l and order m_l [146].[u]

[u] The spherical harmonics can be written as $Y_{l,m_l}(\theta, \phi) = (-1)^m \left[\frac{(2l+1)(l-|m|)!}{4\pi(l+|m|)!}\right]^{\frac{1}{2}} P_{l,m_l}(\cos\theta) e^{im_l\phi}$, where P_{l,m_l} corresponds to the Legendre polynomials. The angular coordinates vary between $[0, \pi]$ for θ and between $[0, 2\pi]$ for ϕ [146].

By considering the electron's spin, the wave function in equation (2.38) must be multiplied by a spin function, σ_{m_s}. Another quantum number is then necessary to describe the i^{th}-electron, the electron spin quantum number, m_s ($= \pm\frac{1}{2}$). Consequently, (a^i) needs to be replaced by (α^i), corresponding to the four quantum numbers (n l m_l m_s) that describe the configuration of the i^{th}-electron. In this case, the spin orbitals $\varphi_i(\alpha^i)$ are [143,146]:

$$\varphi_i(\alpha^i) = \frac{1}{r} R_{n,l}(r) Y_{l,m_l}(\theta,\phi)\sigma_{m_s}, \tag{2.39}$$

To satisfy the Pauli exclusion principle, which states that two or more electrons cannot occupy the same quantum state, the wave functions of the multi-electron ion need to be antisymmetric concerning the simultaneous permutation of the spin and spatial coordinates of any pair of electrons. Thus, the antisymmetric solution of the central field wave functions for N-electrons might be written in the determinantal form (Slater determinant) [143,146]:

$$\mathbf{\Psi} = \frac{1}{\sqrt{N!}} \begin{vmatrix} \varphi_1(\alpha^1) & \varphi_2(\alpha^1) & \ldots & \varphi_N(\alpha^1) \\ \varphi_1(\alpha^2) & \varphi_2(\alpha^2) & \ldots & \varphi_N(\alpha^2) \\ \vdots & \vdots & & \vdots \\ \varphi_1(\alpha^N) & \varphi_2(\alpha^N) & \ldots & \varphi_N(\alpha^N) \end{vmatrix}. \tag{2.40}$$

These wave functions are the basis for the perturbative terms considered next.

The next move is to consider the non-spherically symmetric terms of the free-ion Hamiltonian, i.e., electrostatic repulsion and spin-orbit interactions. These contributions are treated as perturbative terms and split a specific configuration into different energy levels. A new set of basis states capable of fully describing them is necessary. The way to do that is by recurring to a coupling scheme of momenta summation. The most common ones are the LS (or Russell-Saunders) and the *j-j* coupling schemes. The first is a good choice for lighter ions, i.e., when spin-orbit interactions are smaller than the electrostatic ones. The *j-j* coupling scheme is used when Z increases, and the spin-orbit interactions become more significant (heavier ions).

In the case of Ln^{3+}, both interactions are of the same order of magnitude; therefore, none of the coupling schemes gives a precise solution. An intermediate coupling scheme must be employed to determine the energy level structure correctly. However, for the sake of simplicity, their calculation is usually developed from the LS coupling scheme, as will be done next.

In the LS coupling scheme, the orbital angular momenta of electrons are vectorially summed to give a resultant total orbital angular momentum vector $\mathbf{L} = \sum_{i=1}^{N} \mathbf{l}_i$. Likewise, the spin momentum of individual electrons also couple, resulting in a total spin momentum vector $\mathbf{S} = \sum_{i=1}^{N} \mathbf{s}_i$. L and S represent the magnitude of the orbital angular and spin

momenta vectors. Because of the SO interaction, both angular momenta couple, leading to a total angular momentum vector $\mathbf{J} = \mathbf{L} + \mathbf{S}$.[v] The resultant vector $\mathbf{J}$ has a magnitude J, and its projection along the z-axis is represented by M_J. J and M_J are restricted to the values [143]:

$$J = L + S, L + S - 1, \ldots, |L - S| \quad \text{and} \quad M_J = -J, -J + 1, \ldots, J. \tag{2.41}$$

Considering the electrostatic and SO interactions, the degenerated energy states associated with the $4f$ configuration are split into different energy levels called multiplets. The energetic separation between different multiplets (of the order of 10–100 meV or ~10^2–10^3 cm^{-1}) is much smaller than that between $4f^M$ and other excited configurations, like $4f^{M-1}\,5d^1$ (~10 eV or ~10^5 cm^{-1}) [143]. Each multiplet has a degeneracy of $2J$+1 and is characterized by the quantum numbers ($n\ l\ \tau\ L\ S\ J\ M_J$). Here, τ is the seniority number, an additional quantum number that is frequently used to differentiate between terms defined by identical L and S [143,146].

The electronic states associated with multiplets are usually represented using the ${}^{2S+1}L_J$ terms. In the LS notation, L is represented by a capital letter informing about its value; for example, for $L = 0, 1, 2, 3,$ and 4, the letters S, P, D, F, and G are used. For equivalent electrons[w], as is the case of $4f$ electrons, the multiplets can be easily determined when the problem involves only two electrons. As the number of $4f$ electrons to consider increases, determining LS eigenstates becomes more difficult due to many possible combinations and is done computationally.

Taking advantage of Hund's rules, it is possible to determine the quantum numbers that define the fundamental (ground) state without substantial mathematical complications. First, the term with the maximum S value has the lowest energy. For states with the same spin multiplicity, the ground state is that with the highest L. The third and last rule defines that the ground state has the lowest (highest) possible J value for electronic shells that are less (more) than half-filled. The above rules can predict the lowest energy term but not necessarily order all the terms. This happens because the electronic structure of the ion is more accurately described by a configuration interaction and not by a single configuration as considered in the previous analysis [147].

[v] This analysis does not require consideration of electrons not in the $4f$ orbital, since contributions of electrons in filled shells cancel each other, i.e., $\mathbf{L} = \mathbf{S} = 0$.

[w] Equivalent electrons are those that share the same quantum numbers n and l.

Still, as electrostatic and spin-orbit interactions are close in magnitude (intermediate coupling), the multi-electron wave functions are no longer described by the wave functions associated with the quantum numbers ($n\ l\ \tau\ L\ S\ J\ M_J$), i.e., by pure Russell-Saunders terms. Instead, they correspond to linear combinations of states with the same total angular momentum, J. The coefficients of these combinations are referred to as intermediate coupling coefficients. Therefore, one needs to be careful when referring to a $^{2S+1}L_J$ multiplet because it is just a mere indication of the dominant component of the state [143,146].

Electrostatic and spin-orbit interactions give the proper order for the energy splitting of the $4f^M$ configuration. However, additional interactions (e.g., other relativistic effects and configuration interactions) should be considered for a complete and accurate calculation of the energy levels capable of reproducing the experimental results. In that way, the free-ion Hamiltonian can be parametrized with the total effective-operator Hamiltonian given by [143]:

$$\begin{aligned}\mathcal{H}_{\mathrm{FI}} = \ & E_{\mathrm{avg}} + \sum_{k=0,2,4,6} F^k f_k + \zeta_{nl} A_{\mathrm{so}} + \alpha L(L+1) + \beta G(G_2) + \gamma G(R_7) \\ & + \sum_{i=2,3,4,6,7,8} t_i T^i + \sum_{i=0,2,4} m_i M^i + \sum_{i=2,4,6} p_i P^i.\end{aligned} \tag{2.42}$$

The first term (E_{avg}) represents the spherical part of the free-ion and can be omitted without a lack of generality since it only produces an energy shift equal for all the multiplets in a given configuration. The second term, expressed in terms of products of Slater radial integrals (F^k) and angular coefficients (f_k), is the parametrized contribution associated with the electrostatic interaction. The third term contains the spin-orbit interaction, in which ζ_{nl} is a radial integral and A_{so} represents the angular part of the interaction. The fourth, fifth, sixth, and seventh terms of the parametrized Hamiltonian describe the interactions between configurations of the same parity (two- and three-body interactions). α, β, and γ are linear combinations of radial integrals and are treated as adjustable parameters associated with the two-body correction terms; L is the total orbital angular momentum, while $G(G_2)$ and $G(R_7)$ are the eigenvalues of Casimir's operators for the groups G_2 and R_7 (tabulated values [146]). The three-particle configuration interaction terms are considered for $M \geq 3$; t_i and T^i represent the three-body operators and respective parameters. The last two terms of the parametrized Hamiltonian describe spin-spin and spin-other-orbit relativistic interactions. Here, m_i and p_i are the operators for the magnetic corrections, and M^i and P^i are the parameters associated with the respective operators [143]. The various parameters associated with the free-ion operators are adjustable in fitting experimental data.

A complete analysis of the mathematical formalism and the parametrization procedure are beyond this thesis's scope. A more thorough analysis can be found in the dedicated references [143,146,148,149].

The determination of the $^{2S+1}L_J$ states for the different Ln^{3+} is commonly embodied in Dieke's diagram. This representation chart was created for Ln^{3+} in $LaCl_3$ compounds based on the spectra analysis between 0–40000 cm^{-1} [150]. **Figure 2.15** shows the complete $4f$ energy level diagram for Ln^{3+} into LaF_3 hosts calculated by P. Peijzel et al. [151] using the parameters previously determined by W. Carnall et al. [152]. Several contributions have been made over the years in improving such calculations by optimizing the interaction parameters and studying the influence of the host (not considered up to now in this discussion). However, Dieke's diagram is often the basis for analyzing the spectroscopic properties of Ln^{3+} incorporated into crystals, even though slight energetic changes can occur.

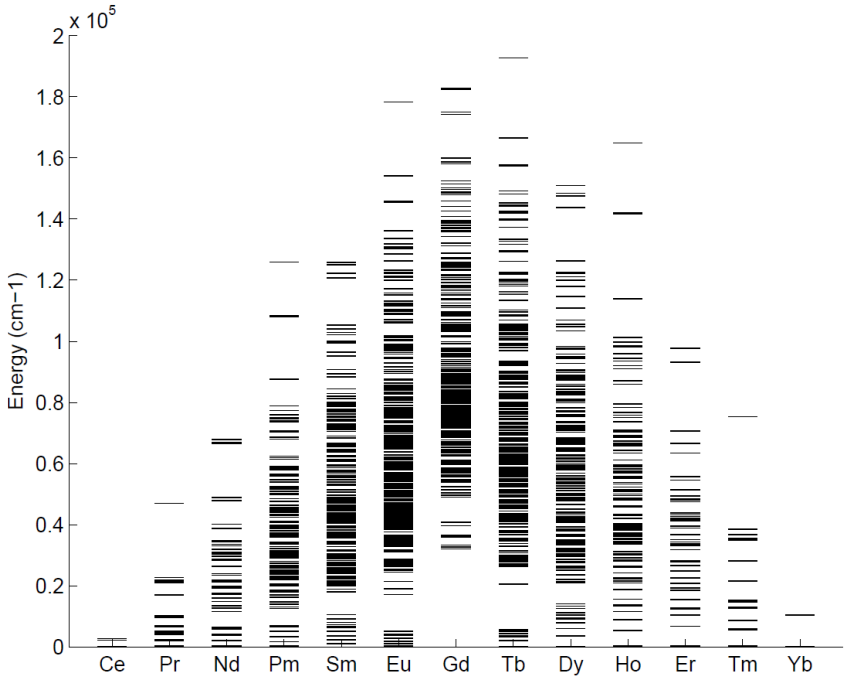

Figure 2.15 Complete $4f^M$ energy level diagram (in cm^{-1}) for Ln^{3+} in LaF_3 compounds (Dieke's diagram). Reprinted from reference [151].

2.5.1.2. Crystal field interactions

When inserted into a crystal, Ln^{3+} experience an electric field generated by the surrounding charge distribution, referred to as a crystal field. Due to the shielding provided by $5s$ and $5p$ electrons, the effect of the crystal field potential (V_{host}) on $4f$ electrons is small

and can be handled as a perturbation to the free-ion Hamiltonian. The Hamiltonian capable of fully describing the electronic structure of Ln^{3+} in solids is then given by:

$$\mathcal{H}_{\mathrm{Ln}} = \mathcal{H}_{\mathrm{FI}} + V_{\mathrm{host}}. \tag{2.43}$$

Although V_{host} does not significantly affect the energetic position of $4f$ levels, it breaks the spherical symmetry of the free-ion, causing the splitting of the $^{2S+1}L_J$ multiplets in a maximum of $2J+1$ sublevels, designated as Stark levels. Nevertheless, the importance of this interaction goes far beyond any energy shift (or splitting); indeed, the most relevant consequence is the admixture of states of different parity into the $4f$ states.

Assuming that the crystal field interaction can be treated as a point charge perturbation on the energy states of the Ln^{3+} free ions, the effective operators of the crystal field interaction should be defined in terms of the tensor operators of spherical harmonics, $C_q^k(i)$. According to B. Wybourne, V_{host} can then be expanded as [146]:

$$V_{\mathrm{host}} = \sum_i \sum_k \sum_{q=-k}^{k} B_q^k \, C_q^k(i). \tag{2.44}$$

Here, B_q^k are the crystal field parameters[x] that account for the radial dependency of the interaction and can be determined empirically from the experimental data. The index i runs over the $4f^M$ electrons of the ion. The values of k and q will be limited by the point symmetry of the ion in the crystal and are determined by the Wigner 3-j symbols[y]. For equivalent $4f$ electrons, the matrix elements of the crystal field Hamiltonian are non-zero only for $k = 0, 2, 4, 6$ (even terms for $k \leq 2l$) and $|q| \leq k$. The non-zero values of q depend on the point group of the site into which the ion is incorporated since the crystal field Hamiltonian has to be invariant under all symmetric operations of the point group [143,146].

The term B_0^0 corresponds to the zero-order of crystal field interaction and is spherically symmetric. Consequently, it does not split the free-ion energy levels but induces an energy shift to all levels in the same $4f^M$ configuration. The remaining terms describe the non-spherical part of the crystal field interaction and are responsible for splitting the $4f$ levels [143,146].

[x] They can also be written in Stevens' notation as $A_k^q \langle r^k \rangle$, with $\langle r^k \rangle$ the average value of r^k.

[y] The Wigner 3-j symbols $\begin{pmatrix} j_1 & j_2 & j_3 \\ m_1 & m_2 & m_3 \end{pmatrix}$ are quantities that arise in considering coupled angular momenta, which are generally used in the evaluation of the matrix elements of the crystal field Hamiltonian (expressed in terms of spherical harmonics) [143].

By treating the crystal-field as point charges, the potential felt by an Ln^{3+} possesses a specific symmetry, the same as the lattice site it occupies, which will act on the free-ion wave functions. Since the crystalline potential is expanded in terms of the spherical harmonics, one can use Group Theory to predict how the free-ion wave functions are transformed under specific symmetry operations[z]. Thus, one can use it to infer the number of Stark levels when the Ln^{3+} are incorporated into a lattice site belonging to a specific point group.

After some mathematical treatment (beyond the scope of this thesis), the non-zero values of q corresponding to a specific symmetry site can be determined. In other words, the non-vanishing crystal-field parameters can be determined by symmetry arguments. When reducing the site symmetry, the number of accessible parameters increases, leading to ${}^{2S+1}L_J$ multiplets being split into more Stark levels. W. Runciman determined the number of Stark levels into which a state of a given J value would split for each site symmetry [153], summarized in **Table 2.7** for integer J values between 0 and 6.[aa] For all point groups within a symmetry class, the splitting of a J-value is the same. The differences between point groups are reflected in the selection rules of the intra-4f transitions. For orthorhombic and lower symmetry, the degeneracy of the states with integer J values is fully lifted, i.e., they split into $2J + 1$ Stark levels.

Table 2.7 Number of Stark levels depending on the site symmetry for Ln^{3+} in a crystal (J integer between 0 and 6) [153].

Symmetry	**Point group**	***J***						
		0	**1**	**2**	**3**	**4**	**5**	**6**
Cubic	O_h, O, T_d, T_h, T	1	1	2	3	4	4	6
Hexagonal	D_{6h}, D_6, C_{6v}, C_{6h}, C_6, D_{3h}, C_{3h}, D_{3d}, D_3, C_{3v}, S_6, C_3	1	2	3	5	6	7	9
Tetragonal	D_{4h}, D_4, C_{4v}, C_{4h}, C_4, D_{2d}, S_4	1	2	4	5	7	8	10
Lower symmetry	D_{2h}, D_2, C_{2v}, C_{2h}, C_2, C_s, S_2, C_1	1	3	5	7	9	11	13

[z] By symmetry operations is meant a coordinates' transformation that does not produce a change in the physical properties of the system.

[aa] It was decided to present only the number of Stark levels to which states with integer J values between 0 and 6 split, as they are the values of interest for Eu^{3+}, the ion that will be studied in this thesis.

Whereas symmetry properties can determine the number of non-vanishing crystal-field parameters (and Stark levels), ascertaining their magnitude is not simple from a theoretical side. Therefore, they are usually obtained by treating them as adjustable parameters when fitting theory to experimental data.

2.5.1.3. Selection rules and Judd-Ofelt theory

A transition between two electronic states $\mathbf{\Psi}_i$ and $\mathbf{\Psi}_f$ can occur only if the matrix element $\mathbf{M} = \langle \mathbf{\Psi}_f | \boldsymbol{\mu} | \mathbf{\Psi}_i \rangle \neq 0$ (integral over all space), where $\boldsymbol{\mu}$ is the operator that connects the initial and final states. In truth, it is unnecessary to calculate $\mathbf{M}$ to ascertain the allowance or forbiddance of a transition. One can recur to the symmetry properties of the wave functions and the transition operator. For instance, the integral is non-zero only if the direct product is symmetric with respect to a symmetry center; that is, the direct product originates a function with even parity[bb]. This is the well-known Laporte's selection rule [68].

An optical transition between two electronic states implies the interaction of the ion with electromagnetic radiation, i.e., it deals with the absorption or emission of a photon. In quantum mechanics, this can be treated by considering a time-dependent perturbation theory to the stationary Hamiltonian of the ion due to the oscillating electromagnetic field. That said, electronic transitions can be assisted by electric dipole (ED), magnetic dipole (MD), or other minor contributions such as electric quadrupole. Depending on the nature of the transition, the transition matrix element can be calculated by replacing the generalized operator $\boldsymbol{\mu}$ with the adequate operator. For instance, the ED moment operator ($\mathbf{p}$) and the MD moment operator ($\mathbf{m}$) are given by [154]:

$$\mathbf{p} = -e \sum_i \mathbf{r}_i \quad \text{and} \quad \mathbf{m} = -\frac{e\hbar}{2m_0 c} \sum_i (\mathbf{L}_i + 2\mathbf{S}_i). \tag{2.45}$$

Then, to infer the allowance or forbiddance of an optical transition, the problem boils down to considering the symmetry properties of the dipole moment operators. On the one hand, the ED moment operator has odd parity since it leads to a sign change under inversion (i.e., $\mathbf{r} \rightarrow -\mathbf{r}$). Consequently, the states involved cannot have the same parity for a transition to be allowed by ED. On the other hand, the MD moment operator has even parity; so, for the matrix element to be non-zero, the wave functions of the initial and final states need to share the parity. The strength of ED transitions is usually much higher (~10^6 times) than those of MD nature [155].

[bb] The parity of the direct product between two functions is simply the product of their parities. For instance, the product of two odd or two even functions give an even function, while the product between an odd and an even function originates a function with odd parity.

Taking into account the parity of the ED and MD operators, pure intra-4*f* transitions within Ln^{3+} are prohibited by ED but are allowed by MD if the following selection rules are obeyed: $\Delta S = 0$, $\Delta L = 0$, and $\Delta J = 0, \pm 1$ ($0 \leftrightarrow 0$ is forbidden) [154]. The first two rules are often broken because the wave functions are not purely described by the LS coupling but instead by the intermediate coupling scheme.

However, experimentally, a bunch of intra-4*f* transition lines is commonly observed, either in absorption or emission spectra, in a much larger number than predicted by the restrictive selection rule on the J quantum number. Furthermore, the intensity of such transitions is too strong to be attributed to higher-order mechanisms (e.g., electric quadrupole). The reasonable explanation is to consider them as having an ED nature, even if they are parity-forbidden [146]. For them to occur, the states involved need not be pure 4*f* states, corresponding to the combination of states with different parity.

J. van Vleck was the first to discuss this problem in 1937, proposing that the crystalline potential would cause an admixture of states of different parities into the pure 4*f* states. The $4f^{M-1}5d^1$ states are the most likely to mix with $4f^M$ states since they are closer in energy compared to other configurations. Such mixing is mediated by the odd-parity terms of V_{host} (i.e., with k odd), which are non-null when the Ln^{3+} incorporate lattice sites without an inversion center. It will perturb the system so that ion's eigenstates no longer have a well-defined parity. Consequently, Laporte's selection rule established for ED transitions is relaxed, and intra-4*f* transitions became allowed by ED [156]. Since these are only possible by the action of the crystal-field, they are designated forced (or induced) ED transitions.

In opposition, when Ln^{3+} occupy centrosymmetric sites, V_{host} has only even-parity terms; thus, the 4*f* wave functions retain their definite parity, and intra-4*f* transitions remain forbidden by ED. These transitions can become allowed if crystal vibrations that can perturb the static crystal-field Hamiltonian have odd symmetry [156]. Still, as the coupling to the lattice is small, their intensity will also be. Later, B. Judd and L. Ofelt worked independently on a quantum mechanical solution to determine the intensities of intra-4*f* transitions, known as the Judd-Ofelt (JO) theory [157,158]. Essentially, the JO theory quantifies the ideas formulated by J. van Vleck. The most remarkable advantage of this theory is that it provides a basis for predicting the radiative transition probability between two states within the $4f^M$ manifold.

The fact that a 4*f* state is slightly admixed with states of different configurations also changes the selection rules on S, L, and J quantum numbers. According to the Judd-Ofelt theory, an intra-4*f* transition is induced ED only if it obeys $\Delta S = 0$, $|\Delta L| \leq 6$, and $|\Delta J| \leq 6$ (if the initial state has $J = 0$, only $|\Delta J| = 2, 4,$ and 6 are valid) [157,158]. **Table 2.8** resumes the selection rules for forced ED and MD transitions.

Table 2.8 Selection rules for intra-4*f* transitions, according to the JO theory [154].

Forced ED transitions	**MD transitions**
$\Delta S = 0$	$\Delta S = 0$
$\|\Delta L\| \leq 6$	$\Delta L = 0$
$\|\Delta J\| \leq 6$ or	$\Delta J = 0, \pm 1$
$\|\Delta \mathrm{J}\| = 2, 4,$ and 6 if the initial or final state has $J = 0$	($J = 0 \leftrightarrow J' = 0$ transitions are forbidden)

According to the JO theory, the intensity of an intra-4*f* transition forced by ED is proportional to [157,158]:

$$\sum_{\lambda=2,4,6} \Omega_\lambda \left|\langle \mathbf{\Psi}_f \| \mathbf{U}^\lambda \| \mathbf{\Psi}_i \rangle\right|^2. \tag{2.46}$$

Ω_λ ($\lambda = 2, 4,$ and 6) are the JO parameters, a set of phenomenological parameters that characterize the strength and the nature of the odd-parity crystal-field acting on the Ln^{3+}. The terms $\left|\langle \mathbf{\Psi}_f \| \mathbf{U}^\lambda \| \mathbf{\Psi}_i \rangle\right|^2$ are the squared reduced matrix elements of the tensor operator $\mathbf{U}^\lambda$; these do not depend on the host and were tabulated for all Ln^{3+} by W. Carnall et al. [159]. Since $\left|\langle \mathbf{\Psi}_f \| \mathbf{U}^\lambda \| \mathbf{\Psi}_i \rangle\right|^2$ is tabulated, the JO parameters, Ω_λ, for a specific Ln^{3+}-host system can be obtained by fitting the experimental absorption or emission spectra in a least squares difference sum.

Once the JO parameters for a given Ln^{3+} incorporation site in the crystalline lattice are known, the total spontaneous emission probability, A_{rad}, associated with a transition between two electronic states $\mathbf{\Psi}_i$ and $\mathbf{\Psi}_f$ can be calculated through [160]:

$$A_{rad} = \frac{64\pi^4 \bar{\nu}^3}{3h(2J+1)} \left[\frac{n(n^2+2)^2}{9} D_{\mathrm{ED}} + n^3 D_{\mathrm{MD}}\right]. \tag{2.47}$$

In this expression, $\bar{\nu}$ is the average transition energy (in cm^{-1}), $2J + 1$ is the degeneracy of the initial state, h is the Planck constant ($= 6.63 \times 10^{-27}$ erg · s), and n is the refractive index of the medium. D_{ED} and D_{MD} are the electric and magnetic dipole strengths (in $\mathrm{esu}^2 \cdot \mathrm{cm}^2$)[cc]; these quantities are zero if a transition is not allowed by forced ED and MD, respectively.

The strength of an induced ED transition can be calculated by [160]:

$$D_{\mathrm{ED}} = e^2 \sum_{\lambda=2,4,6} \Omega_\lambda \left|\langle \mathbf{\Psi}_f \| \mathbf{U}^\lambda \| \mathbf{\Psi}_i \rangle\right|^2, \tag{2.48}$$

[cc] In some references, the symbols S_{ED} and S_{MD} are used instead of D_{ED} and D_{MD} [161].

where e ($= 4.803 \times 10^{-10}$ esu) is the elementary charge. As D_{ED} changes with Ω_λ, it depends on the crystal field acting on the Ln^{3+}. Conversely, the total integrated intensity of a MD allowed transition is mainly independent of the environment, such that D_{MD} can be obtained by the formula [161]:

$$D_{\mathrm{MD}} = (9.273 \times 10^{-21})^2 \times \left|\langle \boldsymbol{\Psi}_f \| (\mathbf{L} + 2\mathbf{S})^\lambda \| \boldsymbol{\Psi}_i \rangle\right|^2. \tag{2.49}$$

in $\mathrm{esu}^2 \cdot \mathrm{cm}^2$.

Once all emission probabilities that depopulate the initial state $\boldsymbol{\Psi}_i$ have been calculated, one can determine how fast the state is depopulated. This corresponds to the radiative lifetime of the excited state $\boldsymbol{\Psi}_i$, τ_{rad}, and can be determined through [161]:

$$\tau_{rad} = \frac{1}{\sum_{\text{all } i \to f'} A_{rad}}. \tag{2.50}$$

The denominator corresponds to the sum of the A_{rad} associated with all the radiative transitions originating from the state $\boldsymbol{\Psi}_i$. This means that stronger emission probabilities and more transitions from a level result in shorter radiative lifetimes. This parameter can also be compared with the lifetime experimentally observed, τ_{obs}, which includes both radiative and non-radiative (multi-phonon decay and energy transfer) processes. Then, the luminescence quantum efficiency of a given transition, Φ, can be defined as the number of emitted photons per excited ion, and it can be estimated by [161]:

$$\Phi = \frac{\tau_{obs}}{\tau_{rad}} = \frac{(A_{rad}^{-1} + W^{-1})}{\tau_{rad}}, \tag{2.51}$$

with W the probability for non-radiative processes.

All these quantities can provide interesting information about the Ln^{3+}-host system. Nevertheless, their determination implies that in a situation where there are several optically active Ln^{3+} centers in a crystal (this is indeed quite common), the contribution of each center needs to be separated because Ω_λ depends on the ion environment in the lattice. Otherwise, this multitude of contributions will affect the calculated parameters and lead to misleading conclusions.

Furthermore, one needs to bear in mind that the selection rule on J will be valid if it remains a "good" quantum number. The crystal field can also cause the admix of electronic states with different J values (J-mixing), relaxing the rule on ΔJ established by the JO theory [154]. This relaxation can affect the determination of the previously mentioned quantities. A well-known example of the breakdown of the selection rules occurs for trivalent europium ions. In this case, the $^7F_0 \leftrightarrow {}^5D_{\mathrm{odd}}$, $^7F_{\mathrm{odd}} \leftrightarrow {}^5D_0$, and $^7F_0 \leftrightarrow {}^5D_0$ transitions are

forbidden considering the selection rules of **Table 2.8**; nevertheless, they are commonly observed in both absorption and emission spectra of Eu^{3+} in different hosts [154,162].

2.5.2. Europium ions in III-N

In the context of this thesis, the incorporation of europium in III-N is a topic of significant importance; therefore, it is pertinent to discuss this particular case. Europium doping can be achieved either by in-situ doping during growth [163–165] or post-growth by ion implantation [166–168]. Regardless of the chosen doping method, europium predominantly replaces a trivalent cation (Eu_{III}), favoring its 3+ charge state; this has been experimentally demonstrated [169–171] and theoretically supported [172–176]. In such a configuration, the Eu^{3+} dopant does not provide additional carriers for conduction, acting as an isoelectronic impurity. This center possesses an unfilled $4f$ core-shell shielded by outer orbitals, so it is generally designated a "structured" isoelectronic impurity.

Eu^{3+} possesses six valence $4f$ electrons. Under the influence of the interactions mentioned above (e.g., electrostatic, SO, crystal field), the $4f^6$ configuration can lift its energetic degeneracy to a maximum of 3003 energy levels[dd]. Following Hund's rules, the ground state of Eu^{3+} is the $^7F_0$. Within the electronic structure of Eu^{3+}, several atomic-like radiative transitions are frequently observed as the ion de-excites from an excited configuration to a lower-energy state.

In III-N, the most prominent transition is often the $^5D_0 \rightarrow {}^7F_2$, which gives rise to a narrow red emission at ~620–625 nm [177–179]. The decay lifetime of this transition is ~200-300 µs [180–182], much slower than the host's excitonic recombination (order of nanoseconds). Luminescence stemming from transitions between the $^5D_0$ excited state and the ^7F_J (with $J = 0–6$) states are also commonly perceived. While the $^5D_0 \rightarrow {}^7F_1$ transition is allowed by MD, the others are induced ED transitions. Transitions like $^5D_0 \rightarrow {}^7F_0$ and $^5D_0 \rightarrow {}^7F_3$, forbidden in the JO theory, become possible due to the relaxation of the selection rule on ΔJ caused by the influence of the crystal field, which admixes states with different J values (J-mixing). In addition to emissions from the $^5D_0$ excited state, one can often identify emission lines from more energetic states, such as $^5D_1$ and $^5D_2$ [177–179]. Observing these more energetic transitions may condition the perceived color, altering it from red to a more orange or yellowish hue.

[dd] The degeneracy of the $4f$ configuration is given by $\frac{14!}{M!(14-M)!}$, with $M = 6$ for Eu^{3+} [162].

While Eu^{3+} tends to substitute the cation, its position in the lattice deviates slightly from the perfect substitutional site by ~0.2 Å along the *c*-axis [170,175,179,183]. The lattice distortion may be caused by the differences in the ionic radius of Eu^{3+} and the metal it replaces (Eu: 0.947 Å, Al: 0.39 Å, Ga: 0.47 Å [184]), as well as in their electronegativity (Eu: 1.20 [185], Al: 1.61, and Ga: 1.81 [9]). A possible consequence of this is the lowering of the local symmetry of the Eu^{3+} compared to the symmetry it would have if it occupied a perfect substitutional C_{3v} symmetry site, altering the mixing of states and transition rates.

For instance, considering the prominent $^5D_0 \rightarrow {}^7F_2$ transition in a site with C_{3v} symmetry, the $^7F_2$ multiplets split into three Stark levels, likely resulting in three emission lines; the singlet $^5D_0$ state is fully degenerated, so it cannot lift more by the action of the crystal field. A reduction of the site symmetry may lift the remaining degeneracy of the $^7F_2$ multiplet, leading to a maximum of five Stark lines (**Table 2.7**) [146,153,162].

2.5.2.1. Optically active Eu^{3+} centers

Native defects and impurities are commonly present in III-N. If these defects are in the vicinities of Eu^{3+}, they will cause additional disturbances of the crystalline potential felt by the ions. Moreover, as theoretical calculations support, substitutional (or near substitutional) Eu^{3+} can form stable complex defects with vacancies, interstitials, and impurities like oxygen [172–174,176]. Considering that several defects may co-exist in the same host, a multitude of Eu^{3+} centers is expected, each of them experiencing a different crystalline field. As a result, if these centers are optically active, they have unique luminescent characteristics (emission and excitation), which can serve as a "fingerprint" to identify them [186].

The general procedure to recognize multiple optically active Eu^{3+} centers involves the study of the Stark lines of the $^5D_0 \rightarrow {}^7F_2$ transition in HR PL experiments, either by varying the excitation wavelength, the excitation density, the polarization conditions, or the temperature. When identifying a center, its emission (excitation) spectrum must be identical in spectral position and relative heights for all its excitation (emission) transitions [144]. Attention is drawn to the difficulty of identifying the local symmetry of a given center because of the superposition of energetically close emission lines. This may lead to the spectral observation of a greater or a lesser number of Stark lines than predicted for a given site symmetry [162]. Furthermore, if the center is in a crystalline environment where the coupling with the lattice is so strong that $5s$ and $5p$ orbitals can no longer efficiently shield the $4f$ orbitals, this may lead to the appearance of vibronic sidebands in the experimental spectra and make lines' assignment even more difficult [143].

Another strategy to identify the minimum number of optically active Eu^{3+} centers in a host is to distinguish the number of lines associated with the $^5D_0 \rightarrow {}^7F_0$ transition; given that

this transition involves two singlet states, a single center is responsible for only one emission peak, whatever the site symmetry. Observing more than one line implies more than one Eu^{3+} center. However, the $^5D_0 \rightarrow {}^7F_0$ transition usually leads to a weak emission and is not observed for all the incorporation sites. This is why this transition only allows determining the minimum number of optically active Eu^{3+} centers.

Several optically active Eu^{3+} centers (up to nine) have been identified in GaN layers [187–190]. Regardless of the doping method, two optically active Eu^{3+} centers dominate the luminescent response of these systems; they are identified as Eu1 (or OMVPE4) and Eu2 (or OMVPE7) [163].[ee] The Eu1 center is characterized by two predominant emission lines at 621.6 nm and 622.5 nm, while the prominent peaks associated with Eu2 occur at 620.8 nm and 621.9 nm. A slight energy shift (~0.1–0.2 nm) may be noticed due to lattice strain [163,191]. Eu1 is the majority center with a typical concentration between ~80–90 %, while Eu2 is a minority center with a relative abundance often lower than ~5 %. Nevertheless, Eu2 gives rise to an intensity comparable to that of Eu1 due to a more efficient excitation for above bandgap excitation [163,192,193]. Hence, a simple comparison of the PL intensity of the various Eu^{3+} centers does not reflect their relative abundance [163].

Although Eu1 and Eu2 can be distinguished in PL experiments, assigning them to a given local environment is not a trivial task; indeed, different proposals for the structure of these centers can be found in the literature. In a first attempt to assign the local structure of Eu1 and Eu2, L. Bodiou et al. proposed that Eu1 could be the isolated Eu_{Ga}, while Eu2 would also be a substitutional or near-substitutional cation center with a closer point defect distorting its local environment (Eu_{Ga}-X, where X represents the point defect) [192]. This complex defect would introduce an energy level in the forbidden gap and could trap carriers, favoring the excitation efficiency of Eu2. In a posterior work, L. Bodiou et al. referred that Eu1 could also be a Eu_{Ga} center perturbed by a more distant defect in the second or third neighboring shell [193].

In contrast, I. Roqan et al. attributed Eu2 to the isolated Eu_{Ga} and Eu1 to a complex defect involving Eu_{Ga} and a nearby defect (Eu_{Ga}-X). Such attribution was based on the dominant contribution from Eu2 after annealing Eu-implanted GaN at high temperatures and pressures, with little or no residual damage. The authors suggested that for such annealing conditions, the concentration of the defects associated with Eu_{Ga} would quench, reducing the contribution from Eu1 to the detriment of Eu2 [194].

[ee] The nomenclature Eu1 (OMVPE4) and Eu2 (OMVPE7) is generally adopted for GaN:Eu samples doped by ion implantation (in-situ doping during growth by MOVPE) [163].

More recently, B. Mitchell et al. assigned the majority Eu1 center to Eu_{Ga} with nitrogen vacancies in the vicinities (Eu_{Ga}-V_N) and Eu2 to isolated Eu_{Ga} or Eu_{Ga} associated with gallium vacancies (Eu_{Ga}-V_{Ga}) at a distance far enough not to perturb the Eu^{3+} [195]. The attribution of the Eu1 center was made based on polarization-dependent PL studies. This center can exist in two microscopic configurations, depending on whether the V_N is axially above Eu^{3+} or in one of the three equivalent off-center positions. In the first case, Eu^{3+} occupies a site with C_{3v} symmetry, whereas in the second the symmetry is lowered to C_{1h}. Theoretical calculations suggested that a Eu_{Ga}-V_N configuration is can be stabilized in both configuration [173,174,176]. In the assignment of Eu2, B. Mitchell et al. considered the increase in the concentration of Eu2 with the number of available V_{Ga} defects in the lattice [195]. These authors further demonstrated that the excitation efficiency of the Eu1 center could be enhanced by pairing such a complex with distant V_{Ga} or Mg acceptors, while Eu2 is likely to pair with oxygen-impurity donors [195,196].

Figure 2.16 presents the spectral shape of the $^5D_0 \rightarrow {}^7F_2$ emission lines attributed to Eu1 and Eu2 in GaN (measured by PL at 12 K) [192]. The local structure of these centers is also illustrated per the proposal by B. Mitchell et al. [195].

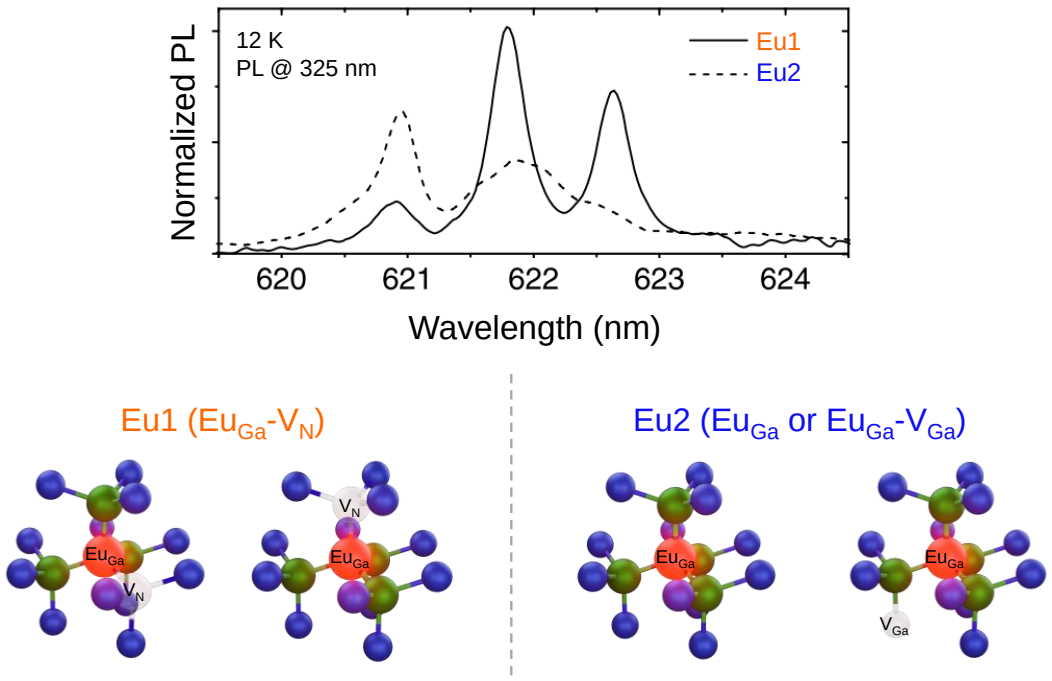

Figure 2.16 PL spectra of Eu1 and Eu2 in GaN, around the $^5D_0 \rightarrow {}^7F_2$ transition (reprinted from reference [192]), and respective structure based on the assignments made by B. Mitchell et al. [195] (considering the ionic radii of N^{3-}, Ga^{3+}, and Eu^{3+} [184]).

Regarding Eu^{3+} centers in AlN hosts, J. Gruber et al. identified various minority sites besides the majority center. Furthermore, they found that the local environment of the majority site was less strained for in-situ doped than for ion-implanted samples [178]. Nevertheless, the identification of the centers and their respective luminescent characteristics have not been explored as much as for Eu^{3+} in GaN hosts. In a distinct but related work, M. J. Soares et al. reported the existence of different erbium centers in AlN thin films [197]. These results suggest that, like in GaN hosts, several Eu^{3+} centers in AlN hosts may exist. Theoretical calculations by S. Petit et al. demonstrated that Eu^{3+} could form complex defects with oxygen impurities and vacancies, with some of these complexes introducing deep levels in the forbidden gap, possibly assisting the excitation process for the intra-$4f^6$ luminescence.

2.5.2.2. Excitation mechanisms of Eu^{3+}

The intra-$4f^6$ luminescence of Eu^{3+} results from the de-excitation of excited electrons state in the $4f$ shell to lower energy states in the same configuration, a process that differs from the recombination mechanisms identified previously in **subsection 2.3.2**. When inserted into semiconductor's hosts, such as III-N, the excitation of Eu^{3+} can proceed in various ways classified as direct or indirect processes [144,181].

Direct excitation corresponds to the process in which Eu^{3+} is photoexcited resonantly to an excited $4f^6$ state.[ff] However, as it deals with intra-ionic transitions from the $^7F_0$ ground state, which are parity forbidden by ED, it rarely yields strong luminescence intensity due to low absorption cross-sections [144,181]. Direct processes also include impact excitation of Eu^{3+} by hot electrons, where the inelastic scattering of hot electrons by Eu^{3+} results in their promotion to an excited $4f^6$ state. This process occurs in CL experiments; it can also occur in EL experiments if the generated electric field is strong enough to accelerate hot electrons with kinetic energy equal to or greater than the energy of the excited $4f^6$ states [198].

On the other hand, indirect mechanisms involve first the excitation of the host, with the energy from the recombination between electrons and holes being transferred non-radiatively (Auger-like process)[gg] to the Eu^{3+} $4f^6$ core states, whose subsequent de-excitation results in the intra-$4f^6$ luminescence [144,198]. Indirect excitation is possible in PL, CL, and EL experiments. The recombination mechanisms that can result in an energy transfer (ET) to the Eu^{3+} core states are discussed below.

[ff] It can also involve excitation to other more configurations, like the $4f^5\ 5d^1$; however, for Eu^{3+}, these transitions generally occur at ~10 eV, impossible to access under optical excitation [143,146].

[gg] It can be interpreted as a three-body interaction between an *e-h* and a $4f$ electron; the recombination energy of the *e-h* is transferred to the $4f$ electron, leaving it in an excited state.

Upon excitation with energy above the host's bandgap, FXs can be formed due to the attraction between electrons and holes free in the bands. As discussed in **subsection 2.3.2**, such entities can recombine radiatively. Additionally, FXs can *i)* undergo inelastic scattering with Eu^{3+} centers transferring their energy (or part of it) to the $4f^6$ core states of Eu^{3+}, or *ii)* become localized at defect traps that introduce levels in the forbidden gap of the host, forming BXs. The defects that can bind excitons may involve or not Eu^{3+}, including "structured" isoelectronic Eu^{3+}, native defects or impurities, and complex defects involving Eu^{3+} and other defects.

Apart from recombining radiatively, BXs can recombine non-radiatively, transferring their energy to the $4f^6$ core states of Eu^{3+} or relaxing non-radiatively through the lattice, i.e., by the emission of phonons. Excitation of defects can also occur for excitation energies below the host's bandgap if the excitation is resonant with the energy levels of the defect in the forbidden gap. The trapped carriers can recombine with the oppositely charged carriers left behind in the bands or attract them to form BXs. The recombination with free carriers and the annihilation of BXs can be radiative or non-radiative through any of the processes identified above, including the ET to Eu^{3+}. The perturbation of the crystalline periodic potential around these defects is strong, with the trapped carriers or bound excitons having tightly localized wave functions. Consequently, the excitation associated with such defects generally leads to broad excitation bands due to the strong electron-phonon coupling [185,199]. Recombination of DAPs can also lead to a non-radiative ET to the $4f^6$ core states of Eu^{3+}.

The predominant mechanism for ET in materials doped with lanthanoids is via dipole-dipole interaction. For an efficient ET to Eu^{3+}, carriers' recombination must energetically overlap the intra-$4f^6$ absorption levels of Eu^{3+}. If the initial and final states are not resonant, the energy mismatch can be overcome by the emission or absorption of phonons; however, the process is as efficient or more efficient the smaller the number of phonons required. The ET also requires spatial proximity between the two centers, being more efficient for closely-associated pairs. This means that defects involving Eu^{3+}, namely "structured" isoelectronic impurities[hh] or complex defects, and others in the vicinities of Eu^{3+} should mediate the process [199–202].

Once Eu^{3+} are in an excited $4f^6$ configuration, they can radiatively de-excite to lower energy states. They can also de-excite non-radiatively by multi-phonon relaxation through the $4f^6$ manifold if the energy levels are closely spaced or by transferring their energy back to the mediating defects. The latter are usually considered to be the main responsible for decreasing the luminescence with increasing temperature [185].

[hh] Despite "structured" isoelectronic impurities have the same valency as the replaced cation, they can bind excitons due to the different ionic radii and electronegativity [185,199].

The indirect mechanisms are generally more efficient than a resonant excitation with excited states of the $4f^6$ configuration, given that the mediating defect's absorption or carrier capture cross-section can overcome the low absorptivity of intra-$4f$ transitions (prohibited by ED) [199]. Furthermore, closely associated defects or complexes can perturb the crystal field perturbation felt by Eu^{3+}, relaxing the selection rules and enhancing the probability of intra-ionic transitions. This means that when promoting the excitation of the $4f^6$ core states of Eu^{3+} via different defects, the emission spectrum will differ due to the favoring of Eu^{3+} centers in the vicinity or associated with the respective mediating defects.

Figure 2.17 provides a schematic representation of the photoexcitation of Eu^{3+} incorporated into III-N, involving direct mechanisms (resonant excitation of the intra-$4f^6$ core-shell) and indirect mechanisms (non-radiative ET from FXs or excitons bound to defect-related traps). In the latter, excitation with energy above and below the host's bandgap is distinguished.

In some instances, it is even possible that the excitation of the intra-$4f^6$ luminescence proceeds through charge transfer directly involving Eu^{3+} if these ions introduce charge-transfer states (CTS) in the forbidden gap of the host. In this case, Eu^{3+} can localize an excited electron by a short-range potential, changing from a valency 3+ to 2+, with Eu^{2+} in its fundamental in $4f^7$ (half-filled shell) configuration, i.e., $^8S_{7/2}$ state. This charge transfer leads to a redistribution of charges around the ion, becoming negatively charged. Consequently, a free hole will be attracted by Coulomb interaction, and the recombination of such entity converts the ion back to its 3+ valency. This process can be either radiative, leaving Eu^{3+} in its fundamental state, or non-radiative, with an ET to the $4f^6$ core states of Eu^{3+} [198,199,203]. However, in this case, the $4f$ orbitals are perturbed, and the wave functions that describe the $4f^6$ states are mixed with wave functions of opposite parity from the CTS, thus increasing the probability of intra-$4f^6$ transitions as they become contributions partially allowed by ED [198,199,203].

Given that a CTS involves a change in the charge state, the equilibrium positions of the atoms change through the lattice relaxation. The CTS can be interpreted from the CC model, similar to that discussed in **sub-subsection 2.3.2.2**. This implies that the excitation bands involved in this process are necessarily broad. As these bands have analogous characteristics to the excitation bands involved in the binding of excitons to defects, it becomes difficult, if not impossible, to distinguish which of the processes is responsible for the broad bands usually involved in the excitation of intra-$4f^6$ luminescence of Eu^{3+}. A schematic representation of this process would be like that involving BXs to defect-related traps, illustrated in **Figure 2.17**.

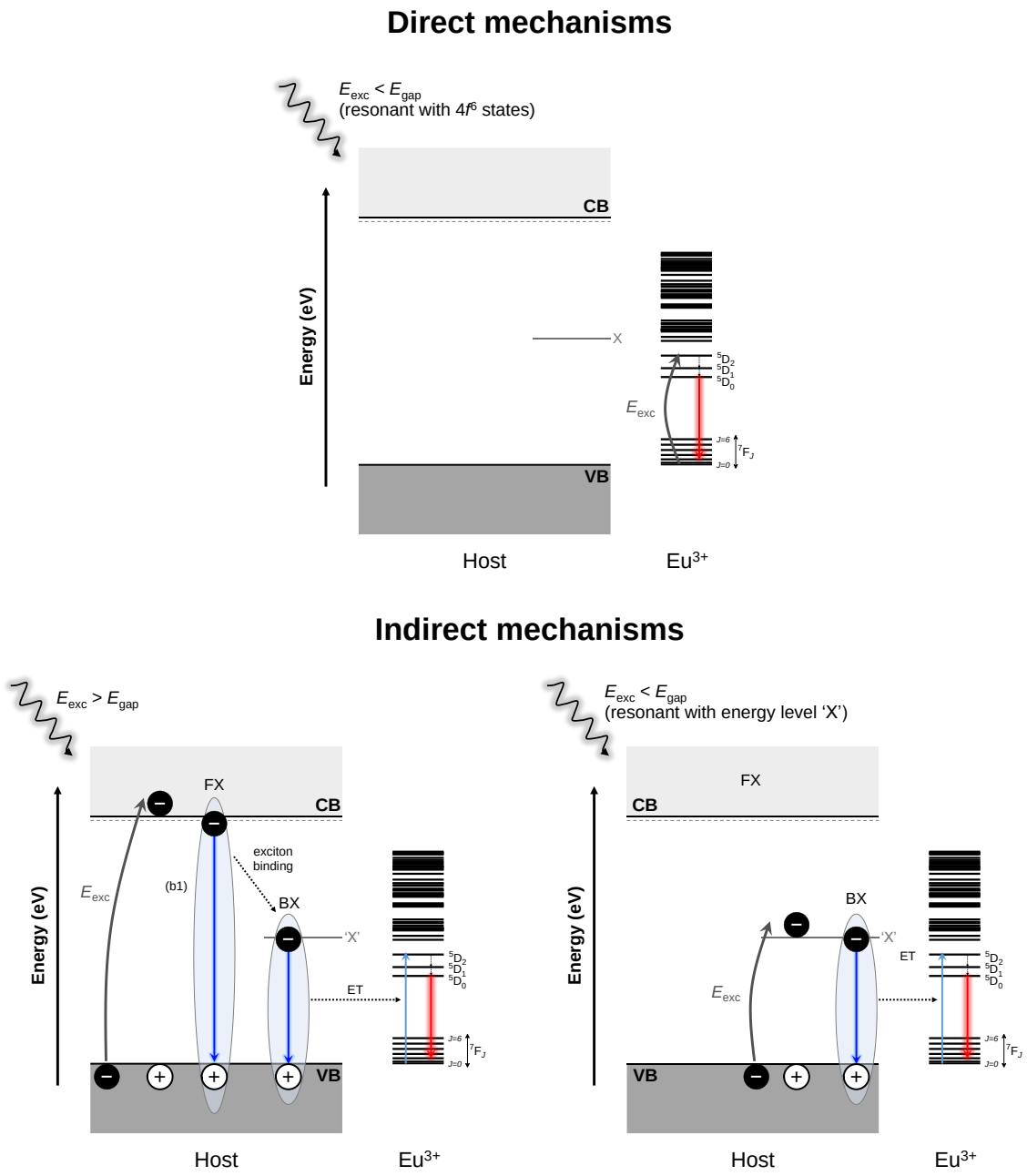

Figure 2.17 Schematics of the direct and indirect mechanisms (involving ET from excitons bound to a defect-related trap 'X' to the $4f^6$ core states of Eu^{3+}) responsible for the photoexcitation of Eu^{3+} in III-N hosts.

Regarding Eu^{3+} in GaN, various authors have reported the excitation channels of the two predominant Eu^{3+} centers in GaN: Eu1 and Eu2. While Eu1 can only be excited with energy above the GaN bandgap, Eu2 can be excited with energy above and below the GaN bandgap. The latter involves a broad excitation band attributed to the non-radiative ET from recombining excitons bound to defects in the vicinity or involving the Eu2 center. The

greater excitation efficiency of Eu2 compared to Eu1 is often correlated with the ability of this defect, with an energy level in the forbidden gap, to capture carriers and localize excitons, favoring the ET to Eu2 [191,192]. Moreover, M. Ishii et al. demonstrated that Eu2 is the favored center under electrical excitation [204]. However, because of the lower abundance of the Eu2 center, the relative intensity of the lines associated with Eu1 tends to increase for higher excitation densities due to a faster saturation of Eu2. Together with the long radiative lifetimes associated with the $^5D_0 \rightarrow {}^7F_2$ transition (~200–300 μs [180–182]), this may condition the output power and the efficiency of this kind of device at high injection levels [186]. Therefore, in order to improve their performance, it is of utmost importance to control the balance of the Eu^{3+} centers, either by favoring the formation of Eu2 by adjusting the doping conditions or enhancing the excitation efficiency of Eu1 by pairing it with impurities or acceptors [163,193,195].

As the AlN molar fraction in AlGaN ternary alloys increases, the bandgap increases, enabling new excitation paths for Eu^{3+}. **Figure 2.18(A)** shows the 15 K PLE response of Eu-implanted AlGaN layers measured at the peak of the $^5D_0 \rightarrow {}^7F_2$ luminescence (from reference [205]). Apart from the band edge absorption, it is possible to notice one or two sub-gap excitation bands: X1 peaking at ~3.2–3.5 eV (FWHM of ~0.4 eV) and X2 peaking at ~4.2–4.5 eV (FWHM of ~0.4 eV). The evolution trend of the peak energy of X1 and X2 with y is presented in **Figure 2.18(B)**, making it possible to notice that X2 emerges for $y > 0.6$ [205]. Although the energy increases with composition, the magnitude of the trend (~200–300 meV from GaN to AlN) is much lower than that of the bandgap energy (~3 eV from GaN to AlN).

Notwithstanding the appearance of the sub-gap bands, above bandgap excitation prevailed as the channel responsible for the most intense intra-$4f^6$ luminescence [205]. This is likely due to the more significant absorption coefficient for the above bandgap excitation, allowing the generation of a greater number of free carriers that can subsequently be trapped at defects, providing either the localization of excitons at defects or a charge-transfer from Eu^{3+} to Eu^{2+}. However, it should be noted that although it causes a stronger luminescence, it does not mean it is the most efficient excitation process; instead, paths involving BXs or CTS should be the most efficient.

From the Dieke diagram associated with Eu^{3+} (**Figure 2.15**), it is possible to note that Eu^{3+} possesses several $4f^6$ levels in the energy region of X1 and X2; this energetic resonance may explain the ET occurrence through such bands. Despite energetic resonance, such an indirect mechanism requires the spatial proximity between the entity transferring the energy and the emitting Eu^{3+} center. Different origins for the X1 and X2 excitation bands have been proposed in the literature.

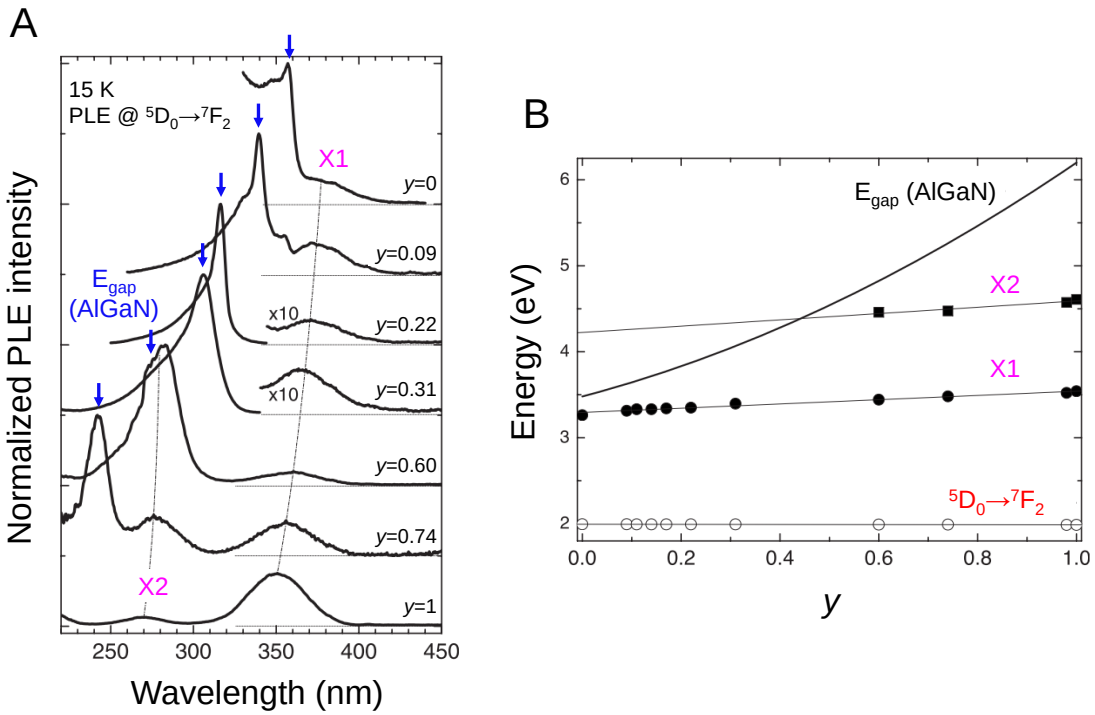

Figure 2.18 (A) 15 K PLE spectra of Eu-implanted AlGaN layers. **(B)** Excitation peak energies of Eu-implanted AlGaN layers derived from PLE as a function of y (open circles correspond to the PL used to monitor the excitation spectra). Reprinted from reference [205].

K. Wang et al. proposed that X1 and X2 involve a charge transfer to the empty $5d^1$ shell of the Eu^{3+} ion leaving the $4f^6$ core states unchanged. By Coulomb interaction, a free hole is attracted to the negatively charged defect, forming an entity analogous to a *d*-exciton; the energy of the recombination of the *d*-exciton is then transferred non-radiatively to the $4f^6$ shell, resulting in the characteristic sharp line luminescence. The authors attributed the two distinct bands to the splitting of the $5d^1$ configuration into high and low spin states separated by ~1 eV [205].

E. Merkx also observed the two broad excitation bands (X1 and X2) in AlN layers doped with Eu^{3+} and proposed they concern CTS involving europium (Eu^{3+} to Eu^{2+}) [206]. They attributed X1 to the CTS related to the substitutional Eu center (Eu_{Al}). This was made based on the proposal of P. Dorenbos for the location of the energy levels of lanthanoid impurities in AlGaN hosts [207,208]. However, P. Dorenbos placed the energy level of the Eu^{3+}/Eu^{2+} CTS of the Eu_{Al} center based on the experimental observation of a similar broad band. The X2 was also attributed to a CTS Eu^{3+} to Eu^{2+} but, in this case, of a complex defect involving Eu_{Al} and oxygen impurities incorporated during growth [206].

In another work, H. Lozykowski et al. argued that the excitons bound to defects involving Eu^{3+} and nearby defects were responsible for various sub-gap excitation bands, leading to an efficient ET to the $4f^6$ core states of Eu^{3+} [209]. Further supporting their arguments, similar excitation bands in the UV region were observed for other Ln^{3+} in AlN, which cannot be explained by CTS considering the energy level location made by P. Dorenbos [25,210–212]. Therefore, they attributed it to the non-radiative ET from bound excitons to defect-related traps involving Eu^{3+} or in their vicinities [25,209].

Furthermore, broad absorption bands in the UV region are commonly observed in AlN (without doping with lanthanoids) and are tentatively assigned to vacancies or oxygen/carbon impurities [95,99,213–215]. In a recent work, L. Peters et al. observed that implantation/irradiation of AlN layers with different ionic species gives rise to an absorption band with spectral characteristics (energy and FWHM) analogous to the X2 band; they proposed that this is related to nitrogen vacancies introduced by implantation [216]. Considering that Eu^{3+} likely forms stable complexes with such defects, this is a likely origin for the excitation of the Eu^{3+} $4f^6$ core states, as suggested by H. Lozykowski et al. [25,209].

2.6. Ion irradiation of III-N

This section describes the mechanisms of interaction between ions and matter. These concepts present a particular relevance within the scope of this thesis, which explores the modification of the optical properties of III-N through ion irradiation techniques. The two cases of interest are particularized: europium-implantation and SHI irradiation of III-N.

2.6.1. Interaction ion-matter

When accelerated ions enter a material, they interact with lattice atoms, leading to energy loss. This energy loss occurs progressively as the ions transverse the material until they lose all the energy and come to rest at a given depth within the material, which is known as the implanted region. The energy transferred to the lattice is described by the total amount of energy lost by an ion per unit length along its trajectory (or total stopping power) and is represented by dE/dx (or S).

The predominant interactions between ions and matter can be categorized into nuclear and electronic interactions, corresponding to elastic collisions with the nuclei and inelastic scattering by electrons, respectively. Neglecting other less probable energy loss mechanisms (e.g., nuclear reactions, bremsstrahlung radiation, or Cherenkov radiation) and taking into account the Born-Oppenheimer approximation, the total stopping power can be considered

as the sum of two independent contributions: S_n, representing nuclear losses, and S_e referring to electronic losses [217,218].

The nuclear interactions result from the scattering of incident ions by the screened nuclear potential of the lattice atoms, with conservation of both momentum and energy in the process. Due to the ballistic nature of the collision, an impinging ion displaces an atom from its equilibrium position. If the energy transferred to the lattice is equal to or greater than the threshold displacement energy (E_d), the atom may be permanently displaced from its regular lattice site, generating a vacancy and occupying an interstitial site. This recoiling atom may still acquire enough kinetic energy to interact with other atoms, contributing to the displacement of other atoms and producing an atomic collision cascade. Since E_d is typically of the order of 10–100 eV, a single ion accelerated to an energy of 10–100 keV can lead to a collisional cascade producing a substantial number of vacancies and interstitials (~100–1000). Clusters and extended defects (e.g., dislocation loops and stacking faults) can also be generated. This results in disorder within the material, and in some cases, it can even induce amorphization [217–220].

Notwithstanding, in nuclear interactions, part of the energy can be inelastically transferred to the lattice, increasing the local lattice temperature. Because of this, some displaced atoms may acquire enough energy to relax back to sites equivalent to their regular lattice sites. This process, where defects recombine due to the thermal energy provided to the lattice instantaneously after implantation, is known as dynamic annealing. The dynamical annealing is likely to be the mechanism that explains why the experimentally measured lattice damage level is generally kept much lower than that predicted by simulation codes, which rarely consider diffusion and annihilation of defects.

On the other hand, electronic interactions correspond to the inelastic scattering of the impinging ions with lattice atoms' electrons. In this case, the ions lose their energy by ionizing and exciting the atoms in the material. The electronic energy loss is deposited in a small zone of some nm in diameter around the ion paths, resulting in a small but highly ionized region with a substantial electron deficiency in its center. This energy is then transferred to the lattice atoms by electron-phonon coupling, initiating various possible effects, such as track formation, local heating (and possibly melting), atomic diffusion, or amorphization [218].

The rate of energy loss by an accelerated ion moving penetrating a material can be predicted through Monte Carlo (MC) calculations implemented on SRIM software [221]. **Figure 2.19** displays the dependence of S_n and S_e values on ion energy for ^{209}Pb ions in GaN derived from SRIM. The two contributions exhibit distinct energy dependencies; still, both increase until they reach a maximum and then decrease. Nuclear losses dominate at lower energies, with the peak occurring for energies of the order of ~1 keV · amu^{-1}. Beyond

~0.1 MeV · amu^{-1}, electronic losses increase significantly and surpassing the nuclear losses, whose contribution diminishes as the ion energy increase because of the high velocity of the ions. At some point, S_n becomes about two orders of magnitude lower than S_e, and its contribution is generally neglected. The peak in the electronic energy loss curve is referred to as Bragg peak and occurs at ~1 MeV · amu^{-1}. Below this peak, S_e is proportional to $E^{1/2}$, and above the peak, S_e is proportional to $1/E$ [217,218].

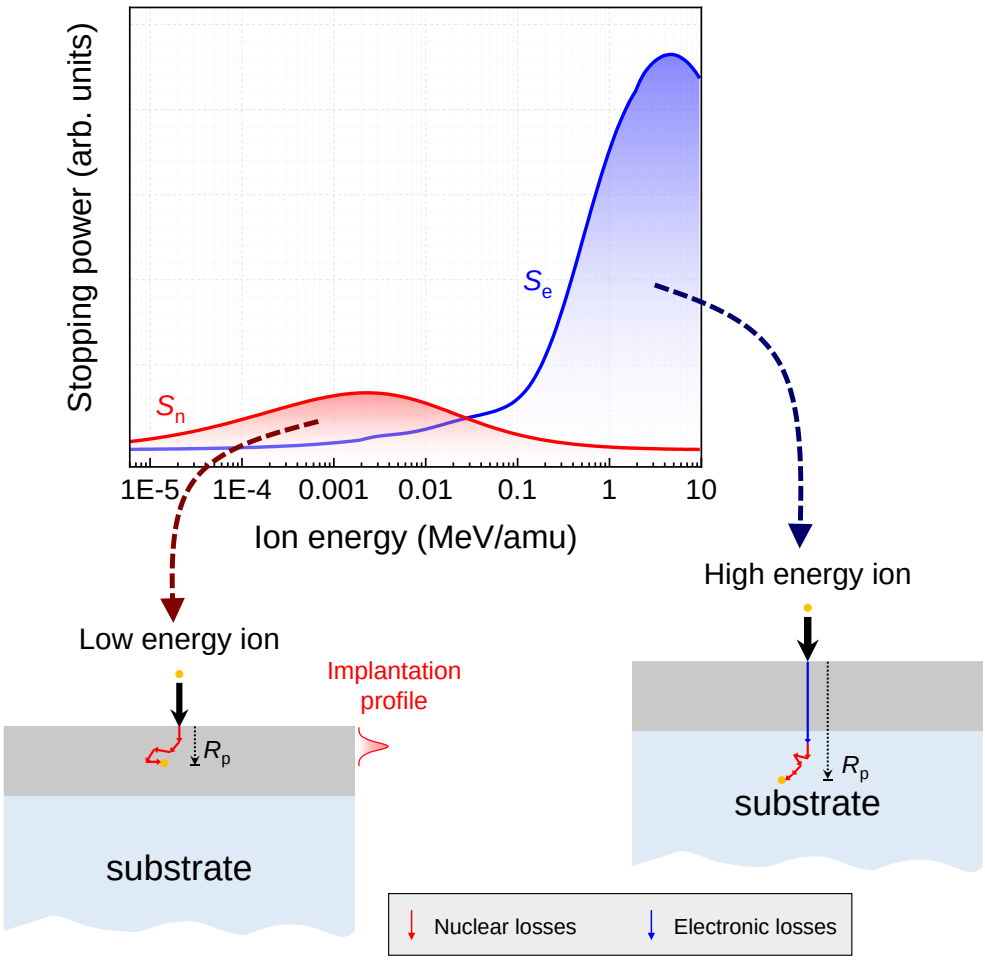

Figure 2.19 Schematics of S_n and S_e as a function of the ion beam energy. Trajectories for low-energy (hundreds of keV) and high-energy (tens of MeV or higher) ions impinging on a material are also represented. Adapted from reference [14].

The trajectories of low-energy (~0.1–1 keV · amu^{-1}) and high-energy (~0.5–10 MeV · amu^{-1}) ions penetrating a material are also illustrated in **Figure 2.19**. In the first case, nuclear interactions dominate; therefore, the incident ions follow a zigzag movement due to the successive nuclear collisions deviating their propagation direction until they come to rest at a distance R_p (penetration depth of the ions in a material). The randomness of

the collisional process means that ions of the same species and with the same energy come to rest in different positions, i.e., they will not be at the same depth; the in-depth profile of the dopant typically follows a broad Gaussian-like distribution.

In contrast, high-energy ions primarily undergo electronic interactions, with their trajectory remaining relatively undisturbed as they transverse the material, i.e., corresponding to a quasi-linear path. However, as these ions lose energy during the passage, the nuclear balance between electronic and nuclear energy loss changes with depth. This means that near their end range (typically a few µm deep), high-energy ions lose energy through ballistic collisions with lattice atoms, presenting zigzag trajectories like low-energy ions. Still, due to the significant penetration depth of high-energy ions in the material, the predominant nuclear losses occur deep in the sample or the substrate [217,218].

2.6.2. Europium-implantation of III-N

Ion implantation is a routine technique in the semiconductors industry in which dopants are purposedly introduced into a material through ion irradiation, implying its occurrence in conditions far from thermodynamic equilibrium. This allows incorporating dopants beyond their solubility limits in a material [220,222]. Precise control of the in-depth distribution of dopants can be attained by adequately adjusting implantation parameters (e.g., ion energy), enabling the realization of vertical devices. Additionally, it allows for lateral patterning using lithographically defined masks [220,222,223].

During europium-implantation of III-N, europium ions are accelerated to relatively low energies, typically ranging from tens to hundreds of keV. Under these conditions, the ions lose their energy primarily through elastic collisions with lattice atoms. While ion implantation is effective in introducing dopants into the host, it also results in a significant concentration of defects due to the ballistic nature of the process. Such defects can negatively impact the structural, optical, and electrical properties of the material.

The formation of defects (nature and distribution) and the distribution profile of europium depend on several factors. One of them is the threshold energy for atomic displacement. For similar implantation conditions, a lower E_d implies a higher probability for atomic displacement and the initiation of atomic collision cascades.

From *ab initio* molecular dynamics calculations, the weighted average values of E_d (over five crystallographic directions) for GaN were 32.4 eV for N atoms and 73.2 eV for Ga atoms [224]. Similarly, for AlN, the following weighted average values of E_d were calculated: 38.8 eV for N atoms and 94.1 eV for Al atoms [225]. The E_d values for N are smaller in both GaN and AlN, which is consistent with experimental works and indicates the N-related defects should be predominant. Furthermore, the E_d values are anisotropic, being highly

dependent on the crystallographic direction, likely due to the different cross-section for collision [224,225].

Another important consideration is that the implantation damage build-up processes in III-N do not follow the typical accumulation of vacancies and interstitials. This is due to efficient dynamic annealing processes, where mobile point defects annihilate during implantation, keeping the damage level relatively low. However, defect annihilation is not perfect, signifying that some generated point defects interact with each other, native defects, or implanted species. This interaction can result in the formation of thermally stable point defect clusters and stacking faults, which may act as traps for free charge carriers and introduce strain in the crystal, disrupting the operationality of the devices. These effects are commonly observed in ion-implanted GaN [226–230].

In AlGaN alloys, the dynamic annealing is enhanced when the Al concentration increases, explaining the higher resistance of AlN to ion irradiation-induced damage. This has been attributed to the higher cohesive energy of the Al–N bonds (11.54 eV/atom) compared to the Ga–N bonds (8.96 eV/atom) [226,231–233]. Still, the nature of the implantation-induced defects in ternary AlGaN alloys and AlN is similar to that found for GaN layers [234–236].

Dynamic annealing has also been proposed as the reason for implanted Eu to incorporate substitutional cation sites (in the trivalent charge state) shortly after implantation into GaN and AlN layers [183,233,237–239]. Nevertheless, intra-$4f^6$ luminescence is generally not observed right after implantation, which is most likely because the implantation-induced defects act as efficient non-radiative de-excitation paths, preventing the excitation of Eu^{3+}. It may also be the case that the environment surrounding the Eu^{3+} is not the most suitable for their optical activation.

The distribution profile of europium and atomic displacements are typically estimated based on MC simulations implemented in the SRIM software [221]. Even so, these do not account for dynamic annealing effects. Experimentally, such information is generally inferred from Rutherford backscattering spectrometry (RBS), X-ray diffraction (XRD), and Raman spectroscopy results. Complementary insights are gathered from examining TEM images [144].

Still, defect formation and dopant distribution do not depend solely on the host. They are also affected by implantation parameters, including ion energy, fluence (i.e., amount of ions accelerated in the beam), temperature, geometry, and ionic species [144,217].

More energetic ions lead to a deeper R_p. However, atomic collisions also increase, resulting in an enhanced defect formation. At the same time, the in-depth distribution of the implanted ions (Gaussian-like profile) broadens compared to implantation with lower energetic ions due to the larger number of collisions [144,217].

In order to have relatively high concentrations of Eu^{3+} in the lattice, the implantation fluence must be high. Besides providing a higher dopant concentration, this implies more atomic collisions, resulting in a more defective material. The effect of the europium fluence on the damage build-up in GaN and AlN layers is reasonably well understood and documented [227–230,235,236]. At low fluences (up to 2×10^{14} cm^{-2} in GaN and 1×10^{15} cm^{-2} in AlN), the damage is low and increases linearly with fluence due to defect formation in well-separated collision cascades; the induced strain also increases progressively. For successively higher fluences, the individual collision cascades start to overlap, and extended defects and point defect clusters start to form and accumulate. Furthermore, for higher fluences, the substitutional fraction decreases [238,239]. Therefore, a loss of the single crystalline order (amorphization) is observed at a given fluence. In GaN, this commences for fluences above 2×10^{15} cm^{-2}, with the formation of a nanocrystalline surface layer, whose thickness increases with fluence [227–230]. Due to the stronger dynamic annealing effects, AlN would amorphized only at extremely high fluences (~10^{17} cm^{-2}); in this case, the amorphization occurs due to the accumulation of stacking faults and point defect clusters in a buried layer (at R_p), instead of at the surface as in GaN layers [229,235,236]. This means that at sufficiently high fluences, irrecoverable damage may occur, being important to avoid such conditions for minimizing the damage level.

Implantation at higher temperatures may promote a more efficient dynamic annealing, resulting in lower damage levels. This increases the fluence threshold level for amorphization. Furthermore, the fraction of Eu^{3+} on substitutional (or near-substitutional) cation sites is often improved [169,238]. Similar findings were observed for AlGaN layers implanted with other lanthanoid ions [240].

Carrying out the implantation in different geometries, i.e., with the incident ions impinging at different angles relative to the *c*-axis of the III-N host, also results in different defect formation and implantation profiles. This happens because the cross-section for elastic collisions is distinct for different crystallographic directions, as seen above from the anisotropic dependence of E_d. For instance, different authors found that the *a*-plane GaN is more resistant to implantation-induced damage than the *c*-plane GaN [241,242].

In specific implantation geometries, the ions can penetrate along low index crystallographic axis, propagating with a reduced probability for nuclear collisions. This results in a deeper R_p of the implanted ions, while implantation-induced damage is minimized. This is called channeling implantation. In III-N, a prone example of channeling effects is noticed when implantation is parallel to the *c*-axis. Channeling implantation of europium into GaN and AlN (along the *c*-axis) results in significantly decreased damage levels compared to implantation performed in a random configuration [144,243–245]. Nevertheless, in such a channeled configuration, the in-depth control of the dopant

distribution is lost, which may be a disadvantage depending on the purpose. Furthermore, it should be noted that the MC simulations implemented in the SRIM software do not consider the channeling effects [221].

2.6.2.1. Thermal annealing

The concurrent generation of defects is the principal disadvantage of ion implantation, rendering the implanted Eu^{3+} optically inactive. To remove implantation-induced disorder and optically activate Eu^{3+}, thermal annealing treatments are essential [220,237].

The annealing temperature is a crucial parameter influencing lattice recovery. Higher temperatures provide more thermal energy to the crystal, increasing the probability of defect annihilation. In III-N, the implantation-induced disorder generally decreases with increasing the annealing temperature [220]. Simultaneously, Eu^{3+} become optically active, and their luminescence becomes more intense, indicating the importance of high annealing temperatures in efficiently activating the implanted ions. This can be attributed to removing non-radiative defects or creating more favorable environments around Eu^{3+} for their excitation and emission during lattice reorganization [170,183,236,244]. Furthermore, L. Bodiou et al. have shown that annealing temperature plays a preponderant role in the balance of Eu1 and Eu2 centers in GaN, with Eu2 favored at elevated annealing temperatures [192,193].

The annealing of defects in III-N is difficult because the extended defects and defect clusters are very stable. Therefore, the annealing treatments realized to recover implantation-induced damage in III-N rarely yield a complete lattice recovery. An empirical rule suggests that for a complete recovery of the lattice to implantation-induced damage, the annealing temperature should be approximately two-thirds of the host's melting temperature [144,237]. Taking into account the melting temperature of GaN (~2500 ℃) and AlN (~3200 ℃) [1], the lattice is expected to fully recover for annealing temperatures near 1600 ℃ and 2100 ℃, respectively. However, III-N degrade at temperatures lower than these values due to nitrogen out-diffusion, which results in gaseous N_2 and Ga droplets on the surface. For instance, GaN dissociates for temperatures starting from ~800–1000 °C (at atmospheric pressure) [1,246–249], while AlN starts to dissociate at ~1500 ℃ [250]. These effects become more pronounced for prolonged annealing due to the establishment of thermodynamic equilibrium conditions. Such a dissociation causes severe damage to III-N and complicates the complete recovery of implantation-induced damage.

Rapid thermal annealing (RTA), which involves short heating periods (up to a few seconds), can partially repair implantation-induced damage without substantial nitrogen loss. Furthermore, since thermodynamic equilibrium is not expected to be reached in such short annealing periods, it can allow for annealing at higher temperatures.

Lanthanoid-implanted AlGaN layers have been treated with RTA at 1000 ℃ and 1200 ℃ under N_2 flow (to avoid dissociation), and it is found that such conditions promote the optical activation of the implanted Ln^{3+} species. Although the recovery of the implantation-induced damage is not complete, it improves for the highest RTA temperature, as does the Ln^{3+}-related luminescence intensity [232,239,240,251], which is unsurprising as the temperature remains below the empirical rule. The choice of a maximum RTA temperature of 1200 ℃ is primarily due to limitations of the heating system rather than sample constraints, particularly for AlGaN samples with high Al nominal compositions.

A promising approach to overcome the existing challenges of implantation-induced damage and lattice recovery was proposed by S. Miranda et al.; it involves sequential multi-step europium implantation and RTA of GaN. This allows for using lower fluences, keeping the induced damage low. At the end of the process, the dopant concentration is equivalent to a high fluence implantation, but the damage is considerably lower [251].

Additional strategies to protect III-N from dissociation include employing capping layers (e.g., an AlN capping layer is used to protect GaN from dissociation at temperatures above 1000 ℃ [252]) and recuring to ultra-high pressure annealing under high N_2 pressures, that enables higher annealing temperatures while avoiding material's decomposition [236,247,253–256].

2.6.2.2. Implantation of NWs

Adopting nanowire structures introduces additional complexities compared to 2D planar structures due to their increased surface-area-to-volume ratio. This implies that the surface properties play a more significant role in implantation and subsequent annealing processes [23].

Molecular dynamics simulations performed on ion-implanted GaN NWs demonstrated an increased sputtering yield compared to bulk structures. Additionally, the implantation-induced defects, which cause a lattice expansion, tend to accumulate near the surface of the NWs [257,258]. D. Faye et al. revealed that the formation of extended defects during ion implantation is suppressed in GaN NWs. Moreover, these NWs exhibit reduced levels of defect-induced strain compared to layered structures [239].

As a preliminary estimation, one can resort to SRIM simulations to predict the distribution of Eu ions and implantation defects in III-N NWs. Nevertheless, it is imperative to bear in mind that SRIM does not consider the three-dimensionality of the NWs, implying that the simulated profile may not reproduce exactly the experimentally obtained profile. Making predictions of ion implantation in NW structures is, in fact, particularly challenging because ions may impinge from both the top (like in 2D planar structures) and the side

facets. Consequently, the distribution of the implanted ions (and damage) relies on the characteristics of the NWs in the ensemble.

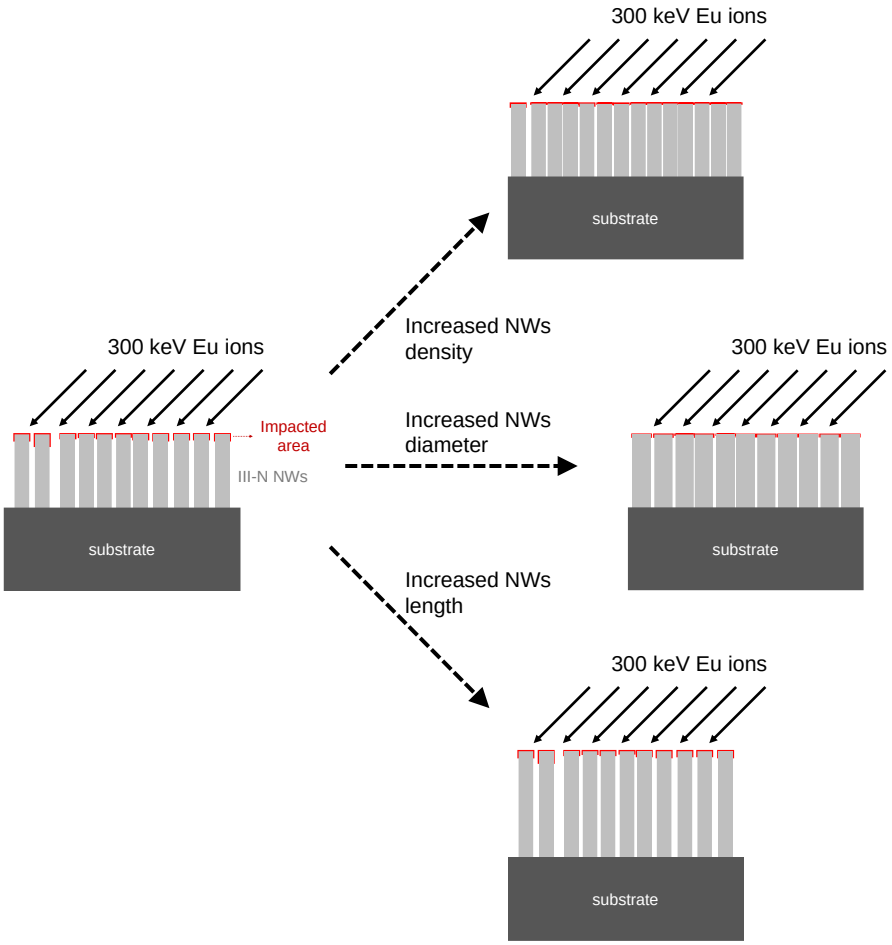

Figure 2.20 Illustration of how the characteristics of the ensemble of NWs can affect shadowing effects during ion implantation.

The characteristics of the adjacent NWs in the ensemble influence the shadowing effects felt by the accelerated ions, affecting the possible area of impact on the NWs. The possible shadowing effects occurring during ion implantation of NWs are illustrated in **Figure 2.20**. These effects depend on the density, diameter, and height of the adjacent NWs, as well as on the implantation angle. An increased density of NWs results in a higher fraction of the ions entering from the top, causing the implantation profile to mimic that of 2D planar structures when the fill factor[ii] is high (above ~90 %). An increase in the diameter also leads to a higher probability of ions entering from the top. Lastly, an increase in the length of the

[ii] Product between NW density and the top cross-sectional area of each NW.

NWs does not modify the implanted volume but results in a reduced ratio between the implanted and non-implanted volumes.

D. Faye et al. modeled the distribution of implanted Eu ions in GaN NWs through MC calculations implemented in the TRI3DYN code [239]. They uncovered that the implanted profiles extend to depths beyond what SRIM simulations predict, most likely due to ions entering through the side facets at different heights (not included in the SRIM). Additionally, they observed that the characteristics of the NWs influence the distribution of Eu ions. **Figure 2.21** shows the simulations for **(A)** an array of 50 nm diameter NWs (length of 2 µm) with a density of 2×10^9 cm^{-2} and **(B)** an array of 100 nm diameter NWs (length of 1 µm) with a density of 7×10^9 cm^{-2}. In the first case, the implantation profile is distributed relatively homogeneously along the entire length of the NWs, with a slight concentration increase in the upper region due to Eu ions entering from the top. Conversely, for the larger and higher density NWs, a substantial portion of Eu ions concentrates within the initial ~100 nm, resembling implantation of 2D planar structures. However, in this case, the profile extends up to ~500 nm due to the non-null probability of ions entering through the side facets. They further measured the profile for optically active Eu^{3+} in CL experiments, which supported the simulated one. The distribution of implantation-induced defects was found to accompany that of the implanted ions [239].

D. Faye et al. also observed that the radial distribution of Eu ions in the NWs is diameter-dependent (**Figure 2.21**). For thinner NWs, the ions that enter through the side facets tend to accumulate in the core. In contrast, for the thicker ones, doping concentration accumulates close to the rim because the limited kinetic energy of the ions prevents them from reaching the core of the NWs.

Analogously to GaN layers, europium-implantation of GaN NWs results in the preferential incorporation of Eu^{3+} into cation substitutional (or near substitutional) sites, especially at low fluences (10^{14} cm^{-2}). However, the substitutional fraction was found to be lower in NWs. A decline in the substitutional fraction with increasing fluence was also reported; this was accompanied by severe surface damage for fluences ~10^{15} cm^{-2} and higher [239].

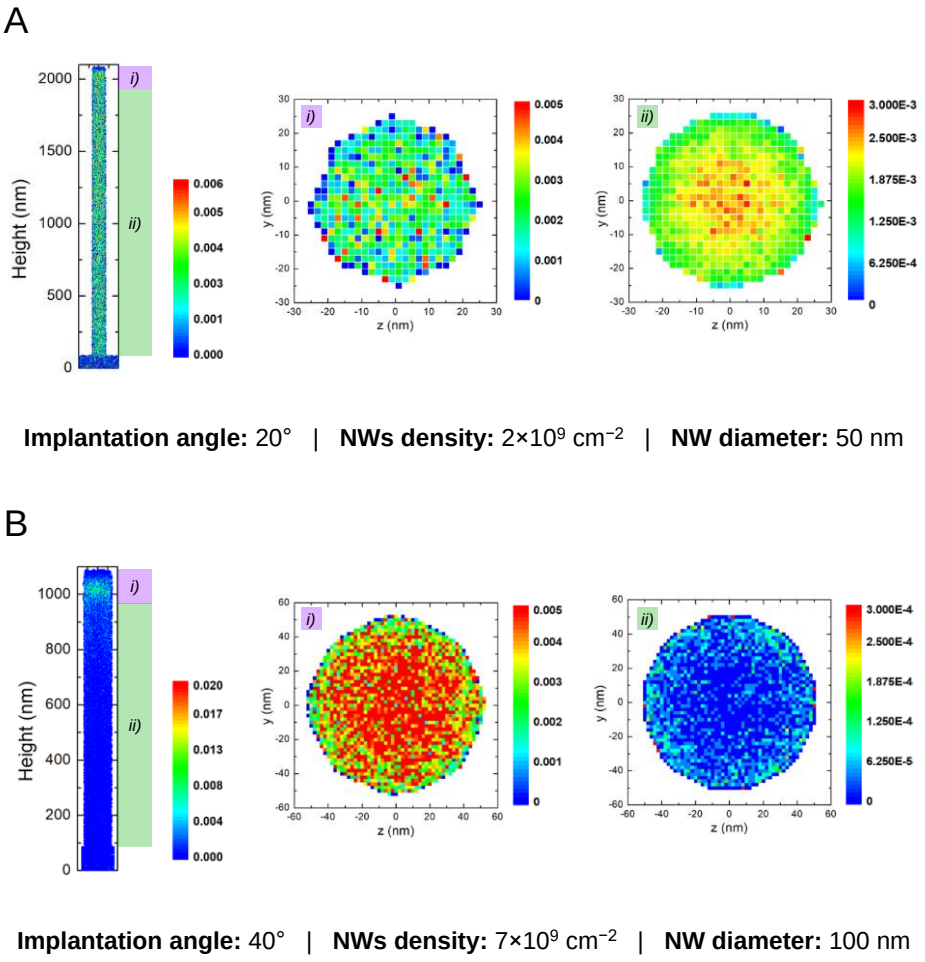

Figure 2.21 TRI3DYN simulations of the radial and longitudinal distribution of Eu ions implanted into an ensemble of GaN with **(A)** 50 nm diameter and density of 2×10^9 cm^{-2} and **(B)** 100 nm diameter and density of 7×10^9 cm^{-2}. The radial distribution corresponds to *i)* integration close to the top of the NWs (first ~50–150 nm) and *ii)* integration from ~150 nm until the NW base. Reprinted from reference [239].

The dissociation of III-N is also expected to be more pronounced in nanowire configurations owing to the increased surface area to volume ratio [23]. RTA is once again a prospective solution to mitigate dissociation during annealing, as it minimizes the probability of thermodynamic equilibrium being reached in such short annealing periods. Indeed, RTA at 1000 °C under N_2 flow was found to reduce the implantation damage and optically activate lanthanoid ions in GaN NWs without severe dissociation [239,259–262]. Nevertheless, D. Faye et al. noted that RTA on GaN NWs implanted with Eu fluences exceeding ~10^{15} cm^{-2} led to the precipitation of Eu, forming local EuN-like cubic structures. This implies that such high fluences should be avoided for device development [239]. No research studies on ion-implanted AlGaN NWs were found.

When comparing GaN NWs and GaN layers implanted with europium in similar conditions (for low fluences) and subjected to RTA treatments, the intra-$4f^6$ luminescence is typically intensified in NWs [239,259]. This is likely due to the suppressed formation of extended defects and defect clusters in NWs.

2.6.3. SHI irradiation of III-N

SHIs are defined as heavy ions with mass equal to or above that of carbon that are accelerated to high energies, typically exceeding tens of MeV [218]. In contrast to ion implantation, SHI irradiation primarily results in energy loss through electronic interactions, with ballistic nuclear collisions contributing minimally to defect formation. The nuclear losses are generally two orders of magnitude lower than the electronic losses. Nevertheless, the electronic losses are sufficient to induce structural modifications in the crystal, rendering SHI irradiation a valuable tool for materials engineering, such as ion beam mixing (i.e., intermixing of atoms at interfaces) or nanostructuring [218,263–265].

The interaction mechanisms of SHIs with semiconductors have been explained through the thermal spike model [218,266]. According to this model, SHIs transverse an interatomic distance in the crystal within a short timescale of 10^{-18} s, leading to the excitation and ionization of lattice atoms along their path. After primary ionizations and excitations, the energetic electrons can further excite other electrons, resulting in a secondary cascade of ionizations and excitation. This creates a highly non-equilibrium cylindrical region with a radius of a few nanometers from the ion trajectory, consisting of hot electrons and a "cold" lattice. Within about $10^{-15} - 10^{-14}$ s, the electronic system undergoes thermalization. Subsequently, electron-phonon coupling leads to lattice heating within a timescale of 10^{-12} s, generating a Gaussian-like temperature profile around the ion's path. If the electronic energy loss surpasses a given threshold, S_{e}^{th}, the material reaches temperatures above its melting point, resulting in localized melting. The value of S_{e}^{th} depends on material properties like density and specific heat capacity. After roughly 10^{-11} s, the heat dissipates to the surrounding cold material, leading to the rapid quenching of the molten phase and a return to thermodynamic equilibrium [218,263–269].

For GaN, the track formation threshold value is still under debate. The following values are reported in the literature: *i)* 15 keV $\cdot$ nm^{-1} [270], *ii)* 17 keV $\cdot$ nm^{-1} [271], and *iii)* higher than 22.8 keV $\cdot$ nm^{-1} [272].

The rapid solid-liquid-solid transitions occurring during the SHI passage form straight tracks along the ion's path, called ion tracks, which may be defective or even amorphous due to ineffective recrystallization. The diameter of such tracks is typically a few nanometers, with the exact dimension being material-specific and dependent on the

electronic energy deposited. The formed ion tracks can be continuous or discontinuous, consisting of a series of damaged fragments [218,263–269].

Atomic diffusion may occur along the track direction during the molten state. When considering interfaces, atomic diffusion between the two sides (intermixing) can occur if both are locally melted [218,263–265]. This intermixing process differs from low-energy ion irradiation, which occurs through ballistic-induced atomic displacements.

Furthermore, in SHI-induced mixing, the impinging ions do not reside in or near the intermixed region (usually at the active region) because of their high penetration depth (up to some micrometers). Consequently, they are implanted in the substrate, where the nuclear losses become predominant. This implies that SHIs do not directly influence the material's optical properties; instead, they affect them indirectly due to the changes caused by their passage.

Despite the reduced nuclear interactions between SHIs and matter, SHI irradiation can generate surface defects (e.g., sputtering and void formation within the initial nanometers of the track) or even cause amorphization. This damage may influence the optical properties of SHI-irradiated III-N since these defects likely introduce detrimental non-radiative de-excitation paths [271–278]. The overall extent of damage tends to increase with increasing ion fluence; for fluences higher than ~10^{13} cm^{-2}, delamination of the III-N films from sapphire substrates was found to occur [274].

2.7. References

[1] H. Morkoç, Handbook of Nitride Semiconductors and Devices, 1st ed., Wiley, Germany, 2008.

[2] J.I. Pankove et al., eds., Gallium Nitride (GaN) I: Semiconductors and Semimetals, 1st ed., Academic Press, United States, 1998.

[3] J.H. Edgar et al., eds., Properties, Processing and Applications of Gallium Nitride and Related Semiconductors, 1st ed., The Institution of Electrical Engineers (INSPEC), United Kingdom, 1999.

[4] I. Gorczyca et al., High pressure phase transition in aluminium nitride, *Solid State Commun.* **79** (1991) 1033–1034. https://doi.org/10.1016/0038-1098(91)90004-F.

[5] I. Gorczyca et al., Band structure and high-pressure phase transition in GaN, AlN, InN and BN, *Phys. B Phys. Condens. Matter.* **185** (1993) 410–414. https://doi.org/10.1016/0921-4526(93)90270-G.

[6] W.F. Hosford, Miller–Bravais Indices for Hexagonal Crystals, in: Mater. Sci., Cambridge University Press, Cambridge, 2006: pp. 21–25.

[7] B. Gil, Physics of Wurtzite Nitrides and Oxides, 1st ed., Springer International Publishing, Switzerland, 2014.

[8] C. Kittel, Introduction to Solid State Physics, 8th ed., John Wiley & Sons, Inc., United States, 2004.

[9] The periodic table of the elements, (n.d.). webelements.com (accessed August 28, 2023).

[10] O. Ambacher, Growth and applications of group III-nitrides, *J. Phys. D. Appl. Phys.* **31** (1998) 2653–2710. https://doi.org/10.1088/0022-3727/31/20/001.

[11] A.R. Denton et al., Vegard's law, *Phys. Rev. A.* **43** (1991) 3161–3164. https://doi.org/10.1002/pssb.19660180251.

[12] J.M. Wagner et al., Properties of strained wurtzite GaN and AlN: Ab initio studies, *Phys. Rev. B - Condens. Matter Mater. Phys.* **66** (2002) 1–20. https://doi.org/10.1103/PhysRevB.66.115202.

[13] C. Kisielowski et al., Strain-related phenomena in GaN thin films, *Phys. Rev. B - Condens. Matter Mater. Phys.* **54** (1996) 17745–17753. https://doi.org/10.1103/PhysRevB.54.17745.

[14] M.D. McCluskey et al., Dopants and Defects in Semiconductors, 1st ed., CRC Press, United States, 2018.

[15] N. Ashcroft et al., Solid State Physics, 1st ed., Harcourt College, United States, 1976.

[16] J.L. Lyons et al., A first-principles understanding of point defects and impurities in GaN, *J. Appl. Phys.* **129** (2021). https://doi.org/10.1063/5.0041506.

[17] M.A. Reshchikov et al., Luminescence properties of defects in GaN, *J. Appl. Phys.* **97** (2005) 1–95. https://doi.org/10.1063/1.1868059.

[18] S. Nakamura et al., The Blue Laser Diode, 1st ed., Springer-Verlag Berlin Heidelberg, Germany, 1997.

[19] R. Calarco et al., Surface-induced effects in GaN nanowires, *J. Mater. Res.* **26** (2011) 2157–2168. https://doi.org/10.1557/jmr.2011.211.

[20] F. Olivier et al., Shockley-Read-Hall and Auger non-radiative recombination in GaN based LEDs: A size effect study, *Appl. Phys. Lett.* **111** (2017). https://doi.org/10.1063/1.4993741.

[21] J. Kou et al., Impact of the surface recombination on InGaN/GaN-based blue micro-light emitting diodes, *Opt. Express.* **27** (2019) A643. https://doi.org/10.1364/oe.27.00a643.

[22] P. Pampili et al., Doping of III-nitride materials, *Mater. Sci. Semicond. Process.* **62** (2017) 180–191. https://doi.org/10.1016/j.mssp.2016.11.006.

[23] C. Ronning et al., Ion beam doping of semiconductor nanowires, *Mater. Sci. Eng. R Reports.* **70** (2010) 30–43. https://doi.org/10.1016/j.mser.2010.07.002.

[24] A.J. Steckl et al., Multiple color capability from rare earth-doped gallium nitride, *Mater. Sci. Eng. B.* **81** (2001) 97–101. https://doi.org/10.1016/S0921-5107(00)00745-5.

[25] H.J. Lozykowski et al., Luminescence and excitation mechanism of Pr, Eu, Tb and Tm ions implanted into AlN, *Microelectronics J.* **36** (2005) 453–455. https://doi.org/10.1016/j.mejo.2005.02.045.

[26] S.D. Carnevale et al., Mixed polarity in polarization-induced p-n junction nanowire light-emitting diodes, *Nano Lett.* **13** (2013) 3029–3035. https://doi.org/10.1021/nl400200g.

[27] P.M. Coulon et al., Dual-polarity GaN micropillars grown by metalorganic vapour phase epitaxy: Cross-correlation between structural and optical properties, *J. Appl. Phys.* **115** (2014). https://doi.org/10.1063/1.4870950.

[28] T. Zywietz et al., Adatom diffusion at GaN (0001) and (000$\bar{1}$) surfaces, *Appl. Phys. Lett.* **73** (1998) 487–489. https://doi.org/10.1063/1.121909.

[29] A.I. Duff et al., Understanding and controlling indium incorporation and surface segregation on in x Ga 1 - X N surfaces: An ab initio approach, *Phys. Rev. B - Condens. Matter Mater. Phys.* **89** (2014) 43–46. https://doi.org/10.1103/PhysRevB.89.085307.

[30] B. Daudin et al., The role of surface diffusion in the growth mechanism of III-nitride nanowires and nanotubes, *Nanotechnology.* **32** (2021) 085606. https://doi.org/10.1088/1361-6528/abc780.

[31] O. Ambacher et al., Pyroelectric properties of Al(In)GaN/GaN hetero- and quantum well structures, *J. Phys. Condens. Matter.* **14** (2002) 3399–3434. https://doi.org/10.1088/0953-8984/14/13/302.

[32] Y. Zhao et al., 30-mW-class high-power and high-efficiency blue semipolar (10$\bar{1}$1) InGaN/GaN light-emitting diodes obtained by backside roughening technique, *Appl. Phys. Express.* **3** (2010) 10–12. https://doi.org/10.1143/APEX.3.102101.

[33] A.E. Romanov et al., Strain-induced polarization in wurtzite III-nitride semipolar layers, *J. Appl. Phys.* **100** (2006). https://doi.org/10.1063/1.2218385.

[34] D.L. Becerra et al., High-power low-droop violet semipolar (30-3-1) InGaN/GaN light-emitting diodes with thick active layer design, *Appl. Phys. Lett.* **105** (2014). https://doi.org/10.1063/1.4900793.

[35] J. Huang et al., eds., Nitride Semiconductor Light-Emitting Diodes (LEDs): Materials, Technologies, and Applications, 2nd ed., Woodhead Publishing, 2018.

[36] K. Shimada, First-principles determination of piezoelectric stress and strain constants of wurtzite III-V nitrides, *Japanese J. Appl. Physics, Part 2 Lett.* **45** (2006). https://doi.org/10.1143/JJAP.45.L358.

[37] M. Cardona et al., eds., Light Scattering in Solids II: basic concepts and instrumentation, 1st ed., Springer-Verlag Berlin Heidelberg, Germany, 1982.

[38] H.W. Kunert, Raman selection rules in C6v4 hexagonal crystals: Allowed combinations and overtones of vibrational modes in wurtzite GaN, *Cryst. Res. Technol.* **38** (2003) 366–373. https://doi.org/10.1002/crat.200310045.

[39] H. Harima, Properties of GaN and related compounds studied by means of Raman scattering, *J. Phys. Condens. Matter.* **14** (2002) R967–R993. https://doi.org/10.1088/0953-8984/14/38/201.

[40] R. Loudon, The Raman effect in crystals, *Adv. Phys.* **13** (1964) 423–482. https://doi.org/10.1080/00018736400101051.

[41] J. Zhang et al., Raman spectra of isotopic GaN, *Phys. Rev. B - Condens. Matter Mater. Phys.*

56 (1997) 14399–14406. https://doi.org/10.1103/PhysRevB.56.14399.

[42] V.Y. Davydov et al., Phonon dispersion and Raman scattering in hexagonal GaN and AlN, *Phys. Rev. B.* **58** (1998) 12899–12907. https://doi.org/10.1103/PhysRevB.58.12899.

[43] V.Y. Davydov et al., Experimental and theoretical studies of phonons in hexagonal InN, *Appl. Phys. Lett.* **75** (1999) 3297–3299. https://doi.org/10.1063/1.125330.

[44] G. Irmer et al., Determination of the charge carrier concentration and mobility in n-gap by Raman spectroscopy, *Phys. Status Solidi.* **119** (1983) 595–603. https://doi.org/10.1002/pssb.2221190219.

[45] D.B. Newell et al., The international system of units (SI), 2019. https://doi.org/10.6028/NIST.SP.330-2019.

[46] NIST, CODATA Internationally recommended 2018 values of the Fundamental Physical Constants, *NIST Ref. Constants, Units, Uncertain.* (2019). https://physics.nist.gov/cuu/Constants/index.html (accessed September 27, 2023).

[47] L.H. Robins et al., Raman spectroscopy based measurements of carrier concentration in n-type GaN nanowires grown by plasma-assisted molecular beam epitaxy, *J. Appl. Phys.* **120** (2016). https://doi.org/10.1063/1.4963291.

[48] P. Perlin et al., Investigation of longitudinal-optical phonon-plasmon coupled modes in highly conducting bulk GaN, *Appl. Phys. Lett.* **67** (1995) 2524. https://doi.org/10.1063/1.114446.

[49] T. Kozawa et al., Raman scattering from LO phonon-plasmon coupled modes in gallium nitride, *J. Appl. Phys.* **75** (1994) 1098–1101. https://doi.org/10.1063/1.356492.

[50] C. Wetzel et al., Electron-Phonon Scattering in Si-Doped GaN, *MRS Proc.* **449** (1996) 567. https://doi.org/10.1557/PROC-449-567.

[51] V.Y. Davydov et al., Raman and photoluminescence studies of biaxial strain in GaN epitaxial layers grown on 6H-SiC, *J. Appl. Phys.* **82** (1997) 5097–5102. https://doi.org/10.1063/1.366310.

[52] F. Demangeot et al., Raman determination of phonon deformation potentials in α-GaN, *Solid State Commun.* **100** (1996) 207–210. https://doi.org/10.1016/0038-1098(96)00410-3.

[53] V. Darakchieva et al., Deformation potentials of the E 1 (TO) and E 2 modes of InN, *Appl. Phys. Lett.* **84** (2004) 3636–3638. https://doi.org/10.1063/1.1738520.

[54] X. Wang et al., Experimental determination of strain-free Raman frequencies and deformation potentials for the E2 high and A1(LO) modes in hexagonal InN, *Appl. Phys. Lett.* **89** (2006). https://doi.org/10.1063/1.2364884.

[55] S. Hernández et al., Raman-scattering study of the InGaN alloy over the whole composition range, *J. Appl. Phys.* **98** (2005). https://doi.org/10.1063/1.1940139.

[56] M.R. Correia et al., Raman study of the A_1(LO) phonon in relaxed and pseudomorphic InGaN epilayers, *Appl. Phys. Lett.* **83** (2003) 4761–4763. https://doi.org/10.1063/1.1627941.

[57] V.Y. Davydov et al., Composition dependence of optical phonon energies and Raman line broadening in hexagonal $Al_xGa_{1-x}N$ alloys, *Phys. Rev. B.* **65** (2002) 125203. https://doi.org/10.1103/PhysRevB.65.125203.

[58] U. Haboeck et al., Lattice dynamics in GaN and AlN probed with first- and second-order Raman spectroscopy, *Phys. Status Solidi C Conf.* **0** (2003) 1710–1731. https://doi.org/10.1002/pssc.200303130.

[59] A. Cros et al., Raman study of the optical phonons in $Al_xGa_{1-x}N$ alloys, *Solid State Commun.* **104** (1997) 35–39. https://doi.org/10.1016/S0038-1098(97)00162-2.

[60] M. Holtz et al., Composition dependence of the optical phonon energies in hexagonal $Al_xGa_{1-x}N$, *J. Appl. Phys.* **89** (2001) 7977–7982. https://doi.org/10.1063/1.1372661.

[61] E.A. Lladó, Vibrational properties of ZnO, group III-nitrides and dilute nitride alloys,

Universitat de Barcelona, 2009. http://dx.doi.org/10.1016/B978-0-444-53175-9.00004-0.

[62] H. Grille et al., Phonons in ternary group-III nitride alloys, *Phys. Rev. B.* **61** (2000) 6091–6105. https://doi.org/10.1103/PhysRevB.61.6091.

[63] R. Loudon et al., Theory of the first-order Raman effect in crystals, *Proc. R. Soc. London. Ser. A. Math. Phys. Sci.* **275** (1963) 218–232. https://doi.org/10.1098/rspa.1963.0166.

[64] P.Y. Yu et al., Fundamentals of semiconductors: physics and materials properties, 4th ed., Springer-Verlag Berlin Heidelberg, Germany, 2010.

[65] W. Richter, Resonant Raman scattering in semiconductors, in: Festkörperprobleme 16, 1st ed., Springer Berlin Heidelberg, Germany, 1976: pp. 121–272.

[66] T. Ruf, Phonon Raman Scattering in Semiconductors, Quantum Wells and Superlattices, 1st ed., Springer-Verlag Berlin Heidelberg, Germany, 1998.

[67] D. Fritsch et al., Band-structure pseudopotential calculation of zinc-blende and wurtzite AlN, GaN, and InN, *Phys. Rev. B - Condens. Matter Mater. Phys.* **67** (2003) 1–13. https://doi.org/10.1103/PhysRevB.67.235205.

[68] J.M. Hollas, Modern Spectroscopy, 4th ed., John Wiley & Sons, Inc., England, 2004.

[69] P.P. Paskov et al., Optical Properties of III-Nitride Semiconductors, in: Handb. GaN Semicond. Mater. Devices, 1st ed., CRC Press, United States, 2017: pp. 87–116.

[70] K.B. Nam et al., Unique optical properties of AlGaN alloys and related ultraviolet emitters, *Appl. Phys. Lett.* **84** (2004) 5264–5266. https://doi.org/10.1063/1.1765208.

[71] Y.P. Varshni, Temperature dependence of the energy gap in semiconductors, *Physica.* **34** (1967) 149–154. https://doi.org/10.1016/0031-8914(67)90062-6.

[72] D.A. Neamen, Semiconductor physics and devices: basic principles, 4th ed., McGraw-Hill, United States, 2012.

[73] B. Monemar, III-V nitrides - important future electronic materials, *J. Mater. Sci. Mater. Electron.* **10** (1999) 227–254. https://doi.org/10.1023/A:1008991414520.

[74] S.M. Sze, Semiconductor devices: physics and technology, 2nd ed., Wiley, United States, 2002.

[75] A. Hangleiter et al., Composition dependence of polarization fields in GaInN/GaN quantum wells, *Appl. Phys. Lett.* **83** (2003) 1169–1171. https://doi.org/10.1063/1.1601310.

[76] J. Li et al., III-Nitrides Light Emitting Diodes: Technology and Applications, 1st ed., Springer Nature Singapore Pte Ltd, Singapore, 2020.

[77] B. Ding, Improving radiative recombination efficiency of green light-emitting diodes, *Mater. Sci. Technol.* **34** (2018) 1615–1630. https://doi.org/10.1080/02670836.2018.1461587.

[78] F. Ren et al., eds., Wide Bandgap Semiconductor-Based Electronics, IOP Publishing, United Kingdom, 2020.

[79] M. Meneghini et al., GaN-based power devices: physics , reliability and perspectives, *J. Appl. Phys.* **130** (2021) 227. https://doi.org/10.1063/5.0061354.

[80] M. Fox, Optical Properties of Solids, 1st ed., Oxford University Press Inc., United States, 2001.

[81] J. Wu, When group-III nitrides go infrared: New properties and perspectives, *J. Appl. Phys.* **106** (2009). https://doi.org/10.1063/1.3155798.

[82] K. Kornitzer et al., Photoluminescence and reflectance spectroscopy of excitonic transitions in high-quality homoepitaxial GaN films, *Phys. Rev. B - Condens. Matter Mater. Phys.* **60** (1999) 1471–1473. https://doi.org/10.1103/PhysRevB.60.1471.

[83] G. Steude et al., Optical investigations of AlGaN on GaN epitaxial films, *MRS Internet J. Nitride Semicond. Res.* **4** (1999) 10–13. https://doi.org/10.1557/s1092578300002532.

[84] F. Yang et al., The origin of the Stokes shift. The line shapes of quantum well exciton absorption and photoluminescence spectra, *Phys. B Phys. Condens. Matter.* **185** (1993) 362–

365. https://doi.org/10.1016/0921-4526(93)90262-5.

[85] R.W. Martin et al., Exciton localization and the Stokes' shift in InGaN epilayers, *Appl. Phys. Lett.* **74** (1999) 263–265. https://doi.org/10.1063/1.123275.

[86] K.P. O'Donnell et al., Origin of Luminescence from InGaN Diodes, *Phys. Rev. Lett.* **82** (1999) 237–240. https://doi.org/10.1103/PhysRevLett.82.237.

[87] K.P. O'Donnell et al., The dependence of the optical energies on InGaN composition, *Mater. Sci. Eng. B Solid-State Mater. Adv. Technol.* **82** (2001) 194–196. https://doi.org/10.1016/S0921-5107(00)00706-6.

[88] T. Onuma et al., Radiative and nonradiative processes in strain-free $Al_xGa_{1-x}N$ films studied by time-resolved photoluminescence and positron annihilation techniques, *J. Appl. Phys.* **95** (2004) 2495–2504. https://doi.org/10.1063/1.1644041.

[89] A. Pierret et al., Growth, structural and optical properties of AlGaN nanowires in the whole composition range, *Nanotechnology.* **24** (2013) 115704. https://doi.org/10.1088/0957-4484/24/11/115704.

[90] M.A. Reshchikov, Measurement and analysis of photoluminescence in GaN, *J. Appl. Phys.* **129** (2021) 121101. https://doi.org/10.1063/5.0041608.

[91] M.A. Reshchikov et al., Two charge states of the C_N acceptor in GaN: Evidence from photoluminescence, *Phys. Rev. B.* **98** (2018) 125207. https://doi.org/10.1103/PhysRevB.98.125207.

[92] J.L. Lyons et al., Carbon impurities and the yellow luminescence in GaN, *Appl. Phys. Lett.* **97** (2010) 152108. https://doi.org/10.1063/1.3492841.

[93] J.L. Lyons et al., Computationally predicted energies and properties of defects in GaN, *Npj Comput. Mater.* **3** (2017) 1–9. https://doi.org/10.1038/s41524-017-0014-2.

[94] T. Mattila et al., Point-defect complexes and broadband luminescence in GaN and AlN, *Phys. Rev. B - Condens. Matter Mater. Phys.* **55** (1997) 9571–9576. https://doi.org/10.1103/PhysRevB.55.9571.

[95] T. Koppe et al., Overview of band-edge and defect related luminescence in aluminum nitride, *J. Lumin.* **178** (2016) 267–281. https://doi.org/10.1016/j.jlumin.2016.05.055.

[96] L. Trinkler et al., UV light induced processes in pure and doped AlN ceramics, *Opt. Mater. (Amst).* **121** (2021) 111550. https://doi.org/10.1016/j.optmat.2021.111550.

[97] T. Koyama et al., Relation between Al vacancies and deep emission bands in AlN epitaxial films grown by N H3 -source molecular beam epitaxy, *Appl. Phys. Lett.* **90** (2007). https://doi.org/10.1063/1.2748315.

[98] A. Sedhain et al., Nature of optical transitions involving cation vacancies and complexes in AlN and AlGaN, *Appl. Phys. Lett.* **100** (2012). https://doi.org/10.1063/1.4723693.

[99] Q. Yan et al., Origins of optical absorption and emission lines in AlN, *Appl. Phys. Lett.* **105** (2014) 0–5. https://doi.org/10.1063/1.4895786.

[100] Q. Zhou et al., Below bandgap photoluminescence of an AlN crystal: Co-existence of two different charging states of a defect center, *APL Mater.* **8** (2020). https://doi.org/10.1063/5.0012685.

[101] D.S.P. Tanner et al., Polar (In, Ga)N/GaN Quantum Wells: Revisiting the Impact of Carrier Localization on the "Green Gap" Problem, *Phys. Rev. Appl.* **13** (2020) 1. https://doi.org/10.1103/PhysRevApplied.13.044068.

[102] B. Damilano et al., Yellow-red emission from (Ga,In)N heterostructures, *J. Phys. D. Appl. Phys.* **48** (2015). https://doi.org/10.1088/0022-3727/48/40/403001.

[103] C. Spindler et al., Excitation-intensity dependence of shallow and deep-level photoluminescence transitions in semiconductors, *J. Appl. Phys.* **126** (2019).

https://doi.org/10.1063/1.5095235.

[104] S. Nakamura et al., High-Power GaN P-N Junction Blue-Light-Emitting Diodes, *Jpn. J. Appl. Phys.* **30** (1991) L1998–L2001. https://doi.org/10.1143/JJAP.30.L1998.

[105] I. Akasaki, Fascinating journeys into blue light (Nobel Lecture), *Ann. Phys.* **527** (2015) 311–326. https://doi.org/10.1002/andp.201500803.

[106] S. Nakamura, Nobel Lecture: Background story of the invention of efficient blue InGaN light emitting diodes, *Rev. Mod. Phys.* **87** (2015) 1139–1151. https://doi.org/10.1103/RevModPhys.87.1139.

[107] J. Neugebauer et al., Atomic geometry and electronic structure of native defects in GaN, *Phys. Rev. B.* **50** (1994) 8067–8070. https://doi.org/10.1103/PhysRevB.50.8067.

[108] C.G. Van De Walle et al., First-principles calculations for defects and impurities: Applications to III-nitrides, *J. Appl. Phys.* **95** (2004) 3851–3879. https://doi.org/10.1063/1.1682673.

[109] H. Wang et al., Calculation of shallow donor levels in GaN, *J. Appl. Phys.* **87** (2000) 7859–7863. https://doi.org/10.1063/1.373467.

[110] A. Shikanai et al., Optical properties of Si-, Ge- and Sn-doped GaN, *Phys. Status Solidi Basic Res.* **235** (2003) 26–30. https://doi.org/10.1002/pssb.200301525.

[111] W. Götz et al., Activation energies of Si donors in GaN, *Appl. Phys. Lett.* **68** (1996) 3144–3146. https://doi.org/10.1063/1.115805.

[112] A. Wolos et al., Properties of metal-insulator transition and electron spin relaxation in GaN:Si, *Phys. Rev. B.* **83** (2011) 165206. https://doi.org/10.1103/PhysRevB.83.165206.

[113] Y. Taniyasu et al., An aluminium nitride light-emitting diode with a wavelength of 210 nanometres, *Nature.* **441** (2006) 325–328. https://doi.org/10.1038/nature04760.

[114] M.H. Breckenridge et al., High n -type conductivity and carrier concentration in Si-implanted homoepitaxial AlN, *Appl. Phys. Lett.* **118** (2021). https://doi.org/10.1063/5.0042857.

[115] W. Götz et al., Hall-effect characterization of III-V nitride semiconductors for high efficiency light emitting diodes, *Mater. Sci. Eng. B Solid-State Mater. Adv. Technol.* **59** (1999) 211–217. https://doi.org/10.1016/S0921-5107(98)00393-6.

[116] A. Hoffmann et al., Local vibrational modes and compensation effects in Mg-doped GaN, *Phys. Status Solidi C Conf.* **0** (2003) 1783–1794. https://doi.org/10.1002/pssc.200303120.

[117] K.B. Nam et al., Mg acceptor level in AlN probed by deep ultraviolet photoluminescence, *Appl. Phys. Lett.* **83** (2003) 878–880. https://doi.org/10.1063/1.1594833.

[118] C. Pfüller et al., Unpinning the Fermi level of GaN nanowires by ultraviolet radiation, *Phys. Rev. B - Condens. Matter Mater. Phys.* **82** (2010) 1–5. https://doi.org/10.1103/PhysRevB.82.045320.

[119] J. Lähnemann et al., Quenching of the luminescence intensity of GaN nanowires under electron beam exposure: Impact of C adsorption on the exciton lifetime, *Nanotechnology.* **27** (2016). https://doi.org/10.1088/0957-4484/27/45/455706.

[120] Z. Fang et al., Si Donor Incorporation in GaN Nanowires, *Nano Lett.* **15** (2015) 6794–6801. https://doi.org/10.1021/acs.nanolett.5b02634.

[121] J. Neugebauer, Surfactants and antisurfactants on group-III-nitride surfaces, *Phys. Status Solidi C Conf.* **0** (2003) 1651–1667. https://doi.org/10.1002/pssc.200303132.

[122] E.N. Aybeke et al., Nanoscale imaging of dopant incorporation in n-type and p-type GaN nanowires by scanning spreading resistance microscopy, *J. Appl. Phys.* **131** (2022) 075701. https://doi.org/10.1063/5.0080713.

[123] R. Vermeersch et al., Shallow donor and DX state in Si doped AlN nanowires grown by molecular beam epitaxy, *Appl. Phys. Lett.* **119** (2021). https://doi.org/10.1063/5.0074454.

[124] R. Vermeersch et al., DX center formation in highly Si doped AlN nanowires revealed by trap

assisted space-charge limited current, *Appl. Phys. Lett.* **120** (2022). https://doi.org/10.1063/5.0087789.

[125] Y. Wu et al., Controlling Defect Formation of Nanoscale AlN: Toward Efficient Current Conduction of Ultrawide-Bandgap Semiconductors, *Adv. Electron. Mater.* **6** (2020) 1–7. https://doi.org/10.1002/aelm.202000337.

[126] S. Zhao et al., Recent advances on p-type III-nitride nanowires by molecular beam epitaxy, *Crystals.* **7** (2017) 18–26. https://doi.org/10.3390/cryst7090268.

[127] N.H. Tran et al., On the mechanism of highly efficient p-type conduction of Mg-doped ultra-wide-bandgap AlN nanostructures, *Appl. Phys. Lett.* **110** (2017). https://doi.org/10.1063/1.4973999.

[128] A.-M. Siladie et al., Mg and In Codoped p-type AlN Nanowires for pn Junction Realization, *Nano Lett.* **19** (2019) 8357–8364. https://doi.org/10.1021/acs.nanolett.9b01394.

[129] E.F. Schubert, Light-emitting diodes, 2nd ed., Cambridge University Press, United States, 2006.

[130] M. Meneghini et al., Thermal droop in III-nitride based light-emitting diodes: Physical origin and perspectives, *J. Appl. Phys.* **127** (2020). https://doi.org/10.1063/5.0005874.

[131] R. Vermeersch et al., Comprehensive Electro-Optical Investigation of a Ga-Doped AlN Nanowire LED for Applications in the UV-C Range, *ACS Appl. Nano Mater.* (2023). https://doi.org/10.1021/acsanm.3c01705.

[132] Y.J. Lee et al., Elucidating the physical property of the InGaN nanorod light-emitting diode: Large tunneling effect, *IEEE J. Sel. Top. Quantum Electron.* **17** (2011) 985–989. https://doi.org/10.1109/JSTQE.2010.2064287.

[133] X. Cao et al., Influence of defects on electrical and optical characteristics of GaN/InGaN-based light-emitting diodes, *Solid State Light. II.* **4776** (2002) 105. https://doi.org/10.1117/12.452581.

[134] H.C. Casey et al., Dominance of tunneling current and band filling in InGaN/AlGaN double heterostructure blue light-emitting diodes, *Appl. Phys. Lett.* **68** (1996) 2867–2869. https://doi.org/10.1063/1.116351.

[135] J.M. Shah et al., Experimental analysis and theoretical model for anomalously high ideality factors (n≫2.0) in AlGaN/GaN p-n junction diodes, *J. Appl. Phys.* **94** (2003) 2627–2630. https://doi.org/10.1063/1.1593218.

[136] C.H. Wang et al., Is it viable to improve light output efficiency by nano-light-emitting diodes?, *Appl. Phys. Lett.* **103** (2013). https://doi.org/10.1063/1.4844715.

[137] K. Mayes et al., High-power 280 nm AlGaN light-emitting diodes based on an asymmetric single-quantum well, *Appl. Phys. Lett.* **84** (2004) 1046–1048. https://doi.org/10.1063/1.1647273.

[138] M. Musolino et al., Understanding peculiarities in the optoelectronic characteristics of light emitting diodes based on (In,Ga)N/GaN nanowires, *Appl. Phys. Lett.* **105** (2014). https://doi.org/10.1063/1.4894241.

[139] M. Musolino et al., A modified Shockley equation taking into account the multi-element nature of light emitting diodes based on nanowire ensembles, *Nanotechnology.* **27** (2016). https://doi.org/10.1088/0957-4484/27/27/275203.

[140] H. Masui et al., Technique to evaluate the diode ideality factor of light-emitting diodes, *Appl. Phys. Lett.* **96** (2010) 2–5. https://doi.org/10.1063/1.3318285.

[141] T.-Y. Seong et al., eds., III-Nitride Based Light Emitting Diodes and Applications, 2nd ed., Springer Nature Singapore Pte Ltd, Singapore, 2013.

[142] IUPAC, Periodic Table of Elements, (2022). https://iupac.org/what-we-do/periodic-table-of-

elements/ (accessed May 9, 2022).

[143] R. Hull et al., eds., Spectroscopic Properties of Rare Earths in Optical Materials, 1st ed., Springer Berlin Heidelberg, Germany, 2005.

[144] K. O'Donnell et al., eds., Rare Earth Doped III-Nitrides for Optoelectronic and Spintronic Applications, 1st ed., Springer Netherlands, Netherlands, 2010.

[145] Atkins Peter et al., Shriver & Atkins' Inorganic Chemistry, 5th ed., Oxford University Press Inc., United States, 2010.

[146] B.G. Wybourne, Spectroscopic Properties of Rare Earths, 1st ed., John Wiley & Sons, Inc., United States, 1965.

[147] J.-C.G. Bünzli et al., Basics of Lanthanide Photophysics, in: Lanthan. Lumin., 1st ed., Springer Berlin Heidelberg, Germany, 2011.

[148] B.R. Judd et al., Intra-Atomic magnetic interactions for f electrons, *Phys. Rev.* **169** (1968) 130–138. https://doi.org/10.1103/PhysRev.169.130.

[149] G. Racah, Theory of Complex Spectra. IV, *Phys. Rev.* **76** (1949) 1352–1365. https://doi.org/10.1103/PhysRev.76.1352.

[150] G.H. Dieke, Spectra and Energy Levels of Rare Earth Ions in Crystals, 1st ed., Interscience Publishers, United States, 1968.

[151] P.S. Peijzel et al., A complete $4f^n$ energy level diagram for all trivalent lanthanide ions, *J. Solid State Chem.* **178** (2005) 448–453. https://doi.org/10.1016/j.jssc.2004.07.046.

[152] W.T. Carnall et al., A systematic analysis of the spectra of the lanthanides doped into single crystal LaF_3, *J. Chem. Phys.* **90** (1989) 3443–3457. https://doi.org/10.1063/1.455853.

[153] W.A. Runciman, Stark-splitting in crystals, *Philos. Mag.* **1** (1956) 1075–1077. https://doi.org/10.1080/14786435608238189.

[154] B.M. Walsh, Judd-Ofelt theory: principles and practices, in: B. Di Bartolo et al. (Eds.), Adv. Spectrosc. Lasers Sens., Springer Netherlands, Netherlands, 2006: pp. 403–433.

[155] R.C. Powell, Physics of Solid-State Laser Materials: Atomic, Molecular and Optical Physics, 1998. http://ir.obihiro.ac.jp/dspace/handle/10322/3933.

[156] J.H.V. Vleck, The Puzzle of Rare-earth Spectra in Solids, *J. Phys. Chem.* **41** (1937) 67–80. https://doi.org/10.1021/j150379a006.

[157] B.R. Judd, Optical Absorption Intensities of Rare-Earth Ions, *Phys. Rev.* **127** (1962) 750–761. https://doi.org/10.1103/PhysRev.127.750.

[158] G.S. Ofelt, Intensities of Crystal Spectra of Rare-Earth Ions, *J. Chem. Phys.* **37** (1962) 511–520. https://doi.org/10.1063/1.1701366.

[159] W.T. Carnall et al., Electronic Energy Levels in the Trivalent Lanthanide Aquo Ions. I. Pr^{3+}, Nd^{3+}, Pm^{3+}, Sm^{3+}, Dy^{3+}, Ho^{3+}, Er^{3+}, and Tm^{3+}, *J. Chem. Phys.* **49** (1968) 4424–4442. https://doi.org/10.1063/1.1669893.

[160] M.H.V. Werts et al., The emission spectrum and the radiative lifetime of Eu^{3+} in luminescent lanthanide complexes, *Phys. Chem. Chem. Phys.* **4** (2002) 1542–1548. https://doi.org/10.1039/b107770h.

[161] C. Gorller-Walrand et al., Spectral intensities of *f-f* transitions in Handbook on the Physics and Chemistry of Rare Earths edited by K.A. Gscheneidner Jr. and L. Eyring (North Holland, Amsterdam, 1998), *Handb. Phys. Chem. Rare Earths.* **25** (1998) 101–264.

[162] K. Binnemans, Interpretation of europium(III) spectra, *Coord. Chem. Rev.* **295** (2015) 1–45. https://doi.org/10.1016/j.ccr.2015.02.015.

[163] Y. Fujiwara et al., Present understanding of Eu luminescent centers in Eu-doped GaN grown by organometallic vapor phase epitaxy, *Jpn. J. Appl. Phys.* **53** (2014) 05FA13. https://doi.org/10.7567/JJAP.53.05FA13.

[164] S. Ichikawa et al., Eu-doped GaN and InGaN monolithically stacked full-color LEDs with a wide color gamut, *Appl. Phys. Express.* **14** (2021) 031008. https://doi.org/10.35848/1882-0786/abe603.

[165] T. Andreev et al., Eu^{3+} location in Eu doped GaN thin films and quantum dots, *Phys. Status Solidi.* **3** (2006) 2026–2029. https://doi.org/10.1002/pssc.200565111.

[166] W.M. Jadwisienczak et al., Visible emission from AlN doped with Eu and Tb ions, *J. Appl. Phys.* **89** (2001) 4384–4390. https://doi.org/10.1063/1.1357467.

[167] K. Lorenz et al., Rare earth doping of III-nitride alloys by ion implantation, *Phys. Status Solidi.* **205** (2008) 34–37. https://doi.org/10.1002/pssa.200776714.

[168] I.S. Roqan et al., Optical and structural properties of Eu-implanted $In_xAl_{1-x}N$, *J. Appl. Phys.* **106** (2009) 1–5. https://doi.org/10.1063/1.3245386.

[169] K. Lorenz et al., Structural and optical characterization of Eu-implanted GaN, *J. Phys. D. Appl. Phys.* **42** (2009). https://doi.org/10.1088/0022-3727/42/16/165103.

[170] U. Wahl et al., Lattice location and optical activation of rare earth implanted GaN, *Mater. Sci. Eng. B Solid-State Mater. Adv. Technol.* **105** (2003) 132–140. https://doi.org/10.1016/j.mseb.2003.08.031.

[171] H.J. Lozykowski et al., Luminescence properties of GaN and $Al_{0.14}Ga_{0.86}N$/GaN superlattice doped with europium, *Appl. Phys. Lett.* **77** (2000) 767–769. https://doi.org/10.1063/1.1306645.

[172] S. Petit et al., Electronic behavior of rare-earth dopants in AlN: A density-functional study, *Phys. Rev. B - Condens. Matter Mater. Phys.* **72** (2005) 4–7. https://doi.org/10.1103/PhysRevB.72.073205.

[173] J.S. Filhol et al., Structure and electrical activity of rare-earth dopants in GaN, *Appl. Phys. Lett.* **84** (2004) 2841–2843. https://doi.org/10.1063/1.1710710.

[174] K. Hoang, Tuning the valence and concentration of europium and luminescence centers in GaN through co-doping and defect association, *Phys. Rev. Mater.* **5** (2021) 034601. https://doi.org/10.1103/PhysRevMaterials.5.034601.

[175] K. Hoang, Rare-earth defects in GaN: A systematic investigation of the lanthanide series, *Phys. Rev. Mater.* **6** (2022) 044601. https://doi.org/10.1103/PhysRevMaterials.6.044601.

[176] S. Sanna et al., Rare-earth defect pairs in GaN: LDA+U calculations, *Phys. Rev. B.* **80** (2009) 104120. https://doi.org/10.1103/PhysRevB.80.104120.

[177] H. Peng et al., Spectroscopic and energy transfer studies of Eu^{3+} centers in GaN, *J. Appl. Phys.* **102** (2007) 073520. https://doi.org/10.1063/1.2783893.

[178] J.B. Gruber et al., Spectroscopic analysis of Eu^{3+} in single-crystal hexagonal phase AlN, *J. Appl. Phys.* **110** (2011) 023104. https://doi.org/10.1063/1.3609076.

[179] T. Monteiro et al., Photoluminescence and lattice location of Eu and Pr implanted GaN samples, *Phys. B Condens. Matter.* **308–310** (2001) 22–25. https://doi.org/10.1016/S0921-4526(01)00656-1.

[180] B. Mitchell et al., Color-Tunablility in GaN LEDs Based on Atomic Emission Manipulation under Current Injection, *ACS Photonics.* **6** (2019) 1153–1161. https://doi.org/10.1021/acsphotonics.8b01461.

[181] B. Mitchell et al., Temporally modulated energy shuffling in highly interconnected nanosystems, *Nanophotonics.* (2020) 1–26. https://doi.org/10.1515/nanoph-2020-0484.

[182] T. Fujiwara et al., Photoluminescence properties of Eu-implanted $Al_xGa_{1-x}N$ ($0 \leq x \leq 1$), *Phys. Status Solidi.* **2** (2005) 2805–2808. https://doi.org/10.1002/pssc.200461431.

[183] M. Peres et al., Optical and structural studies in Eu-implanted AlN films, *Superlattices Microstruct.* **40** (2006) 537–544. https://doi.org/10.1016/j.spmi.2006.07.031.

[184] R.D. Shannon, Revised effective ionic radii and systematic studies of interatomic distances in halides and chalcogenides, *Acta Crystallogr. Sect. A.* **32** (1976) 751–767. https://doi.org/10.1107/S0567739476001551.

[185] H.J. Lozykowski, Kinetics of luminescence of isoelectronic rare-earth ions in III-V semiconductors, *Phys. Rev. B.* **48** (1993) 17758–17769. https://doi.org/10.1103/PhysRevB.48.17758.

[186] B. Mitchell et al., Perspective: Toward efficient GaN-based red light emitting diodes using europium doping, *J. Appl. Phys.* **123** (2018) 160901. https://doi.org/10.1063/1.5010762.

[187] N. Woodward et al., Excitation of Eu^{3+} in gallium nitride epitaxial layers: Majority versus trap defect center, *Appl. Phys. Lett.* **98** (2011) 011102. https://doi.org/10.1063/1.3533806.

[188] K. Lorenz et al., Lattice site location of optical centers in GaN:Eu light emitting diode material grown by organometallic vapor phase epitaxy, *Appl. Phys. Lett.* **97** (2010). https://doi.org/10.1063/1.3489103.

[189] Z. Fleischman et al., Excitation pathways and efficiency of Eu ions in GaN by site-selective spectroscopy, *Appl. Phys. B Lasers Opt.* **97** (2009) 607–618. https://doi.org/10.1007/s00340-009-3605-x.

[190] R. Wakamatsu et al., Luminescence properties of Eu-doped GaN under resonant excitation and quantitative evaluation of luminescent sites, *J. Appl. Phys.* **114** (2013) 043501. https://doi.org/10.1063/1.4816088.

[191] K. Wang et al., Selectively excited photoluminescence from Eu-implanted GaN, *Appl. Phys. Lett.* **87** (2005) 112107. https://doi.org/10.1063/1.2045551.

[192] L. Bodiou et al., Effect of annealing temperature on luminescence in Eu implanted GaN, *Opt. Mater. (Amst).* **28** (2006) 780–784. https://doi.org/10.1016/j.optmat.2005.09.022.

[193] L. Bodiou et al., Optically active centers in Eu implanted, Eu in situ doped GaN, and Eu doped GaN quantum dots, *J. Appl. Phys.* **105** (2009) 043104. https://doi.org/10.1063/1.3078783.

[194] I.S. Roqan et al., Identification of the prime optical center in GaN:Eu^{3+}, *Phys. Rev. B.* **81** (2010) 085209. https://doi.org/10.1103/PhysRevB.81.085209.

[195] B. Mitchell et al., The role of donor-acceptor pairs in the excitation of Eu-ions in GaN:Eu epitaxial layers, *J. Appl. Phys.* **115** (2014) 204501. https://doi.org/10.1063/1.4879253.

[196] B. Mitchell et al., Vibrationally induced center reconfiguration in co-doped GaN:Eu, Mg epitaxial layers: Local hydrogen migration vs. activation of non-radiative channels, *Appl. Phys. Lett.* **103** (2013). https://doi.org/10.1063/1.4846575.

[197] M.J. Soares et al., Structural and optical properties of Er implanted AlN thin films: Green and infrared photoluminescence at room temperature, *Opt. Mater. (Amst).* **33** (2011) 1055–1058. https://doi.org/10.1016/j.optmat.2010.09.005.

[198] M. Godlewski et al., Excitation and recombination processes during electroluminescence of rare earth-activated materials, *Crit. Rev. Solid State Mater. Sci.* **19** (1994) 199–239. https://doi.org/10.1080/10408439408244590.

[199] D.J. Robbins et al., The effects of core structure on radiative and non-radiative recombinations at metal ion substituents in semiconductors and phosphors, *Adv. Phys.* **27** (1978) 499–532. https://doi.org/10.1080/00018737800101434.

[200] D.L. Dexter, A theory of sensitized luminescence in solids, *J. Chem. Phys.* **21** (1953) 836–850. https://doi.org/10.1063/1.1699044.

[201] T. Főrster, 10th Spiers Memorial Lecture. Transfer mechanisms of electronic excitation, *Discuss. Faraday Soc.* **27** (1959) 7–17. https://doi.org/10.1039/DF9592700007.

[202] J. Shaffer et al., Energy Transfer from Donor–Acceptor Pairs to Deep-Lying Impurity States

in Semiconductors, *Phys. Status Solidi.* **38** (1970) 657–663. https://doi.org/10.1002/pssb.19700380217.

[203] T. Hoshina et al., Charge transfer effects on the luminescent properties of Eu^{3+} in oxysulfides, *J. Lumin.* **15** (1977) 455–471. https://doi.org/10.1016/0022-2313(77)90044-8.

[204] M. Ishii et al., Nanoscale determinant to brighten up GaN:Eu red light-emitting diode: Local potential of Eu-defect complexes, *J. Appl. Phys.* **117** (2015) 155307. https://doi.org/10.1063/1.4918662.

[205] K. Wang et al., Luminescence of Eu ions in $Al_xGa_{1-x}N$ across the entire alloy composition range, *Phys. Rev. B.* **80** (2009) 125206. https://doi.org/10.1103/PhysRevB.80.125206.

[206] E.P.J. Merkx et al., Modelling and optimization of UV absorbing photovoltaic windows using a thin film AlN:Eu^{3+} luminescence library, *Sol. Energy Mater. Sol. Cells.* **200** (2019) 110032. https://doi.org/10.1016/j.solmat.2019.110032.

[207] P. Dorenbos et al., Location of lanthanide impurity energy levels in the III-V semiconductor $Al_xGa_{1-x}N$ ($0 \leq x \leq 1$), *Opt. Mater.* **30** (2008) 1052–1057. https://doi.org/10.1016/j.optmat.2007.05.019.

[208] P. Dorenbos et al., Location of lanthanide impurity levels in the III-V semiconductor GaN, *Appl. Phys. Lett.* **89** (2006) 3–6. https://doi.org/10.1063/1.2336716.

[209] H.J. Lozykowski et al., Thermal quenching of luminescence and isovalent trap model for rare-earth-ion-doped AlN, *Phys. Status Solidi Basic Res.* **244** (2007) 2109–2126. https://doi.org/10.1002/pssb.200642152.

[210] M. Peres et al., Influence of the AlN molar fraction on the structural and optical properties of praseodymium-doped $Al_xGa_{1-x}N$ ($0 \leq x \leq 1$) alloys, *Microelectronics J.* **40** (2009) 377–380. https://doi.org/10.1016/j.mejo.2008.07.032.

[211] B. Han et al., Investigation of Luminescence from Dy^{3+} in AlN, *J. Electrochem. Soc.* **154** (2007) J44. https://doi.org/10.1149/1.2392913.

[212] J. Rodrigues et al., Analysis of the Tb^{3+} recombination in ion implanted $Al_xGa_{1-x}N$ ($0 \leq x \leq 1$) layers, *J. Lumin.* **178** (2016) 249–258. https://doi.org/10.1016/j.jlumin.2016.05.018.

[213] L. Jin et al., Optical property in colorless AlN bulk crystals: investigation of native defect-induced UV absorption, *Scr. Mater.* **190** (2021) 91–96. https://doi.org/10.1016/j.scriptamat.2020.08.049.

[214] M. Sall et al., Synergy between electronic and nuclear energy losses for color center creation in AlN, *EPL (Europhysics Lett.* **102** (2013) 26002. https://doi.org/10.1209/0295-5075/102/26002.

[215] M. Sall et al., On the effect of oxygen on the creation of colour centres in swift heavy ion-irradiated AlN, *Nucl. Instruments Methods Phys. Res. Sect. B Beam Interact. with Mater. Atoms.* **536** (2023) 18–22. https://doi.org/10.1016/j.nimb.2022.12.025.

[216] L. Peters et al., A Combination of Ion Implantation and High-Temperature Annealing: The Origin of the 265 nm Absorption in AlN, *Phys. Status Solidi.* (2022). https://doi.org/10.1002/pssa.202200485.

[217] W. Wesch et al., eds., Ion Beam Modification of Solids, 1st ed., Springer International Publishing, Switzerland, 2016.

[218] D.K. Avasthi et al., Swift Heavy Ions for Materials Engineering and Nanostructuring, 1st ed., Springer Netherlands, Netherlands, 2011.

[219] A. V. Krasheninnikov et al., Ion and electron irradiation-induced effects in nanostructured materials, *J. Appl. Phys.* **107** (2010). https://doi.org/10.1063/1.3318261.

[220] C. Ronning et al., Ion implantation into gallium nitride, *Phys. Rep.* **351** (2001) 349–385. https://doi.org/10.1016/S0370-1573(00)00142-3.

[221] J.F. Ziegler et al., SRIM: The stopping and range of ions in matter, 1st ed., United States, 2008.

[222] K. Lorenz, Ion Implantation into Nonconventional GaN Structures, *Physics (College. Park. Md).* **4** (2022) 548–564. https://doi.org/10.3390/physics4020036.

[223] S. Sato et al., Photoluminescence properties of praseodymium ions implanted into submicron regions in gallium nitride, *Jpn. J. Appl. Phys.* **58** (2019) 051011. https://doi.org/10.7567/1347-4065/ab142b.

[224] H.Y. Xiao et al., Threshold displacement energy in GaN: Ab initio molecular dynamics study, *J. Appl. Phys.* **105** (2009). https://doi.org/10.1063/1.3153277.

[225] J. Xi et al., Ab initio molecular dynamics simulations of AlN responding to low energy particle radiation, *J. Appl. Phys.* **123** (2018). https://doi.org/10.1063/1.5009750.

[226] S.O. Kucheyev et al., Dynamic annealing in III-nitrides under ion bombardment, *J. Appl. Phys.* **95** (2004) 3048–3054. https://doi.org/10.1063/1.1649459.

[227] P. Ruterana et al., A mechanism for damage formation in GaN during rare earth ion implantation at medium range energy and room temperature, *J. Appl. Phys.* **109** (2011) 1–7. https://doi.org/10.1063/1.3527944.

[228] B. Lacroix et al., Mechanisms of damage formation in Eu-implanted GaN probed by X-ray diffraction, *EPL (Europhysics Lett.* **96** (2011) 46002. https://doi.org/10.1209/0295-5075/96/46002.

[229] P. Ruterana et al., Mechanisms of damage formation during rare earth ion implantation in nitride semiconductors, *Jpn. J. Appl. Phys.* **52** (2013). https://doi.org/10.7567/JJAP.52.11NH02.

[230] F. Gloux et al., Transmission electron microscopy investigation of the structural damage formed in GaN by medium range energy rare earth ion implantation, *J. Appl. Phys.* **100** (2006). https://doi.org/10.1063/1.2357845.

[231] M. Fialho et al., AlN content influence on the properties of $Al_xGa_{1-x}N$ doped with Pr ions, *Nucl. Instruments Methods Phys. Res. Sect. B Beam Interact. with Mater. Atoms.* **273** (2012) 149–152. https://doi.org/10.1016/j.nimb.2011.07.062.

[232] M. Fialho et al., Lattice site location and luminescence studies of $Al_xGa_{1-x}N$ alloys doped with thulium ions, *Nucl. Instruments Methods Phys. Res. Sect. B Beam Interact. with Mater. Atoms.* **307** (2013) 495–498. https://doi.org/10.1016/j.nimb.2013.01.010.

[233] K. Lorenz et al., Structural and optical characterisation of Eu implanted $Al_xGa_{1-x}N$, *Nucl. Instruments Methods Phys. Res. Sect. B Beam Interact. with Mater. Atoms.* **257** (2007) 307–310. https://doi.org/10.1016/j.nimb.2007.01.020.

[234] S.O. Kucheyev et al., Structural disorder in ion-implanted $Al_xGa_{1-x}N$, *Appl. Phys. Lett.* **80** (2002) 787–789. https://doi.org/10.1063/1.1445478.

[235] S. Leclerc et al., Mechanisms of damage formation in Eu-implanted AlN, *J. Appl. Phys.* **112** (2012). https://doi.org/10.1063/1.4758311.

[236] K. Lorenz et al., High temperature annealing of Europium implanted AlN, *Nucl. Instruments Methods Phys. Res. Sect. B Beam Interact. with Mater. Atoms.* **268** (2010) 2907–2910. https://doi.org/10.1016/j.nimb.2010.05.003.

[237] S.O. Kucheyev et al., Ion implantation into GaN, *Mater. Sci. Eng. R Reports.* **33** (2001) 51–108. https://doi.org/10.1016/S0927-796X(01)00028-6.

[238] K. Lorenz et al., High temperature annealing of rare earth implanted GaN films: Structural and optical properties, *Opt. Mater. (Amst).* **28** (2006) 750–758. https://doi.org/10.1016/j.optmat.2005.09.015.

[239] D.N. Faye et al., Incorporation of Europium into GaN Nanowires by Ion Implantation, *J.*

Phys. Chem. C. **123** (2019) 11874–11887. https://doi.org/10.1021/acs.jpcc.8b12014.

[240] M. Fialho et al., Defect formation and optical activation of Tb implanted $Al_xGa_{1-x}N$ films using channeled implantation at different temperatures, *Surf. Coatings Technol.* **355** (2018) 29–39. https://doi.org/10.1016/j.surfcoat.2018.02.008.

[241] K. Lorenz et al., Implantation damage formation in a-, c- and m-plane GaN, *Acta Mater.* **123** (2017) 177–187. https://doi.org/10.1016/j.actamat.2016.10.020.

[242] N. Catarino et al., Enhanced dynamic annealing and optical activation of Eu implanted a-plane GaN, *EPL (Europhysics Lett.)* **97** (2012) 68004. https://doi.org/10.1209/0295-5075/97/68004.

[243] M. Fialho et al., Impact of implantation geometry and fluence on structural properties of $Al_xGa_{1-x}N$ implanted with thulium, *J. Appl. Phys.* **120** (2016). https://doi.org/10.1063/1.4966120.

[244] K. Lorenz et al., Optical doping and damage formation in AlN by Eu implantation, *J. Appl. Phys.* **107** (2010) 2–6. https://doi.org/10.1063/1.3291100.

[245] T. Nishimura et al., Simulation of channeled implantation of magnesium ions in gallium nitride, *Appl. Phys. Express.* **14** (2021). https://doi.org/10.35848/1882-0786/ac2a55.

[246] I. Grzegory et al., High pressure solution growth of GaN and related compounds, in: J.H. Edgar et al. (Eds.), Prop. Process. Appl. Gall. Nitride Relat. Semicond., INSPEC, The Institution of Electrical Engineers, London, United Kingdom, 1998.

[247] K. Sierakowski et al., High pressure processing of ion implanted gan, *Electron.* **9** (2020) 1–11. https://doi.org/10.3390/electronics9091380.

[248] I. Grzegory et al., III-V Nitrides-thermodynamics and crystal growth at high N_2 pressure, *J. Phys. Chem. Solids.* **56** (1995) 639–647. https://doi.org/10.1016/0022-3697(94)00257-6.

[249] J. Piechota et al., Melting versus Decomposition of GaN: Ab Initio Molecular Dynamics Study and Comparison to Experimental Data, *Chem. Mater.* (2023). https://doi.org/10.1021/acs.chemmater.3c01477.

[250] L. Peters et al., Sublimation behavior of AlN in nitrogen and argon at conditions used for high-temperature annealing, *J. Appl. Phys.* **133** (2023). https://doi.org/10.1063/5.0152054.

[251] S.M.C. Miranda et al., Sequential multiple-step europium ion implantation and annealing of GaN, *Phys. Status Solidi Curr. Top. Solid State Phys.* **11** (2014) 253–257. https://doi.org/10.1002/pssc.201300210.

[252] K. Lorenz et al., High-temperature annealing and optical activation of Eu-implanted GaN, *Appl. Phys. Lett.* **85** (2004) 2712–2714. https://doi.org/10.1063/1.1801686.

[253] N. Ben Sedrine et al., Eu-Doped AlGaN/GaN Superlattice-Based Diode Structure for Red Lighting: Excitation Mechanisms and Active Sites, *ACS Appl. Nano Mater.* **1** (2018) 3845–3858. https://doi.org/10.1021/acsanm.8b00612.

[254] N. Ben Sedrine et al., Optical investigations of europium ion implanted in nitride-based diode structures, *Surf. Coatings Technol.* **355** (2018) 40–44. https://doi.org/10.1016/j.surfcoat.2018.02.004.

[255] D.N. Faye et al., Study of damage formation and annealing of implanted III-nitride semiconductors for optoelectronic devices, *Nucl. Instruments Methods Phys. Res. Sect. B Beam Interact. with Mater. Atoms.* **379** (2016) 251–254. https://doi.org/10.1016/j.nimb.2016.03.028.

[256] S. Porowski et al., Annealing of GaN under high pressure of nitrogen, *J. Phys. Condens. Matter.* **14** (2002) 11097–11110. https://doi.org/10.1088/0953-8984/14/44/433.

[257] M.W. Ullah et al., Atomistic simulation of Er irradiation induced defects in GaN nanowires, *J. Appl. Phys.* **116** (2014) 124313. https://doi.org/10.1063/1.4896787.

[258] W. Ren et al., Molecular dynamics of irradiation-induced defect production in GaN nanowires, *Phys. Rev. B - Condens. Matter Mater. Phys.* **86** (2012) 1–7. https://doi.org/10.1103/PhysRevB.86.104114.

[259] J. Rodrigues et al., Spectroscopic Analysis of Eu^{3+} Implanted and Annealed GaN Layers and Nanowires, *J. Phys. Chem. C.* **119** (2015) 17954–17964. https://doi.org/10.1021/acs.jpcc.5b05101.

[260] J. Rodrigues et al., A comparative study of photo-, cathodo- and ionoluminescence of GaN nanowires implanted with rare earth ions, *Nucl. Instruments Methods Phys. Res. Sect. B Beam Interact. with Mater. Atoms.* **306** (2013) 201–206. https://doi.org/10.1016/j.nimb.2012.12.028.

[261] J. Rodrigues et al., Towards the understanding of the intentionally induced yellow luminescence in GaN nanowires, *Phys. Status Solidi Curr. Top. Solid State Phys.* **10** (2013) 667–672. https://doi.org/10.1002/pssc.201200714.

[262] K. Lorenz et al., Enhanced red emission from praseodymium-doped GaN nanowires by defect engineering, *Acta Mater.* **61** (2013) 3278–3284. https://doi.org/10.1016/j.actamat.2013.02.016.

[263] F.F. Komarov, Nano- and microstructuring of solids by swift heavy ions, *Uspekhi Fiz. Nauk.* **187** (2017) 465–504. https://doi.org/10.3367/ufnr.2016.10.038012.

[264] M. Lang et al., Fundamental Phenomena and Applications of Swift Heavy Ion Irradiations, in: Compr. Nucl. Mater., Elsevier, 2020: pp. 485–516. https://doi.org/10.1016/B978-0-12-803581-8.11644-3.

[265] W. Bolse, Interface modification by swift heavy ions, *Radiat. Meas.* **36** (2003) 597–603. https://doi.org/10.1016/S1350-4487(03)00208-7.

[266] M. Toulemonde et al., Thermal spike model in the electronic stopping power regime, *Radiat. Eff. Defects Solids.* **126** (1993) 201–206. https://doi.org/10.1080/10420159308219709.

[267] N. Medvedev et al., Frontiers, challenges, and solutions in modeling of swift heavy ion effects in materials, *J. Appl. Phys.* **133** (2023) 100701. https://doi.org/10.1063/5.0128774.

[268] F. Aumayr et al., Single ion induced surface nanostructures: A comparison between slow highly charged and swift heavy ions, *J. Phys. Condens. Matter.* **23** (2011). https://doi.org/10.1088/0953-8984/23/39/393001.

[269] M.L. Crespillo et al., Cumulative approaches to track formation under swift heavy ion (SHI) irradiation: Phenomenological correlation with formation energies of Frenkel pairs, *Nucl. Instruments Methods Phys. Res. Sect. B Beam Interact. with Mater. Atoms.* **394** (2017) 20–27. https://doi.org/10.1016/j.nimb.2016.12.022.

[270] M. Sall et al., Track formation in III-N semiconductors irradiated by swift heavy ions and fullerene and re-evaluation of the inelastic thermal spike model, *J. Mater. Sci.* **50** (2015) 5214–5227. https://doi.org/10.1007/s10853-015-9069-y.

[271] F. Moisy et al., Optical bandgap and stress variations induced by the formation of latent tracks in GaN under swift heavy ion irradiation, *Nucl. Instruments Methods Phys. Res. Sect. B Beam Interact. with Mater. Atoms.* **431** (2018) 12–18. https://doi.org/10.1016/j.nimb.2018.06.014.

[272] M. Karlušić et al., Response of GaN to energetic ion irradiation: conditions for ion track formation, *J. Phys. D. Appl. Phys.* **48** (2015) 325304. https://doi.org/10.1088/0022-3727/48/32/325304.

[273] M.C. Sequeira et al., Unravelling the secrets of the resistance of GaN to strongly ionising radiation, *Commun. Phys.* **4** (2021) 51. https://doi.org/10.1038/s42005-021-00550-2.

[274] S.O. Kucheyev et al., Lattice damage produced in GaN by swift heavy ions, *J. Appl. Phys.*

95 (2004) 5360–5365. https://doi.org/10.1063/1.1703826.

[275] M. Ali et al., Reduced photoluminescence from InGaN/GaN multiple quantum well structures following 40 Mev iodine ion irradiation, *Phys. B Condens. Matter.* **404** (2009) 4925–4928. https://doi.org/10.1016/j.physb.2009.08.233.

[276] K. Prabakaran et al., Electronic excitation induced structural and optical modifications in InGaN/GaN quantum well structures grown by MOCVD, *Nucl. Instruments Methods Phys. Res. Sect. B Beam Interact. with Mater. Atoms.* **394** (2017) 81–88. https://doi.org/10.1016/j.nimb.2016.12.042.

[277] M. Sall et al., Electronic excitations induced climb of dislocations in swift heavy ion irradiated AlN and AlxGa1−xN, *Nucl. Instruments Methods Phys. Res. Sect. B Beam Interact. with Mater. Atoms.* **435** (2018) 116–120. https://doi.org/10.1016/j.nimb.2017.12.021.

[278] F. Moisy et al., Role of electronic excitations and nuclear collisions for color center creation in $Al_xGa_{1-x}N$ semiconductors, *Nucl. Instruments Methods Phys. Res. Sect. B Beam Interact. with Mater. Atoms.* **379** (2016) 246–250. https://doi.org/10.1016/j.nimb.2016.02.033.

Chapter 3

Optical activation of europium implanted into AlGaN nanowires for red emitters

3.1. Context

Since the late 1990s and early 2000s, Eu-doped GaN structures have been widely investigated because of their potential use as LEDs in the red spectral region, where conventional InGaN-based LEDs lack efficiency. Although the appeal of this approach waned in the mid-2010s, recent peak EQE values of nearly 10 % (comparable to conventional InGaN LEDs) brought renewed interest to this field of research [1], namely concerning the development of monolithic RGB light emitters for full-color micro-LED displays or ultra-efficient white LEDs [2,3].

Despite recent progress, the performance of red GaN:Eu LEDs is still far behind green InGaN-based LEDs and even further away from blue InGaN-based LEDs, whose state-of-the-art peak EQE values lie around 60 % [4–6] and 80–90 % [7], respectively. Thus, the following steps involve the search for strategies capable of boosting the efficiency of red GaN:Eu LEDs.

One of the ways to improve the performance of these LEDs is to manipulate the optically active Eu^{3+} centers in the host, as the various centers have unique emission and excitation, as well as distinct luminescence efficiencies [8]. This can be done by favoring the formation of the most efficient centers; in line with this thought, T. Inaba et al. proposed the introduction of compressive in-plane strain in GaN as a strategy to favor the formation of Eu2 [9], the favorable center under electrical injection [10]. Another possibility is to modify the local structure of the Eu^{3+}, i.e., creating new centers with higher efficiencies; several authors noticed a substantial enhancement of Eu^{3+} luminescence by co-doping, for example, with Mg or O [8,11–13].

Changing the nitride host from GaN to AlN, going through the ternary alloys, should alter the internal quantum efficiency of red emitters. Although their crystalline structure is the same, the local environment around the incorporated Eu^{3+} is dissimilar, not only because of the replacement of Ga by Al atoms but also because the balance and nature of lattice defects will be distinct, i.e., the stability and formation energies of defects in GaN, AlGaN, and AlN are different. The energetic position of the electronic levels associated with those defects also shifts [14,15]. Furthermore, their tendency to form complex defects with Eu^{3+} varies [16,17]. All this together can promote the formation of Eu^{3+} centers with distinct dynamics regarding excitation and emission that deserve to be studied to understand whether the change host from GaN to AlN is a viable alternative, at least from an optical point of view.

Investigations on the optical activation and efficiency of Eu^{3+} in AlGaN hosts are scarce and limited to 2D planar structures. In most cases, doping was done by ion implantation rather than in situ doping during growth [18–23]. These studies showed that the red luminescence is intensified with increasing the AlN molar fraction up to 0.2–0.5, suggesting a more efficient energy transfer from the host to Eu^{3+}. Further increasing the AlN molar fraction (up to AlN) led to a drop in luminescence intensity; still, the intensity remained above that recorded in GaN hosts. Besides, A. Wakahara et al. reported a lower thermal quenching for Eu-implanted AlGaN hosts with successively higher AlN molar fractions [18], agreeing with observations made by P. N. Favennec et al. for erbium-implanted samples from which they proposed a direct correlation between the intensity of the lanthanoids' emission and semiconductors' bandgap; the emission is more intense for successively wider bandgap semiconductors because of an improved suppression of the thermal quenching [24]. A. Koizumi et al. observed similar behavior for in situ Eu-doped AlGaN layers [21]. The ability of AlGaN hosts over GaN hosts to benefit the luminescence of trivalent lanthanoid ions has also been demonstrated for other ion species, such as terbium, praseodymium, or thulium [25–29].

Likewise, the exploration of nanowire structures is no mere coincidence. NWs have been proposed as the building block of the future, allowing the development of several micro and nano-scale applications, such as micro-LEDs. This relies on the fact that III-N NWs can be grown on highly lattice-mismatched substrates with high crystalline quality (i.e., with a reduced density of extended defects) compared to 2D planar structures because of the eased strain relaxation at the lateral facets [30]. One example is their possible growth directly on Si substrates, providing a cost-effective and scalable platform for device integration with current micro-technology. Furthermore, the NW configuration allows higher incorporation of dopants [31,32] and may lead to an increased light extraction than thin films (depending on their dimensions, morphology, and emission wavelength) [33,34]. Recent studies have

shown that the luminescence of Eu^{3+} in GaN hosts can be enhanced by replacing conventional thin films with nanowires [35–37].

This chapter seeks to deepen the understanding of this subject by studying and comparing the optical activation of Eu-implanted AlGaN NWs, with y varying from 0 to 1, toward their possible use as active regions in future red LEDs at the macro- and micro-scale. Micro-Raman experiments are conducted to infer the crystalline damage introduced during implantation and its recovery after annealing treatments. Steady-state PL, PLE, and CL experiments are done to study the optical properties of the samples and ascertain which host can boost the red Eu^{3+}-related luminescence.

3.2. Experimental details

3.2.1. Description of the samples

3.2.1.1. Growth of AlGaN NWs

The AlGaN NWs studied in this work were grown on top of GaN NWs templates on Si (111) wafers by PAMBE. A 3 nm-thick buffer layer was deposited prior to the NWs' growth to improve their vertical orientation [38]. The AlGaN NWs were grown under N-rich conditions (metal/N ratio: 0.3). The value of y was controlled from 0 (GaN) to 1 (AlN) by adjusting the Al/(Al+Ga) flux ratio; five samples with $y = 0$, $y = 0.3$, $y = 0.5$, $y = 0.75$, and $y = 1$ were grown. Substrate temperature ranged from 800 ℃ (for $y = 0$) to ~860 ℃ ($0 < y < 1$) to 930 ℃ ($y = 1$); the growth time was also different.

Figure 3.1 presents cross-sectional and top-view scanning electron microscopy (SEM) images of **(A)** GaN, **(B)** ternary AlGaN ($y = 0.5$),[jj] and **(C)** AlN NWs; a schematic representation of their structure is included as well. At first glance, SEM images reveal that the three sets of NW ensembles (GaN, ternary AlGaN, and AlN NWs) have different morphological characteristics, such as length (h), diameter (ø), or density; this is caused by the different growth parameters (e.g., substrate temperature and growth time) [39].

The total length of the NWs, corresponding to the AlGaN top section plus the GaN templates, varies from a few hundred nanometers (ternary AlGaN) to a few micrometers (AlN). The length of the top section is ~650–750 nm for GaN, ~190–250 nm for ternary AlGaN, and ~500–700 nm for AlN.

[jj] The morphology of the ternary AlGaN NW is identical; therefore, one decided to show SEM images only for one composition (in the case $y = 0.5$), representing all the others.

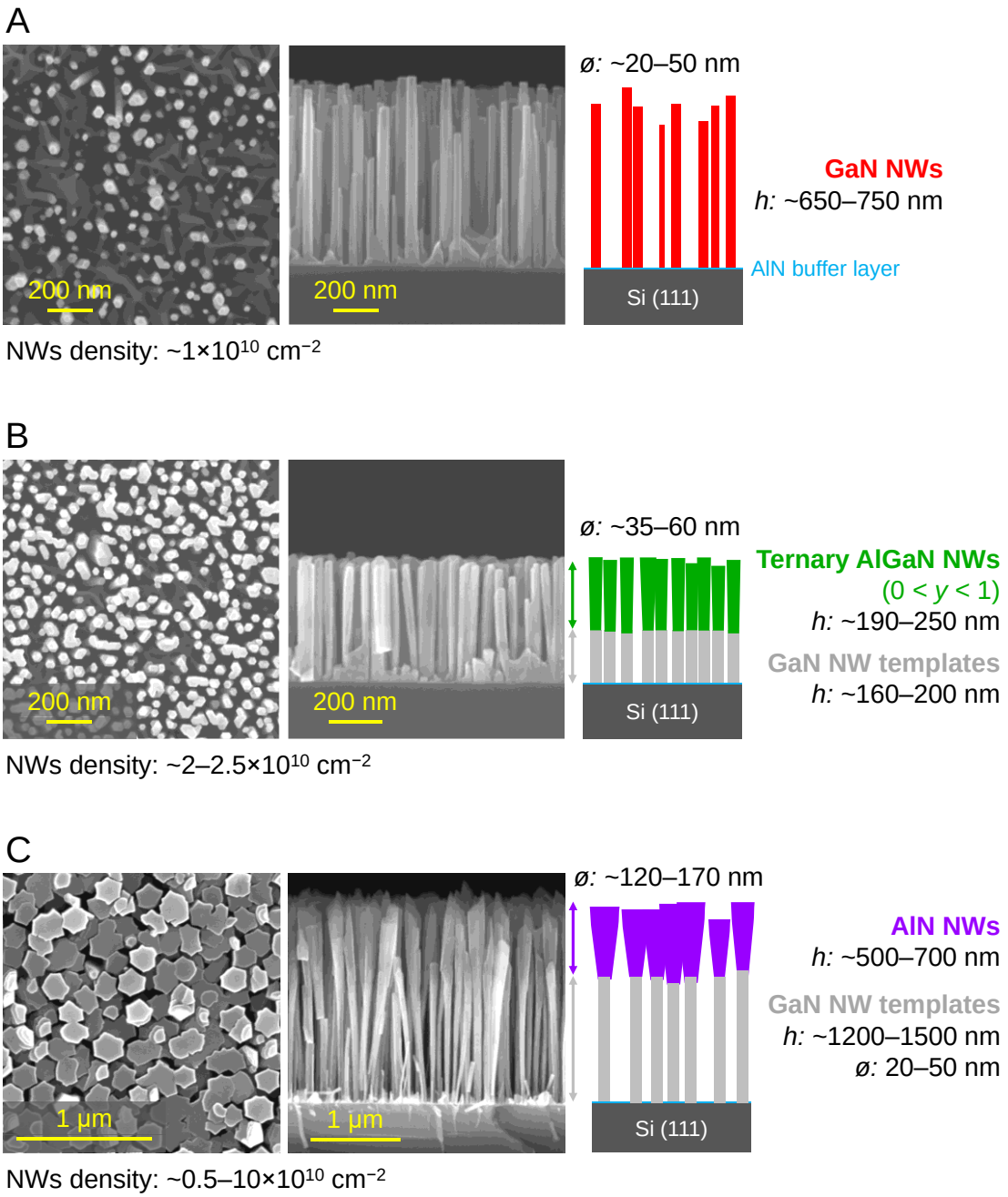

Figure 3.1 Top-view and cross-sectional SEM images of **(A)** GaN, **(B)** ternary AlGaN ($y = 0.5$), and **(C)** AlN NWs. The structure of the three sets of NW ensembles is also schematically illustrated.

The diameter of the GaN NWs templates is identical regardless of the sample, with some heterogeneity found within the ensemble (25–50 nm). The growth of the AlGaN top section results in radial enlargement of the NWs, such that the diameter at the top of the NWs is ~35–65 nm for AlGaN and ~120–170 nm for AlN. The reduced diffusion of Al

adatoms to Ga ones along the sidewalls towards the top of the NWs promotes an increased radial growth rate, explaining the observed radial enlargement [39]. As the radial dimensions of the NWs are one order of magnitude larger than the exciton Bohr radius for III-N [40,41]), no optical confinement effects are expected.

Top-view SEM images reveal different fill factors[kk] (viz., surface coverage) for the three sets of NW ensembles, increasing from GaN to AlN NWs. Moreover, it is possible to notice the partial coalescence of NWs, which can be caused either by NWs bundling [42] or by the contact of nearby NWs due to the radial enlargement at the AlGaN top section [39,43].

It must be taken into account that when growing ternary AlGaN and AlN NWs by PAMBE, a thin Al-rich shell of a few nanometers is often formed around the GaN NWs templates and the AlGaN top section ($y < 1$) because of the higher surface diffusion barrier of Al adatoms along the *c*-axis [39,44–49]. Although it is impossible to identify the shell in the presented SEM images, M. Belloeil showed its presence in the samples studied in this thesis by scanning transmission electron microscopy (STEM) [50]. This Al-rich shell can cover the entire NW length or just a part of it (the upper region), depending on the shadowing effects caused by surrounding NWs.

3.2.1.2. Eu-implantation and RTA treatments

Eu-implantation of AlGaN NWs was performed at RT with ions accelerated at 300 keV. An implantation fluence of 1×10^{14} cm^{-2} (low fluence regime) was used to avoid amorphization and nano-crystallization of the surface, which usually occurs for fluences above 10^{15} cm^{-2} in GaN [37,51–53]. An incidence angle of 45° between the ion beam and the c-axis of the NWs was considered so that the Eu could be incorporated mostly into the AlGaN top section, i.e., preventing implantation into the GaN templates and substrate. During implantation, the samples were rotated around the *c*-axis, yielding a symmetric distribution of Eu and implantation defects around the central axis of the NWs and preventing NWs from bending due to implantation-induced strain gradients.

MC simulations were implemented in the SRIM software to predict the distribution profile of the Eu implanted into GaN and AlN. **Figure 3.2** shows the simulation results [54]. The weighted average values of the displacement threshold energy, E_d, determined by ab initio molecular dynamics, were used as an input parameter [55,56]. The implanted region is anticipated to extend to a depth of ~100–120 nm for both hosts, with a maximum concentration of ~2.3×10^{19} cm^{-3} (0.026 %) and ~2.5×10^{19} cm^{-3} (0.026 %) predicted to occur at a depth of ~40 nm and ~55 nm for GaN and AlN, respectively.

[kk] Fill factor can be understood as the product between NW density.

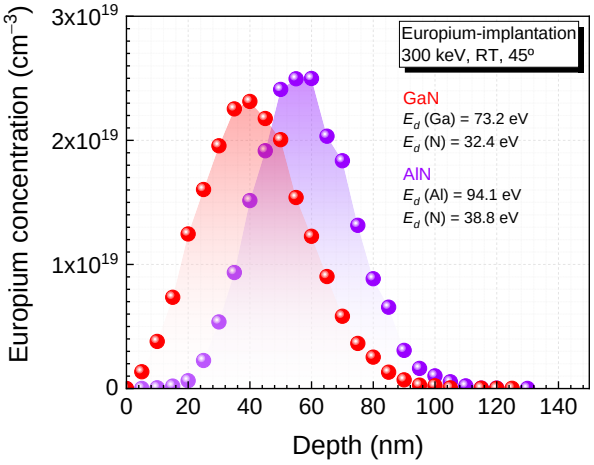

Figure 3.2 Simulated distribution profile for Eu implanted into GaN and AlN obtained with the SRIM software [54].

However, it is worth remembering that SRIM simulations only allow one to obtain a preliminary estimative of the implantation depth, given that the implemented code does not contemplate the three-dimensionality of the NWs. Indeed, according to the results obtained by D. Faye et al. for Eu-implanted GaN NWs [37], the implantation profiles in the AlGaN NWs are expected to extend to depths greater than those predicted by SRIM simulations. As discussed in **sub-subsection 2.6.2.2**, a proper estimation of the distribution profile of Eu-implanted into AlGaN NWs is a complex and sample-dependent process that is beyond the scope of this thesis.

After implantation, AlGaN NWs were subjected to RTA treatments to remove the implantation-induced defects and to activate the Eu^{3+} optically. Resorting to RTA minimizes the possibility of GaN dissociation starting at temperatures of ~800–1000 °C (at atmospheric pressure) [57–59]. The RTA was carried out in an ANNEALSYS As-One 100 RTA processor equipped with halogen lamps to heat the samples via infrared radiation at 1000 °C in flowing N_2 for 30 seconds. The N_2 flow in the RTA chamber may also help to avoid GaN decomposition. The annealing conditions were chosen based on previous results for similar samples [28,35,60,61].

In addition, for the samples with $y > 0$, one decided to test RTA at 1200 °C. The idea is to study the influence of the RTA temperature on the recovery of implantation-induced damage and the optical activation of Eu^{3+}. Regarding the GaN NWs templates, one expects that the AlGaN top section can serve as a capping layer, preventing GaN dissociation at such high RTA temperatures, similar to the method used to protect GaN thin films annealed at high temperatures by using an AlN capping layer [62,63].

3.2.1.3. Samples nomenclature

To facilitate the identification of the samples throughout the presentation and discussion of the results in this chapter, one labeled the samples in the following order:

1. "*n*" defines the NW structure;
2. the number after corresponds to *y* (in %);
3. Eu-implantation conditions, including fluence "*1E14*" and geometry angle "*45*" separated by an underscore;
4. RTA temperature.

Table 3.1 summarizes the nomenclature of all the AlGaN NWs studied in this chapter.

Table 3.1 Nomenclature adopted for the samples studied in this chapter.

y	as-grown	Eu-implantation	RTA	
			1000 °C	1200 °C
0	*n0*	*n0-1E14_45*	*n0-1E14_45-1000*	–
0.3	*n30*	*n30-1E14_45*	*n30-1E14_45-1000*	*n30-1E14_45-1200*
0.5	*n50*	*n50-1E14_45*	*n50-1E14_45-1000*	*n50-1E14_45-1200*
0.75	*n75*	*n75-1E14_45*	*n75-1E14_45-1000*	*n75-1E14_45-1200*
1	*n100*	*n100-1E14_45*	*n100-1E14_45-1000*	*n100-1E14_45-1200*

In certain situations, comparisons are made with commercially available AlGaN layers grown on sapphire substrates. These samples were implanted with Eu and annealed by RTA in the same conditions as the AlGaN NWs. The identification of these samples throughout the chapter is made by replacing the letter "*n*" with the letter "*R*" (meaning reference). Note that the *y* values of the layers are not the same as those of the AlGaN NWs, but their value is indicated in the nomenclature.

3.2.2. Characterization techniques

3.2.2.1. SEM

SEM images were obtained in three different microscopes. The morphology of the as-grown NWs was investigated using a Zeiss Ultra-55 setup with a working distance between 3–6 mm. Secondary electrons were collected by a detector located in the microscope

column (in-lens detector). An acceleration voltage of 10 kV was used to avoid charging effect phenomena, which occur when the material is not conductive enough.

After Eu-implantation and RTA, SEM images were obtained in *i)* a Hitachi SU-70 field emission gun microscope using a working distance of 15–22 mm and a 15 keV electron beam and *ii)* a TESCAN VEGA3 microscope using a working distance of 5 mm and a 30 keV electron beam. Even though it favors the occurrence of charging effects, the worst resolution of the last microscope implied the use of higher acceleration voltages to identify NWs. In both microscopes, secondary electrons were collected by a detector located in the SEM chamber.

3.2.2.2. Micro-Raman

Micro-Raman experiments were conducted in a Horiba Jobin-Yvon LabRAM HR800 spectrometer with a 2400 grooves·mm^{-1} grating (experimental uncertainty of 0.5 cm^{-1}). The 442 nm line of a He-Cd laser was focused on the top of the NWs using a 100× microscope objective with a numerical aperture of 0.9, resulting in a spot area of ~0.8 μm^2. The Raman signal was detected by a charge-coupled device (CCD) in the backscattering configuration $z(x\ \cdot)\bar{z}$, with z parallel to the NWs axis (viz., the c-axis). The system was calibrated using the main peak of a Si reference sample at 520.5 cm^{-1}.

3.2.2.3. Steady-state PL and PLE

PL experiments were carried out in two different spectrometers. In the first, the 325 nm line of a He-Cd laser, with excitation density around 1– 2 W · cm^{-2} and spot area of ~5 mm^2, was used as the excitation source. The luminescence signal was detected in a dispersive system SPEX 1704 Czerny-Turner monochromator (1 m, 1200 grooves·mm^{-1} grating) coupled to a water-cooled Hamamatsu R928 photomultiplier tube (PMT). The excitation light was focused on the sample at an angle of 30° to the surface's normal, while the emitted light was collected at 60° to the surface normal (excitation and detection make a 90° angle to each other). The measured signal was corrected to the response of the system (optics, detector, monochromator) and calibrated using the 2nd-order of the laser emission. For entrance and exit slits of 150 μm, the spectrometer's spectral resolution (bandpass) is ~0.1 nm. In this experimental setup, the samples were mounted in a cold finger of a closed-cycle helium cryostat (pressure of ~10^{-5} Torr), allowing control of the measurement temperature from 14 K to 300 K by heating a resistance near the cold finger. The temperature control was done using a temperature controller connected to a thermocouple close to the resistance.

The other setup used was a Fluorolog 3 Horiba Scientific modular system equipped with a 450 W Xe arc lamp. RT PL (with variable excitation wavelength) and RT PLE

experiments were conducted in this spectrometer. An entrance monochromator defines the excitation wavelength from the UV (~250 nm) to the visible spectral range, while an exit monochromator controls the emission wavelength. A PMT detected the luminescence signal. In this spectrometer, the excitation light was focused on the sample at 60° to the surface normal, while the emitted light was collected at 40° to the surface normal. The presented spectra were corrected to the spectral response of the optical components, the PMT detector, and the Xe lamp. The spectrometer's spectral resolution (bandpass) is set at 3 nm to guarantee an adequate signal intensity. The spot size is much larger than the NW dimensions; thus, as in the previous PL setup, the average response of a few hundred NWs is collected simultaneously.

3.2.2.4. Cathodoluminescence

CL measurements were done at 5 K in an FEI Inspect F50 scanning electron microscope. The luminescence signal was detected using a Horiba Jobin Yvon iHR 550 spectrometer (equipped with 1800 and 600 grooves·mm^{-1} gratings) and a Peltier-cooled Andor Technology Newton DU940 CCD. The applied acceleration voltage was 5 kV, resulting in a CL signal predominantly from the top section of the NWs (~70–190 nm). The beam spot area was ~2 μm^2, leading to the probe of hundreds of NWs in the ensemble. Both excitation and detection were parallel to the *c*-axis of the NWs; the emission was directed toward the spectrometer by a parabolic mirror.

3.2.3. Experimental credits

The growth of the AlGaN NWs was done by Dr. Matthias Belloeil, a former Ph.D. student in Dr. Bruno Daudin's research group (Nanophysics and Semiconductors, CEA, Grenoble, France). The same group kindly provided SEM images of the as-grown NWs. Eu-implantation and RTA were carried out by Professor Katharina Lorenz's group (Laboratory of Accelerators and Radiation Technologies, CTN-IST, Lisbon, Portugal). SEM images of the implanted and annealed NWs were taken with the help of Dr. Manuel Martins and Dr. Ana Violeta Girão (Department of Materials and Ceramic Engineering & CICECO, UA, Aveiro, Portugal), and António Fernandes and Dr. Alexandre Carvalho (Department of Physics & i3N, UA, Aveiro, Portugal). CL measurements were done by Dr. Gwénolé Jacopin (CNRS, Grenoble, France).

3.3. Results and discussion

3.3.1. Structural properties of the AlGaN NWs

RBS/C and XRD are the most commonly used techniques to evaluate implantation-induced damage in III-N 2D structures [53,64–67]. By relating the results of both techniques, it is possible to obtain quantitative information about the implantation depth profile, relative defect fraction, and strain. Furthermore, combining TEM images helps uncover the microscopic nature of the generated defects. The potential of the previous techniques is considerable; however, RBS/C and laboratory XRD are not straightforward when extracting information about implantation in MBE-grown AlGaN NWs because of the slight tilt and twist between individual NWs. In RBS/C, NWs tilt affects channeling, while, in XRD, due to tilt and twist, only a fraction of NWs is well-oriented to measure *a*- and *c*-lattice parameters with accuracy experimentally. After implantation, such determination becomes even worse [37]. Consequently, the whole picture of the implantation-induced damage in AlGaN NWs cannot be accurately done using these techniques.

Micro-Raman spectroscopy constitutes an alternative technique to seek quantitative and qualitative information about the effects of ion implantation in III-N, namely strain and crystalline quality [68–71]. As a part of the research carried out in this chapter, one recurs to micro-Raman spectroscopy under non-resonant conditions (442 nm excitation) to evaluate the effects of Eu-implantation and RTA treatments in the AlGaN NWs. The obtained results are presented and discussed in the following sub-subsections.

3.3.1.1. The micro-Raman response of the as-grown AlGaN NWs

Before going into detail about what happens to the lattice after implantation, one shall understand what information can be extracted from the spectrum of the as-grown samples. **Figure 3.3** shows the non-resonant micro-Raman spectra of all the as-grown AlGaN NWs. Because of the low absorption coefficient of AlGaN (across the entire range of AlN molar fractions), it is possible to obtain scattered signals from the entire length of the NWs and the Si (111) substrate. The response of the Si substrate, which corresponds to a tail in the low-frequency side and a broad unstructured signal between ~600–700 cm^{-1}, is included for comparison. Besides the Si substrate contribution, a well-defined peak associated with the E_{2h} (GaN) phonon of the GaN NWs templates at 567–571 cm^{-1} is identified for all the samples, indicating their growth in the WZ phase. For AlN NWs, the E_{2h} (AlN) phonon is well-defined and peaks at 655 cm^{-1}.

For ternary AlGaN NWs with $y = 0.3$ and $y = 0.5$, a shoulder close to E_{2h} (GaN) appears in the spectrum, and its frequency increases with y; in contrast, for $y = 0.75$, the

shoulder appears at the low-frequency side of the E_{2h} (AlN) phonon. Considering that discussed in **subsection 2.2.3**, these modes are respectively attributed to the E_{2h} (GaN-like) or the E_{2h} (AlN-like) phonon of the ternary AlGaN top section [72–74].

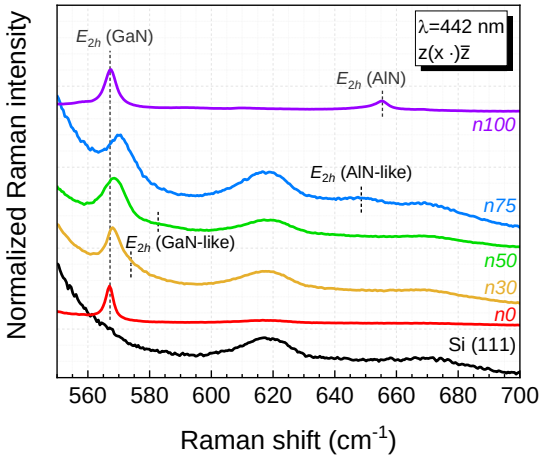

Figure 3.3 Normalized micro-Raman spectra of the as-grown AlGaN NWs. The spectra are vertically shifted for clarity. The spectrum of the Si (111) substrate is plotted for comparison.

The low intensity of the E_{2h} (GaN-like) or E_{2h} (AlN-like) phonon of the ternary AlGaN NWs is likely due to the reduced length of the NWs; note that the relative intensity of the signal coming from the substrate is significantly increased compared to the spectrum of the binary NWs. This, together with the overlapping of the E_{2h} (GaN) phonon signal of the GaN NW templates, makes it challenging to analyze the AlGaN NW top section. In order to do that, a careful deconvolution procedure, similar to that proposed by A. Pierret et al. [48], is applied; firstly, the Si (111) substrate signal is subtracted, and then the remaining signal is fitted using one or two Lorentzian functions depending on the spectral shape.

Figure 3.4 exhibits the results of the deconvolution done for samples **(A)** *n30*, **(B)** *n50*, and **(C)** *n75*. For *n30* and *n50*, the prominent peak reveals an asymmetry of the Raman signal on the high-frequency side; for that reason, two Lorentzian functions are considered. The deconvoluted peak at ~568–569 cm^{-1} corresponds to the E_{2h} (GaN) phonon of the GaN NWs templates, while the shoulder is most likely the E_{2h} (GaN-like) mode of the AlGaN NW top section. For sample *n75*, the peak at ~570 cm^{-1} is symmetric; thus, only one Lorentzian function is considered in the deconvolution. This means the E_{2h} (GaN-like) mode is not detected, as usual for high Al-compositions [72–74]; however, the E_{2h} (AlN-like) mode appears at ~648 cm^{-1}.

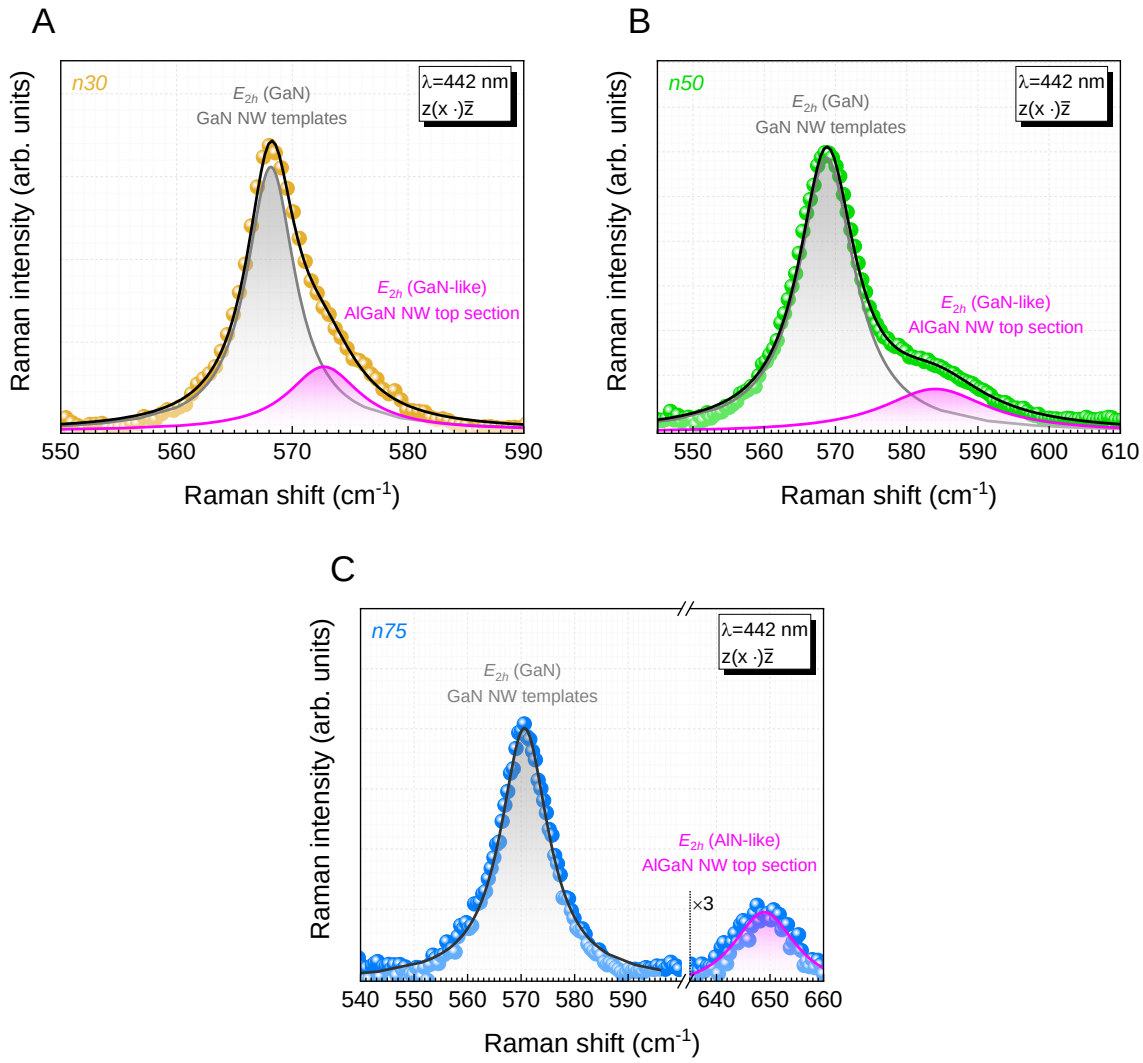

Figure 3.4 Deconvolution of the Raman peaks associated with the GaN NWs templates and the AlGaN top section for samples **(A)** *n30*, **(B)** *n50*, and **(C)** *n75*. Solid black lines correspond to the sum of the two Lorentzian contributions.

Although the experimental uncertainty of 0.5 cm^{-1}, strain inhomogeneities within the ensemble of NWs induce shifts as high as 1 cm^{-1} to the frequency of the E_{2h} phonon; HR-XRD results already revealed similar inhomogeneities in PAMBE-grown AlGaN NWs [75]. Therefore, for binaries, the experimental error associated with determining the frequency of the E_{2h} phonon is 1 cm^{-1}. For ternary AlGaN NWs, the deconvolution procedure introduces a more significant error, up to 3 cm^{-1}, due to the reduced intensity of the signal coming from the NW top section and the overlapping of signal from the GaN NWs templates and the Si substrate.

Figure 3.5 presents the evolution of frequency and FWHM of the two deconvoluted Raman peaks as a function of *y*: **(A)** E_{2h} (GaN-like) and E_{2h} (AlN-like) modes associated with the top section and **(B)** E_{2h} (GaN) phonon of the GaN NWs templates.

For the modes associated with the AlGaN NW top section, **Figure 3.5(A)**, the frequency follows the trend reported by V. Davydov et al. for AlGaN layers [72], suggesting that the average AlN molar fraction of the AlGaN NWs is identical to the nominal one if the top section is fully relaxed. It should be kept in mind that the obtained frequencies translate both composition and strain effects. The FWHM of these peaks is maximum for intermediate compositions (sample *n50*) and minimum for the binaries, which is a common feature in ternary III-N alloys due to the elastic scattering of phonons by compositional fluctuations [72].

In a first attempt to estimate the AlN molar fraction of the AlGaN NWs, one considers the top section to be fully relaxed, which is a reasonable approximation for NWs due to their high aspect ratio ($h > \emptyset$) [48]. For instance, taking into account the dependence reported by V. Davydov et al. for AlGaN layers [72] and the experimental error of 3 cm^{-1}, the phonon frequency of E_{2h} (GaN-like) obtained for sample *n30* corresponds to an AlN molar fraction ranging between ~0.12–0.30. This implies that the frequency obtained corresponds to a wide range of acceptable AlN molar fractions.

Nevertheless, for sample *n100*, the E_{2h} (AlN) phonon peaks at 655 cm^{-1}, which is slightly redshifted compared to the strain-free value (657.4 cm^{-1}) [76]. This means the AlN NW top section is tensile strained because of the growth on GaN NWs templates with a larger in-plane lattice parameter (biaxial expansion). Such a result hints that the AlGaN NW top sections may not be fully relaxed as assumed in the first instance. Instead, they must be biaxially tensile strained by the GaN NWs templates, which would shift the E_{2h} phonon to lower frequencies [77]. Consequently, its disregard means that the previously obtained AlN molar fraction is slightly underestimated. Assuming that the strain induced in the ternary AlGaN top section is analogous to that in AlN, it is possible to estimate the AlN molar fraction by considering two contributions, one from strain [from equation (2.12)] and the other due to compositional effects (dependence reported by V. Davydov et al. [72]); an AlN molar fraction between 0.2 and 0.35 is obtained for sample *n30*. The AlN molar fraction estimated from micro-Raman experiments includes the nominal value for all ternary AlGaN NWs regardless of whether the biaxial strain is considered.

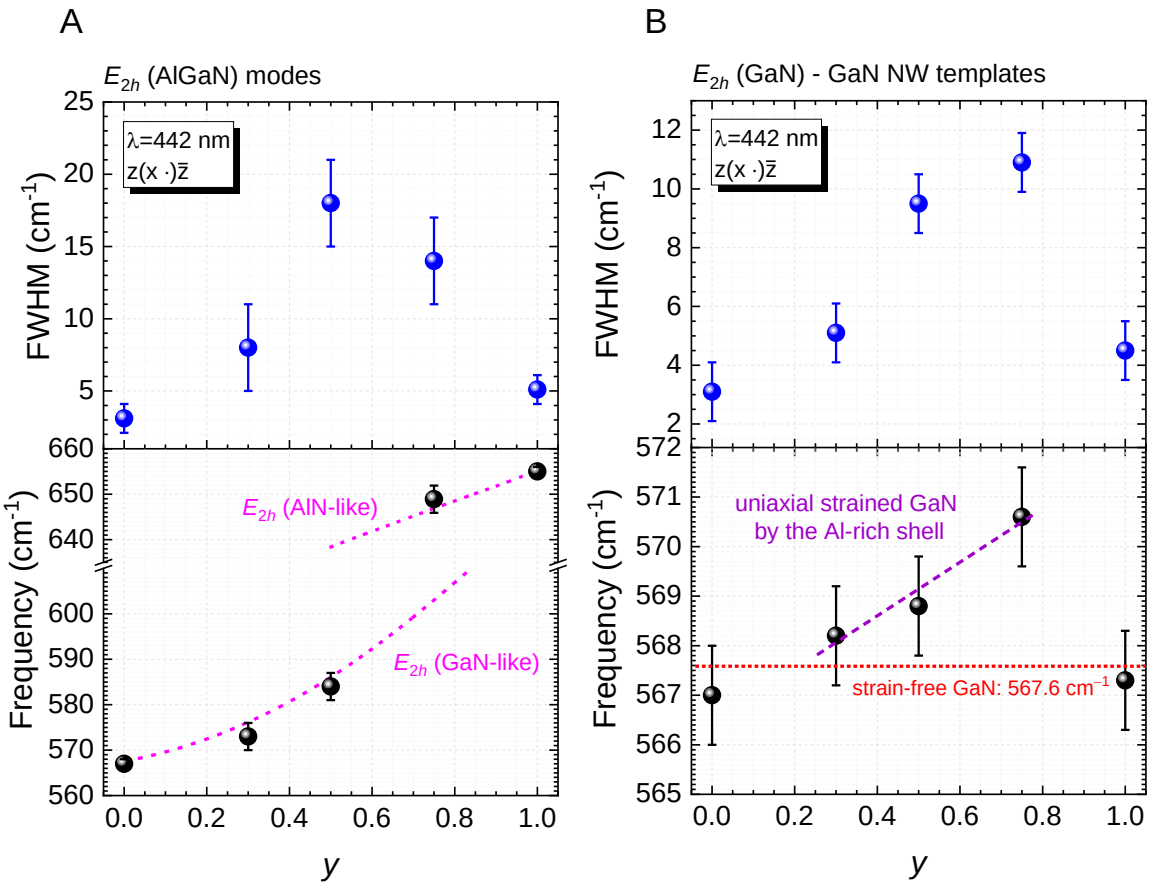

Figure 3.5 Frequency and FWHM evolution of **(A)** E_{2h} (GaN-like) or E_{2h} (AlN-like) modes and **(B)** E_{2h} (GaN) phonon as a function of y. For sample *n0*, the plotted data is the same in both graphs. In **(A)**, the dashed lines correspond to the frequency evolution of E_{2h} (GaN-like) and E_{2h} (AlN-like) modes obtained by V. Davydov et al. for AlGaN layers [72]. In **(B)**, the red dotted line corresponds to the strain-free E_{2h} (GaN) phonon [76], while the violet dashed line is a "guide to the eye" for the evolution of the E_{2h} (GaN) frequency with y for ternary AlGaN NWs.

Let one look at the evolution of the E_{2h} (GaN) phonon related to the GaN NWs templates with y, **Figure 3.5(B)**. The characteristics of this phonon are identical for samples *n0* and *n100*, with the peak frequency coinciding (within the experimental error of 1 cm^{-1}) with the strain-free value of 567.6 cm^{-1} [76]. This indicates that the GaN NWs and the GaN NWs templates of the AlN NWs are relaxed. Nevertheless, for ternary AlGaN NWs, the frequency of the E_{2h} (GaN) phonon successively blueshifts and broadens with y, making it possible to infer that, in this case, the GaN NWs templates are strained. Attending to the structure of the AlGaN NWs (**Figure 3.1**), two hypotheses might explain the introduction of such a strain in the NWs templates: *i)* an uniaxial compression due to the Al-rich shell formed around the templates ($c_{\mathrm{AlGaN}} < c_{\mathrm{GaN}}$) or *ii)* a biaxial compression of the GaN NWs templates due to the growth of the AlGaN section on top of them

($a_{\mathrm{AlGaN}} < a_{\mathrm{GaN}}$). Logically, such a compressive strain is aggravated with increasing y, explaining the larger frequency shifts observed. E. Zielony et al. reported a similar behavior for the E_{2h} (GaN) phonon associated with GaN NW templates when AlGaN NW sections are grown on them [44]. The previous hypotheses justify the strain in the GaN NWs templates of the ternary AlGaN NWs. However, they do not explain why the GaN NW templates are not compressively strained for sample *n100*, where the strain effects would be more significant due to the larger lattice mismatch. In this case, it is proposed that the explanation for this involves the morphological characteristics of the AlN NWs, with the Al-rich shell being unlikely or confined to a reduced height of the GaN NWs templates because of the enhanced shadowing effects to the Al-adatoms, i.e., Al-adatoms are not likely to reach the side facets of the NWs templates. Consequently, and as the GaN NWs templates are very long for AlN NWs (~1 µm long), only a residual fraction of the templates are compressively strained, making it impossible to distinguish signal from this region, contrarily to what happens in ternary AlGaN NWs.

In a separate work, K. Hestroffer et al. discussed the influence of the thickness of an AlN shell formed around GaN NW templates [78]. The authors showed that the E_{2h} (GaN) phonon successively blueshifts with increasing the shell thickness up to 3 nm; for thicker shells, the frequency remains constant at a shift of about 5 cm^{-1}. They also found that the in-plane strain, $\epsilon_{xx}(=\epsilon_{yy})$, is close to zero, which means that the *a*-lattice parameter of the GaN core is not or is very weakly strained by the shell.

Compared to the relaxed frequency, the frequency shifts of the E_{2h} (GaN) phonon measured for the ternary AlGaN NWs studied in this thesis do not exceed 5 cm^{-1} [**Figure 3.5(B)**], in agreement with that observed by K. Hestroffer et al. [78]. Assuming that the thickness of the Al-rich shell is identical for all the samples (a few nanometers thick), the more significant frequency shift observed for higher y [identified by the violet dashed line in **Figure 3.5(B)**] is explained by the increase in the Al-composition of the shell [44]. Accompanying the trend of the peak frequency shift, the FWHM also increases. This may be justified by the heterogeneity of the shell in terms of composition and thickness, causing different strain states within the same NW or in distinct NWs templates [47,78].

3.3.1.2. Eu-implantation of AlGaN NWs: strain and disorder

The previous analysis allowed distinguishing the micro-Raman signals from the AlGaN top section and the GaN NWs templates; notwithstanding, it was particularly tough for the ternary alloys. The objective now is to assess information about the lattice after Eu-implantation. Given that implantation can affect not only the top section but also the templates, it is essential to identify the origin of the signal to analyze the effects caused to each of the sections of the NWs.

Figure 3.6 compares the micro-Raman spectra obtained before and after Eu-implantation for **(A)** GaN and **(B)** AlN NWs. In both cases, the spectral shape changes after implantation, consisting mainly of broad an unstructured bands rather than narrow peaks associated with BZ center phonon lines. The Raman spectrum presents peculiarities that resemble the p-DOS function of the respective lattice, indicating the infliction of crystalline damage by Eu-implantation.

In the micro-Raman spectrum of sample *n100*, one can also identify modes that should be forbidden in the backscattering geometry adopted, namely the E_1(TO) of the GaN NWs templates and the A_1(TO) and the E_1(TO) phonons of the AlN top section. The observation of such modes may be caused by *i)* NWs detached from the substrate and dispersed throughout the sample (possible to occur during sample cut) or *ii)* slight misorientation of the *c*-axis relative to the laser beam incidence.

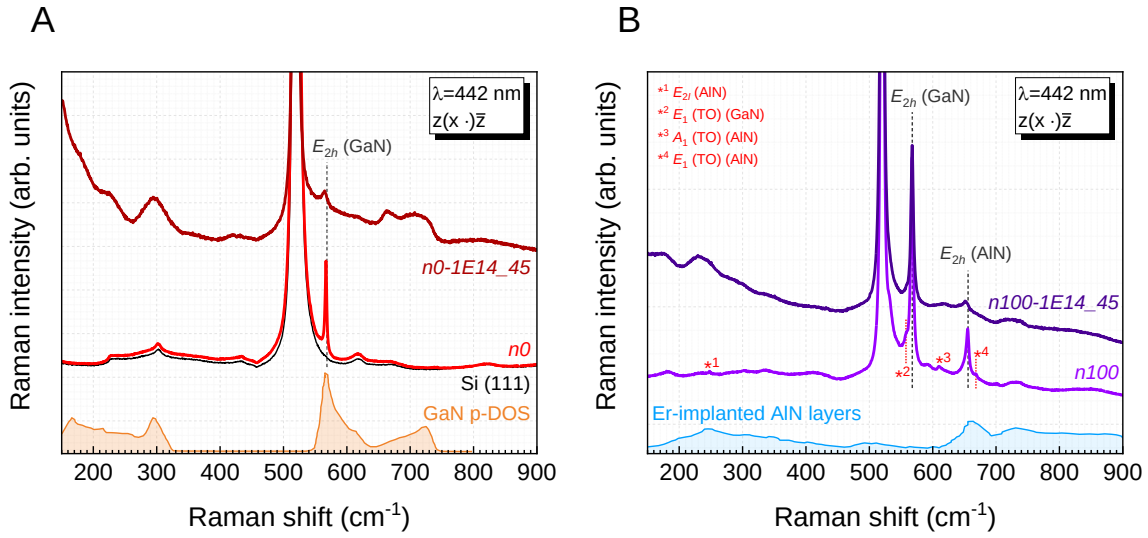

Figure 3.6 Micro-Raman spectra obtained for **(A)** GaN and **(B)** AlN NWs before and after Eu-implantation. The calculated GaN p-DOS and the spectrum of Er-implanted AlN layers (identical to AlN p-DOS) obtained by V. Davydov et al. are plotted for comparison [76].

Besides inference of crystalline damage through the activation of the p-DOS, one can still obtain additional information from the E_{2h} phonon lines. When a crystal is bombarded with ions, the frequency and FWHM of the E_{2h} phonon peak are expected to change because of defects generated in the lattice, whether point defects or the new implanted species. These defects introduce strain within the crystal, shifting the phonon's frequency to higher or lower frequencies depending on the nature and magnitude of the strain. Furthermore, the randomness in the atomic arrangement results in a broadening of the peak [72,79]. As the density of defects (i.e., damage level) increases, the E_{2h} phonon is expected to undergo more

significant deviations and broadening. Therefore, at some point, it becomes challenging to distinguish phonon lines associated with first-order Raman scattering processes for strongly disordered crystals.

For Eu-implanted GaN NWs, the E_{2h} (GaN) phonon shifts to lower frequencies (~2 cm^{-1}), broadens, and its peak intensity decreases; these behaviors agree with the generation of defects. A similar trend is observed for the E_{2h} (AlN) phonon in Eu-implanted AlN NWs, with its frequency red-shifting ~3 cm^{-1}; in this case, the E_{2h} (GaN) phonon related to the GaN NWs templates does not change in frequency, FWHM, or relative intensity, hinting that the templates are unaffected (or only slightly affected) by implantation. In fact, this is expected for sample *n100* because of its high fill factor, which makes the ions enter the NWs mainly from the top, resulting in an implantation profile closer to that simulated for 2D layers. Additionally, the greater length of the AlN NW top sections (~500–700 nm) decreases the probability of Eu reaching the GaN NWs templates during implantation.

Figure 3.7 (A) shows the micro-Raman spectra obtained before and after Eu-implantation for the AlGaN NWs with $y = 0.5$ (representative of the effects observed for the other ternaries). As for the binaries, the spectrum becomes broader after implantation. However, in this case, the detection of the E_{2h} phonon of the AlGaN top section is impossible since its intensity, already weak in the as-grown sample (reduced length of the AlGaN top section and overlap of other more intense signals), is reduced due to implantation-induced disorder. Consequently, this hinders the evaluation of the strain introduced in the ternary AlGaN NWs.

Still, from **Figure 3.7 (A)**, it is possible to obtain information about the GaN NWs templates. Besides a slight broadening and a relative intensity reduction, the characteristics of the E_{2h} (GaN) peak remain almost the same before and after implantation. This result suggests that the templates (or at least a region of them) are affected by Eu-implantation, albeit in a milder way than in the GaN NWs (sample *n0-1E14_45*). In other words, this indicates that although most of the ions reside in the AlGaN top section where the disorder levels should be maximum, a fraction of them still reach the GaN NWs templates. The reduced length of the AlGaN top section and the lower fill factor of ternary AlGaN NWs compared to AlN NWs are the most likely reasons for Eu to reach the templates.

From the isolated spectrum of sample *n50-1E14_45*, it is difficult to associate the broad spectral shape with the p-DOS of the respective lattice because of the inexistence of theoretical or experimental studies in the literature. Nevertheless, when comparing the spectral shape (after background subtraction) obtained for all the implanted NWs in the 640–900 cm^{-1} range, **Figure 3.7(B)**, one can notice a shift of the broad bands towards the high-frequency side with increasing *y*; the spectral shape evolves from what looks like the GaN p-DOS to the AlN p-DOS [76]. For instance, one can observe that the frequencies of

the inflection point (upwards arrow) and the maximum (downwards arrow) at the low-frequency side of the presented spectra vary with y in a similar way to the trend reported for the B_{1h} acoustic phonon in AlGaN layers [72]. These findings suggest that the measured signal comes from the AlGaN NW top sections and that such a section is structurally damaged.

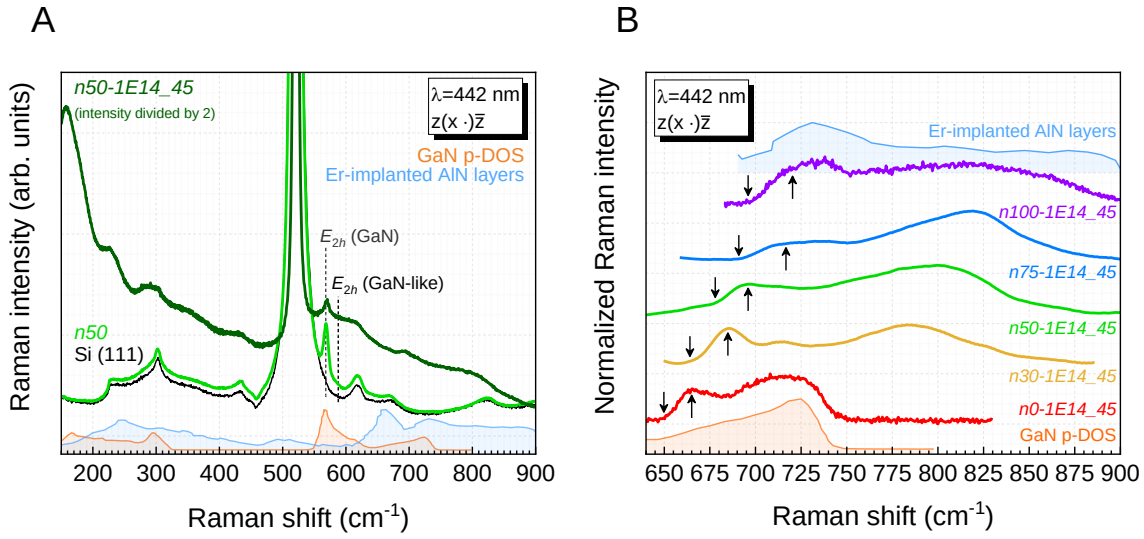

Figure 3.7 (A) Micro-Raman spectra before and after implantation for the ternary AlGaN NWs with $y = 0.5$. **(B)** Comparison of the normalized micro-Raman spectra (after baseline subtraction and smoothing) in the 640–900 cm^{-1} range for all the implanted AlGaN NWs. The calculated GaN p-DOS and the spectrum of Er-implanted AlN layers are plotted for comparison [76].

Due to the impossibility of evaluating the strain introduced in the crystal by implantation-induced defects for ternary AlGaN NWs, the following discussion is restricted to the results obtained for the binaries.

In the first instance, one assumes that the implantation-induced defects and the implanted species exert hydrostatic stress in the crystal ($\sigma_{xx} = \sigma_{yy} = \sigma_{zz} \neq 0$) [60,80,81]. Combining equations (2.8) and (2.12) makes it possible to estimate the induced hydrostatic strain from the measured frequency shift of the E_{2h} phonon. For GaN NWs, the E_{2h} (GaN) phonon measured before and after implantation shifts -2 cm^{-1}, which corresponds to a hydrostatic strain of $\epsilon_{xx} = \epsilon_{yy} = \epsilon_{zz} = (0.09 \pm 0.05)$ %. A positive strain means that the generated defects exert tensile stress in the NWs, resulting in a lattice expansion. Analogously, a strain of magnitude $\epsilon_{xx} = \epsilon_{yy} = (0.11 \pm 0.05)$ % and $\epsilon_{zz} = (0.13 \pm 0.05)$ % can be estimated for Eu-implanted AlN NWs considered the measured E_{2h} (AlN) phonon shift of -3 cm^{-1}. In the case of AlN, the difference between $\epsilon_{xx} = \epsilon_{yy}$ and ϵ_{zz} arises from the anisotropic response to a hydrostatic stress.

The strain magnitude estimated to be introduced in both binary NWs after Eu-implantation is indistinguishable within the estimation uncertainty, which includes the experimental error and the dispersion of values found in the literature for the phonon deformation potentials [82–84]. However, the estimated values are considerably lower than those found in the literature and determined from XRD 2θ–ω scans along symmetric reflections. For example, for GaN and AlN layers implanted with Eu in identical conditions (energy and fluence), the strain measured along the *c*-axis (ϵ_{zz}) was ~0.65–0.75 % [37,53,65], while for GaN NWs, it was ~0.25 % [37]. The lower values found for implanted NWs were explained by *i)* a suppressed formation of defect clusters and *ii)* an eased strain relaxation at the lateral facets [37]. A possible explanation for the discrepancy between the strain values estimated here and those found in the literature is that the stress introduced by Eu-implantation is not described solely by a hydrostatic component, contrary to what was considered in the various references identified.

Establishing the suitable strain model cannot be done only based on the behavior of the E_{2h} phonon since it can change in the same direction in the presence of strain contributions of different natures, as shown previously in **subsection 2.2.2**. For example, the mode shifts to lower frequencies when the GaN lattice undergoes hydrostatic expansion, tensile uniaxial deformation along the *c*-axis, or in-plane biaxial dilatation [77,83]. The same can be said about XRD measurements made in symmetric planes (along the *c*-axis) because they only allow inferences about variations in the *c*-lattice parameter [67]. For this reason, such XRD experiments do not allow the correct attribution of the stress model introduced by implantation-defects in the lattice as being hydrostatic.

A different model is proposed by combining the micro-Raman results obtained in this thesis and the XRD results reported in the literature for similar GaN NWs implanted in identical conditions (energy and fluence) [37]. By taking the measured E_{2h} (GaN) phonon shift of -2 cm^{-1} and the reported $\epsilon_{zz} = 0.25$ % (from ref. [37]), one can estimate that $\epsilon_{xx} (= \epsilon_{yy})$ should vary between -0.02% and 0.01%, depending on the phonon deformation potentials used. Therefore, this model corresponds to the case in which the *a*-lattice parameter is barely unchanged compared to the *c*-parameter. These results might be explained in the following way: implantation-induced defects introduce a hydrostatic pressure that tends to expand the lattice in all directions; however, the *a*-lattice parameter remains coherent to the atomic layers right below. This leads to an additional in-plane biaxial compression counteracting the hydrostatic effect. In other words, in this model, designated as "pseudomorphic-like" model, implantation induces a biaxial stress component that compensates for the hydrostatic pressure in-plane (i.e., $\epsilon_{xx} = \epsilon_{yy} \approx 0$) but aggravates the stress along the *c*-axis.

Figure 3.8 shows the frequency shift of the E_{2h} (GaN) phonon as a function of ϵ_{zz} for different strain regimes. The experimental strain values estimated for sample *n0-1E14_45*, considering the pure hydrostatic and the "pseudomorphic-like" models, are included in the graph.

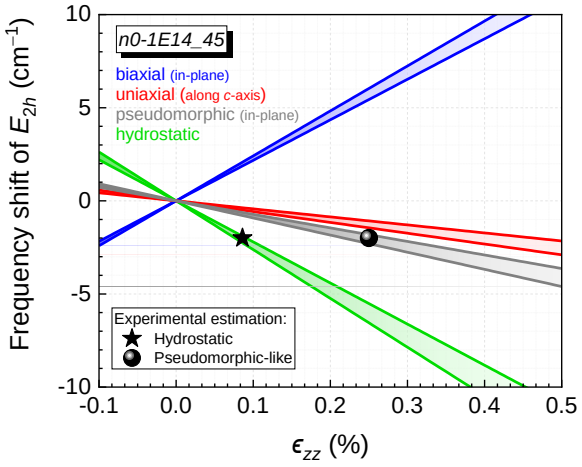

Figure 3.8 Experimentally estimated strain values for the Eu-implanted GaN NWs assuming pure hydrostatic (star) and "pseudomorphic-like" (sphere) models. In the background, the dependences of the E_{2h} (GaN) phonon frequency on ϵ_{zz} (in %) considering different strain regimes are represented [82–84].

In the literature, one can find some papers reporting a similar "pseudomorphic-like" behavior in ion-implanted III-N layers from analyzing reciprocal space maps (RSM) around asymmetric planes. For example, D. Nd. Faye et al. identified the expansion of the lattice along the *c*-axis, while the in-plane parameter was preserved after implantation of AlGaN layers with argon ions (fluence of 1×10^{15} cm^{-2}) [64]. B. Pipeleers et al. found a similar behavior for Er-implanted GaN layers [85]. As referred to at the beginning of this subsection, realizing such XRD measurements in MBE-grown NWs is challenging because of the significant twists found in the NWs ensemble [37]. However, the results found for ion-implanted AlGaN layers suggest the validity, to some extent, of the proposed "pseudomorphic-like" model for Eu-implanted GaN NWs. Comparable findings were also predicted theoretically by M. W. Ullah et al. using Molecular Dynamics simulations to study the effects of 37.5 keV erbium-implantation (fluence of 1×10^{13} cm^{-2}) in GaN NWs; the strain introduced was more significant along the *c*-axis than the in the basal plane [81].

In summary, it is demonstrated that a simple hydrostatic model cannot explain the different results obtained in XRD and micro-Raman experiments for Eu-implanted GaN NWs. A "pseudomorphic-like" model is proposed to provide a more accurate description of

the strain introduced in such structures, agreeing with the XRD results in AlGaN layers and simulations for GaN NWs. Given the similarity of the strain state found in GaN and AlN layers implanted in the same conditions, one hypothesizes that the same strain model should apply to all the AlGaN NWs implanted with Eu, at least for these implantation conditions.

3.3.1.3. Crystalline recovery after RTA

Figure 3.9 shows the micro-Raman response of **(A)** GaN and **(B)** AlN NWs after Eu-implantation and annealing treatments. After RTA, the spectrum evolves towards that of the respective as-grown sample, i.e., the first-order Raman scattering processes become dominant, and the E_{2h} phonon tends to recover the characteristics of that in the as-grown samples. Notwithstanding, the broad bands associated with lattice disorder are still observed, with their relative intensity being reduced with increasing the RTA temperature. These results hint at a partial recovery of the crystalline lattice, with improvements for higher RTA temperatures.

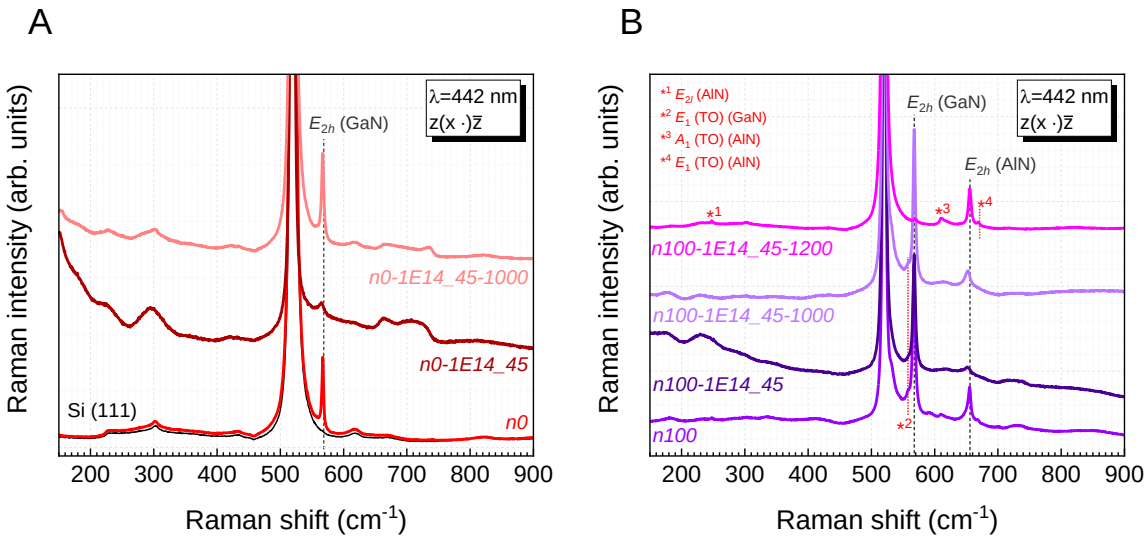

Figure 3.9 Micro-Raman spectra obtained for **(A)** GaN and **(B)** AlN NWs after implantation and RTA treatments.

Another significant finding from the previous spectra is the absence (or drastic intensity reduction) of signal related to GaN NWs templates, the E_{2h} (GaN) phonon, for the AlN NWs annealed at 1200 °C. As the relative intensity of the Si substrate signal is not significantly altered, this suggests that the GaN NWs templates are strongly damaged, i.e.,

the AlN top section cannot effectively protect GaN from dissociation for RTA conducted at 1200 °C.

Figure 3.10 summarizes the frequency and FWHM evolution of the **(A)** E_{2h} (GaN) phonon in GaN NWs and the **(B)** E_{2h} (AlN) phonon in AlN NWs after implantation and subsequent RTA. The represented values correspond to the best-fit model of the phonon modes using Lorentzian functions. As already discussed, the E_{2h} phonon peak shifts to lower frequencies and broadens after implantation. After RTA, the phonon regains the characteristics initially obtained for the as-grown samples. For the AlN NWs, the characteristics of the E_{2h} (AlN) phonon are better recovered when the RTA is done at the highest temperature of 1200 °C.

The evolution of the E_{2h} (AlN) phonon suggests that high RTA temperatures allow for a better crystalline structure recovery. Once enough energy is provided during the annealing, the implantation-induced defects may be removed, reducing defect density. The lower the defect density, the smaller the lattice strain induced and, consequently, the better the structural properties of the crystal. Despite restoring the original (as-grown) phonon peak characteristics, the spectral shape still evidences the low-intensity broad bands, suggesting that a complete recovery is not attained. Even though a better recovery of the AlN lattice is achieved for RTA at 1200 °C, one must bear in mind that such annealing conditions severely damaged the GaN NWs templates.

As already mentioned, the incorporation of Eu into the lattice can also account for the tensile strain observed after implantation due to their significant ionic radius and mass compared to the metallic cation they tend to replace [66,86–89]. However, if this is the main contribution to the E_{2h} phonon frequency shift, it would remain after RTA since, according to literature results, the Eu^{3+} location in the GaN and AlN lattice practically does not change after annealing for low fluences [66,87,88]. Furthermore, considering the low concentration of Eu (below 0.026 %), their contribution is unlikely to affect the macroscopic strain measured by micro-Raman in non-resonant conditions. In contrast, a much higher concentration of defects is expected after implantation because a single accelerated Eu ion colliding with the lattice can displace tens to thousands of lattice atoms. Consequently, these point defects will contribute more to the macroscopic strain. The removal of the implantation-induced defects after RTA likely explains why the average strain introduced by implantation tends to be eliminated.

Although Eu^{3+} is not likely the reason for the macroscopic strain, their incorporation in the lattice implies the existence of compositional fluctuations. Therefore, this may explain the incomplete recovery of the characteristics of the signal from the as-grown samples after RTA.

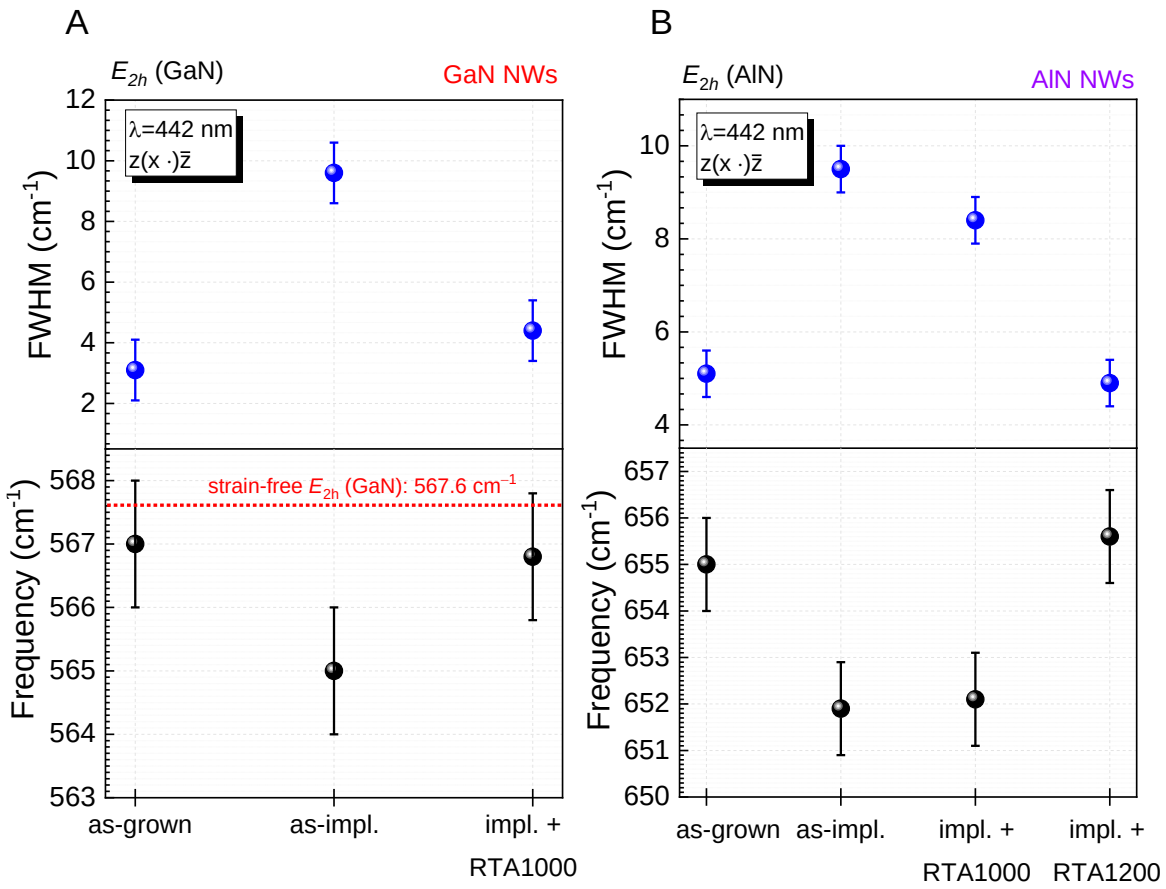

Figure 3.10 Frequency and FWHM evolution of the **(A)** E_{2h} (GaN) phonon in GaN NWs and **(B)** E_{2h} (AlN) phonon in AlN NWs after Eu-implantation and RTA. In these graphs, 'as-impl.' means as-implanted and 'impl. + RTA' refers to the Eu-implanted NWs after RTA.

In the literature, it is possible to find different reports affirming that the initial strain state of GaN layers and NWs implanted with Eu (for fluences below 5×10^{14} cm^{-2}) is recovered after annealing at 1000 °C [37,90]. Nevertheless, the XRD diffractograms showed a slight broadening compared to the as-grown spectrum, attributed to implantation-induced defects remaining after annealing [37,90]. In AlN layers, the implantation damage was reported to be stable upon annealing temperatures up to 1450 °C [91,92]. This incomplete recovery of the initial crystalline state after annealing demonstrated by XRD agrees with the previous discussion of the Raman results for the Eu-implanted GaN and AlN NWs studied in this thesis.

Figure 3.11(A) shows the micro-Raman spectra for AlGaN NWs with $y = 0.5$ after implantation and RTA at 1000 °C and 1200 °C. As in the case of binaries, RTA only provides a partial recovery of the as-grown spectrum, with the broad bands associated with lattice disorder not disappearing completely. Furthermore, for the sample annealed at

1200 °C, the signal from the GaN NWs templates is quenched, agreeing with the previous argument that the AlGaN top section cannot act as a protective capping layer for GaN NWs templates during annealing at high temperatures.

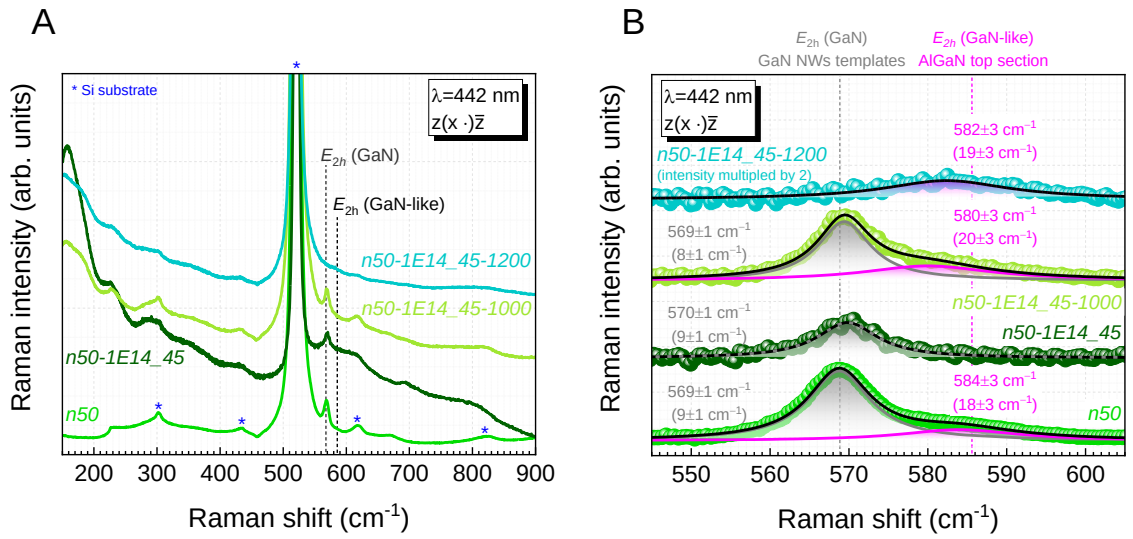

Figure 3.11 (A) Micro-Raman spectra after implantation and RTA for ternary AlGaN NWs with $y = 0.5$. **(B)** Example of the deconvolution of the E_{2h} (GaN) and E_{2h} (GaN-like) peaks for the previous samples; the extracted frequency and FWHM (in parentheses) of each peak are included. The substrate contribution was removed prior to the fitting procedure.

Figure 3.11(B) shows an enlargement of the spectra presented in **Figure 3.11(A)** around the E_{2h} (GaN) and E_{2h} (GaN-like) modes, as well as the corresponding deconvolution results using a procedure similar to that used for the as-grown ternary AlGaN NWs in **sub-subsection 3.3.1.1**.

From such a deconvolution, one can notice that the E_{2h} (GaN) phonon related to the GaN NWs templates is slightly affected by Eu-implantation due to a reduction in their relative intensity compared to the Si substrate signal. After RTA at 1000 °C, the signal is recovered; however, RTA at 1200 °C leads to the non-detection of such mode, which was attributed to GaN dissociation. Regarding the low-intensity signal of the E_{2h} (GaN-like) phonon associated with the ternary AlGaN top section, one cannot detect it after Eu-implantation, consistent with the generation of crystalline damage in the upper section of the NWs. After RTA, this tiny peak reappears, evidencing a recovery of the crystalline properties. Nevertheless, it is impossible to discriminate any influence of implantation-induced strain by evaluating the E_{2h} (GaN-like) mode frequency since the differences between extracted frequencies are within the experimental uncertainty of 3 cm^{-1}.

3.3.1.4. Dissociation of GaN at high RTA temperatures

One of the most significant issues identified previously is the degradation of the GaN NWs templates after RTA at 1200 °C, demonstrated by the significant reduction of the micro-Raman signal related to the E_{2h} (GaN) phonon. Despite this, the Raman signal from the AlGaN section grown on top of the templates remains detectable. In order to try to understand what happened to the NWs' structure, the samples were analyzed by SEM.

Figure 3.12 exhibits low-magnification SEM images of the sample *n100-1E14-1200*, in which it is possible to notice a heterogeneous appearance. This SEM image reveals the emergence of cracks in the sample with substrate lifting, which may occur due to the different thermal expansion coefficients of III-N and Si. Near the cracks (green box), Ga droplets with well-defined spherical shapes and different sizes are noticeable; in these regions, the AlGaN NW top sections do not effectively protect the GaN NWs templates from RTA, becoming more exposed and promoting out-diffusion of nitrogen and formation of Ga droplets on the NWs top. EDX measurements confirmed the formation of Ga droplets.

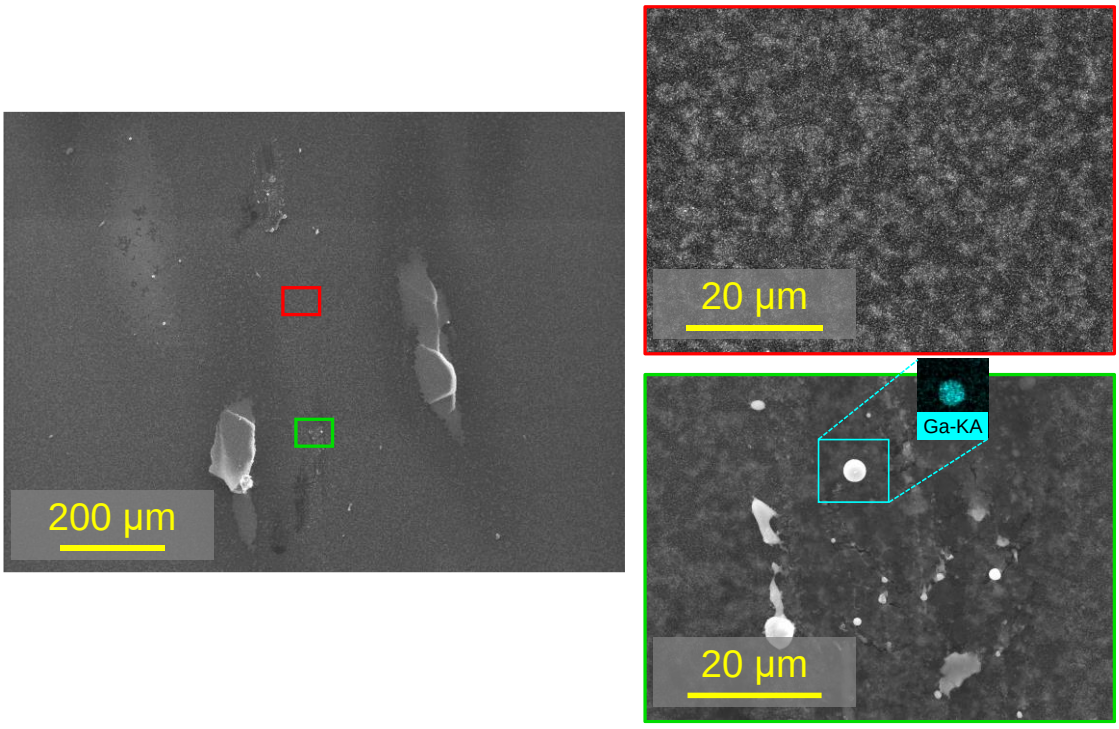

Figure 3.12 Low-magnification SEM images of the sample *n100-1E14_45_1200*. The images on the right correspond to magnifications in the regions indicated in the image on the left (red and green boxes).

Nevertheless, changes can be seen far from the cracks (area represented by the red box). Within this area, the contrast of the signal varies, which can be caused by regions with

different electrical conductivity or regions of NWs of different heights. The latter happens if NWs are detached from the substrate.

Figure 3.13 compares the SEM images obtained for samples *n100-1E14_45-1000* and *n100-1E14_45-1200* at three distinct magnifications. The lower magnification images show significant differences, with the sample annealed at 1000 °C exhibiting a homogeneous appearance like the as-grown AlN NWs, contrasting with what is observed for sample *n100-1E14_45-1200*. The heterogeneities observed in this case are discussed above. The SEM results indicate that GaN decomposes during RTA at 1200 °C, in agreement with micro-Raman findings.

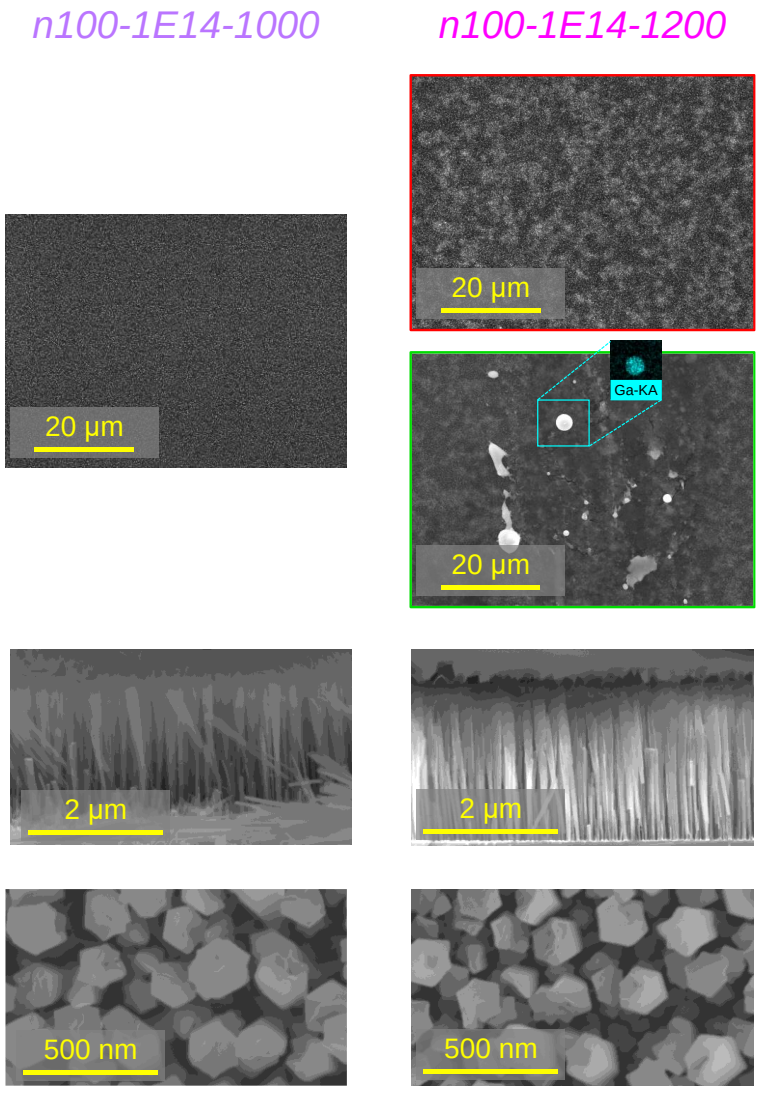

Figure 3.13 Comparison of the SEM images obtained for samples *n100-1E14_45-1000* (left) and *n100-1E14_45_1200* (right). Side by side are images obtained with the same magnification.

Increasing the magnification allows one to perceive that the individual structure of the NWs is similar independently of the RTA temperature; a comparison with the SEM image of the as-grown AlN NWs [in **Figure 3.1(C)**] reveals no differences as well. Interestingly, despite the previous signs of decomposition of GaN NW templates, the NWs retain their vertical orientation and length. This hints that, during RTA at 1200 °C, the surface of the GaN NW templates is the most affected part, while their core should keep sustaining the AlN NW top sections. Although not disclosed here, identical observations are found for the other AlGaN NW samples annealed at 1200 °C.

The dissociation of the GaN NWs templates constitutes a crucial problem that needs to be pondered in future device developments, including LED realization, based on such an approach. However, within the scope of this research, it is not expected to have a critical impact since the primary goal of this study is to evaluate the optical activation of Eu implanted into the AlGaN NW top sections, which are not as severely damaged as the GaN NWs templates by the RTA at 1200 °C. Indeed, micro-Raman results suggest an improvement of the crystalline properties of the AlGaN top sections for RTA at 1200 °C.

3.3.2. Luminescence of the AlGaN NWs

Throughout this subsection, photoluminescence spectroscopy techniques, including PL and PLE are used to evaluate the luminescence features of the Eu-implanted AlGaN NWs. These allow the evaluation of the main mechanisms of recombination and excitation in these samples. However, the available optical excitation sources (Xe lamp and He-Cd laser) do not provide band-to-band excitation of AlGaN hosts with high y (above ~0.6) due to their ultra-wide bandgap. In these cases, optical excitation is only possible if mediated by defects that possess levels within the host's bandgap.

Additional CL experiments are carried out to allow for exciting all the AlGaN NWs above the bandgap. Attention is drawn to the fact that in CL, the excitation source is a high-voltage electron beam that can produce luminescence through all the possible radiative channels available in the sample by impact ionization or excitation.

3.3.2.1. PL and CL spectra of the as-grown AlGaN NWs

Figure 3.14(A) shows the RT PL spectra of the as-grown AlGaN NWs when excited with the Xe lamp. The excitation wavelength is chosen to guarantee band-to-band excitation, which is possible for samples *n0*, *n30*, and *n50*; in these cases, light absorption is high in the top section of the NWs, causing the measured PL signal to come essentially from that region. In contrast, for samples *n75* and *n100*, the excitation wavelength only allows sub-gap excitation. **Figure 3.14(B)** shows the 5 K CL spectra of the as-grown

AlGaN NWs ($0 < y \leq 1$). In these experiments, the interaction extends to depths of about 70–190 nm, signifying that the measured signal comes predominantly from the AlGaN top sections.

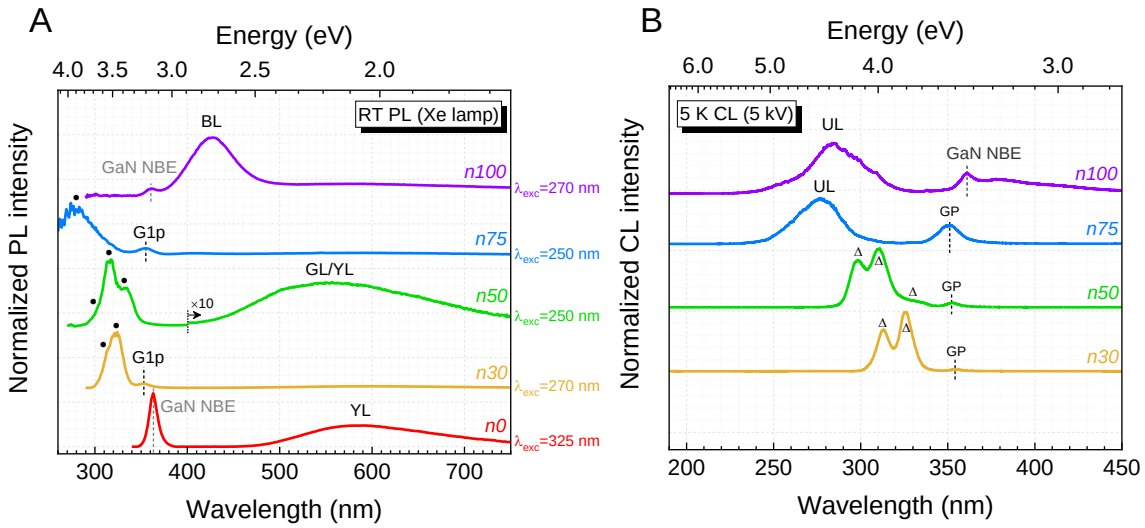

Figure 3.14 Normalized **(A)** RT PL and **(B)** 5 K CL spectra of the as-grown AlGaN NWs.

The PL spectrum of sample *n0* exhibits a peak at 363 nm (~3.4 eV) related to the GaN NBE emission and a broad yellow luminescence band (YL) peaking at ~585 nm (~2.1 eV). Emission bands in the yellow spectral range of the electromagnetic spectrum are common in GaN samples and are caused by lattice defects and impurities; their nature has been under debate since the early stages of GaN. The most accepted origins of these bands involve vacancies and related complexes or carbon-related impurities [93–95].

For sample *n30*, the PL spectrum consists of an asymmetric band in the UV region peaking at 325 nm (~3.8 eV) and a shoulder on the high energy side at ~315 nm (~3.9 eV). This emission corresponds to the AlGaN NBE emission. The observation of two contributions is likely due to the co-existence of regions in the same NW or from different NWs in the ensemble with distinct AlN molar fractions or strain states. In fact, it is often reported in the existence of compositional fluctuations in MBE-grown AlGaN NWs (e.g., irregular Al-rich/Ga-rich superlattice-like structures) due to the nucleation and growth kinetics of AlGaN top sections on GaN NWs templates, as these processes involve Ga and Al adatoms that have distinct diffusivities at the surface of the NWs [39,48,96,97]. In addition to the AlGaN NBE emission, it is possible to observe a low-intensity peak (identified as GP) at ~355 nm (~3.5 eV), the nature of which will be discussed later in this

sub-subsection. Despite a slight shift in peak energy and a reduced width caused by measuring the response at a lower temperature, the 5 K CL response is identical to RT PL.

The luminescence spectra of sample *n50* consist of three peaks at ~300 nm (~4.1 eV), ~315 nm (~3.9 eV), and ~333 nm (~3.7 eV), which are attributed to the AlGaN NBE emission. The observation of various peaks is again associated with compositional fluctuations inherent to ternary AlGaN alloys or strain effects. The PL spectrum also reveals a broad asymmetric luminescence band with contributions in green (GL) and yellow (YL) spectral region, likely due to lattice native defects or impurities in the AlGaN top section or the GaN NWs templates. Although with very low intensity, identical bands are observed for all the as-grown NWs studied. In the CL spectrum, it is possible to identify the GP peaking at ~353 nm (~3.5 eV).

The luminescence of samples *n30* and *n50* suggests the existence of compositional or strain fluctuations, in agreement with reports found in the literature for MBE-grown AlGaN NWs [39,48,96,97]. Nevertheless, the micro-Raman results in **sub-subsection 3.3.1.1** did not allow discerning such fluctuations. This may be due to the reduced scattered signal from the AlGaN top section, contrary to what happens in PL, where most of the measured luminescence comes from this region due to strong light absorption. Furthermore, it must be considered that non-resonant micro-Raman experiments only provided a wide range of values where the AlN molar fraction of the ternary AlGaN alloy can be found due to the uncertainty of the measurement and the fact that compositional and strain effects are indistinguishable.

Returning to the discussion of **Figure 3.14(A)** and **Figure 3.14(B)**, it is possible to verify that the PL and CL spectra obtained for sample *n75* are identical. They exhibit an asymmetric and broad luminescence band in the middle-UV region (UL) between 250 and 300 nm (~5 and 4 eV). The low-intensity peak GP is also detected at ~351 nm (~3.5 eV). As UL is photo-excited with energy below the E_{gap} (AlGaN) for $y = 0.75$, its origin should involve defects or regions in the NWs with lower AlN molar fractions than the nominal value. One will return to the discussion of the origin of this band later in this sub-subsection.

For sample *n100*, the PL spectrum consists of a peak at ~361 nm (~3.4 eV), related to the GaN NBE emission from GaN NW templates, and an intense and broad blue luminescence band (BL) centered at ~430 nm (~2.9 eV). Emission bands in the blue spectral region, which can be excited with energy below the AlN bandgap, are commonly observed in AlN. These are tentatively attributed to defects involving isolated V_{Al} and related complexes with oxygen impurities [15,98–102]. Residual oxygen is among the most common impurities within the MBE chamber [50]. In the 5K CL spectrum, one can identify the GaN NBE emission of the GaN NWs templates, a weak and unstructured emission in the blue

region probably related to the BL, and a broad luminescence band in the middle-UV region identical to the UL observed for sample *n75*.

Figure 3.15 summarizes the PL and CL results, with the peak energies of the different luminescence contributions (except for BL and GL/YL) represented as a function of *y*. These peaks can be grouped into *i)* AlGaN NBE emission peaks, *ii)* low-intensity GP peaks, and *iii)* UL.

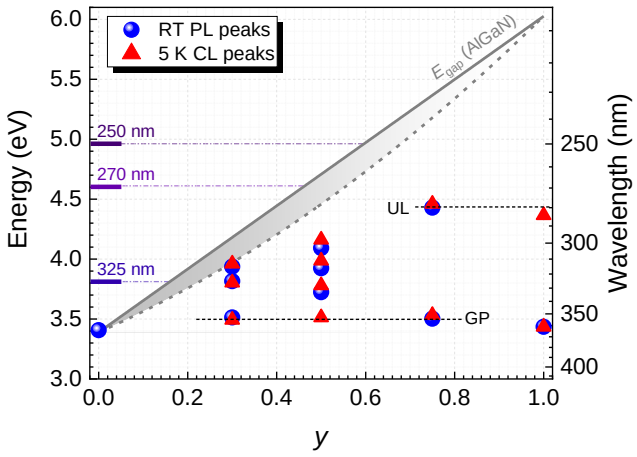

Figure 3.15 Energy of the luminescence peaks observed in RT PL and 5 K CL spectra as a function of *y*. The solid gray curve corresponds to the AlGaN energy bandgap dependence on *y* considering the empirical Vegard's law ($b = 0$ eV), while the dashed gray curve is the same but with $b = 1$ eV [103].

The AlGaN NBE emission peaks tend to accompany the E_{gap} (AlGaN), shifting for higher energies with increasing *y*. For samples *n30* and *n50*, two and three peaks related to the NBE emission are identified, respectively. This was previously attributed to the co-existence of regions in the same NW or from different NWs in the ensemble with distinct AlN molar fractions or strain states. The highest energy peak identified for each sample blueshifts with increasing *y*; however, the peak energies are hundreds of meV below the bandgap energy of AlGaN alloys with such nominal AlN molar fractions. This shift cannot be explained by the formation of the FX, whose binding energies are only some tens of meV [40,41]. The observed shift is likely caused by the recombination of carriers localized at potential minima due to compositional or strain fluctuations in the alloys [104–107]. Therefore, these peaks do not reflect the average composition and strain state of the ternary AlGaN alloys, as obtained from non-resonant micro-Raman experiments; instead, they bring information from localized regions within the alloys responsible for introducing potential minima (e.g., Ga-rich AlGaN sections). Indeed, A. Pierret et al. reported significant Stokes

shifts of ~500 meV for intermediate AlN molar fractions in PAMBE-grown AlGaN NWs [48,96], which is similar in magnitude to that found for the samples studied in this thesis. For samples *n75* and *n100*, no emission associated with the NBE emission is observed in PL or CL experiments.

The low-intensity GP peaks are at slightly higher energies (~100 meV) than the GaN NBE emission in GaN NWs but at much lower energies than expected for the AlGaN NBE emission from the respective alloys. As found in micro-Raman, the GaN NWs templates of ternary AlGaN NWs are uniaxially compressed by the Al-rich shell formed around them (**sub-subsection 3.3.1.1**). Considering the shift of the E_{2h} (GaN) phonon measured for GaN NWs templates (and the strain associated with it) and the electronic deformation potentials of GaN [77], using equations (2.19) and (2.20), the GaN NBE emission is expected to blueshift ~20–100 meV, which is in line with the observed shift. Furthermore, a tenue blueshift is found with increasing y, probably due to the higher AlN molar fraction, as proposed in **subsection 3.3.1.1**. For the as-grown AlN NWs, the GaN NBE emission does not change within the experimental error, in line with the micro-Raman findings. It is proposed that this is caused by the formation of the AlN shell being unlikely or confined to a reduced height of the GaN NWs templates due to shadowing effects during growth.

For samples *n75* and *n100*, the UL appears. This broad and asymmetric luminescence band peaks at ~280 nm (~4.4 eV) regardless of y. As discussed, the UL can be related to defects with energy levels in the forbidden gap of the host or to AlGaN regions in the NWs with different compositions and elastic deformations.

In order to obtain more information about the origin of the UL, CL measurements were carried out with the electron beam focused on single NWs (spot mode). **Figure 3.16** compares the CL response obtained for samples *n75* and *n100* in both average and spot mode. The latter reveals that the UL consists of a bunch of sharp peaks, implying the involvement of highly localized states. A. Pierret et al. observed a similar 5 K PL band at 4.3 eV (~288 nm) for PAMBE-grown AlGaN NWs independently on the nominal AlN molar fraction when exciting above the bandgap; they attributed the quantum-dot-like behavior of the UL to Ga-rich clusters embedded in the AlGaN NW sections, given that defect-related bands would spectrally shift with y [48]. However, despite this being a possibility for sample *n75*, it cannot explain the observation of such sharp lines for sample *n100* since there is no simultaneous exposition to Ga and Al fluxes during growth.

In his Ph.D. thesis, M. Belloeil demonstrated that the AlGaN NW top sections of sample *n75* have Al-rich AlGaN or pure AlN regions [50]. Therefore, one tentatively attributes the UL to point defects in AlN [15,108], with the associated electronic states being strongly localized. Recently, R. Vermeersch et al. also reported a similar emission band in undoped and Ga-doped AlN NWs grown by PAMBE, which they assigned to oxygen impurities [109].

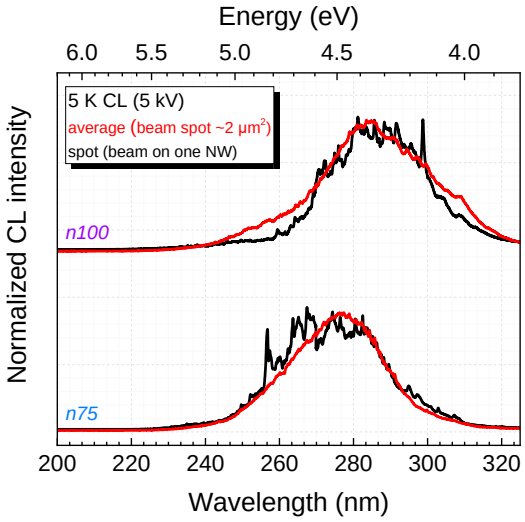

Figure 3.16 Comparison of the 5 K CL spectra obtained for samples *n75* and *n100* in average and spot modes.

3.3.2.2. Optical activation of Eu-implanted into AlGaN NWs

Considering the excitation and detection conditions used before, no luminescence signal associated with the implanted ions could be detected right after implantation.

Figure 3.17 shows the RT PL spectra of **(A)** GaN and **(B)** AlN NWs before and after Eu-implantation and RTA treatment, with GaN NWs being excited above the GaN bandgap ($\lambda_{exc} = 325$ nm) and AlN NWs excited below the AlN bandgap ($\lambda_{exc} = 270$ nm). For both hosts, it is possible to identify various sharp emission lines in the red spectral region due to intra-4f^6 transitions of Eu^{3+} [110–112], indicating the optical activation of the implanted Eu in their trivalent charge state. This result demonstrates that RTA allows Eu^{3+} to become optically active in GaN and AlN NWs, in addition to recovering the crystalline lattice to some extent (as demonstrated in **sub-subsection 3.3.1.3**).

Looking at the PL spectra of GaN NWs in **Figure 3.17(A)**, it is perceived that the response of sample *n0-1E14_45-1000* is markedly distinct from that of *n0*. The predominant radiative recombination paths observed for sample *n0*, the GaN NBE emission and the YL, are replaced by the narrow emission lines of Eu^{3+}. The most intense line peaks at 622 nm and corresponds to the $^5D_0 \rightarrow {}^7F_2$ transition [110]. The strong quenching of the host-related luminescence is likely due to *i)* implantation-induced defects that remain even after RTA at 1000 ℃, responsible for introducing nonradiative de-excitation channels or *ii)* nonradiative ET to Eu^{3+}.

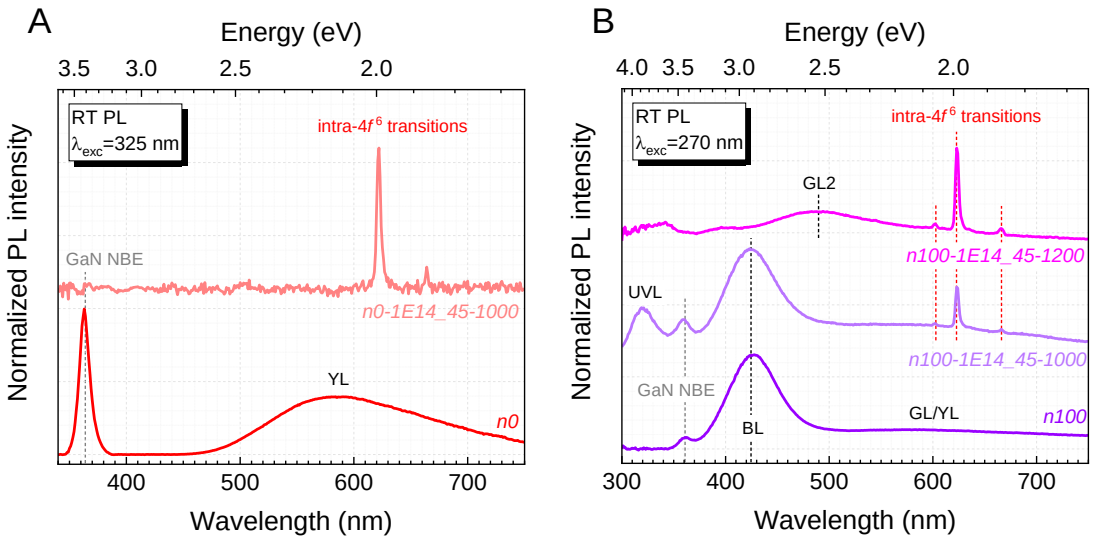

Figure 3.17 Normalized RT PL spectra of **(A)** GaN and **(B)** AlN NWs before and after Eu-implantation and RTA. The excitation source is the Xe lamp. The spectra are normalized to the respective intensity maximum.

The PL spectra of AlN NWs, in **Figure 3.17(B)**, reveal different luminescence contributions. As identified earlier, under such excitation conditions, the PL response of sample *n100* includes the GaN NBE emission, the BL, and the GL/YL. After RTA at 1000 ℃, the PL spectrum resembles that of sample *n100* with two additional contributions: a broad near-UV luminescence band (UVL) centered at ~325 nm (~3.8 eV) and the intra-ionic emission of Eu^{3+}, whose more intense contribution comes from the $^5D_0 \rightarrow {}^7F_2$ transition peaking at ~624 nm. The PL spectrum changes significantly for sample *n100-1E14_45-1200*; compared to sample *n100-1E14_45-1000*, only the intra-4*f*^{6} luminescence remains. A new green luminescence band (named GL2) centered at ~490 nm (~2.5 eV) appears in the spectrum, while the UVL and BL are no longer detected. This suggests that the RTA at 1200 ℃ provides enough energy to the crystalline lattice to reorganize, i.e., it changes the balance of defects in AlN NWs. Furthermore, achieving the optical activation of Eu^{3+} in AlN NWs in these excitation conditions reveals electronic levels in the forbidden gap of AlN capable of exciting the ions.

While in GaN NWs, the GaN NBE emission is strongly quenched after implantation, the same does not occur for AlN NWs since, in this case, the GaN NWs templates are barely unaffected by implantation, i.e., Eu ions tend to become implanted within the long AlN NW top sections. However, the absence of PL signals related to the GaN NWs templates for the sample *n100-1E14_45-1200* points to their severe damage. These behaviors agree with the micro-Raman discussed in the **sub-subsections 3.3.1.2** and **3.3.1.3**.

Figure 3.18 shows the **(A)** RT PL and **(B)** 5 K CL spectra of the Eu-implanted AlGaN NWs after RTA at 1200 °C (1000 °C, for Eu-implanted GaN NWs). When possible, photo-excitation is performed with energy above the host's bandgap, i.e., for samples *n0-1E14_45-1000*, *n30-1E14_45-1200*, and *n50-1E14_45-1200*; otherwise, it proceeds through sub-gap excitation. Intense intra-4f^6 emission lines dominate both PL and CL spectra, demonstrating that Eu^{3+} are optically activated for all the annealed NWs.

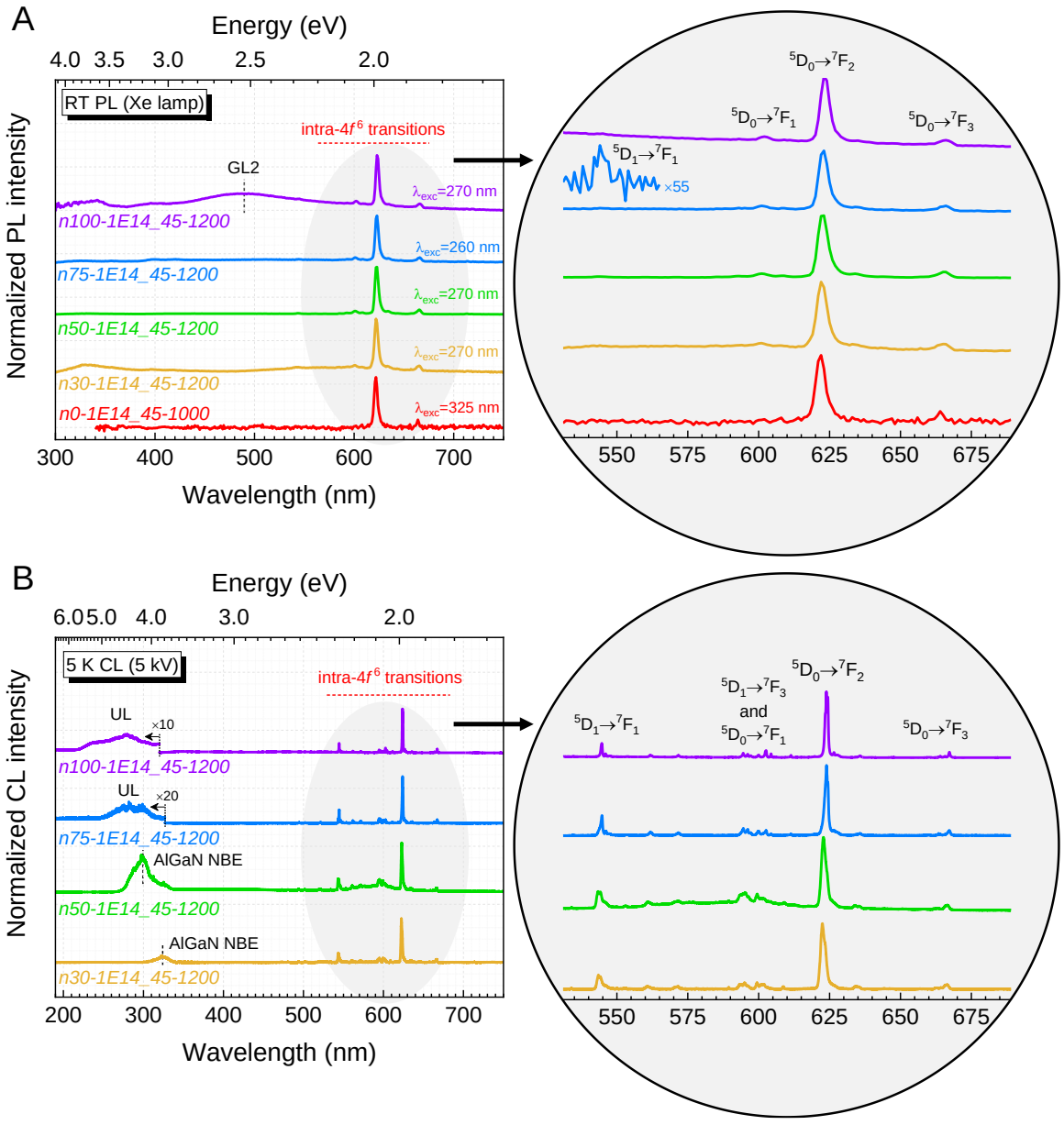

Figure 3.18 Normalized **(A)** RT PL and **(B)** 5 K CL spectra of the Eu-implanted AlGaN NWs after RTA at 1200 °C. Each graph is zoomed around the intra-4f^6 luminescence (on the right side).

In the PL spectra, the $^5D_0 \rightarrow {}^7F_J$ transitions are dominant, with the $^5D_0 \rightarrow {}^7F_2$ transition at ~620–625 nm being the most intense, as typically observed in Eu-doped III-N [19,110,113]. A low-intensity peak related to the $^5D_1 \rightarrow {}^7F_1$ transition could also be identified at ~545 nm; see the magnification in the PL spectrum of sample *n75-1E14_45-1200* in **Figure 3.18(A)** as an example.

The intra-ionic transitions are also the dominant contribution in the 5 K CL spectra shown in **Figure 3.18(B)**; the exception is the spectrum of sample *n50-1E14_45-1200*, in which the AlGaN NBE emission has a comparable intensity. Compared to PL experiments, it is possible to notice a significant increase in the relative intensity of transitions arising from higher energetic states than $^5D_0$, namely the $^5D_1$ state, such that the $^5D_1 \rightarrow {}^7F_1$ transition at ~545 nm is the second most intense transition. This result indicates that the excitation and/or de-excitation mechanisms of Eu^{3+} differ in PL and CL experiments. Indeed, W. Zhu et al. reported similar findings for Eu-doped GaN layers under intense excitation conditions (e.g., CL or high excitation density PL); the authors explained it as a re-excitation of Eu^{3+} excited in the $^5D_0$ state into higher-energy ^5D_J states due to the longer lifetime of $^5D_0$ (of the order of 200 μs) compared to $^5D_1$ and $^5D_2$ (of the order of 2 μs). Once this happens, the re-excited ions can relax back to the $^5D_0$ state or emit from $^5D_1$ and $^5D_2$ [114–116]. In CL, the high-energy of the electron beam used as the excitation source may influence the process because of the much higher excitation density than PL and, therefore, be responsible for the observed changes.

Furthermore, from **Figure 3.18(B)**, one can observe the AlGaN NBE emission for the lower nominal AlN molar fractions (samples *n30-1E14_45-1200* and *n50-1E14_45-1200*). The possibility of detecting the AlGaN NBE emission, the predominant radiative path before implantation (**Figure 3.14**), suggests that RTA at 1200 ℃ allows the recovery of the implantation-induced damage to some extent, in agreement with micro-Raman results. Remember that for GaN NWs, the RTA at 1000 ℃ did not recover the GaN NBE emission [**Figure 3.17(A)**].

3.3.2.3. Excitation of Eu^{3+} in AlGaN NWs

Figure 3.19 shows the PLE spectra of samples **(A)** *n0* and *n0-1E14_45-1000* and **(B)** *n100*, *n100-1E14_45-1000*, and *n100-1E14_45-1200* when fixing the emission wavelength at the maximum of the most intense $^5D_0 \rightarrow {}^7F_2$ transition (i.e., 622 nm for GaN and 624 nm for AlN).

Considering the PL response measured before for GaN NWs, fixing the emission wavelength at 622 nm corresponds to monitoring distinct radiative channels: the YL for sample *n0* and the $^5D_0 \rightarrow {}^7F_2$ transition for sample *n0-1E14_45-1000*. From **Figure 3.19(A)**, it is possible to notice that excitation above the GaN absorption edge at ~360 nm (~3.4 eV)

is the primary excitation path for both samples. Nevertheless, the intra-4f6 luminescence can also be excited through a broad excitation band (hereafter designated by X1)[ll] centered at ~375 nm (~3.3 eV) that is superimposed to the GaN edge and extends to ~425 nm (~2.9 eV). This result demonstrates the possibility of exciting Eu^{3+} in GaN NWs with energy below the bandgap, which implies the involvement of defects with energy levels in the forbidden gap. A similar sub-gap excitation band is often found in Eu-doped GaN layers [117–119].

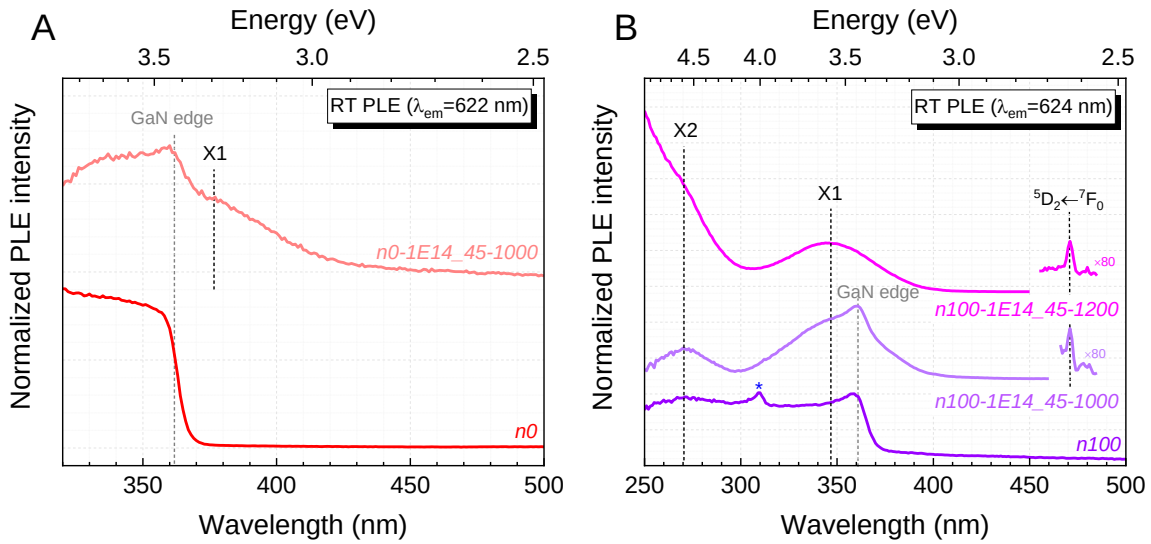

Figure 3.19 Normalized RT PLE spectra of **(A)** GaN and **(B)** AlN NWs when monitoring the emission wavelength at the most intense Eu^{3+} intra-ionic emission ($^5D_0 \rightarrow {}^7F_2$ transition). The asterisk (*) denotes the 2nd-order of the excitation.

The PLE response of AlN NWs shown in **Figure 3.19(B)** by monitoring the emission wavelength at 624 nm corresponds to inspecting two distinct radiative contributions: *i)* GL/YL (samples *n100* and *n100-1E14_45-1000*), and *ii)* $^5D_0 \rightarrow {}^7F_2$ transition (samples *n100-1E14_45-1000* and *n100-1E14_45-1200*). For sample *n100*, the PLE spectrum consists of the GaN absorption edge at ~360 nm (~3.4 eV), which is unsurprising given that the GL/YL was already suspected to have origin in the GaN NWs templates. The PLE spectrum of sample *n100-1E14_45-1000* also reveals the GaN absorption edge; however, two additional broad bands in the UV are discerned: X1 centered at ~350 nm (~3.5 eV) with FWHM of ~55 nm (equivalent to ~0.5 eV), and *ii)* X2 centered at ~270 nm (~4.6 eV) with FWHM of ~30 nm (equivalent to ~0.5 eV). Similar broad excitation bands in the UV have

[ll] One adopts the nomenclature proposed by K. Wang et al. for the two excitation bands commonly observed in Eu-implanted AlGaN layers [20].

already been reported in the literature for Eu-implanted AlGaN layers [20,120–124]. Besides that, a low-intensity peak related to the direct excitation of Eu^{3+} from the ground state $^7F_0$ to the excited state $^5D_2$ can be identified at 471 nm. For sample *n100-1E14_45-1200*, since the high RTA temperature severely damaged GaN NW templates, the PLE spectrum shows only the features involved in the excitation of Eu^{3+} (X1 and X2 broad bands and intra-4*f*^{6} transition peaks), i.e., no GaN absorption edge is detected. Also, a pronounced excitation tail superimposed to X2 is noted at the shorter wavelengths. Given that post-implantation annealing at a higher temperature provides better recovery of the crystalline lattice, such a tail may be related to the onset of band-to-band excitation.

Figure 3.20 shows the PLE response when monitoring different luminescence contributions observed for samples *n100-1E14_45-1000* (UVL, BL, and $^5D_0 \rightarrow {}^7F_2$ transition) and *n100-1E14_45-1200* (GL2 and $^5D_0 \rightarrow {}^7F_2$ transition). The representation of the intensity in the $\log_{10}$ scale allows the identification of an additional low-intensity peak related to the direct excitation of Eu^{3+} at 544 nm ($^5D_1 \leftarrow {}^7F_0$ transition). Furthermore, one can notice that similarly to the Eu^{3+}-related luminescence, defects-related emissions are excited through broad bands in the UV. The BL is excited through an absorption edge that starts at ~335 nm (~3.7 eV) and extends to shorter wavelengths (identified as BL_{exc}), while UVL and GL2 are excited through a UV band similar to X2 that peaks at ~275 nm (~4.5 eV). This means one of two things: *i)* exciting through the X2 band can also give rise to radiative recombination at defects, or *ii)* the absorption bands of the defects responsible for UVL and GL2 are resonant in energy with X2.

Broad absorption UV bands are often observed in AlN; most authors tentatively assign them to vacancies or oxygen/carbon impurities [15,101,125–127]. In a recent work, L. Peters et al. observed that implantation of AlN layers with different ionic species gives rise to an absorption band with spectral characteristics (energy and FWHM) analogous to X2; they proposed that this is related to V_N defects generated by implantation [128]. Furthermore, similar UV bands have been observed to excite other Ln^{3+} implanted into AlN layers (e.g., gadolinium, thulium, terbium, or praseodymium) [26,124,129,130].

According to the results presented and the results found in the literature, it is proposed that the origin of the X1 and X2 bands are defects that introduce energy levels in the forbidden gap of the host. As discussed in **sub-subsection 2.5.2.2**, for ET to Eu^{3+} to be efficient, such defects should be associated with Eu^{3+}, whether complex defects involving Eu^{3+} and other lattice defects or isolated/clustered defects in the close vicinity of Eu^{3+} [123,124,131]. In other words, Eu^{3+} excitation most likely occurs through a non-radiative ET from excitons localized at defect-related traps to 4*f* electrons. For the ET to be efficient, it is also required that a spectral overlap between the defect's emission and intra-4*f*^{6} absorption exists (energetic resonance); if the initial and final states are not

resonant, the energy mismatch may be compensated by the emission (or absorption) of phonons [114,131].

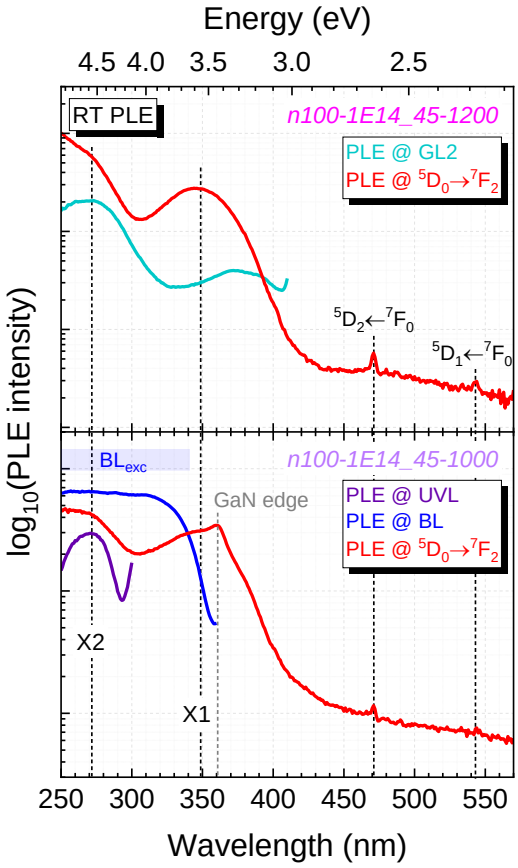

Figure 3.20 RT PLE spectra (in $\log_{10}$ scale) of samples *n100-1E14_45-1000* and *n100-1eE14_45-1200* when monitoring different PL bands.

An exact attribution of the nature of X1 and X2 to specific defects would be merely speculative; however, one can suspect that they are different since excitation through each of these bands gives rise to a distinct RT PL spectrum; this is exemplified for sample *n100-1E14_45-1200* in **Figure 3.21(A)**. Excitation with energy resonant with the X2 band gives rise to GL2, whereas excitation resonant with X1 does not. Furthermore, if those bands have different origins, the Eu^{3+} emission should also be affected because the local potential felt by the ions is no longer the same (i.e., different Eu centers) [132]. In order to inspect that, the RT PL response around the $^5D_0 \rightarrow ^7F_2$ transition, measured with higher resolution (bandpass of 1 nm), is shown in **Figure 3.21(B)**. From this, one can notice that the spectral shape barely changes with the central emission peak at 624 nm for both cases; however, when exciting through X2, shoulders appear at the low wavelength side of the prominent peaks (marked with an arrow). Although the experimental conditions are not ideal for

identifying and distinguishing optically active Eu^{3+} centers (RT measurements and insufficient spectral resolution), the appearance of shoulders is an indication that a new optical center is being excited through X2 compared to X1, hinting that different defects are involved [66]. Still, the conducted experiments do not allow one to say if *i)* two Eu^{3+} centers are simultaneously excited with different efficiencies, *ii)* one center is excited through both bands while the other is not, or *iii)* one center is excited only through X2 and the other only through X1. Note that more than two centers may be contributing to the luminescence.

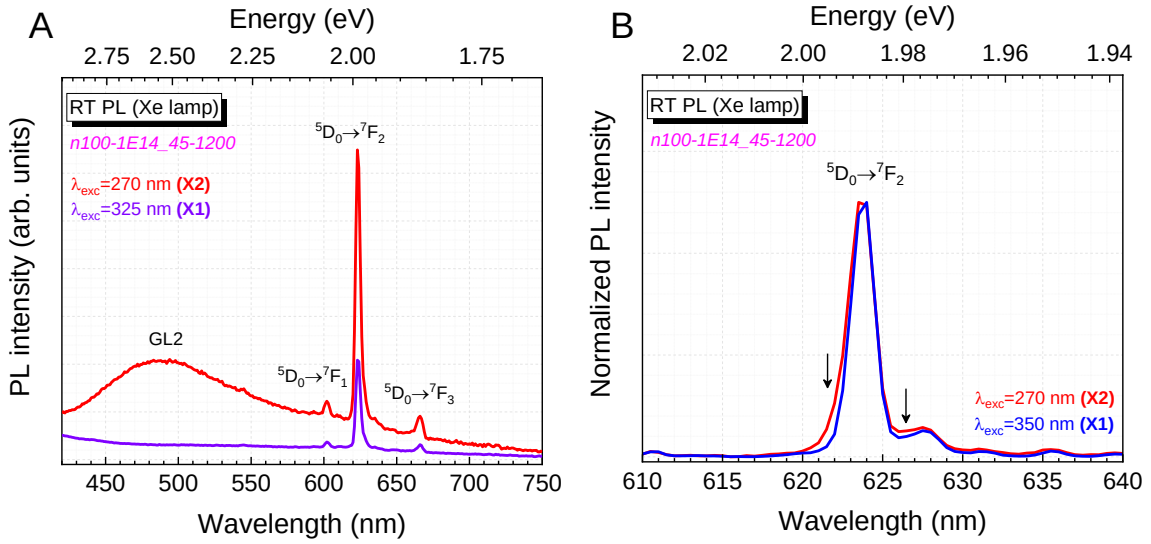

Figure 3.21 Normalized RT PL spectra of sample *n100-1E14_45-1200* when exciting through the X1 and X2 bands: **(A)** in the visible spectral range and **(B)** higher resolution (bandpass: 1 nm) spectra around the $^5D_0 \rightarrow {}^7F_2$ transition. The black arrows identify the spectral regions where differences are noticed.

A picture of the processes involved in the photo-excitation of Eu^{3+} in AlN NWs through the X2 is presented in **Figure 3.22**. First, the defect responsible for the X2 band is excited resonantly, resulting in the formation of a BX with a localized wave function. When the BX recombines, it can transfer its energy non-radiatively to the $4f^6$ core states, triggering the excitation of the Eu^{3+} directly involved (or in the close vicinity) of the defect.

From the Dieke diagram of Eu^{3+} (also represented in **Figure 3.22**), it is possible to notice that Eu^{3+} possesses several $4f^6$ excited levels matching X1 and X2 bands in energy, allowing for ET to occur. Furthermore, these levels are not pure $4f$ states but an admixture of states because of the odd-parity term of V_{host} [133], relaxing Laporte's selection rule for ED transitions. Once excited, Eu^{3+} de-excites through radiative (intra-$4f^6$ luminescence) and

nonradiative (multi-phonon relaxation) processes within the $4f^6$ manifold or by transferring its energy non-radiatively back to X2 [114,131].

Notwithstanding, the ET to Eu^{3+} does not require a total annihilation of the defects-related emission. This may explain why the UVL (sample *n100-1E14_45-1000*) and GL2 (sample *n100-1E14_45-1200*) are observed when exciting through X2. Note that this could also be a mere energetic resonance between the defects that give rise to the excitation band X2 and the responsible for the radiative UVL and GL2.

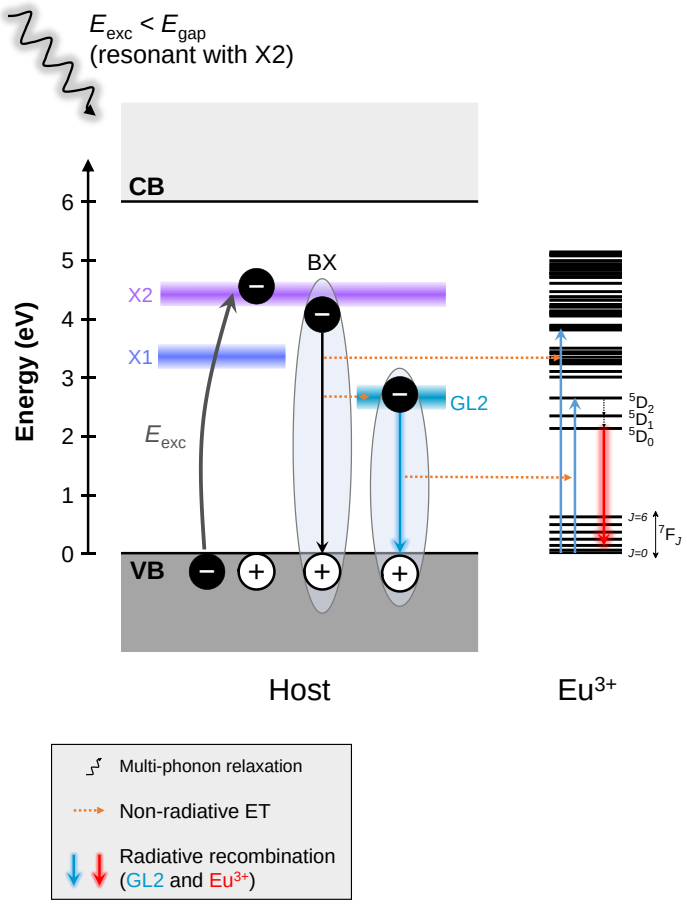

Figure 3.22 Photo-excitation of Eu^{3+} in AlN NWs through the excitation band X2.

Figure 3.23(A) shows RT PLE spectra of the Eu-implanted AlGaN NWs after RTA at 1200 ℃ (1000 ℃, for Eu-implanted GaN NWs) monitored at the $^5D_0 \rightarrow {}^7F_2$ transition peak. With increasing the AlN molar fraction of the ternary AlGaN NWs up to 0.5, the absorption edge shifts to shorter wavelengths, as expected for an AlGaN alloy with higher y. The excitation band X1 also blueshifts with y. For sample *n75-1E14_45-1200*, it is possible to observe a peak at ~250 nm (~5 eV) due to the AlGaN absorption edge; however, this is at an energy ~300–400 meV below the expected for an AlGaN alloy with $y = 0.75$. This is

likely explained by the compositional inhomogeneities found within the same NW or in different NWs of the ensemble. For AlN NWs, it is impossible to detect the absorption edge because it lies outside of the experimentally accessible wavelength range. Furthermore, for $y \geq 0.75$, the sub-gap band X2 appears in the PLE spectrum.

Besides, for $y \geq 0.75$, low-intensity and sharp absorption peaks associated with direct excitation of $4f^6$ states are identified: the $^5D_2 \leftarrow {}^7F_0$ transition at 471 nm and the $^5D_1 \leftarrow {}^7F_0$ transition at 544 nm. The appearance of these peaks suggests that AlGaN hosts with high y may play a relevant role in achieving a more efficient optical activation of Eu^{3+} incorporated by ion implantation, either due to an increased probability of intra-$4f^6$ transitions (crystal field mixing) or a more significant number of the implanted ions contributing to the optical response.

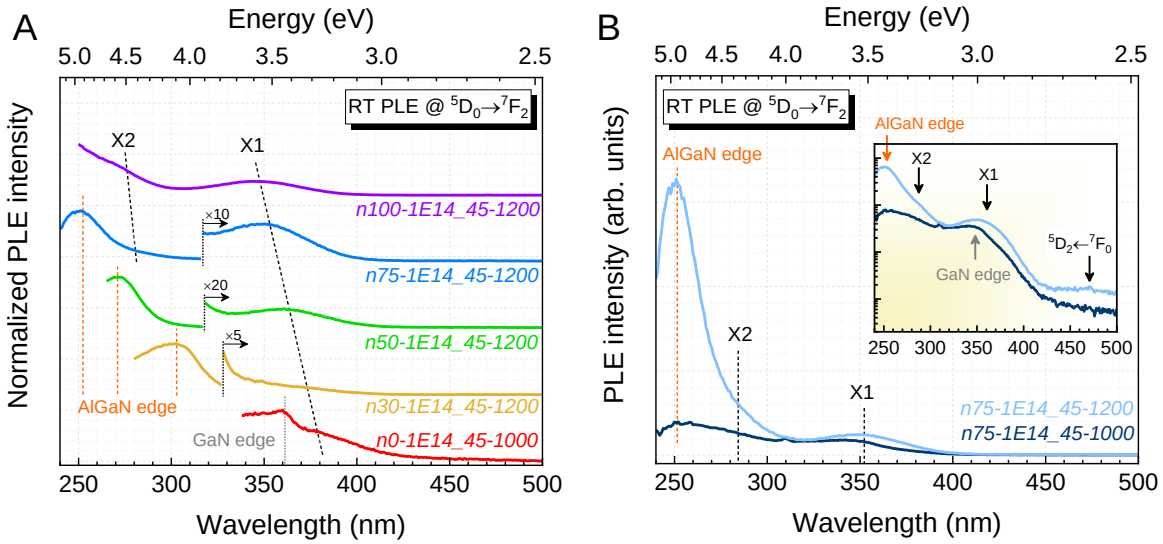

Figure 3.23 (A) Normalized RT PLE spectra of all the implanted AlGaN NWs after RTA at 1200 ℃ (for GaN, it corresponds to RTA at 1000 ℃) when the emission wavelength is set at the $^5D_0 \rightarrow {}^7F_2$ transition. **(B)** Comparison of similar RT PLE spectra obtained for samples *n75-1E14_45-1000* and *n75-1E14_45-1200* (the inset shows the spectra in a $\log_{10}$ scale).

For all samples, band-to-band excitation is the path that leads to a more intense Eu^{3+} emission. This happens because of the high absorption coefficient, resulting in an increased probability of formation of FXs that are subsequently bound to the defects responsible for Eu^{3+} excitation. The absorption cross-section of the defects is not as high as the above bandgap absorption, although the ET process should be more efficient since it does not require the localization of the FX. Furthermore, it is possible to notice that, for the highest RTA temperature, the excitation of Eu^{3+} with energy above the host's bandgap is enhanced. An example is shown in **Figure 3.23(B)** for $y = 0.75$. The relative increase in Eu^{3+} intensity

through band-to-band excitation for the highest RTA temperature is likely due to the reduction of the density of non-radiative defects, i.e., the better recovery of the AlGaN crystalline lattice provided by the RTA at 1200 °C, as discussed in **sub-subsection 3.3.1.3**.

Figure 3.24 summarizes the energies of the bands and peaks involved in the excitation of Eu^{3+} in AlGaN NWs as a function of y. The X1 and X2 excitation bands blueshift with increasing y: X1 shifts ~200–300 meV from GaN to AlN, while X2 shifts less than 100 meV from $y = 0.75$ to AlN. The magnitude of these shifts is smaller than the evolution of the E_{gap} (AlGaN) with y. Furthermore, the peak energies of X1 and X2 bands agree with that reported by K. Wang et al. for Eu-implanted AlGaN layers [20]. Likewise, these authors also showed the above bandgap excitation as the excitation channel responsible for the more intense intra-$4f^6$ luminescence [20]. These results suggest that the excitation of Eu^{3+} in AlGaN layers and NWs is identical.

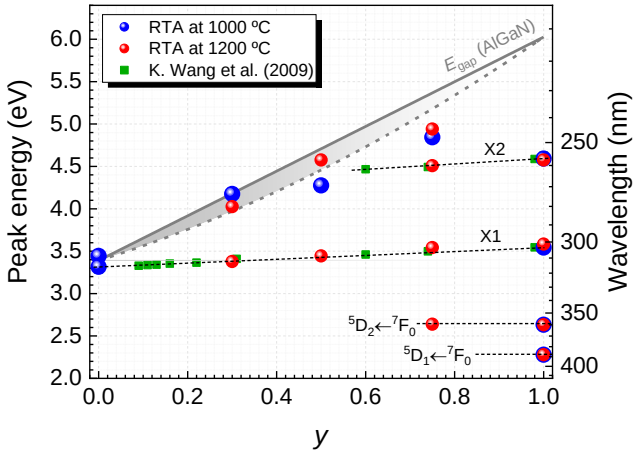

Figure 3.24 Energies of the RT PLE peaks responsible for exciting Eu^{3+} implanted into AlGaN NWs as a function of y. The energies of X1 and X2 reported by K. Wang et al. for Eu-implanted AlGaN layers (15 K PLE) are included for comparison [20]. The E_{gap} (AlGaN) evolution with y is plotted for comparison (solid gray line: $b = 0$ eV, dashed gray line: $b = 1$ eV [103]).

3.3.2.4. Optically active Eu^{3+} centers in AlGaN NWs:

The PL response of Eu^{3+} in AlGaN NWs shown in the previous sub-subsections consists of single peaks associated mainly with transitions from $^5D_0$ to the ^7F_J states. The observation of a single peak is due to the low resolution (higher than 1 nm) of the PL system used, which prevents the distinction of different lines resulting from the energy splitting of the $^{2S+1}L_J$ multiplets into a maximum of $2J + 1$ Stark levels by the action of the crystal field.

The number of Stark levels into which each multiplet splits depends on the site symmetry [134–136], as resumed in **Table 2.7**.

This sub-subsection provides an HR PL study of the fine structure of the most intense $^5D_0 \rightarrow {}^7F_2$ transition from cryogenic temperatures of ~14 K to RT, a common methodology for studying Eu^{3+} centers in GaN [35,66]. However, in this study, the excitation source is a He-Cd laser ($\lambda_{exc} = 325$ nm), so only GaN is excited above the bandgap. For the other AlGaN samples, the excitation of Eu^{3+} is mediated by defects that possess energy levels in the forbidden gap, for instance, through the X1 band. As discussed in **sub-subsection 3.3.2.3**, this can affect the spectral line pattern by favoring specific Eu^{3+} centers closely associated with the defects responsible for X1, while others may be impossible to observe.

Figure 3.25 compares the 14 K HR PL spectrum of samples *n0-1E14_45-1000* and *R0-1E14_45-1000* (Eu-implanted GaN layers) around the most intense $^5D_0 \rightarrow {}^7F_2$ transition.

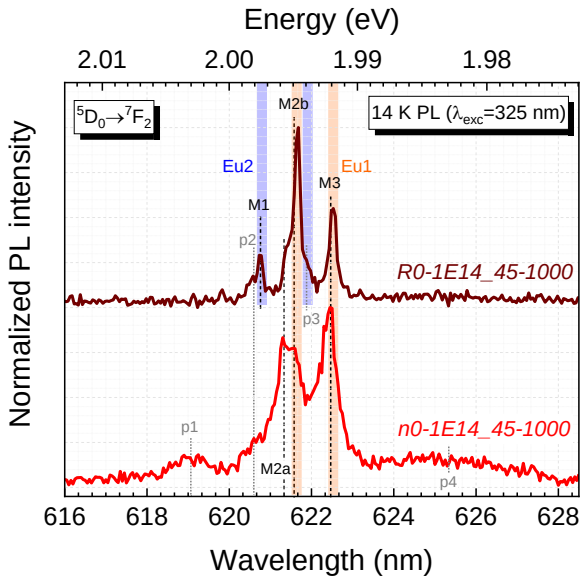

Figure 3.25 Normalized 14 K HR PL spectrum around the $^5D_0 \rightarrow {}^7F_2$ transition for samples *n0-1E14_45-1000* and *R0-1E14_45-1000*. The lines associated with the Eu1 and Eu2 centers are represented in orange and blue [119].

Most of the literature results deal with layered structures, so one starts by discussing the spectrum obtained for sample *R0-1E14_45-1000*. In this case, the $^5D_0 \rightarrow {}^7F_2$ transition consists of three prominent lines at 620.8 nm (M1), 621.8 nm (M2b), and 622.5 nm (M3). Besides those, shoulders can be noticed at ~620.6 nm (p2), ~621.4 nm (M1a), and ~622.0 nm (p3). The detection of six peaks suggests the presence of more than one optically active center since the total splitting of the $^7F_2$ multiplet would result in a maximum of five

emission lines. Nevertheless, it should be considered that other factors can lead to the appearance of more lines than expected, including emission lines associated with other transitions that occur in the same spectral range (e.g., $^5D_1 \rightarrow {}^7F_4$) or vibronic transitions [66]. As no other emissions from the $^5D_1$ state could be detected in PL experiments (see, for example, **Figure 3.17A**), the first hypothesis is excluded. The second is also not expected due to the weak electron-phonon coupling and because the energy difference between the two most energetically distant emission lines is ~6 meV, much lower than the energy of any of the GaN phonons (the E_{2l} phonon, with ~18 meV, has the lowest energy [76]).

The comparison of the PL response of sample *R0-1E14_45-1000* with literature results further strengthens the arguments of at least two optically active Eu^{3+} centers existing. The peaks at 621.8 nm (M2b) and 622.5 nm (M3) coincide with those of the Eu1 center, while the peaks at 620.8 nm (M1) and ~622.0 nm (p3) agree with the Eu2 center, the predominant centers commonly found in Eu-doped GaN layers [8,119,137]. As discussed in **sub-subsection 2.5.2.1**, although these centers can be easily distinguished, their local structure remains unclear [118,137–139]. Still, of the various works reported in the literature, the methodology employed by B. Mitchell et al. is the most reliable; thus, from now on, Eu1 is assumed to be Eu_{Ga} with a V_N in close vicinity and Eu2 as Eu_{Ga} associated with a V_{Ga} [139]. In the first case, two configurations are possible, one with V_N axially above Eu^{3+} (C_{3v} symmetry) and the other with V_N at one of the three equivalent off-center positions (C_{1h} symmetry) [139].

Besides the previously identified lines, the two shoulders at 620.6 nm (p2) and 621.4 nm (M2a) lack identification. While the first peak matches one of the most intense lines of a minority site designated as 'MS 3' by Z. Fleischman et al. [140], the other has no evident correlation with any center reported in the literature.

For sample *n0-1E14_45-1000*, five lines can be identified in the 14 K HR PL spectrum, with the two prominent lines peaking at 621.5 nm (M2) and 622.4 nm (M3). The linewidth of the 621.5 nm peak is larger than that of 622.4 nm, hinting that two different lines are overlapped (621.3 nm – M2a – and 621.7 nm – M2b), similar to sample *R0-1E14_45-1000*. In addition, one can notice a broad peak at ~619 nm (p1), an undistinguishable shoulder at ~620.6 nm (p2), and a broad sideband at ~625.5 nm (p4). The spectral pattern is identical to that obtained for Eu-implanted GaN NWs by J. Rodrigues et al. [35,141]. Furthermore, these authors could resolve the broad peak at ~619 nm and found that it consisted of at least two lines at 618.8 nm and 619.4 nm; therefore, one considers that the unresolved peak at ~619 nm for sample *n0-1E14_45-1000* has at least two contributions. Considering the above, the 14 HR PL spectrum of sample *n0-1E14_45-1000* consists of at least seven lines. Again, as for sample *R0-1E14_45-1000*, observing peaks associated with the $^5D_1 \rightarrow {}^7F_4$ transition is unexpected because of the non-detection of other transitions from the $^5D_1$ state.

Nevertheless, in this case, some peaks can be associated with phonon-assisted transitions, as will be discussed later.

The most intense lines (M2b and M3) agree reasonably well with those of the Eu1 center; however, they exhibit a slight blueshift and a different intensity ratio of the lines than those observed for sample *R0-1E14_45-1000*. Also, the linewidth is larger for sample *n0-1E14_45-1000*. In fact, the emission spectrum of a single center must be identical in position and spectral pattern; thus, the changes observed imply necessarily a modification of the local potential around Eu^{3+}. A possible explanation is the dissimilar strain state in both configurations, inducing different transition probabilities between the $^5D_0$ singlet and the various $^7F_2$ Stark levels.

According to S. Copelman et al., the broad sideband at ~625.5 nm (p4) is associated with a vibronic transition involving the Eu1 center [66,140,142]. Although none of the GaN phonons has this energy (~88–97 cm^{-1}), it is often attributed to a transition assisted by an LVM involving the Eu^{3+} in a Ga substitutional site [66,140,142]. In previous micro-Raman experiments, such frequencies could not be detected because the available notch filter only does not allow measuring Raman shifts below ~100–150 cm^{-1}. Indeed, the strongest coupling of Eu1 in GaN NWs may be related to a different strain state of the lattice, which perturbs in a slightly distinct way the Eu^{3+} centers, resulting in slight energy shifts and different broadening of the emission lines.

No signal of lines associated with the Eu2 center can be identified in the spectrum of sample *n0-1E14_45-1000*, suggesting that the formation of Eu2, generally the most efficient center for photo-excitation above the bandgap [8,118], is unfavorable in GaN NWs than in GaN layers. This may be undesirable for device development, as Eu2 is the most relevant center under electrical injection [10].

Despite the dominance of Eu1, the remaining unidentified lines hint at the presence of more than one optically active Eu^{3+} center. The broad peak at ~619 nm (p1), which is expected to have more than one contribution [35], is tentatively assigned to a minority site designated as MS4 by Z. Fleischman et al. [140]. In the same way, the shoulder at 620.6 nm (p2), also observed in *R0-1E14_45-1000*, is likely due to the minority site MS3. The peak at 621.3 nm (M2a) does not correlate appropriately with any center reported in the literature to date.

These results demonstrate the multiplicity of optically active Eu^{3+} centers in GaN hosts, revealing dissimilarity in NWs and layers. The distinct lattice dynamics between both structures (e.g., defects' stability and strain relaxation) is the most likely reason for such behavior.

Table 3.2 summarizes the peak positions of the $^5D_0 \rightarrow {}^7F_2$ transition identified in samples *n0-1E14_45-1000* and *R0-1E14_45-1000*, as well as their tentative assignment considering literature results.

Table 3.2 Wavelength of lines associated with the $^5D_0 \rightarrow {}^7F_2$ transition for samples *n0-1E14_45-1000* and *R0-1E14_45-1000*. Literature results for Eu-implanted GaN layers (15 K PL) [119,137] and Eu-doped GaN layers (combined excitation and emission spectroscopy) [140] are included.

Transition	Peak	This work (14 K HR PL)		Refs. [119,137]	Ref. [140]
		GaN NWs	GaN layers		
$^5D_0 \rightarrow {}^7F_2$	p1	619.0 (b)		618.7	618.9 **(MS4)**
				619.3	619.6 **(MS4)**
	p2	620.6	620.6 (s)		620.7 **(MS3)**
	M1		620.8	620.8 **(Eu2)**	620.9 **(Eu2)**
	M2a	621.3 (o)	621.4 (s)		
	M2b	621.7 (o)	621.8	621.7 **(Eu1)**	621.6 **(Eu1)**
	p3		621.9 (s)	621.9 **(Eu2)**	621.9 **(Eu2)**
	M3	622.4	622.5	622.5 **(Eu1)**	622.6 **(Eu1)**
	p4	625.5 (b)			

(b) broad peak, (o) overlapped peak, (s) shoulder

Figure 3.26 presents the normalized HR PL spectra of sample *n0-1E14_45-1000* around the $^5D_0 \rightarrow {}^7F_2$ transition when varying the measurement temperature from 14 K to 300 K. With increasing the temperature, the spectrum becomes less resolved due to phonon broadening, hindering a proper distinction of the optically active Eu^{3+} centers for temperatures above ~110 K. Nevertheless, the spectral pattern remains identical, implying that Eu1 center is still the one that leads to a more intense PL signal at RT. Accompanying the line broadening, the emission lines blueshift ~0.2 nm from 14 K to 300 K (i.e., ~0.7 pm·K^{-1}). This slight deviation demonstrates the potential of this approach in obtaining a very stable emission color for a wide range of device operation temperatures. Moreover, the signal-to-noise ratio (SNR) increases with temperature due to the gradual decrease of the PL intensity caused by competitive thermally activated non-radiative processes; this cannot be seen in the spectra of **Figure 3.26** due to normalization. At 300 K, the integrated PL intensity of the $^5D_0 \rightarrow {}^7F_2$ transition is only ~50 % of that measured at 14 K, congruent with that obtained by J. Rodrigues et al. for different Eu-implanted GaN NWs [35].

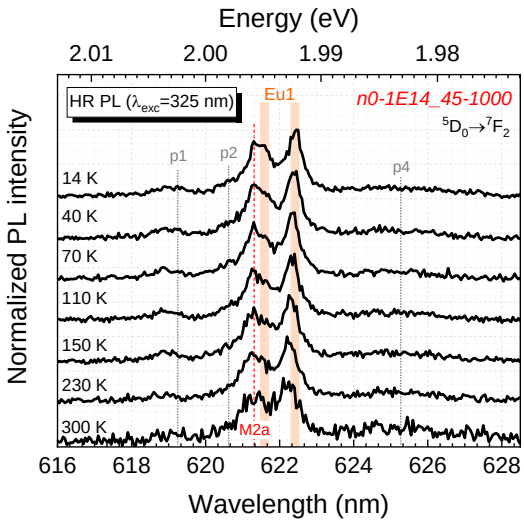

Figure 3.26 Temperature-dependent HR PL spectra of sample *n0-1E14_45-1000* around the $^5D_0 \rightarrow {}^7F_2$ transition. Each spectrum is normalized to its respective maximum.

Figure 3.27 shows the normalized 14 K HR PL spectra of the Eu-implanted AlGaN NWs annealed at **(A)** 1000 ℃ and **(B)** 1200 ℃ around the $^5D_0 \rightarrow {}^7F_2$ transition; **Figure 3.27(B)** also includes the 5 K CL spectra obtained for the same samples. Independently of the RTA temperature, the transition redshifts ~2 nm (from ~622 nm to ~624 nm) with increasing y. This trend is similar to that commonly found in Eu-doped AlGaN layers [20], and it has been attributed to the higher expansion of the $4f^6$ orbitals in hosts with higher y because of the greater electron affinity of Al compared to Ga [18]. The expansion of the $4f^6$ electron cloud results in a decrease of the electronic repulsion and, consequently, in a redshift of the intra-ionic transitions; this is known as the "nephelauxetic effect" [136,143].

In addition to the peak energy shift, the linewidth of the Eu^{3+} emission is larger for ternary AlGaN NWs than for GaN and AlN NWs. In the ternary alloys, Eu^{3+} can replace both Ga or Al, resulting in different optical centers because the environment around each Eu^{3+} is likely to be distinct (random distribution of Ga and Al in the alloy). This and compositional fluctuations contribute to the broadened emission, which makes it impossible to distinguish between emission lines associated with different Eu^{3+} centers [18,26].

Although it is impossible to resolve the various emission lines of Eu^{3+} in ternary AlGaN NWs (and, consequently, the distinction of optically active centers), it is observed that, for the same composition, the spectral shape of the $^5D_0 \rightarrow {}^7F_2$ transition varies with the RTA temperature. For the lowest RTA temperature, it is possible to notice a shoulder on the shorter wavelength side of the prominent peak. This is presumably due to Eu^{3+} being

optically active in the GaN NWs templates since the reduced length of the ternary AlGaN top section makes Eu likely to reach the templates, as discussed in **sub-subsection 3.3.1.2**.

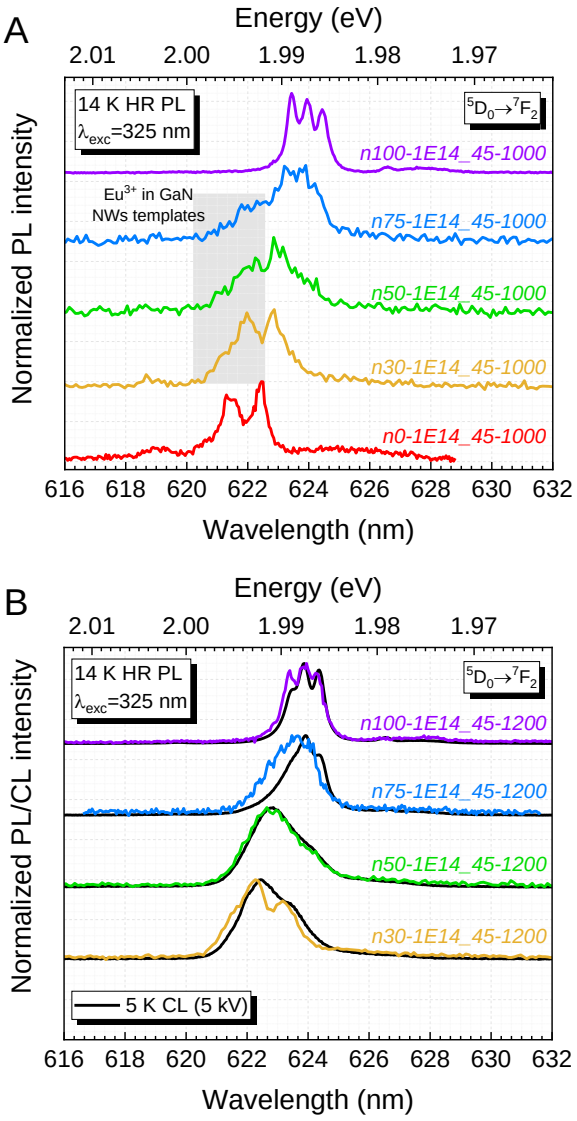

Figure 3.27 Normalized 14 K HR PL spectra around the $^5D_0 \rightarrow {}^7F_2$ transition for the Eu-implanted AlGaN NWs annealed at **(A)** 1000 ℃ and **(B)** 1200 ℃. The latter also includes the 5 K CL spectra of the respective samples (black lines).

For the Eu-implanted AlGaN NWs annealed at 1200 ℃, the signal-to-noise ratio is improved due to their enhanced PL intensity. This will be a matter of further discussion in the following sub-subsection. Furthermore, the shoulder on the shorter wavelength side of the main peak is not present; this further hints at the involvement of Eu^{3+} in the GaN NWs templates, given that RTA at 1200 ℃ severely damages them, explaining why it is not observed.

The comparison between the 5 K CL and 14 K HR PL spectra for sample *n50-1E14_45-1200* reveals no significant differences in the spectral shape and peak position. For samples *n30-1E14_45-1200* and *n75-1E14_45-1200*, the spectra exhibit similar shapes with slightly different peaks' resolution and energy, which can be associated with compositional fluctuations existing within the ensemble of NWs or along the individual NWs within the ensemble of NWs probed. Such dissimilarities may also be related to the different interaction depths of both techniques or their different excitation mechanisms, i.e., a particular center favored in PL may not be favored in CL.

Figure 3.28 provides a direct comparison of the 14 K HR PL spectra for the AlGaN NWs with $y = 0.3$ and $y = 0.75$ annealed at distinct temperatures. This figure allows a better perception of the shoulder attributed to Eu^{3+} in the GaN NWs templates for sample *n75-1E14_45-1000* and its absence for sample *n75-1E14_45-1200* due to GaN dissociation. For the AlGaN NWs with $y = 0.3$, the shoulder related to Eu^{3+} in GaN NWs templates is not easily perceived because of the energy overlap with the Eu^{3+} emission in AlGaN NW top sections. However, it is possible to notice that RTA temperature results in a distinct intensity ratio between the various emission lines in this case, suggesting this parameter *i)* alters the balance of optically active Eu^{3+} centers in the AlGaN NWs, analogously to what has been reported for GaN layers [137], or *ii)* modifies the strain state in the NWs, explaining the slight shifts in peaks' positions – remember that, from micro-Raman experiments, RTA at higher temperatures was found to provide a better recovery of the lattice face to the implantation induced damage.

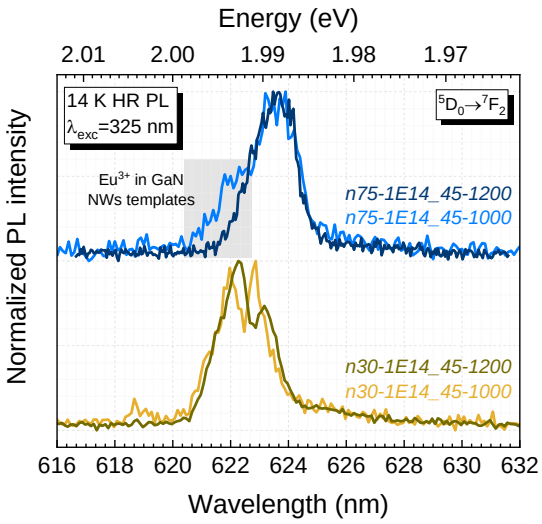

Figure 3.28 Comparison of the normalized 14 K HR PL response of samples *n30-1E14_45-1000* and *n30-1E14_45-1200* (below) and samples *n75-1E14_45-1000* and *n30-1E14_45-1200* (top).

At the extreme of the AlN molar fractions, that is, for AlN NWs, the Eu^{3+}-related lines become narrow again, making it possible to resolve various emission lines (**Figure 3.27**). **Figure 3.29** shows the 14 K HR PL spectrum of sample *n100-1E14_45-1000* around the $^5D_0 \rightarrow {}^7F_2$ transition. Likewise, the spectrum of sample *R100-1E14_45-1000* (Eu-implanted AlN layers annealed at 1000 ℃) is included for comparison.

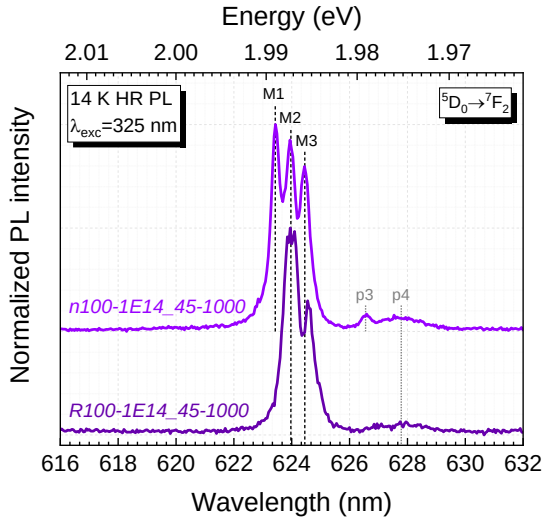

Figure 3.29 Normalized 14 K HR PL spectrum of samples *n100-1E14_45-1000* and *R100-1E14_45-1000* around the $^5D_0 \rightarrow {}^7F_2$ transition.

The spectrum of the sample *R100-1E14_45-1000* is composed of two pronounced peaks at 624.0 nm (M2) and 624.6 nm (M3), as well as a tiny and broad peak at ~627.8 nm (p4). The spectral pattern is identical to the scarce works found in the literature for Eu-doped AlN hosts [20,111]. K. Wang et al. proposed that these lines correspond to a single Eu^{3+} center that could be excited either below ($\lambda_{exc} = 325$ nm) and above the AlN bandgap; in analogy with the majority center observed in GaN, it was designated by Eu1 – this does not mean that they have the same local structure in GaN and AlN [20].

For sample *n100-1E14_45-1000*, the spectrum reveals three pronounced lines at 623.4 nm (M1), 623.9 nm (M2), and 624.4 nm (M3) and other minor intensity peaks; two of them are identified in the graph at 626.6 nm (p3) and ~627.8 nm (p4). The appearance of additional peaks (M1 and p3) suggests that the NW configuration favors the formation of new optically active Eu^{3+} centers, similar to that identified above for Eu-implanted GaN hosts. This is likely explained by the distinct lattice dynamics (defects' formation and strain evolution) of NWs and layers regarding implantation and annealing.

Figure 3.30 compares the 5K CL and 14 K HR PL spectra obtained for sample *n100-1E14_45-1000* in the spectral range of **(A)** 585–675 nm and **(B)** 616–638 nm. The

5 K CL spectrum corresponds to that previously shown in **Figure 3.18(B)**. As identified in **sub-subsection 3.3.2.2**, the relative intensity of the $^5D_1 \rightarrow {}^7F_1$ transition at ~545 nm increases in CL compared to PL experiments. Therefore, it should be possible to distinguish between the transitions arising from the $^5D_0$ and $^5D_1$ states by comparing the spectra presented in **Figure 3.30**.

In **Figure 3.30(A)**, it is possible to distinguish the emission lines that result from the $^5D_0 \rightarrow {}^7F_1$ and $^5D_1 \rightarrow {}^7F_3$ transitions since the relative intensity of the second is enhanced in CL compared to PL, while that of the emission lines of the $^5D_0 \rightarrow {}^7F_1$ transition remain identical in both. A bunch of other emission lines can be noticed in both spectra, including lines associated with $^5D_0 \rightarrow {}^7F_0$, $^5D_0 \rightarrow {}^7F_2$, $^5D_1 \rightarrow {}^7F_4$, and $^5D_0 \rightarrow {}^7F_3$ transitions.

Figure 3.30(B) shows a magnification of **Figure 3.30(A)** around the transitions of minor intensity in the spectral range of 616–638 nm. In addition to the prominent M1, M2, and M3 peaks identified in **Figure 3.29**, at least nine minor intensity peaks could be distinguished in **Figure 3.30(B)**. As already discussed, the $^5D_1 \rightarrow {}^7F_4$ transition occurs in the same spectral range as the $^5D_0 \rightarrow {}^7F_2$ transition; therefore, these low-intensity peaks could be related to any of the transitions. The comparison between PL and CL spectra reveals that only the peak at 626.6 nm (p3) stands out in the CL spectrum, that is, it has a higher relative intensity than in PL experiments. Other peaks, such as p5 at 630.7 nm, p6a at 633.9 nm, and p6b at 634.3 nm, could not be discerned in the PL spectrum; however, in this case, this could be only because of the low intensity of the signal intensity (impossible to distinguish from the noise), rather than be associated with the $^5D_1 \rightarrow {}^7F_4$ transition. J. Gruber et al. made a similar assignment of the peak at 626.6 nm. However, they attributed all the minor intensity lines to the $^5D_1 \rightarrow {}^7F_4$ transition by assuming that Eu would occupy a single optically active center, with Eu^{3+} occupying the perfect substitutional Al site (i.e., with C_{3v} symmetry), i.e., meaning that the $^5D_0 \rightarrow {}^7F_2$ transition would consist of the three most intense lines and the others assigned to the $^5D_1 \rightarrow {}^7F_4$ transition [111].

Assuming that most of the lines found in the spectral range of 616–638 nm are due to the $^5D_0 \rightarrow {}^7F_2$ transition, this implies the existence of multiple optically active Eu^{3+} centers in AlN NWs – remember that a single center leads to a maximum of five Stark lines when the local symmetry is capable of complete lifting the degeneracy of the multiplets. One should not discard the possibility of some of the lines, particularly the broad ones, to be related to transitions assisted by an LVM involving the Eu^{3+} in an Al substitutional site, similar to what was reported in GaN hosts [66,140,142].

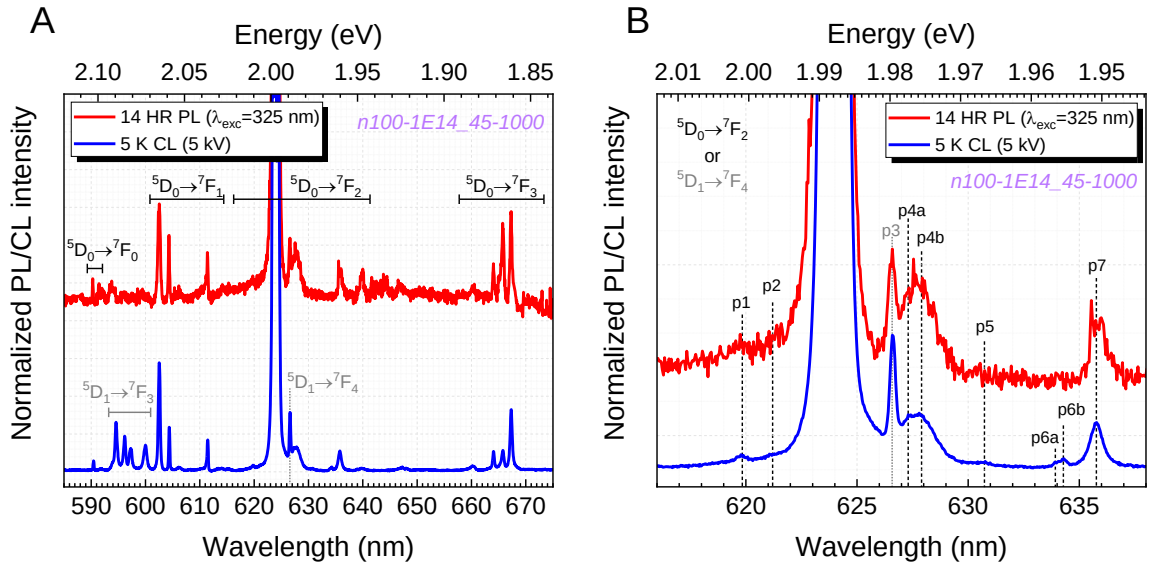

Figure 3.30 (A) Normalized 14 K HR PL and 5 K CL spectra of sample *n100-1E14_45-1000* between 585 and 675 nm e. **(B)** Magnification of the previous spectra between 616 and 638 nm.

Figure 3.31(A) shows an enlargement of the 5 K CL spectra of samples *n100-1E14_45-1000* and *n100-1E14_45-1200* around the $^5D_0 \rightarrow {}^7F_0$ transition. A pronounced peak is identified at 590.4 nm (L2), together with a broad peak at ~591.8 nm (L3); for the sample annealed at the highest temperature, it is also possible to discern a shoulder at 590.2 nm (L1). As this transition involves two states with $J = 0$, each optically active Eu^{3+} center can only give rise to the appearance of a single peak. Therefore, the observation of two and three peaks implies the existence of at least two distinct optical Eu^{3+} centers in AlN NWs. It should be noted that from the previous analysis of excitation-wavelength dependent PL (**Figure 3.21**), one already pointed out the existence of more than one optically active Eu^{3+} center in AlN NWs.

Figure 3.31(B) compares the 14 K HR PL and 5 K CL spectra obtained for samples *n100-1E14_45-1000* and *n100-1E14_45-1200*). The relative PL intensity of lines M1 and M3 varies with the RTA temperature, with the intensity of the first being lower for the highest RTA temperature. The previous findings (i.e., emission lines of Eu-implanted AlN layers and multiple peaks associated with the $^5D_0 \rightarrow {}^7F_0$ transition) suggest that such a change is due to the contribution of two predominant Eu^{3+} centers, whose concentration or excitation efficiency depends on the RTA temperature. In analogy with the nomenclature used for Eu^{3+} centers in GaN, hereafter, one will designate the center responsible for the M1 line as the Eu2, while the M3 line corresponds to the Eu1 center as previously designated by K. Wang et al. [20], that is observed in AlN layers. As the relative intensity of the line M2 seems to be insensitive to the RTA temperature and its linewidth is slightly greater

than M1 and M3, one tentatively attributes it to the combination of two overlapped lines, one related to Eu1 and the other to Eu2. Despite the same nomenclature, it must be remembered that the local structure of the Eu1 and Eu2 centers in GaN and AlN is not necessarily the same.

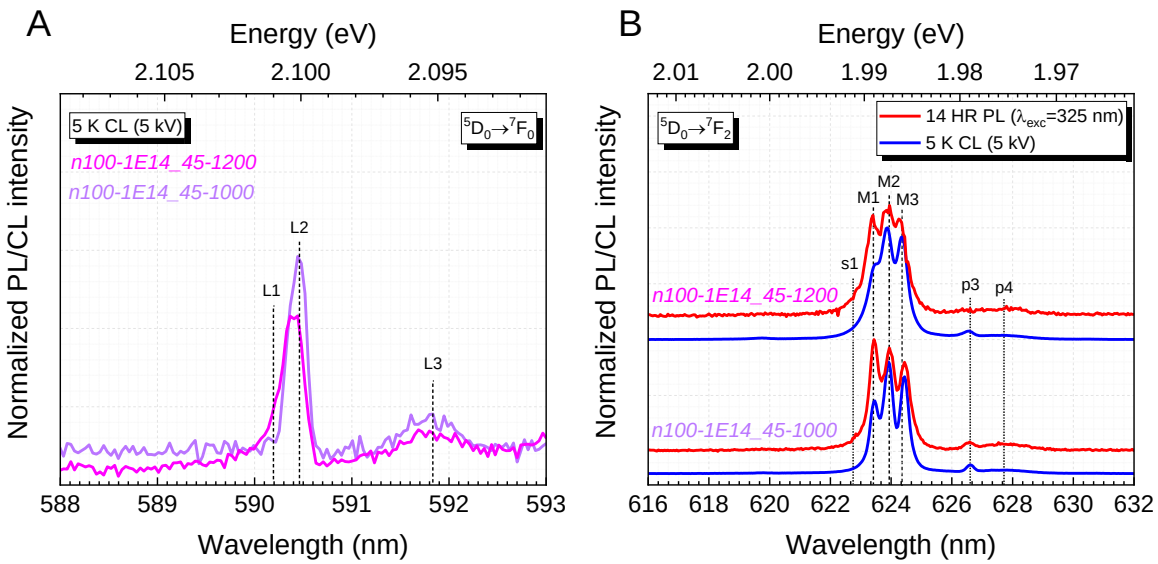

Figure 3.31 (A) 5 K CL spectra of samples *n100-1E14_45-1000* and *n100-1E14_45-1200* around the $^5D_0 \rightarrow ^7F_0$ transition. **(B)** Normalized 14 K HR PL and 5 K CL spectra for the same samples around the $^5D_0 \rightarrow ^7F_2$ transition.

Besides, the ratio between the lines M1 and M3 is also different when comparing the PL and CL responses. In the latter case, M3 is always more intense than M1, suggesting that the excitation efficiency of the two predominant centers depends on the excitation mechanism. Under photo-excitation with $\lambda_{exc} = 325$ nm, the intensity ratio between Eu2 and Eu1 increases compared to excitation with accelerated electrons. The observed differences can also be caused by the distinct in-depth resolution of PL and CL, i.e., Eu1 and Eu2 would not be distributed equally along the NWs *c*-axis. If this is the case, as the interaction depth in CL is ~190 nm and PL probes the entire AlN NW top section, the intensity ratio of Eu2/Eu1 should be higher deeper in the AlN top section of the NWs, i.e., closer to the AlN/GaN interface.

Table 3.3 resumes the peak positions obtained for the $^5D_0 \rightarrow ^7F_2$ and $^5D_1 \rightarrow ^7F_4$ transitions in Eu-implanted AlN NWs (14 K HR PL and 5 K CL) and AlN layers annealed at 1000 °C (14 K HR PL). The peak positions obtained by J. Gruber et al. for AlN single crystals doped in situ with Eu^{3+} are also included. Based on the behavior of the most intense lines and the

results reported in the literature, the assignment of such lines to two optically active Eu^{3+} centers, Eu1 and Eu2, is proposed.

Table 3.3 Assignment of the peaks associated with the $^5D_0 \rightarrow {}^7F_2$ and $^5D_1 \rightarrow {}^7F_4$ transitions observed in Eu-implanted AlN NWs (14 K HR PL and 5 K CL) and those observed for Eu-implanted AlN layers (14 K HR PL). Reported values obtained for in situ doped AlN:Eu single crystals (11 K CL) are included [111].

Transition	Peak	This work					Ref. [111]	Assigned center
		AlN NWs				AlN layers		
		RTA at 1000 °C		RTA at 1200 °C		RTA at 1000 °C		
		14 K PL	5 K CL	14 K PL	5 K CL	14 K PL		
$^5D_0 \rightarrow {}^7F_2$ or $^5D_1 \rightarrow {}^7F_4$	p1	619.7 (li)	619.8 (li)	619.8 (li)	619.7 (li)			
							620.34	
							620.68	
	p2	621.1 (li)	621.1 (li)	621.3 (li)	621.2 (li)			
	M1	623.4	623.5	623.4	623.5			**Eu2**
	M2	623.9	623.9	623.9	623.9	624.0 (2p)	623.95	**Eu1/Eu2**
	M3	624.4	624.4	624.3	624.4	624.6	624.49	**Eu1**
	p3	626.6	626.6	627	626.6		626.66	
							627.0	
	p4a	627.8 (b)	627.3	627.8 (b)	627.6 (b)	627.8		
	p4b		627.8					
							629.0	
	p5		630.7 (li)		630.5 (li)			
	p6a		633.9					
							634.31	
	p6b		634.3		634.3 (li)			
	p7	635.8	635.8	635.7	635.8	636.0	635.79	**Eu1**

(b) broad peak, (li) low-intensity peak, (o) overlapped peak, (s) shoulder

Figure 3.32 displays the normalized HR PL spectra of samples **(A)** *n0-1E14_45-1000* and **(B)** *n100-1E14_45-1200* around the $^5D_0 \rightarrow {}^7F_2$ transition as the temperature increases from 14 K to 300 K. Increasing the temperature makes the Stark lines enlarge because of

phonon broadening, rendering the distinction of the optically active Eu^{3+} centers even more difficult. The emission lines blueshift of ~0.2 nm when increasing the temperature from 14 K to 300 K, similar to what was observed for Eu-implanted GaN NWs (*n0-1E14_45-1000*). Furthermore, the intensity ratio between lines M1 (Eu2) and M3 (Eu1) varies with the temperature, indicating different thermal behaviors. In particular, the Eu1 center is found to be the more stable with temperature, exhibiting a higher contribution to the overall room temperature luminescence regardless of the RTA temperature.

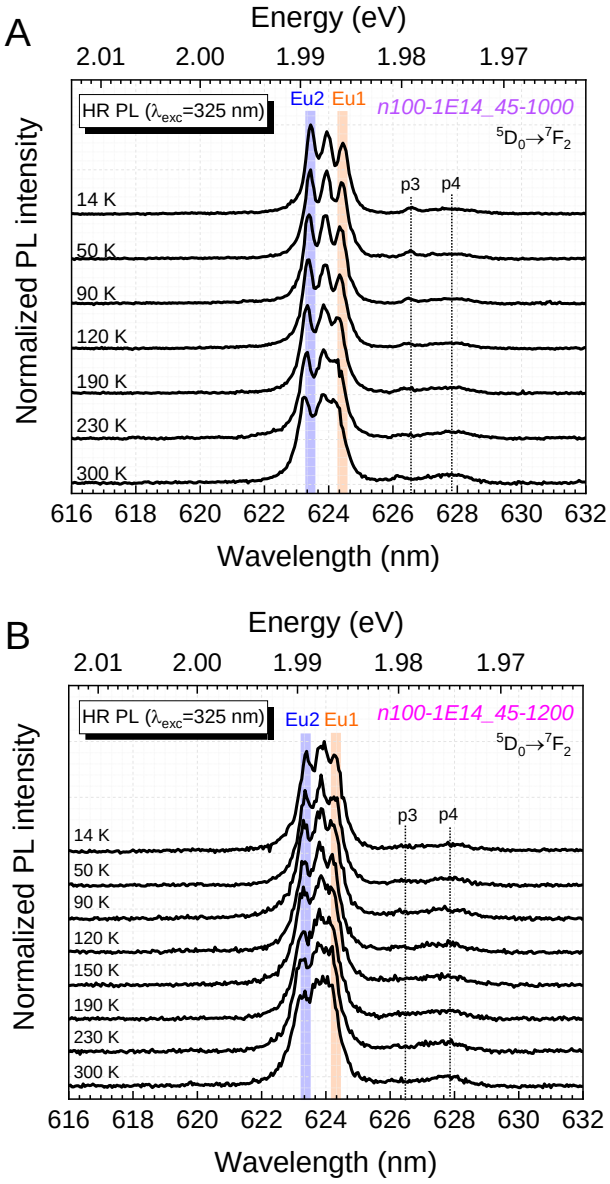

Figure 3.32 Temperature-dependent HR PL spectra around the $^5D_0 \rightarrow {}^7F_2$ transition for samples **(A)** *n100-1E14_45-1000* and **(B)** *n100-1E14_45-1200*. The spectra are normalized to the respective maximum.

3.3.2.5. Eu^{3+}–related luminescence intensity in AlGaN NWs

Thermal behavior of the $^5D_0 \rightarrow {}^7F_2$ transition

The evolution of the integrated PL intensity of the $^5D_0 \rightarrow {}^7F_2$ transition (measured in HR PL spectra presented above from 616 to 632 nm and considering a linear baseline) with temperature for samples *n100-1E14_45-1000* and *n100-1E14_45-1200* is depicted in **Figure 3.33(A)**. The rise in the temperature up to ~120–150 K causes a gradual decrease in PL intensity due to competitive thermally activated non-radiative processes, which should interfere in excitation, de-excitation, or both. Nevertheless, above this temperature, two distinct behaviors are identified. For sample *n0-1E14_45-1000*, the PL intensity continues to quench with increasing temperature. At 300 K, the intensity is ~50 % of the value measured at 14 K.

In contrast, for sample *n0-1E14_45-1200*, above ~120–150 K, the Eu^{3+} PL intensity increases, such that, at 300 K, the intensity is ~80 % of that measured at 14 K. This increase means that there is a thermally activated population mechanism counterbalancing the thermal quenching effect. The origin of this mechanism is yet to be ascertained.

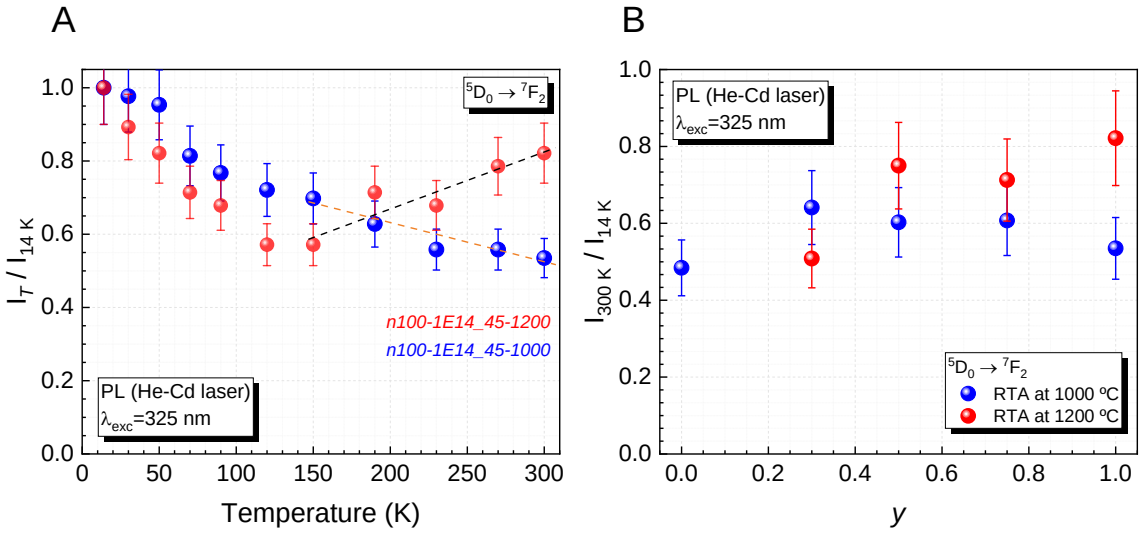

Figure 3.33 (A) Normalized integrated PL intensity of the $^5D_0 \rightarrow {}^7F_2$ transition as a function of the measurement temperature for samples *n100-1E14_45-1000* and *n100-1E14_45-1200*. The dashed lines are a "guide to the eye" of the evolution for temperatures above 150 K (orange for *n100-1E14_45-1000* and black for *n100-1E14_45-1200*). **(B)** Evolution of $I_{300\,K}/I_{14\,K}$ ratio as a function of y for all the implanted and annealed AlGaN NWs.

Figure 3.33(B) resumes the ratio of the integrated PL intensity of the $^5D_0 \rightarrow {}^7F_2$ transition measured at 300 K and 14 K, $I_{300\,K}/I_{14\,K}$, with y for all the AlGaN NWs

implanted and annealed. The procedure used to determine the integrated intensity is the same as that used above for $y = 1$. For the AlGaN NWs annealed at 1000 ℃, the $I_{300\ \mathrm{K}}/I_{14\ \mathrm{K}}$ ratio is roughly constant with y, lying between 50–60 % (the experimental error in determining the integrated PL intensity is overestimated as 5 % of the integrated intensity). After RTA at 1200 ℃, the $I_{300\ \mathrm{K}}/I_{14\ \mathrm{K}}$ ratio increases to ~70–80 % for the samples with $y \geq 0.5$. Such an increase in the ratio may be caused by a better recovery of the crystalline properties and the appearance of a thermally activated channel that contributes to the increase in the PL intensity for temperatures above 150 K. The multitude of optically active Eu^{3+} centers and their distinct activation with RTA temperature can also contribute to this behavior.

Under the assumption that the non-radiative effects are negligible at 14 K, the $I_{300\ \mathrm{K}}/I_{14\ \mathrm{K}}$ ratio can be interpreted as the PL IQE [144]. Therefore, this suggests that both the AlN molar fraction and the RTA temperature play a role in obtaining a more efficient emitting solution based on Eu-implanted AlGaN. Nevertheless, it is not guaranteed that the PL IQE remains the same when varying the excitation wavelength. In other words, when exciting above the host's bandgap (the mechanism that should "mimic" the excitation under electrical injection), the dependence of the luminescence intensity on temperature can differ because the excitation paths are distinct.

Comparison of the integrated intensity of the $^5D_0 \rightarrow {}^7F_2$ transition

The evolution of the Eu^{3+} luminescence intensity in the different AlGaN NWs studied provides information about which y gives rise to a more intense red-light emission. However, it must be considered that beyond the Eu^{3+} radiative transition probability, the measured intensity also relies on factors like excitation and light extraction efficiencies, which are influenced by the excitation source (e.g., photons or electrons) and the detection geometry.

In this study, the following comparisons are made:

1. The RT integrated PL intensity of the $^5D_0 \rightarrow {}^7F_2$ transition for the Eu-implanted AlGaN NWs ($0 < y \leq 1$) after RTA at 1000 ℃ excited with $\lambda_{\mathrm{exc}} = 325$ nm. This corresponds to excite Eu^{3+} through the sub-gap excitation band X1. In addition, for each y, the intensity obtained is compared with that obtained in AlGaN layers implanted and annealed in identical conditions.
2. The RT integrated PL intensity of the $^5D_0 \rightarrow {}^7F_2$ transition for the Eu-implanted AlGaN NWs ($0 \leq y < 1$) when exciting with energy above the host's bandgap. The choice of the excitation wavelength is made considering the peak of the AlGaN edge observed in **Figure 3.23(A)** for the AlGaN NWs annealed at 1200 ℃ and summarized for the remaining NWs in **Figure 3.24**. The measured intensity is corrected to the Xe lamp response for each excitation wavelength.

3. The 5 K integrated CL intensity of the $^5D_0 \rightarrow {}^7F_2$ transition for the Eu-implanted AlGaN NWs ($0 < y \leq 1$) annealed at 1200 ºC. For AlN NWs, the influence of the RTA temperature is further compared.

In each of them, the experimental alignment is maintained so that the influence of the light collection geometry on the measured intensity can be minimized. The measurement error is overestimated to be 5 % of the integrated intensity.

Figure 3.34(A) shows a comparison of the integrated PL intensity for Eu-implanted AlGaN NWs ($0 < y \leq 1$) after RTA at 1000 ºC using the He-Cd laser as the excitation source ($\lambda_{exc} = 325$ nm). The intensity remains roughly constant for ternary AlGaN NWs but increases by approximately an order of magnitude for AlN NWs. The same trend is observed for the AlGaN layers implanted and annealed in identical conditions. Furthermore, the comparison of the intensity obtained in NWs and layers does not differ significantly, as reported by others in the literature [35,37].

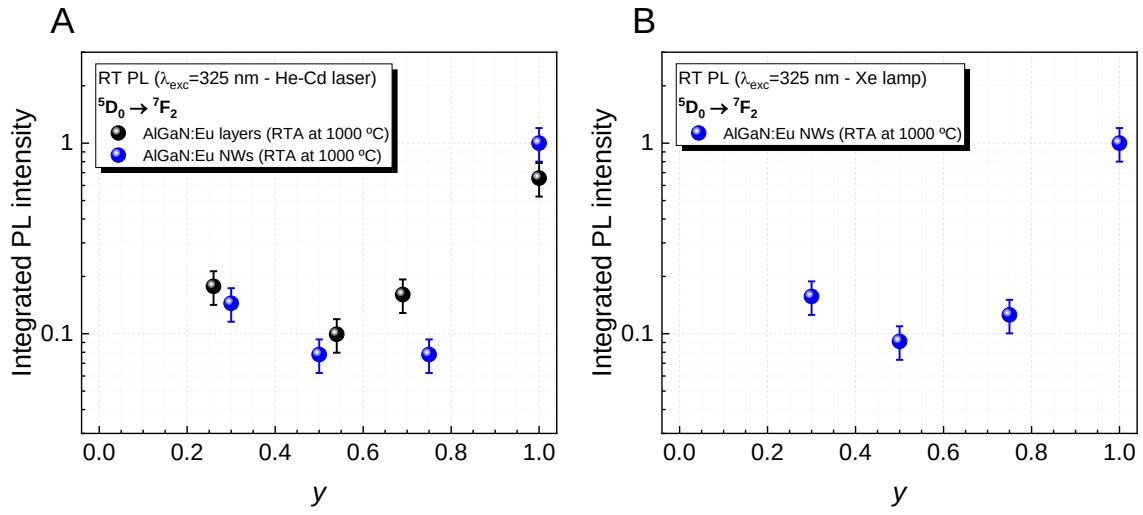

Figure 3.34 RT integrated PL intensity (in $\log_{10}$ scale) of the $^5D_0 \rightarrow {}^7F_2$ transition for the Eu-implanted AlGaN NWs ($y > 0$) after RTA at 1000 ºC, when exciting with the 325 nm light of **(A)** a He-Cd laser and **(B)** a Xe lamp. In **(A)**, data from Eu-implanted AlGaN layers implanted in similar conditions is included. In both, the intensity is normalized to that of the AlN NWs.

Figure 3.34(B) also presents the evolution of the integrated PL intensity for Eu-implanted AlGaN NWs ($0 < y \leq 1$) after RTA at 1000 ºC obtained with $\lambda_{exc} = 325$ nm but now using the Xe lamp as the excitation source. Despite the lower excitation density, the intensity trend with varying y is similar to that obtained with the He-Cd laser.

Based on these findings, one cannot determine unambiguously why the PL intensity of Eu^{3+} remains constant when incorporated into the ternary AlGaN hosts with different y and

suddenly increases in AlN hosts. Assuming that the concentration of implanted ions is the same, several hypotheses can be raised to try to explain the results: *i)* a higher probability of radiative transition, *ii)* a lower probability of non-radiative de-excitation, *iii)* a higher LEE, or *iv)* a higher excitation efficiency (e.g., increased absorption cross-section or favored ET from host to Eu^{3+}).

Above, it was shown that the $I_{300\ K}/I_{14\ K}$ ratio is independent of y for the Eu-implanted AlGaN NWs annealed at 1000 ℃, hinting that the competitive thermally activated non-radiative processes would be identical for all y at this RTA temperature. Hence, the lower probability of non-radiative de-excitation cannot explain the increase in the Eu^{3+} luminescence intensity observed in AlN hosts.

Figure 3.35 presents the evolution of the integrated intensity of the $^5D_0 \rightarrow {}^7F_2$ transition when the AlGaN NWs ($0 \leq y < 1$)are photo-excited with energy above the host's bandgap. Although the excitation wavelength is tuned depending on the AlN molar fraction of the alloy, the absorption coefficient is similar for all of them (~1×10^5 cm^{-1} [145,146]), implying that the penetration depth of the excitation into the NWs is the same in all samples (~100 nm, according to the Beer-Lambert's law). This means one can consider the concentration of implanted ions probed to be identical.

First, the effect that the AlN molar fraction has on the PL intensity of Eu^{3+} is analyzed. For the RTA temperature of 1000 ℃, the intensity increases about one order of magnitude when changing from GaN to the ternary AlGaN NWs; then, it becomes roughly constant with y. This behavior is identical to that found for excitation below the AlGaN bandgap through the X1 band.

In order to assess whether this increase could be due to a greater probability of radiative transition, as proposed before, it is assumed that the dipole strength and energy of the MD-assisted $^5D_0 \rightarrow {}^7F_1$ transition are independent of the host. Therefore, by combining equations (2.47) and (2.50), one can estimate the radiative lifetime as follows [136,147]:

$$\tau_{rad} = A_{\mathrm{MD}} \left(\frac{I_{\mathrm{total}}}{I_{\mathrm{MD}}} \right) = A_{\mathrm{MD},0} n(\lambda)^3 \left(\frac{I_{\mathrm{total}}}{I_{\mathrm{MD}}} \right). \tag{3.1}$$

Here, $n(\lambda)$ is the refractive index of the medium, $A_{\mathrm{MD},0}$ is the spontaneous emission probability for the $^5D_0 \rightarrow {}^7F_1$ transition in vacuum ($A_{\mathrm{MD},0} = 14.65\ s^{-1}$), and $I_{\mathrm{total}}/I_{\mathrm{MD}}$ is the ratio of the total integrated area of the $^5D_0 \rightarrow {}^7F_J$ transitions to the area of the $^5D_0 \rightarrow {}^7F_1$ transition. Considering that the ratio $I_{\mathrm{total}}/I_{\mathrm{MD}}$ is identical for all AlGaN NWs [see **Figure 3.18(A)**], and the refractive index at ~620 nm increases with y [146], then the τ_{rad} should increase as well with y. As τ_{rad} is inversely proportional to A_{rad}, one would expect the spontaneous emission probability to be decrease from GaN to AlN. Therefore, a higher probability of radiative transition should not be the reason that explains why the intensity

is enhanced for Eu^{3+} in ternary AlGaN NWs compared to GaN NWs. Furthermore, by similar arguments, it should not be the reason for the increase in intensity observed in **Figure 3.34** for AlN hosts.

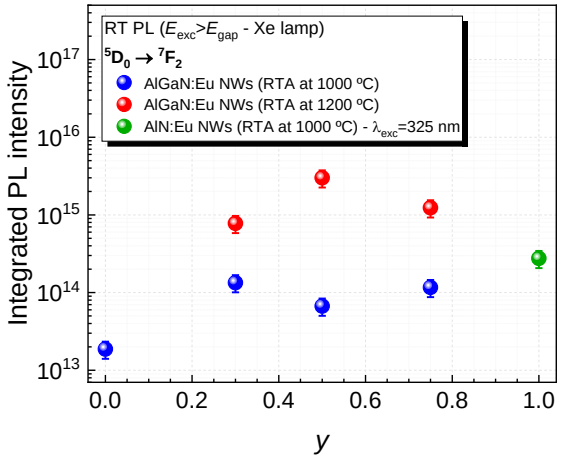

Figure 3.35 Integrated RT PL intensity of the $^5D_0 \rightarrow {}^7F_2$ transition (in $\log_{10}$ scale) as a function of y for the Eu-implanted AlGaN NWs ($0 \leq y < 1$), when excited above the bandgap. The following excitation wavelengths were used: $\lambda_{exc} = 345$ nm for $y = 0$, $\lambda_{exc} = 300$ nm for $y = 0.3$, $\lambda_{exc} = 270$ nm for $y = 0.5$, and $\lambda_{exc} = 250$ nm for $y = 0.75$. The integrated RT PL intensity of sample *n100-1E14_45-1000* when excited with $\lambda_{exc} = 325$ nm (below AlN bandgap) is plotted for comparison.

Nevertheless, the measured intensity for AlGaN NWs exciting above the bandgap is comparable to that of Eu^{3+} implanted into AlN NWs when excited through the X1 band (i.e., below bandgap excitation), which is expected to result in a lower intensity than above bandgap excitation due to the superior absorption coefficient for above bandgap excitation.

For the RTA temperature of 1200 ℃, the intensity of Eu^{3+} is once again barely constant for the ternary AlGaN alloys. However, the intensity increased by about an order of magnitude compared to that obtained for the same compositions but annealed at 1000 ℃. A likely explanation is that the RTA at 1200 ℃ allows for a better recovery of implantation-induced damage, contributing to a more effective anneal of the non-radiative defects introduced during implantation. This hypothesis is congruent with micro-Raman results (**sub-subsection 3.3.1.3**) and with the increased $I_{300\ K}/I_{14\ K}$ ratio observed for the AlGaN NWs annealed at the highest temperature (**sub-subsection 3.3.2.4**). Alternatively, the RTA at higher temperatures can alter the surroundings of the Eu^{3+}, possibly resulting in the formation of more efficient Eu^{3+} centers, for example, in trapping the FX or in transferring the energy to the $4f$ core states of the Eu^{3+}. This idea is coherent with multiple optically active Eu^{3+} centers whose activation depends on the RTA temperature, as found

for Eu^{3+} incorporated into AlN NWs with the distinct balance of Eu1 and Eu2 centers (**sub-subsection 3.3.2.4**).

Figure 3.36 shows the 5 K integrated CL intensity of the $^5D_0 \rightarrow {}^7F_2$ transition as a function of y for the Eu-implanted AlGaN NWs with $y > 0$ after RTA at 1200 ℃. The Eu^{3+} luminescence intensity in AlGaN NWs annealed at 1200 ℃ has an identical evolution to that observed for photo-excitation below the bandgap (**Figure 3.34**), being constant for the ternary AlGaN NWs and increasing about an order of magnitude for AlN NWs. Furthermore, for AlN NWs, the CL intensity of Eu^{3+}-related luminescence increases about twice when the RTA temperature changes from 1000 ℃ to 1200 ℃.

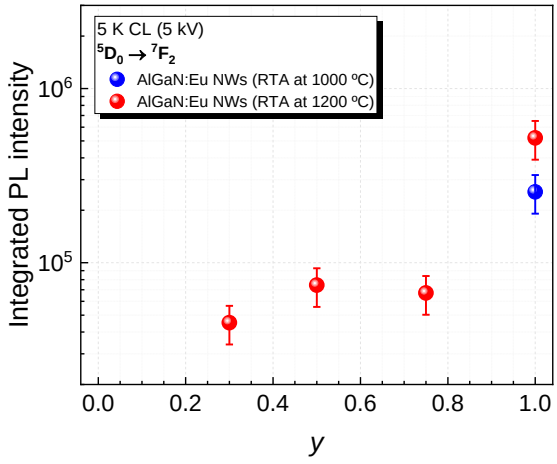

Figure 3.36 Integrated 5 K CL intensity of the $^5D_0 \rightarrow {}^7F_2$ transition for the Eu-implanted AlGaN NWs ($y > 0$) after RTA at 1200 ℃ (in $\log_{10}$ scale) as a function of y. It also includes the intensity measured for sample *n100-1E14_45-1000* (AlN NWs after RTA at 1000 ℃).

The previous results suggest AlN as the host that gives rise to the most intense Eu^{3+}-related luminescence, regardless of whether the excitation is done with photons and electrons. The AlN host is proposed to favor the incorporation of Eu^{3+} as an efficient luminescent agent, leading to a more intense red emission than the other AlGaN hosts evaluated. Furthermore, increasing the RTA temperature from 1000 ℃ to 1200 ℃ resulted in an enhanced Eu^{3+} PL and CL intensity, independently of the AlN molar fraction of the AlGaN NWs. It also boosted the $I_{300\ K}/I_{14\ K}$ ratio.

3.4. Summary

In this chapter, the optical and structural properties of Eu-implanted AlGaN NWs annealed by RTA at 1000 ℃ and 1200 ℃ were studied. The obtained results are summarized as follows:

- The implantation resulted in the formation of defects and the introduction of strain in the crystalline lattice. A "pseudomorphic-like" model was proposed to describe the lattice strain introduced by implantation.
- Subsequent RTA treatments partially recovered the crystalline lattice of the AlGaN top section. A better lattice recovery was achieved for the RTA at 1200 ℃. Besides, the distinct lattice reorganization depending on the RTA temperature results in different densities, distribution, and nature of the existing defects.
- The red emission of Eu^{3+} was attained for all AlGaN NWs after RTA treatments with below and above bandgap excitation. The $^5D_0 \rightarrow {}^7F_2$ transition was the most intense and experienced a peak shift from ~622 nm (in GaN) to ~624 nm (in AlN).
- Two broad sub-gap excitation bands were identified: X1 at ~350 nm and X2 at ~270 nm (only for $y \geq 0.75$). These bands were found to blueshift with y; for example, X1 blueshifted ~200-300 meV from GaN to AlN NWs. Both X1 and X2 were tentatively attributed to defects that introduce energy levels in the forbidden gap of the host. These defects are involved in the non-radiative ET to the $4f^6$ core states of Eu^{3+}.
- Multiple optically active Eu^{3+} centers were distinguished in GaN and AlN NWs. The RTA temperature influenced the relative contribution of the centers in both hosts due to lattice reorganization. Furthermore, differences were observed when comparing the spectral shape of Eu-implanted NW and layered structures (for both GaN and AlN hosts). In ternary AlGaN NWs, the emission broadening due to compositional fluctuations rendered the identification of narrow emission lines associated with distinct optically active Eu^{3+} centers.
- A comparison of the Eu^{3+}-related luminescence intensity in the different AlGaN NWs studied (for the same RTA temperature) demonstrated that the implantation into AlN NWs resulted in a more substantial red-light output. This indicates that AlN NWs promote the incorporation of Eu^{3+} as more efficient luminescent agents than in the other hosts evaluated.

- The RTA at 1200 ℃ also boosted the Eu^{3+}-related luminescence intensity (for the same y). In addition, the $I_{300\,K}/I_{14\,K}$ ratio increased from ~50 % (RTA at 1000 ℃) to ~70–80 % (RTA at 1200 ℃ and $y \geq 0.5$).
- Despite the enhancement in Eu^{3+}-related luminescence intensity and better recovery of the AlGaN top section, the RTA at 1200 ℃ severely degraded the GaN NWs templates due to GaN dissociation at such high temperatures.

In summary, the results showed that incorporating Eu^{3+} in AlN led to a more intense red luminescence output, suggesting these systems have potential to realize more efficient red LEDs based on Eu-doped III-N. Concerning the RTA temperature, this parameter must be restricted to 1000 ℃ unless countermeasures are taken.

3.5. References

[1] B. Mitchell et al., Perspective: Toward efficient GaN-based red light emitting diodes using europium doping, *J. Appl. Phys.* **123** (2018) 160901. https://doi.org/10.1063/1.5010762.

[2] S. Ichikawa et al., Eu-doped GaN and InGaN monolithically stacked full-color LEDs with a wide color gamut, *Appl. Phys. Express.* **14** (2021) 031008. https://doi.org/10.35848/1882-0786/abe603.

[3] M.S. Wong et al., Review—Progress in High Performance III-Nitride Micro-Light-Emitting Diodes, *ECS J. Solid State Sci. Technol.* **9** (2020) 015012. https://doi.org/10.1149/2.0302001JSS.

[4] P. Li et al., Highly efficient InGaN green mini-size flip-chip light-emitting diodes with AlGaN insertion layer, *Nanotechnology.* **30** (2019). https://doi.org/10.1088/1361-6528/aaf656.

[5] Q. Lv et al., Realization of Highly Efficient InGaN Green LEDs with Sandwich-like Multiple Quantum Well Structure: Role of Enhanced Interwell Carrier Transport, *ACS Photonics.* **6** (2019) 130–138. https://doi.org/10.1021/acsphotonics.8b01040.

[6] A.I. Alhassan et al., Development of high performance green c-plane III-nitride light-emitting diodes, *Opt. Express.* **26** (2018) 5591. https://doi.org/10.1364/oe.26.005591.

[7] Y. Narukawa et al., White light emitting diodes with super-high luminous efficacy, *J. Phys. D. Appl. Phys.* **43** (2010). https://doi.org/10.1088/0022-3727/43/35/354002.

[8] Y. Fujiwara et al., Present understanding of Eu luminescent centers in Eu-doped GaN grown by organometallic vapor phase epitaxy, *Jpn. J. Appl. Phys.* **53** (2014) 05FA13. https://doi.org/10.7567/JJAP.53.05FA13.

[9] T. Inaba et al., Emission enhancement and its mechanism of Eu-doped GaN by strain engineering, *Opt. Mater. Express.* **7** (2017) 1381. https://doi.org/10.1364/ome.7.001381.

[10] M. Ishii et al., Nanoscale determinant to brighten up GaN:Eu red light-emitting diode: Local potential of Eu-defect complexes, *J. Appl. Phys.* **117** (2015) 155307. https://doi.org/10.1063/1.4918662.

[11] B. Mitchell et al., Utilization of native oxygen in Eu(RE)-doped GaN for enabling device compatibility in optoelectronic applications, *Sci. Rep.* **6** (2016) 18808. https://doi.org/10.1038/srep18808.

[12] H. Sekiguchi et al., Emission enhancement mechanism of GaN:Eu by Mg codoping, *J. Appl. Phys.* **113** (2013). https://doi.org/10.1063/1.4772950.

[13] J.K. Mishra et al., Strong enhancement of Eu^{+3} luminescence in europium-implanted GaN by Si and Mg codoping, *Appl. Phys. Lett.* **102** (2013) 2011–2014. https://doi.org/10.1063/1.4793207.

[14] J.L. Lyons et al., Computationally predicted energies and properties of defects in GaN, *Npj Comput. Mater.* **3** (2017) 1–9. https://doi.org/10.1038/s41524-017-0014-2.

[15] T. Koppe et al., Overview of band-edge and defect related luminescence in aluminum nitride, *J. Lumin.* **178** (2016) 267–281. https://doi.org/10.1016/j.jlumin.2016.05.055.

[16] S. Petit et al., Electronic behavior of rare-earth dopants in AlN: A density-functional study, *Phys. Rev. B - Condens. Matter Mater. Phys.* **72** (2005) 4–7. https://doi.org/10.1103/PhysRevB.72.073205.

[17] K. Hoang, Rare-earth defects in GaN: A systematic investigation of the lanthanide series, *Phys. Rev. Mater.* **6** (2022) 044601. https://doi.org/10.1103/PhysRevMaterials.6.044601.

[18] A. Wakahara, Impact of AlGaN on luminescence capability of rare-earth ions in AlGaN, *Opt. Mater. (Amst).* **28** (2006) 731–737. https://doi.org/10.1016/j.optmat.2005.09.011.

[19] T. Fujiwara et al., Photoluminescence properties of Eu-implanted $Al_xGa_{1-x}N$ ($0 \leq x \leq 1$), *Phys. Status Solidi.* **2** (2005) 2805–2808. https://doi.org/10.1002/pssc.200461431.

[20] K. Wang et al., Luminescence of Eu ions in $Al_xGa_{1-x}N$ across the entire alloy composition range, *Phys. Rev. B.* **80** (2009) 125206. https://doi.org/10.1103/PhysRevB.80.125206.

[21] A. Koizumi et al., In situ Eu doping into $Al_xGa_{1-x}N$ grown by organometallic vapor phase epitaxy to improve luminescence properties, *Opt. Mater. (Amst).* **41** (2015) 75–79. https://doi.org/10.1016/j.optmat.2014.11.005.

[22] Y. Nakanishi et al., Effects of Al composition on luminescence properties of europium implanted $Al_xGa_{1-x}N$ ($0 \leq x \leq 1$), *Phys. Status Solidi.* **96** (2003) 2623–2626. https://doi.org/10.1002/pssc.200303440.

[23] K. Lorenz et al., Structural and optical characterisation of Eu implanted $Al_xGa_{1-x}N$, *Nucl. Instruments Methods Phys. Res. Sect. B Beam Interact. with Mater. Atoms.* **257** (2007) 307–310. https://doi.org/10.1016/j.nimb.2007.01.020.

[24] P.N. Favennec et al., Luminescence of erbium implanted in various semiconductors: IV, III-V and II-VI materials, *Electron. Lett.* **25** (1989) 718–719. https://doi.org/10.1049/el:19890486.

[25] Y. Nakanishi et al., Improvement of luminescence capability of Tb^{3+}-related emission by $Al_xGa_{1-x}N$, *Phys. Status Solidi.* **240** (2003) 372–375. https://doi.org/10.1002/pssb.200303479.

[26] J. Rodrigues et al., Analysis of the Tb^{3+} recombination in ion implanted $Al_xGa_{1-x}N$ ($0 \leq x \leq 1$) layers, *J. Lumin.* **178** (2016) 249–258. https://doi.org/10.1016/j.jlumin.2016.05.018.

[27] M. Fialho et al., AlN content influence on the properties of $Al_xGa_{1-x}N$ doped with Pr ions, *Nucl. Instruments Methods Phys. Res. Sect. B Beam Interact. with Mater. Atoms.* **273** (2012) 149–152. https://doi.org/10.1016/j.nimb.2011.07.062.

[28] M. Fialho et al., Effect of AlN content on the lattice site location of terbium ions in $Al_xGa_{1-x}N$ compounds, *Semicond. Sci. Technol.* **31** (2016) 035026. https://doi.org/10.1088/0268-1242/31/3/035026.

[29] M. Fialho et al., Lattice site location and luminescence studies of $Al_xGa_{1-x}N$ alloys doped with thulium ions, *Nucl. Instruments Methods Phys. Res. Sect. B Beam Interact. with Mater. Atoms.* **307** (2013) 495–498. https://doi.org/10.1016/j.nimb.2013.01.010.

[30] S. Zhao et al., III-Nitride nanowire optoelectronics, *Prog. Quantum Electron.* **44** (2015) 14–68. https://doi.org/10.1016/j.pquantelec.2015.11.001.

[31] A.M. Siladie et al., Dopant radial inhomogeneity in Mg-doped GaN nanowires, *Nanotechnology.* **29** (2018). https://doi.org/10.1088/1361-6528/aabbd6.

[32] Z. Fang et al., Si Donor Incorporation in GaN Nanowires, *Nano Lett.* **15** (2015) 6794–6801. https://doi.org/10.1021/acs.nanolett.5b02634.

[33] J. Chesin et al., Light extraction in individual GaN nanowires on Si for LEDs, *Nanoepitaxy Mater. Devices IV.* **8467** (2012) 846703. https://doi.org/10.1117/12.970456.

[34] J. Chesin et al., Comparing directed efficiency of III-nitride nanowire light-emitting diodes, *J. Nanophotonics.* **8** (2014) 083095. https://doi.org/10.1117/1.jnp.8.083095.

[35] J. Rodrigues et al., Spectroscopic Analysis of Eu^{3+} Implanted and Annealed GaN Layers and Nanowires, *J. Phys. Chem. C.* **119** (2015) 17954–17964. https://doi.org/10.1021/acs.jpcc.5b05101.

[36] A. Sukegawa et al., Self-Organized Eu-Doped GaN Nanocolumn Light-Emitting Diode Grown by RF-Molecular-Beam Epitaxy, *Phys. Status Solidi.* **216** (2018) 1800501. https://doi.org/10.1002/pssa.201800501.

[37] D.N. Faye et al., Incorporation of Europium into GaN Nanowires by Ion Implantation, *J. Phys. Chem. C.* **123** (2019) 11874–11887. https://doi.org/10.1021/acs.jpcc.8b12014.

[38] R. Songmuang et al., From nucleation to growth of catalyst-free GaN nanowires on thin AlN buffer layer, *Appl. Phys. Lett.* **91** (2007). https://doi.org/10.1063/1.2817941.

[39] B. Daudin et al., The role of surface diffusion in the growth mechanism of III-nitride nanowires and nanotubes, *Nanotechnology.* **32** (2021) 085606. https://doi.org/10.1088/1361-6528/abc780.

[40] J. Wu, When group-III nitrides go infrared: New properties and perspectives, *J. Appl. Phys.* **106** (2009). https://doi.org/10.1063/1.3155798.

[41] K. Kornitzer et al., Photoluminescence and reflectance spectroscopy of excitonic transitions in high-quality homoepitaxial GaN films, *Phys. Rev. B - Condens. Matter Mater. Phys.* **60** (1999) 1471–1473. https://doi.org/10.1103/PhysRevB.60.1471.

[42] V.M. Kaganer et al., Nucleation, Growth, and Bundling of GaN Nanowires in Molecular Beam Epitaxy: Disentangling the Origin of Nanowire Coalescence, *Nano Lett.* **16** (2016) 3717–3725. https://doi.org/10.1021/acs.nanolett.6b01044.

[43] V. Jindal et al., Density functional theoretical study of surface structure and adatom kinetics for wurtzite AlN, *J. Appl. Phys.* **105** (2009). https://doi.org/10.1063/1.3106164.

[44] E. Zielony et al., Strain and lattice vibration mechanisms in GaN-$Al_xGa_{1-x}N$ nanowire structures on Si substrate, *Appl. Surf. Sci.* **588** (2022) 152901. https://doi.org/10.1016/j.apsusc.2022.152901.

[45] R.F. Allah et al., Imaging and analysis by transmission electron microscopy of the spontaneous formation of Al-rich shell structure in $Al_xGa_{1-x}N$/GaN nanowires, *Appl.*

Phys. Express. **5** (2012). https://doi.org/10.1143/APEX.5.045002.

[46] R.F. Allah et al., Structural and chemical evolution of the spontaneous core-shell structures of $Al_xGa_{1-x}N$/GaN nanowires, *Microsc. Microanal.* **20** (2014) 1254–1261. https://doi.org/10.1017/S1431927614000634.

[47] V. Laneuville et al., Double strain state in a single GaN/AlN nanowire: Probing the core-shell effect by ultraviolet resonant Raman scattering, *Phys. Rev. B - Condens. Matter Mater. Phys.* **83** (2011). https://doi.org/10.1103/PhysRevB.83.115417.

[48] A. Pierret et al., Growth, structural and optical properties of AlGaN nanowires in the whole composition range, *Nanotechnology.* **24** (2013) 115704. https://doi.org/10.1088/0957-4484/24/11/115704.

[49] I.M. Høiaas et al., GaN/AlGaN Nanocolumn Ultraviolet Light-Emitting Diode Using Double-Layer Graphene as Substrate and Transparent Electrode, *Nano Lett.* **19** (2019) 1649–1658. https://doi.org/10.1021/acs.nanolett.8b04607.

[50] M. Belloeil, Molecular beam epitaxy growth and optical characterization of GaN/AlGaN nanowire heterostructures emitting in the ultraviolet, Université Grenoble Alpes, 2017.

[51] P. Ruterana et al., A mechanism for damage formation in GaN during rare earth ion implantation at medium range energy and room temperature, *J. Appl. Phys.* **109** (2011) 1–7. https://doi.org/10.1063/1.3527944.

[52] K. Lorenz et al., High-temperature annealing and optical activation of Eu-implanted GaN, *Appl. Phys. Lett.* **85** (2004) 2712–2714. https://doi.org/10.1063/1.1801686.

[53] B. Lacroix et al., Mechanisms of damage formation in Eu-implanted GaN probed by X-ray diffraction, *EPL (Europhysics Lett.)* **96** (2011) 46002. https://doi.org/10.1209/0295-5075/96/46002.

[54] J.F. Ziegler et al., SRIM: The stopping and range of ions in matter, 1st ed., United States, 2008.

[55] H.Y. Xiao et al., Threshold displacement energy in GaN: Ab initio molecular dynamics study, *J. Appl. Phys.* **105** (2009). https://doi.org/10.1063/1.3153277.

[56] J. Xi et al., Ab initio molecular dynamics simulations of AlN responding to low energy particle radiation, *J. Appl. Phys.* **123** (2018). https://doi.org/10.1063/1.5009750.

[57] I. Grzegory et al., High pressure solution growth of GaN and related compounds, in: J.H. Edgar et al. (Eds.), Prop. Process. Appl. Gall. Nitride Relat. Semicond., INSPEC, The Institution of Electrical Engineers, London, United Kingdom, 1998.

[58] K. Sierakowski et al., High pressure processing of ion implanted GaN, *Electron.* **9** (2020) 1–11. https://doi.org/10.3390/electronics9091380.

[59] I. Grzegory et al., III-V Nitrides-thermodynamics and crystal growth at high N_2 pressure, *J. Phys. Chem. Solids.* **56** (1995) 639–647. https://doi.org/10.1016/0022-3697(94)00257-6.

[60] K. Lorenz et al., Enhanced red emission from praseodymium-doped GaN nanowires by defect engineering, *Acta Mater.* **61** (2013) 3278–3284. https://doi.org/10.1016/j.actamat.2013.02.016.

[61] J. Rodrigues et al., GaN:Pr3+ nanostructures for red solid state light emission, *RSC*

Adv. **4** (2014) 62869–62877. https://doi.org/10.1039/c4ra08571j.

[62] E. Nogales et al., Failure mechanism of AlN nanocaps used to protect rare earth-implanted GaN during high temperature annealing, *Appl. Phys. Lett.* **88** (2006) 031902. https://doi.org/10.1063/1.2162797.

[63] K. Lorenz et al., High temperature annealing of rare earth implanted GaN films: Structural and optical properties, *Opt. Mater. (Amst).* **28** (2006) 750–758. https://doi.org/10.1016/j.optmat.2005.09.015.

[64] D.N. Faye et al., Mechanisms of Implantation Damage Formation in $Al_xGa_{1-x}N$ Compounds, *J. Phys. Chem. C.* **120** (2016) 7277–7283. https://doi.org/10.1021/acs.jpcc.6b00133.

[65] S. Leclerc et al., Mechanisms of damage formation in Eu-implanted AlN, *J. Appl. Phys.* **112** (2012). https://doi.org/10.1063/1.4758311.

[66] K. O'Donnell et al., eds., Rare Earth Doped III-Nitrides for Optoelectronic and Spintronic Applications, 1st ed., Springer Netherlands, Netherlands, 2010.

[67] M.A. Moram et al., X-ray diffraction of III-nitrides, *Reports Prog. Phys.* **72** (2009) 036502. https://doi.org/10.1088/0034-4885/72/3/036502.

[68] O. Liubchenko et al., Modification of elastic deformations and analysis of structural and optical changes in Ar+-implanted AlN/GaN superlattices, *Appl. Nanosci.* **0** (2019) 0. https://doi.org/10.1007/s13204-019-01000-w.

[69] W. Limmer et al., Raman scattering in ion-implanted GaN, *Appl. Phys. Lett.* **72** (1998) 2589–2591. https://doi.org/10.1063/1.121426.

[70] M. Kuball, Raman spectroscopy of GaN, AlGaN and AlN for process and growth monitoring/control, *Surf. Interface Anal.* **31** (2001) 987–999. https://doi.org/10.1002/sia.1134.

[71] M. Kuball et al., Thermal stability of GaN investigated by Raman scattering, *Appl. Phys. Lett.* **73** (1998) 960–962. https://doi.org/10.1063/1.122052.

[72] V.Y. Davydov et al., Composition dependence of optical phonon energies and Raman line broadening in hexagonal $Al_xGa_{1-x}N$ alloys, *Phys. Rev. B.* **65** (2002) 125203. https://doi.org/10.1103/PhysRevB.65.125203.

[73] H. Grille et al., Phonons in ternary group-III nitride alloys, *Phys. Rev. B.* **61** (2000) 6091–6105. https://doi.org/10.1103/PhysRevB.61.6091.

[74] M. Holtz et al., Composition dependence of the optical phonon energies in hexagonal $Al_xGa_{1-x}N$, *J. Appl. Phys.* **89** (2001) 7977–7982. https://doi.org/10.1063/1.1372661.

[75] G. Calabrese et al., Radius-dependent homogeneous strain in uncoalesced GaN nanowires, *Acta Mater.* **195** (2020) 87–97. https://doi.org/10.1016/j.actamat.2020.04.045.

[76] V.Y. Davydov et al., Phonon dispersion and Raman scattering in hexagonal GaN and AlN, *Phys. Rev. B.* **58** (1998) 12899–12907. https://doi.org/10.1103/PhysRevB.58.12899.

[77] J.M. Wagner et al., Properties of strained wurtzite GaN and AlN: Ab initio studies, *Phys. Rev. B - Condens. Matter Mater. Phys.* **66** (2002) 1–20. https://doi.org/10.1103/PhysRevB.66.115202.

[78] K. Hestroffer et al., The structural properties of GaN/AlN core-shell nanocolumn heterostructures, *Nanotechnology.* **21** (2010). https://doi.org/10.1088/0957-4484/21/41/415702.

[79] H. Harima, Properties of GaN and related compounds studied by means of Raman scattering, *J. Phys. Condens. Matter.* **14** (2002) R967–R993. https://doi.org/10.1088/0953-8984/14/38/201.

[80] C. Kisielowski et al., Strain-related phenomena in GaN thin films, *Phys. Rev. B - Condens. Matter Mater. Phys.* **54** (1996) 17745–17753. https://doi.org/10.1103/PhysRevB.54.17745.

[81] M.W. Ullah et al., Atomistic simulation of Er irradiation induced defects in GaN nanowires, *J. Appl. Phys.* **116** (2014) 124313. https://doi.org/10.1063/1.4896787.

[82] V.Y. Davydov et al., Raman and photoluminescence studies of biaxial strain in GaN epitaxial layers grown on 6H-SiC, *J. Appl. Phys.* **82** (1997) 5097–5102. https://doi.org/10.1063/1.366310.

[83] J.M. Wagner et al., Phonon deformation potentials of α-GaN and -AlN: An ab initio calculation, *Appl. Phys. Lett.* **77** (2000) 346–348. https://doi.org/10.1063/1.127009.

[84] F. Demangeot et al., Raman determination of phonon deformation potentials in α-GaN, *Solid State Commun.* **100** (1996) 207–210. https://doi.org/10.1016/0038-1098(96)00410-3.

[85] B. Pipeleers et al., Defect accumulation during channeled erbium implantation into GaN, *J. Appl. Phys.* **98** (2005). https://doi.org/10.1063/1.2143120.

[86] R.D. Shannon, Revised effective ionic radii and systematic studies of interatomic distances in halides and chalcogenides, *Acta Crystallogr. Sect. A.* **32** (1976) 751–767. https://doi.org/10.1107/S0567739476001551.

[87] K. Lorenz et al., Structural and optical characterization of Eu-implanted GaN, *J. Phys. D. Appl. Phys.* **42** (2009). https://doi.org/10.1088/0022-3727/42/16/165103.

[88] M. Peres et al., Optical and structural studies in Eu-implanted AlN films, *Superlattices Microstruct.* **40** (2006) 537–544. https://doi.org/10.1016/j.spmi.2006.07.031.

[89] K. Lorenz et al., Optical doping of AlN by rare earth implantation, *Nucl. Instruments Methods Phys. Res. Sect. B Beam Interact. with Mater. Atoms.* **242** (2006) 307–310. https://doi.org/10.1016/j.nimb.2005.08.037.

[90] N. Catarino et al., Enhanced dynamic annealing and optical activation of Eu implanted a-plane GaN, *EPL (Europhysics Lett.* **97** (2012) 68004. https://doi.org/10.1209/0295-5075/97/68004.

[91] K. Lorenz et al., High temperature annealing of Europium implanted AlN, *Nucl. Instruments Methods Phys. Res. Sect. B Beam Interact. with Mater. Atoms.* **268** (2010) 2907–2910. https://doi.org/10.1016/j.nimb.2010.05.003.

[92] K. Lorenz et al., Optical doping and damage formation in AlN by Eu implantation, *J. Appl. Phys.* **107** (2010) 2–6. https://doi.org/10.1063/1.3291100.

[93] M.A. Reshchikov et al., Luminescence properties of defects in GaN, *J. Appl. Phys.* **97** (2005) 1–95. https://doi.org/10.1063/1.1868059.

[94] M.A. Reshchikov et al., Two yellow luminescence bands in undoped GaN, *Sci. Rep.* **8** (2018) 1–11. https://doi.org/10.1038/s41598-018-26354-z.

[95] M.A. Reshchikov et al., Two charge states of the C_N acceptor in GaN: Evidence from photoluminescence, *Phys. Rev. B.* **98** (2018) 125207. https://doi.org/10.1103/PhysRevB.98.125207.

[96] A. Pierret et al., Probing alloy composition gradient and nanometer-scale carrier localization in single AlGaN nanowires by nanocathodoluminescence, *Nanotechnology.* **24** (2013). https://doi.org/10.1088/0957-4484/24/30/305703.

[97] M. Belloeil et al., Nanoscale x-ray investigation of composition fluctuations in AlGaN nanowires, *Nanotechnology.* (2020) 11–14. https://doi.org/10.1088/1361-6528/ab94e1.

[98] L. Trinkler et al., UV light induced processes in pure and doped AlN ceramics, *Opt. Mater. (Amst).* **121** (2021) 111550. https://doi.org/10.1016/j.optmat.2021.111550.

[99] T. Koyama et al., Relation between Al vacancies and deep emission bands in AlN epitaxial films grown by N H3 -source molecular beam epitaxy, *Appl. Phys. Lett.* **90** (2007). https://doi.org/10.1063/1.2748315.

[100] A. Sedhain et al., Nature of optical transitions involving cation vacancies and complexes in AlN and AlGaN, *Appl. Phys. Lett.* **100** (2012). https://doi.org/10.1063/1.4723693.

[101] Q. Yan et al., Origins of optical absorption and emission lines in AlN, *Appl. Phys. Lett.* **105** (2014) 0–5. https://doi.org/10.1063/1.4895786.

[102] Q. Zhou et al., Below bandgap photoluminescence of an AlN crystal: Co-existence of two different charging states of a defect center, *APL Mater.* **8** (2020). https://doi.org/10.1063/5.0012685.

[103] P.P. Paskov et al., Optical Properties of III-Nitride Semiconductors, in: Handb. GaN Semicond. Mater. Devices, 1st ed., CRC Press, United States, 2017: pp. 87–116.

[104] G. Steude et al., Optical investigations of AlGaN on GaN epitaxial films, *MRS Internet J. Nitride Semicond. Res.* **4** (1999) 10–13. https://doi.org/10.1557/s1092578300002532.

[105] F. Yang et al., The origin of the Stokes shift. The line shapes of quantum well exciton absorption and photoluminescence spectra, *Phys. B Phys. Condens. Matter.* **185** (1993) 362–365. https://doi.org/10.1016/0921-4526(93)90262-5.

[106] R.W. Martin et al., Exciton localization and the Stokes' shift in InGaN epilayers, *Appl. Phys. Lett.* **74** (1999) 263–265. https://doi.org/10.1063/1.123275.

[107] K.P. O'Donnell et al., Origin of Luminescence from InGaN Diodes, *Phys. Rev. Lett.* **82** (1999) 237–240. https://doi.org/10.1103/PhysRevLett.82.237.

[108] B. Bastek et al., Analysis of point defects in AlN epilayers by cathodoluminescence spectroscopy, *Appl. Phys. Lett.* **95** (2009) 1–4. https://doi.org/10.1063/1.3154518.

[109] R. Vermeersch et al., Optical properties of Ga-doped AlN nanowires, *Appl. Phys. Lett.* **122** (2023) 091106. https://doi.org/10.1063/5.0137424.

[110] T. Monteiro et al., Photoluminescence and lattice location of Eu and Pr implanted GaN samples, *Phys. B Condens. Matter.* **308–310** (2001) 22–25.

https://doi.org/10.1016/S0921-4526(01)00656-1.

[111] J.B. Gruber et al., Spectroscopic analysis of Eu^{3+} in single-crystal hexagonal phase AlN, *J. Appl. Phys.* **110** (2011) 023104. https://doi.org/10.1063/1.3609076.

[112] V. Katchkanov et al., Photoluminescence studies of Eu-implanted GaN epilayers, *Phys. Status Solidi Basic Res.* **242** (2005) 1491–1496. https://doi.org/10.1002/pssb.200440032.

[113] T. Andreev et al., Optical transitions in Eu^{3+} ions in GaN:Eu grown by molecular beam epitaxy, *Phys. Rev. B - Condens. Matter Mater. Phys.* **73** (2006) 3–8. https://doi.org/10.1103/PhysRevB.73.195203.

[114] B. Mitchell et al., Temporally modulated energy shuffling in highly interconnected nanosystems, *Nanophotonics.* (2020) 1–26. https://doi.org/10.1515/nanoph-2020-0484.

[115] W. Zhu et al., Re-Excitation of Trivalent Europium Ions Doped into Gallium Nitride Revealed through Photoluminescence under Pulsed Laser Excitation, *ACS Photonics.* **5** (2018) 875–880. https://doi.org/10.1021/acsphotonics.7b01090.

[116] B. Mitchell et al., Color-Tunablility in GaN LEDs Based on Atomic Emission Manipulation under Current Injection, *ACS Photonics.* **6** (2019) 1153–1161. https://doi.org/10.1021/acsphotonics.8b01461.

[117] H. Peng et al., Spectroscopic and energy transfer studies of Eu^{3+} centers in GaN, *J. Appl. Phys.* **102** (2007) 073520. https://doi.org/10.1063/1.2783893.

[118] L. Bodiou et al., Optically active centers in Eu implanted, Eu in situ doped GaN, and Eu doped GaN quantum dots, *J. Appl. Phys.* **105** (2009) 043104. https://doi.org/10.1063/1.3078783.

[119] K. Wang et al., Selectively excited photoluminescence from Eu-implanted GaN, *Appl. Phys. Lett.* **87** (2005) 112107. https://doi.org/10.1063/1.2045551.

[120] S. Magalhães et al., Functionalizing self-assembled GaN quantum dot superlattices by Eu-implantation, *J. Appl. Phys.* **108** (2010) 084306. https://doi.org/10.1063/1.3496624.

[121] E.P.J. Merkx et al., Modelling and optimization of UV absorbing photovoltaic windows using a thin film AlN:Eu^{3+} luminescence library, *Sol. Energy Mater. Sol. Cells.* **200** (2019) 110032. https://doi.org/10.1016/j.solmat.2019.110032.

[122] M. Peres et al., The role of the annealing temperature on the optical and structural properties of Eu doped GaN/AlN QD, *Opt. Mater. (Amst).* **33** (2011) 1045–1049. https://doi.org/10.1016/j.optmat.2010.10.025.

[123] H.J. Lozykowski et al., Thermal quenching of luminescence and isovalent trap model for rare-earth-ion-doped AlN, *Phys. Status Solidi Basic Res.* **244** (2007) 2109–2126. https://doi.org/10.1002/pssb.200642152.

[124] H.J. Lozykowski et al., Luminescence and excitation mechanism of Pr, Eu, Tb and Tm ions implanted into AlN, *Microelectronics J.* **36** (2005) 453–455. https://doi.org/10.1016/j.mejo.2005.02.045.

[125] L. Jin et al., Optical property in colorless AlN bulk crystals: investigation of native defect-induced UV absorption, *Scr. Mater.* **190** (2021) 91–96.

https://doi.org/10.1016/j.scriptamat.2020.08.049.

[126] M. Sall et al., Synergy between electronic and nuclear energy losses for color center creation in AlN, *EPL (Europhysics Lett.* **102** (2013) 26002. https://doi.org/10.1209/0295-5075/102/26002.

[127] M. Sall et al., On the effect of oxygen on the creation of colour centres in swift heavy ion-irradiated AlN, *Nucl. Instruments Methods Phys. Res. Sect. B Beam Interact. with Mater. Atoms.* **536** (2023) 18–22. https://doi.org/10.1016/j.nimb.2022.12.025.

[128] L. Peters et al., A Combination of Ion Implantation and High-Temperature Annealing: The Origin of the 265 nm Absorption in AlN, *Phys. Status Solidi.* (2022). https://doi.org/10.1002/pssa.202200485.

[129] M. Peres et al., Influence of the AlN molar fraction on the structural and optical properties of praseodymium-doped $Al_xGa_{1-x}N$ ($0 \leq x \leq 1$) alloys, *Microelectronics J.* **40** (2009) 377–380. https://doi.org/10.1016/j.mejo.2008.07.032.

[130] B. Han et al., Investigation of Luminescence from Dy^{3+} in AlN, *J. Electrochem. Soc.* **154** (2007) J44. https://doi.org/10.1149/1.2392913.

[131] H.J. Lozykowski, Kinetics of luminescence of isoelectronic rare-earth ions in III-V semiconductors, *Phys. Rev. B.* **48** (1993) 17758–17769. https://doi.org/10.1103/PhysRevB.48.17758.

[132] A. Taguchi et al., Multiphonon-assisted energy transfer between Yb 4*f* shell and InP host, *J. Appl. Phys.* **76** (1994) 7288–7295. https://doi.org/10.1063/1.358014.

[133] J.H.V. Vleck, The Puzzle of Rare-earth Spectra in Solids, *J. Phys. Chem.* **41** (1937) 67–80. https://doi.org/10.1021/j150379a006.

[134] B.G. Wybourne, Spectroscopic Properties of Rare Earths, 1st ed., John Wiley & Sons, Inc., United States, 1965.

[135] W.A. Runciman, Stark-splitting in crystals, *Philos. Mag.* **1** (1956) 1075–1077. https://doi.org/10.1080/14786435608238189.

[136] K. Binnemans, Interpretation of europium(III) spectra, *Coord. Chem. Rev.* **295** (2015) 1–45. https://doi.org/10.1016/j.ccr.2015.02.015.

[137] L. Bodiou et al., Effect of annealing temperature on luminescence in Eu implanted GaN, *Opt. Mater.* **28** (2006) 780–784. https://doi.org/10.1016/j.optmat.2005.09.022.

[138] I.S. Roqan et al., Identification of the prime optical center in GaN:Eu^{3+}, *Phys. Rev. B.* **81** (2010) 085209. https://doi.org/10.1103/PhysRevB.81.085209.

[139] B. Mitchell et al., The role of donor-acceptor pairs in the excitation of Eu-ions in GaN:Eu epitaxial layers, *J. Appl. Phys.* **115** (2014) 204501. https://doi.org/10.1063/1.4879253.

[140] Z. Fleischman et al., Excitation pathways and efficiency of Eu ions in GaN by site-selective spectroscopy, *Appl. Phys. B Lasers Opt.* **97** (2009) 607–618. https://doi.org/10.1007/s00340-009-3605-x.

[141] J. Rodrigues et al., A comparative study of photo-, cathodo- and ionoluminescence of GaN nanowires implanted with rare earth ions, *Nucl. Instruments Methods Phys. Res. Sect. B Beam Interact. with Mater. Atoms.* **306** (2013) 201–206. https://doi.org/10.1016/j.nimb.2012.12.028.

[142] S. Copelman et al., Strong crystal field splitting and polarization dependence observed in the emission from Eu^{3+} ions doped into GaN, in: M. Strassburg et al. (Eds.), Light. Devices, Mater. Appl. XXIV, SPIE, 2020: p. 68. https://doi.org/10.1117/12.2544005.

[143] C.K. Jørgensen, Orbitals in atoms and molecules, Academic Press, New York, United States of America, 1962.

[144] M.A. Reshchikov et al., Higher than 90% internal quantum efficiency of photoluminescence in GaN: Si,Zn, *Phys. Status Solidi Curr. Top. Solid State Phys.* **10** (2013) 507–510. https://doi.org/10.1002/pssc.201200664.

[145] J.F. Muth et al., Absorption coefficient, energy gap, exciton binding energy, and recombination lifetime of GaN obtained from transmission measurements, *Appl. Phys. Lett.* **71** (1997) 2572–2574. https://doi.org/10.1063/1.120191.

[146] J.F. Muth et al., Absorption Coefficient and Refractive Index of GaN, AlN and AlGaN Alloys, *MRS Internet J. Nitride Semicond. Res.* **4** (1999) 502–507. https://doi.org/10.1557/S1092578300002957.

[147] M.H.V. Werts et al., The emission spectrum and the radiative lifetime of Eu^{3+} in luminescent lanthanide complexes, *Phys. Chem. Chem. Phys.* **4** (2002) 1542–1548. https://doi.org/10.1039/b107770h.

Chapter 4

Europium-implanted AlN p-n junction nanowires: in the route of red III-N light-emitting diodes

4.1. Context

One of the most appealing properties of III-N is their direct bandgap tunability in the visible spectrum (control of the In-content in InGaN alloys), allowing for the realization of monolithic RGB LEDs. However, as mentioned throughout this thesis, red InGaN-based LEDs suffer from reduced EQE (about 10 % [1,2]) due to poor material quality and strong polarization fields [3–5].

Achieving red LEDs based on III-N with improved performance is vital for micro-LED displays as a monolithic approach would facilitate the joint integration of RGB emitters. As demonstrated in the previous chapter, doping III-N with Eu^{3+} is an alternative method to obtain the red color emission. It benefits from the narrow (atomic-like) radiative transitions between excited and ground states of the partially filled $4f^6$ shell, which is shielded from the surrounding environment by the filled $5s$ and $5p$ outer shells. The emphasis goes to the most intense $^5D_0 \rightarrow {}^7F_2$ transition in the 620–625 nm wavelength range [6–8]. Thanks to the shielding, the emission wavelength is stable against variations in the charge injection levels and the temperature, which is crucial for applications that require high color purity and stability [9–11]; this is a significant benefit compared to red InGaN-based LEDs [1].

In 2009, A. Nishikawa et al. demonstrated for the first time the realization of red LEDs using a p-n junction diode where the active region consisted of an Eu-doped GaN layer. When operating under forward bias, carriers of opposite charge were introduced in the active

layer from each side of the p-n junction. The recombination of electron and hole led to a non-radiative energy transfer to Eu^{3+}, leaving them in an excited $4f^6$ configuration; the subsequent return of Eu^{3+} to the fundamental state resulted in the red luminescence. However, the performance of such LEDs was not good; at 20 mA, the output power was 1.3 µW, and the EQE was only 0.001 % [12]. A year later, the same authors improved the performance of GaN:Eu LEDs by optimizing the growth process. A higher growth pressure enhanced the luminescence intensity and led to a decrease in the thermal quenching of the luminescence intensity from 10 K to 300 K; this was attributed to improvements in the crystalline quality and an increase in the amount of optically active Eu^{3+}. As a result, at 20 mA, the output power increased to 17 µW, and the EQE was 0.04 % [13].

Thereafter, most research studies focused on understanding and manipulating Eu^{3+} centers in GaN [14–16]. Just a few years later, in 2017, W. Zhu et al. reported red GaN:Eu LEDs performing significantly better than the ones of A. Nishikawa. In this case, the active region consisted of a multi-layered structure of 100 pairs of alternating 3 nm-thick GaN:Eu and 6 nm-thick undoped GaN. Under operation at 20 mA, the output power was 375 µW, and the EQE was ~1 %; a maximum EQE of 4.6 % was attained at a current of 1 mA [17]. In 2018, B. Mitchell et al. improved these devices by adjusting the thickness of the undoped GaN layer to 10 nm; the structure of the device is represented in **Figure 4.1(A)**. At a current of 20 mA, these LEDs had an output power of 1.25 mW and an EQE of 3.3 %; a peak EQE of 9.2 % was found for low current levels [18]. The last-mentioned LEDs, whose performance is comparable to red-emitting InGaN-based LEDs, are state-of-the-art LEDs based on the Eu-doped III-N. **Figure 4.1(B)** compares the EL response of GaN:Eu LED and red InGaN-based LEDs [1,18]; one can notice that the first has a narrower emission, conferring better color purity. As mentioned above, their emission wavelength is also much more insensitive to changes in the applied current and temperature.

In the meantime, H. Sekiguchi et al. fabricated red GaN:Eu NW LEDs grown by PAMBE directly on low-resistivity n-type Si (111) substrates for the first time; the device structure was a GaN:Eu active layers sandwiched between p-type GaN and n-type GaN. The LEDs exhibited a rectifying behavior with a turn-on-voltage of 4.9 V under continuous current injection at room temperature [19,20]. In 2023, T. Otabara et al. demonstrated sharp red luminescence from GaN:Eu/GaN core-shell NW LEDs under current injection with a turn-on-voltage of ~10 V [21,22]. Besides the potential of GaN NWs in enhancing the Eu^{3+} luminescence intensity [19,20,23–27], the demonstration of GaN:Eu NW LEDs is fascinating, considering the present attractiveness of III-N NWs for optoelectronics at micro- and nano-scales. For example, micro-LEDs consisting of ensembles of NWs do not require plasma etching treatments; therefore, sidewall damage contributing to SRH nonradiative recombination can be mitigated. As a consequence, using the NW geometry, EQE can be

maintained almost independent of the LEDs' size, as demonstrated by Aledia [28]. Furthermore, NW structures can be employed for flexible optoelectronic applications [29–31].

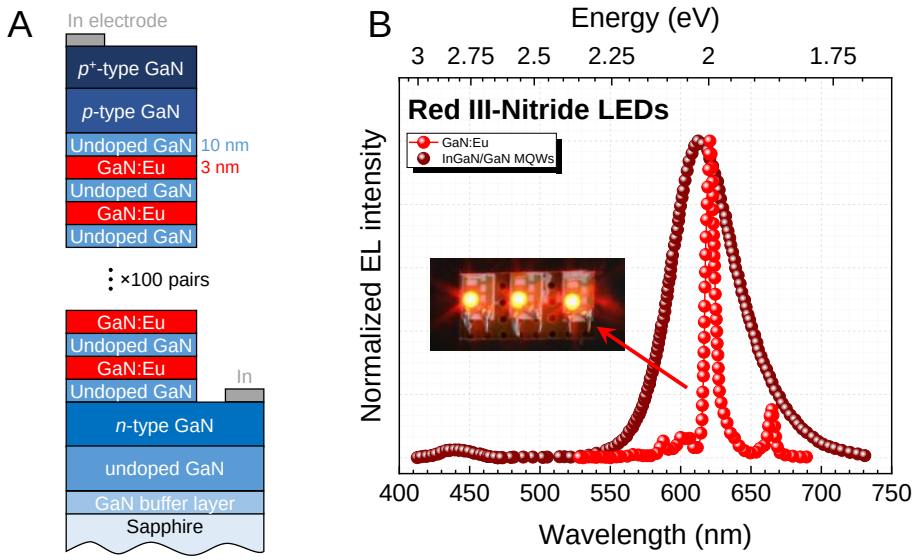

Figure 4.1 (A) Structure of the state-of-the-art GaN:Eu LEDs [18]. **(B)** Normalized EL spectra of state-of-the-art GaN:Eu LEDs [18] (photo is from reference [32]) and InGaN-based LEDs [1] obtained at a current of 20 mA.

The results from **Chapter 3** showed that AlN NW hosts can enhance the luminescence intensity of Eu^{3+} compared to AlGaN NW hosts. Therefore, exploring Eu-implanted AlN NWs for developing red-emitting devices with better optical performance seems tempting. However, one must bear in mind that achieving n- and p-type doping in AlN is not easy because of *i)* the high ionization energies of donors and acceptors, *ii)* incorporation in deep *DX* states, and *iii)* self-compensation. The poor n- and p-type conductivities have been perhaps the most significant limitation in developing efficient AlN and AlGaN-based deep UV LEDs. The NW configuration has been found to enhance dopant incorporation compared to 2D planar counterparts and allow for controlling dopant incorporation in specific configurations (e.g., Si in shallow donor states) [33–36]. However, in NWs, dopants usually present an inhomogeneous radial distribution, affecting the transport properties in the LEDs [37,38].

A second issue concerns the implantation process since, until now, it has never been possible to obtain an electroluminescent response from GaN-based planar LED structures implanted with Ln species, albeit their intra-4*f* luminescence could be observed under photo-excitation [39–41]. D. Faye et al. attributed this behavior to parasitic conduction

paths across the diode structure, likely due to the interaction between implantation-induced defects and pre-existing extended defects [41]; if this is the case, the absence (or at least lower density) of dislocations in NWs may allow for exciting Eu^{3+} through electrical injection. Moreover, AlN hosts are known to suffer less implantation damage than GaN for low fluences typically employed in ion implantation [42–45].

In this chapter, the effects of Eu-implantation and annealing in AlN p-n junction NWs are studied. First, the optical and structural properties of the samples implanted with two fluences (1×10^{14} cm^{-2} and 5×10^{14} cm^{-2}) are evaluated using micro-Raman, PL, PLE, and CL spectroscopy techniques. At the end of the chapter, proof-of-concept red LEDs based on this strategy are demonstrated for the first time, and their preliminary electro-optical characterization is performed.

4.2. Experimental details

4.2.1. Description of the samples

4.2.1.1. Growth of AlN p-n junction NWs

Self-organized AlN NW p-n junctions were grown by PAMBE on GaN NW templates on a low-resistivity n-type doped Si (111) substrate. GaN NW stems and AlN NW top sections were grown under nitrogen-rich conditions (metal/nitrogen ratio of ~0.3) at substrate temperatures of 820 ℃ and 860 ℃, respectively. **Figure 4.2(A)** displays a scheme of the NWs' structure that consists of an n-type doped GaN NWs templates (nominal Si concentration of 10^{20} cm^{-3}) at the bottom, followed by n-type doped AlN NW sections (nominal Si concentration of 10^{19} cm^{-3}), and p-type doped AlN NW sections (nominal Mg concentration of 10^{20} cm^{-3}) at the top. The p-type sections were co-doped with In (nominal concentration of 10^{19} cm^{-3}) as this increases Mg concentration in AlN NWs and, consequently, improves the electrical transport properties [34,46]. The nominal concentration of dopants is estimated considering the calibration reported elsewhere for the same PAMBE equipment, in which the respective cell temperature was correlated with the dopant's concentration measured by EDX [34,35].

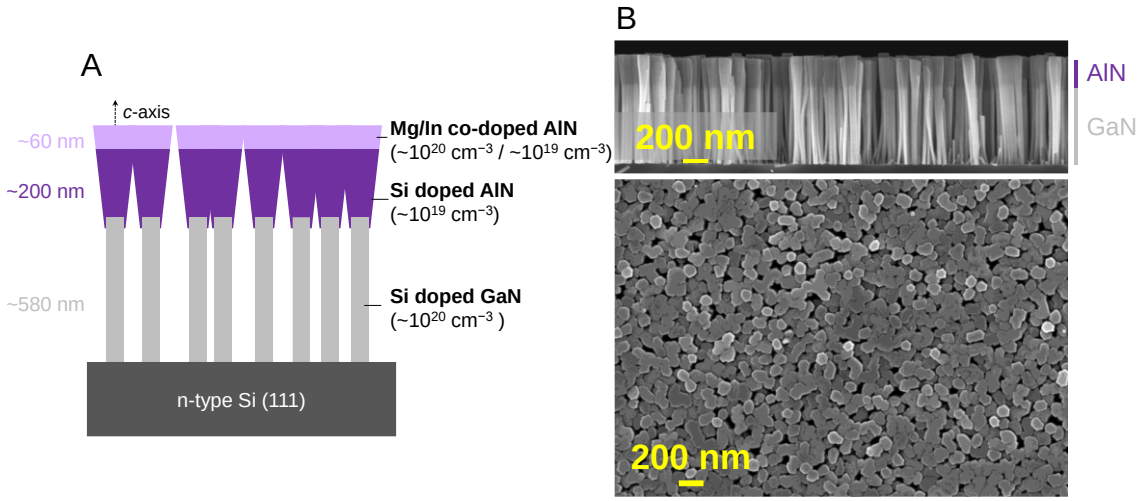

Figure 4.2 (A) Schematic representation of the AlN p-n junction NWs. **(B)** Cross-sectional and top-view SEM images of the as-grown NWs (obtained in a Zeiss Ultra-55 setup with an acceleration voltage of 5 kV).

Figure 4.2(B) shows cross-sectional and top-view SEM images of the as-grown NWs. The NWs are vertically grown along the *c*-axis and have a total length of ~800–850 nm. The first ~580 nm corresponds to GaN NW templates (brighter region), and the remaining to the axial AlN p-n junction. The AlN p-n junction region is estimated to be ~190–210 nm-thick n-AlN and ~50–70 nm-thick p-type AlN based on growth times. The diameter of the NWs is ~45 nm at the GaN NW stems, increasing up to ~90 nm at the AlN sections. The radial enlargement is caused by the limited diffusion of Al adatoms along the sidewalls towards the top, which increases the NW lateral growth rate [47]. This phenomenon, together with the high density of NWs (higher than 10^{10} cm^{-2}), fosters NWs coalescence at the top, which results in high filling factors (above 90 %). Another characteristic that can be observed is the planarity of the NWs.

4.2.1.2. Eu-implantation and RTA treatments

The AlN p-n junction NWs were implanted at RT with 300 keV accelerated europium ions in a configuration parallel to the NWs growth axis (*c*-axis), i.e., channeled implantation. Two different implantation fluences, 1×10^{14} cm^{-2} and 5×10^{14} cm^{-2}, were used to understand how this parameter affects the structural properties of the NWs and the optical activation of Eu^{3+}.

RTA treatments were carried out in an ANNEALSYS AS-One 100 RTA processor equipped with halogen lamps to heat the samples via infrared radiation. RTA was performed in flowing N_2 at 1000 ℃ for 30 seconds. According to the results presented in **Chapter 3**,

higher RTA temperatures allow for a better recovery of the AlN lattice and a stronger intra-$4f^6$ luminescence; however, it results in GaN dissociation. Therefore, as degradation of the GaN NW templates would be critical for the device's development, the RTA temperature was restricted to 1000 ℃ for 30 seconds in flowing N_2.

The idea behind recurring to a channeled implantation geometry is to minimize the generated damage within the AlN NWs since the RTA temperature is limited to 1000 ℃. However, as discussed in subsection 2.6.2, the implantation depth may extend further due to the penetration of the ions through a well-defined and low-index crystallographic axis, with a reduced probability of elastic collisions with target atoms [48–50].

4.2.1.3. LED fabrication

After optical characterization, and in order to provide a proof-of-concept of red Eu-implanted AlN p-n junction NW LEDs, arrays of 100×100 μm^2 indium tin oxide (ITO) pads were fabricated on top of the NWs by photolithographic processes to serve as p-contacts. The backside of the n-type doped Si substrate was directly used as n-contact. Since the NWs density is high, an ensemble of several millions of NWs will contribute to the electrical and optical response of the LEDs.

The thickness of the ITO pads deposited using magnetron sputtering was 100 nm; subsequent annealing at 550 ℃ was performed for 10 minutes in a tubular oven to activate them electrically [34,38]. The high transparency of ITO in the visible spectral region permits the extraction of the red emission from the top of the NWs without significant absorption by the contacts [51]. A high surface area coverage (above 90 %) is of major importance for ensuring that the ITO layer deposits at the top of the NWs [46]. Furthermore, as the p-AlN NW section is very thin, the planarity of the NWs may be significant in preventing short circuits between both sides of the AlN p-n junction.

4.2.1.4. Samples nomenclature

The samples are identified using a nomenclature like that adopted in **Chapter 3**. In this case, a new term to denote the axial p-n junction ("*pn*") is used instead of the previous designation of "*n100*"; furthermore, the implantation geometry angle is omitted as implantation was performed in a channeling configuration. Accordingly, the as-grown sample is named *pn*, while the two implanted and annealed samples are named *pn-1E14-1000* and *pn-5E14-1000*. In some cases, results from an additional sample consisting of non-annealed Eu-implanted AlN p-n junction NWs (fluence of 5×10^{14} cm^{-2}) are presented to elucidate the effects of RTA; this sample is labeled as *pn-5E14*.

In specific circumstances, data from the undoped Eu-implanted AlGaN NWs, discussed in **Chapter 3**, is included for comparison; their nomenclature remains the same as that used previously.

4.2.2. Characterization techniques

4.2.2.1. Micro-Raman

Micro-Raman experiments were conducted in a Horiba Jobin-Yvon HR800 spectrometer. The 325 nm and 442 nm lines of a He-Cd laser were used as excitation. A 600 grooves·mm^{-1} grating (experimental uncertainty of 5 cm^{-1}) and a 40× near UV objective (NA of 0.47) were used for the 325 nm excitation. The 442 nm line of a He-Cd laser was focused on the top of the NWs by a 100× (NA of 0.9) microscope objective, while a 2400 grooves·mm^{-1} grating (experimental uncertainty of 0.5 cm^{-1}) was used. The Raman signal was detected by a CCD in the backscattering geometry $z(x\ \cdot\ )\bar{z}$, with z parallel to the NWs' axis. The system was calibrated using the main peak of a Si reference sample at 520.5 cm^{-1}.

4.2.2.2. Steady-state PL and PLE

PL experiments were carried out in two different systems. In one of the setups, the 325 nm line of a He-Cd laser was used as the excitation source, and the PL signal was measured in a dispersive system SPEX 1704 Czerny-Turner monochromator (1 m, 1200 grooves·mm^{-1} grating) coupled to a water-cooled Hamamatsu R928 photomultiplier tube (PMT). The laser beam excitation density was about 1–2 W·cm^{-2}, and the beam spot was ~5 mm^2; therefore, the collected signal brings information from a few hundred NWs. The excitation light was focused on the sample at 30° to the surface's normal, while the emitted light was collected at 60° to the surface normal. The PL response was corrected to the system's response and calibrated using the 2nd-order of the laser. For entrance and exit slits of 150 µm, the spectrometer's spectral resolution (bandpass) is ~0.1 nm. In this experimental setup, the samples were mounted in a cold finger of a closed-cycle helium cryostat (pressure of 10^{-5} Torr); the temperature was controlled between 14 and 300 K by the heating of a resistance placed close to the cold finger using a temperature controller connected to a thermocouple.

The other PL setup was a Fluorolog 3 Horiba Scientific modular system with a 450 W Xe arc lamp. The excitation and emission wavelengths were controlled by entrance and exit monochromators, allowing for analyzing the samples' PL and PLE response at room temperature. The excitation spot size is much larger than the NW dimensions; thus, as in

the previous PL setup, the average optical response of a few hundred NWs is collected simultaneously. The excitation light was focused on the sample at 60° to the surface's normal, while the emitted light was collected at 40° to the surface normal (front face acquisition mode). The spectrometer's spectral resolution (bandpass) is set at 3 nm to guarantee an adequate signal intensity. The presented spectra were corrected to the spectral response of the optical components, the PMT detector, and the Xe lamp.

4.2.2.3. Cathodoluminescence, electroluminescence, and current-voltage characteristics

CL measurements were done at room temperature in an FEI Inspect F50 scanning electron microscope. The luminescence signal was detected using a Horiba Jobin Yvon iHR 550 spectrometer equipped with 1800 grooves·mm^{-1} grating and a Peltier-cooled Andor Technology Newton DU940 CCD. The beam size was ~20 nm in diameter, and an acceleration voltage of 5 kV was applied, corresponding to an interaction depth of ~150 nm. Two geometries were used with excitation and collection *i)* parallel or *ii)* perpendicular to the *c*-axis of the NWs. In the second case, the electron beam was focused on different positions of the NWs to measure the response along the NWs' length.

Electrical measurements were also carried out inside the SEM chamber at RT. After processing the NWs, i.e., deposition of the ITO p-contacts, the samples were glued on an alumina plate using a silver paste to isolate them from the sample holder electrically. A tungsten tip mounted on nano-manipulators was in contact with the conductive silver ink for the bottom contact, while a second tungsten tip was placed in direct contact with the top ITO pad. The EL signal was then measured using the same spectrometer as in CL experiments. The I-V characteristics of the realized devices were acquired with a Keithley 2636B source meter (detection limit of 0.1 pA).

4.2.3. Experimental data credits

The research presented in this chapter is the result of national and international collaborations within the scope of the projects "Nano-engineering of Wide Bandgap Semiconductors Using Ion Beams" (NASIB) funded by *Fundação para a Ciência e a Tecnologia* (FCT) and "Full Colour Nitride Nanowire Light Emitting Diodes" (FUNN-LED) funded by the bilateral Pessoa Program between Portuguese and French institutions.

The growth of the AlN p-n junction NWs was done by Rémy Vermeersch, a former Ph.D. student in Bruno Daudin's research group (Nanophysics and Semiconductors, CEA, Grenoble, France). The investigation carried out in this group is fully committed to the understanding of p- and n-type doping of AlN and GaN NWs for the realization of deep UV

LEDs [34–38]. Therefore, they provided AlN p-n junction NWs with characteristics like those they have been using for UV LEDs, which were further processed in order to tune the emission to the red. Rémy Vermeersch also did the deposition of the ITO contacts on the NW LEDs, the CL measurements, and the electro-optical characterization (Institut Néel, CNRS, Grenoble, France). Katharina Lorenz's group carried out the Eu-implantation and RTA (Laboratory of Accelerators and Radiation Technologies, CTN-IST, Lisbon, Portugal).

4.3. Results and discussion

4.3.1. Structural properties of the Eu-implanted p-n AlN NWs

In this investigation, one recurs to micro-Raman spectroscopy to obtain information about the crystalline lattice of p-n junction AlN NWs and the effects of Eu-implantation e RTA on these. By using lasers with different wavelengths, different depths of the NW heterostructures can be probed, allowing for examining the infliction of lattice damage in distinct regions of the NW heterostructures. Experiments using two distinct laser excitations are carried out. First, one uses a 442 nm laser excitation to which the NW structures are highly transparent to this excitation; therefore, the micro-Raman signal comes from all the possible regions: p-n AlN top section, GaN NWs templates, and Si substrate. The second excitation is done with the 325 nm line of a He-Cd laser. In this case, due to the strong light absorption in GaN (~1×10^5 cm^{-1} [52]), a penetration depth of ~50 nm in the GaN NWs templates is estimated using Beer-Lambert's law – note that a double absorption needs to be considered for a backscattering geometry. Therefore, the signal comes mainly from the upper part of the GaN NW templates, i.e., close to the interface n-GaN/n-AlN. Furthermore, in this case, Raman scattering occurs under resonant conditions with electronic states of GaN, expectably leading to a substantial enhancement of the scattering intensity of the polar A_1(LO)(GaN) phonon due to Fröhlich interaction [53].

4.3.1.1. Damage evaluation by non-resonant micro-Raman spectroscopy

Figure 3.8(A) shows the micro-Raman spectra of samples *pn* and *pn-5e14* obtained under the 442 nm laser line. The spectrum of the sample *pn* exhibits two Raman peaks, one at 568 ± 1 cm^{-1} related to the E_{2h} phonon of the GaN NW stems [E_{2h} (GaN)] and the other at 654 ± 1 cm^{-1} associated with the E_{2h} phonon of the AlN section [E_{2h} (AlN)]. Despite the experimental accuracy of 0.5 cm^{-1}, strain inhomogeneities within the NWs ensemble induce shifts as high as 1 cm^{-1} to the frequency of the E_{2h} phonon; therefore, the experimental error associated with determining the frequency of the E_{2h} phonon is considered to be 1 cm^{-1}. The

detection of these vibrational modes indicates that the NW heterostructures grow in the hexagonal WZ phase. Furthermore, from the frequencies of these phonons, one can infer that the GaN NW templates grown on a Si (111) substrate are nearly relaxed, assuming the strain-free value as 567.6 cm^{-1} [54]. The same is not valid for the AlN top section since the E_{2h} (AlN) phonon is redshifted compared to the strain-free value of 657.4 cm^{-1} [54]. Such a shift signifies that the AlN top section is biaxially tensile strained due to the growth on GaN stems ($a_{GaN} = 3.189$ Å and $a_{AlN} = 3.112$ Å [55]), similarly to that found in **Chapter 3** for undoped AlN NWs grown on GaN NW templates.

Even though the NW heterostructures studied here consist of AlN and GaN sections doped with Si or Mg, neither LPP modes nor LVMs could be distinguished in the non-resonant micro-Raman spectrum of sample *pn*. On the one hand, as the intensity of LVMs is usually much lower than that of the allowed latttice phonons, the reduced length of the p-AlN section (~60 nm) may explain the non-detection of LVMs associated with Mg incorporation [34,56,57]. On the other hand, besides the frequency shift of the LPP^+ to higher frequencies with increasing free carrier concentration, the LPP^+ also broadens and reduces in intensity [58]. Thus, the non-detection of these coupled modes is tentatively justified by their reduced intensities.

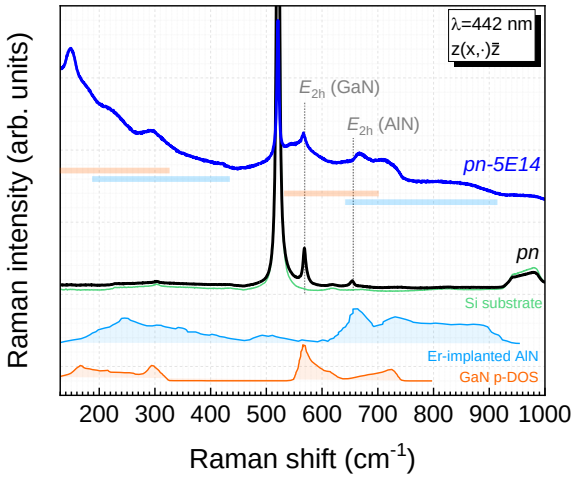

Figure 4.3 Non-resonant micro-Raman spectra of samples *pn* and *pn-5E14*. The calculated GaN p-DOS and the spectrum of Er-implanted AlN layers obtained by V. Davydov et al. [54] are plotted for comparison. Blue and orange horizontal lines close to the spectrum of sample *pn-5e14* correspond to the spectral regions associated with AlN and GaN p-DOS, respectively. The response of the Si (111) substrate is also included.

After Eu-implantation, the micro-Raman spectral shape differs. It consists mainly of broad and unstructured bands rather than narrow peaks associated with BZ center phonon

lines. As can be noticed, the broad features resemble the p-DOS function of both GaN and AlN [54], allowing one to infer that Eu-implantation inflicts crystalline damage in both the AlN NW top sections and GaN NW templates. The first-order Raman peaks also change: the E_{2h} (AlN) phonon is no longer detected while the E_{2h} (GaN) phonon broadens – the FWHM doubles from 6 ± 1 cm^{-1} to 13 ± 1 cm^{-1}.

Monte Carlo simulations, obtained with the SRIM2013 code [59], project an implanted region that extends to a depth of ~150 nm. Maximum Eu ions concentrations of ~2×10^{19} cm^{-3} (0.024 %) and ~1×10^{20} cm^{-3} (0.120 %) for the lowest and highest fluences, respectively, are predicted to occur at ~80 nm. Since the NWs show a high coalescence at the top, the thin layer model would reasonably estimate the vertical distribution of the ions in the structure. However, the SRIM code does not consider channeling effects, resulting in an underestimated implanted range and an overestimated maximum Eu ions concentration. For example, several experimental works have shown that the implanted profile in GaN hosts can extend to depths two or three times deeper than predicted using the SRIM2013 code [50,60–62].

Considering the above, it is conceivable that Eu-implantation affects the GaN NW templates, explaining the previous findings. Still, contrary to what happens to the E_{2h} (AlN) phonon, the observation of the E_{2h} (GaN) phonon at 567 ± 1 cm^{-1}, i.e., without frequency shifting within the experimental error, indicates that the GaN is less affected than AlN. Given that implantation proceeds through the top of the NWs structure, it is expected that the AlN NW top sections are the ones that suffer the most damage, as only a tiny fraction of Eu ions reach the GaN NW templates. Besides, due to the height of the GaN NW templates (~580 nm), it may be the case that only a part of the templates is affected by implantation, i.e., the upper region near the n-GaN/n-AlN interface, while their remaining part is not affected at all. Indeed, this damage distribution may explain why no frequency shift is observed for the E_{2h} (GaN) phonon since micro-Raman measurements using the 442 nm laser line probe the entire depth of the samples.

Figure 4.4(A) displays the micro-Raman spectra of the Eu-implanted AlN p-n junction NWs after RTA at 1000 ℃. The spectral response tends to approach that of the as-grown sample, indicating, to some extent, a recovery of the crystalline damage: the relative intensity of the broad bands associated with lattice disorder decreases, and the first-order Raman scattering processes become dominant again. Furthermore, the characteristics of the E_{2h} (GaN) and E_{2h} (AlN) phonons, i.e., frequency and FWHM, tend to that of the as-grown sample.

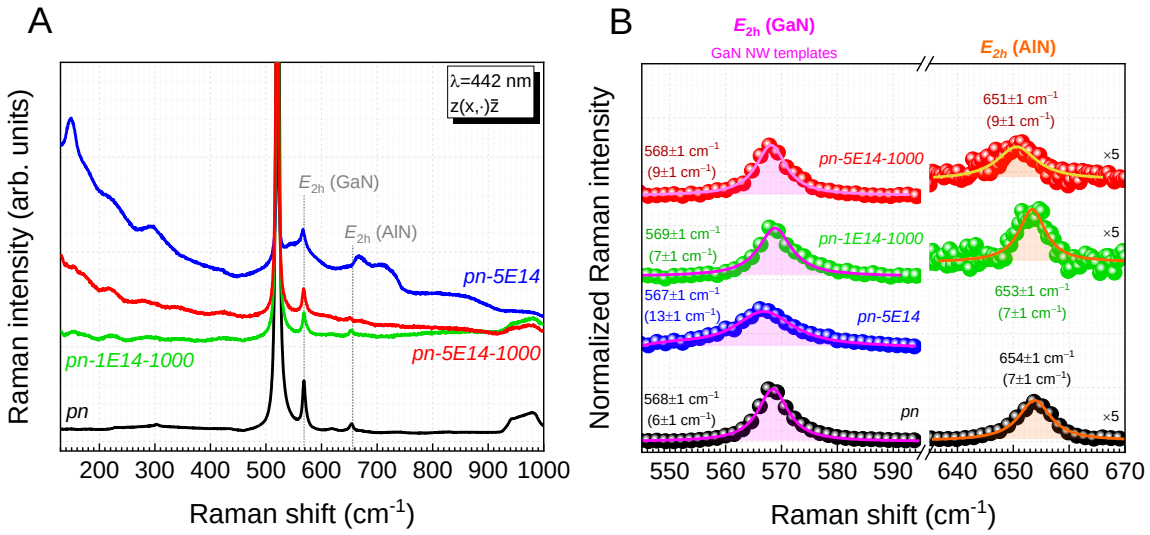

Figure 4.4 (A) Non-resonant micro-Raman spectra of all the NW samples studied. **(B)** Magnification of the previous spectra around the E_{2h} (GaN) and E_{2h} (AlN) after removing the Si substrate contribution. The spectra are normalized to their maximum and vertically shifted.

Figure 4.4(B) magnifies the previous micro-Raman spectra around the E_{2h} (GaN) and E_{2h} (AlN) phonon modes, allowing one to better visualize their behavior with Eu-implantation and RTA treatments; the Lorentzian functions that best fit the experimental data and the respective fitting parameters are included as well.

After RTA, the peak position of the E_{2h} (GaN) phonon remains unchanged within the experimental error of 1 cm^{-1}. This is in line with what had been observed after Eu-implantation (and before RTA), which was tentatively correlated with deeper regions of the unaffected GaN NW templates. Nevertheless, the implantation-induced disorder in the GaN NW templates can be evaluated by the changes in the FWHM of the E_{2h} (GaN) phonon peak. After RTA, the FWHM, which had doubled after implantation, decreases. Even so, independently of the implantation fluence, the FWHM is always higher than that recorded for the as-grown sample, at least due to the introduction of Eu^{3+} in the lattice. For the highest implantation fluence, the FWHM is even greater due to a higher concentration of implantation-induced defects [41,63].

A closer look at the E_{2h} (AlN) phonon allows one to verify that *i)* for sample *n100_pn-1E14-1000*, the phonon peaks at 653 ± 1 cm^{-1} and has a FWHM of 7 ± 1 cm^{-1}, and *ii)* for sample *n100_pn-5E14-1000*, the phonon peaks at 651 ± 1 cm^{-1} and has a FWHM of 9 ± 1 cm^{-1}. In both cases, the SNR is reduced compared to sample *pn*. These results demonstrate that the effects of implantation-induced damage and strain due to lattice expansion are more significant for the highest fluence. This might be caused simultaneously by a higher concentration of Eu in the crystal and a higher density of implantation-induced

defects in the structure [41,63]. According to the discussion in **sub-subsection 3.3.1.3**, the latter hypothesis seems the most reasonable.

By comparing the frequency of the E_{2h} (AlN) phonon in samples *pn-1E14-1000* and *n100-1E14_45-1000* (**sub-subsection 3.3.1.3**), it is possible to verify differences. While in sample *pn-1E14-1000*, the phonon has the same frequency (within the experimental error) as in the respective as-grown sample, the same does not happen for sample *n100-1E14_45-1000*, in which the frequency is lower than that of the as-grown sample *n100* (about 3 cm^{-1}). As implantation fluence and RTA are identical, such differences are tentatively attributed to the lower damage levels provided by channeled implantation geometry [48–50].

The aforementioned results allow one to infer that implantation in channeling conditions results in lower damage levels, which scale with increasing implantation fluence. Furthermore, it is fair to conclude that the RTA at 1000 ℃ allows partial recovery of the crystalline damage introduced by ion implantation in the AlN NW top section. The damage generated in the upper region of the GaN NW templates is also partially recovered.

4.3.1.2. Resonant micro-Raman with electronic states of GaN

Figure 4.5(A) shows the micro-Raman spectra of samples *pn*, *pn-1E14-1000*, and *pn-5E14-1000* obtained with the 325 nm line of a He-Cd laser. For sample *pn*, the spectrum exhibits a prominent peak at 3261 ± 5 cm^{-1} (~3.41 eV), which corresponds to the GaN NBE emission. The intensity of the GaN NBE emission for samples *pn-1E14-1000* and *pn-5E14-1000* is strongly quenched (more than an order of magnitude) and slightly shifts to lower energies. This redshift is more pronounced for the highest fluence (~30 meV). These results confirm that the GaN NW templates are also affected by implantation, particularly the region close to the n-GaN/n-AlN interface.

A closer inspection of the previous micro-Raman spectra (around the yellow shape) allows for distinguishing several peaks, shown in **Figure 4.5(B)**. In addition to the GaN NBE emission, for sample *pn*, two low-intensity Raman peaks are detected at 754 ± 5 cm^{-1} and 1505 ± 5 cm^{-1}, with the frequency of the latter corresponding to about twice the frequency of the first. The first Raman peak corresponds to the A_1(LO) or a *quasi*-LO (GaN) mode, i.e., the mixture of A_1(LO) and E_1(LO) phonons resulting from a slight misorientation between the NWs' *c*-axis and the laser beam incidence. However, the peak position is blueshifted compared to the strain-free frequency of both A_1(LO) and E_1(LO) phonons, respectively 734 cm^{-1} and 741 cm^{-1} [54], indicating that *i)* a compressive uniaxial strain may exist in the upper region of the GaN NW templates [64,65] and/or *ii)* it is no longer a "pure" LO phonon but instead is the coupled mode LPP^+ due to Si-doping of the GaN NW templates [58,66–68]. Both hypotheses will be further discussed below.

Superimposed on the NBE emission, it is possible to observe several sharp peaks. The one at 754 ± 5 cm^{-1} corresponds to the LO (GaN) phonon and does not shift (within the experimental error of 5 cm^{-1}) relative to the as-grown NWs. Assuming that the tensile strain introduced by Eu-implantation follows a "pseudomorphic-like" model due to the generated defects (as proposed in **sub-subsection 3.3.1.2**) and considering the electronic and phonon deformation potentials of GaN, the redshift observed in the GaN NBE emission cannot be distinguished in the LO (GaN) phonon frequency taking into account the experimental error of 5 cm^{-1}.

The other peaks are designated by ω_m, with m an integer value from 2 to 5. To better discern these peaks, a magnification of the previous micro-Raman spectra around the signal of the implanted and annealed AlN p-n junction NWs is shown in **Figure 4.5(B)**. These peaks are at 1505 ± 5 cm^{-1}, 2247 ± 5 cm^{-1}, 2973 ± 5 cm^{-1}, and 3697 ± 5 cm^{-1}; thus, the separation between the consecutive peaks successfully decreases with increasing m.

The appearance of the ω_m peaks can be interpreted as due to a cascade process, as proposed and discussed by R. Martin et al. [69]. According to this model, the absorption of an incident photon (~3.8 eV) with energy above the bandgap leads to the formation of an excited exciton in the continuum of the electronic states. Subsequently, the exciton relaxes through the continuum of states by emitting successive LO (GaN) phonons until it reaches the lowest energy state possible. Therefore, the observed peaks result from the radiative recombination of the exciton as it relaxes through the continuum of electronic states by the emission of phonons. Consistently with this model, the intensity of the peaks increases as they approach the NBE emission peak, that is, when the radiative recombination probability is higher. The fact that separation between consecutive ω_m peaks differ between them and are not equal to LO (GaN), which can be explained as well by this model since higher-order processes involve phonons out of the BZ center, i.e., with $\mathbf{q} \neq 0$.

Returning to the LO (GaN) phonon, **Figure 4.5(C)** compares the micro-Raman response (under resonant conditions) of samples *pn-5E14-1000* and *n0-1E14_45-1000* (i.e., Eu-implanted GaN NWs without Si-doping) around the LO (GaN) phonon. A significant shift of ~20 cm^{-1} to higher frequencies is found for the first sample and a broadening, possibly due to strain or Si-doping effects (assuming that Eu-implantation barely causes any shift within the experimental error). Strain effects can be imposed by the formation of an AlN shell around the GaN NW templates, commonly reported in similar NW structures [70–76]; this would induce a uniaxial compression around the GaN NW templates ($c_{\mathrm{AlN}} < c_{\mathrm{GaN}}$) – in the region of the n-GaN/n-AlN interface where the shell is formed –, resulting in a shift of the LO (GaN) phonon to higher frequencies.

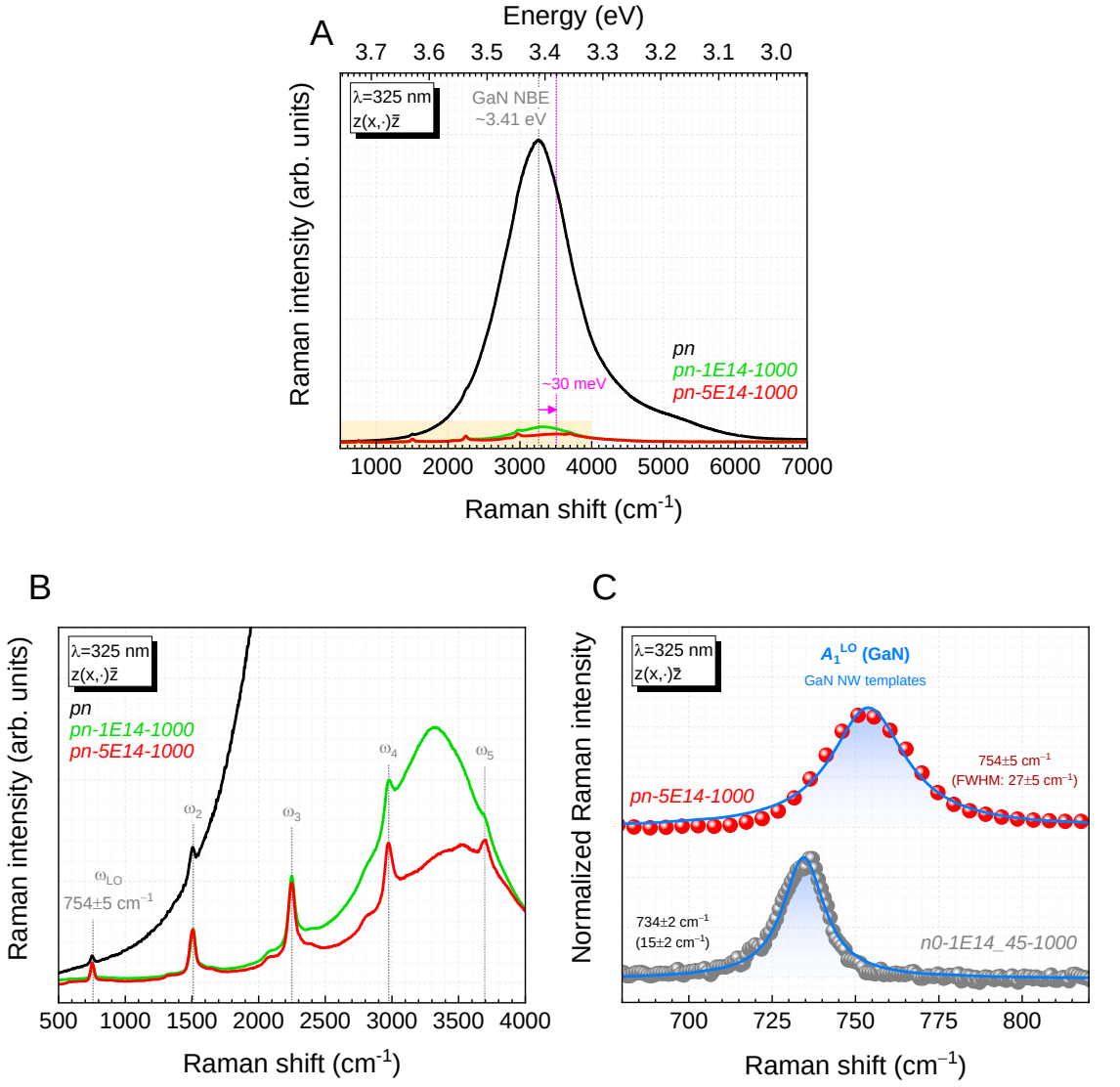

Figure 4.5 (A) Micro-Raman spectra of the AlN p-n junction NWs before and after Eu-implantation and RTA obtained with the 325 nm line of a He-Cd laser in the backscattering geometry $z(x\,\cdot)\bar{z}$. In this case, Raman occurs in resonant conditions with electronic states of GaN. **(B)** Magnification of the previous spectra around the yellow shape to better show the multi-LO (GaN) phonon lines. **(C)** Comparison of the LO (GaN) phonon detected in samples *pn-5E14-1000* and *n0-1E14_45-1000* (the latter spectrum was acquired with an 1800 grooves·mm^{-1} grating).

However, if this strain is the main contributor to the observed shift, the E_{2h} (GaN) phonon would also shift as it is more sensitive to strain, which was not noticed in the previous non-resonant Raman measurements. Therefore, Si-doping should play a significant role in the deviation of the LO (GaN) phonon to higher frequencies due to the interaction between the macroscopic field of the longitudinal phonons and the free carrier plasma

oscillations [58,66–68]. Thus, the detected peak should be the LPP^+ mode associated with the coupling of the LO (GaN) phonon with the free carrier plasma (**sub-subsection 2.2.1**).

The experimental determination of the frequency LPP^+ mode, ω_{LPP^+}, allows one to estimate the concentration of free electrons in the GaN NW templates, n_e. By combining equations (2.10) and (2.11), n_e can be estimated through the following expression [68,77]:

$$n_e = \frac{m_e^* \varepsilon_\infty \varepsilon_0 (2\pi c)^2}{e^2} \cdot \frac{\omega_{LPP^+}^2 (\omega_{LPP^+}^2 - \omega_{LO}^2)}{\omega_{LPP^+}^2 - \omega_{TO}^2}. \quad (4.1)$$

For GaN, it is considered: $m_e^* = 0.2m_0$ [78], $\epsilon_\infty = 5.35$ [79], and $\omega_{LO} = 734.0\ cm^{-1}$ and $\omega_{TO} = 531.8\ cm^{-1}$ (A_1 phonon mode) [54]. By considering the experimentally obtained frequency $754 \pm 5\ cm^{-1}$ for the LPP^+, the estimated concentration of carriers (in this case, electrons) varies between $0.5 - 0.9 \times 10^{18}\ cm^{-3}$. This value is about two orders of magnitude lower than the nominal Si concentration but is still in the range of values that Z. Fang et al. determined (by four-point probe resistivity measurements) for PAMBE-grown Si-doped GaN NWs using similar growth conditions [38]. The estimated values are similar to the free electron concentration required for GaN:Si to exhibit a metallic-like behavior; this was reported to start for concentrations above ~$10^{18}\ cm^{-3}$ [80].

4.3.2. Luminescence of the europium-implanted AlN p-n junction NWs

The focus is now on investigating the optical activation of the Eu-implanted ions in AlN p-n junction NWs after RTA at 1000 ℃. PL and PLE experiments are conducted to evaluate the optical response of the samples, as well as to elucidate the excitation paths below the AlN bandgap energy due to the lack of suitable optical excitation sources in the laboratory to excite them with the above bandgap energy. Additional CL experiments are performed to overcome the excitation light sources' limitations. In this case, the highly energetic electrons can excite Eu ions through all possible direct or indirect mechanisms.

4.3.2.1. Photoexcitation of Eu^{3+} with energy below the AlN bandgap

Figure 2.1 presents the 14 K PL response of the Eu-implanted and annealed AlN p-n junction NWs (for both fluences) using the 325 nm He-Cd laser line as excitation. The PL spectra reveal sharp emission lines corresponding to the intra-$4f^6$ transitions from the excited $^5D_0$ state to the $^7F_{1,2,3}$ states of Eu^{3+}, proving the optical activation of the implanted ions in their trivalent charge state. Low-intensity peaks related to the $^5D_1 \rightarrow {}^7F_1$ and $^5D_0 \rightarrow {}^7F_0$ transitions can also be discerned [81]. The most intense $^5D_0 \rightarrow {}^7F_2$ transition peaks at ~624 nm, indicating that the observed emission is mainly due to Eu^{3+} ions located in the

AlN p-n junction sections – remember that the peak of such transition redshifts from ~622 nm to ~624 nm when the host changes from GaN to AlN (**Figure 3.27**).

Besides intra-4f^6 luminescence, the PL spectra reveal a broad green luminescence band (GL) centered at ~530 nm (~2.3 eV) due to optically active deep-level defects, most likely in the GaN NW templates, as the excitation energy is enough to provide the above bandgap excitation of GaN. Still, based only on these results, it is impossible to rule out that the defects contributing to such luminescence are in the AlN sections of the NW heterostructures. Compared to the GL, the intensity of the Eu^{3+} luminescence increases for the sample implanted with the highest fluence.

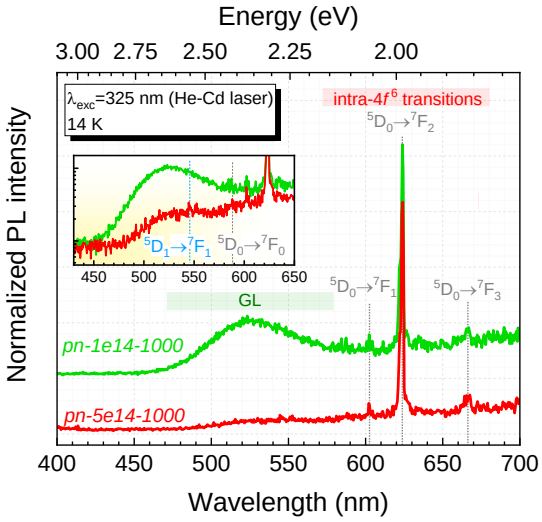

Figure 4.6 14 K normalized PL spectra of samples *pn-1E14-1000* and *pn-5E14-1000*. The spectra were vertically shifted. The inset shows the spectra with intensity in the $\log_{10}$ scale.

Figure 4.7 shows the 14 K HR PL spectra of samples *pn-1E14-1000* and *pn-5E14-1000* around the most intense $^5D_0 \rightarrow {}^7F_2$ transition. Three prominent and well-resolved emission lines can be identified at 623.4 nm (M1), 623.9 nm (M2), and 624.4 nm (M3). Several other peaks can be distinguished at 618.9 nm (m1), 619.3 nm (m2), 621.2 nm (m3), 621.9 nm (m4), 622.8 nm (m5), 626.5 nm (h1), and 627.7 nm (p1). **Table 3.3** compiles the position of all these peaks and compares them with existing data for Eu-implanted GaN NWs and Eu-implanted AlN NWs. To ascertain the origin of these peaks, **Figure 4.7** includes the spectra of samples *n0-1E14_45-1000* (Eu-implanted GaN NWs) and *n100-1E14_45-1000* (Eu-implanted AlN NWs), whose results were already discussed in **Chapter 3**. The three prominent lines (M-peaks) and the peaks at 626.5 nm (h1) and 627.7 nm (p1) originate from the emission of Eu^{3+} implanted into the AlN sections of the NW heterostructures. In contrast, the remaining lines at shorter wavelengths (m-peaks) do not agree with the lines

observed for AlN NWs, but they are close to the positions of Eu^{3+} peaks in GaN NWs. Therefore, the m-peaks are likely due to optically active Eu^{3+} in the GaN NW templates. Nevertheless, one should not discard Mg- and Si-doping of AlN NWs to be responsible for the appearance of new optically active Eu^{3+} centers originating such m-peaks, in similarity to what J. Mishra et al. found in GaN layers co-doped with Eu and Si or Mg [82].

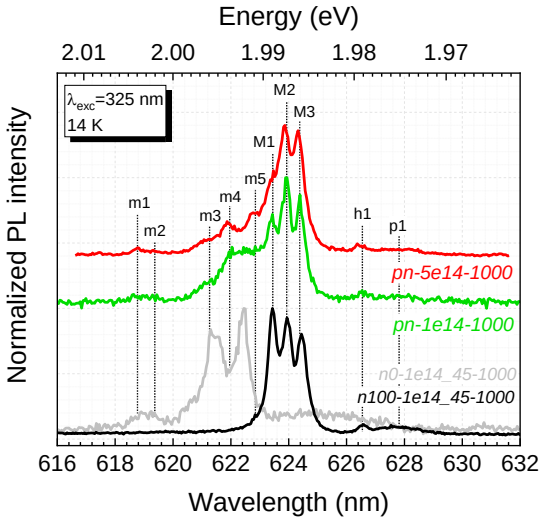

Figure 4.7 14 K normalized HR PL spectra for samples *pn-1E14-1000* and *pn-5E14-1000* around the $^5D_0 \rightarrow {}^7F_2$ transition. The PL spectra of samples *n0-1E14_45-1000* and *n100-1E14_45-1000* are included for comparison.

In **Chapter 3**, peaks M1 and M3 were attributed respectively to the Eu2 and Eu1 centers in AlN NWs, and their relative intensity was found to vary with the RTA temperature. From **Figure 4.7**, one finds that their relative contribution to the luminescence response also changes with implantation fluence; the relative intensity of the M3 line (Eu1) is enhanced when the fluence increases. Furthermore, these lines are slightly broader for the highest fluence, possibly due to the greater implantation-induced disorder level. The larger width and asymmetry of M2 compared to M1 and M3 (for both samples) suggest that such a line corresponds to a superposition of at least two peaks, one that should be related to the Eu1 center and the other to the Eu2; this is similar to that identified for Eu-implanted AlN NWs in **Chapter 3**.

Table 4.1 Compilation of the peaks observed in the 14 K HR PL spectra of samples *pn-1E14-1000* and *pn-5E14-1000* between 616–632 nm. Data from samples *n0-1E14_45-1000* and *n100-1E14_45-1000* (from **Chapter 3**) are also included.

Transition	**Peak**	***pn-1E14-1000*** **(14 K PL)**	***pn-5E14-1000*** **(14 K PL)**	***n0-1E14_45-1000*** **(14 K PL)**	***n100-1E14_45-1000*** **(14 K PL)**
	m1	618.7 (li)	618.9 (li)	619.0 (b)	
	m2	619.3 (li)	619.3 (li)		619.7 (li)
				620.6	
	m3	621.1 (s)	621.2 (s)	621.3 (o)	621.1 (li)
	m4	621.9 (o)	621.9	621.7 (o) **(Eu1)**	
$^5D_0 \rightarrow {}^7F_2$ or $^5D_1 \rightarrow {}^7F_4$	m5	622.7 (o)	622.8	622.4 **(Eu1)**	
	M1	623.4	623.4 (s)		623.4 **(Eu2)**
	M2	623.9	623.9		623.9 **(Eu1/Eu2)**
	M3	624.4	624.3		624.4 **(Eu1)**
				625.5 (b)	
	h1	626.5	626.4		626.6
	p1A	627.7 (b)	627.3		627.8 (b)
	p1B		628.1		

(b) broad peak, (li) low-intensity peak, (o) overlapped peak, (s) shoulder

The local structure of the Eu^{3+} centers in AlN remains to be identified and cannot be accurately done based only on the conducted experiments. However, it is worth mentioning that in GaN hosts, for which most of the research has been carried out, the lattice environment of the Eu^{3+} centers is still open to discussion, with some ambiguities regarding their attribution. The predominant centers in GaN are commonly assigned to complex defects involving Eu^{3+} in a substitutional (or near substitutional) Ga site and nitrogen and gallium vacancies [83–86]. Analogously, theoretical studies in AlN hosts predicted that Eu^{3+} could form stable complexes with vacancies or oxygen impurities [88], likely present in the PAMBE-grown NWs. These complex defects possess levels in the upper third of the forbidden gap, possibly explaining the photoexcitation of such centers with energy below

the AlN bandgap. Therefore, and since implantation generates a high density of vacancies [61], one can speculate a similar local structure for the predominant Eu^{3+} centers in AlN NWs. Furthermore, it would explain why the relative contribution of both centers would vary with RTA temperature and implantation parameters.

By comparing the spectral shape of samples *pn-1E14-1000* and *n100-1E14_45-1000*, it is noticeable that the relative contribution of Eu1 and Eu2 changes as well; Eu1 is intensified for the first sample (i.e., Eu-implanted AlN p-n junction NWs). Two hypotheses can explain it: *i)* different implantation geometry or *ii)* Si- or Mg-doping influence. The total defect density is expected to be lower when implantation is performed in channeling conditions due to the reduced probability for direct collisions with the lattice atoms [48]; furthermore, micro-Raman results proposed lower damage in the sample *pn-1E14-1000*. As a result of different damage levels, the interaction between Eu^{3+} and existing defects should be different, possibly accounting for the changes observed in the relative PL intensity of the Eu1 and Eu2 centers. Furthermore, according to M. Soares et al., trivalent erbium ions were found to be on substitutional sites when implantation was done in a channeled configuration while being displaced from this site for implantation with a certain angle to the *c*-axis [87], hence resulting in centers with distinct emission properties. Besides the implantation geometry, the possibility of Mg and Si doping of AlN promoting specific Eu^{3+} centers cannot be discarded. For example, in GaN:Eu layers, Si co-doping was found to quench the Eu^{3+} luminescence intensity, while Mg co-doping intensified it and promoted not only new optically active centers but also a distinct relative contribution of the predominant ones existing without Mg (Eu1 and Eu2) [82,88]. Furthermore, charge compensation for Mg-doping can occur at the expense of V_N defects [89], increasing the PL intensity of the complex centers involving Eu^{3+} and these defects. If Mg-doping is the reason behind the increase in the relative intensity of the Eu1 center, one can tentatively relate such a center with Eu_{Al}–V_N complex defects. Indeed, B. Mitchell et al. provided strong evidence that the Eu1 center in GaN also involves V_N defects [83]; this would mean a similar structure for the predominant Eu1 center in both hosts.

Figure 4.8 shows temperature-dependent HR PL spectra of samples **(A)** *pn-1E14-1000* and **(B)** *pn-5E14-1000* around the $^5D_0 \rightarrow {}^7F_2$ transition from 14 K to 300 K. For both samples, the integrated PL intensity quenches with increasing the temperature due to competitive thermally activated nonradiative processes. The obtained ratio between the integrated PL intensity measured at 300 K and 14 K, $I_{300\ K}/I_{14\ K}$, is ~50 % independently of the sample; these agree with the value obtained for Eu-implanted AlN NWs after RTA at 1000 ℃ in analogous excitation conditions (see **Figure 3.33**).

In addition to the intensity quenching, the Eu^{3+} emission lines broaden and slightly blueshift with increasing temperature. The broadening renders a proper

identification/resolution of the peaks for temperatures above 150 K. Even though to identify the lines, the spectral shape hints that the Eu1 center has better thermal stability than the Eu2. These findings are once again in line with those presented in **Chapter 3** for Eu-implanted AlN NWs.

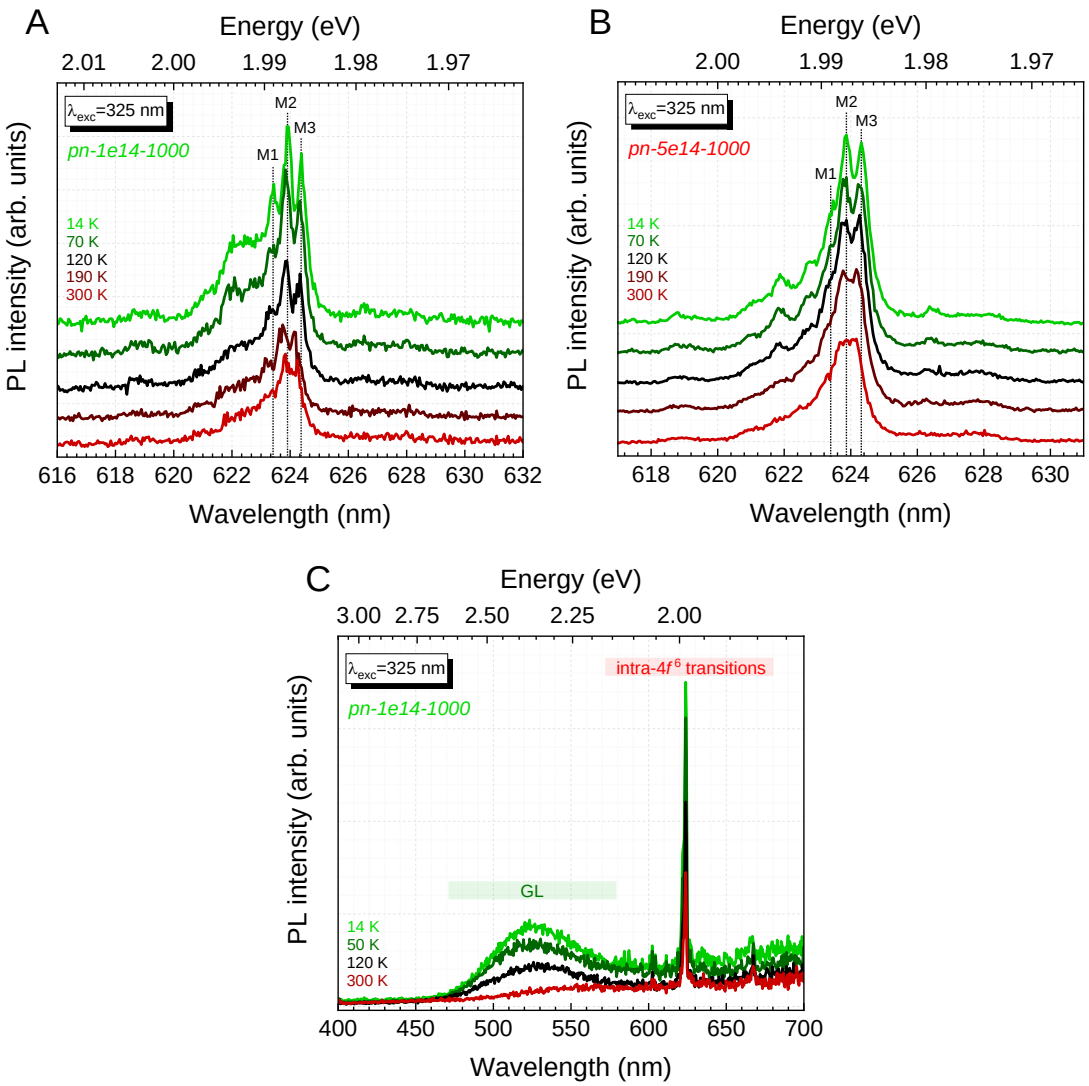

Figure 4.8 Temperature-dependent HR PL spectra of samples **(A)** *pn-1E14-1000* and **(B)** *pn-5E14-1000* around the $^5D_0 \rightarrow {}^7F_2$ transition obtained using the 325 nm line of a He-Cd laser as excitation. **(C)** Temperature-dependent PL spectra of sample *pn-1E14-1000* in the 400–700 nm spectral range.

The intensity of the GL band also quenches with increasing temperature, as exemplified in **Figure 4.8(C)** for sample *pn-1E14-1000*. However, in this case, the decrease is much more pronounced; at 300 K, its integrated intensity is less than 10 % of that at 14 K.

Figure 4.9 compares the RT PL response of samples *pn-1E14-1000* and *pn-5E14-1000* in the 600–635 nm spectral range. The integrated intensity of the Eu^{3+}-related luminescence increases about three times for the sample implanted with the highest fluence. Such an enhancement was predictable due to the higher concentration of Eu in the lattice. However, the emission intensity is lower than expected if a direct proportionality is assumed between Eu concentration and Eu^{3+}-related luminescence intensity. This can be caused by *i)* a higher concentration of competing nonradiative defects in the lattice for sample *pn-5E14-1000* or *ii)* the incorporation of Eu^{3+} in different lattice environments with reduced optical activation efficiency. A similar work conducted in Eu-implanted GaN NWs also found that emission intensity and implantation fluence did not follow a proportional trend 1:1 [24]. The authors found that, for higher fluences, the fraction of Eu in the divalent charge state (2+) increases due to residual implantation defects, and local EuN-like arrangements can be formed. These findings likely explain the smaller increase (compared to the proportional trend 1:1) or saturation of Eu^{3+}-related luminescence intensity in NWs with increasing implantation fluence [24].

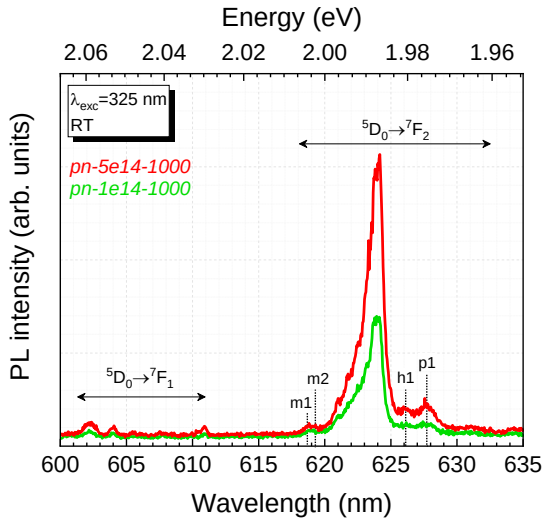

Figure 4.9 RT PL spectra of samples *pn-1E14-1000* and *pn-5E14-1000* (He-Cd laser excitation).

Figure 4.10 compares the PL spectrum of sample *pn-5E14-1000* obtained with the 325 nm excitation of the He-Cd laser and the Xe lamp to infer the influence of the excitation density. In both cases, the spectrum is dominated by the intra-$4f^6$ luminescence, with no change due to the different excitation densities being perceived. Even so, it is possible to notice that the resolution improves in the spectrum obtained with the He-Cd as the excitation source. This is only due to the better resolution of the spectrometer.

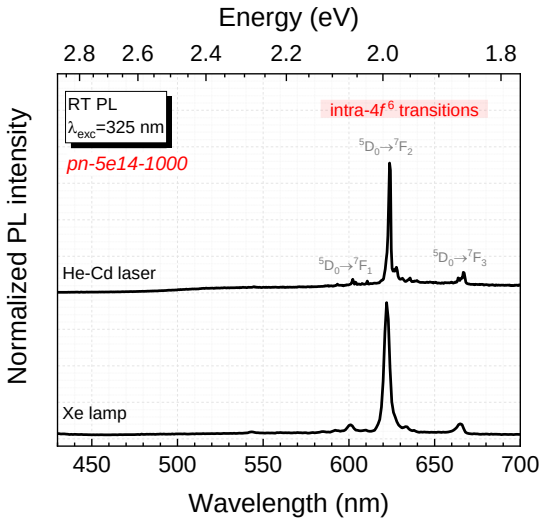

Figure 4.10 Comparison of the normalized RT PL spectra of sample *pn-5E14-1000* obtained with the 325 nm excitation of the He-Cd laser and the Xe lamp.

4.3.2.2. Excitation channels for the Eu^{3+} luminescence

Wavelength-dependent PL and PLE studies are conducted to monitor the excitation paths (below the AlN bandgap) that contribute to the Eu^{3+} luminescence in the NW heterostructures.

Figure 4.11 shows the RT PL spectra of samples *pn*, *pn-1E14-1000*, and *pn-5E14-1000* exciting with 325 nm (Xe lamp). In this case, the luminescence of sample *pn* consists of a blue luminescence band (BL) peaking at ~460 nm (~2.7 eV) and a broad and asymmetric luminescence band in the green/yellow spectral region (GL/YL) peaking at ~570 nm (~2.2 eV), as better noticed in the inset. After Eu-implantation and RTA, the contributions to the luminescence differ, indicating that the nature and balance of defects existing in the NW heterostructures are affected. The BL and the GL/YL are no longer observed, giving rise to a dominant intra-4f^6 luminescence and a broad green luminescence band (GL) peaking at ~520 nm (~2.4 eV).

The broad emission bands are likely due to radiative recombination at deep-level defects in the NW heterostructures. The PL bands observed in the as-grown AlN p-n junction NWs are similar to those observed in GaN and AlN NWs (**sub-subsection 3.3.2.2**); assuming an identical origin, the BL is likely due to defects involving V_{Al} and complex defects involving these and oxygen impurities in the AlN NW sections [90–95], while the GL/YL is tentatively assigned to lattice defects and impurities in the GaN NW templates [96–98].

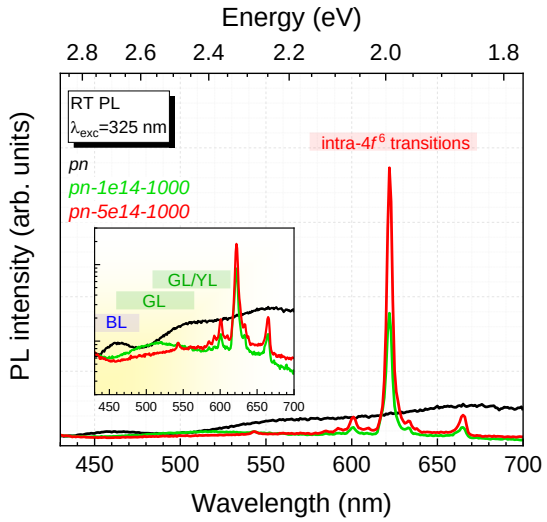

Figure 4.11 RT PL spectra of samples *pn*, *pn-1E14-1000*, and *pn-5E14-1000* obtained with the 325 nm excitation (Xe lamp). The inset shows the spectra in the $\log_{10}$ scale.

Figure 4.12 shows the RT PLE spectra of sample *pn-5E14-1000* when monitoring the $^5D_0 \rightarrow {}^7F_2$ emission. For energy below the AlN bandgap, photo-excitation of Eu^{3+} can occur through two excitation bands in the UV region: *i)* X1 centered at ~350 nm (~3.5 eV) with FWHM of ~55 nm (equivalent to ~0.5 eV), and *ii)* X2 centered at ~270 nm (~4.6 eV) with FWHM of ~30 nm (equivalent to ~0.5 eV). The excitation bands X1 and X2 match those found in Eu-implanted AlN NWs and layers. Besides the X1 and X2 excitation bands, the RT PLE spectrum monitored at the $^5D_0 \rightarrow {}^7F_2$ transition reveals a tiny shoulder at ~364 nm (~3.4 eV) associated with the GaN absorption edge. Such a contribution may come from optically active Eu^{3+} in the GaN NW templates (already suggested by micro-Raman and PL results) or from defects in the GaN NW templates whose emission lies in this spectral region (for example, a possible reminiscent contribution from the broad and asymmetric GL band). Additionally, it is possible to notice a narrow and low-intensity peak at 471 nm; this is related to the $^5D_2 \leftarrow {}^7F_0$ transition and confirms the possibility of directly exciting the Eu^{3+} into excited $4f^6$ states in AlN hosts. The PLE response of sample *pn-1E14-1000* is identical to that of sample *pn-5E14-1000*.

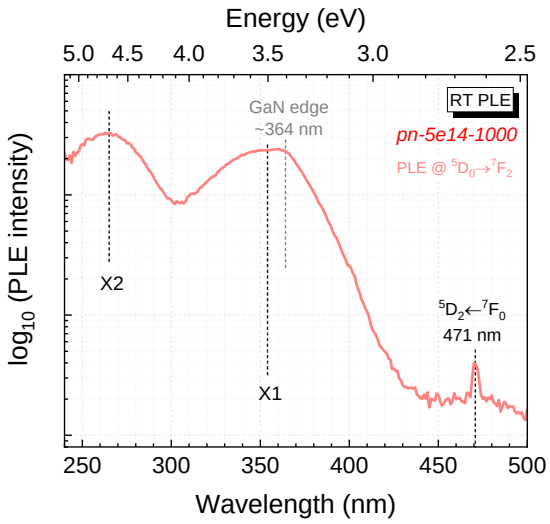

Figure 4.12 RT PLE spectra of sample *pn-5E14-1000*, when monitoring at the maximum of the $^5D_0 \rightarrow {}^7F_2$ transition.

In order to understand whether the recombination channels in the samples are the same when the excitation is done through the two broad bands X1 and X2, PL experiments were done by fixing the emission wavelength of the Xe lamp at 270 nm (i.e., resonant with X2). **Figure 4.13** shows the RT PL spectra of samples *pn*, *pn-1E14-1000*, and *pn-5E14-1000* exciting with 270 nm. Compared to the spectra obtained with $\lambda_{exc} = 325$ nm (in **Figure 4.11**), the response is distinct. The PL spectrum of sample *pn* consists of two maxima in the spectral region of the BL; the inset in **Figure 4.13** reveals that these maxima differ when varying the excitation angle, indicating that the PL signal is modulated by the coherent superposition of multiple reflections in an optical cavity, whose origin is not clear but is tentatively attributed to the reflections between the top of the AlN and the bottom part of the GaN NW section. After Eu-implantation and RTA, and as observed when excited with the 325 nm photons, the BL band is quenched, while the broad and asymmetric GL and the intra-4f^6 emission appear in the PL spectra. However, in this case, it is possible to notice an ultraviolet luminescence (UVL) band centered at ~320 nm (~3.9 eV). The UVL and the GL are only observed after Eu-implantation and RTA; therefore, they are likely due to implantation-induced defects. For example, the UVL is commonly observed in implanted AlN samples, tentatively correlated with implantation-induced defects like V_{Al} and their complexes formed with oxygen impurities. Despite being related to defects similar to those contributing to the BL, the complexes formed are distinct or have a different charge state [90].

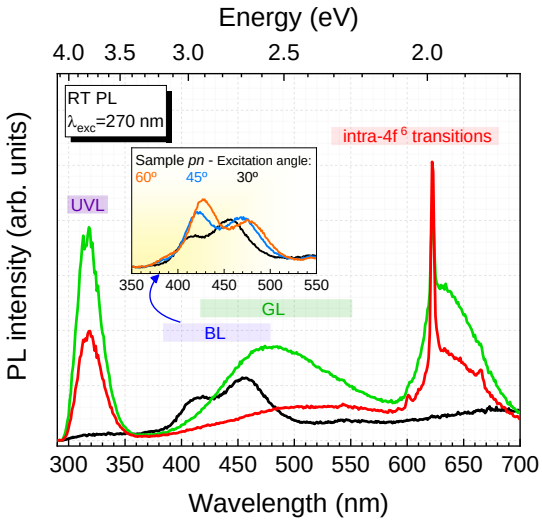

Figure 4.13 RT PL spectra of samples *pn*, *pn-1E14-1000*, and *pn-5E14-1000* obtained with the 270 nm excitation wavelength (Xe lamp). The broad band denoted by an asterisk (*), superimposed to the intra-4f^6 luminescence, corresponds to the 2nd-order contribution of the UVL. The inset shows the PL response of sample pn when changing the excitation angle to the NWs c-axis.

Under both excitations (270 nm and 325 nm), the relative intensity of the Eu^{3+} luminescence compared to deep-level defects' emission (UVL and GL) increases for sample *pn-5E14-1000*, hinting a different balance of radiative defects with increasing the implantation fluence. F. Chen et al. observed that the Eu^{3+} luminescence was enhanced to the detriment of defect-related emission bands with increasing fluence in AlN thin films [99]. Such relative enhancement of the Eu^{3+} luminescence implies that the relaxation mechanisms depend on the implantation fluence. From micro-Raman measurements, defects' density increased for the highest fluence. Thus, a charge redistribution in the crystal may occur, favoring or hindering the formation of some defects. Since no different radiative channels are noticed in the PL spectra of samples *pn-1E14-1000* and *pn-5E14-1000*, such additional defects may introduce nonradiative deexcitation paths. These can also help explain why the Eu^3 luminescence intensity is not proportional to implantation fluence and why the contribution from defects-related emission decreases. Furthermore, as the implantation-induced damage depends on the implantation fluence, it can presumably explain the dissimilar intensity ratio between the Eu1 and Eu2 centers found for both samples in **sub-subsection 4.3.2.1**.

Figure 4.14 compares the RT PLE spectra of sample *pn-5E14-1000* when monitoring the $^5D_0 \rightarrow {}^7F_2$ transition and the UVL. As for the Eu^{3+}-related luminescence, an excitation band in the same spectral range as X2 is the predominant excitation path for the UVL band. As discussed in **Chapter 3**, the results suggest that X1 and X2 cannot be dissociated

from defects with energy levels in the forbidden gap of the host. These defects can be directly related to Eu^{3+}, namely isovalent traps or complex defects involving the ions and lattice defects or impurities, or to defects with Eu^{3+} in their vicinities. In this case, the excitation may proceed through a non-radiative (Auger-like) ET from excitons localized at the defect-related traps to the 4*f* electrons [100–102], requiring proximity between the defect and Eu^{3+} (or direct involvement of them) and resonance between the exciton recombination energy and excited intra-$4f^6$ states of Eu^{3+} [102,103]. Once excited, Eu^{3+} deexcites through radiative (intra-$4f^6$ luminescence) and nonradiative (multi-phonon emission) relaxation within the 4*f* manifold or by transferring its energy non-radiatively back to the host. Notwithstanding, the ET does not require a total quenching of the defects-related emission bands, likely justifying why they are still visible in the PL spectra [102,103].

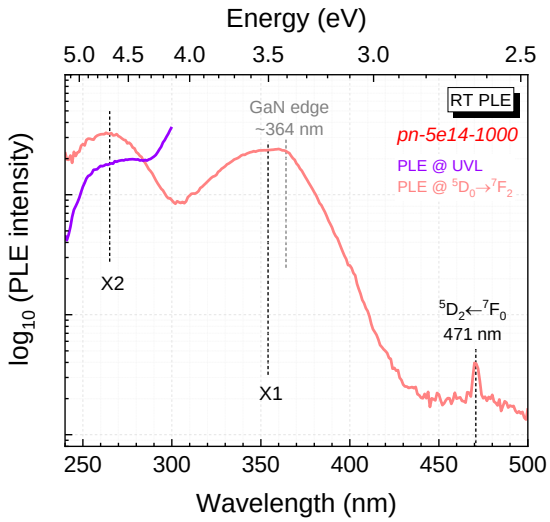

Figure 4.14 RT PLE spectra of sample *pn-5E14-1000*, with the emission wavelength fixed at the maxima of the $^5D_0 \rightarrow {}^7F_2$ transition and the UVL.

4.3.2.3. Exciting Eu^{3+} using high energetic electrons

In CL experiments, the excitation source is a high-voltage electron beam. Therefore, contrary to PL, where photons with specific energy excite the material, the energetic electrons can produce luminescence through all the available radiative channels in the sample. Therefore, in CL, the excitation of Eu^{3+} can proceed through direct (impact excitation by hot electrons) or indirect processes. Indirect ones may involve the previously discussed mechanisms when the excitation energy is below the AlN bandgap (i.e., non-radiative energy transfer from defect-related traps to 4*f* electrons) and responsible

for the PL response, as well as an additional path related to band-to-band excitation of carriers at the AlN p-n junction NWs.

Figure 4.15(A) shows the RT CL spectra of samples *pn-1E14-1000* and *pn-5E14-1000*. The spectra consist of strong emission sharp lines due to transitions from the Eu^{3+} excited states ($^5D_2$, $^5D_1$, and $^5D_0$) to the ^7F_J states. As in PL experiments, the $^5D_0 \rightarrow {}^7F_2$ transition is the most intense one. However, in this case, the relative intensity of the emissions arising from higher energy $4f^6$ excited states (e.g., $^5D_1$ and $^5D_2$) increases, such that the $^5D_1 \rightarrow {}^7F_1$ transition at ~545 nm is the second most intense. This result indicates that the predominant excitation and deexcitation paths for the Eu^{3+} luminescence are dissimilar in PL and CL experiments. As discussed in **Chapter 3**, a possible explanation for such a behavior lies in the longer lifetime of the $^5D_0$ state (of the order of 200–300 μs) compared to the higher energetically $^5D_1$ and $^5D_2$ ones (of the order of 2 μs). The much higher excitation density in CL may lead to a re-excitation of the Eu^{3+} in the $^5D_0$ state into higher ^5D_J states, resulting in a higher probability of radiative decay from such states to the ^7F_J [103–105].

Besides the intra-$4f^6$ luminescence, it is possible to notice the UVL. Its relative intensity decreases for the sample implanted with the highest fluence, as observed previously in PL experiments. Nevertheless, the intensity reduction of the defect-related emission in CL compared to PL indicates that this excitation process favors the Eu^{3+} luminescence over other defect-related radiative paths, corroborating the change in the excitation/deexcitation mechanisms. It is worth mentioning that the AlN NBE emission is not detected in the CL spectra of the Eu-implanted and annealed AlN p-n junction NWs; in fact, it was not observed even in non-implanted samples with similar structure [34], nor in the undoped AlN NWs studied in **Chapter 3**.

The comparison of the CL spectra around the most intense intra-$4f^6$ transitions (between 535–675 nm) for both samples is presented in more detail in **Figure 4.15(B)**. The integrated intensity increases about three times for the sample implanted with the highest fluence, which agrees with the intensity increase previously found in the PL experiments (**Figure 4.9**).

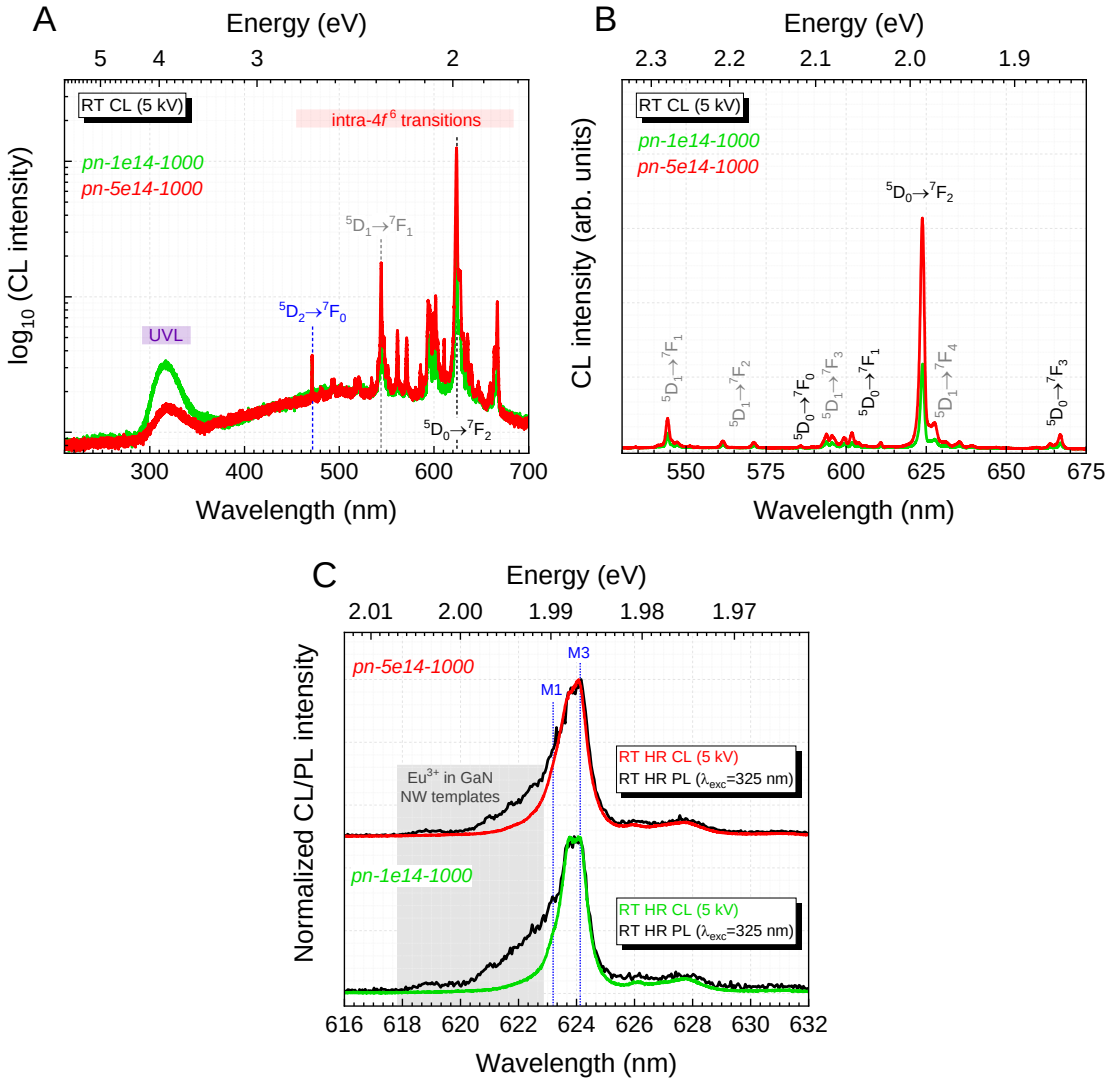

Figure 4.15 (A) RT CL spectra of samples *pn-1E14-1000* and *pn-5E14-1000*. **(B)** Enlargement of the previous spectra around the intra-$4f^6$ luminescence. **(C)** Comparison of the RT HR CL and RT HR PL spectra for both samples around the $^5D_0 \rightarrow {}^7F_2$ transition.

When comparing the spectral shape of the $^5D_0 \rightarrow {}^7F_2$ transition obtained in RT PL and RT CL experiments for both samples, it is possible to notice a shoulder at higher energies in PL, which is not observed in CL – **Figure 4.15(C)**. Taking into account the penetration depth of the PL technique (with $\lambda_{exc} = 325$ nm), which penetrates the entire AlN section and goes up to ~100 nm in the GaN NW templates (the light absorption in GaN is high [52]), compared to CL, which for 5 kV electrons is about ~150 nm (i.e., analysis restricted to the AlN sections), the appearance of the shoulder can be due to optically active Eu^{3+} in the GaN NW templates, strengthening the previous attribution.

By exploring a different CL geometry (excitation and collection perpendicular to the NWs' growth axis – in cross-section) and taking advantage of the spatial resolution of the CL technique, an RT CL intensity map (around the $^5D_0 \rightarrow {}^7F_2$ transition) is done by probing distinct positions of the NW heterostructures along their length, allowing to confirm the localization of the optically active Eu^{3+}. This RT CL intensity map obtained for sample *pn-5E14-1000* is depicted in **Figure 4.16(A)**, as well as the bird-view SEM image of the sample; the green line indicates the line along which the excitation scan was made. It is observed that the highest CL intensity results when probing the n- and p-type AlN sections, confirming that most of the implanted ions reside there. Besides, optically active Eu^{3+} can be found close to the n-GaN/n-AlN interface, as previously unveiled by micro-Raman and PL results. These results confirm that the implanted region extends deeper in the NW heterostructures than predicted in SRIM2013 simulations, which is explained by the channeling effects of implantation done along the *c*-axis [49].

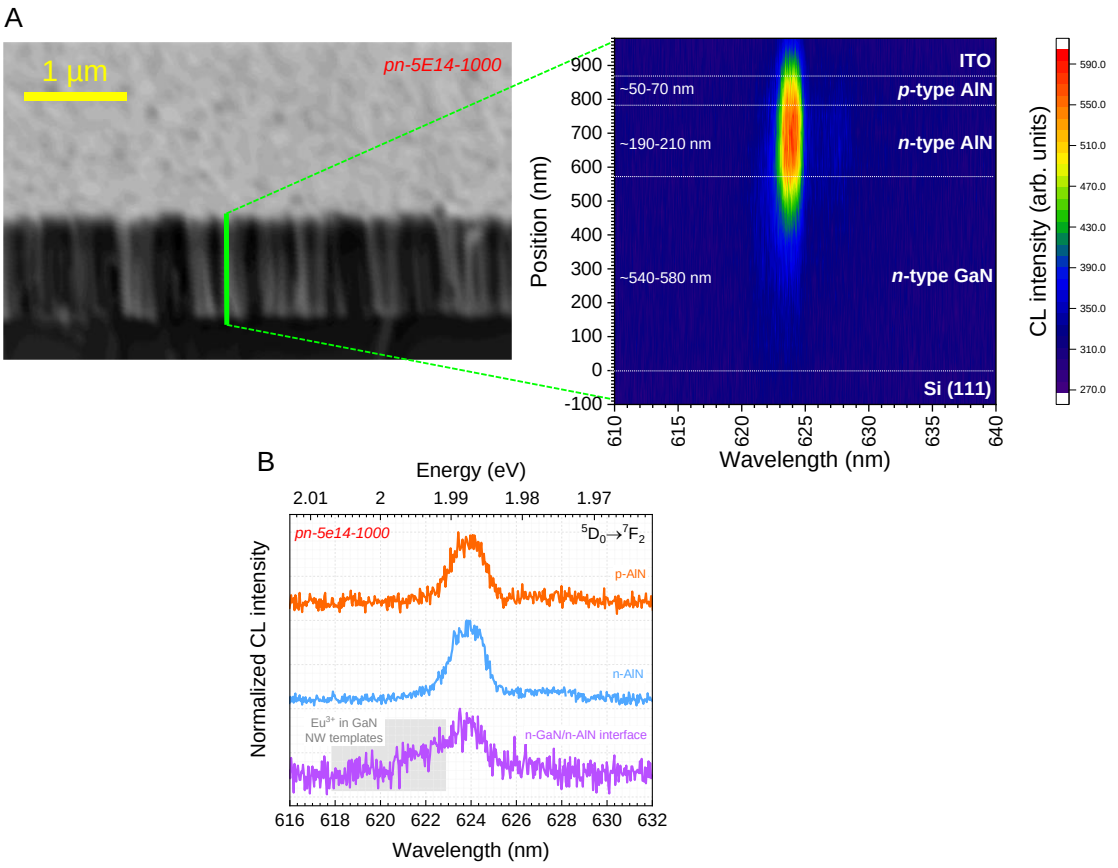

Figure 4.16 (A) Bird-view SEM image and respective RT CL intensity map for sample *pn-5E14-1000* around the $^5D_0 \rightarrow {}^7F_2$ transition. The CL signal was measured by focusing the electron beam along the NWs axis (represented by the green line). **(B)** RT normalized CL spectra of the same sample obtained at distinct heights of the NWs: p-AlN (orange), n-AlN (blue), n-GaN/n-AlN interface (violet). These measurements were done after the deposition of the ITO contact.

Furthermore, in these deeper regions, it is possible to observe a shoulder at the shorter wavelength side of the principal peak of the $^5D_0 \rightarrow {}^7F_2$ transition. The shoulder is better perceived in **Figure 4.16(B)**, where the CL spectra obtained at three distinct heights of the NWs (p-type AlN, n-type AlN, and interface n-GaN/n-AlN) are shown. This result further supports the conclusion from comparing PL and CL spectral shapes around the same transition that the emission at higher energies is due to Eu^{3+} in the GaN NW templates.

4.3.3. Electroluminescence of the proof-of-concept NW LEDs

The deposition of transparent 100×100 μm^2 ITO pads on the top of the AlN p-n junction NW ensembles allows for current injection in the NW heterostructure. At the same time, red light can be extracted with reduced absorption [51]. Initial electroluminescence tests are done on the processed devices to infer the possibility of obtaining the intended intra-$4f^6$ red luminescence.

Figure 4.17(A) shows the RT EL spectrum of a device tested on sample *pn-5E14-1000* when a forward bias of 20 V is applied (positive voltage on the top contact). Tests on two other devices showed a similar EL response. The Eu^{3+}-related luminescence dominates the spectrum; however, additional low-intensity and unstructured signals are observed throughout the visible spectral region, likely due to the radiative recombination at defects. Despite the contribution of the defects, the EL response is more similar to that of CL than that of PL.

For sample *pn-1E14-1000*, only one of the five tested devices exhibits an EL signal (associated with the $^5D_0 \rightarrow {}^7F_2$ transition). In addition to the non-reproducibility, the device that shows an EL response has a very weak signal compared to devices made on sample *pn-5E14-1000* (about two orders of magnitude lower) for a similar applied bias and current flowing through the device, as demonstrated in the inset in **Figure 4.17**. Increasing the bias further caused the device to stop working, possibly because it overheated, damaging it to a point of no return. Such poor performance is puzzling since the difference in the Eu^{3+} luminescence intensity in PL and CL was only two to three times lower for sample *pn-1E14-1000*, in close agreement with the implantation fluences used. Furthermore, micro-Raman results indicated that sample *pn-5E14-1000* had a higher density of defects and strain, hinting that these devices would have a higher failure rate. Therefore, the explanation for this should rely on the processing of the LEDs (ITO contacts' deposition) rather than involving remaining implantation-induced damage or the low concentration of optically active Eu^{3+}.

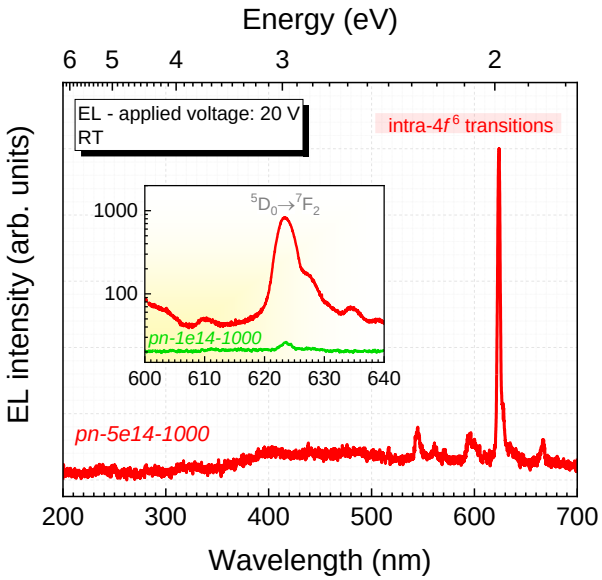

Figure 4.17 RT EL spectrum of a device made on sample *pn-5E14-1000* under a forward bias of 20 V (current of ~1 µA). The inset shows a comparison of the EL response of the previous device with the device made on sample *pn-1E14-1000* that exhibited an EL signal.

Figure 4.18 shows the representative I–V characteristic of the devices made on the *pn* and *pn-5E14-1000* samples. In both cases, the curve presents a diode-like rectifying behavior with a difference of five and two orders of magnitude in the current flowing between −10 and +10 V for *pn* and *pn-5E14-1000*, respectively. Furthermore, after Eu-implantation and RTA, the current flowing under forward bias is reduced by about four orders of magnitude compared to the as-grown samples. In an attempt to describe the behavior of the devices, their I–V characteristics are fitted considering the modified Shockley equation given in equation (2.32) [106]. The best-fit results are presented in the inset of **Figure 4.18**. Two things stand out from the fit: *i)* for low bias (below ~6 V), the model does not properly fit the curve, and *ii)* the ideality factors η obtained at higher bias are $\gg 1$ (~65 for sample *pn* and ~70 for sample *pn-5E14-1000*). Indeed, for III-N NW LEDs, ideality factors higher than ~10 are commonly found in the literature [46,107–111].

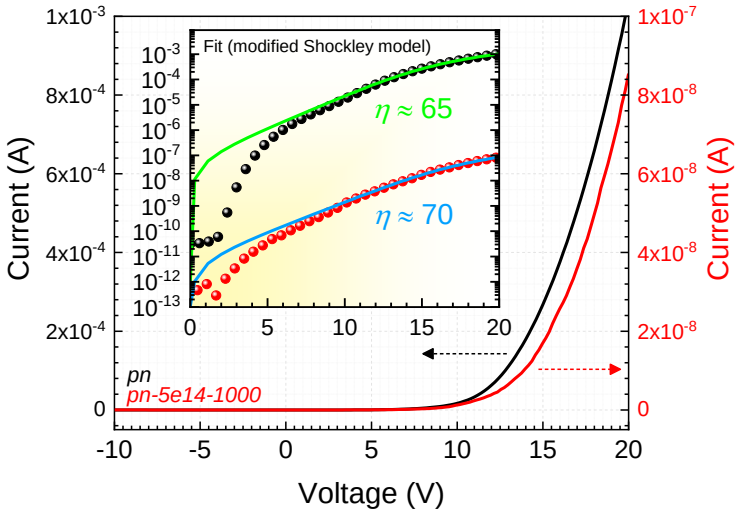

Figure 4.18 Representative I–V characteristic of devices made on samples *pn* and *pn-5E14-1000* (note the different current scales). The inset shows the same graph with the current in the $\log_{10}$ scale; the solid lines correspond to the best-fit results obtained considering the modified Shockley model – equation (2.32).

The high ideality factors imply that the realized devices largely deviate from the ideal behavior of a p-n junction LED. This means that despite having managed to obtain a rectifying behavior, there are problems to be solved regarding the development of LEDs with better electrical performance. These problems may arise from the high resistivity of the n- and p-type doped AlN sections due to the high ionization energy of Si donors (~282 meV in AlN layers [112]; recently, R. Vermeersch et al. showed the presence of shallow donor states with ionization energy of 75 meV in Si-doped AlN NWs [35]) and Mg acceptors (500–600 meV in AlN layers [112,113]). It can also be caused by a high resistance at the existing interfaces (n-Si/n-GaN, n-GaN/n-AlN) or non-optimized Schottky p-contacts (p-AlN/ITO).

R. Vermeersch et al. proposed that at low bias, the carrier transport in AlN p-n junction NWs would be conditioned by trap-assisted tunneling (TAT) mechanism, in which carriers can tunnel through energy barriers by interacting with defect-related traps that possess energy levels in the forbidden gap [107]. This mechanism might explain the disagreement of the Schottky model at low bias.

The increase in resistivity in the NW heterostructure due to reminiscent defects induced by implantation may explain the lower current flowing through the structure. This hypothesis is further corroborated by the increase in the value of the series resistance R_s, which limits the current flow once the p-n junction barrier is lowered. In a simple manner, it can be derived from the linear part of the diode I–V characteristic at high bias:

$R_s = dV/dI|_{\text{at high bias}}$ [106]. The defects resulting from Eu-implantation can increase the resistivity of the NW heterostructure by introducing parasitic radiative or non-radiative recombination paths, as well as by altering the balance of defects in the lattice, possibly resulting in the compensation of Si donors and Mg acceptors, i.e., decreasing the concentration of available free carriers.

Furthermore, one should consider that evaluating the electrical response of an ensemble of NWs is a complex task because of the inhomogeneous electrical properties of different NWs or the coalescence of the NWs in the AlN top sections. On the one side, the first comes from the difficulty in controlling the doping such that carriers' concentration may vary from nanowire to nanowire. In order to consider this effect, M. Musolino et al. proposed a modification of the Shockley model where the ideality factor would vary with the bias, meaning that with increasing the bias, it would be possible to have the contribution of NWs with successively poorer electrical transport properties [108]. The existence of NWs with distinct heights may result in some of them not being electrically connected, contributing to a reduced EL signal and current flowing through the device. On the other side, albeit coalescence can be advantageous for metal deposition, avoiding metal leakage and eventual short-circuits, it can induce the formation of boundary dislocations and stacking faults, which would be detrimental for electrical (preferred conduction paths) and optical (non-radiative recombination) properties [114,115].

Figure 4.19(A) compares the I–V characteristic of the device made on sample *pn-1E14-1000*, for which the EL signal was obtained, with that representative of the devices made on sample *pn-5E14-1000*. As can be seen, the diode-like rectifying behavior is no longer observed for the sample implanted with the lowest fluence. As discussed above, implantation-induced defects and the resulting strain must not be the main reasons behind this behavior; otherwise, these would be aggravated for the highest fluence. A possible explanation for this involves devices' processing.

One key parameter when growing self-spontaneous NWs by PAMBE is the substrate temperature; however, in the PAMBE setup used, it can decrease about 30–40 ℃ from the center to the periphery of the 1-inch radius Si wafers, resulting in NWs with different morphologies and properties (e.g., electrical, optical).

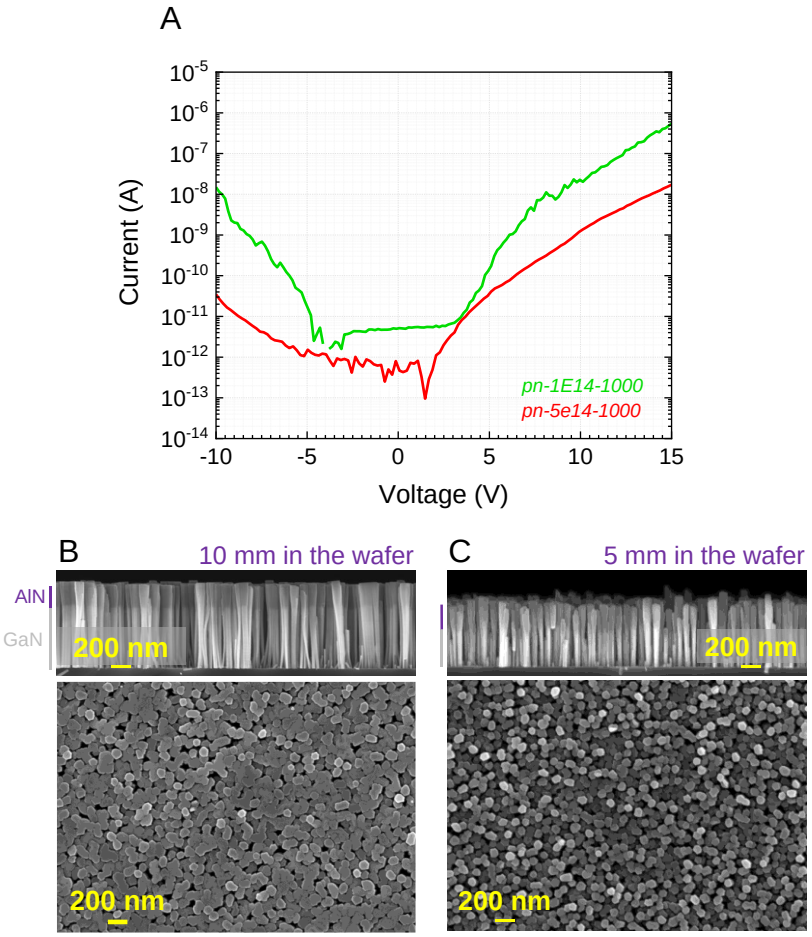

Figure 4.19 (A) Comparison of the I–V characteristics of the operational device on sample *pn-1E14-1000* and one of the devices made on *pn-5E14-1000*. Cross-sectional and top-view SEM images of the as-grown NWs at a distance of **(B)** 10 mm and **(C)** 5 mm from the wafer's center.

Aware of the importance that the position of the studied NWs region on the wafer can have on the optical and electrical properties, pieces of similar regions of the sample (with dimensions of about 5 mm) were studied. Even so, as noticed in **Figure 4.19(B)** and **Figure 4.19(C)**, a slight change of 5 mm in the wafer's position can result in markedly distinct NW morphologies. This can significantly impact the device's behavior. That said, we cannot exclude the possibility that the processed devices are from slightly different regions in the wafer. If this is the case, the NWs height difference (viz., NW surface roughness) observed in **Figure 4.19(B)** may explain the non-rectifying behavior observed for the *pn-1E14-1000* sample. The NW surface roughness, which can be as high as ~100 nm, makes the deposited ITO layer non-conformal, i.e., it can be deposited simultaneously in p-type doped AlN and, in certain NWs, also in the n-type doped section, causing a short

circuit. This would explain the strong failure of the devices, the poor reproducibility, as well as the weak EL signal.

A comparison of the normalized RT luminescence signal around the intra-$4f^6$ transitions obtained for sample *pn-5E14-1000* in CL, EL, and PL ($\lambda_{exc} = 325$ nm) is depicted in **Figure 4.20**. The relative intensity between transitions from the $^5D_0$ state and those from more energetic excited states (e.g., $^5D_1$) is analogous in EL and CL spectra; however, it is significantly higher in PL. This difference was previously tentatively attributed to the re-excitation of already excited Eu^{3+} in the excited $^5D_0$ state to higher energetic states due to the high excitation density in CL and the longer lifetime of the $^5D_0$ state compared to $^5D_1$ and $^5D_2$ states. Nevertheless, in EL experiments, the current density flowing through the devices is very low; therefore, a high excitation density should not explain this effect. Instead, it may be related to changes imposed in the lattice by charge injection, as it can alter the charge balance in the crystal and favor specific excitation or emission paths to the detriment of others. In this case, it should increase the radiative recombination probability from the higher energetic $^5D_1$ and $^5D_2$ states. This led one to conclude that the predominant excitation and deexcitation mechanisms involved in EL are much more identical to those observed in CL than in PL, with the intra-ionic luminescence favored compared to defect-related emission. This implies that *i)* the energy transfer process from the host to the $4f^6$ electrons is favored (compared to recombination at deep-level defects) under charge injection or *ii)* Eu^{3+} are excited directly by hot electrons (impact excitation) instead of involving a non-radiative energy transfer from the host.

Nevertheless, CL and EL signals may result from distinct regions of the NW heterostructures. In CL, Eu^{3+} implanted into the entire AlN NWs can be excited due to an interaction depth of ~150 nm. In contrast, under forward bias electrical injection, electrons (holes) from the n-doped (p-doped) region are injected in the depletion region formed at the p-n junction. This results in the formation of *e-h* pairs, whose recombination can lead to an excitonic emission or an ET to the $4f$ electrons with the successive excitation and radiative deexcitation of Eu^{3+}. As proposed previously, defects in this region can also trap carriers and promote defect-assisted radiative or nonradiative recombination or ET to $4f$ electrons in their vicinity. In addition, the injected carriers can also leak from the depletion region and recombine away from it. The leaking distance depends on the diffusion length of the minority carriers, which, according to the recent results obtained by R. Vermeersch et al., for AlN p-n junctions, correspond to (80 ± 10) nm for electrons in p-type AlN and (205 ± 15) nm for holes in n-type AlN [107].

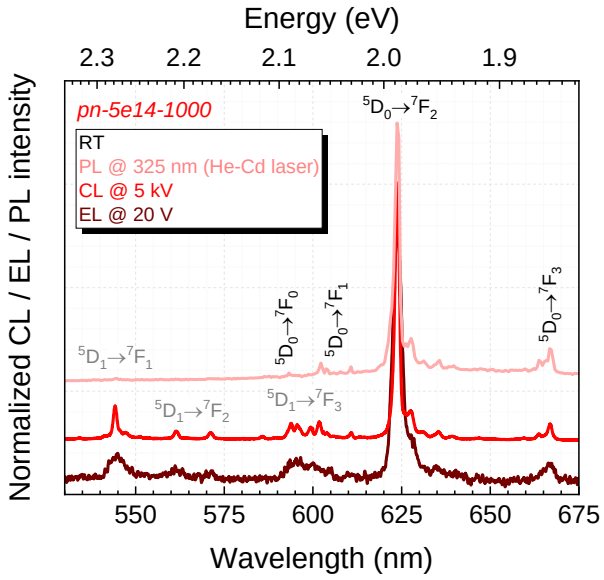

Figure 4.20 Normalized RT CL, RT EL, and RT PL spectra of sample *pn-5E14-1000* around intra-4f^6 transitions. The spectra are vertically shifted for clarity.

Figure 4.21(A) shows the EL spectra of sample *pn-5E14-1000* for different applied voltages (under forward bias), while **Figure 4.21(B)** displays the evolution of the integrated intensity of the $^5D_0 \rightarrow {}^7F_2$ transition with increasing the applied bias. From these, it is possible to notice that the Eu^{3+} luminescence starts to be detectable only at about 12-14 V. The high voltage necessary to produce the red light must be related to the resistive paths connected with the high R_s values due to implantation-induced defects, high ionization energy of donors and acceptors in AlN, and non-optimized p-contacts.

Since the voltage required to have an EL signal is high (above 10 V) and the current density is very low (~10^{-5}–10^{-4} A · cm^{-2}), it is important to consider the possibility of electron-hole generation by impact ionization. In this case, the injected electrons are accelerated by the electric field and may transfer the gained energy to the 4f electrons that become in an excited configuration; the subsequent deexcitation leads to the Eu^{3+}-related emission [116,117]. Considering that the electrical breakdown field is about 4–15 MV · cm^{-1} [118,119], and assuming that the p-type doped AlN section is fully depleted (~50 nm), a voltage of 12 V, corresponding to an electric field of 2.4 MV · cm^{-1}, would not be enough to reach the breakdown field. Therefore, impact ionization is unlikely responsible for the excitation of Eu^{3+}. Based on these results, one can suppose that the injection of carriers in the p-n junction is responsible for the indirect excitation of Eu^{3+} (energy transfer from the host to Eu^{3+}) in the AlN p-n junction NWs studied here. This is consistent with the I–V characteristic of an LED, even though the high resistance of the structure or the non-optimized contacts.

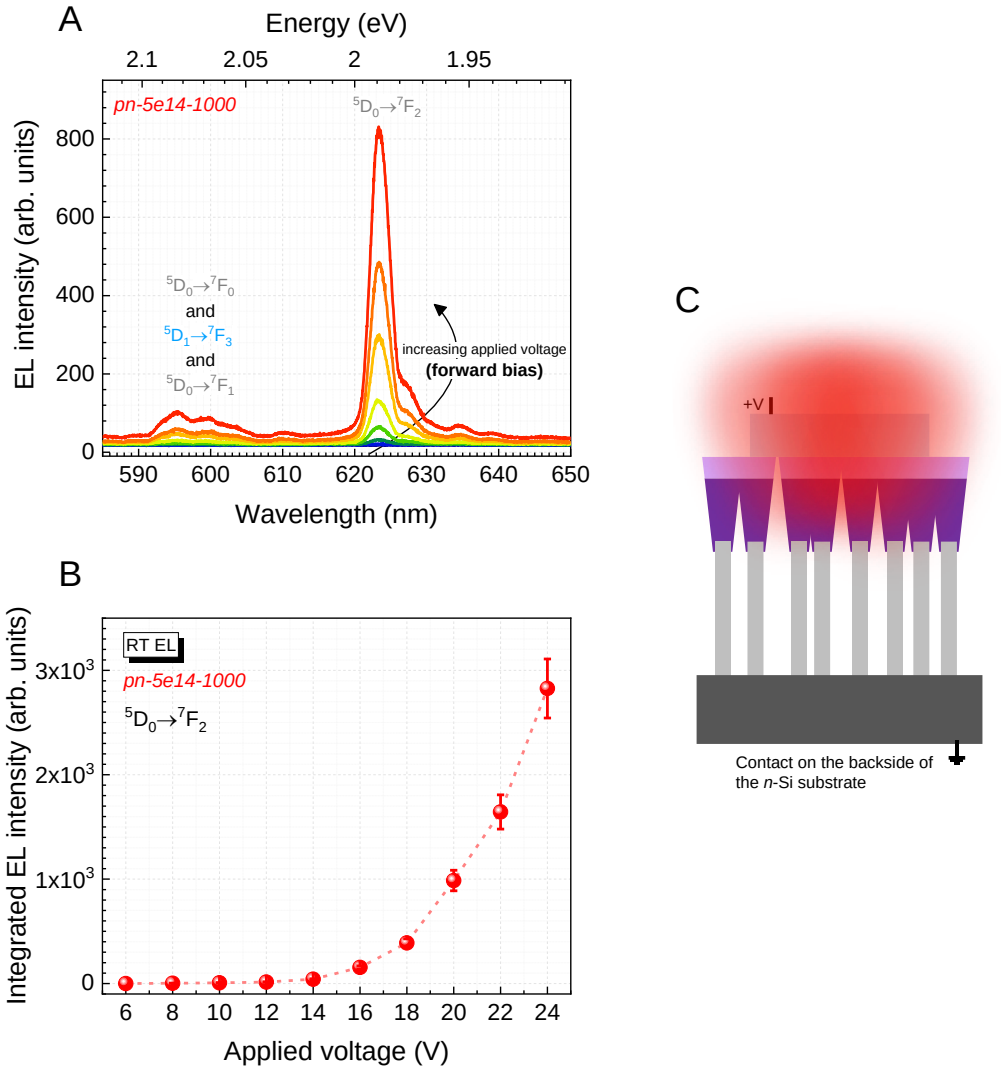

Figure 4.21 (A) EL spectra of a red LED made on sample *pn-5E14-1000* when varying the applied voltage (under forward bias). **(B)** Integrated EL intensity of the $^5D_0 \rightarrow ^7F_2$ transition of the previous LED as a function of the current density flowing through the NW heterostructure. **(C)** Schematic representation of the proof-of-concept red light emitting devices.

Furthermore, with increasing the applied voltage, the EL intensity is successively enhanced, with its dependence on the voltage being analogous to the I–V characteristic of the device. No changes in the Eu^{3+} emission spectral shape and peak position are observed, demonstrating its insensitivity to the applied voltage and current flowing through the device. This, alongside the temperature stability of the emission's peak wavelength, highlights the potential of this proof-of-concept in developing stable LEDs. The predominance of the intra-$4f^6$ luminescence, dominated by the $^5D_0 \rightarrow ^7F_2$ transition, suggests that the approach schematized in **Figure 4.21(C)** can be promising for producing

high-purity (i.e., *quasi*-monochromatic) red-color LEDs based on AlN NWs, even though some challenges need to be addressed.

4.4. Summary

In this chapter, the optical and structural properties of Eu-implanted AlN p-n junction NWs were studied. Then, proof-of-concept red LEDs were realized on such structures. The results obtained are summarized as follows:

- The implantation damaged the crystalline lattice of the AlN p-n junction NWs, which was partially recovered by posterior RTA treatments at 1000 ℃. The damage and strain were higher for the highest fluence used.
- The optical activation of Eu^{3+} was achieved after RTA at 1000 ℃, with the $^5D_0 \rightarrow {}^7F_2$ transition, at ~624 nm, being most intense. The excitation mechanisms were similar to those identified in **Chapter 3** for Eu-implanted undoped AlN NWs, with below bandgap excitation proceeding through X1 and X2 bands or direct excitation of Eu^{3+}.
- The implantation fluence was found to affect the luminescence properties, altering *i)* the relative intensity of the Eu^{3+}-related luminescence with respect to other radiative defects and *ii)* the balance of Eu1 and Eu2 centers.
- A portion of Eu^{3+} was also implanted and optically active in the GaN NWs templates due to channeling effects.
- After the deposition ITO p-contacts on the top of the NWs, the I–V characteristics of the LEDs showed a diode-like rectifying behavior. The remaining implantation-induced defects caused an increase in the resistivity, resulting in a low current flowing through the structure.
- For the LEDs made on sample *pn-5E14-1000*, a red EL signal dominated by the $^5D_0 \rightarrow {}^7F_2$ transition at ~624 nm was obtained under forward bias electrical injection, even if for applied voltages greater than ~12 V. An ET from the host to the $4f^6$ electrons when minority carriers are injected in (or close to) the depletion region might be responsible for the obtained Eu^{3+} emission.

The conducted work allowed the realization of the first successful red LEDs based on Eu-implanted III-N, highlighting the potential of this approach for obtaining red micro- and nano-emitters.

4.5. References

[1] J.-I. Hwang et al., Development of InGaN-based red LED grown on (0001) polar surface, *Appl. Phys. Express.* **7** (2014) 071003. https://doi.org/10.7567/APEX.7.071003.

[2] H. Jiang et al., eds., Micro LEDs, 1st ed., Academic Press, United States, 2021.

[3] O. Ambacher et al., Pyroelectric properties of Al(In)GaN/GaN hetero- and quantum well structures, *J. Phys. Condens. Matter.* **14** (2002) 3399–3434. https://doi.org/10.1088/0953-8984/14/13/302.

[4] B. Damilano et al., Yellow-red emission from (Ga,In)N heterostructures, *J. Phys. D. Appl. Phys.* **48** (2015). https://doi.org/10.1088/0022-3727/48/40/403001.

[5] D. Iida et al., Recent progress in red light-emitting diodes by III-nitride materials, *Semicond. Sci. Technol.* (2021) 0–23. https://doi.org/10.1088/1361-6641/ac3962.

[6] T. Monteiro et al., Photoluminescence and lattice location of Eu and Pr implanted GaN samples, *Phys. B Condens. Matter.* **308–310** (2001) 22–25. https://doi.org/10.1016/S0921-4526(01)00656-1.

[7] T. Andreev et al., Optical transitions in Eu^{3+} ions in GaN:Eu grown by molecular beam epitaxy, *Phys. Rev. B - Condens. Matter Mater. Phys.* **73** (2006) 3–8. https://doi.org/10.1103/PhysRevB.73.195203.

[8] T. Fujiwara et al., Photoluminescence properties of Eu-implanted $Al_xGa_{1-x}N$ ($0 \leq x \leq 1$), *Phys. Status Solidi.* **2** (2005) 2805–2808. https://doi.org/10.1002/pssc.200461431.

[9] S. Ichikawa et al., Eu-doped GaN and InGaN monolithically stacked full-color LEDs with a wide color gamut, *Appl. Phys. Express.* **14** (2021) 031008. https://doi.org/10.35848/1882-0786/abe603.

[10] S. Ichikawa et al., Room-temperature operation of near-infrared light-emitting diode based on Tm-doped GaN with ultra-stable emission wavelength, *J. Appl. Phys.* **127** (2020) 113103. https://doi.org/10.1063/1.5140715.

[11] K. Binnemans, Interpretation of europium(III) spectra, *Coord. Chem. Rev.* **295** (2015) 1–45. https://doi.org/10.1016/j.ccr.2015.02.015.

[12] A. Nishikawa et al., Room-Temperature Red Emission from a p-Type/Europium-Doped/n-Type Gallium Nitride Light-Emitting Diode under Current Injection, *Appl. Phys. Express.* **2** (2009) 071004. https://doi.org/10.1143/APEX.2.071004.

[13] A. Nishikawa et al., Improved luminescence properties of Eu-doped GaN light-emitting diodes grown by atmospheric-pressure organometallic vapor phase epitaxy, *Appl. Phys. Lett.* **97** (2010) 1–4. https://doi.org/10.1063/1.3478011.

[14] N. Woodward et al., Excitation of Eu^{3+} in gallium nitride epitaxial layers: Majority versus trap defect center, *Appl. Phys. Lett.* **98** (2011) 011102. https://doi.org/10.1063/1.3533806.

[15] Y. Fujiwara et al., Present understanding of Eu luminescent centers in Eu-doped GaN grown by organometallic vapor phase epitaxy, *Jpn. J. Appl. Phys.* **53** (2014) 05FA13. https://doi.org/10.7567/JJAP.53.05FA13.

[16] M. Ishii et al., Enhancement in light efficiency of a GaN:Eu red light-emitting diode

by pulse-controlled injected charges, *Appl. Phys. Lett.* **105** (2014) 1–5. https://doi.org/10.1063/1.4900840.

[17] W. Zhu et al., High-Power Eu-Doped GaN Red LED Based on a Multilayer Structure Grown at Lower Temperatures by Organometallic Vapor Phase Epitaxy, *MRS Adv.* **2** (2017) 159–164. https://doi.org/10.1557/adv.2017.67.

[18] B. Mitchell et al., Perspective: Toward efficient GaN-based red light emitting diodes using europium doping, *J. Appl. Phys.* **123** (2018) 160901. https://doi.org/10.1063/1.5010762.

[19] A. Sukegawa et al., Self-Organized Eu-Doped GaN Nanocolumn Light-Emitting Diode Grown by RF-Molecular-Beam Epitaxy, *Phys. Status Solidi.* **216** (2018) 1800501. https://doi.org/10.1002/pssa.201800501.

[20] H. Sekiguchi et al., Stable-wavelength operation of europium-doped GaN nanocolumn light-emitting diodes grown by rf-plasma-assisted molecular beam epitaxy, *Electron. Lett.* **53** (2017) 666–668. https://doi.org/10.1049/el.2017.0447.

[21] T. Otabara et al., Formation and optical characteristics of GaN:Eu/GaN core-shell nanowires grown by organometallic vapor phase epitaxy, *Jpn. J. Appl. Phys.* (2022) 0–23. https://doi.org/10.35848/1347-4065/ac4e4c.

[22] T. Otabara et al., Demonstration of GaN:Eu/GaN nanowire light emitting diodes grown by selective-area organometallic vapor phase epitaxy, *Jpn. J. Appl. Phys.* (2023) 0–23. https://doi.org/10.35848/1347-4065/acbb0f.

[23] H. Sekiguchi et al., Regularly arranged Eu-doped GaN nanocolumns grown by RF-plasma-assisted molecular beam epitaxy through Ti-mask selective-area growth technique, *J. Cryst. Growth.* **511** (2019) 73–78. https://doi.org/10.1016/j.jcrysgro.2019.01.032.

[24] D.N. Faye et al., Incorporation of Europium into GaN Nanowires by Ion Implantation, *J. Phys. Chem. C.* **123** (2019) 11874–11887. https://doi.org/10.1021/acs.jpcc.8b12014.

[25] J. Rodrigues et al., Correction to "Spectroscopic Analysis of Eu^{3+} Implanted and Annealed GaN Layers and Nanowires," *J. Phys. Chem. C.* **120** (2016) 6907–6908. https://doi.org/10.1021/acs.jpcc.6b02591.

[26] J. Rodrigues et al., Spectroscopic Analysis of Eu^{3+} Implanted and Annealed GaN Layers and Nanowires, *J. Phys. Chem. C.* **119** (2015) 17954–17964. https://doi.org/10.1021/acs.jpcc.5b05101.

[27] H. Sekiguchi et al., Structural and optical properties of Eu-doped GaN nanocolumns on (111) Si substrates grown by RF-plasma-assisted molecular beam epitaxy, *Jpn. J. Appl. Phys.* **55** (2016) 05FG07. https://doi.org/10.7567/JJAP.55.05FG07.

[28] Aledia, Strategic agenda by G.Anania, (2021). https://www.aledia.com/en/news/strategic-agenda-by-g-anania (accessed April 8, 2022).

[29] Z. Xing et al., Economically detaching transparent and flexible (Al,Ga)N nanowire films with improved photoelectric response in view of ultraviolet photodetectors, *Mater. Adv.* (2021). https://doi.org/10.1039/D0MA00943A.

[30] J. Jeong et al., Transferable, flexible white light-emitting diodes of GaN p–n junction

microcrystals fabricated by remote epitaxy, *Nano Energy.* (2021) 106075. https://doi.org/10.1016/j.nanoen.2021.106075.

[31] M. Rajan Philip et al., Fabrication of Phosphor-Free III-Nitride Nanowire Light-Emitting Diodes on Metal Substrates for Flexible Photonics, *ACS Omega.* **2** (2017) 5708–5714. https://doi.org/10.1021/acsomega.7b00843.

[32] Y. Fujiwara et al., Eu-doped GaN-Based Red LED for Next-Generation Micro-LED Displays, in: 2022 Int. Conf. Electron. Packag., IEEE, 2022: pp. 35–36. https://doi.org/10.23919/ICEP55381.2022.9795364.

[33] S.M. Sadaf et al., An AlGaN Core–Shell Tunnel Junction Nanowire Light-Emitting Diode Operating in the Ultraviolet-C Band, *Nano Lett.* **17** (2017) 1212–1218. https://doi.org/10.1021/acs.nanolett.6b05002.

[34] A.-M. Siladie et al., Mg and In Codoped p-type AlN Nanowires for pn Junction Realization, *Nano Lett.* **19** (2019) 8357–8364. https://doi.org/10.1021/acs.nanolett.9b01394.

[35] R. Vermeersch et al., Shallow donor and DX state in Si doped AlN nanowires grown by molecular beam epitaxy, *Appl. Phys. Lett.* **119** (2021). https://doi.org/10.1063/5.0074454.

[36] R. Vermeersch et al., DX center formation in highly Si doped AlN nanowires revealed by trap assisted space-charge limited current, *Appl. Phys. Lett.* **120** (2022). https://doi.org/10.1063/5.0087789.

[37] E.N. Aybeke et al., Nanoscale imaging of dopant incorporation in n-type and p-type GaN nanowires by scanning spreading resistance microscopy, *J. Appl. Phys.* **131** (2022) 075701. https://doi.org/10.1063/5.0080713.

[38] Z. Fang et al., Si Donor Incorporation in GaN Nanowires, *Nano Lett.* **15** (2015) 6794–6801. https://doi.org/10.1021/acs.nanolett.5b02634.

[39] N. Ben Sedrine et al., Optical investigations of europium ion implanted in nitride-based diode structures, *Surf. Coatings Technol.* **355** (2018) 40–44. https://doi.org/10.1016/j.surfcoat.2018.02.004.

[40] N. Ben Sedrine et al., Eu-Doped AlGaN/GaN Superlattice-Based Diode Structure for Red Lighting: Excitation Mechanisms and Active Sites, *ACS Appl. Nano Mater.* **1** (2018) 3845–3858. https://doi.org/10.1021/acsanm.8b00612.

[41] D.N. Faye et al., Study of damage formation and annealing of implanted III-nitride semiconductors for optoelectronic devices, *Nucl. Instruments Methods Phys. Res. Sect. B Beam Interact. with Mater. Atoms.* **379** (2016) 251–254. https://doi.org/10.1016/j.nimb.2016.03.028.

[42] Y. Nakanishi et al., Effects of Al composition on luminescence properties of europium implanted $Al_xGa_{1-x}N$ ($0 \leq x \leq 1$), *Phys. Status Solidi.* **96** (2003) 2623–2626. https://doi.org/10.1002/pssc.200303440.

[43] K. Lorenz et al., Structural and optical characterisation of Eu implanted $Al_xGa_{1-x}N$, *Nucl. Instruments Methods Phys. Res. Sect. B Beam Interact. with Mater. Atoms.* **257** (2007) 307–310. https://doi.org/10.1016/j.nimb.2007.01.020.

[44] S.O. Kucheyev et al., Structural disorder in ion-implanted $Al_xGa_{1-x}N$, *Appl. Phys.*

Lett. **80** (2002) 787–789. https://doi.org/10.1063/1.1445478.

[45] D.N. Faye et al., Crystal damage analysis of implanted $Al_xGa_{1-x}N$ ($0 \leq x \leq 1$) by ion beam techniques, *Surf. Coatings Technol.* **355** (2018) 55–60. https://doi.org/10.1016/j.surfcoat.2018.01.020.

[46] R. Vermeersch, Realization of AlN nanowire-based light emitting diodes for UV-C emission, Université Grenoble Alpes, 2023.

[47] B. Daudin et al., The role of surface diffusion in the growth mechanism of III-nitride nanowires and nanotubes, *Nanotechnology.* **32** (2021) 085606. https://doi.org/10.1088/1361-6528/abc780.

[48] M. Fialho et al., Impact of implantation geometry and fluence on structural properties of AlxGa1-xN implanted with thulium, *J. Appl. Phys.* **120** (2016). https://doi.org/10.1063/1.4966120.

[49] K. Lorenz et al., Optical doping and damage formation in AlN by Eu implantation, *J. Appl. Phys.* **107** (2010) 2–6. https://doi.org/10.1063/1.3291100.

[50] T. Nishimura et al., Simulation of channeled implantation of magnesium ions in gallium nitride, *Appl. Phys. Express.* **14** (2021). https://doi.org/10.35848/1882-0786/ac2a55.

[51] A. Antony et al., Influence of target to substrate spacing on the properties of ITO thin films, *Appl. Surf. Sci.* **225** (2004) 294–301. https://doi.org/10.1016/j.apsusc.2003.10.017.

[52] J.F. Muth et al., Absorption coefficient, energy gap, exciton binding energy, and recombination lifetime of GaN obtained from transmission measurements, *Appl. Phys. Lett.* **71** (1997) 2572–2574. https://doi.org/10.1063/1.120191.

[53] D. Behr et al., Resonant Raman scattering in hexagonal GaN, *Appl. Phys. Lett.* **68** (1996) 2404–2406. https://doi.org/10.1063/1.116148.

[54] V.Y. Davydov et al., Phonon dispersion and Raman scattering in hexagonal GaN and AlN, *Phys. Rev. B.* **58** (1998) 12899–12907. https://doi.org/10.1103/PhysRevB.58.12899.

[55] S. Strite, GaN, AlN, and InN: A review, *J. Vac. Sci. Technol. B Microelectron. Nanom. Struct.* **10** (1992) 1237. https://doi.org/10.1116/1.585897.

[56] A. Hoffmann et al., Local vibrational modes and compensation effects in Mg-doped GaN, *Phys. Status Solidi C Conf.* **0** (2003) 1783–1794. https://doi.org/10.1002/pssc.200303120.

[57] A. Kaschner et al., Local vibrational modes in Mg-doped GaN grown by molecular beam epitaxy, *Appl. Phys. Lett.* **74** (1999) 3281–3283. https://doi.org/10.1063/1.123320.

[58] T. Kozawa et al., Raman scattering from LO phonon-plasmon coupled modes in gallium nitride, *J. Appl. Phys.* **75** (1994) 1098–1101. https://doi.org/10.1063/1.356492.

[59] J.F. Ziegler et al., SRIM: The stopping and range of ions in matter, 1st ed., United States, 2008.

[60] K. Lorenz et al., Optical doping of AlN by rare earth implantation, *Nucl. Instruments*

Methods Phys. Res. Sect. B Beam Interact. with Mater. Atoms. **242** (2006) 307–310. https://doi.org/10.1016/j.nimb.2005.08.037.

[61] C. Ronning et al., Ion implantation into gallium nitride, *Phys. Rep.* **351** (2001) 349–385. https://doi.org/10.1016/S0370-1573(00)00142-3.

[62] T. Wojtowicz et al., Microstructural and electrical characterization of Er and Eu implanted gallium nitride, *Mater. Sci. Eng. B Solid-State Mater. Adv. Technol.* **105** (2003) 122–125. https://doi.org/10.1016/j.mseb.2003.08.029.

[63] B. Pipeleers et al., Defect accumulation during channeled erbium implantation into GaN, *J. Appl. Phys.* **98** (2005). https://doi.org/10.1063/1.2143120.

[64] J.M. Wagner et al., Phonon deformation potentials of α-GaN and -AlN: An ab initio calculation, *Appl. Phys. Lett.* **77** (2000) 346–348. https://doi.org/10.1063/1.127009.

[65] J.M. Wagner et al., Properties of strained wurtzite GaN and AlN: Ab initio studies, *Phys. Rev. B - Condens. Matter Mater. Phys.* **66** (2002) 1–20. https://doi.org/10.1103/PhysRevB.66.115202.

[66] P. Perlin et al., Investigation of longitudinal-optical phonon-plasmon coupled modes in highly conducting bulk GaN, *Appl. Phys. Lett.* **67** (1995) 2524. https://doi.org/10.1063/1.114446.

[67] C. Wetzel et al., Electron-Phonon Scattering in Si-Doped GaN, *MRS Proc.* **449** (1996) 567. https://doi.org/10.1557/PROC-449-567.

[68] L.H. Robins et al., Raman spectroscopy based measurements of carrier concentration in n-type GaN nanowires grown by plasma-assisted molecular beam epitaxy, *J. Appl. Phys.* **120** (2016). https://doi.org/10.1063/1.4963291.

[69] R.M. Martin et al., Cascade Theory of Inelastic Scattering of Light, *Phys. Rev. Lett.* **26** (1971) 1241–1244. https://doi.org/10.1103/PhysRevLett.26.1241.

[70] E. Zielony et al., Strain and lattice vibration mechanisms in GaN-$Al_xGa_{1-x}N$ nanowire structures on Si substrate, *Appl. Surf. Sci.* **588** (2022) 152901. https://doi.org/10.1016/j.apsusc.2022.152901.

[71] R.F. Allah et al., Imaging and analysis by transmission electron microscopy of the spontaneous formation of Al-rich shell structure in $Al_xGa_{1-x}N$/GaN nanowires, *Appl. Phys. Express.* **5** (2012). https://doi.org/10.1143/APEX.5.045002.

[72] R.F. Allah et al., Structural and chemical evolution of the spontaneous core-shell structures of $Al_xGa_{1-x}N$/GaN nanowires, *Microsc. Microanal.* **20** (2014) 1254–1261. https://doi.org/10.1017/S1431927614000634.

[73] V. Laneuville et al., Double strain state in a single GaN/AlN nanowire: Probing the core-shell effect by ultraviolet resonant Raman scattering, *Phys. Rev. B - Condens. Matter Mater. Phys.* **83** (2011). https://doi.org/10.1103/PhysRevB.83.115417.

[74] A. Pierret et al., Growth, structural and optical properties of AlGaN nanowires in the whole composition range, *Nanotechnology.* **24** (2013) 115704. https://doi.org/10.1088/0957-4484/24/11/115704.

[75] I.M. Høiaas et al., GaN/AlGaN Nanocolumn Ultraviolet Light-Emitting Diode Using Double-Layer Graphene as Substrate and Transparent Electrode, *Nano Lett.* **19** (2019) 1649–1658. https://doi.org/10.1021/acs.nanolett.8b04607.

[76] K. Hestroffer et al., The structural properties of GaN/AlN core-shell nanocolumn heterostructures, *Nanotechnology.* **21** (2010). https://doi.org/10.1088/0957-4484/21/41/415702.

[77] G. Irmer et al., Determination of the charge carrier concentration and mobility in n-gap by Raman spectroscopy, *Phys. Status Solidi.* **119** (1983) 595–603. https://doi.org/10.1002/pssb.2221190219.

[78] I. Vurgaftman et al., Band parameters for III-V compound semiconductors and their alloys, *J. Appl. Phys.* **89** (2001) 5815–5875. https://doi.org/10.1063/1.1368156.

[79] J. Li et al., III-Nitrides Light Emitting Diodes: Technology and Applications, 1st ed., Springer Nature Singapore Pte Ltd, Singapore, 2020.

[80] A. Wolos et al., Properties of metal-insulator transition and electron spin relaxation in GaN:Si, *Phys. Rev. B.* **83** (2011) 165206. https://doi.org/10.1103/PhysRevB.83.165206.

[81] J.B. Gruber et al., Spectroscopic analysis of Eu^{3+} in single-crystal hexagonal phase AlN, *J. Appl. Phys.* **110** (2011) 023104. https://doi.org/10.1063/1.3609076.

[82] J.K. Mishra et al., Strong enhancement of Eu^{+3} luminescence in europium-implanted GaN by Si and Mg codoping, *Appl. Phys. Lett.* **102** (2013) 2011–2014. https://doi.org/10.1063/1.4793207.

[83] B. Mitchell et al., The role of donor-acceptor pairs in the excitation of Eu-ions in GaN:Eu epitaxial layers, *J. Appl. Phys.* **115** (2014) 204501. https://doi.org/10.1063/1.4879253.

[84] L. Bodiou et al., Effect of annealing temperature on luminescence in Eu implanted GaN, *Opt. Mater. (Amst).* **28** (2006) 780–784. https://doi.org/10.1016/j.optmat.2005.09.022.

[85] L. Bodiou et al., Optically active centers in Eu implanted, Eu in situ doped GaN, and Eu doped GaN quantum dots, *J. Appl. Phys.* **105** (2009) 043104. https://doi.org/10.1063/1.3078783.

[86] S. Sanna et al., Rare-earth defect pairs in GaN: LDA+U calculations, *Phys. Rev. B.* **80** (2009) 104120. https://doi.org/10.1103/PhysRevB.80.104120.

[87] M.J. Soares et al., Structural and optical properties of Er implanted AlN thin films: Green and infrared photoluminescence at room temperature, *Opt. Mater. (Amst).* **33** (2011) 1055–1058. https://doi.org/10.1016/j.optmat.2010.09.005.

[88] D. Lee et al., Control of Eu Luminescence Centers by Codoping of Mg and Si into Eu-Doped GaN, *Jpn. J. Appl. Phys.* **52** (2013) 08JM01. https://doi.org/10.7567/JJAP.52.08JM01.

[89] C. Stampfl et al., Theoretical investigation of native defects, impurities, and complexes in aluminum nitride, *Phys. Rev. B - Condens. Matter Mater. Phys.* **65** (2002) 1552121–15521210. https://doi.org/10.1103/PhysRevB.65.155212.

[90] T. Koppe et al., Overview of band-edge and defect related luminescence in aluminum nitride, *J. Lumin.* **178** (2016) 267–281. https://doi.org/10.1016/j.jlumin.2016.05.055.

[91] L. Trinkler et al., UV light induced processes in pure and doped AlN ceramics, *Opt. Mater. (Amst).* **121** (2021) 111550. https://doi.org/10.1016/j.optmat.2021.111550.

[92] T. Koyama et al., Relation between Al vacancies and deep emission bands in AlN epitaxial films grown by N H3 -source molecular beam epitaxy, *Appl. Phys. Lett.* **90** (2007). https://doi.org/10.1063/1.2748315.

[93] A. Sedhain et al., Nature of optical transitions involving cation vacancies and complexes in AlN and AlGaN, *Appl. Phys. Lett.* **100** (2012). https://doi.org/10.1063/1.4723693.

[94] Q. Yan et al., Origins of optical absorption and emission lines in AlN, *Appl. Phys. Lett.* **105** (2014) 0–5. https://doi.org/10.1063/1.4895786.

[95] Q. Zhou et al., Below bandgap photoluminescence of an AlN crystal: Co-existence of two different charging states of a defect center, *APL Mater.* **8** (2020). https://doi.org/10.1063/5.0012685.

[96] M.A. Reshchikov et al., Luminescence properties of defects in GaN, *J. Appl. Phys.* **97** (2005) 1–95. https://doi.org/10.1063/1.1868059.

[97] M.A. Reshchikov et al., Two yellow luminescence bands in undoped GaN, *Sci. Rep.* **8** (2018) 1–11. https://doi.org/10.1038/s41598-018-26354-z.

[98] M.A. Reshchikov et al., Two charge states of the C_N acceptor in GaN: Evidence from photoluminescence, *Phys. Rev. B.* **98** (2018) 125207. https://doi.org/10.1103/PhysRevB.98.125207.

[99] F. Chen et al., Effects of Eu ions dose and annealing temperature on the structural and optical properties of Eu-implanted AlN thin films, *Superlattices Microstruct.* **129** (2019) 47–53. https://doi.org/10.1016/j.spmi.2019.03.014.

[100] H.J. Lozykowski et al., Thermal quenching of luminescence and isovalent trap model for rare-earth-ion-doped AlN, *Phys. Status Solidi Basic Res.* **244** (2007) 2109–2126. https://doi.org/10.1002/pssb.200642152.

[101] H.J. Lozykowski et al., Luminescence and excitation mechanism of Pr, Eu, Tb and Tm ions implanted into AlN, *Microelectronics J.* **36** (2005) 453–455. https://doi.org/10.1016/j.mejo.2005.02.045.

[102] H.J. Lozykowski, Kinetics of luminescence of isoelectronic rare-earth ions in III-V semiconductors, *Phys. Rev. B.* **48** (1993) 17758–17769. https://doi.org/10.1103/PhysRevB.48.17758.

[103] B. Mitchell et al., Temporally modulated energy shuffling in highly interconnected nanosystems, *Nanophotonics.* (2020) 1–26. https://doi.org/10.1515/nanoph-2020-0484.

[104] W. Zhu et al., Re-Excitation of Trivalent Europium Ions Doped into Gallium Nitride Revealed through Photoluminescence under Pulsed Laser Excitation, *ACS Photonics.* **5** (2018) 875–880. https://doi.org/10.1021/acsphotonics.7b01090.

[105] B. Mitchell et al., Color-Tunablility in GaN LEDs Based on Atomic Emission Manipulation under Current Injection, *ACS Photonics.* **6** (2019) 1153–1161. https://doi.org/10.1021/acsphotonics.8b01461.

[106] E.F. Schubert, Light-emitting diodes, 2nd ed., Cambridge University Press, United States, 2006.

[107] R. Vermeersch et al., Comprehensive Electro-Optical Investigation of a Ga-Doped

AlN Nanowire LED for Applications in the UV-C Range, *ACS Appl. Nano Mater.* (2023). https://doi.org/10.1021/acsanm.3c01705.

[108] M. Musolino et al., A modified Shockley equation taking into account the multi-element nature of light emitting diodes based on nanowire ensembles, *Nanotechnology.* **27** (2016). https://doi.org/10.1088/0957-4484/27/27/275203.

[109] D. van Treeck et al., Electroluminescence and current–voltage measurements of single-(In,Ga)N/GaN-nanowire light-emitting diodes in a nanowire ensemble, *Beilstein J. Nanotechnol.* **10** (2019) 1177–1187. https://doi.org/10.3762/bjnano.10.117.

[110] M. Musolino et al., Understanding peculiarities in the optoelectronic characteristics of light emitting diodes based on (In,Ga)N/GaN nanowires, *Appl. Phys. Lett.* **105** (2014). https://doi.org/10.1063/1.4894241.

[111] C.H. Wang et al., Is it viable to improve light output efficiency by nano-light-emitting diodes?, *Appl. Phys. Lett.* **103** (2013). https://doi.org/10.1063/1.4844715.

[112] Y. Taniyasu et al., An aluminium nitride light-emitting diode with a wavelength of 210 nanometres, *Nature.* **441** (2006) 325–328. https://doi.org/10.1038/nature04760.

[113] K.B. Nam et al., Mg acceptor level in AlN probed by deep ultraviolet photoluminescence, *Appl. Phys. Lett.* **83** (2003) 878–880. https://doi.org/10.1063/1.1594833.

[114] V. Consonni et al., Effects of nanowire coalescence on their structural and optical properties on a local scale, *Appl. Phys. Lett.* **95** (2009) 1–4. https://doi.org/10.1063/1.3275793.

[115] V.M. Kaganer et al., Elastic versus Plastic Strain Relaxation in Coalesced GaN Nanowires: An X-Ray Diffraction Study, *Phys. Rev. Appl.* **6** (2016) 1–13. https://doi.org/10.1103/PhysRevApplied.6.064023.

[116] A.J. Steckl et al., Rare-earth-doped GaN: Growth, properties, and fabrication of electroluminescent devices, *IEEE J. Sel. Top. Quantum Electron.* **8** (2002) 749–766. https://doi.org/10.1109/JSTQE.2002.801690.

[117] J. Heikenfeld et al., Rare-earth-doped GaN switchable color electroluminescent devices, *IEEE Trans. Electron Devices.* **49** (2002) 1545–1551. https://doi.org/10.1109/TED.2002.802663.

[118] M. Meneghini et al., GaN-based power devices : physics , reliability and perspectives, *J. Appl. Phys.* **130** (2021) 227. https://doi.org/10.1063/5.0061354.

[119] F. Martin et al., Thickness dependence of the properties of highly c -axis textured AlN thin films , *J. Vac. Sci. Technol. A Vacuum, Surfaces, Film.* **22** (2004) 361–365. https://doi.org/10.1116/1.1649343.

Chapter 5

Swift-heavy ion irradiation of green-emitting InGaN/GaN multi-quantum wells

5.1. Context

Although the modification of III-Ns using ion beams continues to be discussed, the strategy investigated in this chapter differs from that of the last two. The motivation is no longer the low efficiency of red LEDs but instead solving the efficiency droop of green-emitting III-N LEDs at high current levels [1–4].

Realizing In-composition gradients in the active region of conventional InGaN-based LEDs, i.e., at the InGaN well/GaN barrier interfaces, has been proposed to improve the EQE of such emitters. Theoretical results demonstrated that such gradients can alter the electronic band structure so that both the QCSE and Auger losses can be minimized, pushing up the performance of the LEDs at high current levels [5–7]. Besides theoretical results, S. Han et al. obtained an experimental improvement of EQE using trapezoidal QWs instead of the conventional rectangular QWs at high current densities [8].

The In-composition gradients during growth can be controlled by adjusting the flux of the In and Ga precursor reaching the sample. However, controlling it at the nanoscale is challenging. Post-growth treatments are a different way of possibly realizing such compositional gradients. Thermal annealing and low-energy (tens to hundreds keV) irradiation followed by thermal annealing have already been used to generate a mixture of In and Ga atoms at the QW interfaces, a process known as QWI [9]. In the first case, the MQW structures are subjected to high-temperature annealing treatments (1300–1400 ℃) to allow atomic inter-diffusion and high pressures (up to 15 kbar) to avoid surface decomposition [10,11]. In the second approach, low-energy ion irradiation promotes QWI due to atomic displacements caused by elastic collisions between the ions and the target nuclei. These nuclear interactions generate point defects that act as nonradiative

recombination centers and degrade emission efficiency (even at low irradiation fluences of ~10^{11}–10^{12} cm^{-2}). Therefore, post-irradiation thermal annealing is mandatory to recover the damage introduced in the crystalline structure. The thermal treatment can also favor QWI since irradiation breaks III-N bonds, facilitating inter-diffusion at the interfaces during annealing [9,12]. Furthermore, due to the low energy used in the irradiation process, the penetration depth of the ions is reduced, leading to a high concentration of implanted species in the active region, influencing both electrical and optical properties.

When using SHIs, the interaction between ion-matter occurs mainly through electronic excitation. Hence, due to the intense local ionization, solid-liquid-solid transitions can be induced in the material for tens to hundreds of picoseconds, promoting the formation of long and straight cylindrical ion tracks along the path [13]. Atomic diffusion along the track direction may also happen during the molten state [14,15]. Resorting to the irradiation of InGaN/GaN with SHIs may constitute an opportunity to obtain the pretended QWI with a reduced contribution of ballistic nuclear collisions [16]. To induce the creation of ion tracks and QWI, S_e should be higher than S_e^{th} [17]. The reported threshold values for track formation in GaN present some dispersion: *i)* 15 keV · nm^{-1} [18], *ii)* 17 keV · nm^{-1} [19], and *iii)* higher than 22.8 keV · nm^{-1} [20].

In addition to the possibility of QWI with an expected low density of point defects in the active region, the higher penetration depth of SHI causes them to be far from the active region, not interfering directly with the optical properties. Despite the diminished nuclear interaction between ion and matter, SHI irradiation can also generate surface defects (e.g., sputtering and formation of voids within the first nanometers of the track), recover pre-damaged crystals, or even cause amorphization of the crystal [14,21].

The potential for SHI irradiation to cause QWI exists, yet studies about their impacts on InGaN/GaN MQWs are still scarce. So far, K. Prabakaran et al. have studied the optical properties of InGaN/GaN QW structures irradiated with 100 MeV Au^{7+} ions (fluence of 1×10^{11} cm^{-2} and 5×10^{12} cm^{-2}). Based on PL and XRD measurements, they claimed the occurrence of intermixing [22]. Nevertheless, the physical mechanisms for such intermixing are far from being understood.

The work provided in this chapter combines the use of non-destructive optical spectroscopy techniques (optical transmittance, micro-Raman, PL, and PLE) to investigate the effects of ^{129}Xe SHI irradiation on the optical and structural properties of green-emitting InGaN/GaN MQWs. The energy of the ion beam is varied from 82 MeV to 38 MeV (S_e between 21.5 keV · nm^{-1} and 13.0 keV · nm^{-1}, respectively), allowing one to infer the effects with energies close to the threshold for track formation in GaN. Independent RBS/C experiments are made to validate the methodology adopted and analyze the results carried out in this work. The main goal of such a study is to evaluate the pertinence of this approach

as a tool for obtaining QWI in InGaN/GaN MQW structures toward realizing more efficient green-light emitters.

5.2. Experimental details

5.2.1. Description of the samples

5.2.1.1. InGaN MQWs

The samples studied in this chapter consist of *c*-oriented InGaN/GaN MQWs grown by MOVPE on a 3 μm-thick GaN template layer on a (0001) Al_2O_3 substrate. The MQW region corresponds to a five-period structure of 2.7 nm-thick InGaN wells and 11 nm-thick GaN barriers, starting and ending with an 11 nm-thick GaN layer.

Additionally, commercial *c*-plane GaN thin films (~10 m thick) grown by metalorganic chemical vapor deposition (MOCVD) on Al_2O_3 substrates are available for comparison.

5.2.1.2. ^{129}Xe SHI irradiation

The MQWs were irradiated at RT with ^{129}Xe SHIs in a *quasi*-normal incidence (6° tilt) relative to the normal of the sample surface. The energy of the ion beam was controlled from 82 MeV to 38 MeV by placing Al foils of different thicknesses before the sample, allowing it to deaccelerate the ^{129}Xe ions that initially had an energy of 92 MeV. The GaN thin films were irradiated under similar conditions. **Figure 5.1(A)** provides a schematic representation of the InGaN/GaN MQWs and the irradiation geometry.

In order to predict the penetration depth of the ^{129}Xe ions in the sample, Monte Carlo simulations for ^{129}Xe irradiated GaN layers were done using the SRIM software [23]. These were made assuming the effect of 2.7 nm-thick InGaN wells would be negligible. Considering the energies used, the end-of-range of the ions occurs in the substrate because their penetration depth in GaN is higher than 5 μm, greater than the thickness of the GaN-based structure. Furthermore, such calculations estimate the energy loss contributions, S_e and S_n, at the samples' surface. **Figure 5.1(B)** shows the evolution of the S_e and S_n values with the ^{129}Xe ion beam energy (in GaN). With this information, one can estimate that S_e varies from 21.5 keV · nm^{-1} to 13.0 keV · nm^{-1} for InGaN/GaN MQWs irradiated with ^{129}Xe ions when the energy decreases from 82 MeV to 36 MeV (violet-shaded region in the graph). These energy values are around the threshold values for track formation in GaN reported in the literature (15–23 keV · nm^{-1} [18–20]), expectably allowing for irradiating the InGaN/GaN MQWs with energy above and below the threshold. At the same time, the S_n

shows an opposite behavior and increases from 0.23 keV · nm^{-1} to 0.42 keV · nm^{-1}. The nuclear losses are about two orders of magnitude lower than the electronic ones.

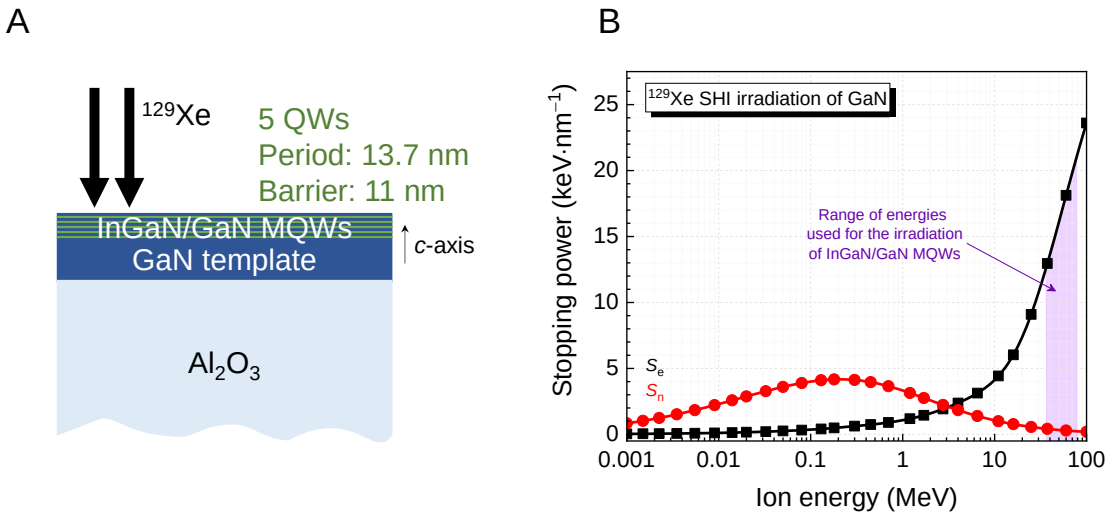

Figure 5.1 (A) InGaN/GaN MQW structure and ^{129}Xe SHI irradiation geometry. **(B)** S_e and S_n as a function of ^{129}Xe ion beam energy in GaN layers obtained by Monte Carlo simulations using the SRIM software [23].

5.2.1.3. Samples nomenclature

Table 5.1 summarizes the irradiation conditions and presents the adopted nomenclature of the InGaN/GaN MQW samples studied in this chapter. The nomenclature is identical for *c*-oriented GaN layers, but the initial term "*MQW*" is replaced by "*GaN*."

Table 5.1 ^{129}Xe SHI energy conditions of the InGaN/GaN MQWs studied and corresponding S_e and S_n values at the samples' surface.

Sample	Energy (MeV)	S_e (keV · nm^{-1})	S_n (keV · nm^{-1})
MQW-asgr	–	–	–
MQW-38	38	13.0	0.42
MQW-74	74	20.3	0.27
MQW-82	82	21.5	0.23

5.2.2. Characterization techniques

5.2.2.1. Optical transmittance

The UV/Visible optical transmittance of the InGaN/GaN MQWs before and after Xe SHI irradiation was measured at RT using a double-beam Shimadzu UV-2100 spectrometer in transmission mode. The signal was detected using a Hamamatsu R928 PMT. Two lamps were used to cover the spectral region 190–900 nm: a halogen lamp for the longer wavelengths and a deuterium lamp for the shorter ones. The lamp switching was set at 360 nm, possibly resulting in the appearance of a little bump in the spectrum.

5.2.2.2. Micro-Raman

Micro-Raman experiments were done in a Horiba Jobin-Yvon LabRAM HR800 spectrometer with a CCD for detection. Three different excitations were used: the 325 nm and the 442 nm lines of a He-Cd laser and the 632.8 nm line of a He-Ne laser. For the 325 nm laser line, a 600 grooves $\cdot$ mm^{-1} grating (experimental uncertainty of 5 cm^{-1}) and a 40$\times$ near UV objective (NA of 0.47) were used. A 50$\times$ objective (NA of 0.5) and a 1200 grooves $\cdot$ mm^{-1} grating were used for the remaining lines (experimental uncertainty of 3 cm^{-1} and 2 cm^{-1}, respectively, for 442 nm and 632.8 nm). The Raman signal was collected in the backscattering geometry $z(x\ \cdot\ )\bar{z}$, given in Porto's notation, with z perpendicular to the samples' surface (i.e., parallel to the c-axis). The system was calibrated using the peak of a Si reference sample at 521 cm^{-1}.

5.2.2.3. Rutherford backscattering spectrometry

RBS experiments were performed on a Van de Graaff AN-2500 type-A accelerator facility using a 2 MeV $^{4}He^{+}$ ion beam. The backscattered ions were detected at 165° using a silicon p-i-n diode detector. The aligned spectra, i.e., in a channeled configuration, were recorded by aligning the ion beam with the crystal c-axis. Additionally, for the as-grown InGaN/GaN MQWs, a random spectrum (non-channeled configuration) was acquired by applying a 5° tilt relative to the crystal c-axis and rotating the sample during the measurement. The latter was done to compare the signal backscattered in both geometries and extract information about irradiation damage. Post-irradiation damage was then evaluated by MC simulations using the computational code McChasy [24,25].

5.2.2.4. Photoluminescence and photoluminescence excitation

RT PL and PLE experiments were carried out in a Fluorolog 3 Horiba Scientific modular system equipped with a 450 W Xe arc lamp. The excitation and emission wavelengths were

controlled by entrance and exit monochromators, and the luminescent signal was collected with a PMT detector. The excitation light was focused on the sample at 60° to the surface normal, while the emitted light was collected at 40° to the surface normal. The presented spectra were corrected to the spectral response of the optical components, the PMT detector, and the Xe lamp.

5.2.3. Experimental data credits

InGaN/GaN MQWs were kindly provided by Professor Christian Wetzel (RPI, Troy, NY, United States). SHI irradiation was carried out by Dr. Clara Grygiel at the Grand Accélérateur National d'Ions Lourds (GANIL, CIMAP, Caen, France). RBS/C measurements and analysis were done by Dr. Przemysław Jóźwik, a former post-doc in the investigation group of Professor Katharina Lorenz (Laboratory of Accelerators and Radiation Technologies, CTN-IST, Lisbon, Portugal). MC simulations using the McChasy code were also run and interpreted by Dr. Przemysław Jóźwik.

5.3. Results and discussion

5.3.1. Optical transmittance

The RT optical transmittance spectra of the InGaN/GaN MQWs before and after irradiation are shown in **Figure 5.2A**. For *MQW-asgr*, the spectrum reveals a well-defined GaN NBE absorption at 365 nm (3.4 eV) and a slight absorption tail, emphasized by a shaded yellow shape, with an onset around 460 nm (~2.7 eV) related to the InGaN band edge. The perceived interference fringe pattern is due to the coherent superposition of multiple reflections in the GaN-based film.

In this case, the GaN bandgap energy ($E_{\mathrm{gap}}^{\mathrm{eff}} = 3.4$ eV) was determined by converting the previous graph into a plot of absorbance, A, where $A = -\log_{10} T$, versus photon energy, E_{ph}, and then fitting the experimental curve with a sigmoidal function of the type [26,27]

$$A(E_{\mathrm{ph}}) = \frac{A_0}{1 + \exp\left(\frac{E_{\mathrm{gap}}^{\mathrm{eff}} - E_{\mathrm{ph}}}{\Delta E}\right)}. \tag{5.1}$$

A_0 is a constant, and ΔE is equivalent to the width of the Urbach tail, which generally correlates with the crystalline disorder. The obtained ΔE from the fit is 12 meV, which is identical to the typical value found for GaN planar structures [28].

After irradiation, the GaN band edge slightly redshifts by about 40 meV and becomes less steep, i.e., ΔE increases [inset of **Figure 5.2(A)**]. The transparency in the visible

spectral range is reduced, as seen in the photos of the samples displayed in **Figure 5.2(B)**. Furthermore, an irradiation-induced absorption band (designated by irr-AB) emerges at ~455 nm (~2.7 eV) with an FWHM of ~35 nm (~0.2 eV); this band is superimposed with the interference fringes and the InGaN absorption tail making its perception difficult in some cases. These results suggest that ^{129}Xe SHI irradiation generates defects that introduce localized electronic states near the electronic bands of GaN (ΔE increases) [29] and a mid-gap state responsible for the absorption at ~2.7 eV that can be related to defects in GaN (barriers and/or template) and InGaN.

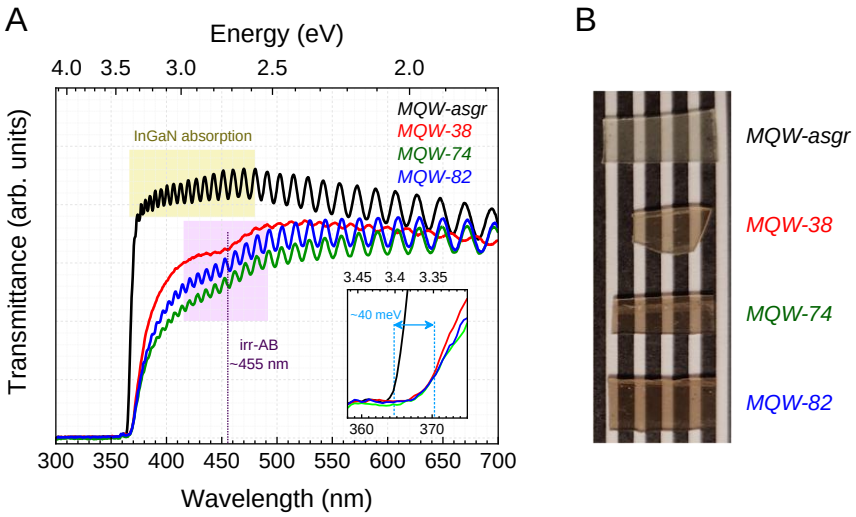

Figure 5.2 (A) Transmittance spectra of the InGaN/GaN MQWs before and after ^{129}Xe SHI irradiation. The inset enlarges the spectra around the GaN absorption edge. **(B)** Photo of the samples.

Aiming to clarify the origin of the irr-AB, the transmittance of the *c*-plane GaN layers irradiated under similar conditions is evaluated. From the spectra shown in **Figure 5.3**, one can notice that irradiation generates an absorption band with similar characteristics (energy position and FWHM) as that found for InGaN/GaN MQWs; for that reason, the same nomenclature of irr-AB is adopted. Also, the GaN absorption edge becomes less steep and redshifts about 40 meV compared to the as-grown sample. Such a result hints that the mid-gap states are related to GaN rather than InGaN.

F. Moisy et al. found the appearance of a similar absorption band in GaN layers irradiated with distinct ionic species. Its origin was tentatively linked to V_{Ga} defects, whose concentration was correlated with the number of atomic displacements triggered by nuclear elastic collisions [30]. Density functional theory (DFT) studies also predicted that the charge-state transition level of V_{Ga} (2−/3−) occurs at around this energy, 2.6–2.8 eV [31,32].

Thus, one can tentatively link the observed irr-AB band with the induction of such defects by ^{129}Xe SHI irradiation in the GaN lattice (barriers and/or template).

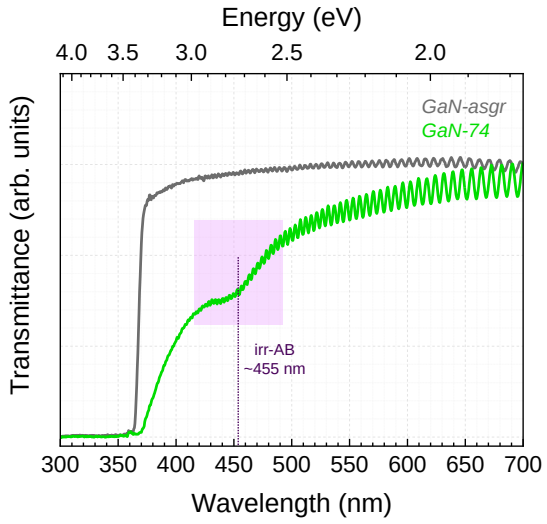

Figure 5.3 Transmittance spectra of GaN films before and after irradiation with 74 MeV accelerated ^{129}Xe SHI beam.

5.3.2. Micro-Raman

To further investigate the effects of ^{129}Xe SHI irradiation on the structure of the InGaN/GaN MQWs, micro-Raman spectroscopy is used. Although optical transmittance provides important information regarding the influence of irradiation on the electronic states, micro-Raman experiments can offer additional knowledge about lattice dynamics. As the lattice vibrations cause a periodic modulation of the electronic structure, Raman scattering is also sensitive to the electronic states, with the scattered signal being intensified near critical points of the electronic band structure [33]. Therefore, the use of distinct laser lines allows one to benefit from resonant and non-resonant excitation conditions with electronic states of GaN or InGaN, which are helpful to infer both the crystalline and electronic structures of the InGaN/GaN MQWs and how they are affected by ^{129}Xe SHI irradiation.

5.3.2.1. Non-resonant micro-Raman analysis

Figure 5.4 presents the micro-Raman spectra of the irradiated InGaN/GaN MQWs using the 632.8 nm laser line. Under this excitation, the optical transparency along the structure is high, making it possible to probe the entire sample's volume. Furthermore, as

the scattering volume in the MQWs is reduced, stronger contributions are expected to come from the GaN template and the Al_2O_3 substrate.

For the *MQW-asgr* sample, the three vibrational modes of WZ GaN allowed in the backscattering geometry $z(x\ \cdot\ )\bar{z}$ are detected at 142 ± 2 cm^{-1} [E_{2l} (GaN)], 569 ± 2 cm^{-1} [E_{2h} (GaN)], and 734 ± 2 cm^{-1} [A_1(LO) (GaN)]. Additional peaks related to the sapphire substrate are observed at ~418 cm^{-1} (A_{1g}) and ~750 cm^{-1} (E_g) [34], confirming that the 632.8 nm laser line probes the entire sample in depth.

After irradiation, and alongside the observation of the allowed first-order GaN phonons, distinct features appear in the spectra, which include *i)* an increase of background signal on the low-frequency side and *ii)* two new broad bands peaking at 300 cm^{-1} and 670 cm^{-1} associated with peculiarities of the GaN p-DOS. These observations are typical in damaged GaN structures and are associated with lattice disorder [30,35]. Notwithstanding the appearance of such features, first-order Raman scattering processes still dominate the spectra. Furthermore, it is not discerned any frequency shift of the BZ phonons (within the experimental uncertainty of ±2 cm^{-1}) nor an increase in the FWHM, hinting that ^{129}Xe SHI irradiation does not modify the strain state of the GaN template, at least considering the sensitivity of the technique.

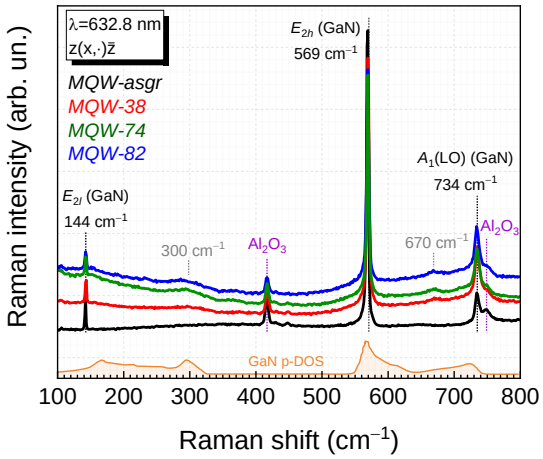

Figure 5.4 Micro-Raman spectra of the InGaN/GaN MQWs before and after SHI irradiation, obtained with the 632.8 nm line of a He-Ne laser. The p-DOS of GaN is included [36].

The previous results suggest that the sample as a whole is not seriously compromised; otherwise, the spectra would resemble the GaN p-DOS, as commonly observed in strongly disordered lattices [36]. Still, the intensity ratio between first-order processes and disorder-related features decreases slightly with increasing S_e, meaning that the damage level should be to some extent higher with increasing the ^{129}Xe SHI beam energy. Two possibilities

can justify such a behavior: *i)* the concentration of irradiation-induced defects is indeed low throughout the sample and only slightly increases with S_e, or *ii)* there are distinct regions in the sample with different concentrations of defects, for example, one with a higher concentration of defects responsible for the appearance of broad disorder-related bands and other comprising most of the sample's volume which is almost unaffected making the Raman spectrum to be dominated by first-order processes.

5.3.2.2. Resonant micro-Raman with electronic levels of GaN

A micro-Raman study performed using the 325 nm laser line is conducted to elucidate the previous hypotheses proposed to explain the damage distribution in the samples. In this case, the optical absorption in GaN and InGaN sections is high [37], causing the signal to come essentially from the upper region of the sample (~50 nm, considering the double absorption in backscattering geometry). Therefore, the analyzed volume is restricted under these conditions, with the most significant contribution arising from the GaN barriers. Moreover, under this excitation, Raman scattering occurs resonantly with the electronic band states of GaN, which shall lead to a substantial enhancement of the scattering intensity of the polar A_1(LO) (GaN) phonon in the GaN barriers due to Fröhlich interaction [38].

Figure 5.5(A) shows the micro-Raman spectra of the irradiated InGaN/GaN MQWs using the 325 nm laser line. For all the samples, the spectra reveal the two allowed phonons from GaN: E_{2h} (GaN) at 569 ± 5 cm^{-1} and A_1(LO) (GaN) at 734 ± 5 cm^{-1}, with the relative intensity of the latter favored due to the resonance with electronic levels of GaN. The two broad bands, previously associated with lattice disorder, can also be identified indistinguishably at 300 cm^{-1} and 670 cm^{-1}. It must be said that, for sample *MQW-asgr*, an intense GaN NBE luminescence tail is superimposed on the Raman signal, hindering the detection of the latter. Therefore, comparing the micro-Raman response before and after irradiation is impossible. After irradiation, as it strongly quenches the NBE luminescence intensity of GaN (shown and discussed later in **subsection 5.3.4**), the Raman signal can be detected without problems.

Figure 5.5(B) demonstrates the schematic representation of the geometry used in the Raman experiments as well as the penetration depth of 325 nm and 632.8 nm laser lines in the samples. When comparing the response obtained with both excitations, it is possible to notice that the phonons from the first BZ center [E_{2h} (GaN) and A_1(LO) (GaN)] are found at identical frequencies. However, their relative intensity differs due to energetic resonance with electronic states, translated by the intensity enhancement of A_1(LO) (GaN) under UV excitation. Furthermore, when using the 325 nm laser line, the spectral shape is more similar to the GaN p-DOS, reflecting the activation of phonons from the entire BZ due to crystalline disorder [36]. These findings suggest that the samples' surface region (i.e., the InGaN/GaN

MQWs) suffers more severe damage after ^{129}Xe SHI irradiation than deeper regions in the structure (e.g., the GaN template).

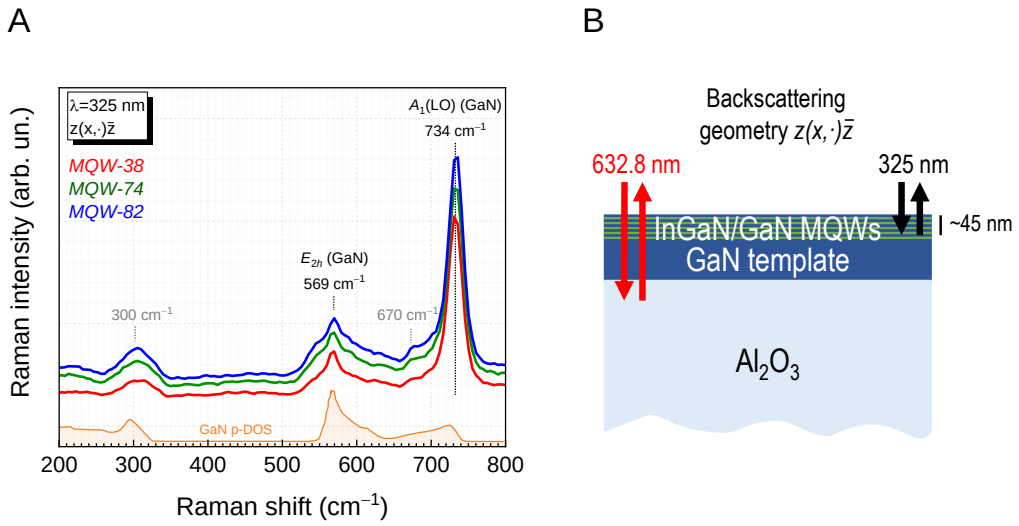

Figure 5.5 (A) Micro-Raman spectra of the InGaN/GaN MQWs before and after SHI irradiation, obtained with the 325 nm line of a He-Cd laser. The calculated p-DOS of GaN is included [36]. **(B)** Scheme of the micro-Raman scattering geometry used in the experiments and the penetration depth of both laser lines in the structure.

5.3.2.3. Resonant micro-Raman with electronic levels of InGaN MQWs

Given the reduced scattering volume of InGaN, no information from the MQWs could be perceived in the previous micro-Raman spectra. A possible way to access information from this region is to take advantage of resonance but, this time, with electronic states of InGaN. To attain this, the 442 nm (~2.8 eV) line of a He-Cd laser is used as excitation since it is close in energy to the InGaN absorption tail [previously shown in **Figure 5.2(A)**]. In this case, the scattering intensity of the polar A_1(LO) (InGaN) phonon is strongly enhanced due to Fröhlich interaction, making it possible to assess what happens in the InGaN MQWs [39–43].

Figure 5.6(A) shows the resonant Raman spectra of the MQWs after irradiation using the 442 nm laser line. Two bands can be identified in the spectra for all samples, one at 568 ± 3 cm^{-1} related to the E_{2h} (GaN) phonon and a broad band centered at ~730 cm^{-1} that may include contributions from InGaN, GaN, and Al_2O_3. It must be noted that for sample *MQW-asgr*, a strong luminescence contribution hampered the detection of the Raman signal, preventing an important comparison of the response before and after irradiation.

The micro-Raman spectra are deconvoluted using Lorentzian functions to distinguish the various contributions; **Figure 5.6(B)** shows an example of this procedure for sample *MQW-74*. The deconvolution considers two additional Gaussian functions to adjust better the contributions from background between 600–650 cm^{-1} and above 750 cm^{-1}. As a result, it is possible to identify the E_{2h} (GaN) phonon at 568 ± 3 cm^{-1} and the A_1(LO) (GaN) at 735 ± 3 cm^{-1} related to GaN (barriers and/or template). These values are comparable (within the experimental error) with those obtained with the previous excitations. Other features are uncovered: *i)* a disorder-related band at 670 cm^{-1}, *ii)* the A_{1g} and E_g phonons from the sapphire substrate peaking at 418 cm^{-1} (A_{1g}) and 750 cm^{-1} respectively, and *iii)* a peak at 720 ± 3 cm^{-1} likely related to the A_1(LO) (InGaN) mode.

Before making a clear conclusion about the assignment of the 720 cm^{-1} peak, it is necessary to consider all the resonance channels that can participate in this process. For instance, the 442 nm excitation is also resonant with electronic states associated with defects in GaN, namely the irr-AB [as seen in **Figure 5.2(A)**], which can mask the signal coming from InGaN and condition the analysis. In order to infer the influence of the defect states in the resonance profile, the micro-Raman response of sample GaN-74 is obtained under the same experimental conditions and compared with that of sample *MQW-74*, **Figure 5.6(C)**; remember that the absorption band irr-AB is observed for both the MQWs and GaN layers after irradiation. From this comparison, one can notice that the A_1(LO) (GaN) phonon intensity enhancement does not occur for irradiated GaN layers. Thus, one can rule out the involvement of the mid-gap defect states introduced in GaN after SHI irradiation to the intensity increase of the 720 cm^{-1} signal; instead, this result points out to the resonance with electronic levels of InGaN MQWs and the peak to be related to the A_1(LO) (InGaN) vibrational mode.

According to M. R. Correia et al., it is not possible to distinguish In-compositions, x, between 0.05 and 0.2 in pseudomorphic InGaN layers due to the opposite effects of composition and compressive strain to phonon frequency; in this case, the frequency of the A_1(LO) (InGaN) phonon lies between ~728–730 cm^{-1} [39]. Moreover, the CLT for relaxation of InGaN layers with $x < 0.25$ is predicted to be higher than 10 nm [44], hinting that the InGaN MQWs studied in this work grow coherently on GaN barriers (i.e., $a_{\mathrm{GaN}} = a_{\mathrm{InGaN}}$). Therefore, considering both compositional and biaxial strain effects, the total expected shift of the A_1(LO) (InGaN) phonon relative to A_1(LO) (GaN) is given by $\Delta\omega = \Delta\omega_x + \Delta\omega_s$. From equation (2.14), $\Delta\omega_x = -153x$. In turn, considering that a biaxial strain is introduced in the MQWs, the second term is expressed by $\Delta\omega_s = 2\left(a_\lambda - \frac{C_{13}}{C_{33}} b_\lambda\right) \frac{a_{\mathrm{GaN}} - a_{\mathrm{InN}}}{a_{\mathrm{InGaN}}} x$ [43]. Interpolating the values of the elastic constants, C_{13} and C_{33}, and the in-plane lattice parameter, a_{InGaN}, for $x = 0.15$–0.30 and taking the deformation potentials a_λ and b_λ associated with the A_1(LO) phonon reported for GaN [45], $\Delta\omega_s = (80 \pm 3)x$. Therefore, a

shift of 14 cm^{-1} relatively to the A_1(LO) (GaN) phonon corresponds to an In-composition ~0.2. However, it should be to noted that, if relaxation occurs for InGaN thicknesses below the CLT as proposed by S. Lazić et al. [43], the x value obtained by the above procedure for the InGaN MQWs is overestimated.

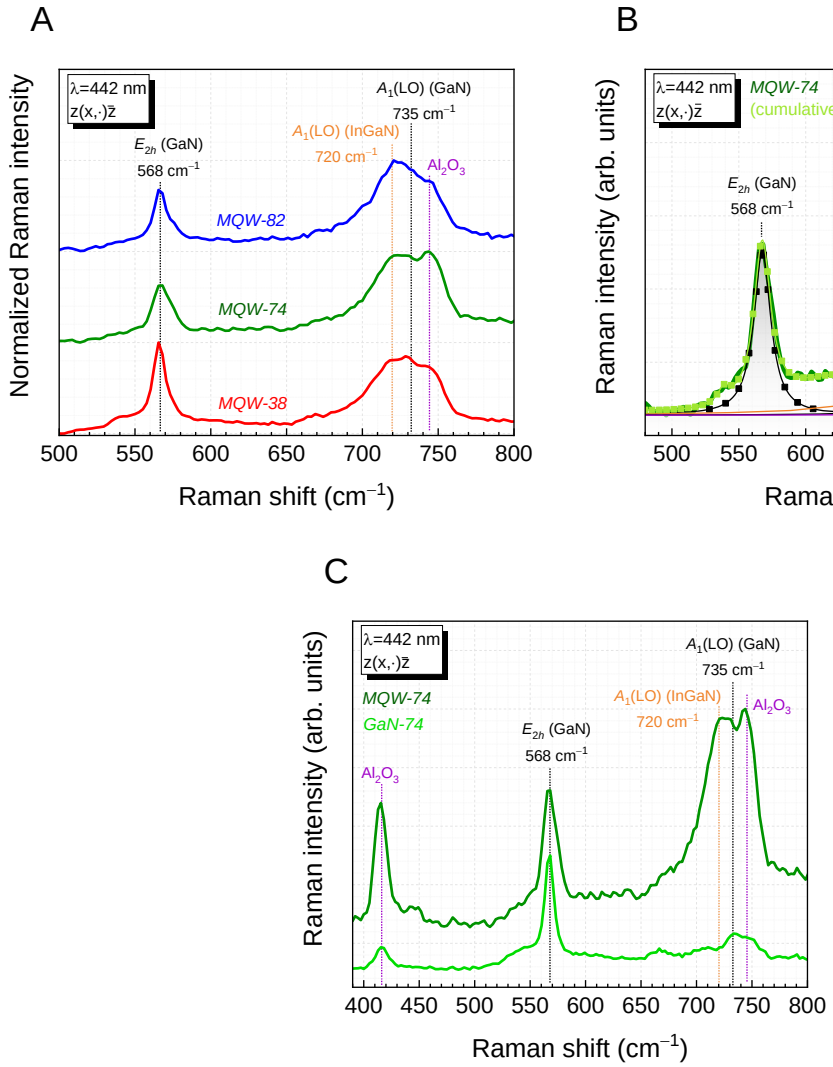

Figure 5.6 (A) Resonant micro-Raman spectra of the SHI irradiated InGaN/GaN MQWs using the 442 nm laser line. **(B)** Example of the procedure used to deconvolute the Raman signal from the previous spectra for sample *MQW-74*. **(C)** Comparison of the micro-Raman spectra of samples *MQW-74* and *GaN-74* obtained with the 442 nm excitation.

Besides, a closer look at the intensity ratio between A_1(LO) (InGaN) and E_{2h} (GaN) phonons, $I_{A_1(\mathrm{LO})(\mathrm{InGaN})}/I_{E_{2h}(\mathrm{GaN})}$, indicates the existence of differences as the ion beam energy changes [**Figure 5.6(A)**]. According to the deconvolution procedure, exemplified in **Figure 5.6(B)** for the highest irradiation energies (74 MeV and 82 MeV), the intensity

ratio doubles the value obtained for sample *MQW-36*. This points to a modification in the resonance profile with the electronic states of InGaN MQWs, with an approximation of the excitation energy for the higher SHI energies. A change in the In/Ga ratio (i.e., the occurrence of intermixing at the InGaN/GaN interfaces) could be responsible for the modification in the electronic resonance profile. Indeed, for these SHI energies, S_e is higher than most of the threshold energy values for track formation in GaN proposed in the literature [18–20]; this strengthens the hypotheses that In/Ga intermixing (along the track direction) may occur during the molten state reached after the passage of the ^{129}Xe SHI with energies of 74 MeV and 82 MeV.

5.3.3. Rutherford backscattering spectrometry measurements

Independent RBS/C measurements are conducted to support the previous conclusions made by Raman spectroscopy. This technique helps clarify questions about the crystalline damage and its in-depth profile introduced in the InGaN/GaN MQWs after their irradiation with ^{129}Xe SHI.

In a very simplified manner, an RBS/C experiment consists of detecting backscattered ions (and their respective energy) resulting from the elastic collisions between high-energy incident ions and atomic nuclei of the host. In a channeled experiment, the incident beam is aligned with a crystalline axis; therefore, the number of backscattered ions is expected to be low; the probability of an incident ion being backscattered in a channeled experiment scales up with the density of structural defects in the crystal. The comparison of such a response with the number of backscattered ions in a random/non-channeled configuration, mimicking the response of a completely disordered (amorphous) material, can give an estimation of the number of defects in the crystal. Furthermore, the ion beam also loses energy in the path before and after the collision, resulting in backscattered ions with different energies; this allows one to infer the in-depth distribution of defects since backscattered ions (resulting from the interaction with a given atomic nuclei) with successively lower energies come from a deeper region of the material [46].

Figure 5.7(A)–(C) show the RBS/C spectra of the InGaN/GaN MQWs after and before SHI irradiation acquired along the ⟨0001⟩ direction; the different plots correspond only to magnifications around different energy windows. From the high-energy to the low-energy side of the spectra, the first bump corresponds to backscattered ions by In-atoms, while the second plateau starting at ~1650 keV comes from the backscattered ions resulting from the collision with the Ga-atoms. After ^{129}Xe SHI irradiation, the backscattered signal increases compared to the response of the *MQW-asgr* sample. Although far from the random spectrum of the as-grown MQWs, the spectral shape tends to evolve in this direction with increasing the SHI beam energy, meaning that the introduced damage scales with that

parameter, which is in close agreement with micro-Raman results. A thorough analysis of the RBS/C will follow.

Using the McChasy software [24,25], the simulation of the random spectrum allows estimating the In-composition of the MQWs to be ~0.21, assuming a nominal QW thickness of 2.7 nm. Such a value matches the x value estimated by micro-Raman under 442 nm resonant excitation, confirming the validity of the methodology and analysis performed in **subsection 5.3.2**.

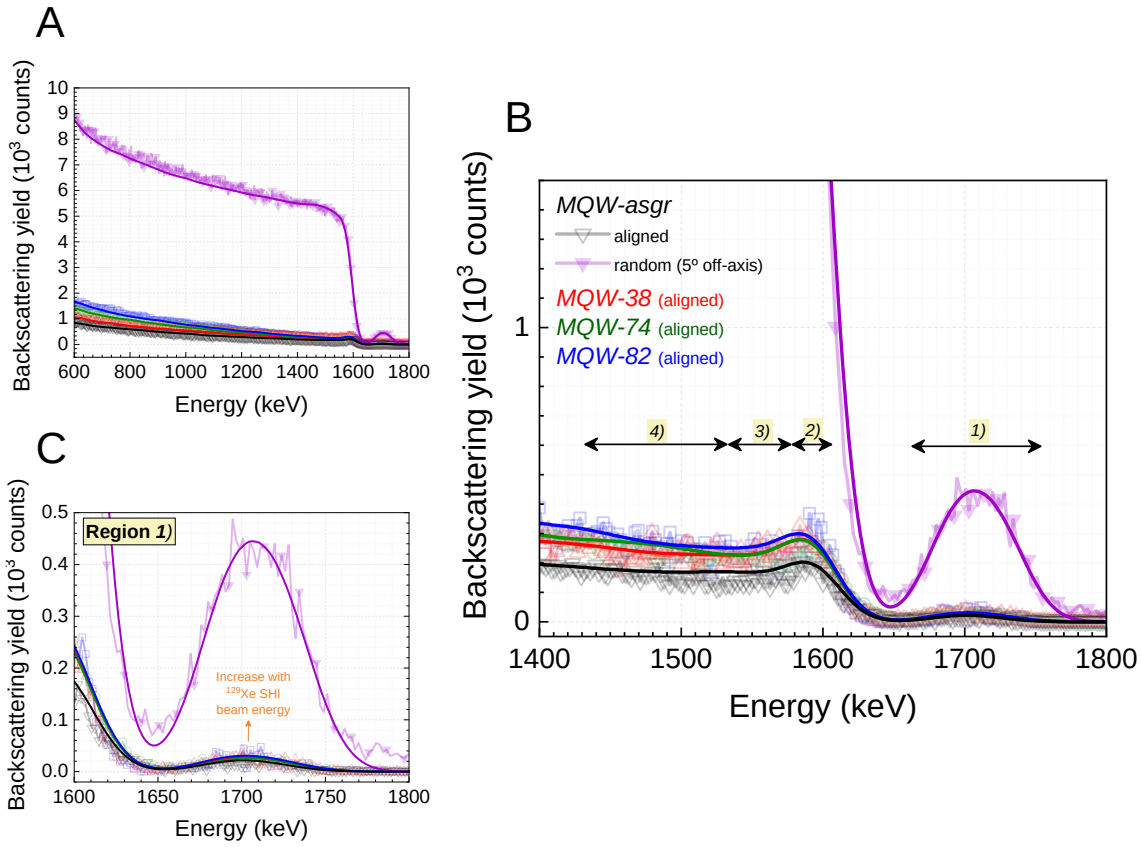

Figure 5.7 (A) RBS/C spectra of InGaN/GaN MQWs before and after SHI irradiation, obtained along the ⟨0001⟩ direction (aligned spectra). The random spectrum (5° off-axis) obtained for sample *MQW-asgr* is also included. Solid lines correspond to the MC simulations obtained using the McChasy code [24,25]. **(B)** Magnification of the previous spectra between 1400–1800 keV; the different energy windows to measure χ_{min} are represented: *1)* In-signal, *2)* Ga-signal from the MQWs close to the surface, *3)* Ga-signal from the MQWs close to the GaN template, and *4)* Ga-signal from the first ~120 nm of the GaN template. **(C)** Magnification around the energy window *1)*, i.e., 1600–1800 keV.

Moreover, as mentioned above, it is possible to extract information about the crystalline quality of the samples from the RBS/C spectra. This is done by calculating the minimum

yield (χ_{min}), defined as the ratio of the RBS signal in the aligned spectrum to that of the random one within a region of interest. To do such an analysis, the signal from four different energy windows is considered: *1)* In-atoms localized within the MQWs (1675–1745 keV), *2)* Ga-atoms localized within the MQWs closer to the surface (1580–1605 keV), *3)* Ga-atoms localized within the MQWs but close to the interface with the GaN template (1533–1580 keV), and *4)* Ga-atoms localized within the first ~120 nm of the GaN template (1433–1533 keV). It is important to note that it is not possible to distinguish between the Ga signal from the barriers and the MQWs. The χ_{min} values for each energy window considered are summarized in **Table 5.2**. The low minimum yield of the MQW-asgr reveals a high crystalline quality of the samples before irradiation [9]. After irradiation, χ_{min} increases due to the presence of lattice defects responsible for increasing the backscattering yield. The introduced damage can be quantified by calculating the relative defect fraction (f_D) that is given by $f_D = \frac{\chi_{aligned}^{irr} - \chi_{aligned}^{as-grown}}{\chi_{random}}$; the values obtained for each energy window are also included in **Table 5.2**.

Table 5.2 Summary of the χ_{min} and f_D values obtained from the RBS/C spectra for the InGaN/GaN MQWs before and after ^{129}Xe SHI irradiation.

Sample	**In – MQWs** (1675–1745 keV)		**Ga – MQWs surface** (1580–1675 keV)		**Ga – deeper in MQWs** (1533–1580 keV)		**Ga – GaN template** (1433–1533 keV)	
	χ_{min} (%)	f_D (%)	χ_{min} (%)	f_D (%)	χ_{min} (%)	f_D (%)	χ_{min} (%)	f_D (%)
MQW-asgr	3.2 ± 0.2	–	6.6 ± 0.3	–	2.8 ± 0.2	–	2.7 ± 0.2	–
MQW-38	5.2 ± 0.3	1.9 ± 0.2	8.9 ± 0.3	2.3 ± 0.2	4.4 ± 0.3	1.6 ± 0.2	4.4 ± 0.3	1.7 ± 0.2
MQW-74	5.4 ± 0.3	2.1 ± 0.2	8.6 ± 0.3	2.0 ± 0.2	4.2 ± 0.2	1.5 ± 0.2	4.2 ± 0.3	1.4 ± 0.2
MQW-82	5.7 ± 0.3	2.5 ± 0.2	10.1 ± 0.4	3.5 ± 0.2	4.6 ± 0.3	1.7 ± 0.2	4.6 ± 0.3	1.9 ± 0.2

Despite the different ^{129}Xe SHI energies, only the f_D values of the signal lying close to the surface suggest a significant damage increase (above 2 %). Their increase with the ion beam energy implies higher defect levels. The damage levels of GaN in a deeper region of the MQWs and the GaN template are identical within the uncertainty. These results indicate a higher density of defects on the samples' surface, particularly in the first MQWs, corroborating the previous micro-Raman analysis.

MC simulations using the McChasy code are carried out to trace the damage profile [24,25]. The corresponding in-depth distribution of defects, modeled as randomly displaced atoms (RDAs), is shown in **Figure 5.8**; for all the irradiated samples, defects are

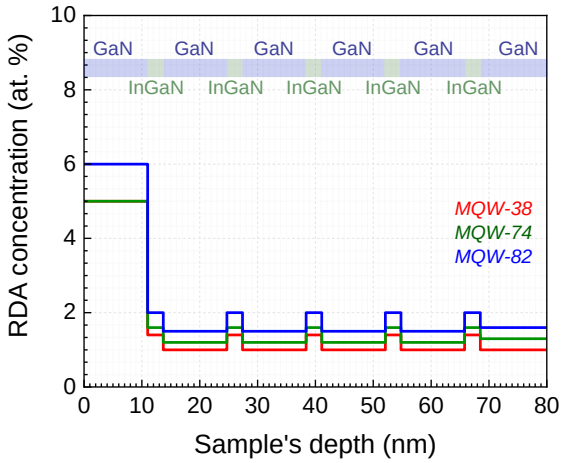

Figure 5.8 Depth-distribution of RDAs in the first 80 nm of the SHI irradiated InGaN/GaN MQWs extracted from the MC simulations using the McChasy code [24,25].

found to be predominant at the surface. However, to obtain a proper fit in the lowest energy region of the RBS/C spectra for samples *MQW-74* and *MQW-82*, it was necessary to consider the generation of dislocations in the GaN template with densities of 1×10^{9} cm^{-2} and 1.5×10^{9} cm^{-2}, respectively.

The results obtained in this chapter agree reasonably well with those reported recently for *c*-oriented GaN thin films irradiated with ^{129}Xe SHI in the same range of energies and fluence by M. Sequeira et al. [21,47]. Based on RBS/C results, they found that ^{129}Xe SHIs induced nearly no damage in the bulk crystal. They also found that the most damaged region was the surface due to sputtering, which led to the formation of voids and nano-hills. Low-density structures near the surface were also identified in high-resolution and Fresnel TEM images [**Figure 5.9(A)** and **Figure 5.9(B)**] [21,47].

Furthermore, M. Sequeira et al. developed a Two Temperature Model – Molecular Dynamics (TTM-MD) simulation scheme capable of describing the interaction of SHI with GaN. Using it, they demonstrated that ^{129}Xe irradiation (for $S_e > 14.9$ keV $\cdot$ nm^{-1}) induces a thermal spike such that the lattice temperature goes up to 9000 K (highly above the melting temperature of GaN of ~2500 K at atmospheric pressure), forming a cylindrical track of molten material, where atomic diffusion can occur. Even though recrystallization of part of the molten region occurs some picoseconds after the SHI passage, discontinuous tracks, consisting essentially of small clusters of point defects, still exist close to the surface. The presence of superficial voids for depths up to 5 nm and 18 nm for energies of 45 MeV and 70 MeV, respectively, was also shown [21]. The damaged core of the track was found to have a maximum radius of only 0.7 ± 0.2 nm; for a fluence of 2×10^{12} cm^{-2} and under the assumption that track overlap is not occurring, only 3% of the sample is damaged at the

end of the SHI passage with predominance to the surface [21,47]. The formation of dislocations in GaN layers irradiated in similar conditions was also predicted using MD simulations. **Figure 5.9(C)** and **Figure 5.9(D)** show some of the TTM-MD simulation results obtained by these authors for GaN layers irradiated with 70 MeV ^{129}Xe SHI [21].

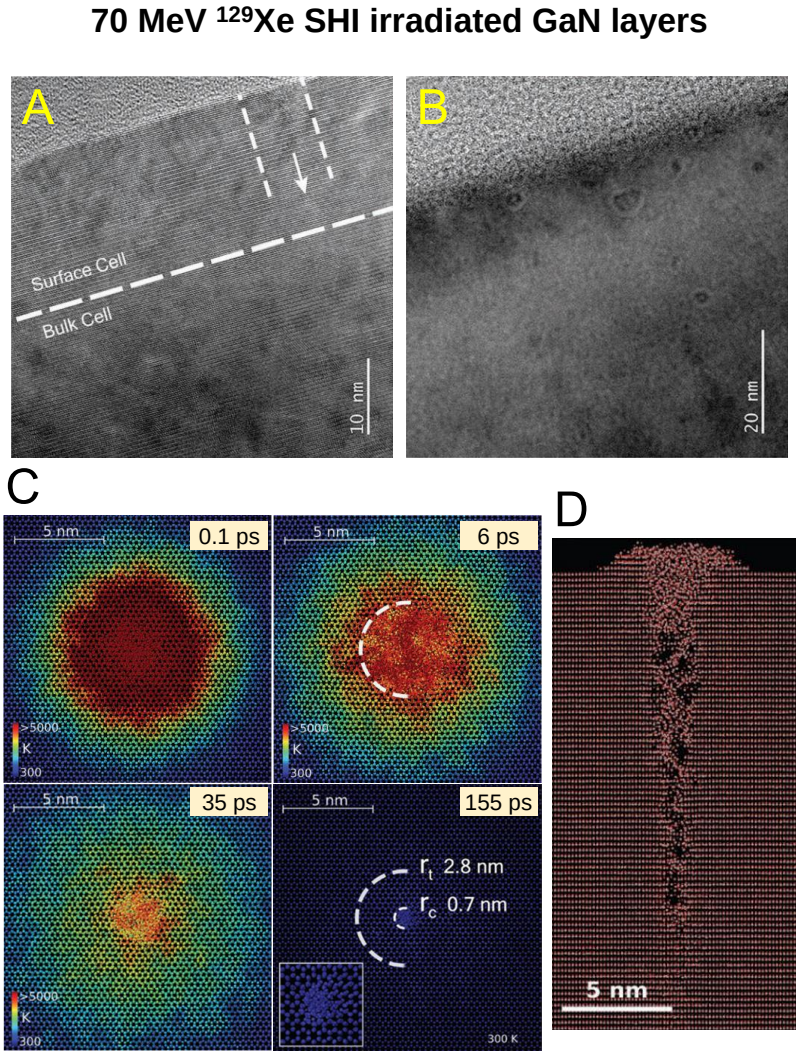

Figure 5.9 (A) HR-TEM image and **(B)** Fresnel contrast TEM image of a GaN layer irradiated with 70 MeV ^{129}Xe SHIs. The white arrow in **(A)** indicates a possible SHI track. **(C)** TTM-MD simulation results for GaN layers impacted by a 70 MeV ^{129}Xe SHI (top-view). The temperature evolution in the GaN cell is represented from 0.1 ps to 155 ps after the ion impact. **(D)** Cross-sectional images of the simulated track near the surface, being possible to notice a discontinuous defective track is seen. The images presented here are reprinted from [47].

The TTM-MD simulations and TEM results of M. Sequeira et al. led to the same conclusion relative to the low damage level determined from RBS/C and non-resonant

micro-Raman (632.8 nm excitation). In turn, when using the 325 nm resonant excitation, only the surface region is probed (~45 nm), as it is the most affected region by SHI irradiation with clusters of point defects, voids, and nano hills, the Raman spectral shape resembles the GaN p-DOS due to a more significant lattice disorder. The fact that the results from the two distinct and independent methodologies lead to similar results demonstrates the robustness of this discussion.

5.3.4. Photoluminescence and photoluminescence excitation

PL and PLE experiments are carried out to access information about the localization of the emitting states of InGaN/GaN MQWs and their respective excitation pathways before and after ^{129}Xe SHI irradiation.

Figure 5.10 depicts the RT PL spectra of *MQW-asgr*, *MQW-38*, and *MQW-82* samples when excited above the GaN bandgap energy. For *MQW-asgr*, the PL spectrum reveals the GaN NBE emission peak at 363 nm (3.4 eV) and a broad and intense green/yellow luminescence (GL/YL) band with a maximum at ~550 nm (2.3 eV). The GL/YL is modulated by optical interference caused by the superposition of multiple reflections in the GaN-based film. Under these excitation and detection conditions, detecting luminescence after irradiation is impossible. Such extinction in the PL intensity is likely caused by the surface damage created by irradiation (clusters of point defects, voids, and nano hills), which can contribute substantially to non-radiatively de-exciting the optically excited carriers. In a similar and contemporaneous work, Y. Wang et al. also observed that SHI irradiation seriously degrades the luminescence of InGaN/GaN UV LEDs, emitting at ~390 nm, due to the generation of detrimental defects; the leakage current increases as well [48].

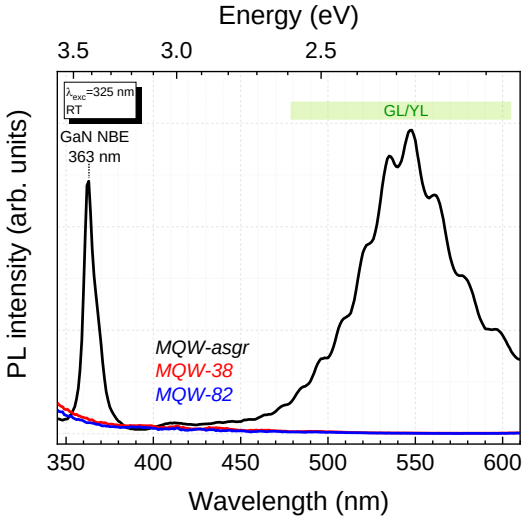

Figure 5.10 RT PL spectra of samples *MQW-asgr*, *MQW-38*, and *MQW-82* exciting at 325 nm (3.8 eV). The tail below 380 nm in the spectra of the irradiated samples is due to direct excitation light reaching the detector.

Notably, distinct contributions can participate in the GL/YL band: InGaN excitonic emission and deep-level defects in both GaN and InGaN lattices. **Figure 5.11(A)** shows the normalized PLE spectra when monitoring the emission wavelength at distinct GL/YL band positions for sample *MQW-asgr*. Two excitation paths can be distinguished: *i)* the GaN absorption edge at the lower wavelength side and *ii)* an excitation tail that extends from the GaN edge up to ~450 nm (~2.75 eV) due to InGaN absorption. Although excitation above the GaN band gap gives rise to the entire GL/YL band, the same does not happen when excitation is accomplished through the second path. In that case, only a narrow contribution of the GL/YL, between ~510–570 nm (~2.4–2.2 eV), is excited through InGaN. This result implies that at least two emitting centers contribute to the green/yellow luminescence, one involving localized excitons in InGaN and another related to deep-level defects in GaN that give rise to a broader emission. In GaN layers, such defect-related emission is often assigned to defects involving carbon impurities [49–51]. Carbon and oxygen impurities are common impurities in undoped III-Ns grown by MOVPE, being introduced either from the precursors or from the release of gases from the reactor components [52]. Nevertheless, given the complexity of the GL/YL band in GaN, the involvement of other defects cannot be excluded, particularly those involving lattice defects like V_{Ga} and associated complex defects [31,32,53–55].

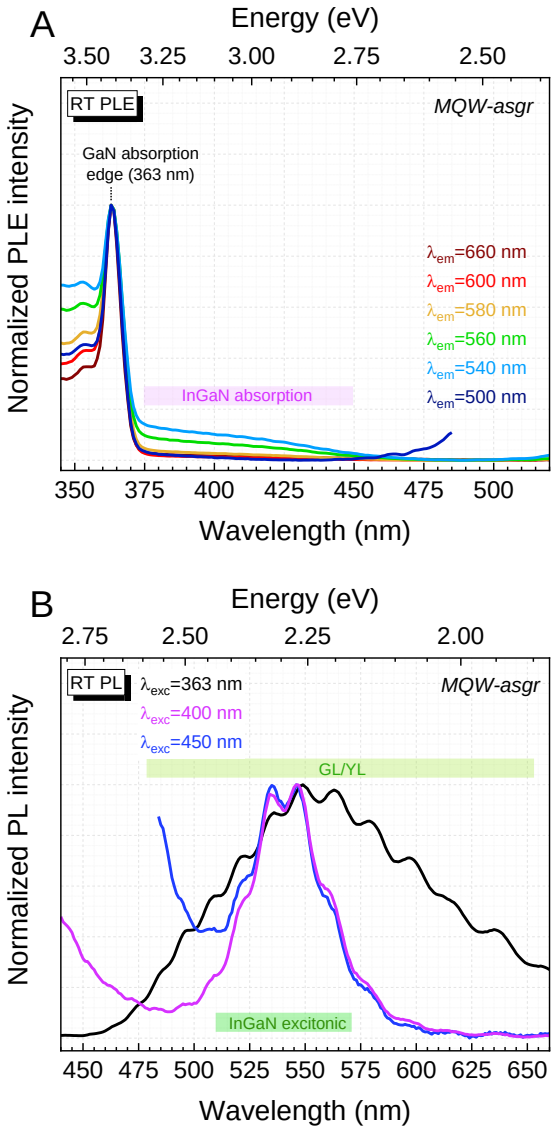

Figure 5.11 (A) RT PLE spectra of *MQW-asgr* monitoring at different emission wavelengths of the GL/YL. **(B)** RT PL spectra of the same sample for excitation above ($\lambda_{exc} = 363$ nm) and below ($\lambda_{exc} = 400$ nm and $\lambda_{exc} = 450$ nm) the GaN bandgap energy.

The changes in the spectral shape of the GL/YL band in sample *MQW-asgr* under different excitation wavelengths can be better analyzed in **Figure 5.11(B)**. From this, it is possible that the InGaN excitonic emission peaks at ~540 nm (~2.3 eV). Considering the correlation between the InGaN effective bandgap (E_{gap}^{eff}) and the emission maximum (E_{PL}) proposed by K. O' Donnell et al. for different types of InGaN structures ($E_{PL} = 1.45E_{gap}^{eff} - 1.54$), one can predict that E_{gap}^{eff} should be at ~2.65 eV. This value closely matches the onset of the absorption tail found in the PLE spectrum. Assuming once again that this is affected by compositional effects and the biaxial strain resulting from the

coherent growth of InGaN on GaN barriers, an In-composition of 0.23–0.24 can be estimated using the following expression: $E_{\mathrm{gap}}^{\mathrm{eff}} = 0.7x + 3.4(1-x) - 1.65(1-x) + 0.79x$ [56]. However, it is important to consider that in MQWs, the PL peak energy can be redshifted due to QCSE [57] and compositional fluctuations in the QWs [58], which can result in an overestimation of x. In turn, the assumption of coherent growth of InGaN to the GaN barriers results in an underestimation x.

Returning to **Figure 5.10**, it is essential to understand whether the GL/YL after irradiation is extinguished by removing the associated defects or by changing the excitation pathways. To unveil it, PLE spectra are obtained by monitoring distinct emission wavelengths of the GL/YL (i.e., considering a similar spectral range to that of the *MQW-asgr* sample). **Figure 5.12(A)** shows the RT PLE spectra for sample *MQW-82*, confirming that the GL/YL band is not quenched; the excitation channels differ. After irradiation, the GL/YL band cannot be excited with energy above the GaN bandgap. A possible reason for this involves the non-radiative defects generated near the surface; these can introduce energy levels in the GaN mid-gap that act as traps for electrons (holes) optically excited to the GaN CB (VB), which would act as nonradiative recombination channels [59–61]. This possibly explains why it is not detected any UV/visible luminescence (with the experimental conditions used) when GaN band-to-band excitation happens. Instead, after irradiation, the GL/YL band is excited through an excitation band identical to the irr-AB (in energy position and FWHM).

Nevertheless, after ^{129}Xe SHI irradiation, there are other defects formed in GaN with energy levels in the forbidden gap, namely the one that can absorb light with energy below the GaN bandgap [irr-AB, previously observed in **Figure 5.2(A)**]. In this case, the excitation of the contribution of the GL/YL band due to defects in GaN is possible, revealing that irradiation introduces a new excitation channel. By varying the excitation along the irr-AB, the spectral shape of the GL/YL band does not change. It should be mentioned that the absorption through InGaN may overlap with irr-AB, hindering the identification of the InGaN absorption onset and, consequently, the existence of deviations resulting from In/Ga intermixing, which had been previously suggested to occur in micro-Raman experiments under electronic resonance conditions.

The comparison between the GL/YL excitation processes before and after irradiation can be seen in **Figure 5.12(B)**. Here, it is possible to identify that, after irradiation, the preferential excitation pathway for the YL/GL is through the absorption band generated and centered at ~455 nm (~2.7 eV), independently of the electronic energy loss of the SHIs, at least within the range studied.

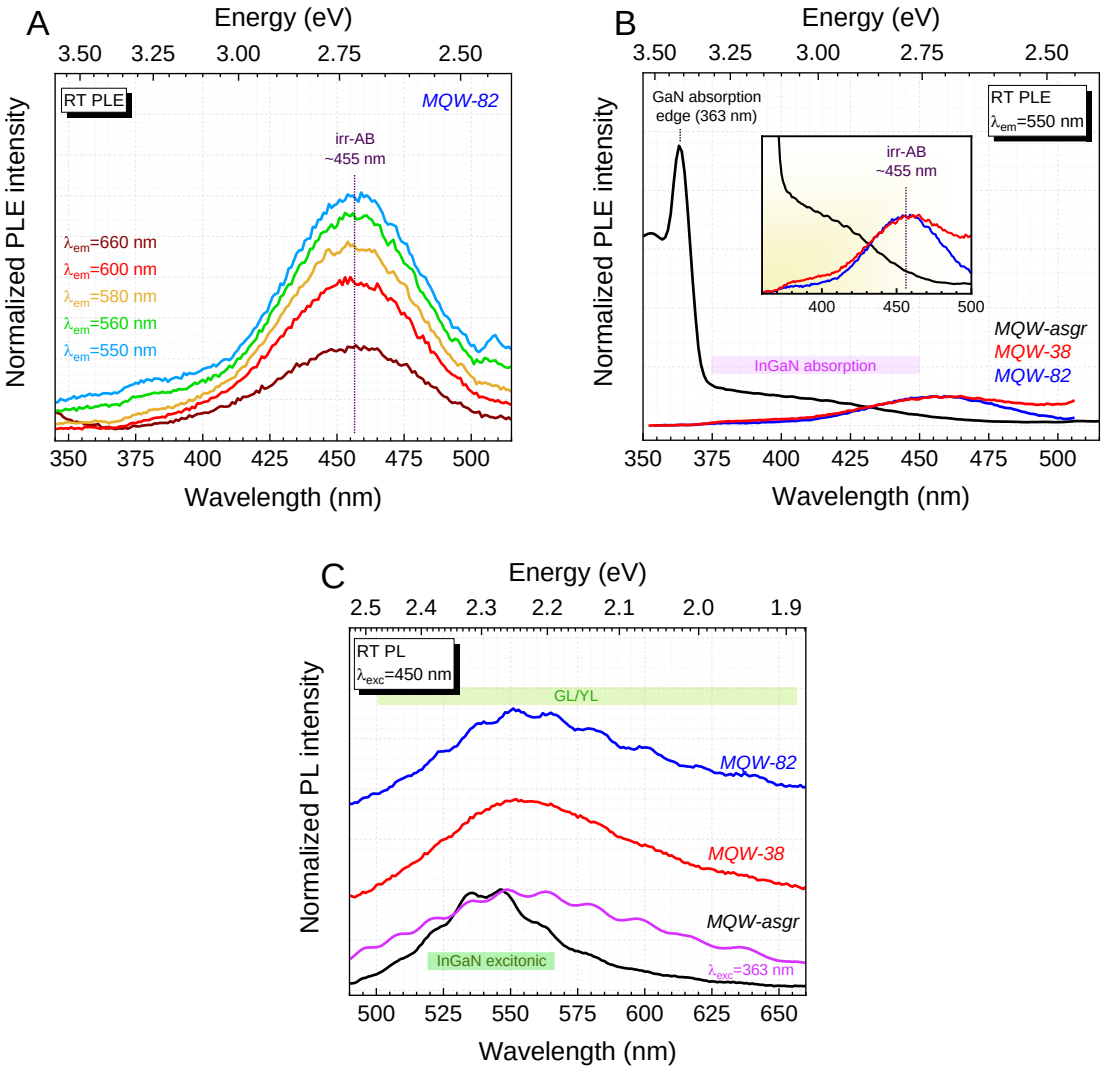

Figure 5.12 (A) RT PLE spectra of sample *MQW-82* monitoring at different emission wavelengths. **(B)** Normalized RT PLE of samples *MQW-asgr*, *MQW-38*, and *MQW-82* when monitoring the GL/YL peak. The spectra of the irradiated samples are normalized to the intensity maximum of the irr-AB, while that of sample *MQW-asgr* is normalized by the intensity at 400 nm. **(C)** RT PL spectra of the same samples using $\lambda_{exc} = 450$ nm. For *MQW-asgr*, an additional spectrum ($\lambda_{exc} = 363$ nm) is included for comparison.

Figure 5.12(C) shows the normalized RT PL spectra of *MQW-asgr*, *MQW-38*, and *MQW-82* samples when excited with 440 nm light. This energy excites through InGaN and irr-AB, the last only for irradiated samples. The PL spectrum of *MQW-asgr*, when exciting with 360 nm light, is also included in **Figure 5.12(C)**. Despite the strong quenching in PL integrated intensity (it is more than two orders of magnitude) and differences in the excitation mechanisms of the GL/YL, its spectral shape is analogous to that of the sample

MQW-asgr obtained for excitation above the GaN bandgap. This suggests that the contributions to the GL/YL band remain identical despite the different excitation pathways.

Figure 5.13 presents an illustration that summarizes the effects of ^{129}Xe SHI irradiation on the InGaN/GaN MQWs and their luminescence.

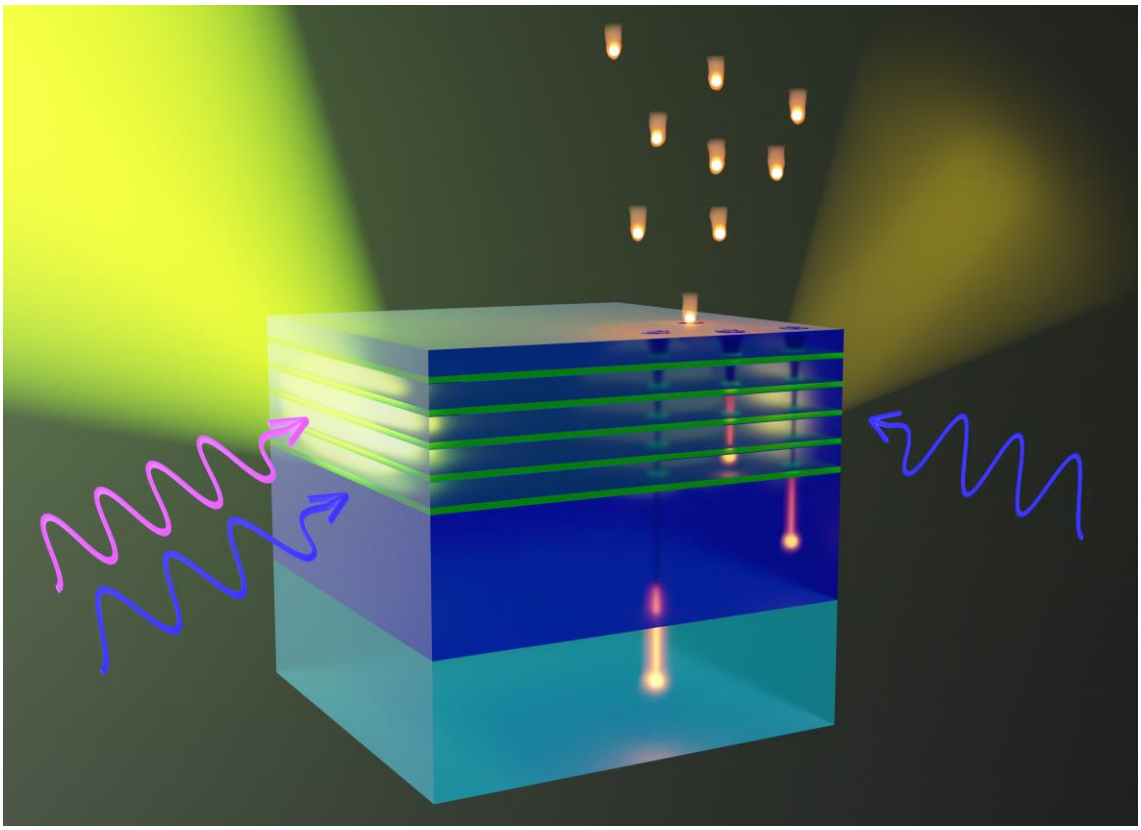

Figure 5.13 Illustration of the effects of ^{129}Xe SHI irradiation on the luminescence of InGaN/GaN MQWs. This image is the back cover art of the "Exploring swift-heavy ion irradiation of InGaN/GaN multiple quantum wells for green-emitters: the use of Raman and photoluminescence to assess the irradiation effects on the optical and structural properties," published in the *Journal of Materials Chemistry C* (Volume **9**, 2021, pp. 8809).

5.4. Summary

In this chapter, the effects of ^{129}Xe SHI irradiation with energies between 38 MeV and 82 MeV on the optical and structural properties of InGaN/GaN MQWs were explored. The following results were obtained:

- A profile of the structural damage induced by SHI irradiation was identified by micro-Raman spectroscopy results. By combining different excitation wavelengths under resonant and non-resonant conditions, the surface of the samples was found to be the most affected region, with a higher concentration of defects detrimental to the luminescent characteristics of the MQWs.
- Independent RBS/C measurements and MC simulations revealed a similar in-depth damage profile.
- The overall damage introduced only slightly increases with increasing the ^{129}Xe SHI beam energy in the studied range of energies.
- The resonance profile in InGaN changed with the irradiation energy, as evidenced in micro-Raman experiments by the increase in the relative intensity of A_1^{LO} (InGaN) for higher irradiation energies (74 MeV and 82 MeV). This was proposed to be due to QWI.
- Two distinct contributions for the GL/YL were distinguished for the sample *MQW-asgr*: *i)* InGaN excitonic emission and *ii)* GaN deep-level defects emission.
- After SHI irradiation, a strong quenching of the intensity of GL/YL was observed, accompanied by a change in the excitation processes. An electronic state in the GaN mid-gap (responsible for the absorption band irr-AB centered at ~2.75 eV and tentatively attributed to V_{Ga} defects) was found to participate in the excitation of the contribution from GaN-related defects to the GL/YL.
- It was impossible to discern the distinct GL/YL contributions (and consequently QWI) from PL/PLE experiments after SHI irradiation due to the spectral overlap of irr-AB and InGaN absorption edge.

In summary, it is possible to infer that using SHI might result in the pretended QUI. However, it also results in defects detrimental to the luminescence of the InGaN/GaN MQWs, conditioning light emission and extraction efficiencies. Therefore, instead of improving the performance of the LEDs due to the QWI, this approach ends up being harmful to them.

References

[1] C. Weisbuch et al., The efficiency challenge of nitride light-emitting diodes for lighting, *Phys. Status Solidi Appl. Mater. Sci.* **212** (2015) 899–913. https://doi.org/10.1002/pssa.201431868.

[2] M. Meneghini et al., Thermal droop in III-nitride based light-emitting diodes: Physical origin and perspectives, *J. Appl. Phys.* **127** (2020). https://doi.org/10.1063/5.0005874.

[3] J. Li et al., III-Nitrides Light Emitting Diodes: Technology and Applications, 1st ed., Springer Nature Singapore Pte Ltd, Singapore, 2020.

[4] T.-Y. Seong et al., eds., III-Nitride Based Light Emitting Diodes and Applications, 2nd ed., Springer Nature Singapore Pte Ltd, Singapore, 2013.

[5] M. Auf Der Maur et al., Band gap engineering approaches to increase InGaN/GaN LED efficiency, *Opt. Quantum Electron.* **44** (2012) 83–88. https://doi.org/10.1007/s11082-011-9536-x.

[6] M. Auf der Maur et al., Efficiency Drop in Green InGaN/GaN Light Emitting Diodes: The Role of Random Alloy Fluctuations, *Phys. Rev. Lett.* **116** (2016) 027401. https://doi.org/10.1103/PhysRevLett.116.027401.

[7] K.P. O'Donnell et al., It's not easy being green: Strategies for all-nitrides, all-colour solid state lighting, *Phys. Status Solidi - Rapid Res. Lett.* **6** (2012) 49–52. https://doi.org/10.1002/pssr.201100206.

[8] S.-H. Han et al., Improvement of efficiency droop in InGaN/GaN multiple quantum well light-emitting diodes with trapezoidal wells, *J. Phys. D. Appl. Phys.* **43** (2010) 354004. https://doi.org/10.1088/0022-3727/43/35/354004.

[9] K. Lorenz et al., Quantum well intermixing and radiation effects in InGaN/GaN multi quantum wells, in: J.-I. Chyi et al. (Eds.), Proceeding SPIE - Gall. Nitride Mater. Devices XI, 2016: p. 97480L. https://doi.org/10.1117/12.2211429.

[10] C.C. Chuo et al., Interdiffusion of in and Ga in InGaN/GaN multiple quantum wells, *Appl. Phys. Lett.* **78** (2001) 314–316. https://doi.org/10.1063/1.1339991.

[11] M.D. McCluskey et al., Interdiffusion of In and Ga in InGaN quantum wells, *Appl. Phys. Lett.* **73** (1998) 1281–1283. https://doi.org/10.1063/1.122149.

[12] M.A. Sousa et al., Luminescence studies on green emitting InGaN/GaN MQWs implanted with nitrogen, *Sci. Rep.* **5** (2015) 6–11. https://doi.org/10.1038/srep09703.

[13] M. Toulemonde et al., Thermal spike model in the electronic stopping power regime, *Radiat. Eff. Defects Solids.* **126** (1993) 201–206. https://doi.org/10.1080/10420159308219709.

[14] M. Lang et al., Fundamental Phenomena and Applications of Swift Heavy Ion Irradiations, in: Compr. Nucl. Mater., Elsevier, 2020: pp. 485–516. https://doi.org/10.1016/B978-0-12-803581-8.11644-3.

[15] W. Bolse, Interface modification by swift heavy ions, *Radiat. Meas.* **36** (2003) 597–603. https://doi.org/10.1016/S1350-4487(03)00208-7.

[16] W.J. Weber et al., The role of electronic energy loss in ion beam modification of

materials, *Curr. Opin. Solid State Mater. Sci.* **19** (2015) 1–11. https://doi.org/10.1016/j.cossms.2014.09.003.

[17] D.K. Avasthi et al., Swift Heavy Ions for Materials Engineering and Nanostructuring, 1st ed., Springer Netherlands, Netherlands, 2011.

[18] M. Sall et al., Track formation in III-N semiconductors irradiated by swift heavy ions and fullerene and re-evaluation of the inelastic thermal spike model, *J. Mater. Sci.* **50** (2015) 5214–5227. https://doi.org/10.1007/s10853-015-9069-y.

[19] F. Moisy et al., Optical bandgap and stress variations induced by the formation of latent tracks in GaN under swift heavy ion irradiation, *Nucl. Instruments Methods Phys. Res. Sect. B Beam Interact. with Mater. Atoms.* **431** (2018) 12–18. https://doi.org/10.1016/j.nimb.2018.06.014.

[20] M. Karlušić et al., Response of GaN to energetic ion irradiation: conditions for ion track formation, *J. Phys. D. Appl. Phys.* **48** (2015) 325304. https://doi.org/10.1088/0022-3727/48/32/325304.

[21] M.C. Sequeira et al., Unravelling the secrets of the resistance of GaN to strongly ionising radiation, *Commun. Phys.* **4** (2021) 51. https://doi.org/10.1038/s42005-021-00550-2.

[22] K. Prabakaran et al., Electronic excitation induced structural and optical modifications in InGaN/GaN quantum well structures grown by MOCVD, *Nucl. Instruments Methods Phys. Res. Sect. B Beam Interact. with Mater. Atoms.* **394** (2017) 81–88. https://doi.org/10.1016/j.nimb.2016.12.042.

[23] J.F. Ziegler et al., SRIM: The stopping and range of ions in matter, 1st ed., United States, 2008.

[24] P. Jozwik et al., Advanced Monte Carlo Simulations for Ion-Channeling Studies of Complex Defects in Crystals, in: 2020: pp. 133–160. https://doi.org/10.1007/978-3-030-37790-8_8.

[25] P. Jozwik et al., Monte Carlo simulations of ion channeling in crystals containing dislocations and randomly displaced atoms, *J. Appl. Phys.* **126** (2019) 195107. https://doi.org/10.1063/1.5111619.

[26] R.W. Martin et al., Exciton localization and the Stokes' shift in InGaN epilayers, *Appl. Phys. Lett.* **74** (1999) 263–265. https://doi.org/10.1063/1.123275.

[27] K.P. O'Donnell et al., Origin of Luminescence from InGaN Diodes, *Phys. Rev. Lett.* **82** (1999) 237–240. https://doi.org/10.1103/PhysRevLett.82.237.

[28] M.A. Jacobson et al., Absorption spectra of GaN: Film characterization by Urbach spectral tail and the effect of electric field, *J. Cryst. Growth.* **230** (2001) 459–461. https://doi.org/10.1016/S0022-0248(01)01246-5.

[29] J.F. Wager, Real- and reciprocal-space attributes of band tail states, *AIP Adv.* **7** (2017). https://doi.org/10.1063/1.5008521.

[30] F. Moisy et al., Effects of electronic and nuclear stopping power on disorder induced in GaN under swift heavy ion irradiation, *Nucl. Instruments Methods Phys. Res. Sect. B Beam Interact. with Mater. Atoms.* **381** (2016) 39–44. https://doi.org/10.1016/j.nimb.2016.05.024.

[31] J.L. Lyons et al., First-principles theory of acceptors in nitride semiconductors, *Phys.*

Status Solidi. **252** (2015) 900–908. https://doi.org/10.1002/pssb.201552062.

[32] J.L. Lyons et al., Computationally predicted energies and properties of defects in GaN, *Npj Comput. Mater.* **3** (2017) 1–9. https://doi.org/10.1038/s41524-017-0014-2.

[33] T. Ruf, Phonon Raman Scattering in Semiconductors, Quantum Wells and Superlattices, 1st ed., Springer-Verlag Berlin Heidelberg, Germany, 1998.

[34] P.G. Li et al., Raman and photoluminescence properties of α-Al_2O_3 microcones with hierarchical and repetitive superstructure, *Mater. Lett.* **64** (2010) 161–163. https://doi.org/10.1016/j.matlet.2009.10.032.

[35] M. Katsikini et al., Raman study of Mg, Si, O, and N implanted GaN, *J. Appl. Phys.* **94** (2003) 4389–4394. https://doi.org/10.1063/1.1606521.

[36] V.Y. Davydov et al., Phonon dispersion and Raman scattering in hexagonal GaN and AlN, *Phys. Rev. B.* **58** (1998) 12899–12907. https://doi.org/10.1103/PhysRevB.58.12899.

[37] J.F. Muth et al., Absorption coefficient, energy gap, exciton binding energy, and recombination lifetime of GaN obtained from transmission measurements, *Appl. Phys. Lett.* **71** (1997) 2572–2574. https://doi.org/10.1063/1.120191.

[38] D. Behr et al., Resonant Raman scattering in hexagonal GaN, *Appl. Phys. Lett.* **68** (1996) 2404–2406. https://doi.org/10.1063/1.116148.

[39] M.R. Correia et al., Raman study of the A_1(LO) phonon in relaxed and pseudomorphic InGaN epilayers, *Appl. Phys. Lett.* **83** (2003) 4761–4763. https://doi.org/10.1063/1.1627941.

[40] M.R. Correia et al., Raman spectroscopy studies in InGaN/GaN wurtzite epitaxial films, *MRS Proc.* **639** (2000) G6.10. https://doi.org/10.1557/PROC-639-G6.10.

[41] J. Wagner et al., Effect of strain and associated piezoelectric fields in InGaN/GaN quantum wells probed by resonant Raman scattering, *Appl. Phys. Lett.* **74** (1999) 3863–3865. https://doi.org/10.1063/1.124205.

[42] D. Behr et al., Evidence for compositional inhomogeneity in low in content (InGa)N obtained by resonant Raman scattering, *Appl. Phys. Lett.* **73** (1998) 241–243. https://doi.org/10.1063/1.121768.

[43] S. Lazić et al., Resonant Raman scattering in strained and relaxed InGaN/GaN multi-quantum wells, *Appl. Phys. Lett.* **86** (2005) 1–3. https://doi.org/10.1063/1.1861496.

[44] S. Pereira et al., Structural and optical properties of InGaN/GaN layers close to the critical layer thickness, *Appl. Phys. Lett.* **81** (2002) 1207–1209. https://doi.org/10.1063/1.1499220.

[45] J.M. Wagner et al., Phonon deformation potentials of α-GaN and -AlN: An ab initio calculation, *Appl. Phys. Lett.* **77** (2000) 346–348. https://doi.org/10.1063/1.127009.

[46] W.-K. Chu et al., Backscattering spectrometry, Academic Press, California, United States, 1978.

[47] M.C. Sequeira et al., Examining Different Regimes of Ionization-Induced Damage in GaN Through Atomistic Simulations, *Small.* **18** (2022). https://doi.org/10.1002/smll.202102235.

[48] Y. Wang et al., Degradation mechanisms of InGaN/GaN UVA LEDs under swift

heavy ion irradiation: role of defects, *Semicond. Sci. Technol.* (2021) https://doi.org/10.1088/1361-6463/aad7de. https://doi.org/10.1088/1361-6641/ac1b13.

[49] J.L. Lyons et al., Carbon impurities and the yellow luminescence in GaN, *Appl. Phys. Lett.* **97** (2010) 152108. https://doi.org/10.1063/1.3492841.

[50] M.A. Reshchikov et al., Two yellow luminescence bands in undoped GaN, *Sci. Rep.* **8** (2018) 1–11. https://doi.org/10.1038/s41598-018-26354-z.

[51] M.A. Reshchikov et al., Two charge states of the C_N acceptor in GaN: Evidence from photoluminescence, *Phys. Rev. B.* **98** (2018) 125207. https://doi.org/10.1103/PhysRevB.98.125207.

[52] I.M. Watson, Metal organic vapour phase epitaxy of AlN, GaN, InN and their alloys: A key chemical technology for advanced device applications, *Coord. Chem. Rev.* **257** (2013) 2120–2141. https://doi.org/10.1016/j.ccr.2012.10.020.

[53] M.A. Reshchikov et al., Luminescence properties of defects in GaN, *J. Appl. Phys.* **97** (2005) 1–95. https://doi.org/10.1063/1.1868059.

[54] A. Sedhain et al., Nature of deep center emissions in GaN, *Appl. Phys. Lett.* **96** (2010) 151902. https://doi.org/10.1063/1.3389497.

[55] N. Ben Sedrine et al., Photoluminescence studies of a perceived white light emission from a monolithic InGaN/GaN quantum well structure, *Sci. Rep.* **5** (2015) 3–9. https://doi.org/10.1038/srep13739.

[56] E. Sakalauskas et al., Dielectric function and bowing parameters of InGaN alloys, *Phys. Status Solidi Basic Res.* **249** (2012) 485–488. https://doi.org/10.1002/pssb.201100334.

[57] O. Ambacher et al., Pyroelectric properties of Al(In)GaN/GaN hetero- and quantum well structures, *J. Phys. Condens. Matter.* **14** (2002) 3399–3434. https://doi.org/10.1088/0953-8984/14/13/302.

[58] D. Carvalho et al., Quantitative Chemical Mapping of InGaN Quantum Wells from Calibrated High-Angle Annular Dark Field Micrographs, *Microsc. Microanal.* **21** (2015) 994–1005. https://doi.org/10.1017/S143192761501301X.

[59] W. Shockley et al., Statistics of the recombinations of holes and electrons, *Phys. Rev.* **87** (1952) 835–842. https://doi.org/10.1103/PhysRev.87.835.

[60] R.N. Hall, Electron-Hole Recombination in Germanium, *Phys. Rev.* **87** (1952) 387–387. https://doi.org/10.1103/PhysRev.87.387.

[61] T. Goudon et al., On the Shockley-read-hall model: Generation-recombination in semiconductors, *SIAM J. Appl. Math.* **67** (2007) 1183–1201. https://doi.org/10.1137/060650751.

Chapter 6

Conclusion

6.1. Main conclusions

This thesis was devoted to studying the optical and structural properties of III-Ns modified by ion irradiation techniques. In this context, two different strategies were investigated, with the final goal of evaluating their viability for obtaining more efficient green and red III-N LEDs, whose EQE is below that of blue LEDs. One of the strategies consisted of implanting AlGaN NWs with Eu to take advantage of their red intra-$4f^6$ luminescence at characteristic wavelengths for realizing red LEDs (**Chapters 3** and **4**). The second approach involved the irradiation of InGaN/GaN MQWs with ^{129}Xe SHIs, aiming to achieve QWI and produce more efficient green-light emitters (**Chapter 5**).

6.1.1. Eu-implantation of AlGaN NWs

In **Chapter 3**, the optical and structural properties of Eu-implanted AlGaN NWs ($0 \leq y \leq 1$), grown by PAMBE on GaN NWs templates on Si-substrates, were studied. These samples were also subjected to RTA treatments at 1000 °C and 1200 °C. The main objective of this research was to evaluate the role of y on the optical activation of Eu^{3+}, culminating in identifying the optimal y value for which the Eu^{3+}-related red luminescence is the most intense. The effects of the RTA temperature were also evaluated.

From such a study, it was possible to infer that Eu-implantation generated lattice defects and strain. It was proposed that the resulting lattice deformation follows a "pseudomorphic-like" model in which a biaxial stress component compensates for the hydrostatic pressure component, impeding the lattice to expand or contract in-plane ($\epsilon_{xx} = \epsilon_{yy} \approx 0$) and aggravating the changes in the c-lattice parameter of the NWs compared to the pure hydrostatic model.

Subsequent RTA treatments allowed a partial recovery of the implantation-induced damage and the initial strain state of the lattice. Furthermore, RTA treatments were necessary to attain the optical activation of Eu^{3+}. For all the NWs, the $^5D_0 \rightarrow {}^7F_2$ transition was the most intense luminescent contribution of Eu^{3+}, and it was excited with energy above and below the host's bandgap. Band-to-band excitation was identified as the channel that

gives rise to the most intense luminescence. For the below bandgap excitation, two broad bands were noticed: X1 at ~350 nm observed for all samples and X2 at ~270 nm observed only for $y \geq 0.75$. These bands experienced a blueshift of similar magnitude with increasing y; for example, X1 blueshifted ~200–300 meV from GaN to AlN NWs. X1 and X2 bands compare to the sub-gap excitation bands commonly observed in Eu-implanted AlGaN layers, indicating that the excitation of Eu^{3+} is similar in AlGaN NWs and AlGaN layers. It was proposed that these bands are related to defects that are involved in the non-radiative ET to the $4f^6$ core states of Eu^{3+}. In addition, for $y \geq 0.75$, low-intensity and sharp absorption peaks associated with direct excitation of $4f^6$ states were identified: the $^5D_2 \leftarrow ^7F_0$ transition at 471 nm and the $^5D_1 \leftarrow ^7F_0$ transition at 544 nm.

HR PL experiments conducted at 14 K allowed the identification of several narrow emission lines due to crystal field splitting and their attribution to various optically active Eu^{3+} centers in GaN and AlN NWs. For the ternary AlGaN NWs, the broadening of the Stark lines due to compositional fluctuations hindered the identification of multiple centers. For GaN NWs, excitation above the bandgap resulted in a spectrum dominated by lines associated with Eu1, the majority center commonly in GaN layers. Other emission lines with a much lower intensity could be noticed and were correlated with additional minority sites. Curiously, no lines associated with Eu2, the most efficient Eu^{3+} center in GaN layers, were identified in the spectrum of Eu-implanted GaN NWs, suggesting their formation is not favored in NW structures. For AlN NWs, two predominant optically active Eu^{3+} centers were found when exciting with below the AlN bandgap energy. These were designated Eu1 and Eu2 by spectral similarity with the predominant centers in GaN hosts. In AlN layers, no signal contribution from Eu2 is observed. These results suggest that the different lattice dynamics between III-Ns layers and NWs (i.e., defects' stability and strain relaxation) alter the Eu^{3+} center's formation probability for the same implantation and annealing conditions.

The RTA temperature was found to have a significant role in controlling the formation of a given center to the detriment of others. For example, in AlN NWs, the relative intensity of Eu2 decreased for the highest RTA temperature. For the ternary AlGaN NWs, the changes in the broader spectral shape with the RTA temperature seemed to indicate that more than one optically active Eu^{3+} exists, and their formation depends on the RTA temperature.

A comparison of the Eu^{3+}-related luminescence integrated intensity in the different AlGaN NWs (for the same RTA temperature) showed that Eu^{3+} incorporated into AlN NWs led to an increase in integrated intensity of about one order of magnitude regardless of whether the excitation is done with photons or electrons. Moreover, similar intensities were measured for the Eu^{3+}-related luminescence in AlN NWs and AlN layers, indicating no significant improvement in dopant incorporation or light extraction.

Besides controlling the formation of Eu^{3+} centers, the RTA temperature also affected the measured intensity of the Eu^{3+}-related luminescence. For each AlGaN NWs, the intensity was the highest for the RTA at 1200 °C. Furthermore, by increasing the RTA temperature from 1000 ℃ to 1200 ℃, the $I_{300\,K}/I_{14\,K}$ ratio increased from ~50 % (obtained for all y) to ~70–80 % (obtained for $y \geq 0.5$). Such improvements were tentatively attributed to a better recovery of the AlGaN crystalline lattice provided by the RTA at 1200 ℃, which was possible to identify in micro-Raman experiments. The RTA at 1200 ℃ simultaneously promoted a decrease in the density of non-radiative defects and a reorganization in the nearby environment of Eu^{3+} so that they become more efficient in generating the red light. Nevertheless, the RTA at 1200 ℃ severely degraded the GaN NWs templates due to GaN dissociation.

This presumably led to a diminished density of non-radiative defects, enhancing the luminescence. Alternatively, it can also be due to the lattice reorganization that promoted a change in the nearby environment of the Eu^{3+} so that they become more efficient in generating the red light.

Summarizing, from this study, one inferred that the y of the AlGaN hosts and the RTA temperature play a crucial role in the optical activation of Eu^{3+}. Furthermore, it was identified that Eu-implanted into AlN hosts annealed at 1200 °C led to the strongest luminescence of Eu^{3+}. This further suggests that these systems should be explored to realize more efficient red LEDs based on Eu-doped III-N. However, if no countermeasures are taken to avoid the degradation of the GaN NWs templates, the RTA temperature should be restricted to 1000 ℃.

Based on the previous conclusions, AlN p-n junction NWs (grown on n-doped GaN NWs templates on n-doped Si substrates by PAMBE) were implanted with Eu, aiming to achieve proof-of-concept red LEDs. Since the RTA temperature could not be increased above 1000 ℃ to avoid degradation of the GaN NWs templates, the implantation was carried out in a channeled geometry to minimize implantation-induced damage. In addition, two implantation fluences (1×10^{14} cm^{-2} and 5×10^{14} cm^{-2}) were used to study the impact of fluence on the structural and optical properties of the system. These results were discussed in **Chapter 4**.

The optical and structural properties of these structures were not so different from the previously studied set of samples. In this case, it was found that the damage level and the resulting strain in the AlN lattice were lower due to the channeled implantation geometry; the damage scaled up with increasing implantation fluence. Subsequent RTA led to the partial recovery of the lattice affected by implantation and to the optical activation of Eu^{3+} in AlN, dominated by the $^5D_0 \rightarrow {}^7F_2$ transition at ~624 nm (AlN). The excitation mechanisms of Eu^{3+} were identical to those mentioned above, with below bandgap excitation proceeding

through X1 and X2 bands or direct excitation of the ions. However, due to channeling effects, it was possible to identify that a portion of Eu^{3+} was also implanted and optically active in the GaN NWs templates, indicating that the implantation profile was not optimized in the AlN p-n region of the NWs.

The integrated PL and CL intensity of the Eu^{3+}-related luminescence increased by about two to three for the sample implanted with the highest fluence due to the more significant concentration of Eu^{3+} introduced in the lattice. At the same time, the relative contribution from other radiative defects decreases with increasing fluence, resulting in a purer red color. However, the emission intensity was lower than expected if assumed a direct proportionality between concentration and luminescence intensity. Two hypotheses were proposed to explain this: *i)* an increased density of competing non-radiative defects due to the higher damage levels or *ii)* the incorporation of Eu^{3+} in different lattice environments with lower optical activation efficiency.

After the deposition of ITO electrical contacts on the top of the AlN p-n junction NWs, red LEDs could be realized for the sample implanted with the highest fluence. The I-V characteristics of the LEDs revealed a diode-like rectifying behavior. Despite that, large ideality factors were obtained, implying that the realized devices largely deviate from the ideal behavior of the p-n junction. These deviations were attributed to a high resistivity of the n- and p-type doped AlN sections or high interface resistances. A non-optimized p-contact can also contribute to that. The comparison of I-V characteristics of the AlN p-n junctions before and after Eu-implantation revealed a significantly lower current flowing through the structure at the same applied voltage. Such an increase in resistivity after implantation was attributed to the defects induced by implantation, which RTA at 1000 ℃ did not remove.

For such LEDs, it was possible to detect a red EL signal dominated by the $^5D_0 \rightarrow {}^7F_2$ transition (as in PL and CL experiments), even if only for applied voltages above ~12 V. This was also attributed to the high resistive paths due to implantation-induced defects and high ionization energies of donors and acceptors, as well as non-optimized p-contacts. The red EL signal was intensified with increasing the applied voltage, while the emission's spectral shape remained the same, demonstrating the color stability of the device. This, alongside the temperature stability of the emission's peak wavelength, highlights the potential of this proof-of-concept in developing stable LEDs.

Although far from optimization, successful red LEDs based on Eu-implanted III-Ns were realized. This highlights the potential of this approach for obtaining red micro- and nano-emitters.

6.1.2. ^{129}Xe SHI irradiation of InGaN/GaN MQWs

In **Chapter 5**, the effects of ^{129}Xe SHI irradiation with energies between 38 and 82 MeV on the optical and structural properties of InGaN/GaN MQWs were investigated using optical spectroscopic techniques.

The irradiation of the samples introduced structural damage. Through micro-Raman spectroscopy, it was possible to define an in-depth profile of the damage. By combining different excitation wavelengths under resonant and non-resonant conditions, it was found that the sample's surface is the most affected region. This region was found to have a higher concentration of defects, which affect not only the crystalline structure but also the luminescent characteristics of the InGaN/GaN MQWs. Independent RBS/C measurements and Monte Carlo simulations led to similar results.

It was noticed that the damage introduced only slightly increases with increasing the ^{129}Xe SHI beam energy in the studied range. Nevertheless, the irradiation energy changed the excitation resonance profile in InGaN, as identified in micro-Raman experiments by the increase in the relative intensity of A_1(LO) (InGaN) for the irradiation energies of 74 and 82 MeV, corresponding to S_e equal to or above 20.3 keV $\cdot$ nm^{-1}. This was tentatively attributed to QWI at the interfaces of the MQWs due to diffusion of Ga and In atoms during the molten state reached a few picoseconds after the SHIs passage.

PL/PLE experiments allowed distinguishing two contributions for the green luminescence observed in the *MQW-asgr* sample. Those contributions were related to *i)* the InGaN emission and *ii)* the GL/YL related to deep-level defects in GaN. After SHI irradiation, an electronic state in the GaN mid-gap (responsible for irr-AB centered at ~2.75 eV), able to absorb light in the same energy region of the InGaN absorption tail, was found to participate in the excitation of GaN-related defect GL/YL. It was impossible to discern the occurrence of QWI from PLE experiments due to the spectral overlap of irr-AB and InGaN absorption edge. Furthermore, the InGaN emission was strongly quenched.

Considering the results, it is possible to infer that using SHI to obtain QWI in InGaN/GaN MQWs is seriously compromised from a technological point of view. This happens because the irradiation introduces superficial defects detrimental to the emission of the MQWs.

6.2. Future work

To deepen the understanding and overcome some of the problems identified concerning the approaches studied in this thesis, one proposes some research ideas for future work.

6.2.1. Eu-implantation of AlGaN NWs

An important research to be conducted in this field involves the identification of which Eu^{3+} centers are most efficient in AlN hosts. Similarly to what was done in the past for Eu^{3+} in GaN hosts, where Eu2 was identified as the most efficient center, this can be done by combined excitation-emission spectroscopy. After that, optimization and control of the implantation and annealing conditions that favor the most efficient Eu^{3+} centers are required.

Another issue to be solved is to avoid GaN dissociation at high annealing temperatures, given that these are required for a better recovery of the implantation-induced damage and an improved optical activation of Eu^{3+}. Various solutions are proposed to mitigate this problem:

- Getting rid of GaN NWs templates is the "easiest" solution; however, due to the high growth temperatures required to nucleate AlN NWs directly on Si substrates, the growth was impossible in the PAMBE chamber used.
- Changes in the growth of AlN/GaN NW structures for the AlN shell that covers part of the GaN NWs templates to be more effective in protecting them from dissociation. This can be done by controlling the morphological characteristics of the NWs during growth, like diameter, height, and density.
- Passivate the NWs before or after implantation (e.g., with Al_2O_3) so the passivation layer would protect the NWs during annealing. Furthermore, if passivation is done before implantation, it can also reduce the sputtering of surface atoms during implantation, contributing to a reduced density of surface defects, which generally introduce non-radiative paths. However, this approach requires removing the top passivated layer before contact deposition.
- The realization of ultra-high-pressure annealing treatments (in N_2 ambient) is another possibility since, in these conditions, GaN can sustain higher annealing temperatures without dissociating.

Although proof-of-concept red LEDs based on Eu-implanted AlN NWs have been demonstrated, their optimization requires going further in fundamental research regarding the electro-optical properties of these systems. These should involve new approaches to improve p- and n-type conductivity in AlN; in this regard, the research can benefit from the studies carried out parallelly in AlN NWs intending to develop more efficient far UV LEDs. Elucidating the impact the p-contact can have on the electrical properties of the LEDs and clarifying the mechanisms responsible for the excitation of the Eu^{3+} is crucial. At the same time, it is essential to minimize the defects generated by implantation, which can be done

by optimizing the implantation and annealing conditions. In this context, the dissociation of GaN NWs templates mentioned above must be considered. Understanding all these aspects is crucial for improving the performance of such LEDs, which, due to the high voltage necessary to trigger the EL signal and the low current flowing through the NW heterostructures, are far from being competitive with the existing red LEDs based on III-Ns.

Even though AlN hosts have promoted a more intense and efficient optical activation of Eu^{3+} compared to GaN hosts, it is not clear yet that this benefit translates into an improvement of the electro-optical properties of the realized LEDs. Therefore, it would be interesting to test the realization of red Eu-implanted GaN p-n junction LEDs and compare their behavior with AlN-based ones.

From a technological application point of view, evaluating how the performance of Eu-implanted III-Ns LEDs compares with the doping in situ ones, whether they are layered or nanowire structures, is important. Further comparisons with conventional red InGaN-based LEDs are also needed.

Another attractive opportunity to explore this field is the implantation of III-N NWs with other Ln species to realize LEDs of different colors (e.g., with Tm^{3+} for blue or Tb^{3+} for green). The use of lithographically defined masks in the implantation process would enable easier lateral integration of multi-color NW LEDs on the same wafer to realize, for example, RGB displays at the micro- or nano-scale. In particular, this could be done directly on Si substrates, providing a cost-effective and scalable platform for device integration with current micro-electronics.

6.2.2. ^{129}Xe SHI irradiation of InGaN/GaN MQWs

Regarding the irradiation of InGaN/GaN MQWs with SHIs, one of the possibilities for removing the detrimental defects to the luminescence of the MQWs is to carry out subsequent thermal treatments. Initial tests have already been made, with the realization of RTA treatments at 800 ℃ not showing significant improvements to the luminescence. Despite this, it may be worth conducting additional tests at higher annealing temperatures and for longer times.

From a different perspective, one can also consider using a sacrificial capping layer. As the surface region is the most affected by SHI irradiation with clusters of point defects, voids, and nano hills, using a sacrificial layer to accumulate such defects would leave the active region of the LED free from them. This layer would need to be removed after SHI irradiation.

6.3. Final remarks

The potential of Eu-implantation of AlN NWs for developing red LEDs was demonstrated, with the first Ln-implanted III-N NW LED being realized. Side-by-side with in situ doping, incorporating Eu^{3+} into III-N NWs by ion implantation to obtain more efficient red LEDs has room for progression. This approach can further benefit from advances made in the field of AlGaN and AlN NWs for far UV LEDs, as well as the use of III-N NWs for the realization of micro-LEDs.

On the other hand, even if it allows obtaining QWI, irradiation of InGaN/GaN MQWs with SHIs seems not a viable solution from a technological point of view. As the primary purpose is to achieve more efficient LEDs, the quenching of the luminescence from the active region due to detrimental defects generated by irradiation conditions their use.

List of scientific outputs

During the development of this thesis, the research results were presented at several national and international conferences as oral and poster presentations, as well as published in peer-reviewed international journals. Below, a bibliographic compilation of these outputs is presented.

Publications as the first author relevant to this thesis

J. P. S. Cardoso, G. Jacopin, D. Nd. Faye, A. M. Siladie, B. Daudin, E. Alves, K. Lorenz, T. Monteiro, M. R. P. Correia, and N. Ben Sedrine, "Eu^{3+} optical activation engineering in $Al_xGa_{1-x}N$ nanowires for red solid-state nano-emitters," *Applied Materials Today* **22** (2021) 100893. https://doi.org/10.1016/j.apmt.2020.100893

These results were discussed in **Chapter 3**.

J. P. S. Cardoso, N. Ben Sedrine, P. Jóźwik, M. C. Sequeira, C. M. Wetzel, C. Grygiel, K. Lorenz, T. Monteiro, and M. R. Correia, "Exploring swift-heavy ion irradiation of InGaN/GaN multiple quantum wells for green-emitters: the use of Raman and photoluminescence to assess the irradiation effects on the optical and structural properties," *Journal of Materials Chemistry C* **9** (2021) 8809. https://doi.org/10.1039/D1TC01603B

These results were discussed in **Chapter 4**.

J. P. S. Cardoso, M. R. P. Correia, R. Vermeersch, D. Verheij, G. Jacopin, J. Pernot, T. Monteiro, S. Cardoso, K. Lorenz, B. Daudin, and N. Ben Sedrine, "Europium-implanted AlN nanowires for red light-emitting diodes," *ACS Applied Nano Materials* **5** (2022) 972. https://doi.org/10.1021/acsanm.1c03654

These results were discussed in **Chapter 5**.

Other publications as first author

J. P. S. Cardoso, G. Jacopin, D. Nd. Faye, A. M. Siladie, B. Daudin, E. Alves, K. Lorenz, T. Monteiro, M. R. P. Correia, and N. Ben Sedrine, "Eu^{3+} optical activation engineering in $Al_xGa_{1-x}N$ nanowires for red solid-state nano-emitters," *Applied Materials Today* **22** (2021) 100893. https://doi.org/10.1016/j.apmt.2020.100893

Most of the research was conducted within the scope of the master's thesis.

Other publications

O. Kalu, C. Rodríguez-Fernández, **J. P. S. Cardoso**, M. R. P. Correia, A. Cantarero, G. Rojas, J. A. D. Moller, and A. Reyes-Rojas, "Near band edge and defect emissions in wurtzite $Cd_{0.025}Mg_{0.10}Zn_{0.875}O$ nanocrystals," *Optical Materials* **118** (2021) 111227. https://doi.org/10.1016/j.optmat.2021.111227

The contribution to this work involved the realization of PL experiments and respective data analysis.

P. Jóźwik, **J. P. S. Cardoso**, D. F. Carvalho, M. R. P. Correia, M. C. Sequeira, S. Magalhães, D. Nd. Faye, C. Grygiel, I. Monnet, A. S. Bross, C. Wetzel, E. Alves, and K. Lorenz, "Damage in InGaN/GaN bilayers upon Xe and Pb swift heavy ion irradiation," *Physical Chemistry Chemical Physics* **24** (2022) 25773-25787. https://doi.org/10.1039/D2CP02526D

The contribution to this work involved the realization of micro-Raman experiments, respective data analysis, and writing part of the manuscript.

Oral communications as presenting author

"Europium-implanted AlN nanowires: a route for red nano-emitters," oral presentation at the VIII Annual Meeting i3N (2023) Leiria, Portugal.

"Europium-Implanted AlN p-n Junction Nanowires – Towards the Realization of Red Light-Emitting Devices," poster presentation at the International Workshop on Nitride Semiconductors (2022) Berlin, Germany.

"Demonstration of Red-Light Emitting Devices Based on Europium-Implanted AlN p-n Junction Nanowires," oral presentation at the 22nd International Conference on Ion Beam Modification of Materials (2022) Lisbon, Portugal.

"Optical properties InGaN/GaN multiple quantum wells irradiated with swift-heavy ions," oral presentation at the 17th International Conference in Advanced Materials (2021) Aveiro, Portugal.

"The effects of swift-heavy ions on the luminescence of group III-nitride structures," online oral presentation at the E-MRS Spring Meeting (2021).

"Generating new excitation pathways for the green emission of InGaN/GaN MQWs by Xe swift-heavy ion irradiation," online poster presentation at the 9th European Nanoanalysis Symposium (2020).

"Spectroscopic study of Xe swift-heavy ion radiation effect on III-nitride nanostructures," poster presentation at the Summer School on Wide-Bandgap nitride devices (2019) Ghent, Belgium.

"*Exploring the optical activation of Eu ions in $Al_xGa_{1-x}N$ nanowire structures for red solid-state nano-emitters,"* poster presentation at the conference Materiais (2019) Lisbon, Portugal.

"Spectroscopic study of Xe swift-heavy ion radiation effect on III-nitride nanostructures," poster presentation at the conference Materiais (2019) Lisbon, Portugal.

Other oral communications

"Optical activation of different rare-earth ions implanted into AlN nanowires," poster presentation by M. R. P. Correia at the E-MRS Spring Meeting (2023) Strasbourg, France.

"Ion Implantation and Defect Engineering in Wide Bandgap Semiconductor Nanostructures," invited talk by K. Lorenz at the E-MRS Fall Meeting (2022) Warsaw, Poland.

"Molecular Beam Epitaxy Grown GaN-Nanowires-Based p-i-n Structures on a Diamond Substrate Via Pre-Orienting Layer," oral presentation by T. K. Ng at the conference WOCSDICE/EXMATEC (2022) Azores, Portugal.

"Eu-doped AlGaN for solid-state red emitters," online invited talk by N. Ben Sedrine at the conference EXMATEC (2022).

"Probing the optical properties of III-V nanowires for optoelectronic applications," poster presentation by N. Ben Sedrine at the Nanowire Week (2022) Pisa, Italy.

"Tuning MBE-grown $Al_xGa_{1-x}N$ nanowires on Si for red solid-state nano-emitters," oral presentation by N. Ben Sedrine at the E-MRS Spring Meeting (2019) Nice, France.

"Effect of Xe swift heavy ion radiation on the optical properties of III-nitride nanostructures," poster presentation by M. R. P. Correia at the E-MRS Spring Meeting (2019) Nice, France.

"Emission properties of wide bandgap nanostructures," invited talk by T. Monteiro at the conference Materiais (2019) Lisbon, Portugal.

"Optical properties of III-V nanostructures for optoelectronic applications," oral presentation by N. Ben Sedrine at the Nanophotonics and Micro/Nano Optics International Conference (2018) Rome, Italy.

"Spectroscopic studies of III-V nanostructures for optoelectronic applications," oral presentation by N. Ben Sedrine at the International Conference on Advanced Laser Technologies (2018) Tarragona, Spain.

"III-V nanostructures for optoelectronic applications: a spectroscopic study," poster presentation by N. Ben Sedrine at the Nanoanalysis Symposium (2018) Dresden, Germany.